Structure, Reactivity and *In Crystallo* Chemistry of Group IX and XI Organometallic Systems

Chloe-Louise Johnson

Doctor of Philosophy

University of York

Department of Chemistry

January 2025

Abstract

This thesis describes the application of solid-state techniques to the pursuit of catalytically relevant organometallic systems and provides a comparison between the solution and solid-state behaviour of such complexes. *Chapter 1* provides a summary of existing research on the solid-state chemistry of organometallic complexes, with particular focus on single-crystal to single-crystal (SC-SC) transformations. Brief introductions to the fundamentals of gold(I) *π*-alkyne catalysis and group IX pincer complexes are also discussed.

Chapter 2 describes the synthesis of a silver(I) [Ag(NBE)(η^2:η^2-BAr^F_4)] zwitterion and proposes an equilibrium between a dichloromethane solvent complex and a Ag···H–C agostic complex in the solution-state, in contrast to its solid-state behaviour. Investigation into the zwitterion as a source of Ag[BAr^F_4] is also demonstrated by exemplar ligand substitution, single electron redox, and salt metathesis reactions.

Chapter 3 presents the first examples of sequential solid/gas reactivity of a gold(I) *π*-ethylene complex, enabling the isolation of a variety of new complexes featuring alkene, carbonyl and amine ligands, [(**L1**)Au(L)][BAr^F_4] (**L1** = tris-2-(4,4'-di-tert-butylbiphenyl)phosphine; L = C_2H_4, CO, NH_3, NMe_3, NMe_2H, isobutylene, C_2H_4). The H/D exchange of a gold(I) ammonia complex is also reported and solid-state techniques are employed to prevent the solvent induced reactivity observed in the solution. Additionally, *in crystallo* methodologies and use of a bulky phosphine ligand support the isolation of the first reported gold(I) *π*-acetylene complex, the isolation of which has thus far been hindered by deleterious solution-state pathways.

Chapter 4 builds upon the work presented by Weller on the application of SC-SC techniques to Brookhart's [(^{tBu}PONOP)Ir(Me)(H)][BAr^F_4] system, by comparing it to the solution and solid-state chemistry of a similar ligand featuring adamantyl substituents, ^{Ad}PONOP. In the solid-state, SC-SC loss of methane *in vacuo* is not observed whilst the complex readily liberates methane in solution and SC-SC reaction with H_2, highlighting the difference in solution and solid-state behaviour.

Declaration

The work presented in this thesis was carried out by the thesis author under the supervision of Professor Andrew S. Weller and Professor Simon B. Duckett at the University of York, unless otherwise stated. I declare that this is original work, unless otherwise stated, and has not been submitted previously for any qualification at this, or any other, institution.

Chloe-Louise Johnson

University of York, January 2025

Acknowledgements

The first thanks must go to my supervisors *Professor Andrew Weller* and *Professor Simon Duckett*: Thank you for the wonderful opportunity that this PhD turned out to be. I have learnt so much from you both, and appreciate how supportive and motivating you have been. I will always value my time in the Weller and Duckett groups. *Andy:* You put so much time and energy into the group not only with science but also with all of the pub trips, curries and group adventures, especially when walking the streets of Edinburgh at midnight in an unrelenting search to find my first deep fried mars bar. Thank you for that. *Simon:* Thank you for always making time to help set up an experiment or answer any questions. I'm still amazed at the NMR powerhouse you have built in CHyM, and I thank you for letting me be a part of it.

I must especially thank some of the brilliant postdocs who have helped me during my PhD; *CDMG*, *Laurence* and *Kris* for their expertise and advice over the years. *Matt:* Thank you for welcoming me to the ways of the Weller group back in '21 and your patience ever since. You were simultaneously the best audience and harshest critic for my bad jokes. Old Country has regained an excellent chemist. *Laurence*: From you I inherited my beloved Schlenk line and the ability to eat ripe bananas (maybe not as ripe as you, but I would use the term expired to describe those). Thank you for your calming presence and subtle humour when I joined the group. *Kris*: You have made a wonderful fumehood neighbour, thank you for always bouncing ideas around with me. I'm so glad we have ten more months of annoying Chloe VB with our air guitar performances and singing in the lab.

To my other fellow Wellers: thank you for the intellectual, mental and emotional support, it's been a pleasure to work alongside you all, but there are a few I must especially mention. *Mat*: From day one of our PhDs we have gone through this rollercoaster together and I'm so glad of it. Despite being the polar opposites of one another we became close friends and you've kept me sane when the results were driving me otherwise. I've never met anyone with a determination like yours and it leaves me with no doubt that you're going to have a brilliant career. *Joe*: I must thank you also, "*why?"*,† because between your sense of humour and your

rather interesting playlists there was never a dull moment in the lab. I remain in awe of your ability to talk science and I know yours will also be a career to keep an eye on. *Helena*: I don't know whose idea it was to put my desk next to yours in the office but I'm sure they weren't aware of the chaos that would unfold. I miss shrieking with laughter as we played with toy cars on the office floor or flamenco danced around the lab. Please visit for the next WWR. *Chloe VB*: I didn't think I could blush at hearing the word Duck but somehow, you make it happen. Thank you for all of the gossip at the glovebox, and for being one of the most genuine people I have met. It's safe to say that the T-1000 is an upgrade. *Jack*: I'm very glad my supervision didn't scare you off during your MChem and you decided to stick around for a PhD. Your framed autograph of Dwayne 'the Rock' Johnson secret santa present still resides proudly above my desk. *Rebecca*: Trieste was one of my favourite trips of my PhD, and a big part of that was the many an Aperol Spritz and Limoncello we shared, thanks for being a great Airbnb-mate. I'm glad you've finally migrated into the Weller lobe. *Alex* and *Dom*: Although I haven't had a chance to work alongside you both, I'm glad that that will soon change. You both make excellent additions to the group and I'm looking forward to my time on Team AB.

And to the rest of this wonderful era of Wellers and Ducketts; *Callum, Vicky A, Vicky L, Dean, Sam, Spencer, Pav, Claire, Kieren, Ben T, Ben C, Matthew, Samira, Natalia*: I have loved these past few years and a good deal of that goes to all of you.

Much of this work would not have been possible without the efforts of my collaborators, and so to *Drs Jesús Campos* and *Miquel Navarro*: Thank you for the wonderful opportunity to collaborate, and for hosting me in beautiful Sevilla. To *Professor Stuart Macgregor*, *Dr Arif Sajjad*, *Daniel Storm*: Thank you for your computational work and for all of the Macgrellers. I'm sorry for all of the solvent in my structures. To all of the technical staff at York, especially *Dr Vicky A*, *Dr Adrian Whitwood, Heather Fish, Dr Matthew Davy*: Thank you for your valuable help and advice, and your hard work throughout the years.

To the wonderful friends I've made here in York, in chemistry and beyond: Thank you for all of the Brew York shenanigans, movie nights, and rotations around that Popworld dancefloor. But mostly thank you for reminding me that Shest Canem.

I wouldn't be who I am today without my family – *Ryan*, *Nan Edwards*, *Granddad*, *Nan Johnson, Kim*, *Luke*, *Jess, Teresa, Dave, Katie, Dan*. But a special thank you to *Mom* and *Dad*: I wouldn't be here without you (literally), thank you for always loving and encouraging me, you're my biggest supporters. *Luke*: You may not be here to see your favourite cousin finish her PhD, but I know you'd secretly be proud. I'll have a jägerbomb for you. And to my partner *Dean*: Thank you for supporting me to the end, into the very fires of this thesis. I promise I'll repay the favour when it's your turn. Whilst I am grateful for all of the opportunities this PhD has given me, most of all I'm grateful that it gave me the chance to meet you.

Abbreviations and Symbols

Å	ångströms (10^{-10} m)
Ad	adamantyl
adp	atomic displacement parameter
Ar^{Cl}	3,5-dichlorophenyl
Ar^{F}	3,5-bis(trifluoromethyl)phenyl
$Ar^{F'}$	3,5-difluorophenyl
Ar^{SF5}	3,5-bis(pentafluorosulfanyl)phenyl
ATR	Attenuated Total Reflectance
Bp	bis(pyrazoyl)borate
calc	calculated
Cy	cyclohexyl
COD	1,5-cycloctadiene
COE	cyclooctene
d_8	mixing time
dcpe	1,2-bis(di-cyclohexylphosphino)ethane
dcpm	1,2-bis(di-cyclohexylphosphino)methane
DEPT	Distortionless Enhancement by Polarisation Transfer
DFT	Density Functional Theory
dibpe	1,2-bis(di-*iso*-butylphosphino)ethane
dppe	1,2-bis-(diphenylphosphino)ethane
dtbpe	1,2-bis(di-*tert*-butylphosphino)ethane
ESI-MS	Electrospray Ionisation Mass Spectrometry
EXSY	Exchange Spectroscopy
fwhm	full width at half maximum
GC-MS	Gas Chromatography-Mass Spectrometry
ΔG	change in Gibbs energy
ΔH	change in enthalpy
HMBC	Heteronuclear Multiple Bond Correlation
HSQC	Heteronuclear Single Quantum Coherence
hr	hour(s)
Hz	Hertz (s^{-1})

IGMH	Independent Gradient Model with Hirshfeld partitioning
IR	Infrared Spectroscopy
^{i}Pr	*iso*-propyl
IPr	1,3-bis(2,6-diisoprop-ylphenyl)imidazol-2-ylidene
IPr*	N,N'-bis(2,6-bis(diphenylmethyl)-4-methoxy-phenyl)imidazole-2-ylidene
^{iPr}PONOP	(di-*iso*propylphosphino)-2,6-dioxypyridine
J	Joules
J	scalar coupling constant
kcal	kilocalorie (1 kcal = 4.184 kJ)
L1	tris-2-(4,4'-di-tert-butylbiphenyl)phosphine
L2	bis(di-adamantylphosphino)-2,6-dioxypyridine
m	multiplet
M	mol dm^{-3}
Me	methyl
Me_2bipy	4,4'-dimethylbipyridine
Mes	mesityl (3,5-trimethylphenyl)
MicroED	Microcrystal Electron Diffraction
min	minute(s)
mL	millilitre
MOF	Metal-organic framework
m/z	mass-to-charge ratio
NBA	norbornane (bicyclo[2.2.1]heptane)
NBD	2,5-norbornadiene (bicyclo[2.2.1]hept-2,5-diene)
NBE	norbornene (bicyclo[2.2.1]hept-2-ene)
NBO	Natural Bond Orbital
NCI	non-covalent interaction
NHC	*N*-heterocyclic carbene
NMR	Nuclear Magnetic Resonance
NOESY	Nuclear Overhauser Effect Spectroscopy
OTf	trifluoromethanesulfonate
Ph	phenyl
ppm	parts per million
Pz	pyrazolyl
QTAIM	Quantum Theory of Atoms In Molecules

SC-SC	Single-crystal to single-crystal
SCXRD	Single-crystal X-ray diffraction
ΔS	change in entropy
SIDipp	1,3-bis(2,6-diisopropylphenyl)imidazolin-2-ylidene
SMOC	Surface Modified Organometallic Chemistry
SMOM	Solid-state Molecular Organometallic Chemistry
SOF	Site Occupancy Factor
SSNMR	Solid-state Nuclear Magnetic Resonance
t	time
T	temperature
^{t}Bu	*tert*-butyl
^{tBu}PONOP	(di-*tert*-butylphosphino)-2,6-dioxypyridine
tetraglyme	tetraethylene glycol dimethyl ether
TMEDA	Tetramethylethylenediamine
TMP	tetramethylpyrazine
VT	Variable Temperature
WCA	Weakly Coordinating Anion
XRD	X-ray diffraction
ν	frequency

Key Compounds

Chapter 1

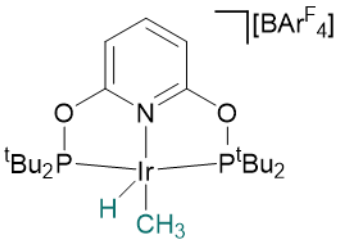

1.50

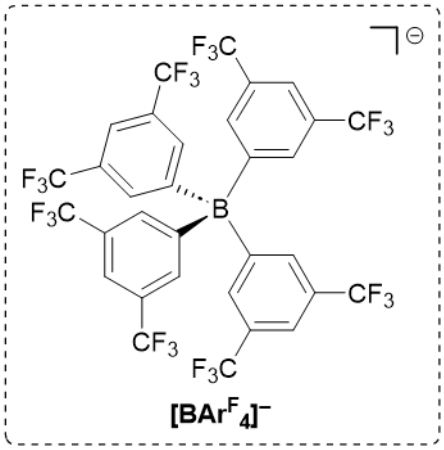

Chapter 2

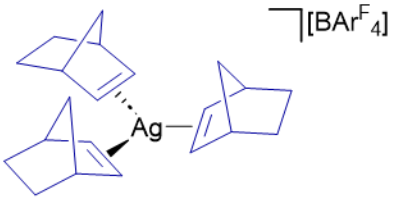

2.1

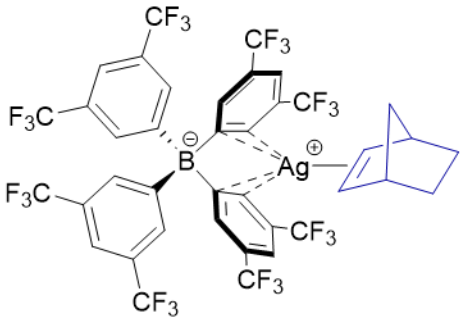

2.2

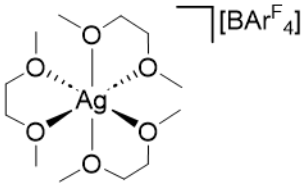

2.3

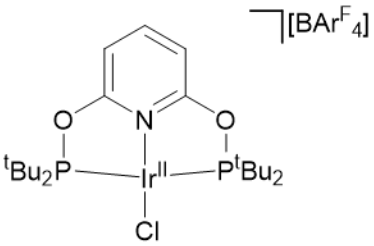

2.4

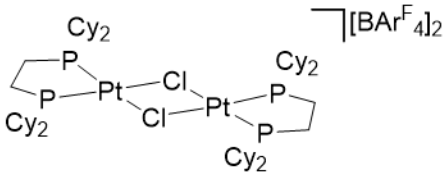

2.5

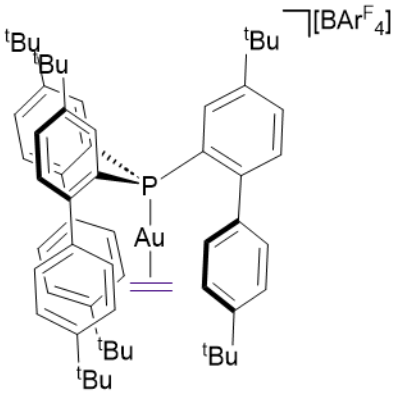

3.1

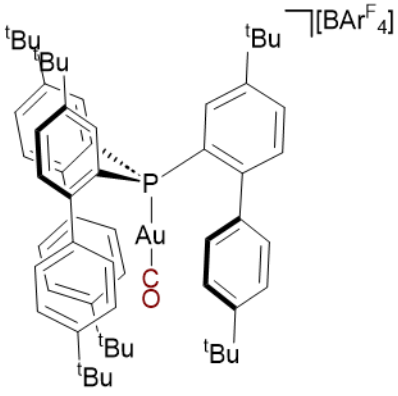

3.2

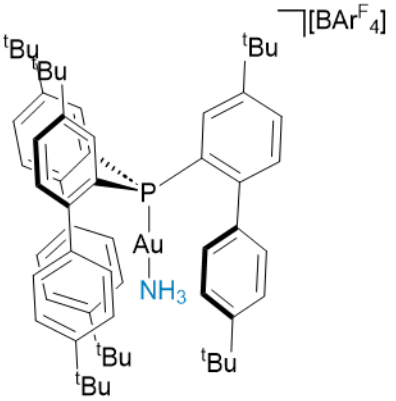

3.3

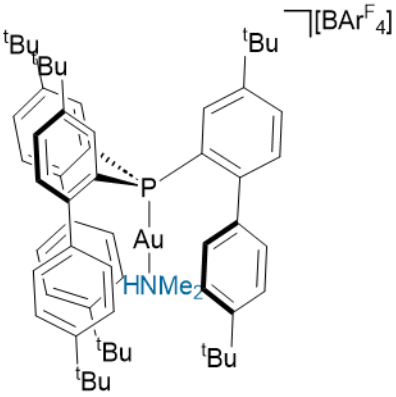

3.4

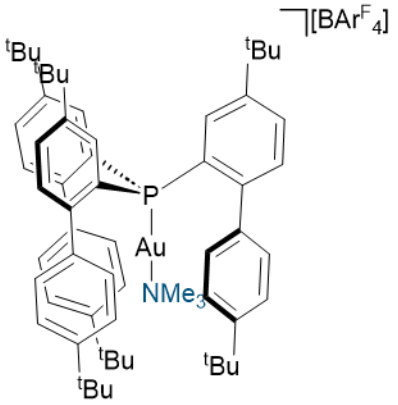

3.5

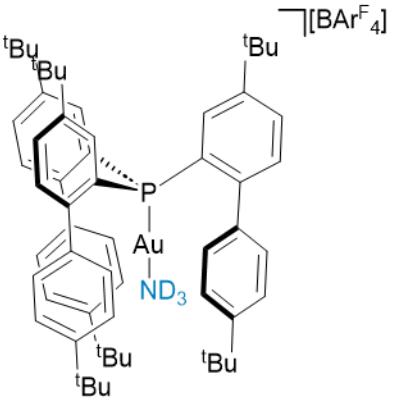

D_3-3.3

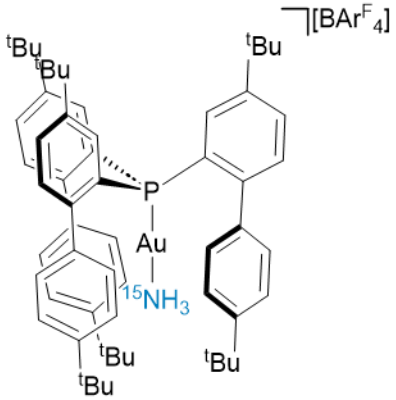

^{15}N-3.3

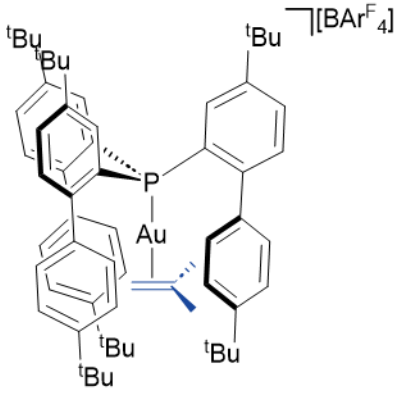

3.6

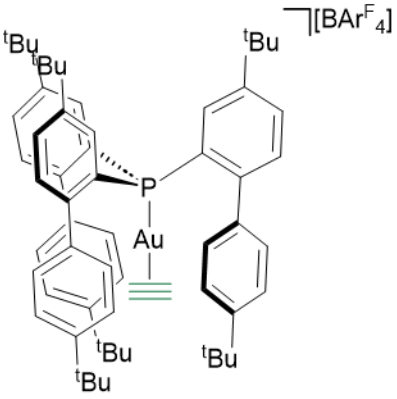

3.7

Chapter 4

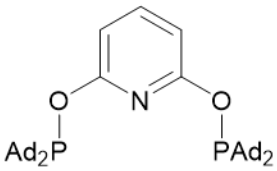

L2

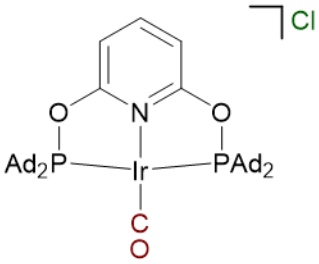

4.1

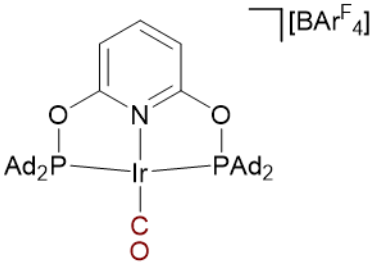

4.2

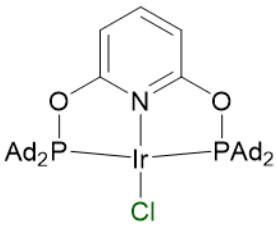

4.3

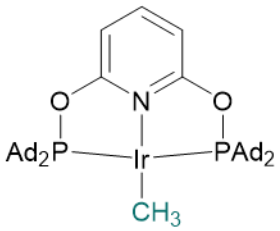

4.4

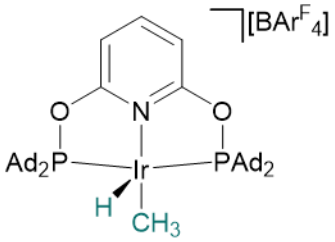

4.5

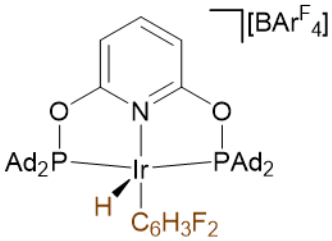

4.6

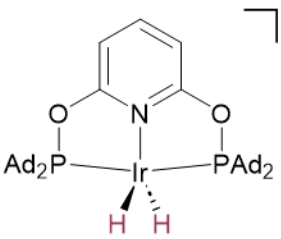

4.7

Table of Contents

Abstract ii

Declaration iii

Acknowledgements iv

Abbreviations and Symbols vii

Key Compounds x

1 Introduction 1

1.1 Solid-state Organometallic Chemistry 1

1.1.1 Solid-state Molecular Organometallic (SMOM) chemistry 6

1.1.2 The $[BAr^{F}_{4}]^{-}$ lattice: a stabilising crystalline framework 15

1.1.3 The solid-state chemistry of group XI 22

1.2 Solution-state catalytic alkyne transformations with gold(I) 27

1.3 Iridium pincer complexes for *in crystallo* chemistry 32

1.4 Conclusions and Thesis Aims 37

1.5 References 37

2 Synthesis and reactivity of a silver(I) [Ag(NBE)(η^2:η^2-BAr^{F}_{4})] zwitterion 42

2.1 Introduction 42

2.2 Synthesis, characterisation and reactivity of $[Ag(NBE)_3][BAr^{F}_{4}]$ (2.1) 47

2.3 The isolation of a coordinated $[BAr^{F}_{4}]^{-}$ adduct, [Ag(NBE)(η^2:η^2-BAr^{F}_{4})] (2.2) 54

2.4 [Ag(NBE)(η^2:η^2-BAr^{F}_{4})] (2.2) as a source of $Ag[BAr^{F}_{4}]$ 65

2.5 Summary and Conclusions 71

2.6 Experimental 71

2.6.1 $[Ag(NBE)_3][BAr^{F}_{4}]$ (2.1·DFB) 72

2.6.2 [Ag(NBE)(η^2:η^2-BAr^{F}_{4})] (2.2) 73

2.6.3 $[Ag(DME)_3][BAr^{F}_{4}]$ (2.3) 74

2.6.4 $[(^{tBu}PONOP)IrCl][BAr^{F}_{4}]$ (2.4) 75

2.6.5 $[(dcpe)PtCl]_2[BAr^{F}_{4}]_2$ (2.5) 75

2.7 References 76

3 Synthesis and SC-SC reactivity of a gold(I) *π*-ethylene system 79

3.1 Introduction 79

3.2 Synthesis and characterisation of [(**L1**)Au(η^2-C_2H_4)][BAr^{F}_{4}] (3.1) 83

3.2.1 Two crystalline polymorphs of complex 3.1 83

3.2.2 Variable temperature SCXRD of complex 3.1 87

3.2.3 Solution-state NMR spectra of complex 3.1 89
3.3 Exploring the SMOM reactivity of complex 3.1 92
3.3.1 The SC-SC synthesis of a gold(I) carbonyl complex, 3.2 93
3.3.2 Solid/gas reactivity with amines 98
3.3.3 H/D exchange with complex 3.3 110
3.3.4 SC-SC reactivity with isobutylene 120
3.4 Isolation of a gold(I) acetylene complex (3.7) *via in crystallo* techniques 125
3.4.1 Solid-state characterisation of complex 3.7 129
3.4.2 Solution-state characterisation of complex 3.7 131
3.4.3 Computational analysis of complex 3.7 136
3.5 Summary and Conclusions 140
3.6 Experimental 141
3.6.1 [(**L1**)Au(η^2-C_2H_4)][BAr^F_4] (3.1) 141
3.6.2 [(**L1**)Au(CO)][BAr^F_4] (3.2) 142
3.6.3 [(**L1**)Au(NH_3)][BAr^F_4] (3.3) 143
3.6.4 Independent synthesis of [(**L1**)Au(ND_3)][BAr^F_4] (D_3-3.3) 144
3.6.5 [(**L1**)Au($^{15}NH_3$)][BAr^F_4] (^{15}N-3.3) 145
3.6.6 [(**L1**)Au(NMe_2H)][BAr^F_4] (3.4) 146
3.6.7 [(**L1**)Au(NMe_3)][BAr^F_4] (3.5) 147
3.6.8 [(**L1**)Au(H_2CCMe_2][BAr^F_4] (3.6) 148
3.6.9 [(**L1**)Au(η^2-C_2H_2)][BAr^F_4] (3.7) 149
3.6.10 [(**L1**)Au(η^2-$^{13}C_2H_2$)][BAr^F_4] (^{13}C-3.7) 151
3.7 References 152
4 A new Ir(I)/Ir(III) adamantyl pincer system **155**
4.1 Introduction 155
4.2 Synthesis of the adamantyl pincer ligand, **L2** 161
4.3 Synthesis of an iridium(III) methyl hydride complex, 4.5 163
4.4 Characterisation of complex 4.5 176
4.5 C–H activation of 1,2-difluorobenzene with complex 4.5 190
4.6 *In crystallo* chemistry of complex 4.5 197
4.7 Summary and Conclusions 209
4.8 Experimental 210
4.8.1 (di-adamantylphosphino)-2,6-dioxypyridine (**L2**) 210
4.8.2 [(**L2**)Ir(CO)]Cl (4.1) 211

4.8.3 [(**L2**)Ir(CO)][BAr^F_4] (4.2) 212
4.8.4 [(**L2**)IrCl] (4.3) 213
4.8.5 [(**L2**)Ir(Me)] (4.4) 214
4.8.6 [(**L2**)Ir(Me)(H)][BAr^F_4] (4.5) 215
4.8.7 [(**L2**)Ir(Ar)(H)][BAr^F_4] (4.6) 217
4.8.8 [(**L2**)$Ir(H)_2$][BAr^F_4] (4.7) 218
4.8.9 EXSY Data for complex 4.5 219
4.8.10 C–H activation of 1,2-difluorobenzene by complexes 4.5 and 1.50 220
4.9 References 221
5 Overview **223**
6 Future Work **224**
7 Appendix **225**
6.1 General Considerations 225
6.2 Single-Crystal X-ray Diffraction 226
6.2.1 Crystallographic Data Tables 226
6.3 Computational Methods 238
6.4 References 238

Chapter 1: Introduction

1.1 Solid-state Organometallic Chemistry

Organometallic catalysis often relies on the generation of highly reactive, low-coordinate organometallic complexes which can activate substrates.[1, 2] The majority of industrial processes featuring organometallic catalysts focus on the homogeneous phase, and benefit from the fact that their activity can be optimised by ligand design as their active sites are often more easily studied than bulk heterogeneous catalysts. However, solution-state reactivity presents challenges such as catalyst dimerization, which can lead to deactivation, solvent-induced side reactions, which lead to by-products, and separation challenges, which result in poor product recovery.[3] A solid state approach to organometallic transformations tackles these challenges by removing the solvent,[4] enabling the investigation of chemically interesting reactivity without these deleterious effects.

An example of solid state chemistry overcoming the challenges incurred by reactivity in the solution-state is provided by the iridium (complex **1.1**) catalysed hydrogenation of CO_2 to methanol,[5] which is an industrially relevant, high in demand chemical currently largely produced from syngas.[6] In this example, although mononuclear, dinuclear and trinuclear iridium catalysts were investigated, the dinuclear complex resulted in the highest conversion to methanol and was thus selected as the focus of this work. In the solution-state (water solvent), catalysis yields formic acid as the major product due to ligand exchange of the formate intermediate with the water solvent (Scheme 1.1 B). This hinders further reactivity of the formate intermediate with H_2, and the liberated formic acid is also in equilibrium with H_2 and CO_2, limiting methanol production under solution conditions. In contrast, in the solid state ligand exchange with water is prevented and the formate intermediate can react further with H_2 to form methanol in a solid/gas reaction with complex **1.1** as an amorphous solid. Methanol is the major product of the solid/gas reaction, with only a negligible amount of formic acid observed in the residual solid catalyst (Scheme 1.1 A). Another advantage of this process is

that gas phase methanol can easily be separated from the catalyst and is not contaminated by the less volatile formic acid, nor CO or CH_4 after condensation, and the iridium catalyst can be recycled by the addition of more CO_2 and H_2.

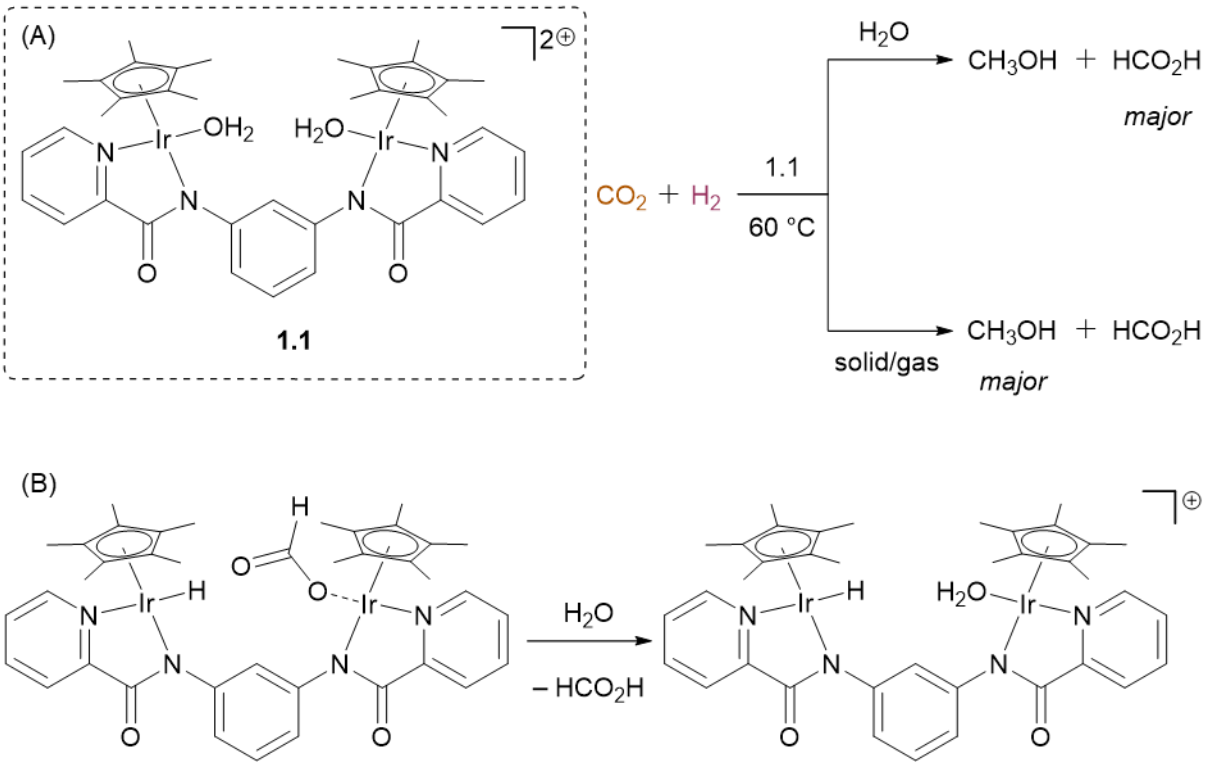

Scheme 1.1 (A) The difference in methanol production *via* the hydrogenation of CO_2 in solution and the solid state. (B) Solution-state ligand exchange of the proposed formate intermediate with water (solvent), which is prevented in the solid state.

There are several techniques for enabling reactive metal-ligand complexes to achieve organometallic transformations in the solid state, such as surface modified organometallic chemistry (SMOC),[7] metal-organic frameworks (MOF),[8, 9] mechanochemistry,[10] and *in crystallo* chemistry.[11] For the purpose of this thesis, detailed discussion shall be limited to the last, as *in crystallo* chemistry shall be a continuous theme throughout this work.

Throughout this thesis, the term *in crystallo* chemistry refers to chemical transformations within crystalline materials which usually, but not always, retain bulk crystallinity over the course of the reaction. Those which do retain single-crystallinity are described as single-crystal to single-crystal (SC-SC) or topochemical reactions. Topochemical reactions are directed by the crystalline lattice and retain a defined lattice during the reaction, whilst SC-SC reactions may

involve the addition of external reagents and the lattice may change during the reaction. Some SC-SC reactions are investigated entirely within one single-crystal, but those which occur within the bulk of organometallic single-crystals have been described as Solid-state Molecular Organometallic (SMOM) chemistry by Weller.[12, 13] Solid/gas reactions involve the bulk reactivity of gaseous substrates with solid inorganic material. A solid/gas reaction may occur within a crystalline material (*in crystallo*) or may involve reactivity of amorphous or powdered solids.

One of the earliest examples of *in crystallo* organometallic transformations dates back to 1991, when Bianchini and coworkers investigated the substitution of an N_2 ligand in the single-crystalline cobalt tetraphosphine complex, $[(PP_3)Co(N_2)][BPh_4]$ (**1.2**) [PP_3 = tris((diphenylphosphino)ethyl)phosphine], for gaseous ligands such as C_2H_2, C_2H_4, H_2CO and CO in both solution and the solid state to make the complexes **1.3-1.5** (Scheme 1.2).[14] This is a solid/gas reaction but not SC-SC, as crystallinity is lost upon formation of complexes **1.3-1.5**. In the case of C_2H_2, C−H bond activation resulted in the formation of an $[(PP_3)Co(H)(C{\equiv}CH)][BPh_4]$ (**1.4**) intermediate capable of undergoing a 1,3-hydride shift at 65 °C to form the vinylidene complex $[(PP_3)Co(C{=}CH_2)][BPh_4]$ (**1.5**). Bianchini also noted that the yields of the solid/gas reactions were reduced, or even non-existent in the case of C_2H_4 and MeCHO, upon changing the $[BPh_4]^-$ anion for the smaller anions $[BF_4]^-$, $[PF_6]^-$ or $[OTf]^-$ (OTf = trifluoromethanesulfonate). This alludes to the impact of the counterion on reactivity in the solid state, as will be discussed in section 1.1.2.

Bianchini subsequently compared the solution and solid state reactivity of the microcrystalline complex $[(triphos)Ir(H)_2(\eta^2\text{-}C_2H_4)][BPh_4]$ [triphos = 1,1,1-tris(diphenylphosphinomethyl)ethane] with H_2 to form amorphous $[(triphos)Ir(H)_2(\sigma\text{-}H_2)][BPh_4]$ *via* solid/gas reactivity.[15] Whilst this compound is not stable in solution, readily yielding $[(triphos)Ir(H)_3]$, benzene and triphenylborane in THF, it is indefinitely stable in the solid state under an inert atmosphere, and can even survive a short time in air. This reactive ethylene dihydride system also undergoes solid/gas oligomerisation of acetylene to yield a mixture of

benzene, cyclohexa-1,3-diene, butadiene and allyl hydride complexes.[16] This process also works in solution, however only the benzene and butadiene complexes are observed, likely due to loss of ethylene from the coordination sphere.

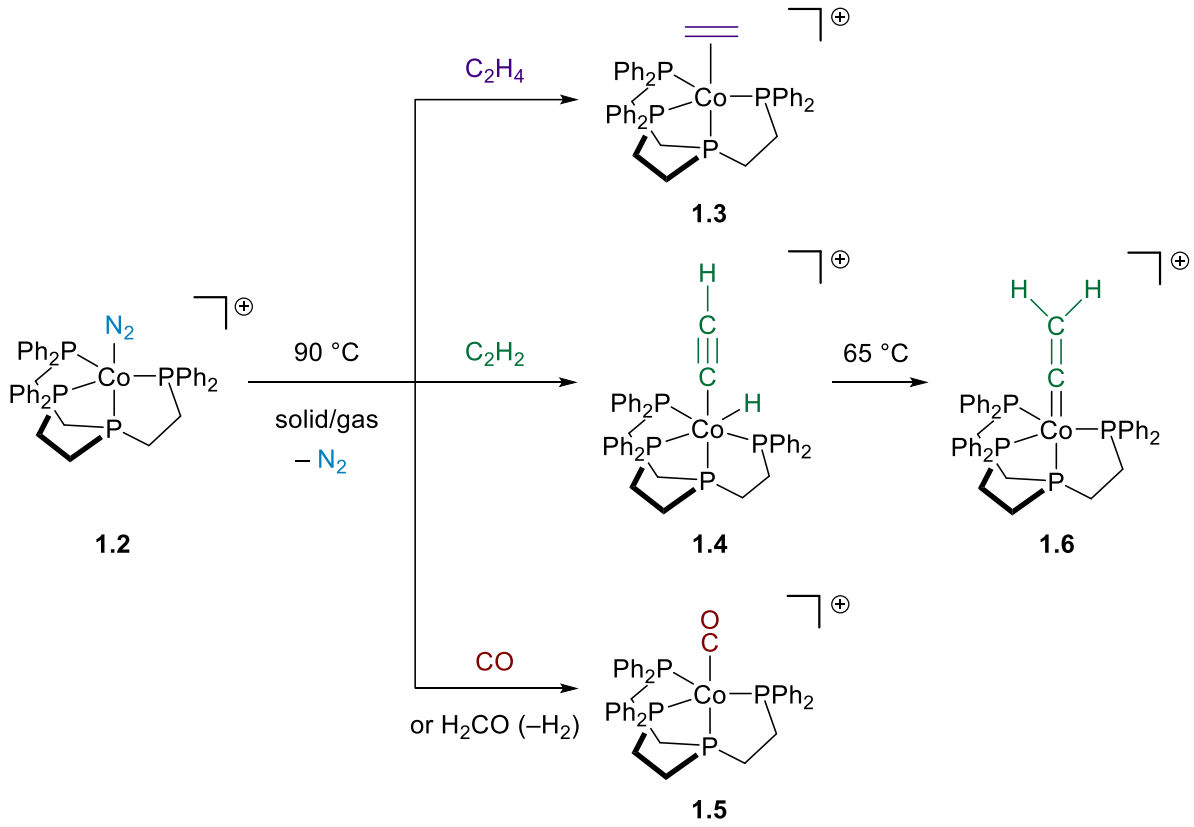

Scheme 1.2 Solid state ligand substitution of **1.2** with C_2H_2, C_2H_4, H_2CO and CO. $[BPh_4]^-$ anion not shown. Note reaction with formaldehyde eliminates H_2 to form the carbonyl complex.

Solid/gas reactivity can also be used to access complexes utilised in catalysis. For example Brookhart and colleagues investigated the SC-SC substitution of N_2 in [(^{Ar}POCOP)Ir(N_2)] (**1.7**; Figure 1.1 A) for various small gases, yielding the corresponding [(^{Ar}POCOP)Ir(L)] (**1.8**; L = C_2H_4, CO, NH_3, O_2 and H_2) complexes, the latter of which was shown to be an active catalyst in ethylene hydrogenation.[17] Despite crystals of [(^{Ar}POCOP)Ir(N_2)] being non-porous, gases were able to move through channels created by the organisation of the toluene solvent (Figure 1.1 B).

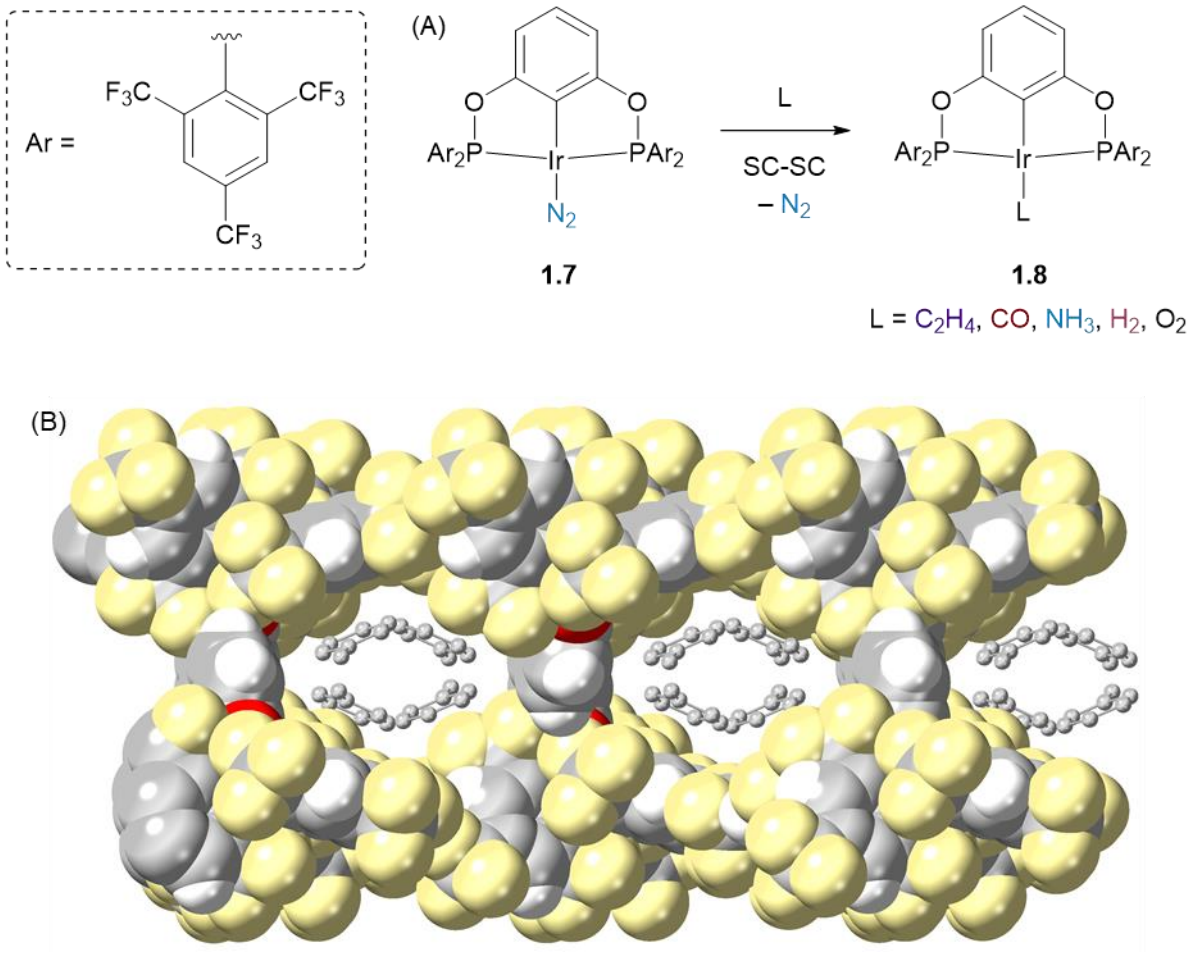

Figure 1.1 (A) The SC-SC transformations of an iridium(I) pincer system. (B) The channels in complex **1.7**, which are created by the toluene solvent (ball and stick), depicted as Van der Waals radii.

Another useful stimulus for *in crystallo* reactivity is light. For example, in 2017 Powers demonstrated the SC-SC photoextrusion of N_2 from a ruthenium azide (**1.9**) to form the highly reactive metallonitrene (**1.10**; Figure 1.2).[18] Similar photocrystallographic reactivity has also been explored by Schneider and colleagues.[19] Such metallonitrenes are proposed intermediates in C−H amination catalysis yet are only observed transiently in solution, demonstrating how *in crystallo* techniques can be used to isolate reactive intermediates relevant to catalysis.[20, 21]

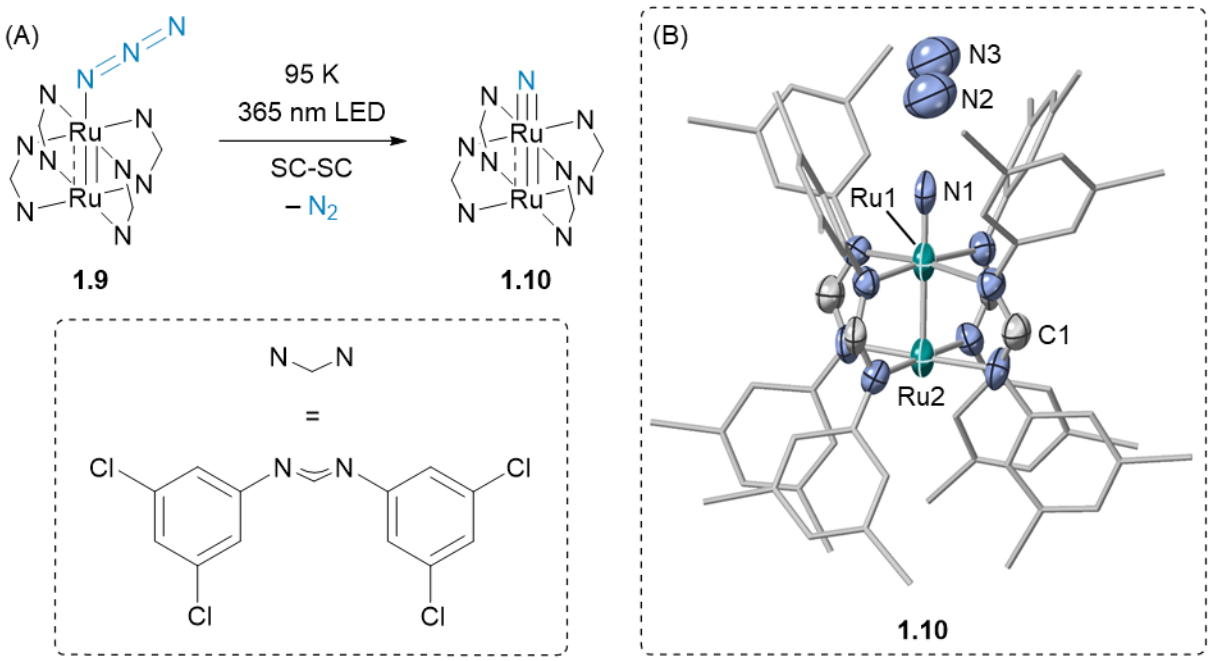

Figure 1.2 (A) The SC-SC isolation of the metallonitrene complex **1.10** *via* photolysis. (B) The molecular structure of complex **1.10**, collected at 95 K, showing the dissociated N_2 remaining within the crystal lattice. Displacement ellipsoids are set at 50% probability level. Hydrogen atoms are omitted for clarity.

1.1.1 Solid-state Molecular Organometallic (SMOM) chemistry

Another example of the application of *in crystallo* chemistry for the isolation of highly reactive intermediates was presented in 2012, when Weller and coworkers reported the first example of a crystallographically characterised *σ*-alkane complex developed by applying solid/gas SC-SC techniques to the hydrogenation of a Rh(I)-alkene complex. Addition of H_2 to the Rh(I)-alkene complex, [(dibpe)Rh(NBD)][BAr^F_4] (**1.11**; dibpe = 1,2-bis(di-*iso*-butylphosphino)ethane; NBD = norbornadiene; Ar^F = 3,5-bis(trifluoromethyl)phenyl), affords the *σ*-alkane complex, [(dibpe)Rh(NBA)][BAr^F_4] (**1.12**) (NBA = norbornane), *via* hydrogenation of the NBD ligand (Figure 1.3 A, B).[22] Complex **1.12** is not stable in solution, liberating NBA even at 163 K in $CDCl_2F$. Previously *σ*-alkane complexes, which are key intermediates in C−H activation processes, had only been observed transiently in solution *via* low temperature *in situ* NMR (Nuclear Magnetic Resonance) methods or fast time-resolved IR (Infrared Spectroscopy), due to their short lifetimes even at cryogenic temperatures.[23-29] This is due to the fact that alkane ligands, binding via weak three-centre-two-electron bonding with typical M···H−C bond

enthalpies of less than 15 kcal mol^{-1},[30-32] are poor ligands on account of the strong (i.e. the bond dissociation enthalpy of $H_3C{-}H$ = 104 kcal mol^{-1}),[33] and non-polar nature of the C−H bonds which are also sterically crowded. Therefore, traditional solution-state methods cannot be used to isolate *σ*-alkane complexes on the timescale required for crystallisation, but such complexes can be accessed using this solid state methodology. Whilst other groups have utilised SC-SC reactions, as detailed previously, Weller describes those which occur in the bulk as SMOM chemistry.[12, 13]

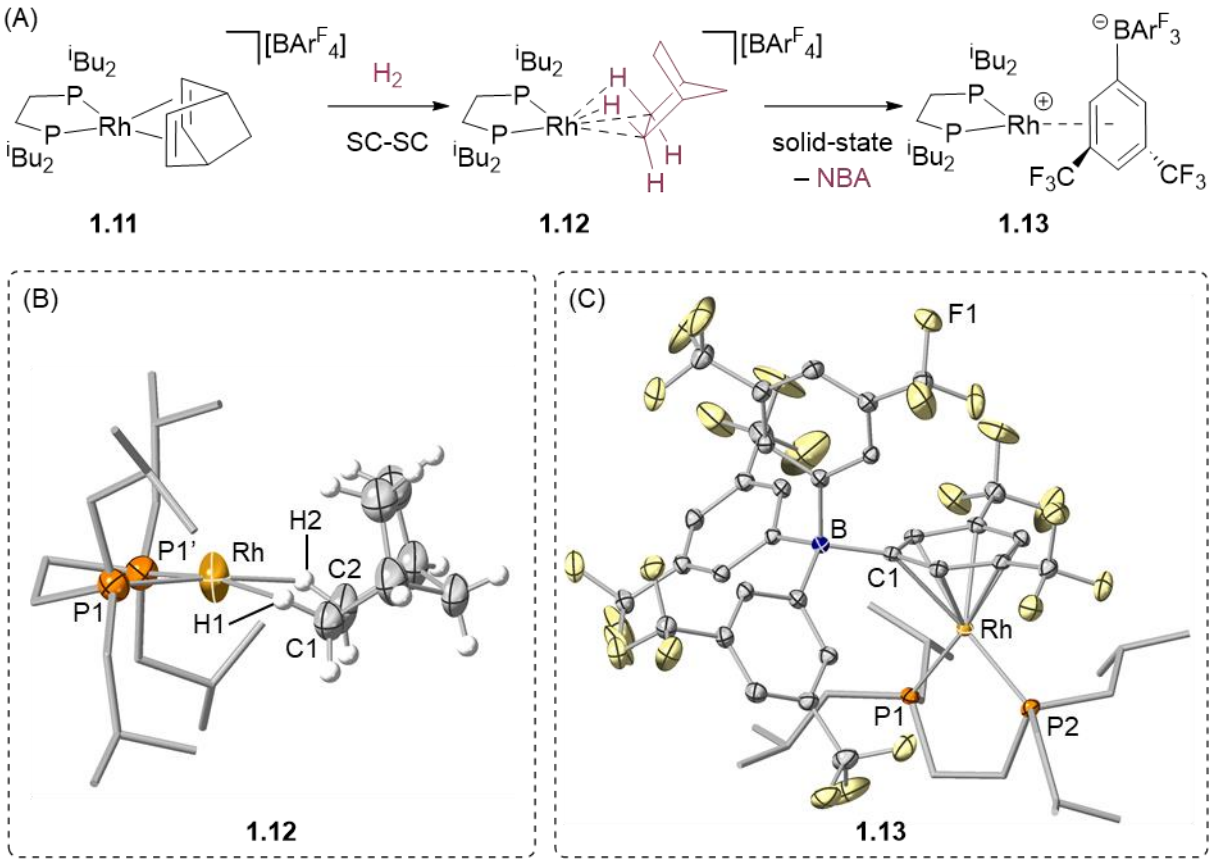

Figure 1.3 (A) The SC-SC hydrogenation of complex **1.11** to afford the crystallographically characterised *σ*-alkane complex, **1.12**, and it's subsequent formation of the zwitterion [(dibpe)Rh(η^6-$C_6H_3(CF_3)_2$)BAr^F_3] (**1.13**). (B) The molecular structures of complexes **1.12** and (C) **1.13**. Displacement ellipsoids are set at 50% probability level. Select hydrogen atoms and $[BAr^F_4]^-$ counterion (**1.12**) are omitted for clarity.

In both solution and the solid state, complex **1.12** converts to the zwitterion [(dibpe)Rh(η^6-$C_6H_3(CF_3)_2$)BAr^F_3] (**1.13**) *via* coordination of the $[BAr^F_4]^-$ anion, liberating NBA in the process.[22] Although this complex forms as an amorphous solid due to the extreme structural

rearrangement required to coordinate the $[BAr^F_4]^-$ anion, its structure was determined through independent synthesis (Figure 1.3 C). This solid state reorganisation was subsequently prevented by changing the substituent group of the phosphine ligand from ^{i}Bu to Cy (cyclohexyl) to form [(dcpe)Rh(NBA)][BAr^F_4] (**1.14**; dcpe = 1,2-bis(di-cyclohexylphosphino)ethane), which is stable under an argon atmosphere in the solid state for months at 298 K.[34] In the solution-state, complex **1.14** eliminates NBA above 197 K in CD_2Cl_2 and converts to the zwitterionic complex [(dcpe)Rh(η^6-$C_6H_3(CF_3)_2$)BAr^F_3] (**1.15**) at 253 K. However, unlike complex **1.13**, complex **1.15** is relatively unstable in solution, forming in relatively low yield alongside minor decomposition products, including free $[BAr^F_4]^-$, which grow in over time.

Weller's application of SMOM techniques to access the crystallographically characterised *σ*-alkane complex **1.12** has since been supplemented by the isolation of a number of linear and branched *σ*-alkane complexes of similar chelating phosphine rhodium(I) systems, including propane, pentane, isobutane, hexane, cyclohexane, 2-methylbutane, 3-methyl pentane and cyclooctane,[35-38] from the corresponding alkene. The highly reactive, open shell cobalt(I) analogue [(dcpe)Co(NBA)][BAr^F_4], which begins to decompose after 2 hrs in oil at 100 K, has also been synthesised using these SMOM techniques.[39]

Some of these described SMOM *σ*-alkane systems can undergo selective C–H activation, as evidenced by the addition of D_2 to complex **1.14** which results in SC-SC H/D exchange of the protons on the NBA ligand to form the partially deuterated *exo*-D_4-**1.14** complex after 16 hrs. Addition of D_2 to [(dcpe)Rh(NBD)][BAr^F_4] (**1.16**) instead results in the formation of the partially deuterated *endo*-D_4-**1.14** complex after 5 min, which proceeds to form the *endo*-*exo*-D_8-**1.14** when left for a total of 16 hrs (Scheme 1.3).[40] This contrasts to the solution-state selectivity, which liberates *endo*-D_2-*exo*-D_2-NBA upon hydrogenation of complex **1.16** with D_2. The labelling in these isotopomers and isotopologues were deduced by SSNMR and single-crystal neutron diffraction studies. They were further supported by GC-MS and solution-state ^{1}H/^{2}H

NMR spectroscopy of the eliminated NBA, which is liberated upon forming the corresponding zwitterion **1.15** in the solution-state.

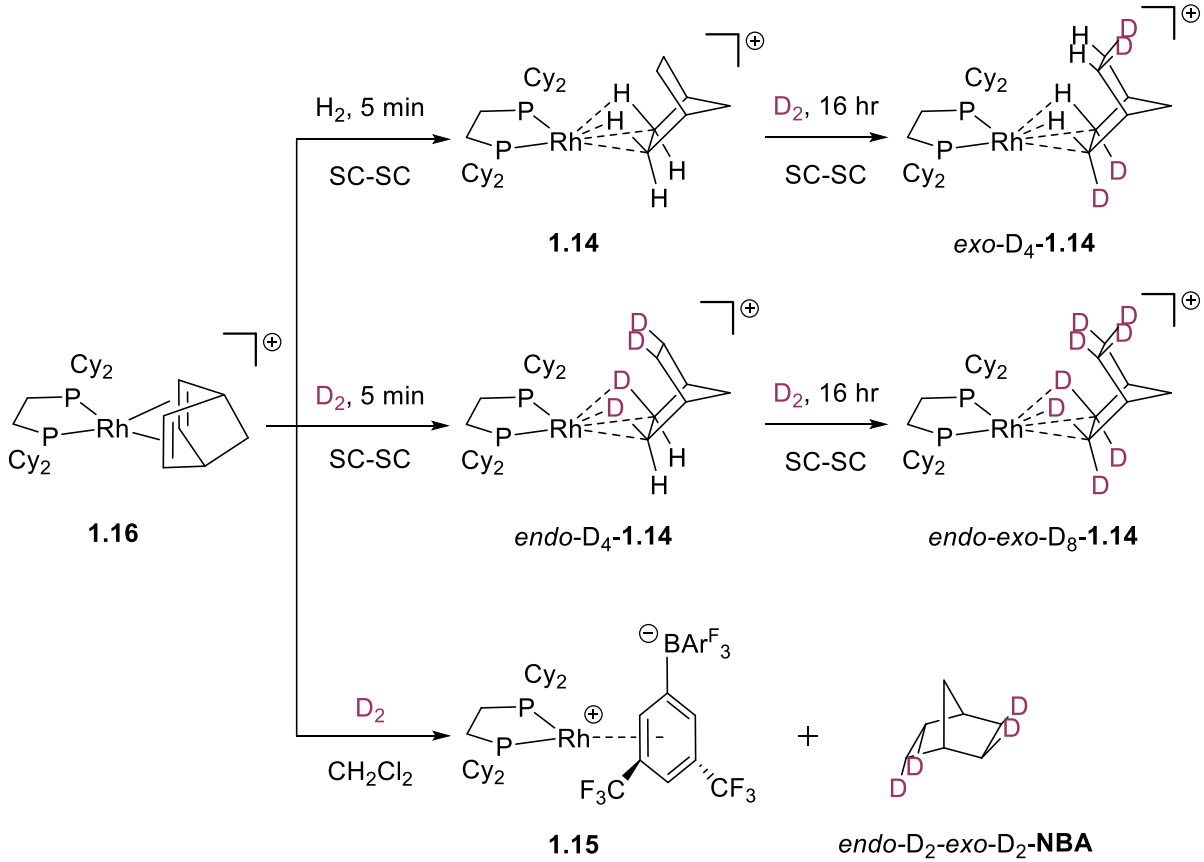

Scheme 1.3 Selective H/D exchange of the NBA ligand in the solid and solution-state with a rhodium(I) SMOM motif.

Regioselectivity can also be controlled by altering the phosphine substituents, and whilst [(dcpp)Rh(NBA)][BAr^F_4] (**1.17**; dcpp = 1,2-bis(dicyclohexylphosphino)propane) binds *via* *endo*-C–H···Rh interactions similar to complex **1.14**, switching to ^{t}Bu substituents binds the alkane *via* *exo*-C–H···Rh interactions due to the subtly different microenvironment within the crystal lattice of [(dtbpp)Rh(NBA)][BAr^F_4] (**1.18**; dtbpp = 1,2-bis(di-*tert*-butylphosphino)propane) (Scheme 1.4).[41] This demonstrates the tuneability of SMOM systems to access various different binding modes.

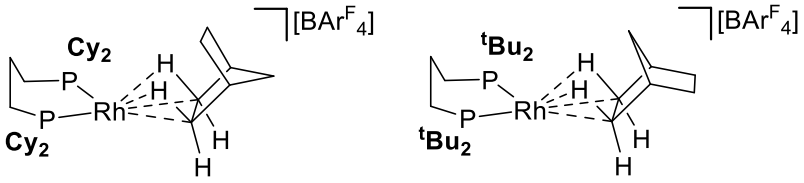

endo-**1.17** *exo*-**1.18**

Scheme 1.4 Phosphine ligand controlled regioselectivity of alkane binding.

Similar to Bianchini's solid/gas and Brookhart's SC-SC work discussed previously, SMOM systems can also be utilised in ligand exchange reactions. The alkane ligand in [(dibpe)Rh(NBA)][BAr$^F_4$] (**1.12**) can be substituted for C_2H_4 and C_4H_6 to give the corresponding alkene complexes, **1.19** and **1.20** respectively in a solid/gas reaction (Figure 1.4 A).[42] Crystallinity is lost upon formation of complexes **1.19** and **1.20**, but these complexes can be recrystallised in solution. However, complex **1.19** is unstable in solution at 298 K in the absence of an ethylene atmosphere, forming either the zwitterionic complex **1.13** in dichloromethane, or the solvent complex [(dibpe)Rh(η^6-1,2-$F_2C_6H_4$)][BAr$^F_4$] in 1,2-difluorobenzene, but is stable in the solid state even under vacuum. This further demonstrates the importance of undergoing this chemistry in the solid state, due to the greater stability observed compared to the solution-state.

The onward solid/gas reactivity of complex **1.20** to substitution of the butadiene ligand was also investigated with NH_3 and CO, yielding the respective bis-ammonia (**1.21**) or bis-carbonyl (**1.22**) complexes as amorphous solids which can be recrystallised in solution. The reaction of complex **1.21** with D_2 has also been investigated. Complex **1.21** undergoes selective H/D exchange of the ammonia ligands with D_2 in both the solution (1,2-difluorobenzene) and solid state (Figure 1.4 B). The latter reaction not only retains crystallinity, but is also one of the first examples of H/D exchange of an organometallic ammonia complex in the solid state, with the other example being that of an implied [(Cp*)Ir(H)$_2$(NH_3)] (Cp* = pentamethylcyclopentadienyl) complex in an argon matrix at 10 K, as shown by IR spectroscopy.[43] Several cases of NH_3/D_2 exchange have been observed in the solution-state.[44-46]

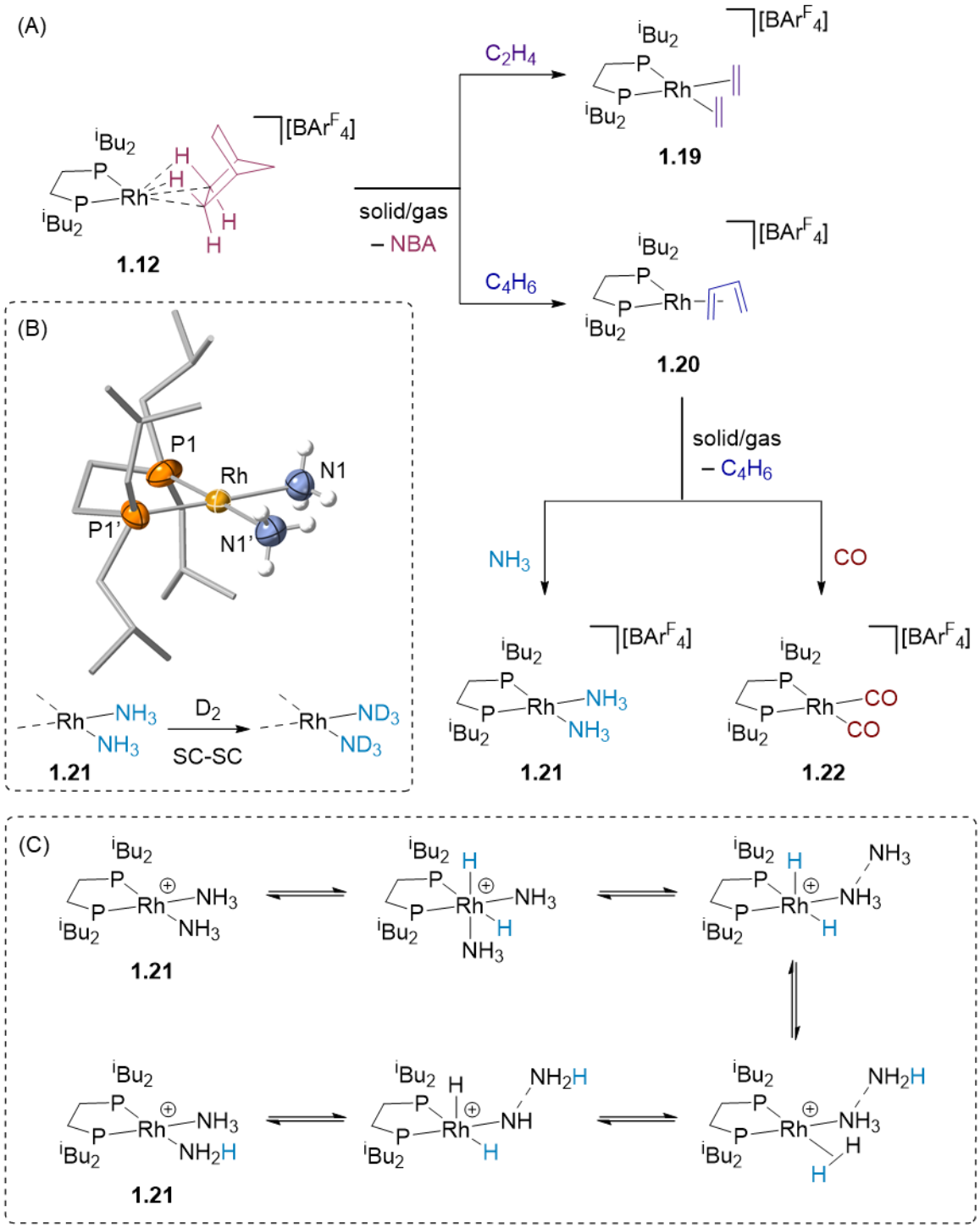

Figure 1.4 (A) *in crystallo* ligand exchange of complex **1.12** with C_2H_4 and C_4H_6 to form the corresponding alkene complexes **1.19** and **1.20** respectively, and further substitution of **1.20** for NH_3 and CO to form complexes **1.21** and **1.22**. (B) The molecular structure of complex **1.21** and it's SC-SC H/D exchange with D_2. Displacement ellipsoids are set at 50% probability level. The $[BAr^F_4]^-$ anion is omitted for clarity. (C) The calculated reaction pathway for H/H exchange of the bound ammonia ligand of complex **1.21**.

The mechanism of H/H exchange of complex **1.21** was calculated (DFT, Density Functional Theory) to occur *via* oxidative addition of H_2 to give a rhodium(III) dihydride,

[(dibpe)Rh(NH_3)$_2$(H)$_2$][BAr^F_4]. The ammonia ligand *trans* to one of the hydride ligands dissociates and interacts with the bound ammonia ligand *via* hydrogen bonding. The outer-sphere ammonia then deprotonates one of the hydride ligands and transfers a proton to the remaining hydride ligand. Finally, reductive elimination of H_2 regenerates complex **1.21**.

The cationic rhodium systems utilised in SMOM chemistry can also be applied to industrially relevant *in crystallo* catalysis such as the hydrogenation of alkenes. *Via* gas phase ^{1}H NMR spectroscopy, complexes **1.12, 1.13** and **1.19**-**1.22** were probed as ethylene hydrogenation catalysts, revealing the precatalysts containing alkene ligands to be the most active. For instance, the NBD complex **1.11** (3 mg, ~0.002 mmol) promotes complete conversion of ethylene (1 atm, ~0.08 mmol) to ethane in less than 2 min.[42] Meanwhile, the zwitterionic complex **1.13** is a slow solid/gas catalyst (ca. 5% conversion after 25 min) which is in contrast to its rapid activity in the solution-state, likely due to the complex being unable to undergo ring slippage and reveal a vacant site within the lattice. This demonstrates the confinement on reactivity imposed by the solid state. In order to investigate if catalysis occurs fastest at the surface or throughout the bulk, the surface of the crystals was passivated with CO, since the carbonyl compound **1.22** demonstrated relatively low activity. CO-passivated crystals of complex **1.20** demonstrated slower conversion compared to the original catalyst complex **1.20**, suggesting that the most active sites reside at the surface, which was supported by the rate of catalysis also increasing upon using smaller particle sizes as the surface area was increased.

The norbornane complex **1.14**, as well as the ethylene complex [(dcpe)Rh(C_2H_4)$_2$][BAr^F_4] (**1.23**), have also proved to be excellent SC-SC catalysts in the isomerisation of 1-butene to a mixture of cis- and trans-2-butenes. For example, complex **1.23** reaches the thermodynamic equilibrium position of 97% 2-butenes with a cis:trans ratio of 1:2 after 6 min.[12] Whilst this was initially performed under batch conditions, this also occurs under a stream of 1-butene in a solid state flow reactor using complex **1.14** as the catalyst.[47] However, the catalytic activity of complex **1.14** drops after 3 hr due to formation of the butadiene deactivation product complex

1.20, which can be reactivated by addition of H_2 (Scheme 1.5). In comparison, catalytic lifetime can be increased to 90 hr by switching the phosphine substituent from Cy to ^{t}Bu with [(dtbpe)Rh(NBA)][BAr^F_4] (dtbpe = 1,2-bis(di-*tert*-butylphosphino)ethane), which does not form the corresponding butadiene compound. This demonstrates the potential utility of SMOM chemistry in catalysis, even under industrially relevant flow conditions.

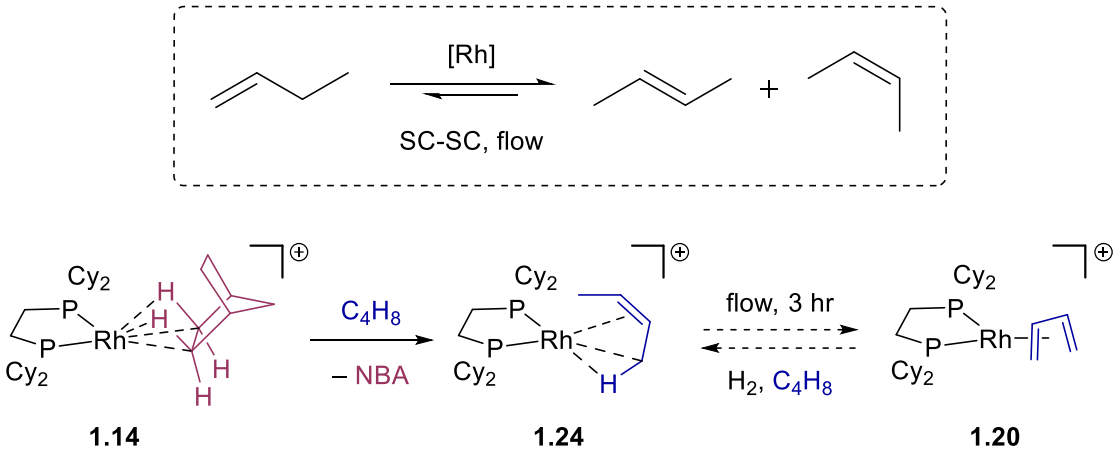

Scheme 1.5 The solid/gas isomerisation of 1-butene under flow conditions and the deactivation of the rhodium catalyst *via* formation of the butadiene complex.

Related reactivity has been further explored with other alkenes, such as propene. In solution, addition of C_3H_6 to [(dcpe)Rh(NBA)][BAr^F_4] (**1.14**) results in the formation of the bis-propene complex [(dcpe)Rh(C_3H_6)$_2$][BAr^F_4] (**1.25**), whilst in the SC-SC reaction, the mono-propene complex [(dcpe)Rh(C_3H_6)][BAr^F_4] (**1.26**) is instead formed,[12] yet again demonstrating the utility of SMOM chemistry in accessing complexes which cannot be isolated in the solution-state (Figure 1.5). The propene ligand in complex **1.26** is bound as a *π*-coordinated alkene with a Rh···H−C agostic interaction and demonstrates fluxional behaviour in both solution and the solid state, likely *via* C−H activation to form the *π*-allyl hydride intermediate, [(dcpe)Rh(H)(C_3H_5)][BAr^F_4], as shown by deuterium scrambling during the solid/gas catalytic isomerisation of 3,3,3-d_3-propene.

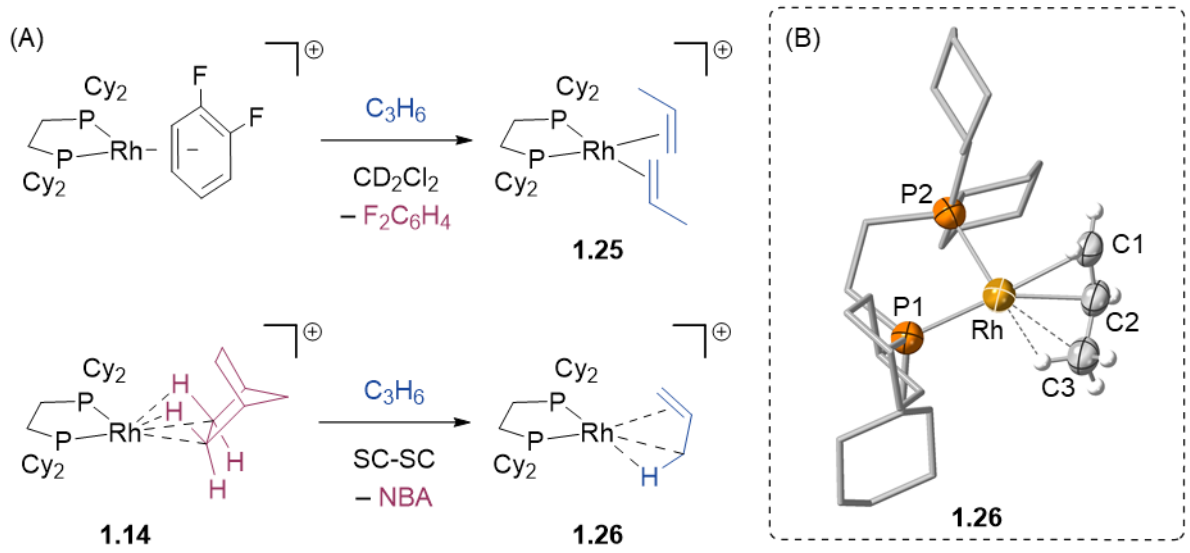

Figure 1.5 (A) The solution *vs* solid state synthesis of mono- or bis-propene complexes. (B) The molecular structure of complex **1.26**. Displacement ellipsoids are set at 50% probability level. $[BAr^F{}_4]^-$ anion omitted for clarity.

Solid/gas hydrogenation catalysis has been further explored using *para*-H_2 (a nuclear-spin isomer of H_2) with propene, 1-butene, propyne and 1-butyne. Parahydrogen-induced polarisation (PHIP) transfer is a useful tool to interrogate catalytic processes and the efficiency of hydrogen transfer by monitoring the resulting signal enhancement in the corresponding ^{1}H NMR spectra.[48] This often assists in the identification of products and even the detection of catalytic intermediates.[49, 50] In the propane formed from hydrogenation, high levels of PHIP (85%) were observed using [(dtbpe)Rh(C_3H_6)][$BAr^F{}_4$] (**1.27**) at 298 K, allowing for single scan gas phase ^{1}H and ^{13}C NMR spectra to be obtained (Figure 1.6).[51] This demonstrates that the pairwise transfer of *para*-H_2 is highly efficient in SMOM catalysts. This was compared to the dcpe analogue (**1.26**) which, whilst polarisation effects are initially observed, results in the formation of the zwitterionic deactivation product complex **1.15**, demonstrating the importance of catalyst choice in SMOM catalysis.

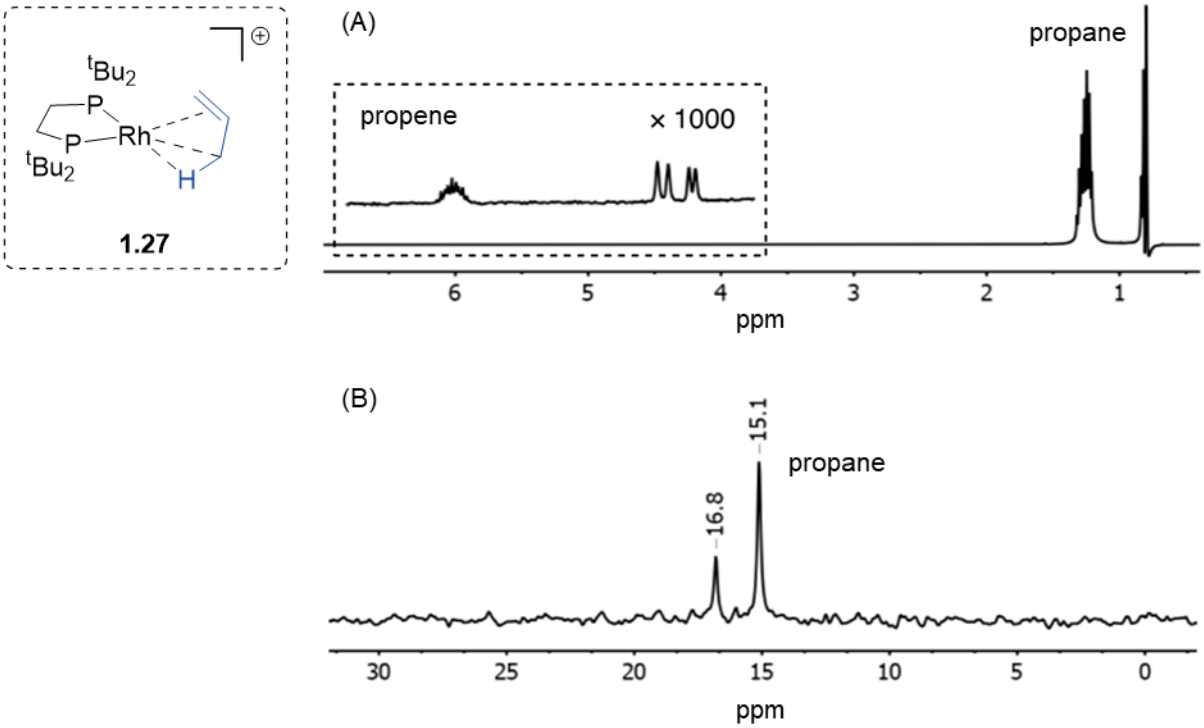

Figure 1.6 Single-scan (A) ^{1}H and (B) ^{13}C-INEPT NMR spectra of propene hydrogenation showing the scale of PHIP signal enhancement in propane observed when complex **1.27** reacts a 3.5 bar of a 1:2.5 mixture of propene and *para*-H_2, inset shows propene signal relatively scaled ×1000.

1.1.2 The $[BAr^F_4]^-$ lattice: a stabilising crystalline framework

The remarkable stability of the aforementioned cationic rhodium *σ*-alkane complexes is proposed to be due to the regular arrangement of $[BAr^F_4]^-$ anions. The anions form a well-defined cavity, encapsulating and stabilising the reactive metal centre *via* non-covalent interactions in a variety of different packing motifs, the most common of which includes octahedral (Figure 1.7 A)[41] and bicapped square prismatic geometries.[36, 37] The octahedral packing arrangement encapsulates one cation within six $[BAr^F_4]^-$ anions, whilst the bicapped square prism forms a motif of ten anions and can accommodate two crystallographically equivalent cations. The increased stabilisation provided by the $[BAr^F_4]^-$ anions was calculated to be up to 50% by comparing the computed solid state energy interaction terms of [(dcpe)Rh(NBA)][BAr^F_4] (**1.14**) (33.1 kcal mol^{-1}) compared to that of the molecular alkane binding energy (147.1 kcal mol^{-1}).[36, 52] This stabilisation was highlighted further by the Independent Gradient Model with Hirshfeld partitioning (IGMH) plot of complex **1.14**, which

displays weakly stabilising interactions between the CH-CH_2-CH bridge of the NBA ligand and the neighbouring $[BAr^F{}_4]^-$ aromatic rings, as depicted by the broad green isosurfaces (Figure 1.7 B).

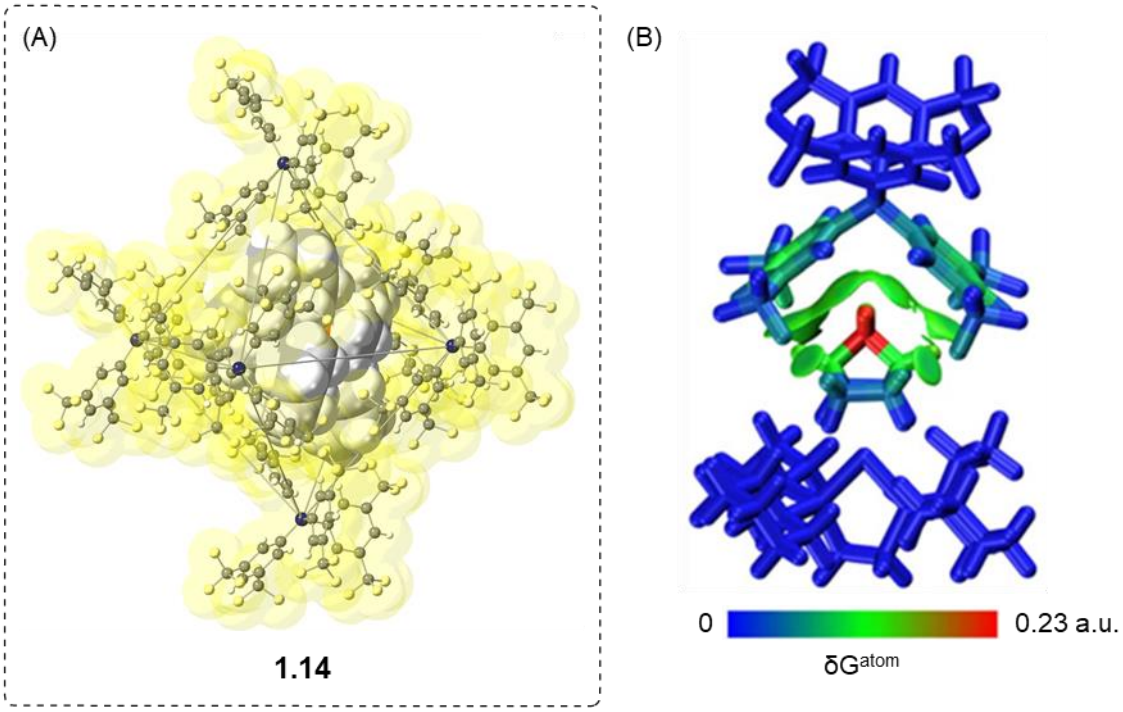

Figure 1.7 (A) The extended solid state structure of complex **1.14**, showing the octahedral arrangement of $[BAr^F{}_4]^-$ anions depicted as Van der Waals radii. (B) IGMH plot of complex **1.14**. The colour of the atoms highlights which atoms contribute most significantly to the non-covalent interactions, wherein the red atoms contribute the most.

This organisation of $[BAr^F{}_4]^-$ anions, with each aryl ring featuring two CF_3 groups, into a regular framework also creates hydrophobic channels which enable substrate ingress and product egress, during which crystallinity is usually retained. This is similar to how the toluene solvent channels in Brookhart's [(^{Ar}POCOP)Ir(N_2)] (**1.7**) facilitate movement of gases within the non-porous crystal.[17] It is hypothesised that the CF_3 groups undergo a concerted "geared" motion which allows for the transport of gases,[42] akin to the work of Brammer and coworkers who proposed that the role of the fluorinated substituents within the non-porous coordination polymer [[$Ag_4(O_2C(CF_2)_2CF_3)_4(TMP)_3$] (TMP = tetramethylpyrazine) was pivotal in the mechanism of reversible SC-SC uptake of ROH (R = Me, Et, ^{i}Pr) vapour to yield [[$Ag_4(O_2C(CF_2)_2CF_3)_4(TMP)_3(ROH)_2$].[53]

The $[BAr^F_4]^-$ anion is thus of considerable importance, not only in the stabilisation it provides to a reactive cation, but also to support gas transport through the crystal for both the ingress of reactants and egress of products, similar to that found in metalloenzymes.[54-56] This was made especially apparent in the reversible uptake of dichloromethane solvent and xenon gas within the non-porous fluorous channels of [(dcpm)Rh(NBD)][BAr^F_4] (dcpm = 1,2-bis(di-cyclohexylphosphino)methane). The $[BAr^F_4]^-$ anion framework acts as the host, encapsulating the guest CH_2Cl_2 or Xe molecules within the crystalline lattice to form [(dcpm)Rh(NBD)][$(CH_2Cl_2)_{0.75}$⊂BAr^F_4] (**1.28**) and [(dcpm)Rh(NBD)][$(Xe)_{0.5}$⊂BAr^F_4] (**1.29**) respectively in a SC-SC manner (Figure 1.8).[57]

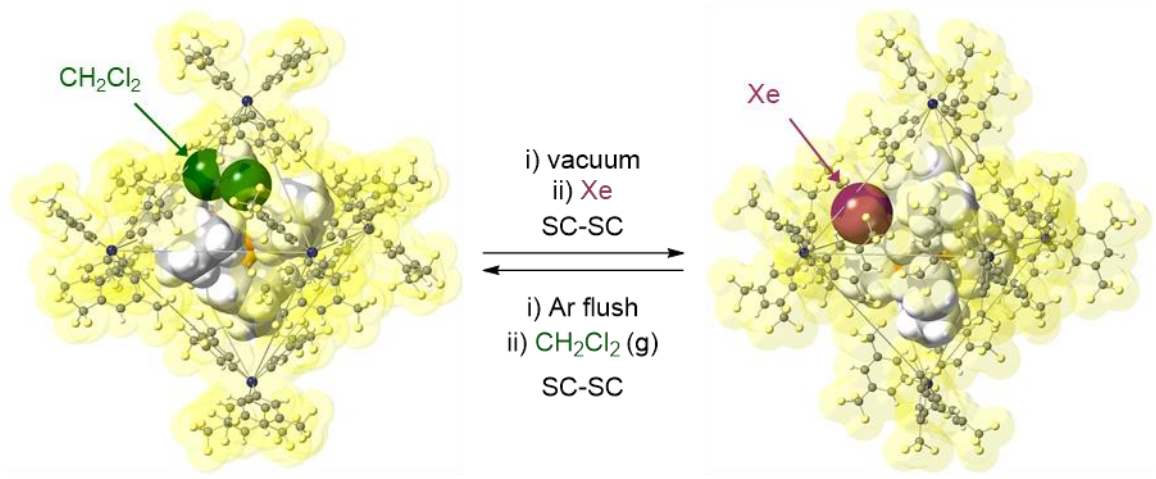

Figure 1.8 The reversible SC-SC uptake of CH_2Cl_2 and Xe within a crystal lattice as shown by the solid state octahedral $[BAr^F_4]^-$ structures depicted as Van der Waals radii. CH_2Cl_2 is removed from the lattice under vacuum for 24 hrs, whilst Xe can be removed under an argon flush for 2 min.

Despite it's well-defined, ordered structure, the $[BAr^F_4]^-$ lattice framework typically used in SMOM chemistry is remarkably adaptive even within the solid state, often being able to withstand large structural rearrangements in order to support *in crystallo* reactivity. For instance, the ^{iPr}PONOP (^{iPr}PONOP = (di-*iso*-propylphosphino)-2,6-dioxypyridine) ligand of the propene complex [(^{iPr}PONOP)Ir(C_3H_6)][BAr^F_4] (**1.31**) moves by 90° within the $[BAr^F_4]^-$ lattice during the SC-SC reaction with H_2 to form [(^{iPr}PONOP)Ir(C_3H_6)($H)_2$][BAr^F_4] (**1.32**, Figure 1.9).[58] This results in an increase in the unit cell volume (2975 to 3033 Å^3).

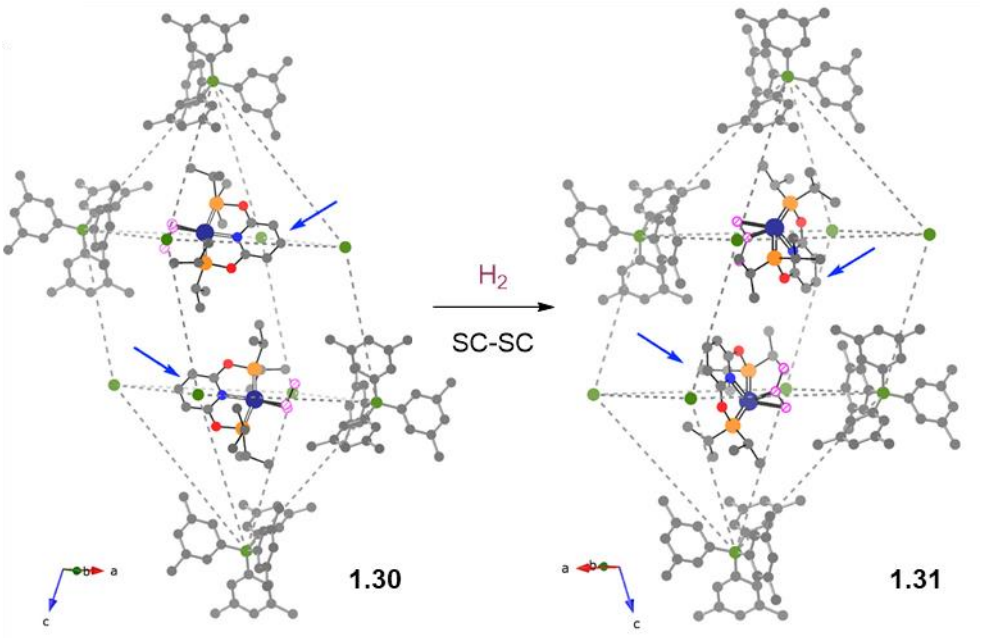

Figure 1.9 The rearrangement of the ^{iPr}PONOP ligand (indicated by blue arrows) within the bicapped square prismatic $[BAr^F{}_4]^-$ arrangements in the solid state during reaction of complex **1.31** with H_2, taken from the original text and depicted by ball and stick format.[58] Fluorine and hydrogen atoms are omitted for clarity.

Another example of the flexibility of the $[BAr^F{}_4]^-$ framework comes from the *in crystallo* reaction of the pincer complex $[(^{iPr}PONOP)Mn(CO)_2(THF)][BAr^F{}_4]$ (**1.32**) with CO to yield $[(^{iPr}PONOP)Mn(CO)_3][BAr^F{}_4]$ (**1.33**). In both precursor and product, the $[BAr^F{}_4]^-$ anions are arranged in a bicapped square prismatic packing motif with ten anions encapsulating two cations. However, there is a significant lateral movement during the reaction which is associated with a large change in volume (**1.32**, 6306; **1.33**, 2835 Å^3). As highlighted by SEM (Scanning Electron Microscopy, Figure 1.10 a and b), this results in the crystals fracturing due to the mechanical stress of undergoing a space group change and subsequent reordering of the $[BAr^F{}_4]^-$ framework, in addition to the loss of hexane lattice solvent and the eliminated THF molecule (Figure 1.10).[59] Despite this, these complexes retained micro-crystallinity and were analysed using MicroED (Microcrystal Electron Diffraction) techniques.[60, 61]

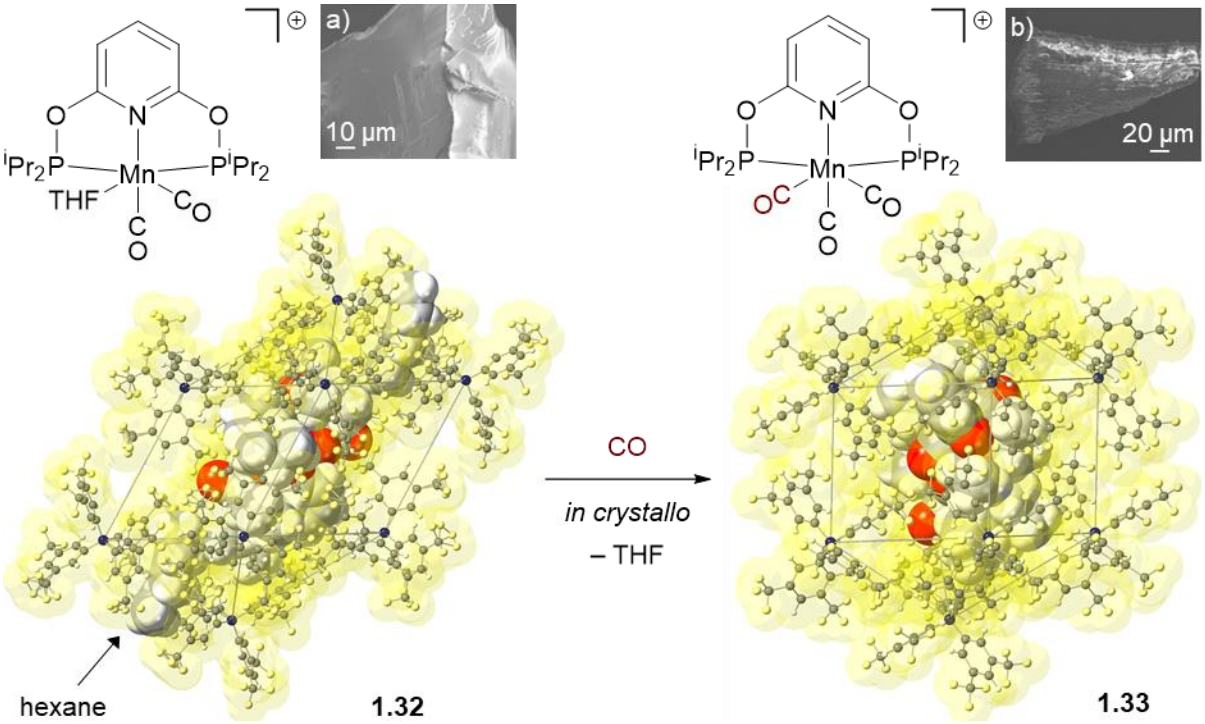

Figure 1.10 The rearrangement of the solid state $[BAr^F{}_4]^-$ arrangements during reaction of complex **1.32** with CO, depicted as Van der Waals radii. SEM images (a) before and (b) after the transformation, showing the fracturing within the crystal on the µm scale.

Another example of the plasticity of $[BAr^F{}_4]^-$ based SMOM systems is the case of [Rh(dtbpe)(NBA)][$BAr^F{}_4$] (**1.35**). Long-range crystalline order was lost during the solid/gas synthesis of complex **1.35** from [Rh(dtbpe)(NBD)][$BAr^F{}_4$] (**1.34**), but crystalline order was subsequently restored upon addition of 1-butene gas to form a 60:40 mixture of the 1-butene (**1.36**) and *cis*-2-butene complexes (**1.37**) respectively in an order/disorder/order phase transition (Figure 1.11).[47]

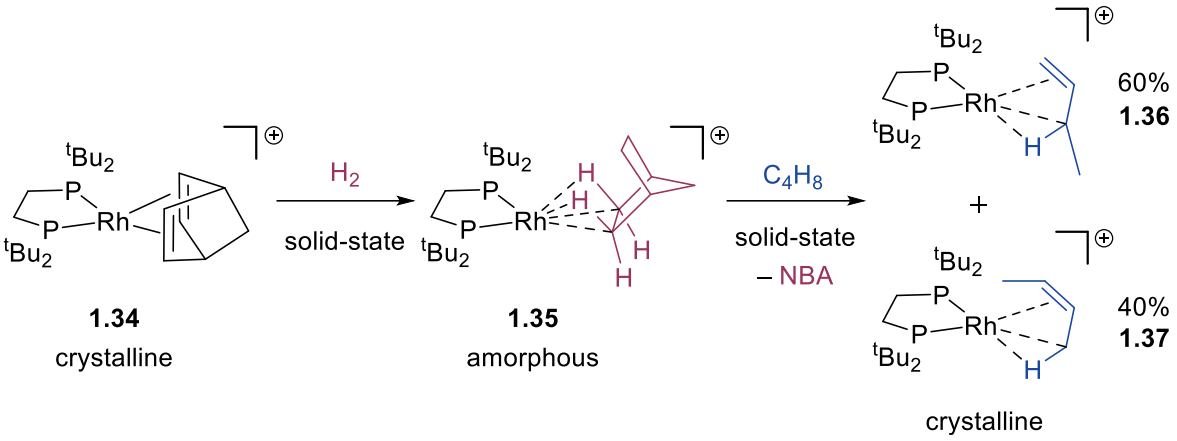

Figure 1.11 The solid state phase transition during hydrogenation of complex **1.34** and subsequent addition of 1-butene.

These examples of SC-SC rearrangements within the lattice were less significant than that required to coordinate the $[BAr^F_4]^-$ anion in order to form the zwitterionic complex [(dibpe)Rh(η^6-$C_6H_3(CF_3)_2$)BAr^F_3] (**1.13**) discussed in section 1.1.1, and so it is unsurprising that complex **1.13** loses crystallinity and forms a completely amorphous material.[22] The ability of these systems utilised in SMOM chemistry to retain crystallinity despite significant changes within the lattice is of relevance to chapters 3 and 4 of this thesis, where the effect of loss of lattice solvent during *in crystallo* transformations shall be discussed.

Throughout these discussions it has become evident that the $[BAr^F_4]^-$ anion is important in stabilising the crystal lattice to support SC-SC reactivity, and this is also apparent in the numerous attempts to alter the anion. Exchanging $[BAr^F_4]^-$ for $[BAr^{Cl}_4]^-$ (Ar^{Cl} = 3,5-dichlorophenyl) in the hydrogenation of [(dibpe)Rh(NBD)]$^+$ results in coordination of the anion to form the zwitterion **1.13** with no observation of the alkane intermediate.[62] As previously discussed in section 1.1.1, [(dcpe)Rh(NBA)]$^+$ (**1.16**) shows no coordination of $[BAr^F_4]^-$ (**1.15**) even after months at 298 K in the solid state. Switching the anion to $[BAr^{Cl}_4]^-$, $[BAr^{F'}_4]^-$ ($Ar^{F'}$ = 3,5-difluorophenyl) and $[BPh_4]^-$ results in the respective analogues of the aryl-coordinated complex **1.15**. This was demonstrated by monitoring the conversion of complex **1.16** to [(dcpe)Rh(NBA)]$^+$ (**1.14**) and complex **1.15**, and it was determined that only $[BAr^F_4]^-$ converts fully to complex **1.14** with no observation of complex **1.15** (Scheme 1.6).[63] As previously

discussed in section 1.1.1, complex **1.16** is an active catalyst in the isomerisation of 1-butenes to 2-butenes,[12] and thus in order to further explore the effect of the anion used, these complexes were probed as SC-SC butene isomerisation catalysts. Complex **1.16**[BPh_4] demonstrated no catalytic activity, halting at zwitterion **1.15**[BPh_4], whilst complexes **1.16**[$BAr^{F'}{}_4$] and **1.16**[$BAr^{Cl}{}_4$] reached 72 and 88% conversion respectively after 2 min, compared to the 96% conversion observed for the corresponding $[BAr^F{}_4]^-$ catalyst. The presence of electron-withdrawing CF_3 groups in order to make the anion sufficiently weakly coordinating, as well as phosphine choice, are vital to this chemistry to prevent formation of the zwitterionic deactivation product. Investigation into the use of other weakly coordinating anions, such as $[B(C_6F_5)_4]^-$, $[Al(OC(CF_3)_3)_4]^-$ or $[Al(OCH(CF_3)_2)_4]^-$, with these rhodium(I) systems led to intractable oils which could not be crystallised.[34, 64]

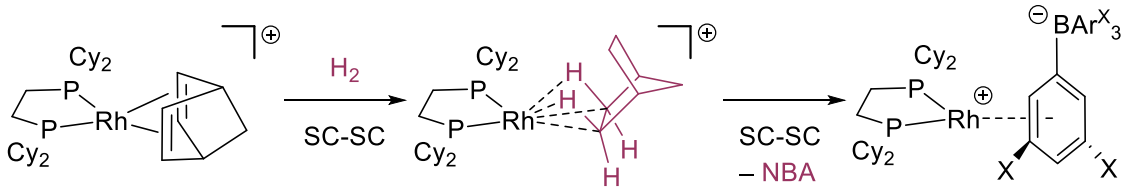

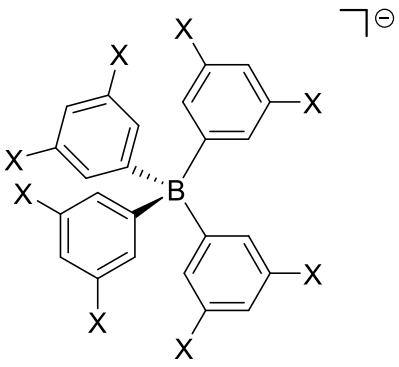

	1.16	1.14	1.15
X = **H**	0	0	100%
F	14%	17%	69%
Cl	0	25%	75%
CF_3	0	100%	0

Scheme 1.6 The selectivity of the formation of cation **1.14** with different anions, as measured by $^{31}P\{^1H\}$ SSNMR (solid-state NMR) spectroscopy taken 1 hr after H_2 addition.

An alternative anion which has proven successful in SMOM chemistry is $[BAr^{SF5}{}_4]^-$ (Figure 1.12, Ar^{SF5} = 3,5-bis(pentafluorosulfanyl)phenyl). Crystals of [(dcpe)Rh(NBA)][$BAr^{SF5}{}_4$], synthesised from the SC-SC hydrogenation of [(dcpe)Rh(NBD)][$BAr^{SF5}{}_4$] with H_2, are remarkably stable up to 170 °C as well as in a pentane suspension, unlike

[(dcpe)Rh(NBA)][BAr^{F}_{4}] (**1.14**) which decomposes at 80 °C or rapidly forms the zwitterion **1.15** when placed in a pentane slurry, owing to increased non-covalent interactions of [BAr^{SF5}_{4}]$^{-}$.[65] However, these crystals are synthetically challenging to isolate, and most crystals proved too small for single-crystal XRD (X-ray diffraction) and thus required the use of more challenging MicroED techniques to analyse the SC-SC reactivity.

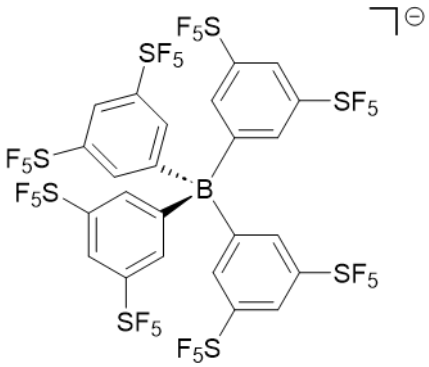

[BAr^{SF5}_{4}]$^{-}$

Figure 1.12 The structure of the anion [BAr^{SF5}_{4}]$^{-}$.

1.1.3 The solid-state chemistry of group XI

Despite the numerous examples of rhodium, iridium, and even cobalt SC-SC transformations,[22, 39, 58] SMOM chemistry has largely been limited to the group IX metals. While limited, investigation into manganese and rhenium compounds has been reported,[59] but beyond that there is much left to be explored. One focus of this thesis shall be on expanding this SMOM methodology to the group XI metals in order to access solution-state inaccessible intermediates, an objective which will be discussed further in section 1.2.

Solid/gas reactivity with group XI metal-ligand complexes only began to emerge within the last 10 years, dating back to the example reported by Brammer and coworkers discussed in section 1.1 which featured the reversible SC-SC uptake of ROH vapour within a silver(I) coordination polymer.[53] This has since been followed by the reversible *in crystallo* binding of C_2H_4 to [$((CF_3)_2Bp)Cu]_3$ (**1.38**; Bp = bis(pyrazoyl)borate) to afford [$((CF_3)_2Bp)Cu(C_2H_4)$] (**1.39**), which eliminates C_2H_4 upon gentle heating and vacuum (Figure 1.13). Although this is not a

SC-SC reaction, likely owing to the significant structural rearrangement required to form a monomeric species from a trimer, this process retains bulk crystallinity as shown by powder X-ray diffraction. A column of $[((CF_3)_2Bp)Cu]_3$ proved effective in the selective purification of ethylene (0.995:0.005 ethylene:ethane) from an ethylene/ethane mixture in the solid state.[66] Dias more recently reported analogous chemistry with silver, wherein C_2H_4 reversibly binds to various fluorinated pyrazolate silver(I) trimer complexes to form dimeric silver(I) ethylene complexes. One of which is $[(4\text{-Br-}3,5\text{-}(CF_3)_2Pz)Ag(C_2H_4)]_2$ (Pz = pyrazolyl), which cannot be accessed in the solution-state, but the structure can be indirectly obtained under 10 bar C_2H_4 at 220 K *via in situ* powder XRD.[67] As well as this, an unusual $[((CF_3)_2Pz)Ag(C_2H_4)]_3$ trinuclear complex was observed, which Dias noted could potentially be an intermediate in the trimer-to-dimer transformations observed for the other complexes discussed in this work. As will be discussed in more detail in section 1.2, group XI metal *π*-alkene and alkyne complexes are difficult to stabilise owing to the relatively weak metal-ligand interactions, therefore these are impressive examples of utilising bulky, fluorinated ligands and solid state methodologies to isolate such complexes in the solid state.

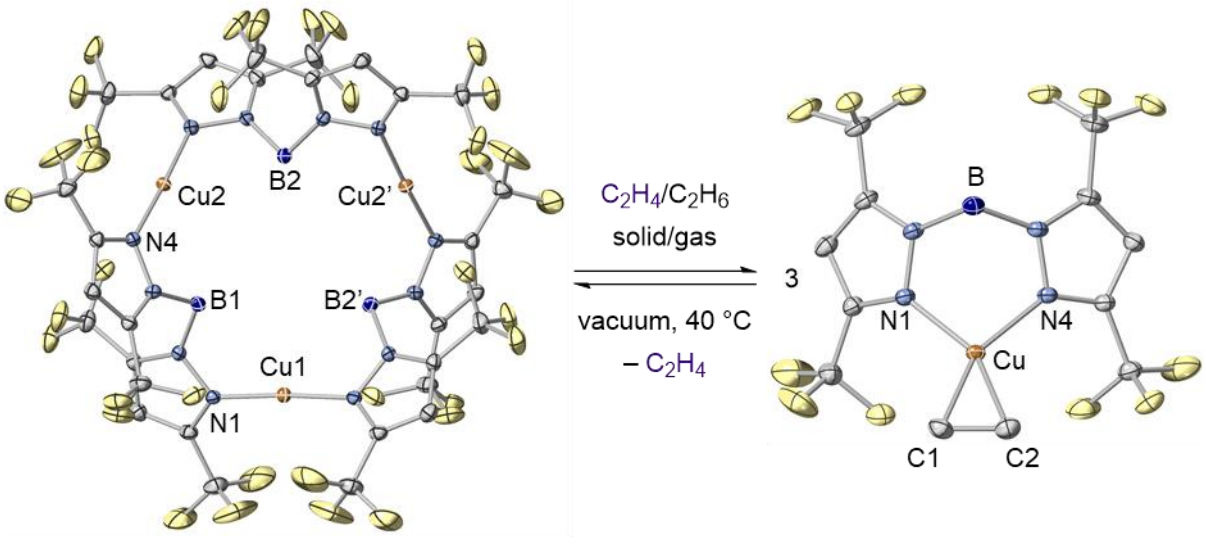

1.38 **1.39**

Figure 1.13 Solid/gas selective and reversible ethylene binding of a copper(I) complex from an ethylene/ethane mixture. Displacement ellipsoids are set at 50% probability level and hydrogen atoms are omitted for clarity.

Recently Tran and colleagues presented the SC-SC stepwise insertion of CO_2 into the copper(I) hydride bridged complex $[(IPr^*)Cu(H)]_2$ (**1.40**; IPr* = N,N'-bis(2,6-bis(diphenylmethyl)-4-methoxy-phenyl)imidazole-2-ylidene). SC-SC reactivity enabled the isolation of the single CO_2 insertion product $[(IPr^*)Cu]_2(\mu\text{-}1,3\text{-}O_2CH)(\mu\text{-}H)$ (**1.41**) after 15 min, which then proceeded to the bis-formate complex $[(IPr^*)Cu]_2(\mu\text{-}1,3\text{-}O_2CH)(\mu\text{-}1,1\text{-}O_2CH)$ (**1.42**) when left for 3 hr (Figure 1.14).[68] The latter displays two different bonding modes of the bridging formate, binding in both a κ'κ'-1,1 and κ'κ'-1,3 motif. Such complexes are proposed intermediates in CO_2 reduction yet are not stable in the solution-state, instead forming the monomeric complex $[(IPr^*)Cu(\mu\text{-}1,1\text{-}O_2CH)]$ (**1.43**). This further demonstrates the utility of *in crystallo* chemistry in accessing otherwise inaccessible catalytic intermediates.

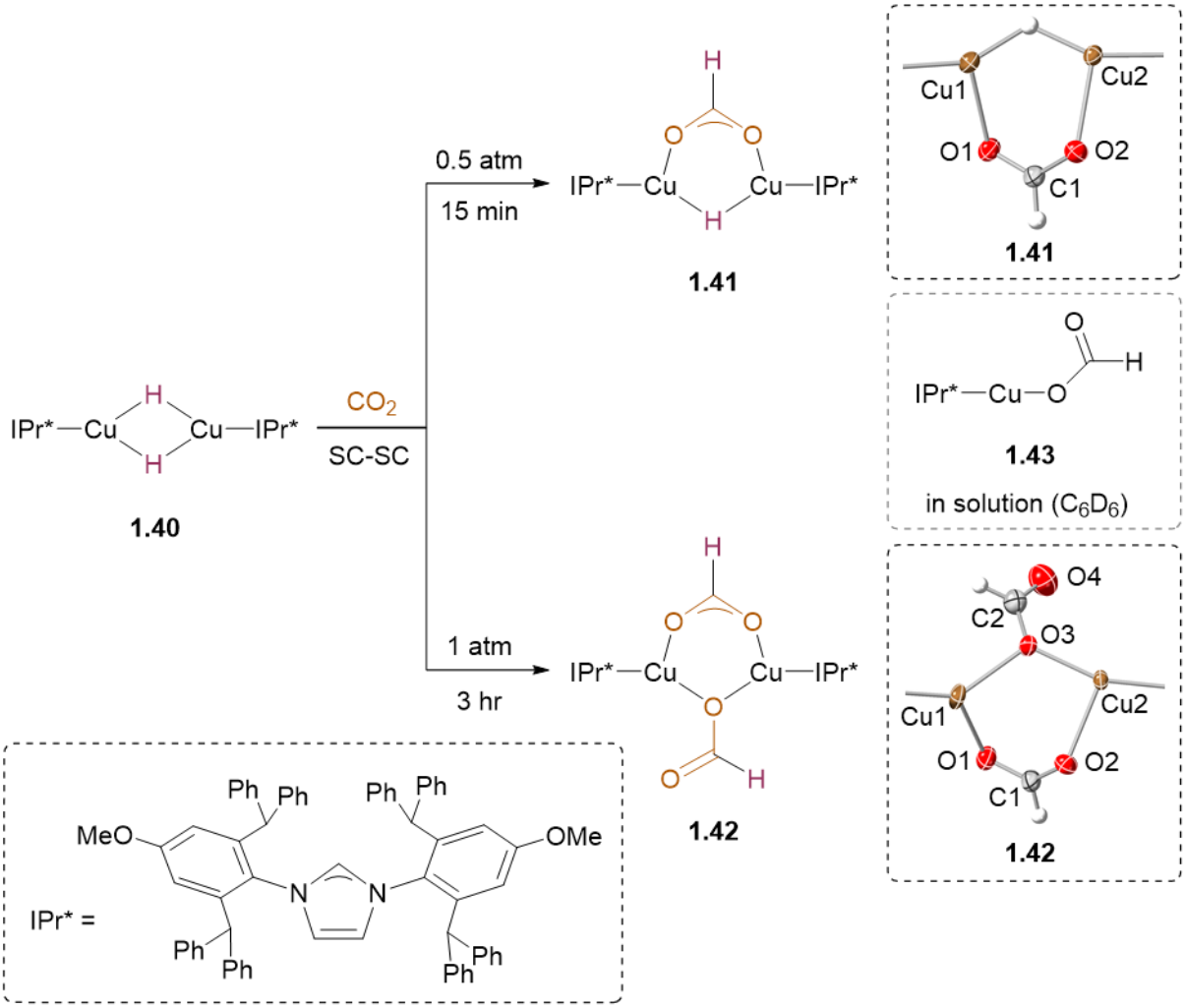

Figure 1.14 The isolation of mono- and bis-formate dimers *via* SC-SC CO_2 insertion, and the central $[Cu]_2$ fragments of the molecular structures showing the different formate binding modes. Dissolving either crystals in C_6D_6 forms the monomeric complex. Displacement ellipsoids are set at 50% probability level.

Besides solid/gas reactivity, the solid state chemistry of group XI also includes that of polymorph-to-polymorph transitions, for which reports describe the application of physical stimuli to induce *in crystallo* transformations with gold complexes. In the case of phenyl(phenyl isocyanide)gold(I) (**1.44**), a needle prick on one single-crystal triggers a domino-like, kinetic to thermodynamic transformation across the bulk of the crystals (**α-1.44**, $P\bar{1}$) in a SC-SC manner within 15 hours in order to access a new, thermodynamically stable polymorph in a new space group (**β-1.44**, $I\bar{4}2d$, Figure 1.15).[69] This bulk change can also be induced by seeding single-crystals with a single-crystal of the opposite polymorph. These changes result in differences in photoluminescence between the initial, kinetic, polymorph (**α-1.44**) with C−H···π intermolecular interactions and the thermodynamic polymorph which has Au···Au aurophilic interactions (**β-1.44**). Polymorphs **α-1.44** and **β-1.44** can also be crystallised from solution by altering the crystallisation conditions (rapid *vs* slow cooling).

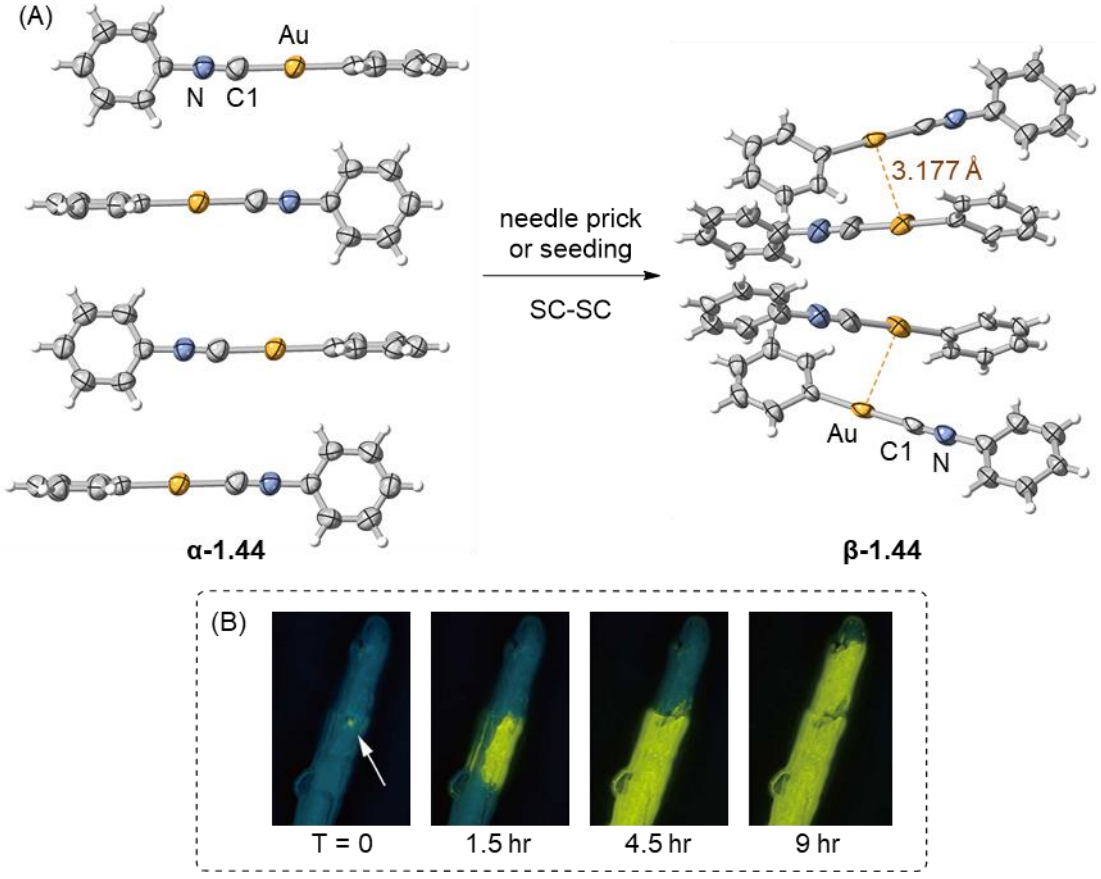

Figure 1.15 (A) The molecular structures of polymorphs **α-1.44** and **β-1.44**, showing the needle-prick induced SC-SC polymorph transition. Displacement ellipsoids are set at 50% probability level. (B) Photos showing the phase transformation across a crystal of polymorph **α-1.44** over time. The white arrow highlights the point of the needle-prick upon the crystal.

A similar SC-SC polymorph transition occurs with $Au_2(\mu\text{-dppe})_2X_2 \cdot 2(\text{solvent})$ (**1.45**; dppe = 1,2-bis-(diphenylphosphino)ethane; X = Br, I; solvent = acetone or dichloromethane), which reversibly converts between polymorphs *via* exposure to solvent vapour or air/vacuum, resulting in alterations in the aurophilic interactions and thus a change in luminescence (Figure 1.16).[70, 71] However, the absorbed solvent molecule is not exchangeable and applying dichloromethane vapour to polymorph ***β*-1.45** simply results in the reformation of polymorph ***α*-1.45** with no change to the acetone lattice solvent. This demonstrates that in this rather unusual example, solvent vapour can induce changes in the crystalline lattice structure but not the composition of the compound.

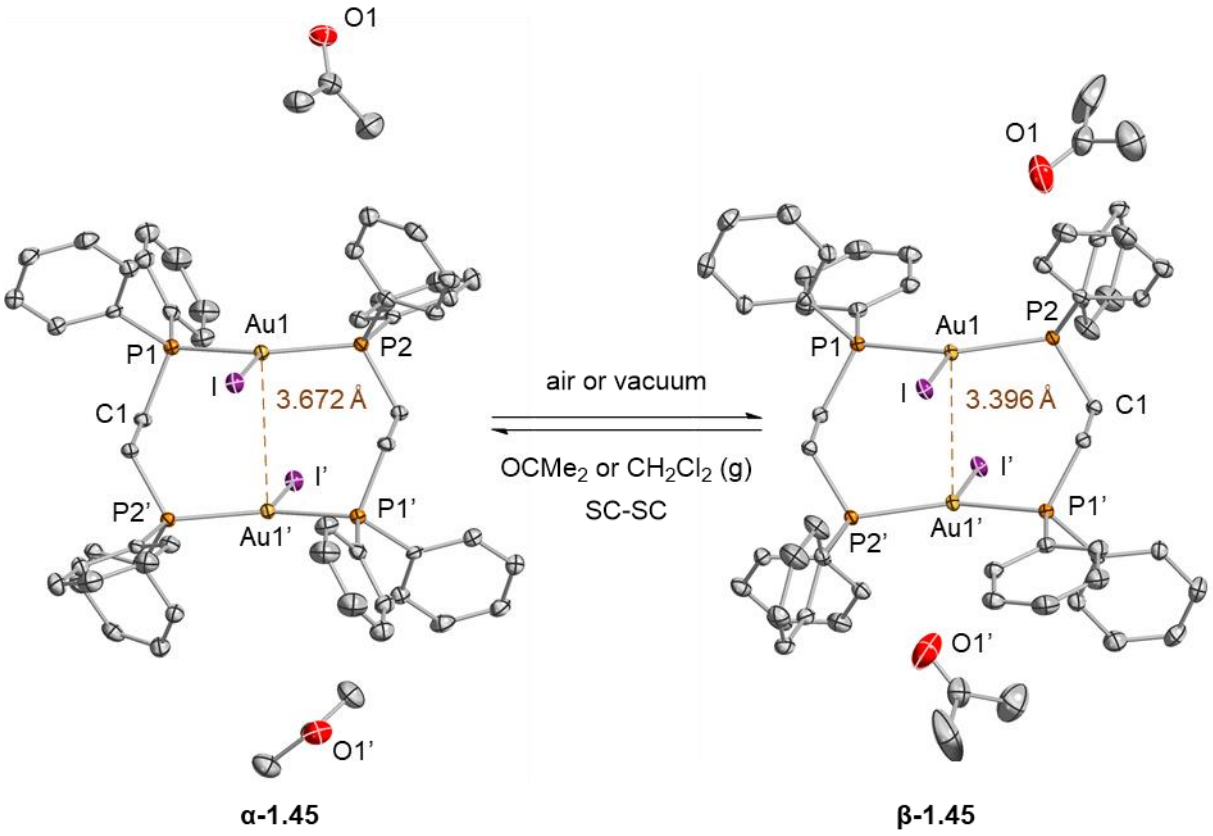

Figure 1.16 The reversible SC-SC solvent vapour induced polymorph transition of complex **1.45** as shown by molecular structures, with Au1···Au2 interactions of 3.6720(2) Å (***α*-1.40**) and 3.3955(2) Å (***β*-1.40**). Displacement ellipsoids are set at 50% probability level and hydrogen atoms are omitted for clarity.

The topotactic chemistry of gold also includes the X-ray induced SC-SC reduction of the crown ether complex [K(18-crown-6)][$AuCl_4$] to [K(18-crown-6)][$AuCl_2$].[72] This process is irreversible,

and also undergoes a space group change from $P\bar{1}$ to $C2/c$. These are rare examples of polymorph-to-polymorph transitions within the single-crystalline state, and help demonstrate the rich potential of gold in solid state organometallic chemistry.

Other examples of group XI solid state chemistry include examples of ligand substitutions with solvent suspensions of MOF-supported copper(I) complexes,[73, 74] and vapochromic metal chain complexes such as $\{Tl[Au(C_6Cl_5)_2])_n\}$ which demonstrate that the coordination of volatile compounds to metal ions alters the M···M interactions.[75]

Despite the numerous examples discussed in section 1.1, there is still much left to be explored for the *in crystallo* chemistry of the coinage metals. Chapter 3 of this thesis shall report the application of a group XI system in *in crystallo* transformations.

1.2 Solution-state catalytic alkyne transformations with gold(I)

Gold(I) complexes have recently emerged as excellent catalysts (selective, high yielding, mild conditions)[76] in transformations of alkynes due to their ability to activate bound ligands to nucleophilic attack, even with traditionally poor nucleophiles such as water and methanol.[77, 78] A common proposed intermediate for the mechanism of these processes are gold(I) *π*-alkyne complexes, for example in the gold(I) catalysed reaction of methanol and propyne (Scheme 1.7).[77, 79-81] For this mechanism catalysis is initiated by coordination of propyne to the cationic gold(I) complex generated *in situ* by the protonolysis of $[(Ph_3P)Au(CH_3)]$ with methanesulfonic acid, to give the *π*-alkyne intermediate **A**. This then proceeds with associative attack of the methanol (**B**) and 1,3-hydrogen migration (**D**), as calculated by DFT. Finally, ligand exchange with propyne yields 2-methyoxypropene and returns intermediate **A**.

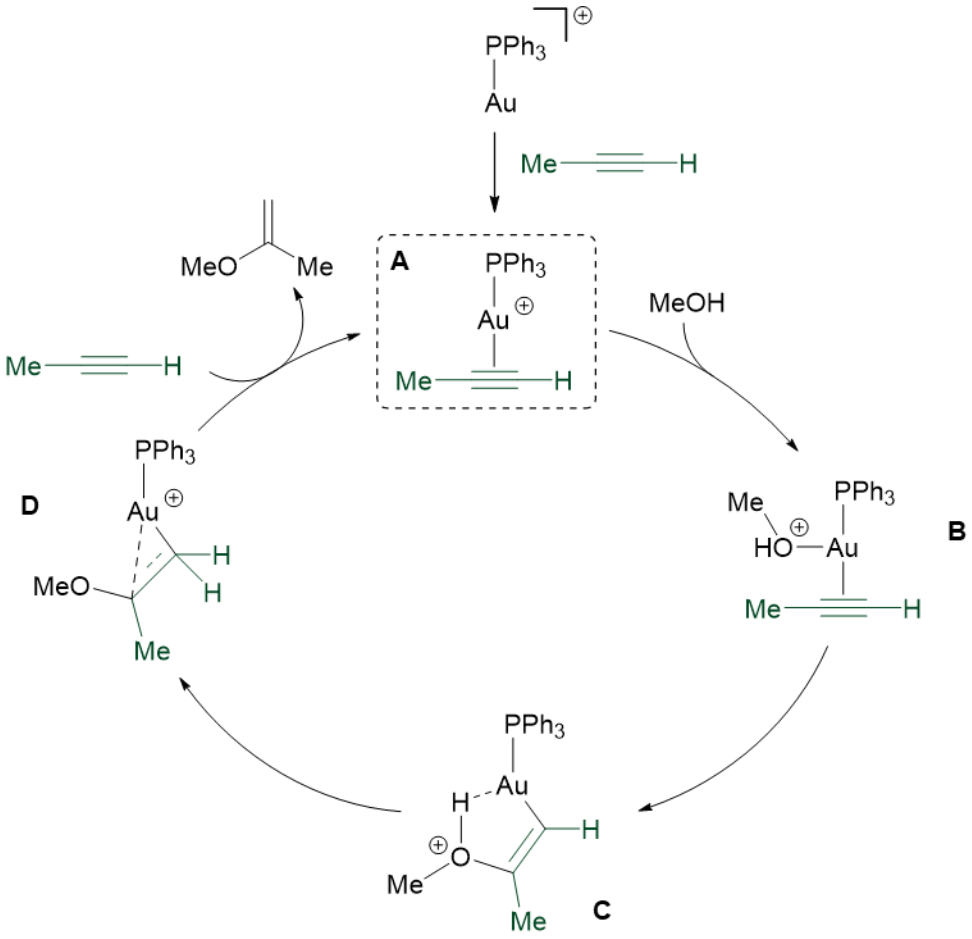

Scheme 1.7 The proposed mechanism for the reaction of methanol and propyne *via* a gold(I) *π*-alkyne intermediate (A).

There are several gold(I) *π*-alkyne complexes structurally characterised which often are supported by auxiliary ligands such as NHCs (*N*-heterocyclic carbenes).[82-84] This includes [(IPr)Au(η^2-cyclooctyne)][SbF_6] (IPr = 1,3-bis(2,6-diisoprop-ylphenyl)imidazol-2-ylidene), which is a proposed intermediate in the gold catalysed isomerisation of cyclooctyne to ring-fused bicyclic alkenes.[85] The structure of [Au(EtC≡CEt)Cl], free from a supporting auxiliary ligand, is also known and is stabilised by Au···Au (3.36260(15) Å) contacts.[86] Despite these stabilising aurophilic interactions, [Au(EtC≡CEt)Cl] decomposes at room temperature even in the solid state. Such instability is also observed in other gold(I) *π*-alkyne complexes, for example [Au(cyclododecyne)Cl] and even the NHC-supported [(IPr)Au(cyclododecyne)][SbF_6] decompose even in the solid state above 0 and –20 °C respectively.[87] [(SIPr)Au(EtC≡CEt)][BF_4] (SIPr = 1,3-bis(2,6-diisopopylphenyl)-imidazolidene), a catalyst in

the hydrofluorination of alkynes, decomposes in solution but is stable in the solid state for 2 weeks.[88]

Russell and coworkers described the synthesis of the first dicoordinate gold *π*-alkyne compounds also bearing a phosphine ligand, [(^{t}Bu$_3$P)Au(η^2-RC≡CR')][SbF$_6$] (R = Me, SiMe$_3$ (**1.46**); R' = ^{t}Bu).[89] In the case of R = SiMe$_3$, the reaction continued to form a trinuclear *σ*,*π*-acetylide species, wherein a bridging ^{t}BuC≡C$^-$ ligand is bound to two gold centres in a three-centre-two-electron fashion and the third gold centre via *π*-coordination (**1.47**; Figure 1.17). Similar desilylation reactivity with bis(trimethylsilyl)acetylene yields the *σ*,*π*-tetragold acetylide complex [((^{t}Bu$_3$P)Au)$_4$(C$_2$)][SbF$_6$]$_2$, which displays two gold centres bound to the alkyne in a *σ*-manner whilst the other two gold centres *π*-coordinate. Numerous other multinuclear *σ*,*π*-acetylide complexes are known,[90-92] some of which have been reported as a decomposition product of the corresponding gold *π*-alkyne, for instance in the case of [(IPr)Au(HC≡CPh)][SbF$_6$] which forms the dinuclear *σ*,*π*-complex upon warming to 0 °C.[93]

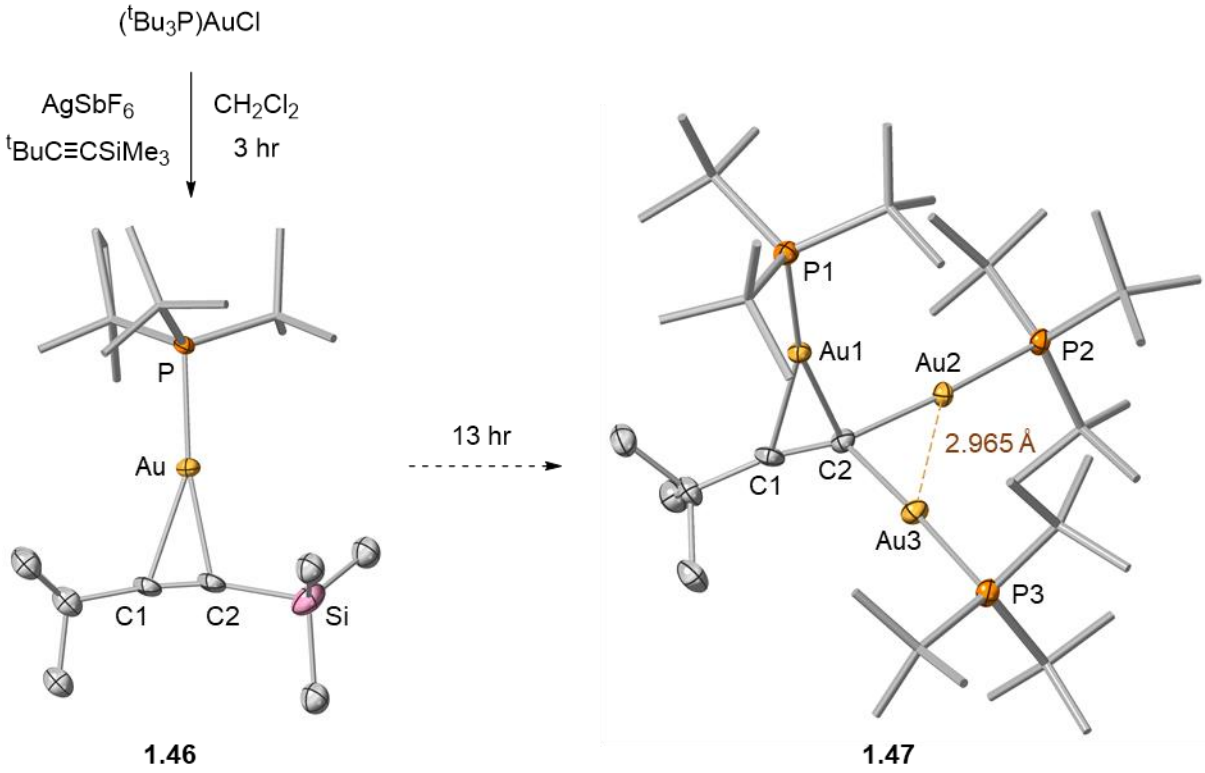

Figure 1.17 Synthesis of the dicoordinate gold(I) alkyne complex **1.46** and onward reactivity to the *σ,π*-trigold acetylide. Note the aurophilic interaction, Au2···Au3. Displacement ellipsoids are set at 50% probability level. [SbF$_6$]$^-$ anions and hydrogen are atoms omitted for clarity.

Whilst there are examples of *σ*,*π*-acetylide complexes being active in catalysis,[91, 94, 95] in the [(^{t}BuXPhos)Au(NCMe)][X] (^{t}BuXPhos = 2-di-*tert*-butylphosphino-2′,4′,6′-tri-*iso*-propylbiphenyl; X = OTf, NTf_2, BF_4, SbF_6, $BAr^F{}_4$) catalysed reaction of phenylacetylene with 2-methylstyrene, the corresponding *σ*,*π*-digold(I) complex is believed to be the deactivation product.[96] Demonstrating the importance of the anion used, the greatest conversion was observed when $[X]^- = [BAr^F{}_4]^-$, as the bulky and weakly coordinating nature of the anion decreases the stability of the corresponding Brønsted acid formed upon deprotonation of the terminal alkyne, thus discouraging formation of the *σ*,*π*-acetylide. Further examples of multinuclear *σ*,*π*- complexes as unreactive resting states which decrease catalyst efficiency have been reported,[97, 98] and therefore the focus of this section shall be on the active *π*-alkyne compounds.

In contrast to the several examples featuring substituted alkynes, there are no reported gold(I) complexes supporting the simplest of all alkynes, acetylene, despite acetylene being an important C_2 chemical feedstock in various transformations including cyclopropanation and aryloxyvinylation.[99, 100] The isolation of such intermediates is challenging due to weak metal-ligand interactions, similar to that of metal-ethylene compounds. Classically, alkenes and alkynes bind to metal centres *via* a mixture of electrostatic interactions and synergic bonding. The latter is described by the Dewar-Chatt-Duncanson model, which is a combination of *σ*-donation from the alkyne and *π*-backbonding from the metal into the $\pi^*_{C\equiv C}$ antibonding orbital (Figure 1.18).[101, 102] However, a d^{10} cation M(I) (M = Cu, Ag, Au) has relatively contracted filled metal *d*-orbitals, resulting in poor overlap between the gold 5*d* and the antibonding $\pi^*_{C\equiv C}$ orbitals, and thus reduced *π*-backbonding.[103]

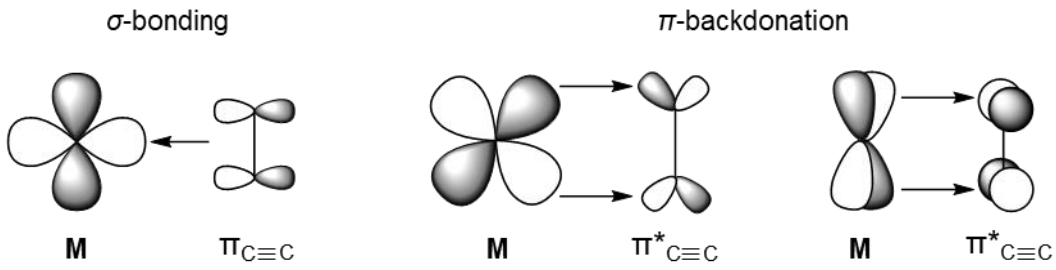

Figure 1.18 The classical Dewar-Chatt-Duncanson model of metal-alkyne bonding for a d^n metal, showing the *σ*-donation from a *π*-orbital of the alkyne to a vacant orbital of the metal and *π*-backbonding from a filled metal *d*-orbital into the $\pi^*_{C\equiv C}$ antibonding orbital.

Whilst there have been no gold(I) acetylene complexes crystallographically or even spectroscopically described, there are several examples of tri- and tetracoordinate *π*-acetylene complexes of the other coinage metals (Figure 1.19 A).[104-107] Whilst the majority of these complexes are relatively stable under inert conditions, $[Ag(C_2H_2)_3][Al(OC(CF_3)_3)_4]$ loses acetylene above –20 °C even in the solid state.[108] Dias reported several copper(I) and silver(I) *π*-acetylene complexes supported by scorpionate ligands, including $[(H_2C(3,5\text{-}(CH_3)_2Pz)_2)Ag(\eta^2\text{-}C_2H_2)][SbF_6]$ (**1.48**; Figure 1.19 B), and explored their relative stabilities under a variety of conditions.[109] Whilst these reported complexes were stable in the solid state under an acetylene atmosphere, tridentate complexes featuring bis(pyrazolyl) ligands experienced partial C_2H_2 dissociation under nitrogen and complete dissociation when placed under vacuum both in solution and the solid state, which in most cases is reversible and can regenerate the acetylene complexes when placed back under an atmosphere of acetylene. In comparison, several of the four-coordinate tris(pyrazolyl)borate compounds that were explored by Dias were remarkably stable in air for 16 hours in both solution and the solid state. Despite this stability with copper(I) and silver(I), Dias also noted that all attempts to make the gold(I) analogues led to rapid decomposition in solution, demonstrating the elusive nature of gold(I) *π*-acetylene complexes.

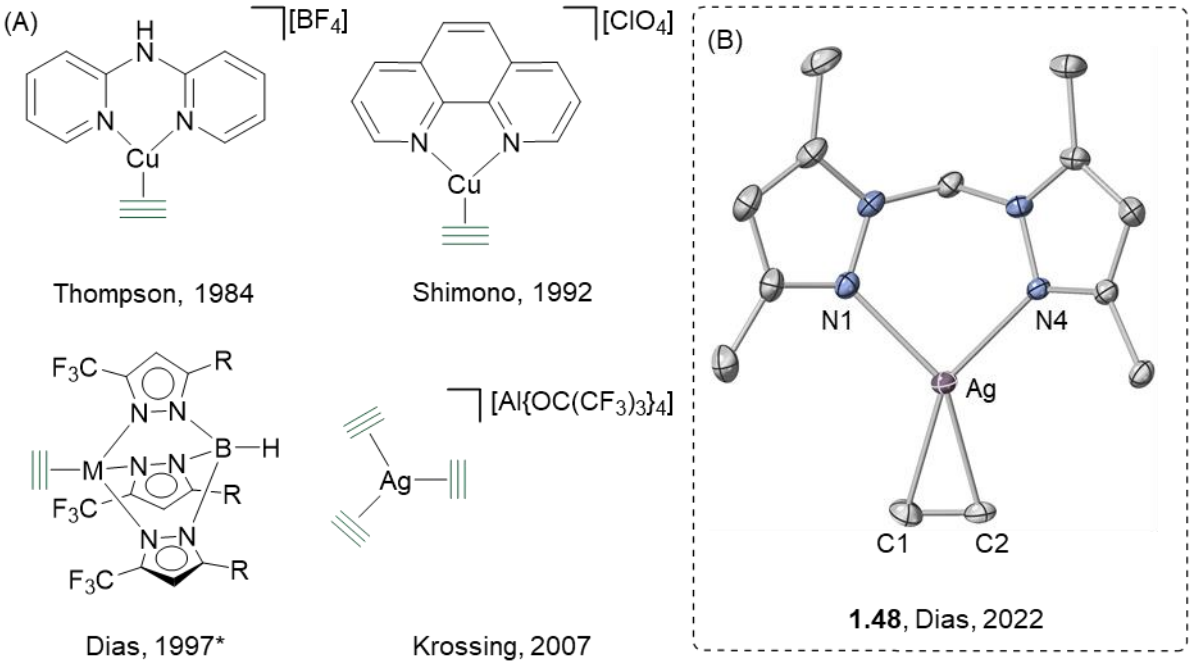

Figure 1.19 (A) Structurally characterised group XI *π*-acetylene complexes. * M = Cu, Ag; R = Ph, CF_3. (B) The cationic structure of complex **1.48**. The $[SbF_6]^-$ anion and hydrogen atoms are omitted for clarity.

The synthesis of the first gold(I) *π*-acetylene complex would be of fundamental interest to this field due to the valuable insight it would provide on the nature of such intermediates and their metal-ligand bonding interactions, a concept which shall be explored further in chapter 3.

1.3 Iridium pincer complexes for *in crystallo* chemistry

Phosphorus based pincer ligands are of great interest in organometallic chemistry due to their ability to stabilise a variety of oxidation states *via* the chelating phosphine donors and enforce certain geometries due to their rigid *mer*-tridentate structure.[110] They also provide steric and electronic control by altering the phosphine substituents, the ligand backbone, and the central atom (E) (Scheme 1.8 A). Although a wide variety of these ligands are known, this discussion shall focus on the PONOP (E = N, X = O) and POCOP (E = C, X = O) type ligands. Chapter 4 of this thesis focuses on iridium pincer complexes, which have been widely studied for C–H activation, for instance in the dehydrogenation of alkanes to alkenes using iridium(I) POCOP catalysts,[111, 112] which has even been shown to occur under continuous flow conditions in the solid state using a supported catalyst (SMOC) (**1.49**; Scheme 1.8 B).[113]

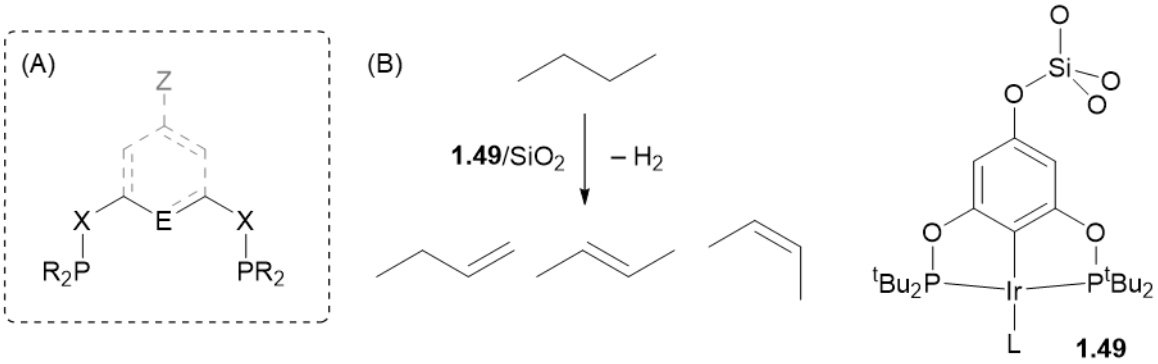

Scheme 1.8 (A) The generic structure of phosphorus pincer ligands. Common E = C, N; X = O, $(CH_2)_n$, NH; Z = H, alkyl, aryl, halogen. (B) The dehydrogenation of butane *via* an iridium(I) POCOP catalyst (**1.49**; L = C_2H_4, CO). This catalyst is both air stable and thermally stable up to 340 °C. SiO_4 represents the silica surface.

Brookhart and colleagues utilised these ligand scaffolds to isolate the iridium(III) methyl hydride complex [(^{tBu}PONOP)Ir(Me)(H)][BAr^F_4] (**1.50**; ^{tBu}PONOP = (di-*tert*-butylphosphino)-2,6-dioxypyridine) from the reaction of [(^{tBu}PONOP)Ir(Me)] with [$H(OEt_2)_2$][BAr^F_4] (Scheme 1.9 A). This was the first crystallographically characterised example of an iridium(III) alkyl hydride species, which are proposed intermediates in iridium(I) alkane dehydrogenation catalysis such as that described above. As evidenced by EXSY (exchange spectroscopy) NMR experiments, complex **1.50** undergoes rapid site exchange of the Ir–H and Ir–Me *via* the transient iridium(I) *σ*-methane complex [(^{tBu}PONOP)Ir(CH_4)][BAr^F_4] in solution at –105 °C ($\Delta G^{\ddagger}$ = 9.3 kcal mol^{-1}).[114] Further verification for a *σ*-methane intermediate comes from the reaction of complex **1.50** with D_2, which loses methane to form an iridium(III) dihydride complex with evidence of deuterium scrambling into the Ir–Me, which is further supported by DFT calculations.[115] Similar reactivity with the rhodium analogue results in the formation of one of the few reported *σ*-methane complexes, [(^{tBu}PONOP)Rh(CH_4)][BAr^F_4] (**1.51**, Scheme 1.9 B), which can be observed using NMR spectroscopy at –110 °C in $CDCl_2F$.[23] However, at 298 K complex **1.50**, *via* reductive coupling, and complex **1.51** rapidly lose methane in the solution-state, leading to decomposition.

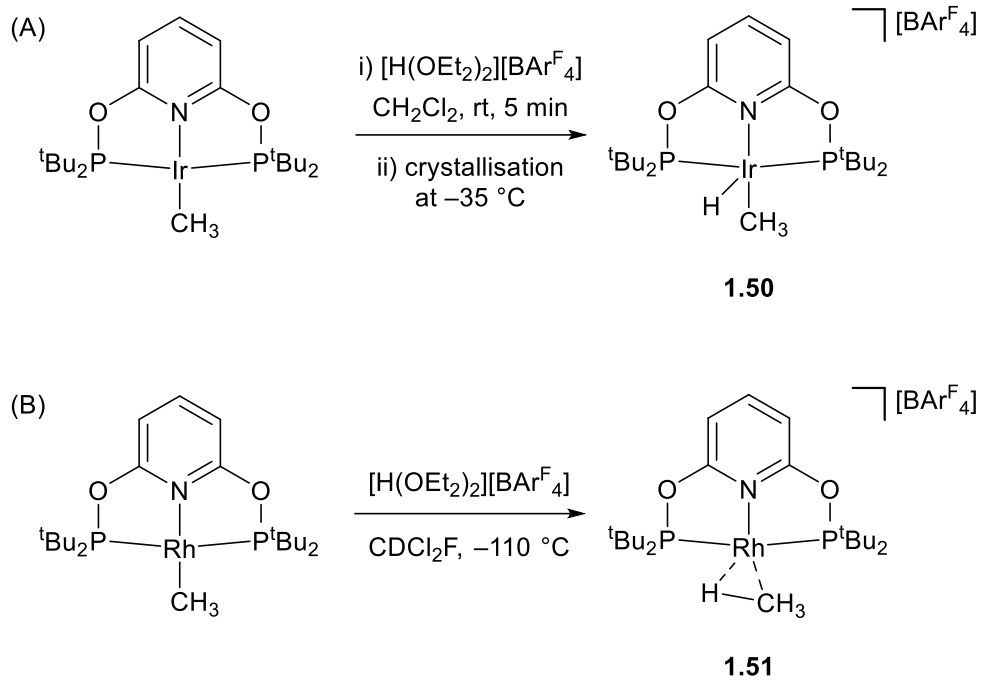

Scheme 1.9 The synthesis of (A) complex **1.50** from an iridium(I) methyl precursor and (B) the *σ*-methane complex, **1.51**.

As discussed in section 1.1, pincer ligand systems have the potential to undergo SC-SC reactivity, as evidenced by the work of Brookhart (ligand substitution of [(^{Ar}POCOP)Ir(N_2)])[17] and Weller (addition of hydrogen to [(^{iPr}PONOP)Ir(C_3H_6)][BAr^F_4] and *in crystallo* reactivity of [(^{iPr}PONOP)Mn($CO)_2$(THF)][BAr^F_4]).[58, 59] Another recent example includes a highly reactive iridium(I) methylidene complex (**1.52**), which is synthesised from the same iridium(I) methyl precursor as complex **1.50**. The SC-SC reactivity of the electrophilic Ir=CH_2 was probed with H_2, CO and NH_3 (Scheme 1.10).[116]

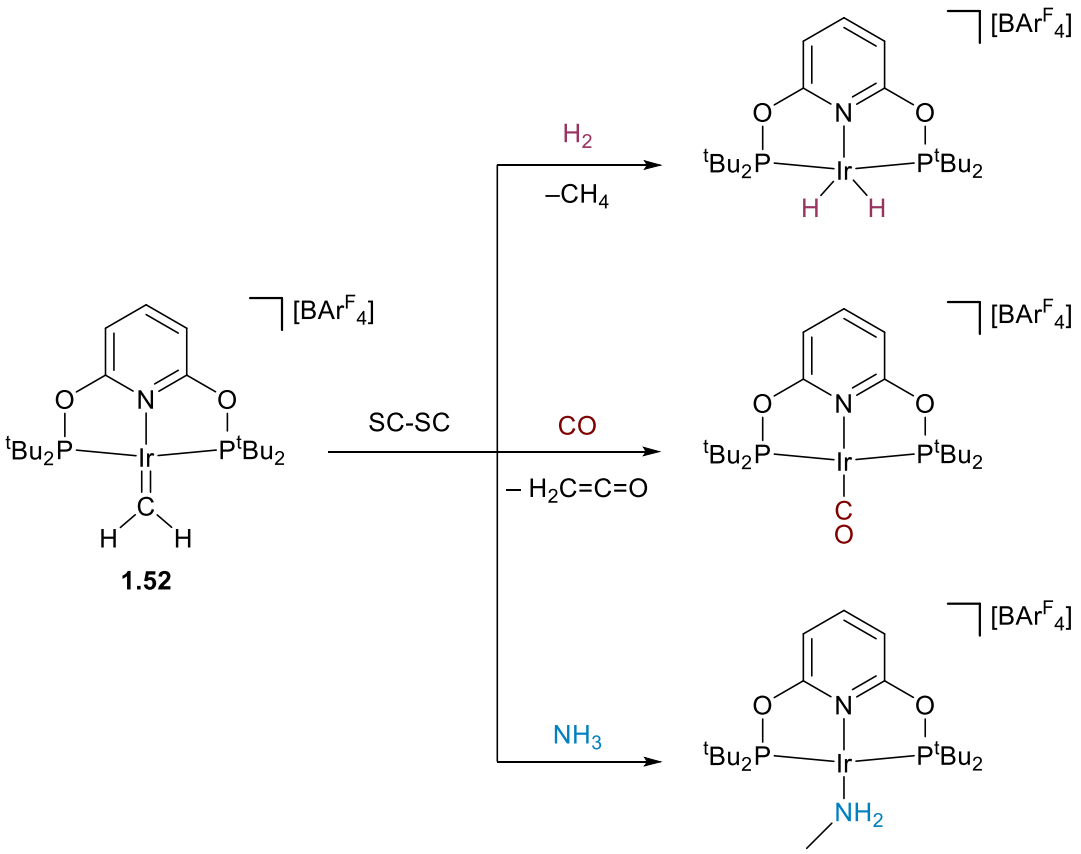

Scheme 1.10 The SC-SC reactivity of a highly reactive methylidene complex, **1.52**.

This prompted Weller and coworkers to investigate the SC-SC reactivity of Brookhart's system **1.50**, which crystallises in two different, separable, space groups ($P2_1/n$ and $C2/c$) and is stable for months at 298 K in the solid state, and remarkably even stable in a suspension of degassed water after 1 week. When placed under high vacuum (5×10^{-5} mbar) at 80 °C, complex **1.50** liberates methane to yield a reactive iridium(III) cyclometalated complex, **1.53** (Figure 1.20).[117] Complex **1.53** activates methane at 80 °C, suggesting that complex **1.53** can reversibly reductively eliminate the cyclometalated ^{t}Bu group to form a transient 14 electron iridium(I) [(^{tBu}PONOP)Ir][BAr$^F_4$] species which then rapidly reacts with methane, as supported by DFT calculations and deuterium labelling studies. However, this results in a pressure dependent equilibrium between complex **1.53** and the regenerated complex **1.50**, showing that C–H activation using this system is hindered by competition with the relatively stable cyclometalated complex. Complex **1.53** also dehydrogenates ethane, resulting in the formation of the known ethylene and dihydride complexes[118] in a 1:1 mixture.

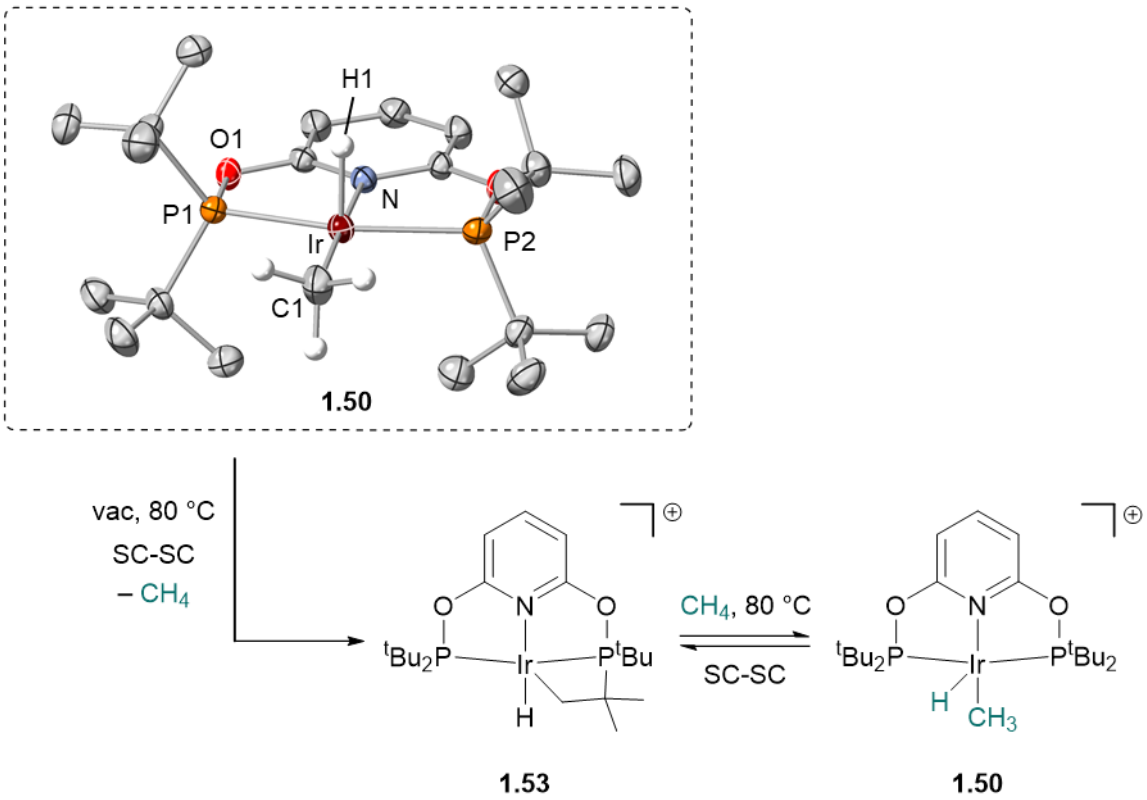

Figure 1.20 The cationic structure of **1.50** in the $P2_1/n$ space group, as determined by single-crystal neutron diffraction, and the *in crystallo* activation of methane *via* an iridium(III) cyclometalated complex, **1.53**. Select hydrogen atoms and $[BAr^F{}_4]^-$ anion are omitted for clarity. Displacement ellipsoids are set at 50% probability level.

In this context, the aforementioned 'cyclometalation' of ligands describes the C–H activation of the ligand *via* a transition metal to form a metallacycle containing a new M–C bond. Cyclometalation is often reversible, and so this ligand cooperativity can mediate reactivity by forming these metallacycle intermediates.[119] Cyclometalation can occur by activation of the substituents, as is seen in the example described above by Weller and coworkers, or the ligand backbone in the case of pincer ligands which contain acidic CH_2 and NH moieties as exemplified by Shaw and Milstein.[120-123] Aside from the aforementioned complex **1.53**, other iridium(III) cyclometalated complexes are known with POCOP, PCP and PNP pincer ligands with ^{t}Bu and *neo*-pentyl substituents,[124-127] and have demonstrated onward reactivity. For instance, the subsequent addition of CO to a cyclometalated *neo*-pentyl complex forms the corresponding iridium(I) CO adduct with the *neo*-pentyl substituent no longer cyclometalated.[128]

Chapter 4 shall continue to explore the solution and solid state chemistry of well-defined iridium pincer complexes by investigating a new iridium pincer system which does not cyclometalate the ligand, therefore providing a contrast to the chemistry described by Weller.

1.4 Conclusion and Thesis Aims

This chapter has provided a summary of existing literature on the solid-state chemistry of organometallic complexes, with a key focus on single-crystal to single-crystal (SC-SC) transformations due to their particular relevance to the work presented in this thesis. The fundamentals of gold(I) π-alkyne catalysis and group IX pincer complexes have also been discussed to provide background to the work presented in chapters 3 and 4 of this thesis.

The examples described in this chapter highlight the numerous advantages of applying solid-state techniques to organometallic chemistry. However, despite these clear advantages, organometallic research is dominated by solution-state reactivity. The overarching aim of this thesis is to expand SMOM chemistry beyond that of rhodium(I) σ-alkane complexes to other late transition metals, specifically iridium, silver and gold complexes, and compare the solution and solid-state behaviour of these target organometallic systems in order to demonstrate the utility of SMOM chemistry.

1.5 References

1. J. F. Hartwig, *Organotransition Metal Chemistry. From Bonding to Catalysis*, University Science Books: Sausalito, 2010.
2. C. Vogt and B. M. Weckhuysen, *Nat. Rev. Chem.*, 2022, **6**, 89-111.
3. C. R. H., *Chem. Rev.*, 2015, **115**, 127-150.
4. N. J. Coville and L. Cheng, *J. Organomet. Chem.*, 1998, **571**, 149-169.
5. R. Kanega, N. Onishi, S. Tanaka, H. Kishimoto and Y. Himeda, *J. Am. Chem. Soc.*, 2021, **143**, 1570-1576.
6. G. A. Olah, *Angew. Chem. Int. Ed.* 2005, **44**, 2636-2639.
7. C. Copéret, *Nat. Energy*, 2019, **4**, 1018-1024.
8. R. J. Young, M. T. Huxley, E. Pardo, N. R. Champness, C. J. Sumby and C. J. Doonan, *Chem. Sci.*, 2020, **11**, 4031-4050.
9. J. Albalad, C. J. Sumby, D. Maspoch and C. J. Doonan, *CrystEngComm*, 2021, **23**, 2185-2195.
10. J.-L. Do and T. Friščić, *ACS Cent. Sci.*, 2017, **3**, 13-19.
11. K. A. Reid and D. C. Powers, *Chem. Comm.*, 2021, **57**, 4993-5003.
12. F. Mark Chadwick, A. I. McKay, A. J. Martinez-Martinez, N. H. Rees, Tobias Krämer, S. A. Macgregor and A. S. Weller, *Chem. Sci.*, 2017, **8**, 6014-6029.

13. A. J. Martínez-Martínez, B. E. Tegner, A. I. McKay, A. J. Bukvic, N. H. Rees, G. J. Tizzard, S. J. Coles, M. R. Warren, S. A. Macgregor and A. S. Weller, *J. Am. Chem. Soc.*, 2018, **140**, 14958-14970.
14. C. Bianchini, M. Peruzzini and F. Zanobini, *Organometallics*, 1991, **10**, 3415-3417.
15. C. Bianchini, S. Moneti, M. Peruzzini and F. Vizza, *Inorg. Chem.*, 1997, **36**, 5818-5825.
16. C. Bianchini, P. Frediani, M. Graziani, J. Kaspar, A. Meli, M. Peruzzini and F. Vizza, *Organometallics*, 1993, **12**, 2886-2887.
17. Z. Huang, P. S. White and M. Brookhart, *Nature*, 2010, **465**, 598-601.
18. A. Das, J. H. Reibenspies, Y.-S. Chen and D. C. Powers, *J. Am. Chem. Soc.*, 2017, **139**, 2912-2915.
19. J. Sun, J. Abbenseth, H. Verplancke, M. Diefenbach, B. de Bruin, D. Hunger, C. Würtele, J. van Slageren, M. C. Holthausen and S. Schneider, *Nat. Chem.*, 2020, **12**, 1054-1059.
20. A. Das, C.-H. Wang, G. P. Van Trieste III, C.-J. Sun, Y.-S. Chen, J. H. Reibenspies and D. C. Powers, *J. Am. Chem. Soc.*, 2020, **142**, 19862-19867.
21. J. M. Smith, *Prog. Inorg. Chem.*, 2014, **58**, 417-470.
22. S. D. Pike, A. L. Thompson, A. G. Algarra, D. C. Apperley, S. A. Macgregor and A. S. Weller, *Science*, 2012, **337**, 1648-1651.
23. W. H. Bernskoetter, C. K. Schauer, K. I. Goldberg and M. Brookhart, *Science*, 2009, **326**, 553-556.
24. G. E. Ball, *Spectrosc. Prop. Inorg. Organomet. Compd.*, 2010, **41**, 262-287.
25. J. D. Watson, L. D. Field and G. E. Ball, *Nat. Chem.*, 2022, **14**, 801-804.
26. J. D. Watson, L. D. Field and G. E. Ball, *J. Am. Chem. Soc.*, 2022, **144**, 17622-17629.
27. S. A. Bartlett, N. A. Besley, A. J. Dent, S. Diaz-Moreno, J. Evans, M. L. Hamilton, M. W. D. Hanson-Heine, R. Horvath, V. Manici, X.-Z. Sun, M. Towrie, L. Wu, X. Zhang and M. W. George, *J. Am. Chem. Soc.*, 2019, **141**, 11471-11480.
28. S. Geftakis and G. E. Ball, *J. Am. Chem. Soc.*, 1998, **120**, 9953-9954.
29. Bruce K. McNamara, Jake S. Yeston, Robert G. Bergman and C. Bradley Moore, *J. Am. Chem. Soc.*, 1999, **121**, 6437-6443.
30. C. Hall and R. N. Perutz, *Chem. Rev.*, 1996, **96**, 3125-3146.
31. E. A. Cobar, R. Z. Khaliullin, R. G. Bergman and M. Head-Gordon, *Proc. Nat. Acad. Sci. USA*, 2007, **104**, 6963-6968.
32. A. J. Cowan, P. Portius, H. K. Kawanami, O. S. Jina, D. C. Grills, X.-Z. Sun, J. McMaster and M. W. George, *Proc. Nat. Acad. Sci. USA*, 2007, **104**, 6933-6938.
33. Branko Ruscic, Maritoni Litorja and R. L. Asher, *J. Phys. Chem. A*, 1999, **103**, 8625-8633.
34. S. D. Pike, F. M. Chadwick, N. H. Rees, M. P. Scott, A. S. Weller, T. Krämer and S. A. Macgregor, *J. Am. Chem. Soc.*, 2015, **137**, 820-833.
35. A. I. McKay, A. J. Bukvic, B. E. Tegner, A. L. Burnage, A. J. Martínez-Martínez, N. H. Rees, S. A. Macgregor and A. S. Weller, *J. Am. Chem. Soc.*, 2019, **141**, 11700-11712.
36. A. J. Bukvic, A. L. Burnage, G. J. Tizzard, A. J. Martínez-Martínez, A. I. McKay, N. H. Rees, B. E. Tegner, T. Krämer, H. Fish, M. R. Warren, S. J. Coles, S. A. Macgregor and A. S. Weller, *J. Am. Chem. Soc.*, 2021, **143**, 5106-5120.
37. F. M. Chadwick, N. H. Rees, A. S. Weller, T. Krämer, M. Iannuzzi and S. A. Macgregor, *Angew. Chem. Int. Ed.*, 2016, **55**, 3677-3681.
38. L. R. Doyle, M. R. Galpin, S. K. Furfari, B. E. Tegner, A. J. Martínez-Martínez, A. C. Whitwood, S. A. Hicks, G. C. Lloyd-Jones, S. A. Macgregor and A. S. Weller, *Organometallics*, 2022, **41**, 284-292.
39. T. M. Boyd, B. E. Tegner, G. J. Tizzard, A. J. Martínez-Martínez, S. E. Neale, M. A. Hayward, S. J. Coles, S. A. Macgregor and A. S. Weller, *Angew. Chem. Int. Ed.*, 2020, **59**, 6177-6181.
40. F. M. Chadwick, T. Krämer, T. Gutmann, N. H. Rees, A. L. Thompson, A. J. Edwards, G. Buntkowsky, S. A. Macgregor and A. S. Weller, *J. Am. Chem. Soc.*, 2016, **138**, 13369-13378.

41. S. K. Furfari, B. E. Tegner, A. L. Burnage, L. R. Doyle, A. J. Bukvic, S. A. Macgregor and A. S. Weller, *Chem. Eur. J.*, 2021, **27**, 3177-3183.
42. S. D. Pike, T. Krämer, N. H. Rees, S. A. Macgregor and A. S. Weller, *Organometallics*, 2015, **34**, 1487-1497.
43. A.-K. Jungton, C. Herwig, T. Braun and C. Limberg, *Chem. Eur. J.*, 2012, **18**, 10009-10013.
44. R. Koelliker and D. Milstein, *J. Am. Chem. Soc.*, 1991, **113**, 8524-8525.
45. E. Khaskin, M. A. Iron, L. J. W. Shimon, J. Zhang and D. Milstein, *J. Am. Chem. Soc.*, 2010, **132**, 8542-8543.
46. R. M. Brown, J. B. Garcia, J. Valjus, C. J. Roberts, H. M. Tuononen, M. Parvez and R. Roesler, *Angew. Chem. Int. Ed.*, 2015, **54**, 6274-6277.
47. A. J. Martínez-Martínez, C. G. Royle, S. K. Furfari, K. Suriye and A. S. Weller, *ACS Catal.*, 2020, **10**, 1984-1992.
48. D. Blazina, S. B. Duckett, T. K. Halstead, C. M. Kozak, R. J. K. Taylor, M. S. Anwar, J. A. Jones and H. A. Carteret, *Magn. Reson. Chem.*, 2005, **43**, 200-208.
49. S. B. Duckett and N. J. Wood, *Coord. Chem. Rev.*, 2008, **252**, 2278-2291.
50. G. Buntkowsky, F. Theiss, J. Lins, Y. A. Miloslavina, L. Wienands, A. Kiryutin and A. Yurkovskaya, *RSC Adv.*, 2022, **12**, 12477-12506.
51. M. R. Gyton, C. G. Royle, S. K. Beaumont, S. B. Duckett and A. S. Weller, *J. Am. Chem. Soc.*, 2023, **145**, 2619-2629.
52. M. A. Sajjad, S. A. Macgregor and A. S. Weller, *Faraday Discuss.*, 2023, **244**, 222-240.
53. I. J. Vitórica-Yrezábal, S. Libri, J. R. Loader, G. M. Espallargas, M. Hippler, A. J. Fletcher, S. P. Thompson, J. E. Warren, D. Musumeci, M. D. Ward and L. Brammer, *Chem. Eur. J.*, 2015, **21**, 8799-8811.
54. Y. Montet, P. Amara, A. Volbeda, X. Vernede, E. C. Hatchikian, M. J. Field, M. Frey and J. C. Fontecilla-Camps, *Nat. Struct. Biol.*, 1997, **4**, 523-526.
55. D. A. Whittington, A. C. Rosenzweig, C. A. Frederick and S. J. Lippard, *Biochem.*, 2001, **40**, 3479-3482.
56. S. J. Lee, M. S. McCormick, S. J. Lippard and U.-S. Cho, *Nature*, 2013, **494**, 380-384.
57. A. J. Martínez-Martínez, N. H. Rees and A. S. Weller, *Angew. Chem. Int. Ed.*, 2019, **58**, 16873-16877.
58. C. G. Royle, L. Sotorrios, M. R. Gyton, C. N. Brodie, A. L. Burnage, S. K. Furfari, A. Marini, M. R. Warren, S. A. Macgregor and A. S. Weller, *Organometallics*, 2022, **41**, 3270-3280.
59. J. C. Goodall, M. Arif Sajjad, E. A. Thompson, S. J. Page, A. M. Kerrigan, H. T. Jenkins, J. M. Lynam, S. A. Macgregor and A. S. Weller, *Chem. Comm.*, 2023, **59**, 10749-10752.
60. B. L. Nannenga and T. Gonen, *Nat. Methods*, 2019, **16**, 369-379.
61. R. J. A., E. D. S. and G. T., *Curr Opin Struct Biol.*, 2017, **46**, 79-86.
62. S. D. Pike and A. S. Weller, *Dalton Trans.*, 2013, **42**, 12832-12835.
63. A. I. McKay, A. J. Martínez-Martínez, H. J. Griffiths, N. H. Rees, J. B. Waters, A. S. Weller, T. Krämer and S. A. Macgregor, *Organometallics*, 2018, **37**, 3524-3532.
64. I. Krossing, *Chem. Eur. J.*, 2001, **7**, 490-502.
65. L. R. Doyle, E. A. Thompson, A. L. Burnage, A. C. Whitwood, H. T. Jenkins, S. A. Macgregor and A. S. Weller, *Dalton Trans.*, 2022, **51**, 3661-3665.
66. A. Noonikara-Poyil, H. Cui, A. A. Yakovenko, P. W. Stephens, R.-B. Lin, B. Wang, B. Chen and H. V. R. Dias, *Angew. Chem. Int. Ed.*, 2021, **60**, 27184-27188.
67. H. V. R. Dias, D. Parasar, A. A. Yakovenko, P. W. Stephens, Á. Muñoz-Castro, M. Vanga, P. Mykhailiuk and E. Slobodyanyuk, *Chem. Sci.*, 2024, **15**, 2019-2025.
68. E. A. Patrick, M. E. Bowden, J. D. Erickson, R. M. Bullock and B. L. Tran, *Angew. Chem. Int. Ed.*, 2023, **62**, e202304648.
69. H. Ito, M. Muromoto, S. Kurenuma, S. Ishizaka, N. Kitamura, H. Sato and T. Seki, *Nat. Commun.*, 2013, **4**.

70. S. H. Lim, M. M. Olmstead and A. L. Balch, *J. Am. Chem. Soc.*, 2011, **133**, 10229-10238.
71. S. H. Lim, M. M. Olmstead and A. L. Balch, *Chem. Sci.*, 2013, **4**, 311-318.
72. N. K. Sethi, A. C. Whitwood and D. W. Bruce, *Inorg. Chem.*, 2018, **57**, 13524-13532.
73. R. A. Peralta, M. T. Huxley, J. Albalad, C. J. Sumby and C. J. Doonan, *Inorg. Chem.*, 2021, **60**, 11775-11783.
74. M. Asgari, S. Jawahery, E. D. Bloch, M. R. Hudson, R. Flacau, B. Vlaisavljevich, J. R. Long, C. M. Brown and W. L. Queen, *Chem. Sci.*, 2018, **9**, 4579-4588.
75. E. J. Fernández, J. M. López-de-Luzuriaga, M. Monge, M. E. Olmos, J. Pérez, A. Laguna, A. A. Mohamed and J. John P. Fackler, *J. Am. Chem. Soc.*, 2003, **125**, 2022-2023.
76. H. Schmidbaur and A. Schier, *Organometallics*, 2010, **29**, 2-23.
77. J. H. Teles, S. Brode and M. Chabanas, *Angew. Chem. Int. Ed.*, 1998, **37**, 1415-1418.
78. E. Mizushima, K. Sato, T. Hayashi and M. Tanaka, *Angew. Chem. Int. Ed.*, 2002, **41**, 4563-4565.
79. V. Lavallo, G. D. Frey, S. Kousar, B. Donnadieu and G. Bertrand, *Proc. Nat. Acad. Sci. USA*, 2007, **104**, 13569-13573.
80. T. Lauterbach, A. M. Asiri and A. S. K. Hashmi, *Adv. Organomet. Chem.*, 2014, **62**, 261-297.
81. R. Dorel and A. M. Echavarren, *Chem. Rev.*, 2015, **115**, 9028-9072.
82. P. Schulte and U. Behrens, *Chem. Comm.*, 1998, 1633-1634.
83. A. Das, C. Dash, M. Yousufuddin, M. A. Celik, G. Frenking and H. V. R. Dias, *Angew. Chem. Int. Ed.*, 2012, **51**, 3940-3943.
84. M. M. Hansmann, F. Rominger, M. P. Boone, D. W. Stephan and A. S. K. Hashmi, *Organometallics*, 2014, **33**, 4461-4470.
85. A. Das, Y. Hua, M. Yousufuddin, T. R. Cundari, J. Jeon and H. V. R. Dias, *Eur. J. Inorg. Chem.*, 2016, **2016**, 995-1001.
86. J. Wu, P. Kroll and H. V. R. Dias, *Inorg. Chem.*, 2009, **48**, 423-425.
87. S. Flügge, A. Anoop, R. Goddard, W. Thiel and A. Fürstner, *Chem. Eur. J.*, 2009, **15**, 8558-8565.
88. Jennifer A. Akana, Koyel X. Bhattacharyya, Peter Müller and J. P. Sadighi, *J. Am. Chem. Soc.*, 2007, **129**, 7736-7737.
89. T. N. Hooper, Michael Green and C. A. Russell, *Chem. Comm.*, 2010, **46**, 2313-2315.
90. A. Grirrane, H. Garcia, A. Corma and E. Álvarez, *Chem. Eur. J.*, 2013, **19**, 12239-12244.
91. A. S. K. Hashmi, T. Lauterbach, P. Nösel, M. H. Vilhelmsen, M. Rudolph and F. Rominger, *Chem. Eur. J.*, 2013, **19**, 1059-1065.
92. A. Gómez-Suárez, S. Dupuy, A. M. Z. Slawin and S. P. Nolan, *Angew. Chem. Int. Ed.*, 2013, **52**, 938-942.
93. T. J. Brown and R. A. Widenhoefer, *Organometallics*, 2011, **30**, 6003-6009.
94. A. Grirrane, H. Garcia, A. Corma and E. Álvarez, *ACS Catal.*, 2011, **1**, 1647-1653.
95. Paul Ha-Yeon Cheong, Philip Morganelli, Michael R. Luzung, K. N. Houk and F. D. Toste, *J. Am. Chem. Soc.*, 2008, **130**, 4517-4526.
96. A. Homs, C. Obradors, D. Lebœuf and A. M. Echavarren, *Adv. Synth. Catal.*, 2014, **356**, 221-228.
97. C. Obradors and A. M. Echavarren, *Chem. Eur. J.*, 2013, **19**, 3547-3551.
98. A. Simonneau, F. Jaroschik, D. Lesage, M. Karanik, R. Guillot, M. Malacria, J.-C. Tabet, J.-P. Goddard, L. Fensterbank, V. Gandon and Y. Gimbert, *Chem. Sci.*, 2011, **2**, 2417-2422.
99. D. Scharnagel, I. Escofet, H. Armengol-Relats, M. E. d. Orbe, J. N. Korber and A. M. Echavarren, *Angew. Chem. Int. Ed.*, 2020, **59**, 4888-4891.
100. T. Medina-Gil, A. Sadurní, L. A. Hammarback and A. M. Echavarren, *ACS Catal.*, 2023, **13**, 10751-10755.
101. M. J. S. Dewar, *Bull. Soc. Chim Fr.*, 1951, **18**, C71-79.
102. J. Chatt and L. A. Duncanson, *J. Chem. Soc.*, 1953, 2939-2947.

103. E. Soriano and J. Marco-Contelles, *Structure, Bonding, and Reactivity of Reactant Complexes and Key Intermediates*, Springer, Berlin, Heidelberg, 2011.
104. J. S. Thompson and J. F. Whitney, *Inorg. Chem.*, 1984, **23**, 2813-2819.
105. M. Munakata, S. Kitagawa, I. Kawada, M. Maekawa and H. Shimono, *J. Chem. Soc., Dalton Trans.*, 1992, 2225-2230.
106. H. V. Rasika Dias, Ziyun Wang and W. Jin, *Inorg. Chem.*, 1997, **36**, 6205-6215.
107. A. Noonikara-Poyil, A. Muñoz-Castro and H. V. R. Dias, *Molecules*, 2022, **27**, 16.
108. A. Reisinger, N. Trapp, I. Krossing, S. Altmannshofer, V. Herz, M. Presnitz and W. Scherer, *Angew. Chem. Int. Ed.*, 2007, **46**, 8295-8298.
109. A. Noonikara-Poyil, S. G. Ridlen, I. Fernández and H. V. R. Dias, *Chem. Sci.*, 2022, **13**, 7190-7203.
110. D. Morales-Morales, *Rev. Soc. Quim. Mex.*, 2004, **48**, 338-346.
111. Inigo Göttker-Schnetmann, Peter White and M. Brookhart, *J. Am. Chem. Soc.*, 2004, **126**, 1804-1811.
112. D. Morales-Morales, R. o. Redón, C. Yung and C. M. Jensen, *Inorg. Chim. Acta*, 2004, **357**, 2953-2956.
113. B. Sheludko, M. T. Cunningham, A. S. Goldman and F. E. Celik, *ACS Catal.*, 2018, **8**, 7828-7841.
114. W. H. Bernskoetter, S. K. Hanson, S. K. Buzak, Z. Davis, P. S. White, R. Swartz, K. I. Goldberg and M. Brookhart, *J. Am. Chem. Soc.*, 2009, **131**, 8603-8613.
115. J. Campos, S. Kundu, D. R. Pahls, M. Brookhart, E. Carmona and T. R. Cundari, *J. Am. Chem. Soc.*, 2013, **135**, 1217-1220.
116. K. M. Altus, M. A. Sajjad, M. R. Gyton, A. C. Whitwood, S. J. Page, S. A. Macgregor and A. S. Weller, *Organometallics*, 2024, DOI: 10.1021/acs.organomet.4c00119.
117. M. R. Gyton, M. A. Sajjad, D. J. Storm, K. M. Altus, J. C. Goodall, C. L. Johnson, S. J. Page, A. J. Edwards, R. Piltz, S. B. Duckett, S. A. Macgregor and A. S. Weller, *J. Am. Chem. Soc.*, Submitted, ja-2024-18122t.
118. M. Findlater, K. M. Schultz, W. H. Bernskoetter, A. Cartwright-Sykes, D. M. Heinekey and M. Brookhart, *Inorg. Chem.*, 2012, **51**, 4672-4678.
119. M. Albrecht, *Chem. Rev.*, 2010, **110**, 576-623.
120. L. Schwartsburd, M. A. Iron, L. Konstantinovski, E. Ben-Ari and D. Milstein, *Organometallics*, 2011, **30**, 2721-2729.
121. M. Feller, Y. Diskin-Posner, L. J. W. Shimon, E. Ben-Ari and D. Milstein, *Organometallics*, 2012, **31**, 4083-4101.
122. H. D. Empsall, E. M. Hyde, R. Markham, W. S. McDonald, M. C. Norton, B. L. Shaw and B. Weeks, *J. Chem. Soc., Chem Commun.*, 1977, 589-590.
123. C. Crocker, R. J. Errington, W. S. McDonald, K. J. Odell, B. L. Shaw and R. J. Goodfellow, *J. Chem. Soc., Chem Commun.*, 1979, 498-499.
124. H. A. Y. Mohammad, J. C. Grimm, K. Eichele, H.-G. Mack, B. Speiser, F. Novak, M. G. Quintanilla, W. C. Kaska and H. A. Mayer, *Organometallics*, 2002, **21**, 5775-5784.
125. T. Yano, Y. Moroe, M. Yamashita and K. Nozaki, *Chem. Lett.*, 2008, **37**, 1300-1301.
126. A. V. Polukeev, S. A. Kuklin, P. V. Petrovskii, A. S. Peregudov, F. M. Dolgushin, M. G. Ezernitskaya, A. A. Koridze and A. V. Polukeev, *Russ. Chem. Bull.*, 2010, **59**, 745-749.
127. A. V. Polukeev and M. Tasić, *Dalton Trans.*, 2023, **52**, 7701-7708.
128. J. E. Smart, I. Prokes, B. Leforestier and A. B. Chaplin, *Organometallics*, 2024, **43**, 1143-1154.

Chapter 2: Synthesis and reactivity of a silver(I) [Ag(NBE)(η^2:η^2-BAr^F_4)] zwitterion

The experimental work presented in this chapter was carried out in collaboration with Jack Heaton (complex **2.3** and preliminary data for complex **2.4**) and Dr Kristof Altus (complex **2.5**) at the University of York. Solid-State NMR (SSNMR) data was collected by Dr Matthew Gyton at the University of York.

2.1 Introduction

The use of weakly coordinating anions (WCA) is of fundamental importance to organometallic chemistry, as they offer a potential route to generate highly reactive cations which possess a latent vacant or "virtual vacant" site necessary for catalytic processes that involve the coordination of substrates to a reactive cationic metal centre.[1, 2] For example, [(Cp*)(PMe_3)Ir(Me)($ClCH_2Cl$)][BAr^F_4], which is stabilised by the WCA [BAr^F_4]$^-$, is active in the C–H activation of methane and terminal alkanes due to the lability of the CH_2Cl_2 ligand which provides access to the reactive 16-electron intermediate [(Cp*)(PMe_3)Ir(Me)][BAr^F_4].[3] As demonstrated in Section 1.1.2, the [BAr^F_4]$^-$ anion, in particular, is of importance to SMOM chemistry as the weakly coordinating nature of [BAr^F_4]$^-$ is needed to stabilise highly reactive intermediates such as σ-alkane complexes.[4-6] However, in some cases the π-system of the [BAr^F_4]$^-$ anion can coordinate to the metal centre to form zwitterionic complexes, even in the solid state. For example, [(dipbe)Rh(NBA)][BAr^F_4] (**1.12**) converts to the anion coordinated compound [(dipbe)Rh(η^6-$C_6H_3(CF_3)_2$)BAr^F_3] (**1.13**) in the solid state *via* loss of the NBA ligand (Scheme 2.1 A).[4] There are also several examples of rhodium(I) [BAr^F_4]$^-$ zwitterions known which have been synthesised in solution (Scheme 2.1 B).[7-11]

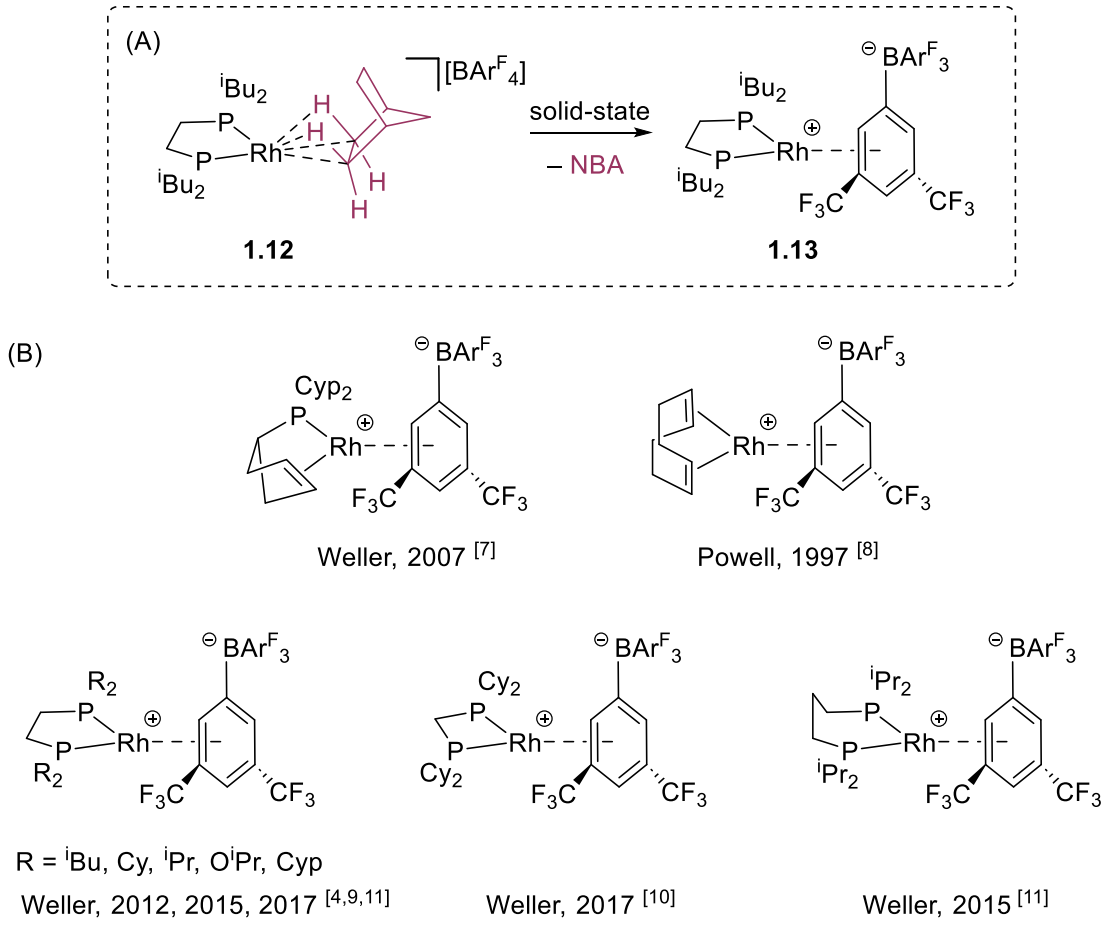

Scheme 2.1 (A) The solid state formation of the π-coordinated [BAr$^F_4$]$^-$ zwitterion, [(dipbe)Rh(η^6-C$_6$H$_3$(CF$_3$)$_2$)BAr$^F_3$], which proceeds with a loss of crystallinity. (B) Examples of crystallographically characterised rhodium(I) [BAr$^F_4$]$^-$ zwitterions. Cyp = cyclopentyl, O^{i}Pr = isopropoxide.

Organometallic complexes with vacant sites are often generated using Na[BAr$^F_4$], which acts as a halide abstraction agent and introduces the WCA [BAr$^F_4$]$^-$ into the system. Na[BAr$^F_4$] can be synthesised free of solvent, i.e. naked "Na$^+$",[12] which is crucial in preventing quenching of the vacant site *via* coordination of solvent such as THF, MeCN and Et$_2$O. Similar to Na[BAr$^F_4$], Ag[BAr$^F_4$] is another important reagent in salt metathesis reactions due to it being able to abstract a halide and introduce a WCA.[13-16] Ag[BAr$^F_4$] is also used as an oxidant,[17] for example in the single electron oxidation of the iridium(I) dinitrogen compound [(^{tBu}POCOP)Ir(N$_2$)] to the iridium(II) complex [(^{tBu}POCOP)Ir(N$_2$)][BAr$^F_4$] (Scheme 2.2 A), which activates dihydrogen to form a mixture of the iridium(III) complex [(^{tBu}POCOP)Ir(H)$_2$] and iridium(V) [(^{tBu}POCOP)Ir(H)$_4$].[18] Similar rhodium(I) dinitrogen systems, [(^{R}POCOP)Rh(N$_2$)] (R = ^{t}Bu, ^{i}Pr),

undergo oxidation by Ag[BAr$^{F}_{4}$] to form the rhodium(II) complexes, followed by subsequent B–C bond cleavage of [BAr$^{F}_{4}$]$^{-}$ to form rhodium(III) aryl complexes (Scheme 2.2 B).[19]

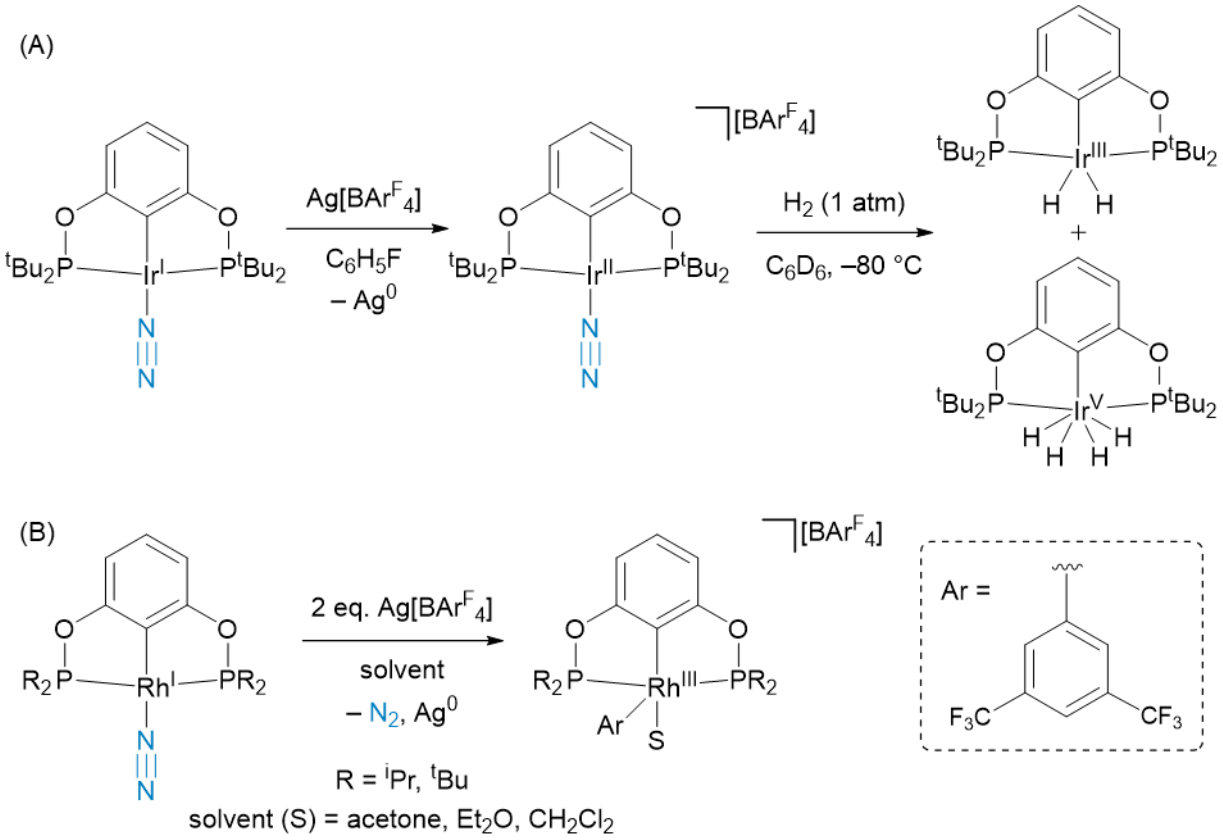

Scheme 2.2 The single electron redox chemistry of Ag[BAr$^{F}_{4}$] to form (A) a paramagnetic iridium(II) complex, which activates H_2, and (B) a rhodium(III) aryl product formed as a result of [BAr$^{F}_{4}$]$^{-}$ B–Ar^{F} bond cleavage.

Despite its synthetic importance, all reported syntheses of Ag[BAr$^{F}_{4}$] describe it as having solvent (S) of coordination, e.g. [Ag(S)$_n$][BAr$^{F}_{4}$]. For example, complexes of acetonitrile, [Ag(NCMe)$_2$][BAr$^{F}_{4}$], or diethyl ether, [Ag(OEt$_2$)$_x$][BAr$^{F}_{4}$] (x = 1-2), have been proposed.[20, 21] However, the use of acetonitrile or diethyl ether salts of Ag[BAr$^{F}_{4}$] in catalyst preparation can result in quenching of the vacant site and hinder formation of the desired product.[19, 22-24]

As well as accessing a solvent-free Ag[BAr$^{F}_{4}$] salt, it was hypothesised that a Ag[BAr$^{F}_{4}$] complex might undergo solid/gas transformations with gaseous substrates, such as CO and C_2H_4, and add to the numerous examples of SC-SC chemistry of group XI complexes discussed in Section 1.1.3.

It was hypothesised that a Ag[BAr^F_4] complex free of solvent might exist as a silver(I) [BAr^F_4]$^-$ zwitterion as silver(I) salts are often "arene-phillic", as demonstrated by the silver(I) carborane complex [Ag(CB_9H_{19})].[25] There are three reported examples of silver(I) coordinated to [BAr^F_4]$^-$, two of which are [(κ^2-$I_2C_6H_4$)Ag(η^2:η^2-BAr^F_4)] and [(bipy)Ag(η^2:η^1-BAr^F_4)] (bipy = 2,2′-bipyridine) (Figure 2.1).[8, 26] In these complexes the [BAr^F_4]$^-$ anion coordinates to the *ipso*- and *ortho*- positions of two of the aryl rings, in contrast to the η^6 coordination to one aryl ring observed with rhodium(I).

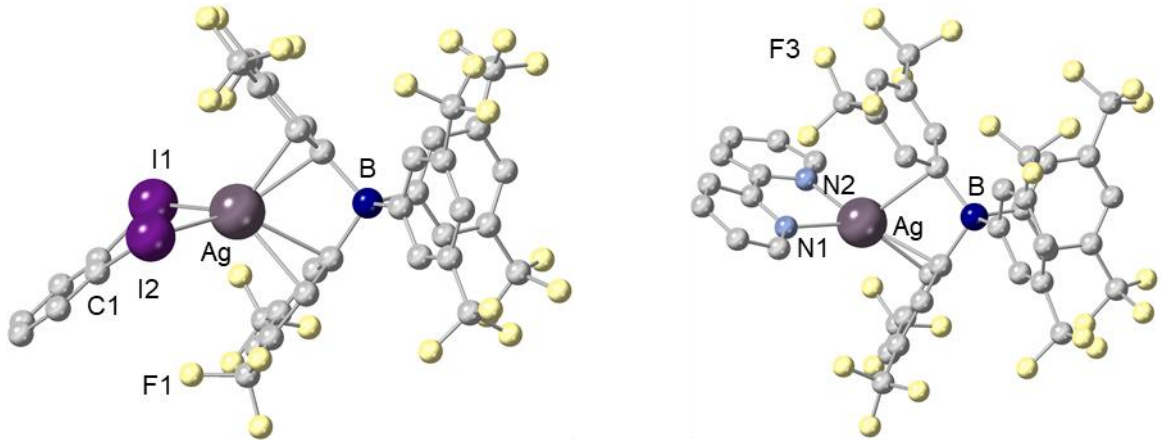

Figure 2.1 Crystallographically characterised examples of [BAr^F_4]$^-$ anion coordination to silver(I). The structures are displayed as ball and stick representation due to the lack of thermal ellipsoid parameter information provided.

The third example of silver(I) coordinated to [BAr^F_4]$^-$ is the heterobimetallic complex [(η^1:η^1-BAr^F_4)$AgFe(CO)_5$] wherein the silver is coordinated through the *ipso*- positions of two of the [BAr^F_4]$^-$ aryl rings (Figure 2.2).[27] The weak binding nature of the [BAr^F_4]$^-$ ligand was demonstrated by the addition of $Fe(CO)_5$ to [(η^1:η^1-BAr^F_4)$AgFe(CO)_5$] to form [$Ag(Fe(CO)_5)_2$][BAr^F_4], with the [BAr^F_4]$^-$ acting as a discrete counterion in the product. The addition of one equivalent of Me_2bipy (4,4'-dimethylbipyridine) also replaces the [BAr^F_4]$^-$ ligand to form [(Me_2bipy)$AgFe(CO)_5$][BAr^F_4]. The [BAr^F_4]$^-$ and $Fe(CO)_5$ ligands can also both be readily displaced by Et_2O or $PMes_3$ (Mes = 2,4,6-trimethylphenyl) to form [$Ag(OEt_2)_3$][BAr^F_4] and [$Ag(PMes_3)_2$][BAr^F_4] respectively.

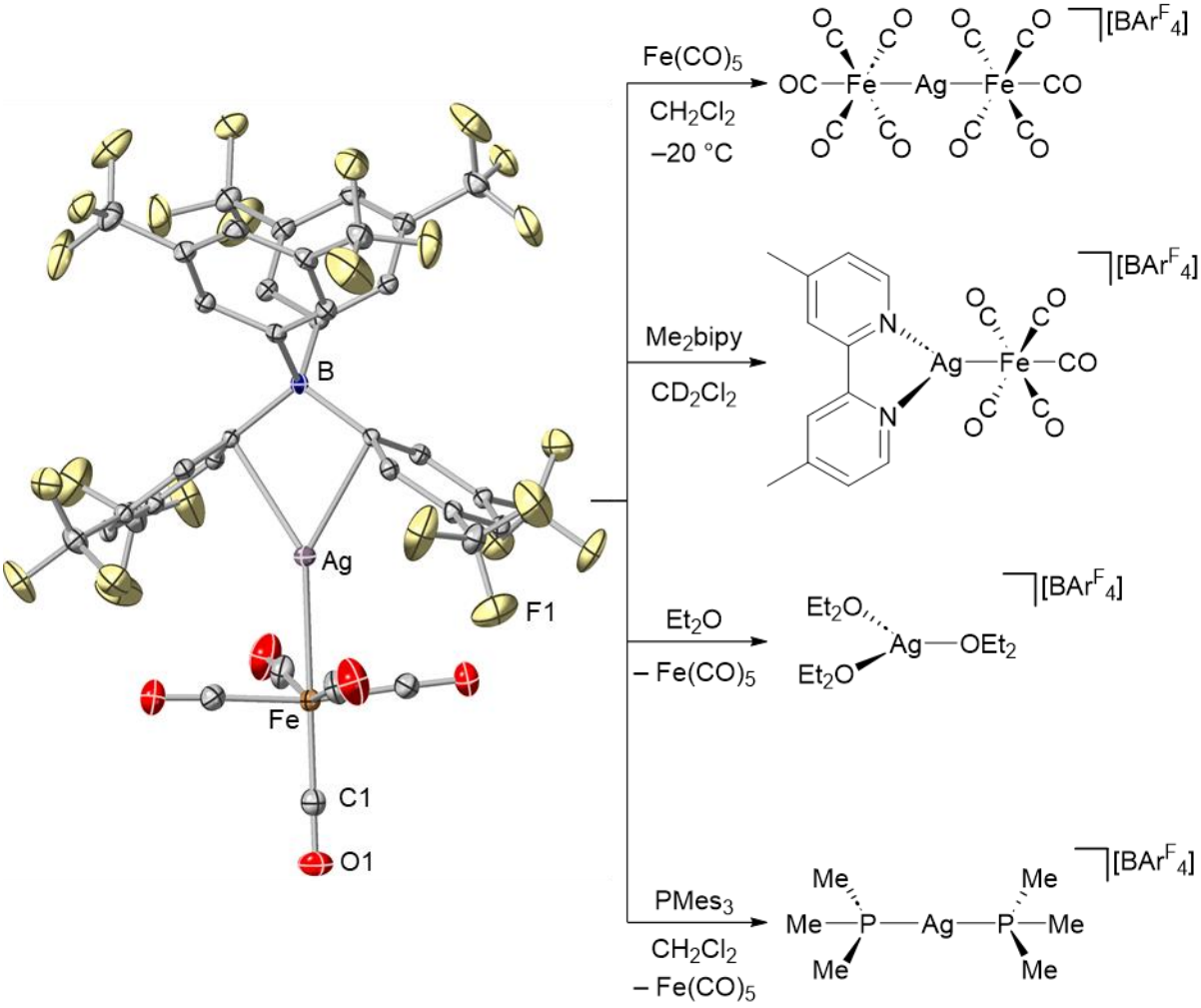

Figure 2.2 The molecular structure of [(η^1:η^1-BAr^F_4)AgFe(CO)$_5$] and its ligand substitution reactivity with Fe(CO)$_5$, Et_2O and $PMes_3$.

It was hypothesised that [Ag(NBE)$_3$][BAr^F_4] (**2.1**, NBE = norbornene), for which the [Ag(NBE)$_3$][SbF_6] counterpart is known,[28] might lose NBE under vacuum in a SC-SC reaction to form a highly reactive Ag[BAr^F_4] zwitterion free of solvent, in a similar way to how rhodium(I) [BAr^F_4]$^-$ coordinated complexes such as [(dibpe)Rh(η^6-$C_6H_3(CF_3)_2$)BAr^F_3] (**1.13**) form in the solid state. While complex **2.1** does not form the intended Ag[BAr^F_4] by SC-SC reactivity, a new silver(I) [BAr^F_4]$^-$ coordinated zwitterion, [Ag(NBE)($\eta^2\eta^2$-BAr^F_4)] (**2.2**), was instead isolated. This chapter reports on the synthesis and characterisation of complex **2.2** and investigation into its use as a source of Ag[BAr^F_4], as demonstrated by three exemplar reactions: ligand substitution, salt metathesis and single electron oxidation.

2.2 Synthesis, characterisation and reactivity of $[Ag(NBE)_3][BAr^F_4]$ (Complex 2.1)

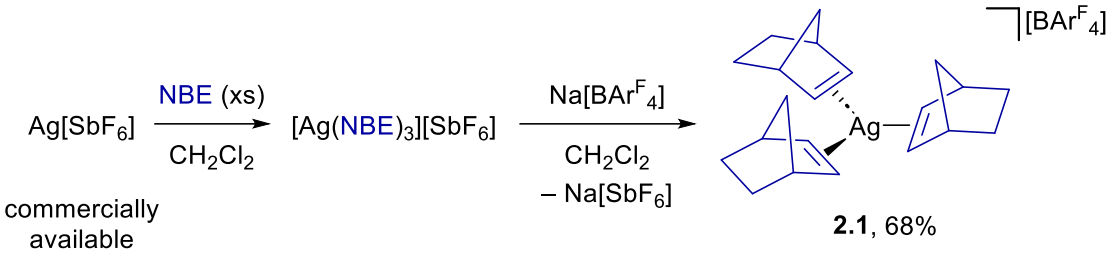

Scheme 2.3 The synthesis of $[Ag(NBE)_3][BAr^F_4]$ (**2.1**), xs = excess.

The precursor complex, $[Ag(NBE)_3][SbF_6]$, was synthesised according to the literature procedure *via* the addition of excess NBE to $Ag[SbF_6]$ in dichloromethane at room temperature, followed by crystallisation from dichloromethane/hexane at –20 °C.[28] Subsequent anion metathesis with $Na[BAr^F_4]$ in dichloromethane and filtration at room temperature, followed by recrystallisation from 1,2-difluorobenzene/hexane or dichloromethane/hexane at –20 °C afforded colourless crystals of $[Ag(NBE)_3][BAr^F_4]$•0.9(1,2-$F_2C_6H_4$) (**2.1·DFB**, 188 mg, 68%) or $[Ag(NBE)_3][BAr^F_4]$•0.7(CH_2Cl_2) (**2.1·CH_2Cl_2**, 85 mg, 64%) respectively (Scheme 2.3). The cation in the crystal structure of complex **2.1·CH_2Cl_2** is not well-defined, and the structure contains several highly disordered, partial occupancy CH_2Cl_2 solvent molecules. In comparison, the cation in complex **2.1·DFB** is more ordered, and the lattice 1,2-difluorobenzene (0.9 occupancy) molecule can be suitably modelled. The ^{1}H NMR (CD_2Cl_2) spectra for **2.1·CH_2Cl_2** and **2.1·DFB** are identical with the exception of the lattice solvent, and therefore further discussion is limited to complex **2.1·DFB**.

In the solution ^{1}H NMR (CD_2Cl_2) spectrum of complex **2.1·DFB** (Figure 2.3 A) broad singlets are observed corresponding to the *ortho*- and *para*-BAr^F_4 protons at δ 7.73 (8H) and δ 7.57 (4H). Overlapping signals corresponding to 1,2-difluorobenzene are also observed at δ 7.19 and 7.12 as multiplets with a total integral of 3.7H rather than 4H, indicating that a 1,2-difluorobenzene molecule resides within the crystal lattice with a partial occupancy of ~0.9 relative to the *ortho*-BAr^F_4 signal, as seen in the molecular structure. Hexane signals at δ 1.30 (1.7H) and 0.88 (1.4H) are also observed corresponding to the CH_2 and CH_3 protons

respectively, suggesting that there is also ~0.2 hexane within the lattice, although this is too low occupancy to be observed in the crystal structure (*vide infra*). There are two possible orientations of the NBE ligands, however only one set of signals corresponding to the NBE ligand are observed, suggesting that the NBE ligands are equivalent on the timescale of the NMR experiment. Therefore, the solution-state structure shall be presented as a syn/syn/syn arrangement for the remainder of this thesis (Figure 2.3 B). No evidence of coupling to silver (^{107}Ag: I = ½, 51.8%; ^{109}Ag: I = ½, 48.2%) is observed, likely due to dynamic behaviour (*vide infra*) of the NBE ligands 'self-decoupling', similar to the lack of ^{107}Ag/^{109}Ag coupling reported for $[Ag(\eta^2\text{-}C_2H_4)_3][Al(OC(CF_3)_3)_4]$.[29] The alkene proton of the NBE ligand, H_a, would be expected to be a pair of concentric doublets with such coupling, but is instead observed as a singlet at δ 6.19 (6H), shifted downfield compared to free NBE (δ 5.98, CD_2Cl_2).[28] Although limited discussion is presented for the ^{1}H NMR spectra of $[Ag(NBE)_3][SbF_6]$,[28] the alkene resonance (δ 6.42, CD_2Cl_2) is observed at a significantly different chemical shift to complex **2.1·DFB**. A difference in chemical shift is also observed in the ^{13}C NMR (CD_2Cl_2) spectrum, in which the alkene carbons, C_a, are observed at δ 131.4 compared to δ 132.6 for $[Ag(NBE)_3][SbF_6]$. A singlet is also observed at δ 3.16 (6H) for the bridgehead protons H_b, closer to that of $[Ag(NBE)_3][SbF_6]$ (δ 3.20). The *exo*- and *endo*-H_c protons are observed as doublets ($^2J_{HH}$ = 8 Hz) at δ 1.78 (6H) and 1.02 (6H) respectively, similar to $[Ag(NBE)_3][SbF_6]$ (δ 1.77 and 1.01 respectively). The bridging CH_2 protons appear in separate environments as doublets ($^2J_{HH}$ = 9 Hz) at δ 1.18 (3H) and δ 0.74 (3H), revealing them to be diastereotopic and coupled to one another. Whilst complex **2.1·DFB** is stable for weeks in the absence of light, it forms metallic silver(0) as a distinctive silver mirror on the walls of the NMR tube and free NBE, as shown by ^{1}H NMR spectroscopy, due to the light sensitivity of silver(I).

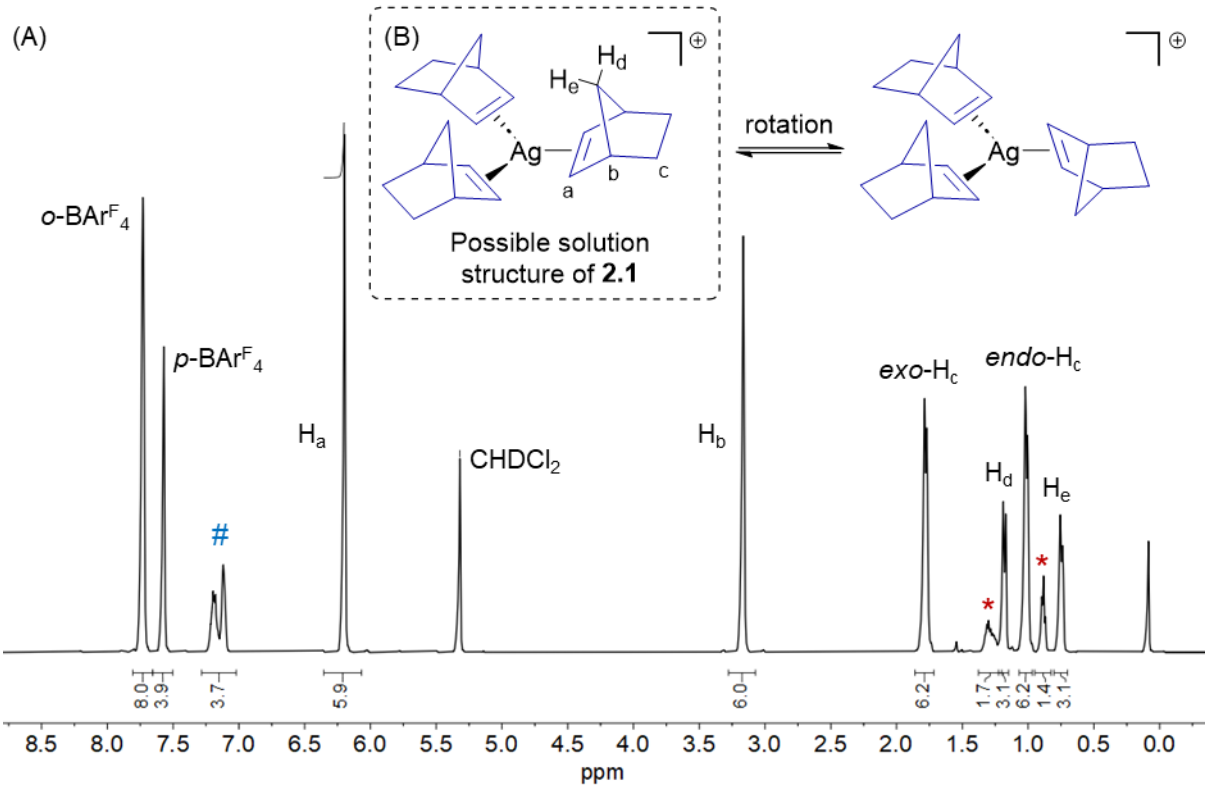

Figure 2.3 (A) The ^{1}H NMR spectrum of complex **2.1·DFB** (500 MHz, CD_2Cl_2, 298 K). # Denotes lattice 1,2-difluorobenzene, * denotes lattice hexane. (B) The fast rotation between possible orientations of the NBE ligands of **2.1·DFB**, resulting in a time averaged structure observed in solution. The dotted box highlights the structure which shall be drawn for the remainder of this thesis.

One of the diasteretopic protons, H_e, resides above the alkene bond of the NBE ligand and in close proximity to the metal centre, thus within the 'cone of shielding' created by the *π*-electrons of the C=C double bond, shifting it relatively upfield to δ 0.74. This was identified by the 1D selective ROESY (Rotating Frame Overhauser Enhancement Spectroscopy) spectrum of **2.1·DFB** (Figure 2.4). The ROESY spectrum, centred upon the peak at δ 0.74, shows an opposite phase peak at δ 6.19 (H_a) and 3.16 (H_b), indicative of through space correlations. No such cross peak is observed when centred upon the peak at δ 1.18 (H_d). TOCSY (Total Correlation Spectroscopy) peaks are observed for the H_d and *endo*-H_c peaks at δ 1.18 and 1.02, as evident by the peaks being of the same phase as the selected peak at δ 0.74, due to these peaks being relatively close in chemical shift and coupling to one another. Whilst their assignments are not discussed, diasteretopic protons are also observed in the ^{1}H NMR spectrum of $[Ag(NBE)_3][SbF_6]$ at δ 1.18 and 0.84, and free NBE at δ 1.29 and 1.10.[28]

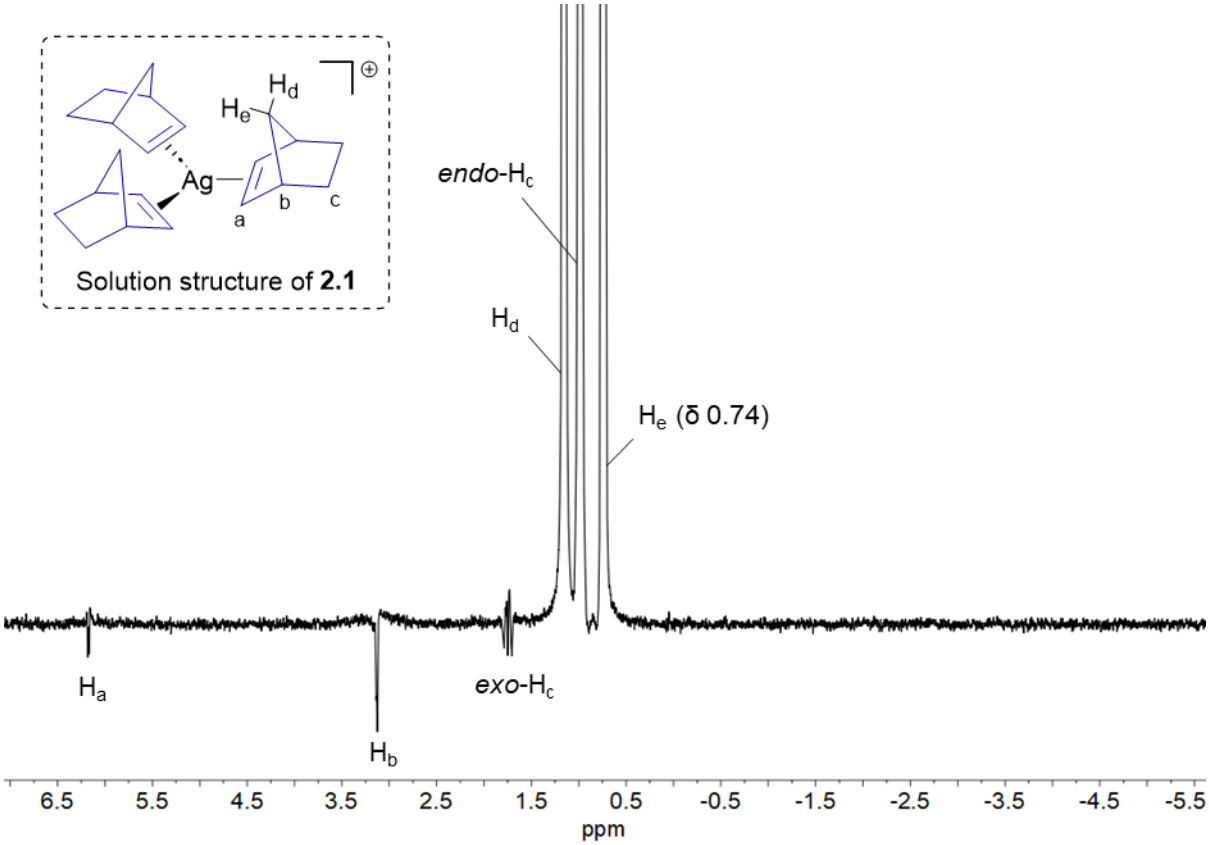

Figure 2.4 The 1D selective ^{1}H ROESY spectrum of complex **2.1**, centred on δ 0.74. Positive phase peaks denote TOCSY correlations, negative phase peaks denote through space ROE correlations. (500 MHz, CD_2Cl_2, 298 K).

Complex **2.1·DFB** crystallises in the space group $P2_1/n$. The structure of the cation in complex **2.1·DFB** shows a trigonal planar geometry, with three NBE ligands coordinated (Figure 2.5 A), similar to $[Ag(NBE)_3][SbF_6]$.[28] In the solid-state structure of complex **2.1·DFB**, all NBE ligands are bound in an *exo*- manner through their C=C bonds, with one CH_2 bridgehead pointing the opposite way to the other two NBE ligands in a syn/anti arrangement (Figure 2.5 B). This is in contrast to the C_{3v} symmetry observed in solution by NMR spectroscopy and different from the crystal structure of $[Ag(NBE)_3][SbF_6]$,[28] for which the NBE ligands are orientated in a syn/syn arrangement. This reflects the ability of these ligands to orientate themselves based on the surrounding environment within the crystal ($[BAr^F{}_4]^-$ *vs* $[SbF_6]^-$). Besides this structural difference, the bond metrics in complex **2.1·DFB** are similar to $[Ag(NBE)_3][SbF_6]$.[28] The Ag–C bond distances of 2.369(8) – 2.431(8) Å are similar to $[Ag(NBE)_3][SbF_6]$ (2.397(3) and 2.420(3) Å). The C–C alkene distances (1.348(10), 1.36(1)

and 1.357(12) Å) are also the same within error of $[Ag(NBE)_3][SbF_6]$ (1.369(4) Å), as well as free NBE (1.334(1) Å).[30] There is also a fractional 1,2-difluorobenzene (0.9 occupancy) molecule within the lattice, in agreement with the relative integral in the ^{1}H NMR spectrum of complex **2.1·DFB**. No evidence of heptane is within the lattice despite being present in the ^{1}H NMR spectrum, due to its low occupancy (~0.2).

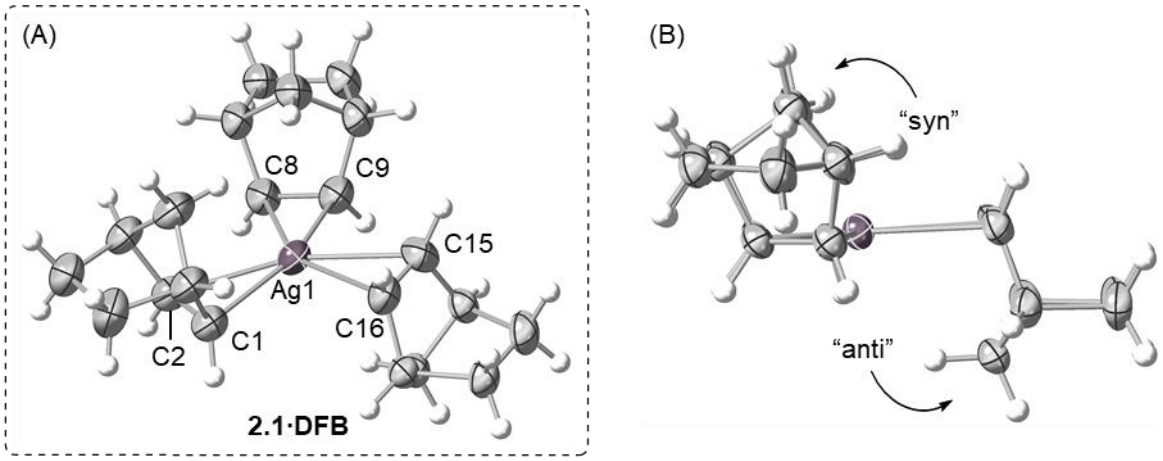

Figure 2.5 (A) The molecular structure of the isolated cation of **2.1·DFB**. Displacement ellipsoids are set at 30% probability level. Selected bond distances (Å): Ag1–C1, 2.369(8); Ag1–C2, 2.424(8); Ag1–C8, 2.410(6); Ag1–C9, 2.413(8); Ag1–C15, 2.431(8); Ag1–C16, 2.398(7); C1–C2, 1.348(10); C8–C9, 1.36(1); C15–C16, 1.357(12). Selected bond angles (°): C1–Ag1–C15, 120.3(3); C1–Ag1–C8, 123.6(3); C8–Ag1–C15, 116.0(3). (B) The syn/anti *exo*-binding of the NBE ligands in complex **2.1·DFB**.

In the solid state, the $[BAr^F_4]^-$ anions in complex **2.1·DFB** are arranged in an octahedron with six anions encapsulating two crystallographically equivalent cations (Figure 2.6). As discussed in section 1.1.2, the stabilising octahedral framework has repeatably been shown to support SMOM reactivity, such as in the formation of rhodium σ-alkane complexes, although these report only one cation encapsulated within the octahedron.[11] There are several short C–H···F contacts (< 2.8 Å) between the NBE ligand and the neighbouring $[BAr^F_4]^-$ environment, for example H15A···F15 (2.42(2) Å), H21B···F22 (2.52(2) Å) H1···F5 (2.55(3) Å), and H2···F5 (2.76(3) Å). No close (< 2.8 Å) C–H···F contacts are observed for the third NBE ligand due to it lying within the centre of the octahedron, pointing toward the second cation and further away from the nearby $[BAr^F_4]^-$ anions.

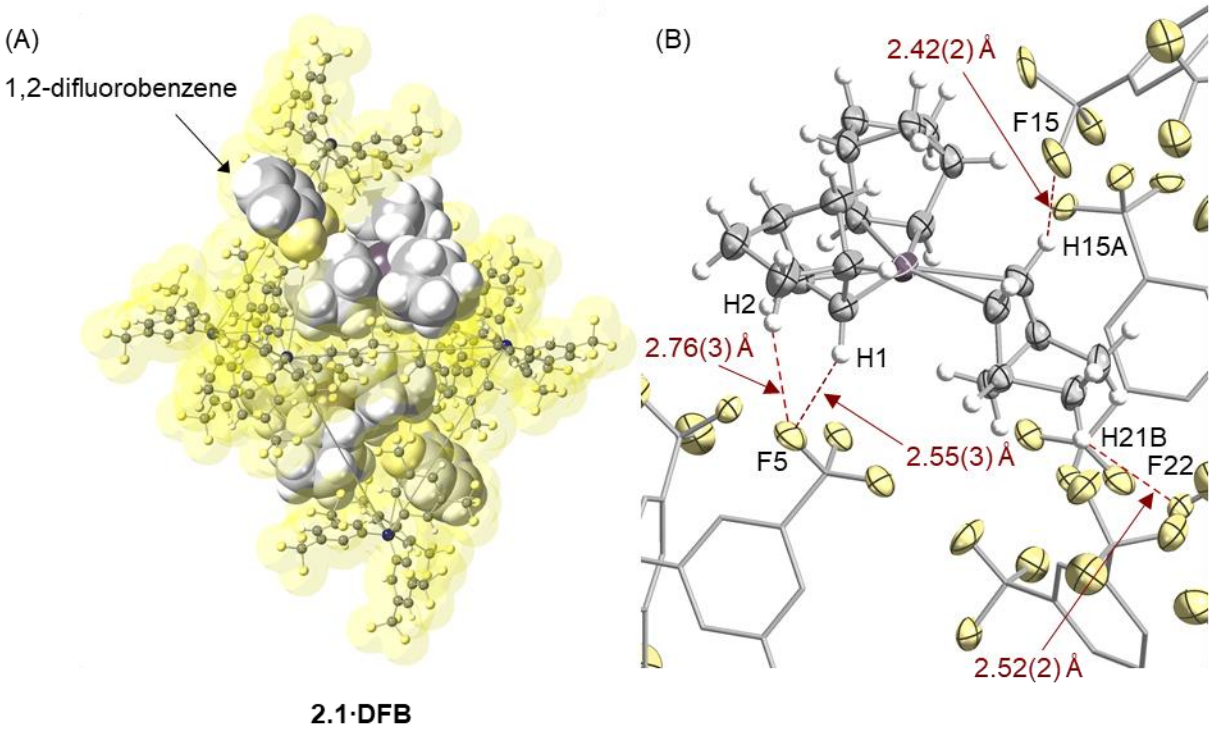

Figure 2.6 (A) The extended solid-state structure of complex **2.1·DFB**, showing the octahedral arrangement of $[BAr^{F}_{4}]^{-}$ anions and 1,2-difluorobenzene lattice solvent, depicted as Van der Waals radii. (B) A depiction of complex **2.1·DFB** showing close C–H···F contacts (< 2.8 Å) between the NBE ligands and a neighbouring $[BAr^{F}_{4}]^{-}$ anion.

The two distinct NBE environments (syn/anti) observed in the solid-state structure of complex **2.1·DFB** suggests that the NBE ligands are undergoing an exchange process on the NMR timescale in solution, making the environments for the bound NBE ligands equivalent and preventing the observation of coupling to $^{107}Ag/^{109}Ag$. This may either be due to fast rotation of the ligands, or through rapid exchange. Exchange could occur through several mechanisms, including in an associative or dissociative manner (Scheme 2.4). Although more complicated schemes are possible such as bimolecular pathways, this is beyond the scope of this thesis and may be explored using DOSY (Diffusion-ordered Spectroscopy) experiments as future work. Evidence for dissociative exchange of NBE comes from the dissociation of NBE to form [Ag(NBE)(η^2:η^2-BAr^{F}_{4})] (**2.2**), as is further detailed in Section 2.3. The low temperature ^{1}H NMR (CD_2Cl_2) spectrum of complex **2.1·DFB** at 193 K shows only one set of NBE signals with no signs of broadening. The signals are shifted slightly (193 K: δ 6.01, 3.09, 1.65, 1.01, 0.92, 0.49; 298 K: δ 6.19, 3.16, 1.78, 1.18, 1.02, 0.74) due to the temperature

dependence of chemical shift. The lack of new features in the ^{1}H NMR spectrum suggests that rotation of the NBE ligands must be rapid even at low temperatures, so that only the time averaged structure is observable in solution.

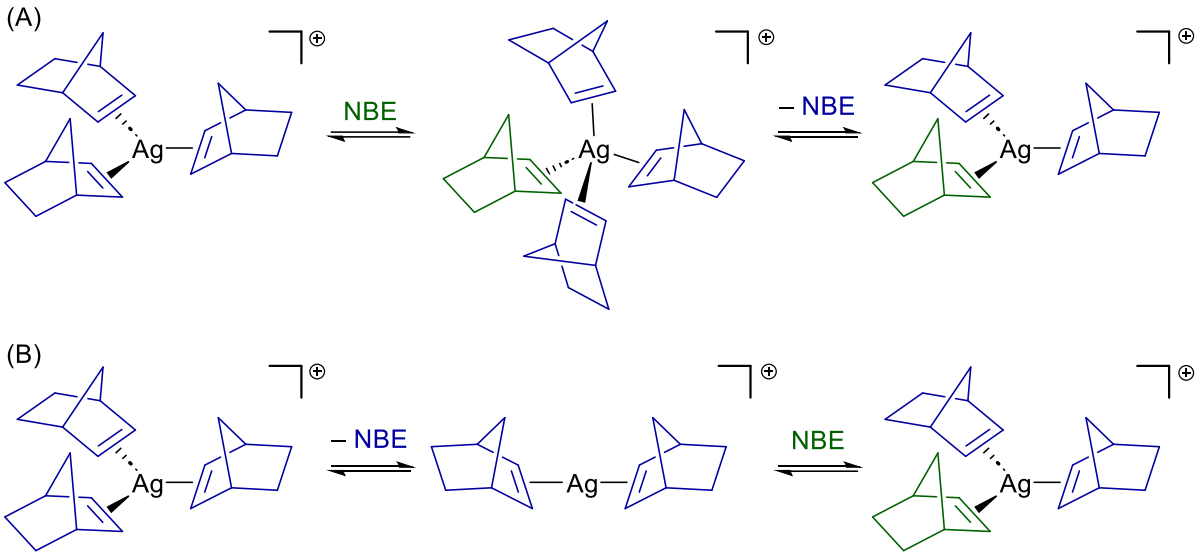

Scheme 2.4 Two plausible mechanisms based on (A) associative and (B) dissociative processes for the fast exchange of the bound NBE ligands in complex **2.1·DFB**.

Exchange of the NBE ligands was confirmed by addition of one equivalent of NBE to a CD_2Cl_2 solution of complex **2.1·DFB**. The resulting ^{1}H NMR spectrum reveals only one set of NBE peaks which are observed at the expected frequency averaged position for the corresponding signals of complex **2.1·DFB** and free NBE, when their populations are considered. The alkene protons are observed at δ 6.14, which matches that of the calculated weighted average position (δ 6.14) of complex **2.1·DFB** (δ 6.19) and free NBE (δ 5.98).[28] This is similar to the fast exchange of free and bound C_2H_4 reported for $[Ag(\eta^2\text{-}C_2H_2)_3][Al(OC(CF_3)_3)_4]$ in the presence of excess ethylene,[29] and confirms that the bound NBE ligands are in very rapid exchange with free NBE at 298 K. In the presence of excess NBE exchange is likely to occur *via* an associative process, forming a four-coordinate intermediate. A four-coordinate intermediate is reasonable as the similar silver(I) complex, $[Ag(\eta^2\text{-}C_2H_2)_4][Al(OC(CF_3)_3)_4]$,[31] is known.

Despite its regular octahedral framework, attempted SC-SC ligand exchange experiments of complex **2.1·DFB** with CO (2 bar absolute, 24 hr) and C_2H_4 (2 bar absolute, 24 hr) were unsuccessful, as evident by the ^{1}H NMR spectrum of the dissolved crystals, which remained unchanged from that of complex **2.1·DFB**. No change was observed upon placing complex **2.1·DFB** under dynamic vacuum (10^{-3} mbar, 24 hr, 298 K) by SCXRD and NMR (CD_2Cl_2) spectroscopy, demonstrating that Ag[BAr^F_4] cannot be synthesised by the SC-SC loss of NBE from complex **2.1·DFB**.

2.3 The isolation of a coordinated $[BAr^F_4]^-$ adduct, [Ag(NBE)(η^2:η^2-BAr^F_4)] (2.2)

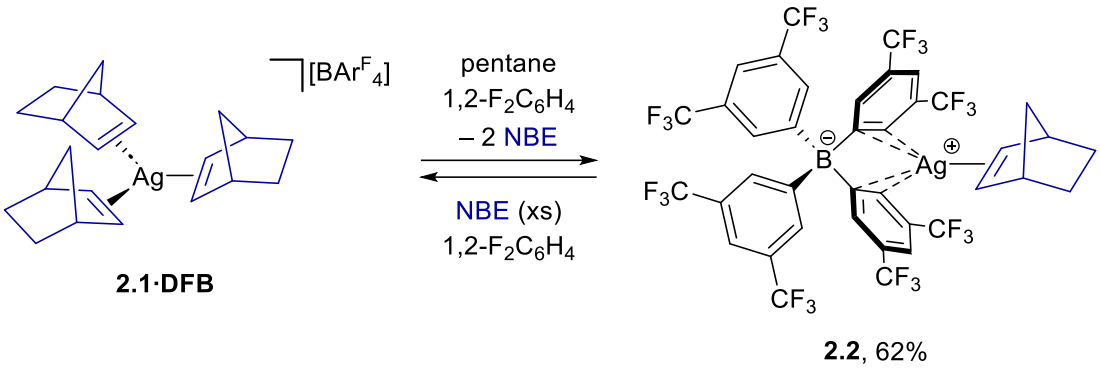

Scheme 2.5 The synthesis of [Ag(NBE)(η^2:η^2-BAr^F_4)] (**2.2**).

While complex **2.1·DFB** proved unreactive in the solid state to CO, C_2H_4 and vacuum, the lability of its NBE ligands in solution on the laboratory timescale is evident by the formation of [Ag(NBE)(η^2:η^2-BAr^F_4)] (**2.2**). Addition of pentane to a 1,2-difluorobenzene solution of complex **2.1·DFB** at room temperature results in the formation of a white precipitate which was washed with pentane three times, yielding complex **2.2** as a white powder, as evident by the ^{1}H NMR (CD_2Cl_2) spectrum (*vide infra*). Crystallisation from 1,2-difluorobenzene/hexane at –20 °C for 72 hours results in the isolation of colourless crystals of complex **2.2** (206 mg, 62%, Scheme 2.5). This process is reversible, and adding NBE to a 1,2-difluorobenzene solution of complex **2.2** reforms complex **2.1·DFB** as shown by ^{1}H NMR spectroscopy (*vide infra*).

Complex **2.2** crystallises in the space group $P2_1/c$. The resulting solid-state structure reveals that the silver(I) centre is located within the cleft of two aryl rings of the $[BAr^F_4]^-$ anion and is

exo-bound to a single NBE ligand (Figure 2.7). The $[BAr^{F}_{4}]^{-}$ anion acts as a bidentate ligand and coordinates to the silver in an η^2:η^2 manner with Ag1···C8, Ag1···C9, Ag1···C16 and Ag1···C17 distances of 2.559(2), 2.544(2), 2.496(2), 2.596(2) Å respectively. These Ag···C distances are similar to those measured in [(η^1:η^1-BAr^{F}_{4})AgFe(CO)$_5$] (2.5183(18) Å)[27] and [(κ^2-$I_2C_6H_4$)Ag(η^2:η^2-BAr^{F}_{4})] (2.581(3), 2.571(3) and 2.507(3) Å), and [(bipy)Ag(η^2:η^1-BAr^{F}_{4})] (2.640(3), 2.424(3) and 2.493(3) Å).[8] The Ag···C distances of complex **2.2** are similar to silver–arene complexes more generally, for instance silver(I) mono-anionic carborane complexes which tend to have silver–anion distances of 2.4–2.6 Å.[25, 32] In the solid-state structure of complex **2.2**, the Ag(I) centre resides closer to the NBE ligand than the $[BAr^{F}_{4}]^{-}$ anion as shown by Ag1–C1 and Ag1–C2 distances to the NBE ligand of 2.340(3) and 2.326(3) Å, which are shorter than Ag1–C8, Ag1–C9, Ag1–C16 and Ag1–C17 (2.559(2), 2.544(2), 2.496(2), 2.596(2) Å respectively). The alkene C1–C2 distance of 1.355(4) Å of complex **2.2** is similar to complex **2.1·DFB** (1.348(10), 1.36(1) and 1.357(12) Å). The Ag1–C1 and Ag1–C2 distances of complex **2.2** are also similar to the Ag–C bond lengths of complex **2.1·DFB** (2.369(8) – 2.431(8) Å). The C8–C9 and C16–C17 distances of the coordinated aryl rings (1.4086(34) and 1.4170(29) Å respectively) sit within the range of the C_{ipso}–C_{ortho} bond lengths of the non-coordinated rings in complexes **2.2** and **2.1·DFB** (1.3794(77)–1.4167(76) Å), showing that the structure of the $[BAr^{F}_{4}]^{-}$ anion is unaffected by coordination. The closest C–H···F contacts between the NBE ligand and the coordinated $[BAr^{F}_{4}]^{-}$ anion are H4B···F3 (2.893(4) Å) and H4B···F9 (3.195(2) Å), which are longer than that of the closest distances between the NBE ligand and the uncoordinated $[BAr^{F}_{4}]^{-}$ anionic framework in **2.1·DFB** (2.42(2), 2.52(2), 2.55(3) Å and 2.76(3) Å).

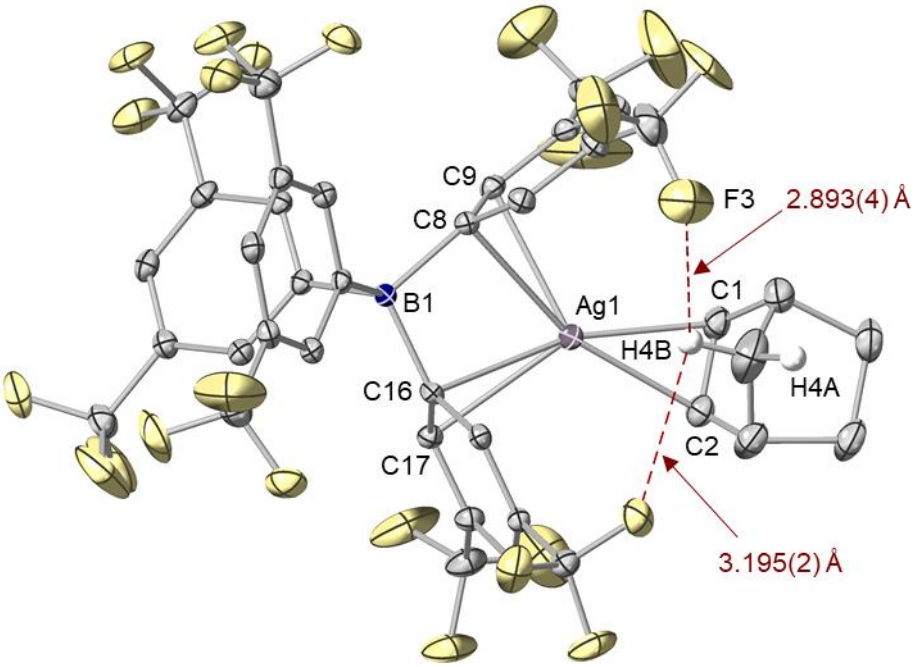

Figure 2.7 The molecular structure of the isolated cation of **2.2**. Displacement ellipsoids are set at 50% probability level and select hydrogen atoms are omitted for clarity. Selected bond distances (Å): Ag1–C1, 2.340(3); Ag1–C2, 2.326(3); Ag1–C8, 2.559(2); Ag1–C9, 2.544(2); Ag1–C16, 2.496(2); Ag1–C17, 2.596(2); C1–C2, 1.355(4); C8–C9, 1.4086(34); C16–C17, 1.4170(29). Selected bond angles (°): C1–Ag1–C2, 33.77(9); C8–Ag1–C9, 32.05(7); C16–Ag1–C17, 32.24(7); C1–Ag1–C8, 130.83(8); C1–Ag1–C17, 142.65(8); C8– Ag1–C17, 85.35(7).

In the ^{1}H NMR (CD_2Cl_2) spectrum of complex **2.2** at 298 K (Figure 2.8 A) only two broad singlets are observed corresponding to the *ortho*- and *para*-BAr^{F}_{4} protons at δ 7.88 (8H) and 7.75 (4H) respectively, shifted downfield slightly compared to that of complex **2.1·DFB** (δ 7.73 and 7.57) which shows the $[BAr^{F}_{4}]^{-}$ anion as uncoordinated. If the $[BAr^{F}_{4}]^{-}$ were to be coordinated in solution in the same way as in the solid state, five $[BAr^{F}_{4}]^{-}$ signals would be expected to be observed in the ^{1}H NMR spectrum due to the inequivalent environments for the coordinated and uncoordinated aryl rings, similar to that of [(dibpe)Rh(η^6-$C_6H_3(CF_3)_2$)BAr^{F}_{3}] (**1.13**). Two sets of $[BAr^{F}_{4}]^{-}$ signals are observed in the ^{1}H NMR spectrum of complex **1.13** (δ 7.62 (6H), 7.41 (3H), 7.36 (1H) and 6.74 (2H)), which shows the $[BAr^{F}_{4}]^{-}$ to be bound in an η^6 manner, resulting in the coordinated aryl ring being inequivalent to the three unbound rings.[4] The presence of only two signals corresponding to $[BAr^{F}_{4}]^{-}$ is indicative of time-averaged T_d symmetry for the $[BAr^{F}_{4}]^{-}$ anion in solution, meaning that it is either fluxional, or not bound to the silver(I) centre. Though not often discussed in detail, a single environment

for the $[BAr^F_4]^-$ anion is not unusual for silver(I) $[BAr^F_4]^-$ complexes. Whilst there are no reported NMR spectroscopy data for $[(\kappa^2\text{-}I_2C_6H_4)Ag(\eta^2{:}\eta^2\text{-}BAr^F_4)]$ and $[(bipy)Ag(\eta^2{:}\eta^1\text{-}BAr^F_4)]$,[8] the ^1H NMR (CD_2Cl_2) spectrum of $[(\eta^1{:}\eta^1\text{-}BAr^F_4)AgFe(CO)_5]$ reports only one set of environments for $[BAr^F_4]^-$ at δ 7.88 (8H) and 7.75 (4H), in contrast to its solid-state structure which is similar to that of complex **2.2**.[27]

Further evidence that the $[BAr^F_4]^-$ anion does not adopt the same structure in solution as the solid state comes from the ^{11}B NMR (CD_2Cl_2) spectrum of complex **2.2**, for which a singlet is observed at δ –6.8, similar to that of free $[BAr^F_4]^-$ in complex **2.1·DFB** (δ –6.6) and Na$[BAr^F_4]$ (δ –6.5, d_8-THF).[12] In contrast, the peak occurs at δ –7.6 (C_6F_6) in the ^{11}B NMR spectrum of complex **1.13**,[4] where the $[BAr^F_4]^-$ anion is shown to be strongly bound in solution. These data combined suggest that $[BAr^F_4]^-$ is free in a solution of complex **2.2**. Future work might include further demonstrating this using a DOSY experiment.

At 298 K one set of signals corresponding to the NBE ligand are observed in the ^1H NMR spectrum. The alkene proton H_a is observed as a singlet at δ 5.79 (2H), shifted upfield relative to complex **2.1·DFB** (δ 6.19), with no evidence of coupling to $^{107}Ag/^{109}Ag$ observed. The bridgehead protons H_b are observed at δ 2.81 (2H), whilst the *exo*-H_c and *endo*-H_c are observed as doublets ($^2J_{HH}$ = 9 Hz) at δ 1.66 (2H) and 0.79 (2H) respectively. The diastereotopic bridging protons H_d and H_e are observed at δ 1.00 (1H) and 0.05 (1H) respectively, with H_e being significantly shifted from complex **2.1·DFB** (δ 1.18, H_d; 0.74, H_e). Approximately 5% 1,2-difluorobenzene remains within the lattice as shown by overlapping signals at δ 7.19 and 7.12 (0.2H), yet this is not observed in the crystal structure due to its low fractional occupancy. Within hours at 298 K in CD_2Cl_2, unidentified peaks grow in the aryl region. This change is ascribed to decomposition, forming a mixture of products in the ^1H NMR spectrum, including free NBE and metallic silver(0) as a distinctive silver mirror on the walls of the NMR tube. Attempts to crystallise this decomposition mixture were unsuccessful.

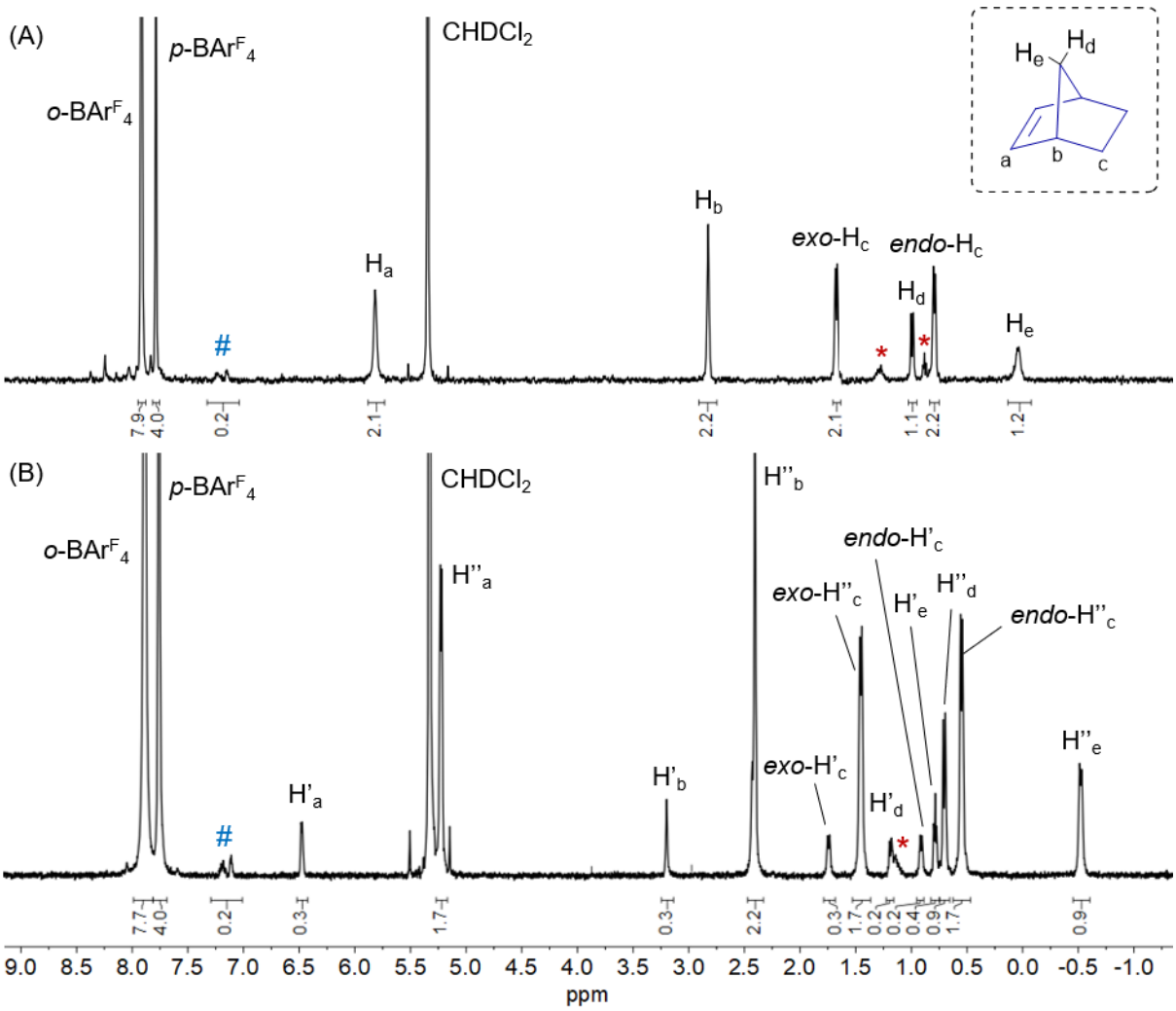

Figure 2.8 The ^{1}H NMR spectra of complex **2.2** at (A) 298 K, 5 minutes after sample preparation, and (B) 193 K (500 MHz, CD_2Cl_2). # Denotes lattice 1,2-difluorobenzene, H'$_x$ and H''$_x$ denote the two different sets of NBE signals.

Given the slow solution-state decomposition observed at 298 K, the low temperature ^{1}H NMR (CD_2Cl_2) spectrum of complex **2.2** was collected (Figure 2.8 B). At 193 K the $[BAr^F{}_4]^-$ signals remain unchanged (δ 7.88, 8H, *ortho*-$BAr^F{}_4$; 7.75, 4H, *para*-$BAr^F{}_4$), while two sets of NBE signals are observed in a 0.3:1.7 ratio relative to those of *ortho*-$BAr^F{}_4$. The corresponding two signals for the alkene proton H'$_a$ and H''$_a$ are observed as doublets at δ 6.47 (0.3H) and 5.21 (1.7H) with slightly different coupling constants ($^{3}J_{HH}$ = 5, = 7 Hz respectively). These peaks coalesce at 298 K into signal at δ 5.79 (2H), shifted slightly from the calculated weighted average position of δ 5.40. This suggests that there are two different compounds containing NBE present at 193 K, which interconvert rapidly at 298 K, and that the equilibrium lies slightly

towards that of the species presenting the peak at δ 6.47 at 298 K. The rest of the inequivalent NBE signals at 193 K were assigned *via* the exchange cross peaks in the ^{1}H NOESY NMR spectrum at 193 K (Figure 2.9). The NBE bridgehead protons H_b are observed at δ 3.19 (0.3H) and 2.40 (2H), whilst the *exo*-H_c protons are observed as doublets ($^{2}J_{HH}$ = 9 Hz) at δ 1.73 (0.3H) and 1.45 (1.7H), and the *endo*-H_c protons are observed at δ 0.91 (0.4H) and 0.54 (1.7H) respectively. The diastereotopic bridging proton H_d is observed at δ 1.18 (0.2H) and 0.71 (0.9H), whilst H_e are observed at δ 0.78 (0.2H) and –0.52 (0.9H), with the last being significantly shifted upfield relative to complex **2.1·DFB** (δ 0.74).

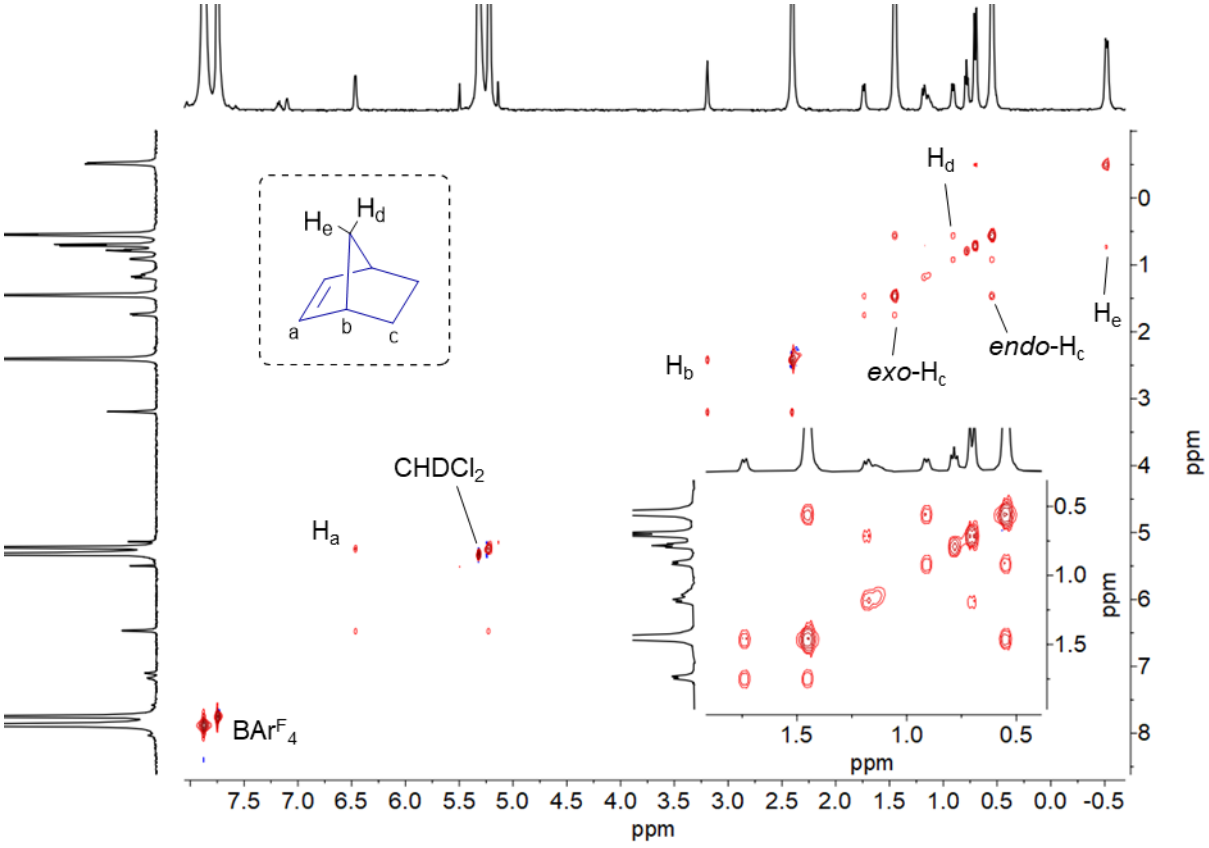

Figure 2.9 The ^{1}H NOESY NMR spectrum of complex **2.2** at 193 K. Cross peaks of positive phase indicate exchange between sites according to the NBE proton positions. The inset shows the δ 0.4–1.9 region for clarity. (500 MHz, CD_2Cl_2, 193 K).

Given that the ^{1}H and ^{11}B NMR spectra suggest that the $[BAr^F_4]^-$ anion is not bound in solution, it is plausible that complex **2.2** could instead form a solvent complex in solution such as $[(NBE)Ag(CD_2Cl_2)][BAr^F_4]$ (Scheme 2.6). As discussed in Section 2.1, silver(I) solvent complexes are known with acetonitrile, diethyl ether and 1,2-diiodobenzene.[8, 20, 21] The

dichloromethane complexes $[(CH_2Cl_2)Ag(Al(OC(CH_3)(CF_3)_2)_4)]$ and $[Ag(CH_2Cl_2)_3][F(Al(OC(CF_3)_3)_3)_2]$ have also been reported, and in the case of the latter the dichloromethane molecules can be removed under vacuum in 24 hrs.[26, 33] Despite lattice 1,2-difluorobenzene also being present in the mixture, it is unlikely that one of the complexes corresponds to a 1,2-difluorobenzene complex due to it being in too low occupancy (0.2 H, 5% 1,2-difluorobenzene) relative to *ortho*-BAr^F_4. The peak corresponding to H_e of the major component (H_e'') is observed at δ –0.52. This negative chemical shift could be due to either a ring current effect or indicative of an agostic complex. Considering that the data suggests that the $[BAr^F_4]^-$ anion is not bound in solution, it is unlikely to be due to a ring current effect and could instead be due to the formation of a Ag···H–C interaction (Scheme 2.6), although no $^{107}Ag/^{109}Ag$ coupling is observed. Agostic complexes of the coinage metals are rare,[34-36] yet low temperature NMR spectroscopy has previously been used to identify a Au···H–C agostic interaction in a gold(III) alkyl complex, which was confirmed by computational analysis.[37] Due to time constraints this could not be investigated further, however future work includes a low temperature ^{109}Ag-^1H HMBC experiment of complex **2.2**, which would confirm the presence of an agostic interaction by comparing the spectra to that of complex **2.1·DFB**, as a correlation would be expected to be observed to the peak at δ –0.52 if it is an agostic interaction. Comparison of the low temperature ^{13}C NMR spectra would also be useful as the $^1J_{CH}$ coupling constant would be expected to decrease upon the formation of an agostic interaction due to donation of the C–H bond to the silver(I) centre.

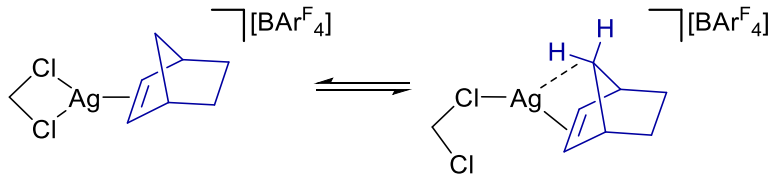

Scheme 2.6 The equilibrium between potential structures of the silver(I) NBE solvent complexes formed upon dissolution of complex **2.2**, which would account for the observed NMR spectroscopic behaviour.

The weighted average provides information on the limit of fast exchange. However, the chemical shifts of the NBE signals at 298 K do not follow the calculate weighted average based on the corresponding peaks at low temperature. The alkene proton H_a and the diastereotopic proton H_e are most significantly shifted from their corresponding weighted average positions, likely due to their close proximity to the silver(I) centre. For example, the NBE alkene peaks δ 6.47 (0.3H) and 5.21 (1.7H) coalesce at δ 5.79 (2H) at 298 K, shifted from the calculated weighted average position at δ 5.40. The diastereotopic proton H_e is observed at δ 0.78 (0.15H) and –0.52 (0.85H) and coalesces at δ 0.05 (1H), shifted from the calculated weighted average position at δ –0.16. The observed shift from the weighted average is indicative of a change in structure which results in a more positive ΔS value. The origin of this entropic gain could be due to the κ_1-dichloromethane ligand having greater degrees of freedom, or the rotating NBE ligand. At higher temperatures this would result in a more negative –TΔS term, and thus a more negative ΔG value (ΔG = ΔH–TΔS).

In 1,2-difluorobenzene at 298 K, the ^{1}H NMR spectrum of complex **2.2** shows a single set of signals corresponding to NBE at δ 5.88 (singlet, 2H, H_a), 2.90 (singlet, 2H, H_b), 1.61 (doublet, $^2J_{HH}$ = 9 Hz, 2H, H_c), 1.01 (doublet, $^2J_{HH}$ = 9 Hz, 1H, H_d), 0.76 (doublet, $^2J_{HH}$ = 9 Hz, 2H, H_c), and 0.22 (singlet, 1H, H_e), downfield compared to the corresponding shifts in CD_2Cl_2 at 298 K (δ 5.79, 2.81, 1.66, 1.00, 0.79, 0.05). The *ortho*- and *para*-BAr^F_4 protons are observed at δ 8.44 (8H) and 7.86 (4H) respectively, shifted from complex **2.2** in CD_2Cl_2 (δ 7.88, 8H, *ortho*-BAr^F_4; 7.75, 4H, *para*-BAr^F_4) due to solvent effects of 1,2-difluorobenzene. Signals for *ortho*- and *para*-BAr^F_4 tend to be observed at a more downfield region in 1,2-difluorobenzene, as seen in $[Rh(P^tBu_2H)_2(\eta^2\text{-}H_3B{\cdot}P^tBu_2H)][BAr^F_4]$ for which the *ortho*- and *para*-BAr^F_4 protons are observed at δ 8.33 and 7.68 respectively.[38] The mixture is stable for weeks at 298 K, demonstrating the stability of complex **2.2** in 1,2-difluorobenzene compared to that in dichloromethane which decomposes within 24 hours. Crystallisation of complex **2.2** in 1,2-difluorobenzene/hexane at –20 °C shows no evidence of a $[(NBE)Ag(1,2\text{-}F_2C_6H_4)][BAr^F_4]$ by SCXRD and ^{1}H/^{19}F NMR, as only that of complex **2.2** is observed.

Due to the solution-state instability of complex **2.2** at 298 K, the $^{13}C\{^{1}H\}$ NMR (CD_2Cl_2) spectrum could not be obtained. In the $^{13}C\{^{1}H\}$ SSNMR spectrum of complex **2.2** at 298 K (Figure 2.10) one set of signals corresponding to NBE are observed at δ 48.1, 42.8 and 21.5. The peak at δ 42.8 was assigned to C_b using a solid-state polarisation inversion experiment[39] analogous to a DEPT (Distortionless Enhancement by Polarisation Transfer) experiment, which are often used in the solution-state to determine the degree of substitution of carbon atoms (*ie* C, CH, CH_2, CH_3) and aid in the assignment of spectra. This is similar to that assigned to C_b for complex **2.1·DFB** in the solution-state (δ 43.2), consequently the peaks at δ 48.1 and 21.5 were assigned as C_d and C_c respectively by comparison to complex **2.1·DFB**. The aryl region displays multiple broad, overlapping features between δ 117.9–134.7 corresponding to the alkene carbon of the NBE ligand and the $[BAr^F_4]^-$ anion environments, so that the alkene carbon environment could not be identified. Two broad peaks for the *ipso*-BAr^F_4 carbons are observed at δ 161.8 and 158.7 due to the two distinct $[BAr^F_4]^-$ environments for the coordinated and non-coordinated aryl rings, analogous to the two environments reported in the $^{13}C\{^{1}H\}$ SSNMR spectrum of the $[BAr^F_4]^-$ coordinated complex **1.13** (δ 155.2, 159.2).[4] In comparison, one environment tends to be observed for the *ipso*-BAr^F_4 carbon of discrete $[BAr^F_4]^-$ complexes such as in the $^{13}C\{^{1}H\}$ SSNMR spectrum of [(dibpe)Rh(NBA)][BAr^F_4] (**1.12**, δ 164.3) or the solution $^{13}C\{^{1}H\}$ NMR spectrum of Na[BAr^F_4] (δ 162.8, d_8-THF).[12] Therefore, the two $[BAr^F_4]^-$ environments observed for complex **2.2** suggest that the $[BAr^F_4]^-$ anion is coordinated in the solid state at 298 K, consistent with the SCXRD structure, throughout the bulk material.

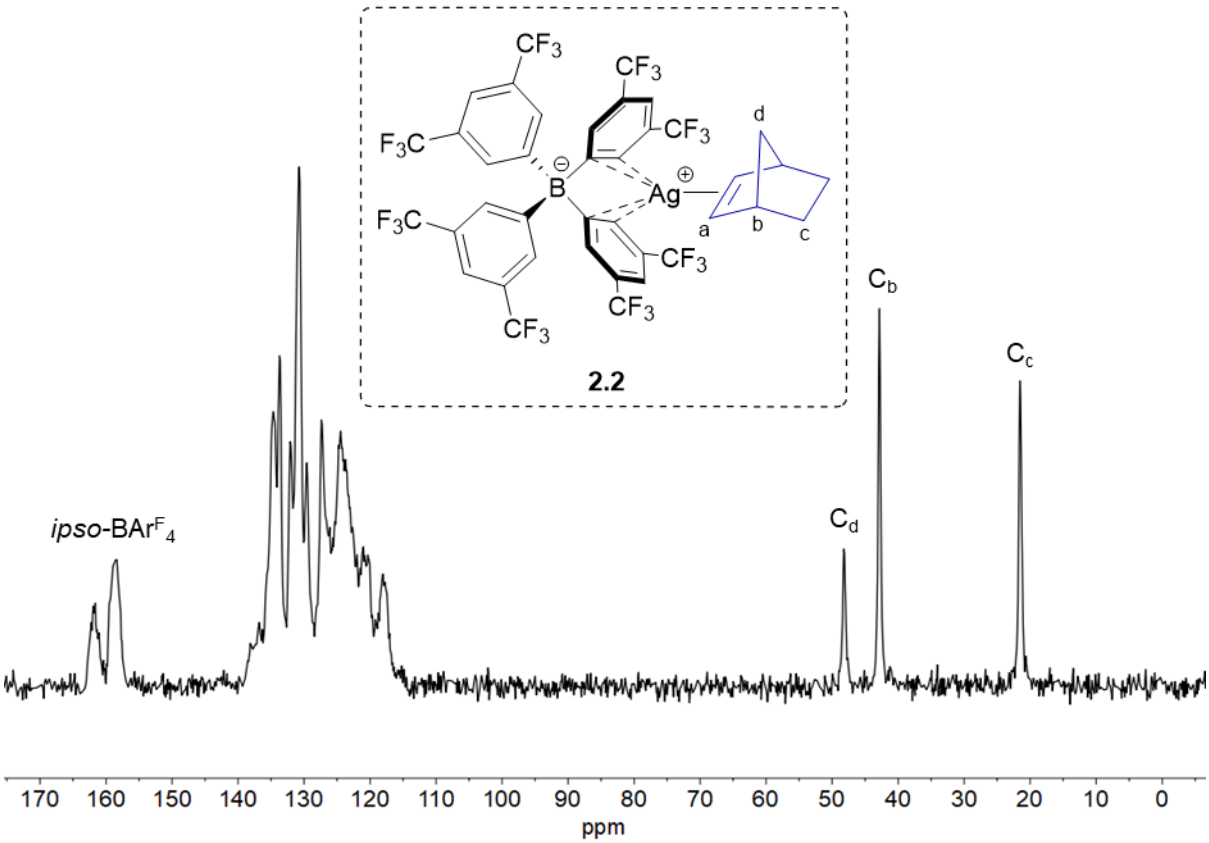

Figure 2.10 Solid-state $^{13}C\{^1H\}$ CPTOSS MAS NMR spectrum of complex **2.2** (100 MHz, 10 kHz spin rate, 298 K).

The possibility of forming a solvent complex from complex **2.2** was further investigated by dissolving the complex in DME (1,2-dimethoxyethane) at room temperature. This results in the substitution of both the $[BAr^F_4]^-$ and the NBE ligand to form $[Ag(DME)_3][BAr^F_4]$ (**2.3**, 85 mg, 49%) due to the more strongly binding nature of DME compared to NBE. This is analogous to that described for $[(\eta^1{:}\eta^1\text{-}BAr^F_4)AgFe(CO)_5]$ which readily loses $[BAr^F_4]^-$ and $Fe(CO)_5$ in Et_2O to form the corresponding $[Ag(OEt_2)_3][BAr^F_4]$.[27] Crystallisation from 1,2-dichloroethane/hexane at –20 °C affords colourless crystals of complex **2.3**, which crystallise in the space group *P*nna. The molecular structure shows that the silver(I) sits on a special position and has three DME ligands coordinated (Figure 2.11), resulting in half of the molecule being crystallographically equivalent, as highlighted by O1 and O1'.

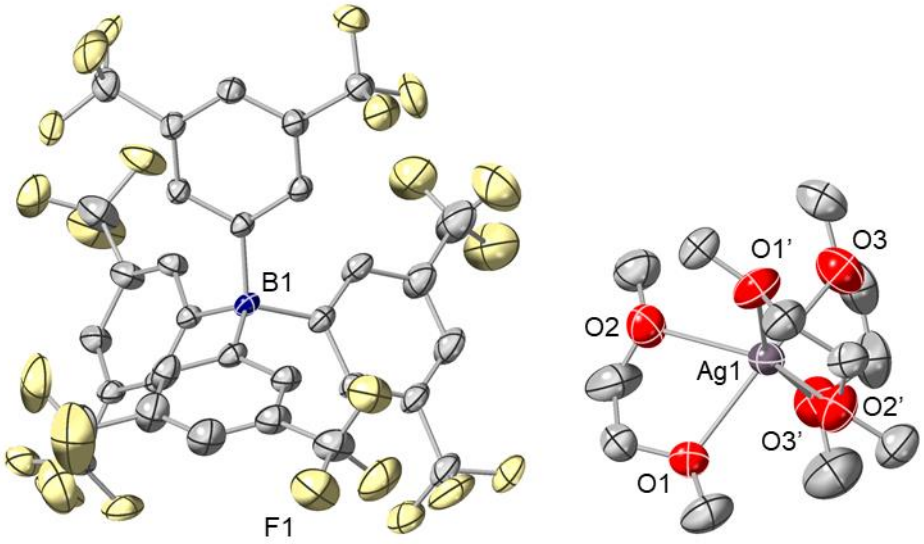

Figure 2.11 The molecular structure of complex **2.3**. Displacement ellipsoids are set at 50% probability level. Hydrogen atoms are omitted for clarity. Selected bond distances (Å): Ag1–O1, 2.456(4); Ag1–O2, 2.483(4); Ag1–O3, 2.405(4). Selected bond angles (°): O1–Ag1–O2, 68.85(12); O2–Ag1–O3, 105.61(15).

In the solution ^{1}H NMR (CD_2Cl_2) spectrum of complex **2.3**, singlets corresponding to the *ortho*- and *para*-BAr^F_4 protons are observed at δ 7.76 (8H) and δ 7.60 (4H). The ethyl and methoxy protons of the DME ligand are observed as singlets at δ 3.55 (12H) and 3.38 (18H) respectively, shifted downfield slightly of free DME (δ 3.49 and 3.34 respectively).[40] A singlet is observed in the solution ^{11}B NMR (CD_2Cl_2) spectrum of complex **2.3** at δ –6.7, within the same region as complexes **2.1·DFB** (δ –6.8) and **2.2** (δ –6.6), consistent with uncoordinated $[BAr^F_4]^-$.

2.4 [Ag(NBE)(η^2:η^2-BAr$^F_4$)] (2.2) as a source of Ag[BAr$^F_4$]

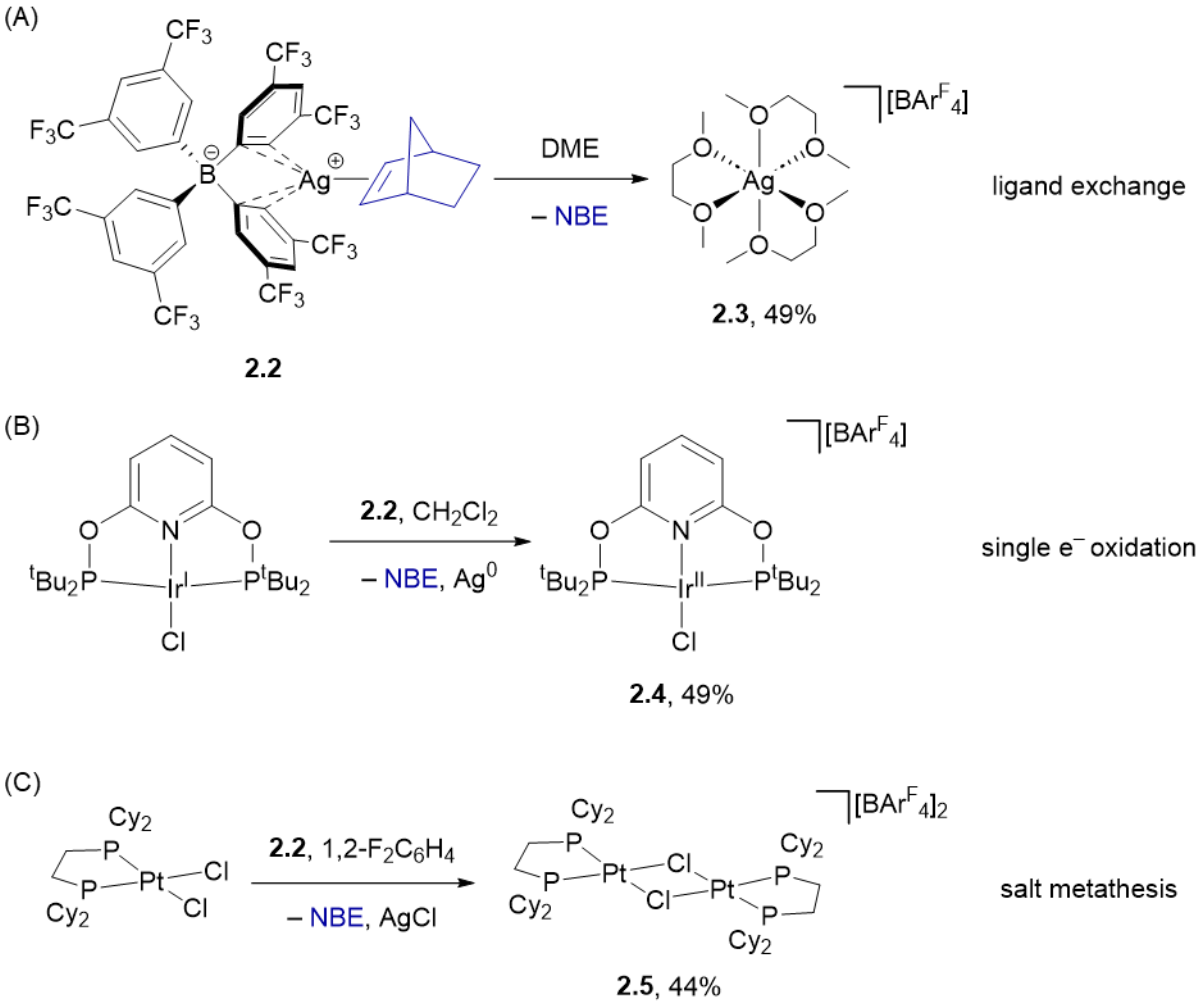

Scheme 2.7 Reactivity of complex **2.2** with (A) DME, (B) [(^{tBu}PONOP)IrCl] and (C) [(dcpe)PtCl$_2$].

Whilst the envisioned naked Ag[BAr$^F_4$] salt could not be accessed from complexes **2.1** or **2.2**, the solution-state lability of the NBE and [BAr$^F_4$]$^-$ ligands in complex **2.2** is evident from variable temperature NMR spectroscopy and the isolation of complex **2.3** *via* ligand exchange with DME (Scheme 2.7 A). This prompted the investigation of complex **2.2** as a source of Ag[BAr$^F_4$] in single electron oxidation and salt metathesis reactions. Two exemplar reactions were chosen: i) the generation of an iridium(II) complex from an iridium(I) precursor (Scheme 2.7 B); ii) the halide abstraction of a platinum(II) dichloride complex to form a platinum(II) dimer (Scheme 2.7 C), as shall be discussed *vide infra*.

Iridium(II) complexes are key intermediates in the iridium(III) catalysed reduction of quinones,[41] and have also been shown to activate small molecules such as H_2 and O_2.[18] For example, de Bruin reported the first iridium(II) ethylene complex $[(Me_3\text{-tpa})Ir(C_2H_4)][PF_6]_2$ (Me_3-tpa = *N*,*N*,*N*-tri((6-methyl-2-pyridyl)methyl)amine) which reacts with O_2 to form the iridium(III) formylmethyl complex $[(Me_3\text{-tpa})Ir(CH_2CHO)(NCMe)][PF_6]_2$. This reactivity towards O_2 is different to that of the iridium(I) analogue $[(Me_3\text{-tpa})Ir(C_2H_4)][PF_6]$, which instead forms the peroxoethylene complex $[(Me_3\text{-tpa})Ir(C_2H_4)(O_2)][PF_6]$.[42] Iridium(II) complexes are often accessed from the oxidation of iridium(I) complexes with ferrocenium or $Ag[PF_6]$,[43-45] and, as discussed in Section 2.1, $Ag[BAr^F{}_4]$ can also promote the single electron oxidation of iridium(I) and rhodium(I) POCOP compounds.[18] The similar ligand scaffold ^{tBu}PONOP was chosen to investigate the redox chemistry of complex **2.2**. The reaction of complex **2.2** and [(^{tBu}PONOP)IrCl][46] in dichloromethane at room temperature resulted in the immediate precipitation of silver(0) as a black precipitate, liberation of free NBE (^{1}H NMR spectroscopy) and the formation of the paramagnetic iridium(II) compound $[(^{tBu}PONOP)IrCl][BAr^F{}_4]$ (**2.4**, Scheme 2.7 B) as a dark red solution.

In the solution ^{1}H NMR (CD_2Cl_2) spectrum taken during the reaction of complex **2.2** with [(^{tBu}PONOP)IrCl] (Figure 2.12 A) singlets are observed corresponding to the *ortho*- and *para*-BAr^F protons at δ 7.56 (8H) and δ 7.34 (4H). The spectrum also shows broad peaks at δ 34.45 (fwhm = full width at half maximum = ~ 644 Hz, 1H) and 8.88 (fwhm = ~ 70 Hz, 2H) which correspond to the *para*- and *meta*-aryl CH protons of the pyridine backbone ring respectively. Pyridine environments in PONOP ligands are usually observed as a well-defined triplet and doublet, for instance at δ 7.82 and 6.38 ($^3J_{HH}$ = 8 Hz) respectively as reported for [(^{tBu}PONOP)IrCl].[46] The broad and significantly shifted peaks observed in complex **2.4** are characteristic of paramagnetic compounds, which contain one or more unpaired electron.[45] The ^{t}Bu protons, which are observed at δ 1.43 for the [(^{tBu}PONOP)IrCl] precursor, are observed at δ 17.45 (fwhm= ~ 657 Hz, 32H)due to their close proximity to the paramagnetic low spin d^7 iridium centre. Sharp signals corresponding to free NBE are also observed, for

instance the alkene proton at δ 5.98.[28] The NBE was removed by crystallisation from dichloromethane/hexane at room temperature, which afforded dark red crystals of complex **2.4** (15 mg, 49%). A signal in the $^{31}P\{^{1}H\}$ NMR spectrum of complex **2.4** was not observed due to the paramagnetism.

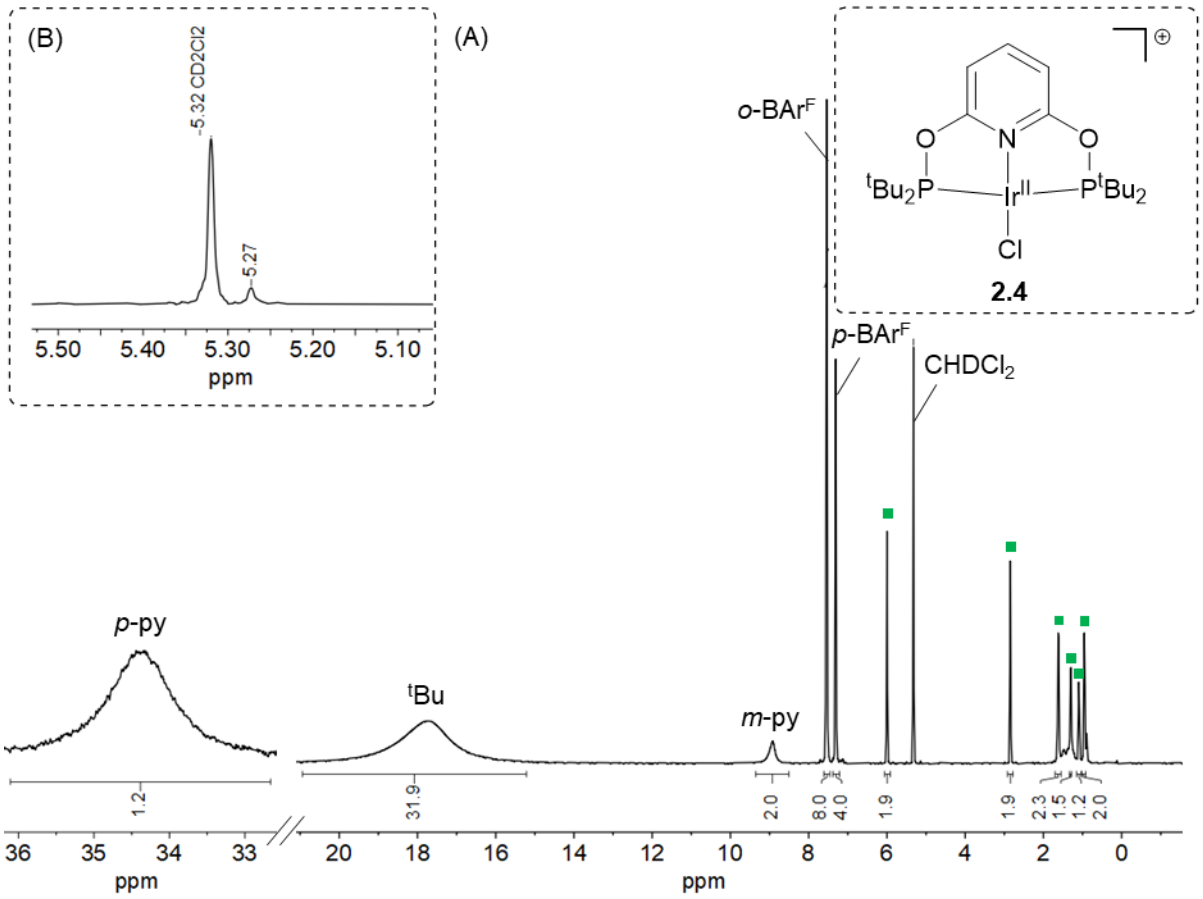

Figure 2.12 (A) The ^{1}H NMR spectrum of the reaction of complex **2.2** with [(^{tBu}PONOP)IrCl], ■ denotes free NBE signals. The y-gain of the δ 34.45 region was increased ×10 due to the broadness of the peak. (B) The solvent region of the ^{1}H NMR spectrum of complex **2.4**, containing a flame-sealed capillary of CD_2Cl_2 for Evans' measurement (500 MHz, CD_2Cl_2, 298 K).

The effective magnetic moment was measured *via* the Evans method[47, 48] using crystals of complex **2.4** (CD_2Cl_2, 298 K, Figure 2.12 B) to be μ_{eff} = 1.706 μ_B, which is consistent with one unpaired electron as would be expected for a low spin d^7 square planar complex. This is similar to the magnetic moment of [(^{tBu}POCOP)Ir(OTf)][BAr^F_4] (1.75 μ_B).[18]

Complex **2.4** crystallises in the space group $P2_1/n$ and the associated molecular structure displays a square planar geometry (Figure 2.13) with Ir1–Cl1 and Ir1–N2 distances of

2.2900(6) and 2.022(2) Å respectively, and Ir–P distances of 2.2924(6) and 2.2867(6) Å. Whilst the crystal structure of the iridium(I) [(^{tBu}PONOP)IrCl] has not yet been reported and thus cannot be compared, an elongation of the Ir–P distances may be expected for complex **2.4** relative to [(^{tBu}PONOP)IrCl]. Several examples of iridium(II) complexes are reported which describe the lengthening of M–P distances upon removal of an electron.[49, 50] For example, a lengthening of the relative Ir–P distances in the reported [(^{tBu}POCOP)Ir(N_2)][BAr^F_4] (2.313(1), 2.316(2) Å) is observed upon oxidation from [(^{tBu}POCOP)Ir(N_2)] (2.2764(11), 2.2778(11) Å), as well as a shortening of the Ir–C bond to the POCOP ligand (2.017(4) to 1.979(5) Å) due to stronger σ-donation to the iridium(II) which is more electrophilic than iridium(I).[18]

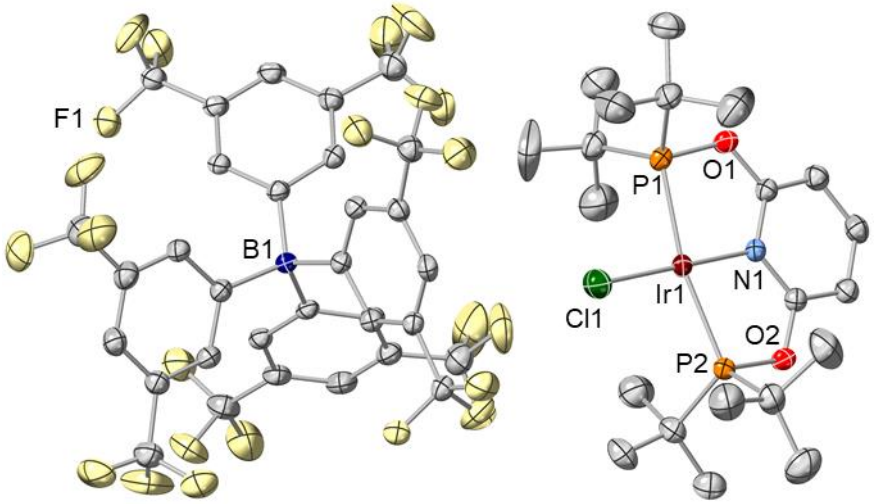

Figure 2.13 The molecular structure of complex **2.4**. Displacement ellipsoids are set at 50% probability level. Hydrogen atoms are omitted for clarity. Selected bond distances (Å): Ir1–Cl1, 2.2900(6); Ir1–P1, 2.2924(6); Ir1–P2, 2.2867(6); Ir1–N2, 2.022(2). Selected bond angles (°): P1–Ir1–Cl1, 98.21(3); P2–Ir1–Cl1, 98.47(3); P1–Ir1–N1, 81.67(6); P2–Ir1–N1, 81.58(6).

To investigate the use of complex **2.2** as a salt metathesis reagent, the synthesis of the platinum(II) complex [(dcpe)PtCl]$_2$[BAr^F_4]$_2$ (**2.5**) was explored. Complex **2.5** is reported to be the product of the reactions of a) hydrochloric acid with [(dcpe)Pt(Me)(OEt_2)][BAr^F_4] or b) [(dcpe)Pt(Me)(Cl)][BAr^F_4] with [H(OEt_2)$_2$][BAr^F_4].[51] Both of these routes are multistep syntheses from [(dcpe)$PtCl_2$], and so it was hypothesised that complex **2.5** could instead be synthesised directly from [(dcpe)$PtCl_2$] in a relatively straightforward reaction from complex **2.2**.

Complex **2.2** and [(dcpe)$PtCl_2$] were combined in 1,2-difluorobenzene at room temperature, immediately forming AgCl rather than Ag(0) as observed in the synthesis of complex **2.4**, which was removed upon filtration. The subsequent layering of 1,2-difluorobenzene/hexane at room temperature resulted in colourless crystals of complex **2.5** (8 mg, 44%, Scheme 2.7 C, Figure 2.14 A). Complex **2.5** crystallises in the space group $P\bar{1}$. The molecular structure displays a dimeric structure wherein the two crystallographically equivalent platinum(II) centres are bridged by two chloride ligands with a Pt1–Cl1 distance of 2.39815(3) Å, which is longer than the Pt–Cl distances in the monomeric [(dcpe)$PtCl_2$] (2.366(2), 2.365(2) Å).[52] The similar platinum(II) dimer species, [{(η^7-$C_7H_6PCy_2$)Ti(η^5-$C_5H_4PCy_2$)}$PtCl]_2[BAr^F{}_4]_2$, which is synthesised from the reaction of [{(η^7-$C_7H_6PCy_2$)Ti(η^5-$C_5H_4PCy_2$)}$PtCl_2$][$BAr^F{}_4$] with K[$BAr^F{}_4$] (Figure 2.15 C), experiences a similar elongation of the Pt–Cl bonds (2.3711(6), 2.3779(6) to 2.4002(8), 2.4234(8) Å).[53] The Cl1–Pt1–Cl1' angle (~ 83.812°) is smaller than that of Cl1–Pt1–Cl2 in [(dcpe)$PtCl_2$] (89.23(9)°) as to be expected upon forming a chloride bridged dimer. The Pt1–P distances (2.22398(2), 2.22502(4) Å) are within error of [(dcpe)$PtCl_2$] (2.222(2), 2.225(2) Å).

In the solution ^{1}H NMR (CD_2Cl_2) spectrum of complex **2.5** singlets are observed corresponding to the *ortho*- and *para*-$BAr^F{}_4$ protons at δ 7.73 (8H) and δ 7.56 (4H). The dcpe signals are observed as overlapping multiplets δ 2.20–1.46. The $^{31}P\{^1H\}$ NMR (CD_2Cl_2) spectrum reveals a singlet at δ 74.2 with ^{195}Pt satellites ($^1J_{PPt}$ = 3654 Hz) (Figure 2.14 B), shifted downfield and with a bigger Pt–P coupling constant than that of the [(dcpe)$PtCl_2$] precursor (δ 65.1, $^1J_{PPt}$ = 3573 Hz).[54] The larger Pt–P coupling constant of complex **2.5** compared to [(dcpe)$PtCl_2$] is consistent with the chloride ligands having weaker *trans*-influence when bridging two metal centres. A similar Pt–P coupling constant increase is seen upon dimerization of [(dppe)$PtCl_2$] (dppe = 1,2-bis-(diphenylphosphino)ethane; δ 41.6, $^1J_{PPt}$ = 3619 Hz)[55] to form [(dppe)$PtCl]_2[OTf]_2$ (δ 52.3, $^1J_{PPt}$ = 3780 Hz).[56]

The NMR data and molecular structure of complex **2.5** are consistent with a platinum(II) diamagnetic complex, demonstrating that complex **2.2** has acted as a halide abstraction agent

in the synthesis of complex **2.5**, rather than an oxidant as seen in the synthesis of complex **2.4**.

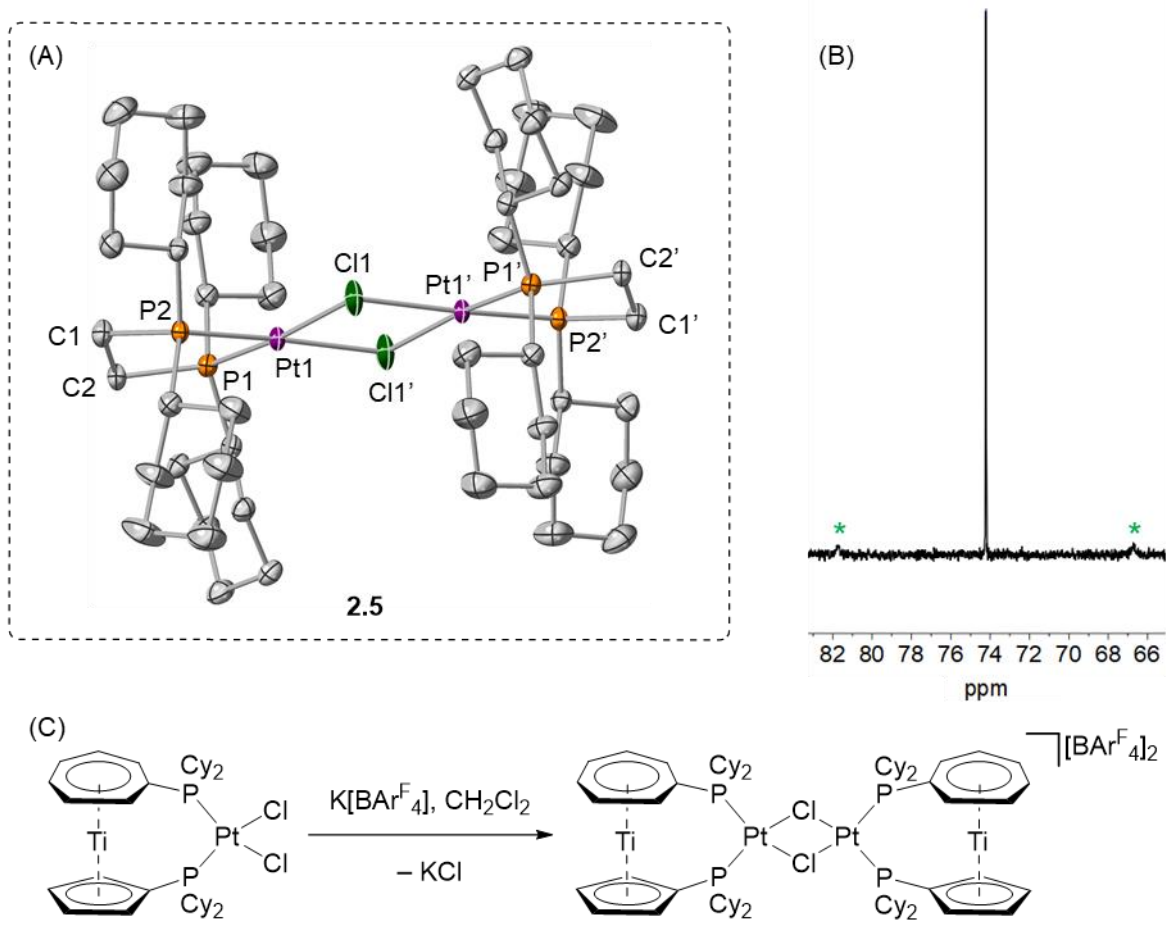

Figure 2.14 (A) The grown cation structure of complex **2.5**. Displacement ellipsoids are set at 50% probability level. Hydrogen atoms and $[BAr^F_4]^-$ anions are excluded for clarity. Selected bond distances (Å): Pt1–Cl1, 2.39815(3); Pt1–P1, 2.22398(2); Pt1–P2, 2.22502(4). Selected bond angles (°): P1– Pt1–P2, 87.5999(12); P1– Pt1–Cl1, 175.90164(7); P2– Pt1–Cl1, 94.9577(12). (B) The $^{31}P\{^1H\}$ NMR spectrum of complex **2.5** (242 MHz, CD_2Cl_2, 298 K), * denotes ^{195}Pt satellites. (C) The literature reaction of [{(η^7-$C_7H_6PCy_2$)Ti(η^5-$C_5H_4PCy_2$)}$PtCl_2$][BAr^F_4] and K[BAr^F_4] to form [{(η^7-$C_7H_6PCy_2$)Ti(η^5-$C_5H_4PCy_2$)}PtCl]$_2$[BAr^F_4]$_2$.

Given the solution-state lability of the NBE and $[BAr^F_4]^-$ ligands of complex **2.2** shown in the formation of complexes **2.3**–**2.5**, the SC-SC reactivity with complex **2.2** was also explored. However, complex **2.2** demonstrates no reactivity in the solid state in the attempted SC-SC reactions with CO (2 bar absolute) and C_2H_4 (2 bar absolute), or under vacuum (10^{-3} mbar) for which no change was observed after 24 hrs by SCXRD and solution-state ^1H NMR

spectroscopy. This prompted investigation into different systems for the SMOM chemistry of group XI, as is detailed in chapter 3.

2.5 Summary and Conclusions

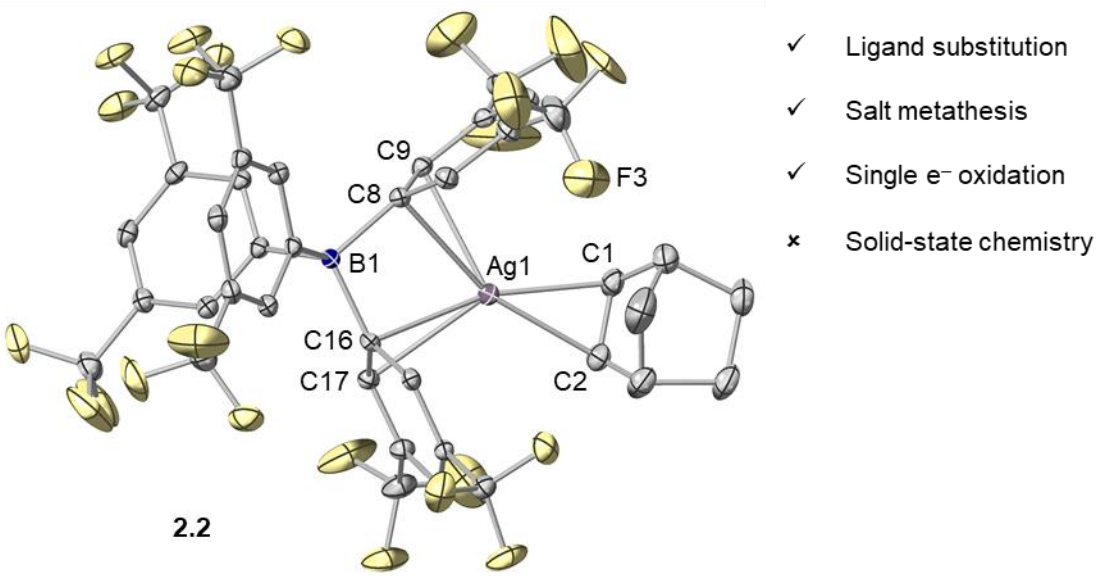

Figure 2.15 A summary of the work presented in chapter 2 of this thesis.

This chapter has presented the formation of the new silver(I) NBE complexes $[Ag(NBE)_3][BAr^F_4]\cdot 0.9(F_2C_6H_4)$ (**2.1·DFB**) and $[Ag(NBE)(\eta^2{:}\eta^2\text{-}BAr^F_4)]$ (**2.2**, Figure 2.15). The characterisation of complex **2.2** in the solution (NMR spectroscopy) and solid-state (SSNMR spectroscopy, XRD) has been compared, and suggests that **2.2** exists as a different species in solution, potentially a dichloromethane solvent complex which is in rapid exchange with a proposed Ag···H–C agostic complex. Onward reactivity of the zwitterionic complex **2.2** has also been investigated as a potential source of $Ag[BAr^F_4]$ for use in salt metathesis and single electron redox reactions, as demonstrated by the formation of the new compounds $[Ag(DME)_3][BAr^F_4]$ (**2.3**) and $[(^tBuPONOP)IrCl][BAr^F_4]$ (**2.4**) as well as the known $[(dcpe)PtCl]_2[BAr^F_4]_2$ (**2.5**). Attempts at SC-SC transformations with complexes **2.1·DFB** and **2.2** proved unsuccessful despite the solution-state lability of the NBE ligand.

2.6 Experimental

For general procedures see appendix section 7.1 of this thesis. Na[BAr^F_4],[12] $[Ag(NBE)_3][SbF_6]$,[28] [(^{tBu}PONOP)IrCl][46] and [(dcpe)$PtCl_2$][54] were prepared according to literature methods. All chemical shifts (δ) are quoted in ppm and coupling constants (*J*) in Hz. The magnetic moment of complex **2.4** was determined by the Evans method[47, 48] using the shift of the residual solvent proton resonance in a CD_2Cl_2 solution of complex **2.4** (9.8 mg, 0.35 mL) compared to the signal of CD_2Cl_2 in a sealed capillary at 298 K on a Bruker AVIIIHD 500 MHz spectrometer.

2.6.1 $[Ag(NBE)_3][BAr^F_4]$ (2.1·DFB)

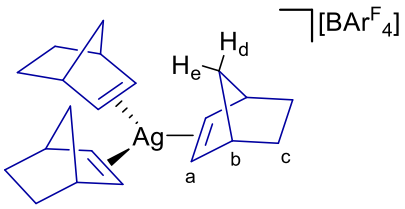

A suspension of Na[BAr^F_4] (199 mg, 0.22 mmol) in dichloromethane (5 mL) was added to a solution of $[Ag(NBE)_3][SbF_6]$ (140 mg, 0.22 mmol) in dichloromethane (5 mL). The reaction mixture was stirred at room temperature for 2 hr then filtered via cannula. Crystallisation from 1,2-difluorobenzene/hexane at –20 °C afforded colourless crystals of complex **2.1·DFB**. (Yield: 188 mg, 0.15 mmol, 68%)

^{1}H NMR (500 MHz, CD_2Cl_2, 298 K): δ 7.73 (br s, 8H, *ortho*-BAr^F_4), 7.57 (s, 4H, *para*-BAr^F_4), overlapping 7.19 and 7.12 (m, 3.7H, 1,2-$F_2C_6H_4$), 6.19 (s, 6H, H_a), 3.16 (s, 6H, H_b), 1.78 (d, $^2J_{HH}$ = 8 Hz, 6H, *exo*-H_c), 1.30 (m, 1.7H, hexane), 1.18 (d, $^2J_{HH}$ = 9 Hz, 3H, H_d), 1.02 (dm, $^2J_{HH}$ = 8 Hz, 6H, *endo*- H_c), 0.88 (m, 1.4H, hexane), 0.74 (d, $^2J_{HH}$ = 9 Hz, 3H, H_e).

^{13}C{^{1}H} NMR (125 MHz, CD_2Cl_2, 298 K): δ 162.1 (q, $^1J_{CB}$ = 50 Hz, *ipso*-BAr^F_4), 135.2 (s, *ortho*-BAr^F_4), 131.4 (s, C_a) 129.3 (q, $^2J_{CF}$ = 32 Hz, *meta*-BAr^F_4), 124.9 (q, $^1J_{CF}$ = 272 Hz, CF_3), 117.9 (m, $^3J_{CF}$ = 4 Hz, *para*-BAr^F_4), 48.0 (s, $C_{d/e}$), 43.2 (s, C_b), 34.5 (hexane), 23.8 (C_c), 22.8 (hexane), 14.2 (hexane).

$^{11}B\{^{1}H\}$ NMR (192 MHz, CD_2Cl_2, 298 K): δ -6.6 (s).

ESI-MS m/z (CH_2Cl_2) found (calculated) for $Ag_1C_{21}H_{30}$ $[M]^+$: 389.1393 (390.3350).

Elemental analysis calc for $C_{53}H_{42}Ag_1B_1F_{24}\cdot 0.7(C_6H_4F_2)$: C 51.52; H 3.39; N 0; found: C 44.84; H 1.85; N 0. Repeat attempts also led to discrepancies between the found and calculated values, the reason for which could not be identified but is potentially due to residual $Ag[SbF_6]$ and solvent. Despite this, the complex was pure by NMR, SCXRD, and ESI-MS, and so was used for subsequent reactivity.

2.6.2 [Ag(NBE)(η^2:η^2-BAr^F_4)] (2.2)

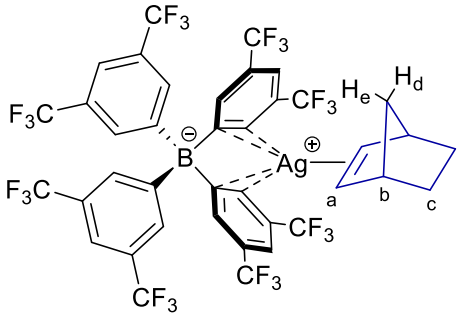

A solution of complex **2.1·DFB** (194 mg, 0.31 mmol) in 1,2-difluorobenzene (5 mL) was precipitated out with pentane. The solution was removed *via* cannula and the white solid dried *in vacuo,* then precipitated from 1,2-difluorobenzene/pentane twice more. Crystallisation from 1,2-difluorobenzene/hexane at –20 °C afforded colourless crystals of complex **2.2**. (Yield: 206 mg, 0.19 mmol, 62%).

^{1}H NMR (500 MHz, CD_2Cl_2, 193 K): δ 7.88 (s, 8H, *ortho*-BAr^F_4), 7.75 (s, 4H, *para*-BAr^F_4), 6.47 (d, $^3J_{HH}$ = 5 Hz, 0.3H, H'$_a$), 5.21 (d, $^3J_{HH}$ = 7 Hz, 1.7H, H''$_a$), 3.19 (s, 0.3H, H'$_b$), 2.40 (s, 2H, H''$_b$), 1.73 (d, $^3J_{HH}$ = 9 Hz, 0.3H, *exo*-H'$_c$), 1.45 (d, $^3J_{HH}$ = 9 Hz, 1.7H, *exo*-H''$_c$), 1.18 (br d, $^3J_{HH}$ = 9 Hz, 0.2H, H'$_d$), 0.91 (d, $^3J_{HH}$ = 8 Hz, 0.4H, *endo*-H'$_c$), 0.78 (t, $^3J_{HH}$ = 7 Hz, 0.2H, H'$_e$), 0.71 (d, $^3J_{HH}$ = 9 Hz, 0.9H, H''$_d$), 0.54 (d, $^3J_{HH}$ = 8 Hz, 1.7H, *endo*-H''$_c$), –0.52 (d, $^3J_{HH}$ = 9 Hz, 0.9H, H''$_e$).

^{1}H NMR (500 MHz, CD_2Cl_2, 298 K): δ 7.88 (s, 8H, *ortho*-BAr^{F}_4), 7.75 (s, 4H, *para*-BAr^{F}_4), 5.79 (s, 2H, H_a), 2.81 (s, 2H, H_b), 1.66 (d, $^{2}J_{HH}$ = 9 Hz, 2H, exo-H_c), 1.00 (d, $^{2}J_{HH}$ = 9 Hz, 1H, H_d), 0.79 (d, $^{2}J_{HH}$ = 9 Hz, 2H, endo-H_c), 0.05 (br s, 1H, H_e).

^{1}H NMR (600 MHz, 1,2-$F_2C_6H_4$, 298 K): δ 8.41 (s, 8H, *ortho*-BAr^{F}_4), 7.86 (s, 4H, *para*-BAr^{F}_4), 5.88 (s, 2H, H_a), 2.90 (s, 2H, H_b), 1.63 (d, $^{2}J_{HH}$ = 9 Hz, 2H, H_c), 1.03 (d, $^{2}J_{HH}$ = 10 Hz, 2H, H_d), 0.75 (d, $^{2}J_{HH}$ = 9 Hz, 1H, H_c), 0.24 (br s, 1H, H_e).

^{11}B{^{1}H} NMR (192 MHz, 1,2-$F_2C_6H_4$, 298 K): δ -6.8 (s).

^{13}C{^{1}H} SSNMR (100 MHz, 10 kHz spin rate, 298 K): δ 161.8 (*ipso*-BAr^{F}_4), 158.4 (*ipso*-BAr^{F}_4), 134.9, 133.7, 132.1, 130.6, 129.6, 127.4, 124.6, 120.7, 118.1 (BAr^{F}_4 and NBE alkene environments), 48.1 (C_d), 42.8 (C_b), 21.5 (C_c).

Elemental analysis calc for $C_{39}H_{22}Ag_1B_1F_{24}$: C 43.97; H 2.08; N 0; found: C 44.04; H 2.04; N 0.

2.6.3 [Ag(DME)$_3$][BAr^{F}_4] (2.3)

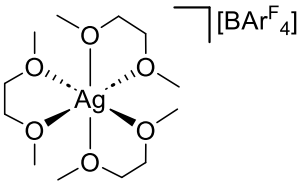

Complex **2.2** (149 mg, 0.14 mmol) in 1,2-dimethoxyethane (2 mL) was stirred for 1 hr then dried *in vacuo*. Crystallisation from 1,2-dichloroethane/hexane at –20 °C afforded colourless crystals of complex **2.3**. (Yield: 85 mg, 0.07 mmol, 49 %).

^{1}H NMR (500 MHz, CD_2Cl_2, 298 K): δ 7.76 (s, 8H, *ortho*-BAr^{F}_4), 7.60 (s, 4H, *para*-BAr^{F}_4), 3.55 (s, 12H, $(CH_3OC\underline{H}_2)_2$), 3.38 (s, 18H, $(C\underline{H}_3OCH_2)_2$).

^{13}C{^{1}H} NMR (125 MHz, CD_2Cl_2, 298 K): δ 162.1 (q, $^{1}J_{CB}$ = 50 Hz, *ipso*-BAr^{F}_4), 135.0 (s, *ortho*-BAr^{F}_4), 130.2 (s, *meta*-BAr^{F}_4), 124.4 (q, $^{1}J_{CF}$ = 272 Hz, CF_3), 118.0 (s, *para*-BAr^{F}_4), 72.0 (s, $(CH_3O\underline{C}H_2)_2$), 59.7 (s, $(\underline{C}H_3OCH_2)_2$), 44.2 (1,2-dichloroethane).

^{11}B NMR (160, CD_2Cl_2, 298 K): δ -6.7 (s).

Elemental analysis calc for $C_{44}H_{42}Ag_1B_1F_{24}O_6$: C 42.57; H 3.41; N 0; found: C 42.97; H 3.46; N 0.

2.6.4 [(^{tBu}PONOP)IrCl][BAr^F_4] (2.4)

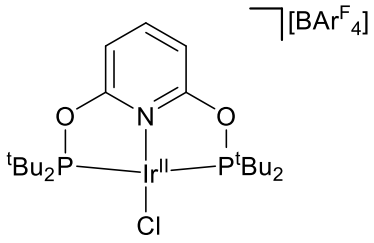

A solution of complex **2.2** (21 mg, 0.020 mmol) and [(^{tBu}PONOP)IrCl] (16 mg, 0.025 mmol) in dichloromethane (2 mL) was stirred at room temperature, immediately forming a black precipitate which was filtered off *via* cannula. The layering with dichloromethane/hexane for crystallisation at room temperature resulted in the formation of dark red crystals of complex **2.4**. (Yield: 15 mg, 0.010 mmol, 49%).

^{1}H NMR (500 MHz, CD_2Cl_2, 298 K): δ 34.45 (br s, 1H, *para*-py) 17.45 (br s, 32H, ^{t}Bu), 8.88 (br s, 2H, *meta*-py), 7.56 (s, 8H, *ortho*-BAr^F_4), 7.34 (s, 4H, *para*-BAr^F_4).

^{13}C{^{1}H} NMR (125 MHz, CD_2Cl_2, 298 K): δ 162.0 (q, $^1J_{CB}$ = 50 Hz, *ipso*-BAr^F_4), 135.0 (s, *ortho*-BAr^F_4), 129.0 (q, $^2J_{CF}$ = 32 Hz, *meta*-BAr^F_4), 124.7 (q, $^1J_{CF}$ = 272 Hz, CF_3), 117.7 (s, *para*-BAr^F_4).

Evans' measurement (500 MHz, CD_2Cl_2, 298 K): μ_{eff} = 1.706.

Elemental analysis calc for $C_{53}H_{51}Ir_1P_2N_1O_2Cl_1B_1F_{24}$: C 42.71; H 3.45; N 0.94; found: C 43.11; H 3.63; N 0.95.

2.6.5 [(dcpe)PtCl]$_2$[BAr^F_4]$_2$ (2.5)

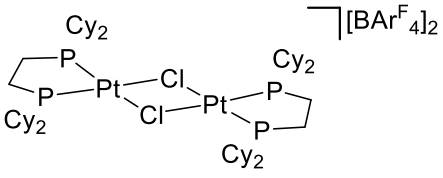

Synthesis adapted from literature procedure.[51]

1,2-difluorobenzene (2 mL) was added to an ampoule containing [(dcpe)$PtCl_2$] (8 mg, 0.012 mmol) and complex **2.2** (13 mg, 0.012 mmol) and stirred for 5 minutes prior to removal of all volatiles *in vacuo*. The white solid was then extracted with 1,2-difluorobenzene (1 mL) and filtered via cannula. The layering of 1,2-difluorobenzene/hexane yielded colourless crystals of complex **2.5**, which were washed with hexane (3 x 2 mL). (Yield: 8 mg, 0.005 mmol, 44 %)

^{1}H NMR (CD_2Cl_2, 600 MHz, 298 K): δ 7.73 (s, *ortho*-$BAr^F{}_4$, 16H), 7.56 (s, *para*-$BAr^F{}_4$), 2.20-2.10 (m, 16H), 1.96-1.87 (m, 24H), 1.85-1.77 (m, 16H), 1.46-1.22 (m, 40H).

^{1}H{^{31}P} NMR (CD_2Cl_2, 600 MHz, 298 K): δ 7.73 (s, *ortho*-$BAr^F{}_4$, 16 H), 7.56 (s, *para*-$BAr^F{}_4$), 2.20-2.10 (m, 16H), 1.96-1.87 (m, 24H), 1.85-1.77 (m, 16H), 1.46-1.22 (m, 40H).

^{13}C{^{1}H} NMR (CD_2Cl_2, 150 MHz, 298 K): δ 162.2 (*ipso*-$BAr^F{}_4$), 135.2 (*ortho*-$BAr^F{}_4$), 129.3 (qq, $^2J_{CF}$ = 31.5 Hz; $^4J_{CF}$ = 2.80 Hz, *meta*-$BAr^F{}_4$), 125.0 (q, $^1J_{CF}$ = 274 Hz, CF_3), 117.9 (sept, $^3J_{CF}$ = 4.3 Hz, *para*-$BAr^F{}_4$), 35.7 (d, J_{CP} = 34 Hz), 29.9, 28.8, 26.9, 25.8.

^{31}P{^{1}H} NMR (CD_2Cl_2, 242 MHz, 298 K): δ 74.2 (s', $^1J_{PPt}$ = 3654 Hz)

2.7 References

1. S. H. Strauss, *Chem. Rev.*, **1993**, *93*, 927-942.
2. I. Krossing and I. Raabe, *Angew. Chem. Int. Ed.*, **2004**, *43*, 2066-2090.
3. B. A. Arndtsen and R. G. Bergman, *Science*, **1995**, *270*, 1970-1973.
4. S. D. Pike, A. L. Thompson, A. G. Algarra, D. C. Apperley, S. A. Macgregor and A. S. Weller, *Science*, **2012**, *337*, 1648-1651.
5. A. J. Bukvic, A. L. Burnage, G. J. Tizzard, A. J. Martínez-Martínez, A. I. McKay, N. H. Rees, B. E. Tegner, T. Krämer, H. Fish, M. R. Warren, S. J. Coles, S. A. Macgregor and A. S. Weller, *J. Am. Chem. Soc.*, **2021**, *143*, 5106-5120.
6. M. A. Sajjad, S. A. Macgregor and A. S. Weller, *Faraday Discuss.*, **2023**, *244*, 222-240.
7. Thomas M. Douglas, Eduardo Molinos, Simon K. Brayshaw and A. S. Weller, *Organometallics*, **2007**, *26*, 463-465.
8. J. Powell, A. Lough and T. Saeed, *J. Chem. Soc., Dalton Trans.*, **1997**, 4137-4138.
9. A. I. McKay, T. Krämer, N. H. Rees, A. L. Thompson, K. E. Christensen, S. A. Macgregor and A. S. Weller, *Organometallics*, **2017**, *36*, 22-25.
10. A. L. Colebatch, A. I. McKay, N. A. Beattie, S. A. Macgregor and A. S. Weller, *Eur. J. Inorg. Chem.*, **2017**, 4533-4540.
11. S. D. Pike, F. M. Chadwick, N. H. Rees, M. P. Scott, A. S. Weller, T. Krämer and S. A. Macgregor, *J. Am. Chem. Soc.*, **2015**, *137*, 820-833.
12. A. J. Martínez-Martínez and A. S. Weller, *Dalton Trans.*, **2019**, *48*, 3551-3554.
13. Y. Hayashi, J. J. Rohde and E. J. Corey, *J. Am. Chem. Soc.*, **1996**, *118*, 5502-5503.

14. W. E. Buschmann and J. S. Miller, *Chem. Eur. J.*, **1998**, *4*, 1731-1737.
15. K. J. Miller, T. T. Kitagawa and M. M. Abu-Omar, *Organometallics*, **2001**, *20*, 4403-4412.
16. E. Poverenov, I. Efremenko, G. Leitus, J. M. L. Martin and D. Milstein, *Organometallics*, **2013**, *32*, 4813-4819.
17. M. J. Bezdek, S. Guo and P. J. Chirik, *Inorg. Chem.*, **2016**, *55*, 3117-3127.
18. N. Hidalgo, J. J. Moreno, I. García-Rubio and J. Campos, *Angew. Chem. Int. Ed.*, **2022**, *61*, e202206831.
19. H. Salem, L. J. W. Shimon, G. Leitus, L. Weiner and D. Milstein, *Organometallics*, **2008**, *27*, 2293-2299.
20. J. H. Golden, P. F. Mutolo, E. B. Lobkovsky and F. J. DiSalvo, *Inorg. Chem.*, **1994**, *33*, 5374-5375.
21. Y. Zhang, E. Herdtweck, J. Mink and F. E. Kühn, *New J. Chem.*, **2005**, *29*, 366-370.
22. C. M. Frech, L. J. W. Shimon and D. Milstein, *Organometallics*, **2009**, *28*, 1900-1908.
23. M. Gandelman, L. Konstantinovski, H. Rozenberg and D. Milstein, *Chem. Eur. J.*, **2003**, *9*, 2595-2602.
24. J. G. Bazemore, C. W. Padgett and B. Quillian, *J. Coord. Chem.*, **2021**, *74*, 306-314.
25. Z. Xie, T. Jelinek, R. Bau and C. A. Reed, *J. Am. Chem. Soc.*, **1994**, *116*, 1907-1913.
26. I. Krossing, *Chem. Eur. J.*, **2001**, *7*, 490-502.
27. G. Wang, Y. S. Ceylan, T. R. Cundari and H. V. R. Dias, *J. Am. Chem. Soc.*, **2017**, *139*, 14292-14301.
28. M. Fianchini, H. Dai and H. V. R. Dias, *Chem. Comm.*, **2009**, 6373-6375.
29. A. Reisinger, N. Trapp, C. Knapp, D. Himmel, F. Breher, H. Rüegger and I. Krossing, *Chem. Eur. J.*, **2009**, *15*.
30. J. Min, J. Benet-Buchholz and R. Boese, *Chem. Comm.*, **1998**, 2751-2752.
31. A. Reisinger, N. Trapp, I. Krossing, S. Altmannshofer, V. Herz, M. Presnitz and W. Scherer, *Angew. Chem. Int. Ed.*, **2007**, *46*, 8295-8298.
32. N. J. Patmore, C. Hague, J. H. Cotgreave, M. F. Mahon, C. G. Frost and A. S. Weller, *Chem. Eur. J.*, **2002**, *8*, 2088-2098.
33. A. Bihlmeier, M. Gonsior, I. Raabe, N. Trapp and I. Krossing, *Chem. Eur. J.*, **2004**, *10*, 5041-5051.
34. X. Ribas, C. Calle, A. Poater, A. Casitas, L. Gómez, R. Xifra, T. Parella, J. Benet-Buchholz, A. Schweiger, G. Mitrikas, M. Solà, A. Llobet and T. D. P. Stack, *J. Am. Chem. Soc.*, **2010**, *132*, 12299-12306.
35. M. Joost, S. Mallet-Ladeira, K. Miqueu, A. Amgoune and D. Bourissou, *Organometallics*, **2013**, *32*, 898-902.
36. A. E. Nako, A. J. P. White and M. R. Crimmin, *Dalton Trans.*, **2015**, *44*, 12530-12534.
37. F. Rekhroukh, L. Estévez, C. Bijani, K. Miqueu, A. Amgoune and D. Bourissou, *Angew. Chem. Int. Ed.*, **2016**, *55*, 3414-3418.
38. M. A. Huertos and A. S. Weller, *Chem. Comm.*, **2012**, *48*, 7185-7187.
39. X. L. Wu, S. T. Burns and K. W. Zilm, *J. Magn. Reson. A*, **1994**, *111*, 29-36.
40. G. R. Fulmer, A. J. M. Miller, N. H. Sherden, H. E. Gottlieb, A. Nudelman, B. M. Stoltz, J. E. Bercaw and K. I. Goldberg, *Organometallics*, **2010**, *29*, 2176-2179.
41. Z. Liu, R. J. Deeth, J. S. Butler, A. Habtemariam, M. E. Newton and P. J. Sadler, *Angew. Chem. Int. Ed.*, **2013**, *52*, 4194-4197.
42. B. d. Bruin, T. P. J. Peters, S. Thewissen, A. N. J. Blok, J. B. M. Wilting, R. d. Gelder, J. M. M. Smits and A. W. Gal, *Angew. Chem. Int. Ed.*, **2002**, *41*, 2135-2138.
43. K. K. Pandey, *Coord. Chem. Rev.*, **1992**, *121*, 1-42.
44. D. G. H. Hetterscheid, M. Klop, R. J. N. A. M. Kicken, J. M. M. Smits, E. J. Reijerse and B. d. Bruin, *Chem. Eur. J.*, **2007**, *13*, 3386-3405.
45. J. Meiners, M. G. Scheibel, M.-H. Lemée-Cailleau, S. A. Mason, M. B. Boeddinghaus, T. F. Fässler, E. Herdtweck, M. M. Khusniyarov and S. Schneider, *Angew. Chem. Int. Ed.*, **2011**, *50*, 8184-8187.
46. W. H. Bernskoetter, S. K. Hanson, S. K. Buzak, Z. Davis, P. S. White, R. Swartz, K. I. Goldberg and M. Brookhart, *J. Am. Chem. Soc.*, **2009**, *131*, 8603-8613.

47. D. F. Evans, *J. Chem. Soc.*, **1959**, 2003-2005.
48. S. K. Sur, *J. Magn. Reson.*, **1989**, *82*, 169-173.
49. A. G. Orpen and N. G. Connelly, *Organometallics*, **1990**, *9*, 1206-1210.
50. M. C. MacInnis, J. C. DeMott, E. M. Zolnhofer, J. Zhou, K. Meyer, R. P. Hughes and O. V. Ozerov, *Chem*, **2016**, *1*, 902-920.
51. Wayde V. Konze, B. L. Scott and G. J. Kubas, *J. Am. Chem. Soc.*, **2002**, *124*, 12550-12556.
52. J. T. Mague, M. J. Fink and C. A. Recatto, *Acta Crystallogr., Sect. C.*, **1993**, *49*, 1176-1178.
53. S. Tröndle, T. Bannenberg, M. Freytag, P. G. Jones and M. Tamm, *Organometallics*, **2019**, *38*, 4351-4362.
54. M. Hackett and G. M. Whitesides, *J. Am. Chem. Soc.*, **1988**, *110*, 1449-1462.
55. G. Annibale, M. Bortoluzzi, G. Marangoni and B. Pitteri, *Transit. Met. Chem.*, **2005**, *30*, 748-750.
56. F. E. Hahn, D. Klusmann and T. Pape, *Eur. J. Inorg. Chem.*, **2008**, *2008*, 4420-4424.

Chapter 3: Synthesis and SC-SC reactivity of a gold(I) *π*-ethylene system

The experimental work presented in this chapter was carried out in collaboration with Dr Miquel Navarro and Dr Jesús Campos at the Instituto de Investigaciones Químicas and University of Sevilla. The synthesis of complex **3.7** was conducted at the Instituto de Investigaciones Químicas and University of Sevilla by the thesis author, funded by the Wild Visiting Scholars Fund from the University of York. SSNMR data was collected by Dr Matthew Gyton or Dr Kristof Altus at the University of York. Computational work (Section 3.4.3) was conducted by Daniel Storm and Dr Arif Sajjad under the supervision of Professor Stuart Macgregor at the University of St Andrews.

Part of the work presented in this chapter has been published: C. L. Johnson, *et. al. Angew. Chem. Int. Ed.* **2024**, e202404264.

3.1 Introduction

As described in section 1.2, the coinage metals experience relatively weak metal-ligand interactions with alkene ligands, such as ethylene, due to poor overlap between the contracted d^{10} cation orbitals and alkene π^* antibonding orbitals, which results in a minimal backdonation contribution to bonding. Despite this, several coinage metal *π*-ethylene complexes are known, including the most simple homoleptic complexes, $[M(\eta^2\text{-}C_2H_4)_3][X]$ (M = Cu, Ag, Au; X = $Al(OC(CF_3)_3)_4$, SbF_6).[1-5] Whilst numerous *π*-ethylene complexes of copper and silver are known, gold(I) *π*-ethylene complexes are relatively rare, and include several tricoordinate complexes bearing bidentate phosphine or amine ligands (Figure 3.1).[6-10]

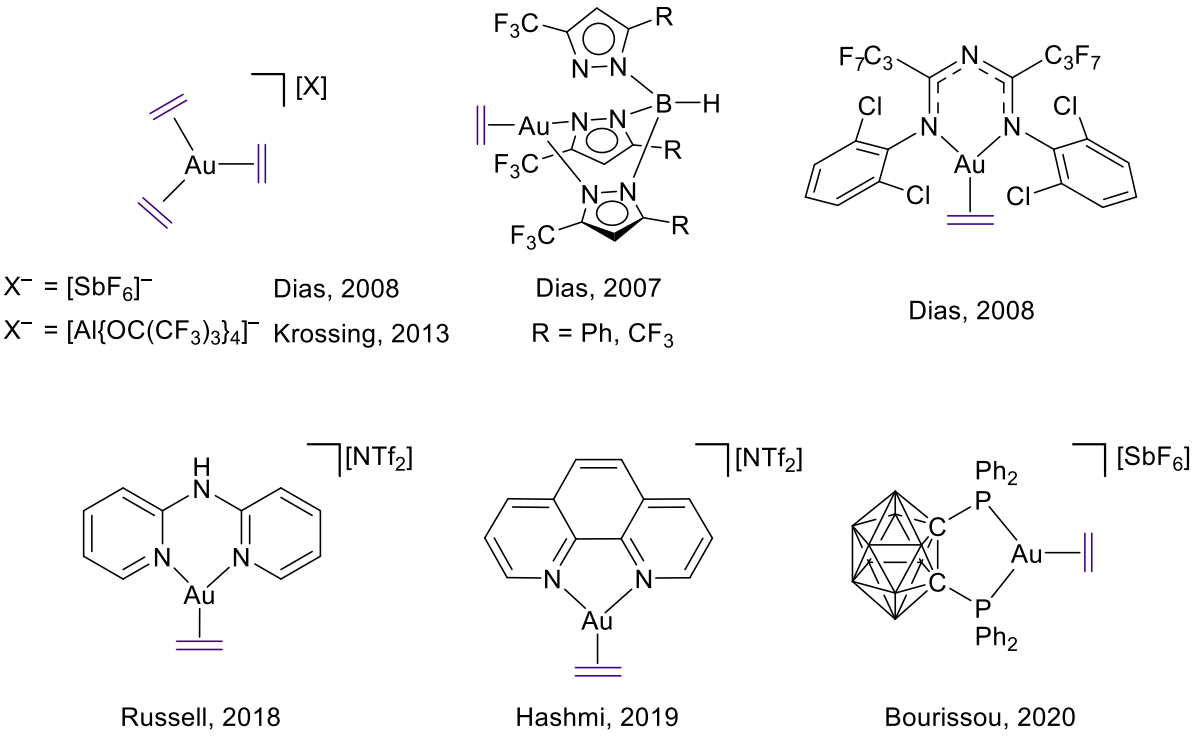

Figure 3.1 Structurally characterised gold(I) *π*-ethylene complexes.

The Campos group recently reported the synthesis of the first dicoordinate gold(I) *π*-ethylene complex, [(**L1**)Au(η^2-C_2H_4)][SbF_6] (**L1** = tris-2-(4,4′-di-tert-butylbiphenylyl)phosphine, Scheme 3.1).[11, 12] This was followed by the synthesis of a number of gold(I) *π*-ethylene complexes featuring other bulky phosphine ligands, such as $PMes_3$ and PMe_2Ar^{Dipp} (Mes = mesityl; Ar^{Dipp} = 2,6-(2,6-^{i}Pr$_2$-C_6H_3)$_2$$C_6H_3$).[13] However, attempts to isolate [(PPh_3)Au(η^2-C_2H_4)][SbF_6] led to the formation of [(PPh_3)$_2$Au][SbF_6] and Au(0), demonstrating that the bulky phosphine ligands **L1**, $PMes_3$ and PMe_2Ar^{Dipp} are required to kinetically stabilise the gold(I) *π*-ethylene group. In the absence of an ethylene atmosphere, decomposition to the corresponding [(phosphine)$_2$Au][SbF_6] and Au(0) was observed in solution for all of these complexes except [(**L1**)Au(η^2-C_2H_4)][SbF_6], which is stable even after weeks in solution, highlighting the remarkable stability imparted by the sterically demanding ligand **L1**.

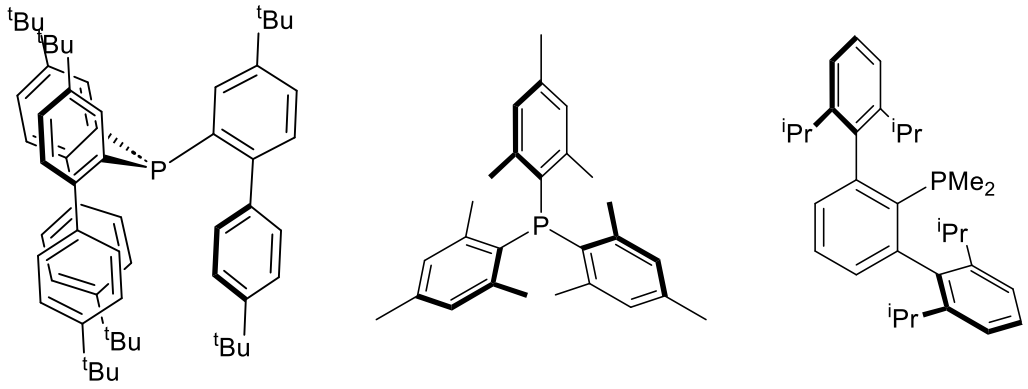

L1 $PMes_3$ PMe_2Ar^{Dipp}

Scheme 3.1 The structure of the phosphine ligands **L1**, $PMes_3$ and PMe_2Ar^{Dipp} used in the formation of gold(I) *π*-ethylene complexes for ethylene hydroamination catalysis.

The $[(L)Au(\eta^2\text{-}C_2H_4)][SbF_6]$ (L = **L1**, $PMes_3$ and PMe_2Ar^{Dipp}) complexes were shown to be catalytically active in the hydroamination of ethylene with imidazolidine-2-one in the solution-state, with $[(\mathbf{L1})Au(\eta^2\text{-}C_2H_4)][SbF_6]$ displaying 100% conversion to 1,2-ethylimidzaolidin-2-one in 18 hr under relatively mild conditions (1 bar ethylene, 80 °C, Scheme 3.2 A). $[(\mathbf{L1})Au(\eta^2\text{-}C_2H_4)][SbF_6]$ also proved reactive to substitution of the ethylene ligand with CO to form $[(\mathbf{L1})Au(CO)][SbF_6]$, which is in equilibrium with the starting ethylene complex (K_{eq} = 113, Scheme 3.2 B). Considering this solution-state reactivity and stability of the gold(I) *π*-ethylene adduct with ligand **L1**, it was postulated that the $[(\mathbf{L1})Au(\eta^2\text{-}C_2H_4)]^+$ cation might undergo similar ligand exchange reactions in the solid state under SMOM-type SC-SC conditions.

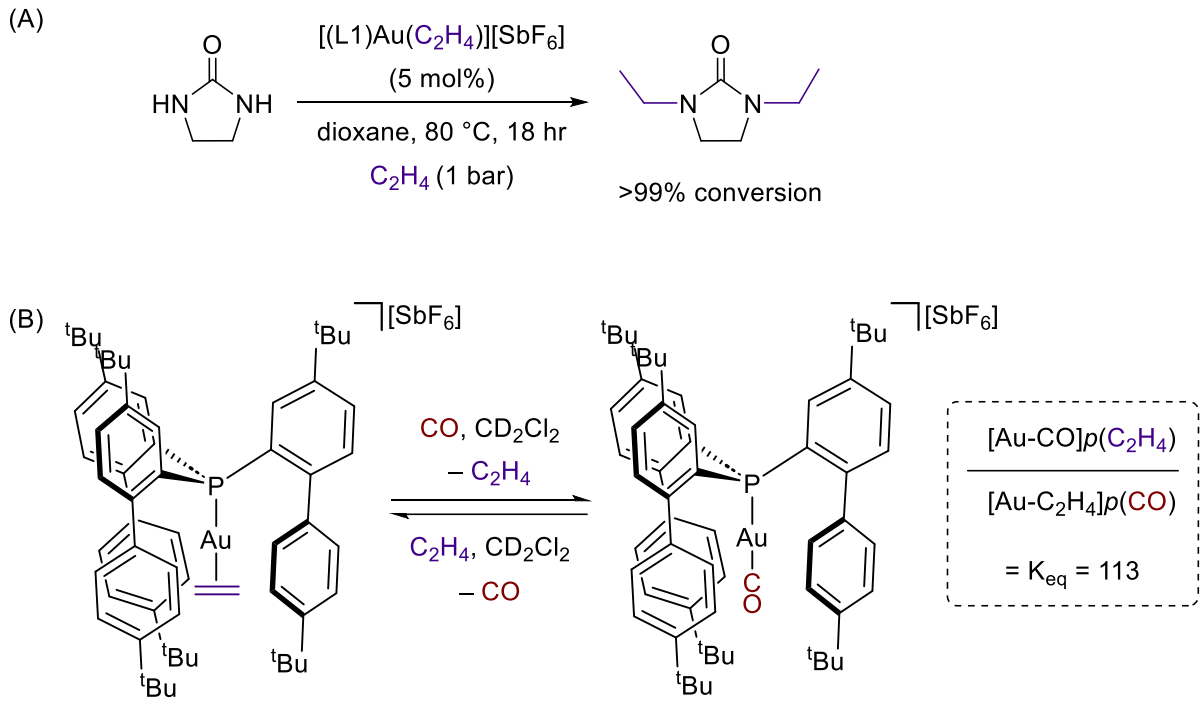

Scheme 3.2 (A) The catalytic solution-state hydroamination of ethylene with [(**L1**)Au(η^2-C_2H_4)][SbF_6]. (B) The solution-state equilibrium between [(**L1**)Au(η^2-C_2H_4)][SbF_6] and [(**L1**)Au(CO)][SbF_6], with an equilibrium constant, K_{eq}, of 113.

This chapter describes the synthesis and characterisation of [(**L1**)Au(η^2-C_2H_4)][BAr^F_4] and an investigation of its *in crystallo* reactivity with gaseous substrates to form [(**L1**)Au(L)][BAr^F_4] (L = CO, NH_3, $NHMe_2$, NMe_3, isobutylene and acetylene). As described in section 1.2, direct observation of gold(I) *π*-acetylene complexes have yet to be reported due to their rapid solution-state decomposition.[14] It was hypothesised that application of the same SMOM methodologies used to access highly reactive *σ*-alkane intermediates (section 1.1.1),[15] combined with the kinetic stabilisation provided by the bulky phosphine ligand **L1**, might allow for the synthesis of the first gold(I) *π*-acetylene complex, [(**L1**)Au(η^2-C_2H_2)][BAr^F_4].

3.2 Synthesis and characterisation of [(L1)Au(η²-C₂H₄)][BAr$^F_4$] (3.1)

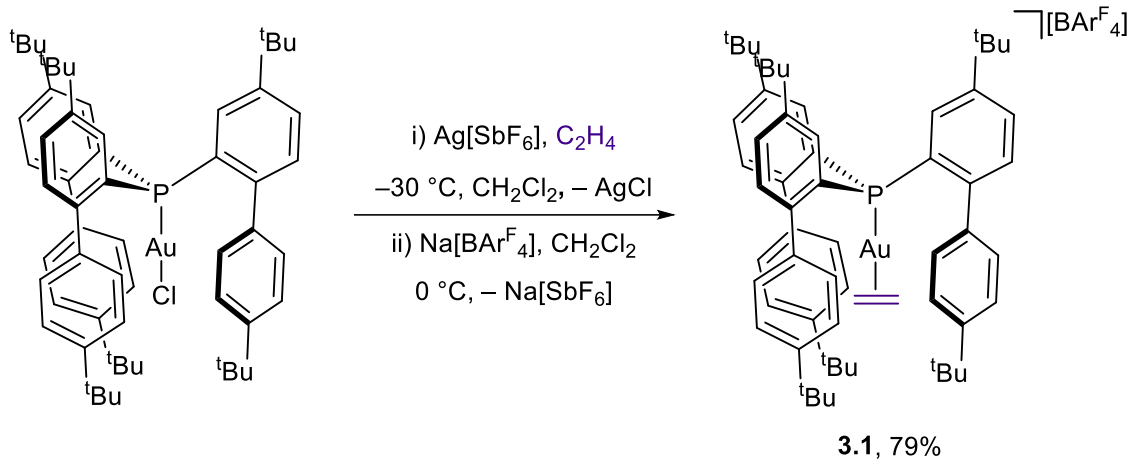

Scheme 3.3 The synthesis of [(**L1**)Au(η²-C_2H_4)][BAr$^F_4$] (**3.1**).

The known precursor complex, [(**L1**)Au(η²-C_2H_4)][SbF_6], was synthesised according to the literature procedure[11] *via* the dropwise addition of Ag[SbF_6] to [(**L1**)AuCl] in dichloromethane solution under an ethylene atmosphere (2 bar absolute) at –30 °C, followed by filtration through Celite at room temperature. Crystallisation from dichloromethane/hexane at –20 °C afforded colourless crystals of [(**L1**)Au(η²-C_2H_4)][SbF_6]. Attempted SC-SC reactions with [(**L1**)Au(η²-C_2H_4)][SbF_6] and CO (2 bar absolute) were hindered by relatively poor quality crystals which did not retain crystallinity upon addition of CO gas and incomplete reaction (~40% conversion). Therefore, the [SbF_6]$^-$ anion was exchanged for the well-known WCA [BAr$^F_4$]$^-$, which often provides better quality crystals. This was achieved by anion metathesis of [(**L1**)Au(η²-C_2H_4)][SbF_6] with Na[BAr$^F_4$] in dichloromethane and filtration at 0 °C, followed by crystallisation from 1,2-difluorobenzene/heptane at –20 °C. This afforded analytically pure colourless crystals of [(**L1**)Au(η²-C_2H_4)][BAr$^F_4$]•(1,2-$F_2C_6H_4$)(heptane) (**3.1**, Scheme 3.3) which were suitable for SC-SC study.

3.2.1 Two crystalline polymorphs of complex 3.1

Complex **3.1** crystallises in two different polymorphs in space groups $P2_1/n$ (*α*-**3.1**) and $P\bar{1}$ (*β*-**3.1**). Consideration of their extended lattice structure shows that both polymorphs *α*-**3.1** and *β*-**3.1** form similar bicapped square prismatic packing arrangements of ten [BAr$^F_4$]$^-$ anions

encapsulating two crystallographically identical cations (Figure 3.2). The packing of polymorph *α*-**3.1** appears slipped compared with *β*-**3.1** and possesses a larger cell volume (8979.581 Å^3) compared to polymorph *β*-**3.1** (5040.827 Å^3). The polymorphs also differ in their lattice solvents, as polymorph *α*-**3.1** has 1,2-difluorobenzene (0.35 occupancy) fractionally occupied within the lattice, whilst polymorph *β*-**3.1** has both 1,2-difluorobenzene (0.90 occupancy) and heptane (0.75 heptane) within the lattice.

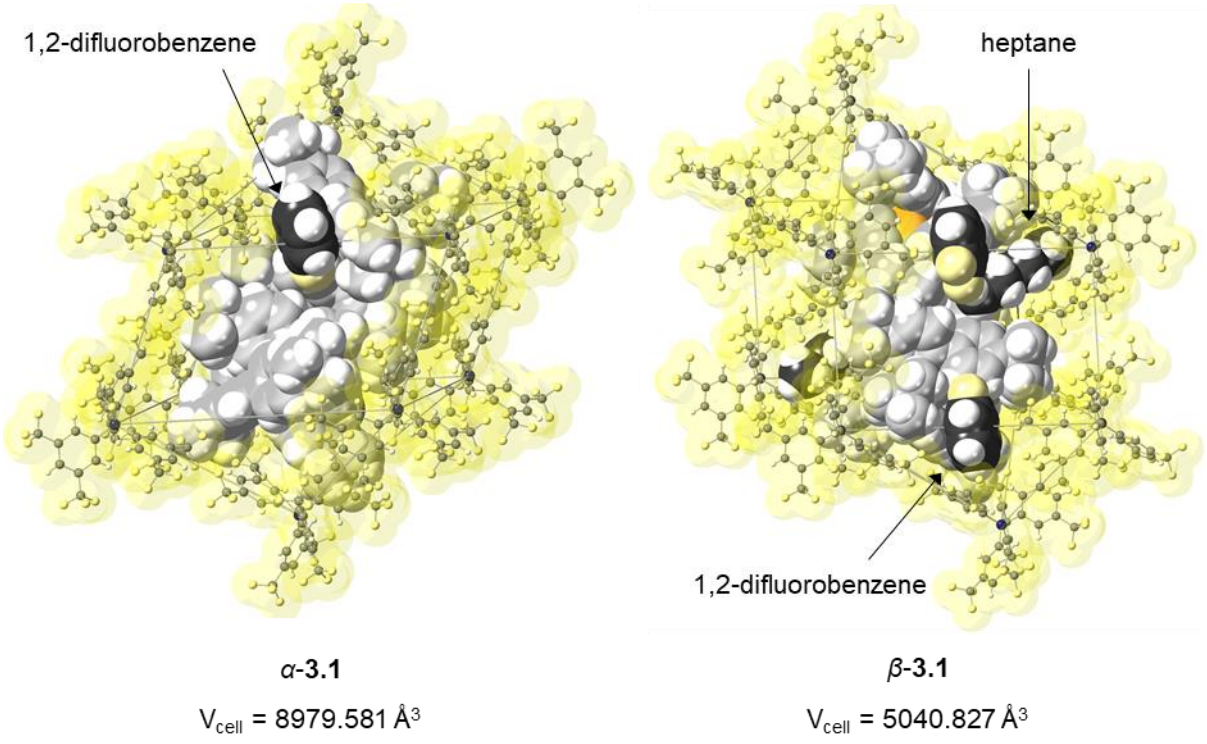

Figure 3.2 The extended solid-state structure of the two polymorphs of **3.1**, showing the bicapped square prismatic arrangements of $[BAr^F{}_4]^-$ anions and 1,2-difluorobenzene and heptane lattice solvents, depicted as Van der Waals radii.

Polymorphs *α*-**3.1** and *β*-**3.1** both lose solvent under vacuum, as shown by the disappearance of solvent peaks in the $^{13}C\{^1H\}$ SSNMR spectrum of the ensemble of polymorphs *α*-**3.1** and *β*-**3.1** after 20 hrs under vacuum when compared with argon-flushed crystals (10^{-3} mbar, Figure 3.3 A and B). Aside from the disappearance of the solvent peaks, no other significant changes are observed upon application of vacuum to the ensemble of polymorphs *α*-**3.1** and *β*-**3.1** in the $^{13}C\{^1H\}$ SSNMR spectrum, and the ethylene ligand is retained as shown by the peak at δ 109.4. In the $^{13}C\{^1H\}$ solution NMR spectrum the ethylene environment is observed as a

doublet at δ 109.4 ($^2J_{CP}$ = 9 Hz). Two peaks are observed in the $^{31}P\{^1H\}$ SSNMR spectrum of the ensemble of polymorphs *α*-**3.1** and *β*-**3.1** at δ 16.6 and 11.7 (Figure 3.3 C), due to the crystallographically inequivalent phosphorus environments of the two distinct crystal morphologies of complex **3.1**, *α*-**3.1** and *β*-**3.1**. In solution only one peak is observed at δ 13.0. Whilst coupling to the quadrupolar ^{197}Au (I = 3/2) nucleus has been reported previously in ^{31}P SSNMR spectra,[16-18] no such coupling is observed for complex **3.1**.

Due to their similar size and colourless nature, polymorphs *α*-**3.1** and *β*-**3.1** can only be distinguished through the screening of crystals using SCXRD. However, polymorph *β*-**3.1** is particularly sensitive to solvent loss under vacuum, consequently resulting in multiply faceted crystals which did not diffract (Figure 3.3 D).

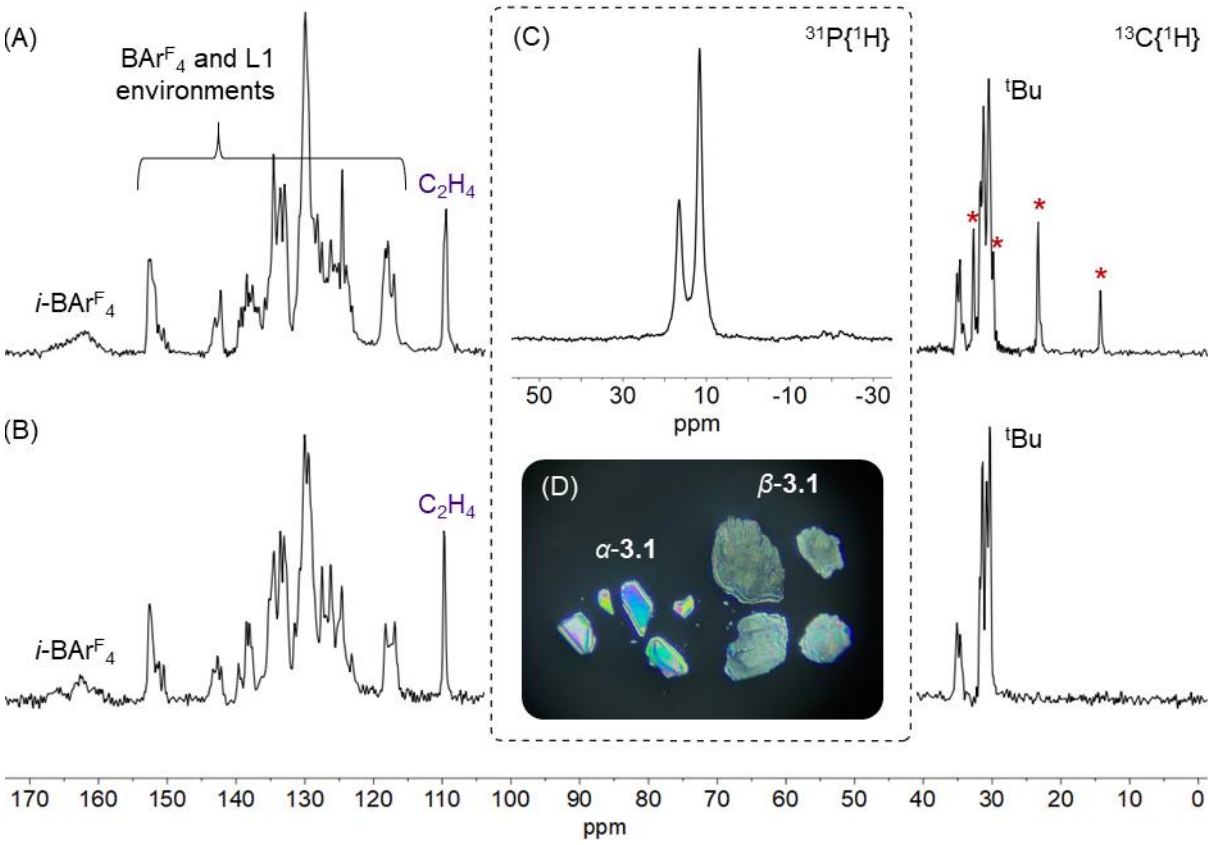

Figure 3.3 The solid-state $^{13}C\{^1H\}$ CPTOSS MAS NMR spectrum of the ensemble of polymorphs *α*-**3.1** and *β*-**3.1** (A) after 30 minutes argon purge and (B) after 20 hr under dynamic vacuum (100 MHz, 10 kHz spin rate, 298 K). * Denotes lattice heptane, which is lost under vacuum. (C) The solid-state $^{31}P\{^1H\}$ CP MAS NMR spectrum of the ensemble of polymorphs *α*-**3.1** and *β*-**3.1** (162 MHz, 20 kHz spin rate, 298 K). (D) Image of the crystals of both polymorphs of complex **3.1** after 20 hr vacuum (10^{-3} mbar).

This observed loss of crystallinity is reflected in the changes shown in the powder X-ray diffraction pattern of the mixture of polymorphs *α*-**3.1** and *β*-**3.1** before and after exposure to vacuum (Figure 3.4 A). Some of the sharp, well-defined peaks are lost, as highlighted by the difference plot (Figure 3.4 B), leading to a broadening of the pattern as is characteristic of amorphous material. Some crystallinity is still retained in the final pattern due to polymorph *α*-**3.1** remaining crystalline, as confirmed by the measurement of the SCXRD structure of *α*-**3.1** after vacuum.

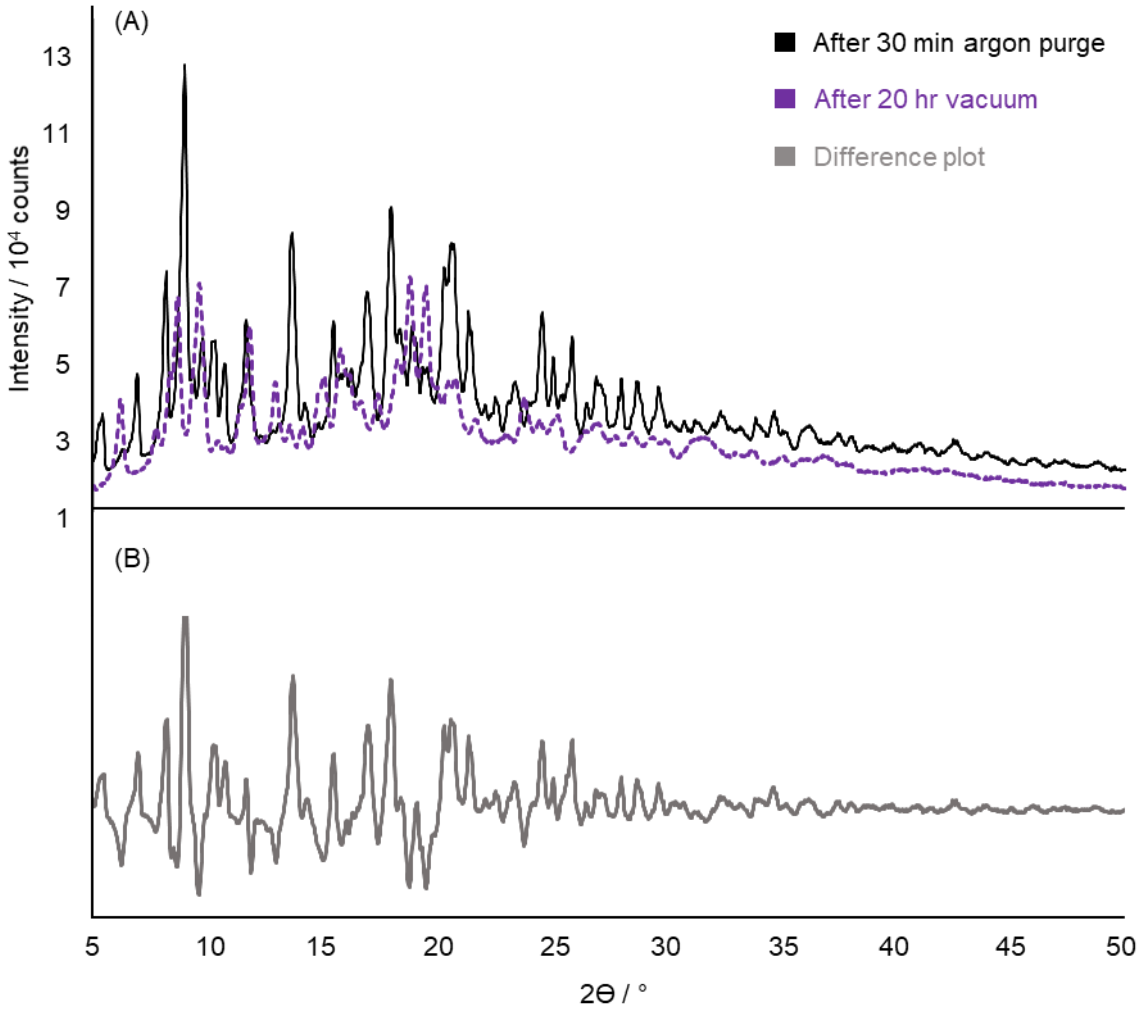

Figure 3.4 (A) Powder X-Ray Diffraction plots of complex **1.3** before (black) and after 20 hr of vacuum (purple). (B) Difference plot of the powder diffraction patterns before and after exposure to vacuum.

Previously it has been reported that different morphologies of the same compound often have differing reactivity and stability in SC-SC reactions,[19-21] in such cases it is important to isolate

a single polymorph.[22] However, due to the similar size and colourless nature of crystals of polymorphs *α*-**3.1** and *β*-**3.1**, the polymorphs could not be separated mechanically or through different crystallisation conditions (solvents: 1,2-difluorobenzene, dichloromethane, pentane, hexane, heptane, methyl cyclohexane; temperatures: room temp, 5 °C, –20 °C, –80 °C; techniques: layering, vapour diffusion). As shown by solution-state and solid-state NMR of the bulk material following SC-SC reactivity (*vide infra*), both polymorphs *α*-**3.1** and *β*-**3.1** show the same reactivity, therefore, the reactivity and characterisation of polymorphs *α*-**3.1** and *β*-**3.1** is discussed as an ensemble with the exception of the SCXRD structures.

3.2.2 Variable temperature SCXRD of complex 3.1

Polymorphs *α*-**3.1** and *β*-**3.1** display the same cation structure within error, showing the ethylene η^2 bound to the gold(I) centre (*α*-**3.1**, 100 K: C1–C2, 1.302(5) Å; *β*-**3.1**, 110 K: C1–C2, 1.310(5) Å) therefore discussion of the cation structure shall be limited to polymorph *α*-**3.1**. *α*-**3.1** has a similar structure to [(**L1**)Au(η^2-C_2H_4)][SbF_6],[11] consisting of a linear geometry around the gold centre with ethylene coordinated in an η^2 fashion with a P1–Au1–centroid(C1···C2) angle of 178.570(17)°. (Figure 3.5 A). At 150 K the C1–C2 distance (1.199(6) Å) is shorter than free ethylene (1.313 Å)[23] and other dicoordinate gold(I) ethylene complexes reported by Campos (1.353(15) – 1.384(10)) Å.[13] This effect is similar to the artificially short acetylene C–C distances observed in [Ag(C_2H_2)$_3$][Al{OC(CF_3)$_3$}$_4$] (1.127(19), 1.120(17) Å), [Ag(C_2H_2)$_4$][Al{OC(CF_3)$_3$}$_4$] (1.092(7) Å) and [(HB(3,5-(CF_3)$_2$Pz)$_3$)Cu(C_2H_2)] (1.134(7) Å),[14, 24] compared to free acetylene (1.2033(2) Å)[25] which are reported to be due to "thermal smearing" and electron density anisotropy of the acetylene ligand. It has been proposed by Campos that the reduction in bond length could be in part due to negligible *π*-backdonation from the cationic d^{10} gold(I) centre to the $\pi^*_{C=C}$ orbital, as electrostatic effects have a greater contribution to bonding than *π*-backdonation. An alternative explanation is that there is either a slow equilibrium between multiple unresolved components within the crystal structure which could not be suitably modelled, or a fast dynamic torsional libration of the C–C bond occurs in the solid state. Torsional libration results in an artificial shortening of

experimentally determined bond distances, as classically demonstrated for 1,2-diphenylethane, where the measured central C–C distance increases at lower temperature as torsional librations are reduced [100 K, 1.529(3) Å; 240 K, 1.506(5) Å].[26] A variable temperature SCXRD experiment was carried out for complex *α*-**3.1**, showing that the C1–C2 distance decreases at higher collection temperatures [100 K, 1.302(5); 150 K, 1.199(6); 200 K, 1.089(9); 250 K, 1.04(1); 298 K, 1.037(12) Å] (Figure 3.2 B), consistent with torsional libration. The Au–C bond lengths (i.e. 2.219(3) Å at 100 K) lie within the range of known dicoordinate and tricoordinate gold(I)-ethylene complexes [2.089(2) – 2.268(5) Å][3, 6, 8, 13] and also shorten at higher temperature due to the torsional libration of the ethylene bond [100 K, 2.219(3), 2.219(3) Å; 298 K, 2.178(6), 2.188(7) Å]. In comparison, the Au1–P1 distance changes minimally from 100 K (2.2830(4) Å) to 298 K (2.2750(7) Å), demonstrating that only the C1–C2 bond experiences significant torsional libration. There are no close Au···Au contacts, and thus no stabilising aurophilic interactions,[27, 28] due to the steric constraints of the phosphine ligand which surrounds the gold centre.

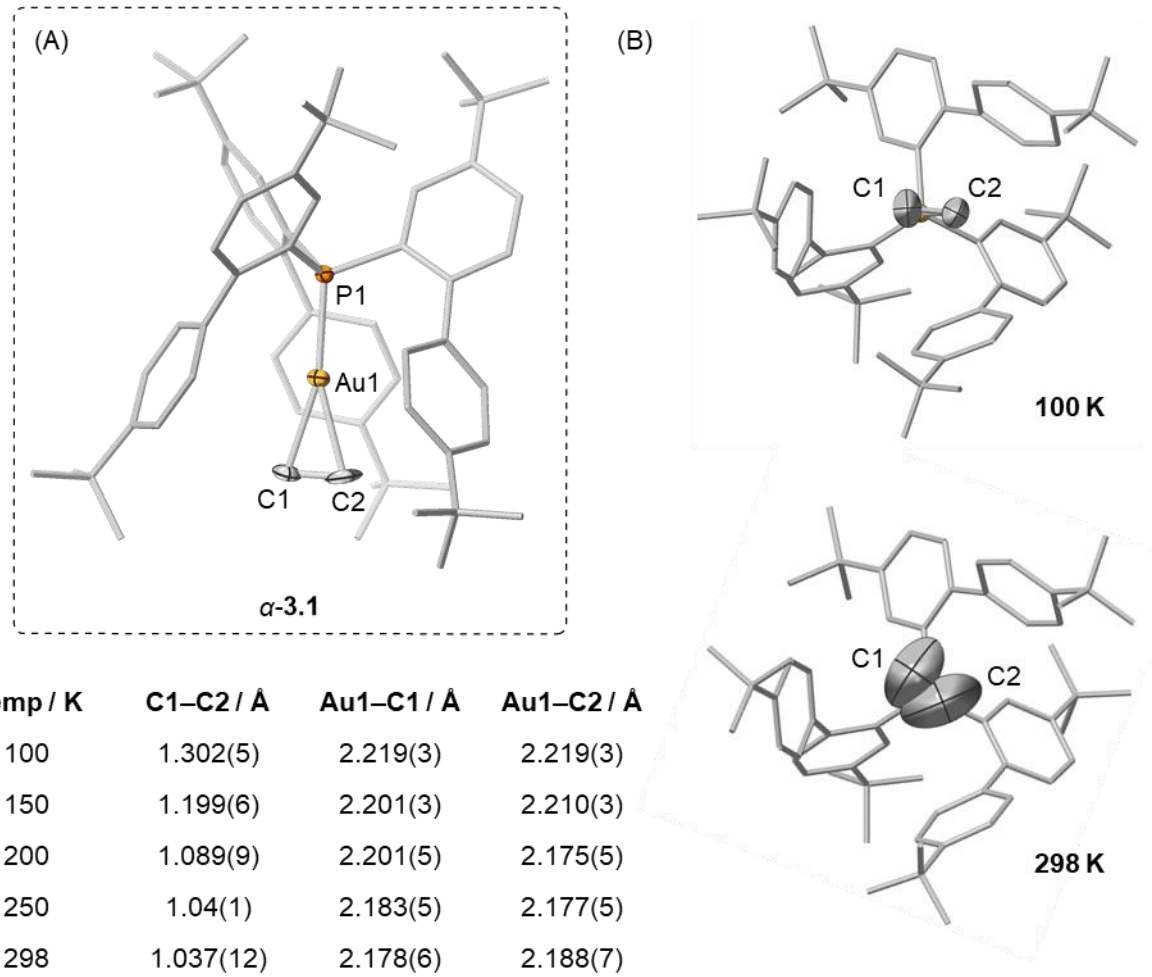

Temp / K	C1–C2 / Å	Au1–C1 / Å	Au1–C2 / Å
100	1.302(5)	2.219(3)	2.219(3)
150	1.199(6)	2.201(3)	2.210(3)
200	1.089(9)	2.201(5)	2.175(5)
250	1.04(1)	2.183(5)	2.177(5)
298	1.037(12)	2.178(6)	2.188(7)

Figure 3.5 (A) The molecular structure of the isolated cation of polymorph *α*-**3.1** collected at 100 K. Displacement ellipsoids are set at 50% probability level. Hydrogen atoms, lattice solvent and $[BAr^F{}_4]^-$ anion are excluded for clarity. (B) Alternative representation of polymorph *α*-**3.1** showing the torsional disorder at 100 K and 298 K, highlighting the ethylene atomic displacement parameters (adp's), with a table noting selected bond distances of polymorph *α*-**3.1** at different data collection temperatures. Au1–P1 bond distances (Å): 2.2830(4), 100 K; 2.2806(7), 150 K; 2.2786(7), 200 K; 2.2764(7), 250 K; 2.2750(7), 298 K. Select bond angles (°): P1–Au1–centroid(C1···C2), 178.570(17).

3.2.3 Solution-state NMR spectra of complex 3.1

The ^{1}H NMR (CD_2Cl_2) spectrum of the dissolved ensemble of polymorphs *α*-**3.1** and *β*-**3.1** (Figure 3.6 A) is analogous to that of the known precursor [(**L1**)Au(η^2-C_2H_4)][SbF_6],[11] with the addition of multiplet peaks corresponding to the *ortho*- and *para*-$BAr^F{}_4$ protons at δ 7.72 and 7.56 respectively, the latter of which overlaps with one the aryl environments of the biphenyl phosphine ligand, H_a. Multiplets corresponding to the 1,2-difluorobenzene lattice solvent are observed at δ 7.18-7.22, overlapping with the phosphine aryl environments, as well as a triplet peak at δ 0.88 corresponding to the terminal CH_3 of heptane. The peak corresponding to the

CH_2 of heptane is overlapping with the two signals of the *tert*-butyl protons of the phosphine ligand at δ 1.27-1.25. The alkene protons are observed as a complex AA'BB'X multiplet between δ 3.79 – 3.63 at 500 MHz, upfield relative to free ethylene (δ 5.40)[29] and $[(PMes_3)Au(\eta^2\text{-}C_2H_4)][SbF_6]$ (δ 5.46).[13] The inequivalent proton environments are observed as an AA'BB'X spin system (X = ^{31}P) in contrast to the one ethylene environment observed for other gold(I) ethylene complexes such as $[(PMes_3)Au(\eta^2\text{-}C_2H_4)][SbF_6]$ (δ 5.46).[13] The ethylene carbon is observed as a doublet ($^2J_{CP}$ = 9 Hz) at δ 109.4 in both the solution (CD_2Cl_2) and the solid-state $^{13}C\{^1H\}$ NMR spectrum, upfield of free ethylene (δ 123.2).[29] The single carbon environment could be due to a mirror plane, however two sets of signals corresponding to ligand **L1** would be expected if a mirror plane were to be present, yet only one set of signals are observed. This may be observed due to the ethylene ligand spinning, making the carbons equivalent, or due to two signals occurring at coincident chemical shifts. This is captured in the torsional libration shown in the variable temperature SCXRD experiment. The AA'BB'X spin system arises from the alkene protons being diastereotopic due to the biphenyl phosphine ligand **L1** (Figure 3.6 B).

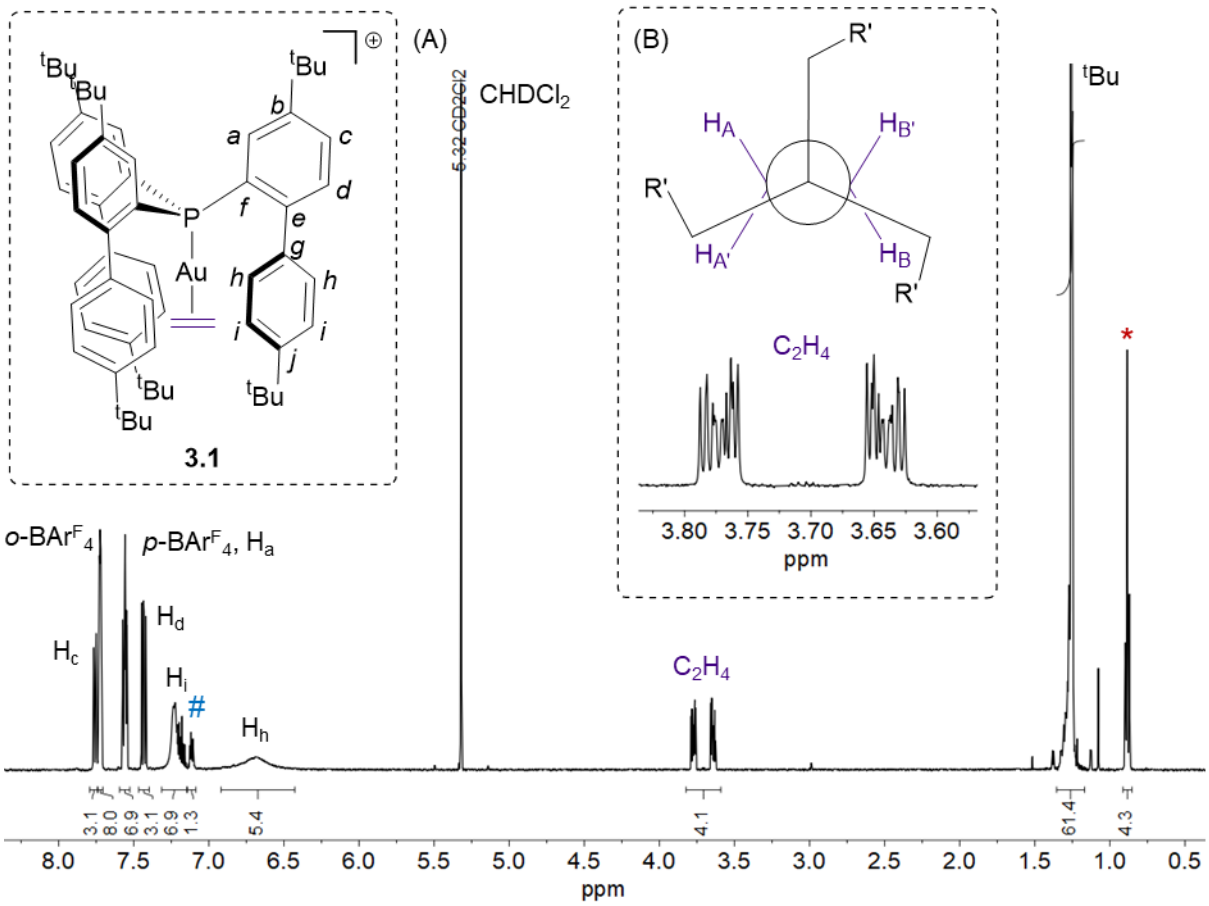

Figure 3.6 (A) The ^{1}H NMR spectrum of the dissolved ensemble of polymorphs *α*-**3.1** and *β*-**3.1** (500 MHz, CD_2Cl_2, 298 K). # Denotes lattice 1,2-difluorobenzene, * denotes lattice heptane. The inset highlights the ethylene proton environment. (B) The Newman projection down the P–Au bond, showing the diastereotopic proton environments. R' = 2-(4,4′-di-tert-butylbiphenylyl).

The upfield shift of the alkene protons could be due to a ring current effect from the nearby aromatic rings of the phosphine ligand wherein the circulation of delocalised *π*-electrons induce an additional magnetic field upon the alkene protons, shielding the environment so that it shifts upfield. This ring current effect is proposed as the aryl groups of the biphenyl phosphine ligand sit in close proximity to the ethylene, as shown by the solid-state molecular structure in which the closest H–centroid(C(x)···C(y)) distances are 3.2924(12), 3.2639(32) and 3.5042(14) Å in complex *α*-**3.1** (Figure 3.7) for which the protons are in their calculated positions. Ring current effects have been observed with SMOM complexes previously, for instance the bridgehead protons of the NBA ligand in [(dcpe)Rh(NBA)][BAr^F_4] (**1.14**) are observed at δ –1.82 in the ^{1}H projection of the ^{1}H-^{13}C HETCOR SSNMR spectrum, relatively

upfield due to the NBA ligand being situated within the cleft created by the $[BAr^{F}_{4}]^{-}$ anion. The proton–centroid distances of complex **1.14** are 2.502 and 2.548 Å, which are shorter than that observed for complex *α*-**3.1** (3.2924(12), 3.2639(32) and 3.5042(14) Å), resulting in a more significant upfield shift for complex **1.14**. Similar ring current effects have also been observed in supramolecular host-guest complexes.[30] For instance, when acetonitrile is held within an open C_{60} cage, the methyl protons of acetonitrile experience a strong ring current effect and are observed at δ –11.91 in the ^{1}H NMR spectrum ($CDCl_3$), significantly upfield relative to free acetonitrile (δ 2.10).[31] The proton–centroid distances between the methyl protons and the closest C_{60} rings lie within the range 2.2837(14) – 2.3308(13) Å, much shorter proton–centroid distances than that of complex *α*-**3.1**, resulting in a less significant ring current effect for complex *α*-**3.1**.

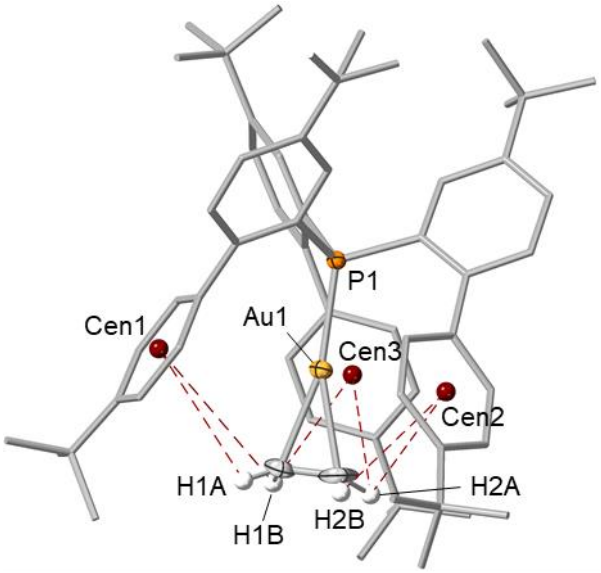

α-**3.1**

Figure 3.7 The molecular structure of the isolated cation of polymorph *α*-**3.1** collected at 100 K. The C(53)···C(58), C(25)···C(30), and C(9)···C(14) centroids are labelled as Cen1, Cen2 and Cen3 respectively. Displacement ellipsoids are set at 50% probability level. Hydrogen atoms, lattice solvent and $[BAr^{F}_{4}]^{-}$ anion are excluded for clarity. Select bond distances (Å): H1A–Cen1, 3.2924(12); H1B–Cen1, 4.2152(17); H2A–Cen2, 3.8455(37); H2B–Cen2, 3.2639(32); H1B–Cen3, 3.5042(14); H2A–Cen3, 3.8853(5).

3.3 Exploring the SMOM reactivity of complex 3.1

As discussed in section 1.1.2, the bicapped square prismatic framework of $[BAr^{F}_{4}]^{-}$ anions, which is observed for both polymorphs of complex **3.1**, has previously been reported to

support SMOM reactivity,[32, 33] such as in the formation of rhodium *σ*-alkanes complexes and manganese or iridium pincer complexes that show SC-SC reactivity.[34] The SMOM reactivity of complex **3.1** with gaseous substrates (CO, NH_3, NMe_2H, NMe_3, isobutylene) was therefore explored. As described in section 3.1, [(**L1**)Au(CO)][SbF_6] has been reported previously and is synthesised in the solution-state from [(**L1**)Au(η^2-C_2H_4)][SbF_6],[11] and was therefore the starting point to this work.

3.3.1 The SC-SC synthesis of a gold(I) carbonyl complex, 3.2

The SC-SC addition of CO (4 bar absolute, 10 minutes) to the ensemble of polymorphs *α*-**3.1** and *β*-**3.1** resulted in the isolation of [(**L1**)Au(CO)][BAr^F_4] (**3.2**, Figure 3.8 A) as colourless crystals, in 100% conversion as shown by ^{1}H and ^{31}P{^{1}H} NMR (CD_2Cl_2) spectroscopy following this SC-SC reaction. This reaction is reversible, and addition of ethylene (2 bar absolute, 10 minutes) to complex **3.2** quantitively reforms complex **3.1** as shown by ^{1}H and ^{31}P{^{1}H} NMR spectroscopy following the SC-SC reaction. Whilst only one polymorph (*β*-**3.1**) was measured by SCXRD, two overlapping peaks are observed at δ 8.6 and 5.7 in the ^{31}P{^{1}H} SSNMR of complex **3.2**, suggesting that two polymorphs are present in the crystalline mixture.

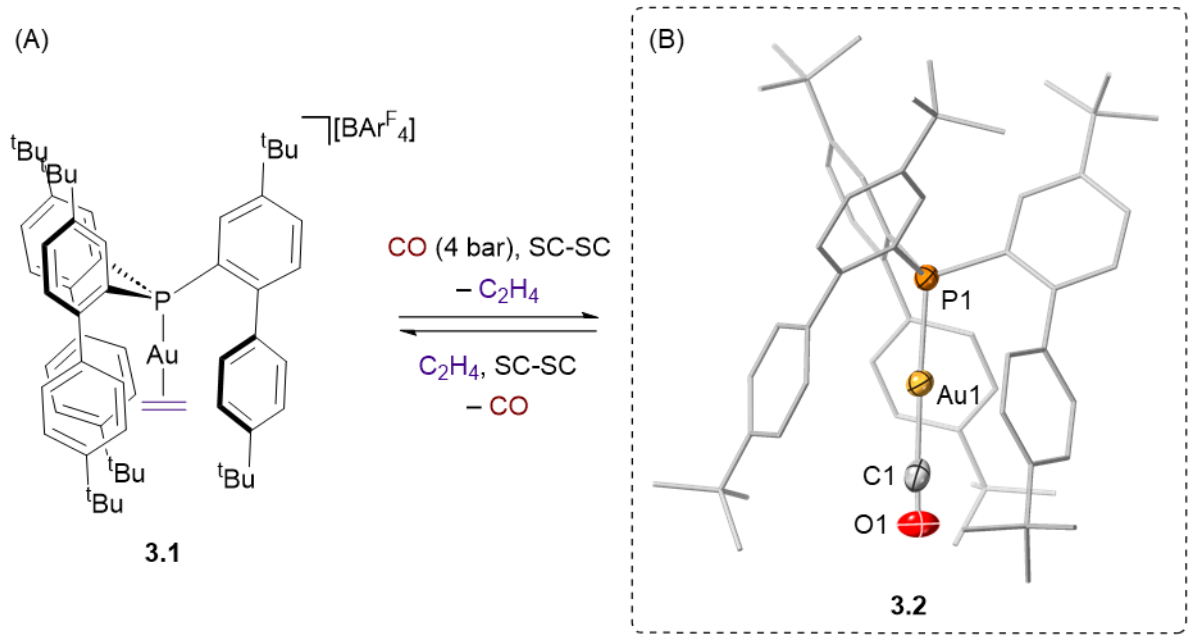

Figure 3.8 (A) The reversible SC-SC synthesis of [(**L1**)Au(CO)][BAr$^F_4$] (**3.2**). (B) the molecular structure of the isolated cation of complex *β*-**3.2**. Displacement ellipsoids are set at 50% probability level. Hydrogen atoms, lattice solvent and [BAr$^F_4$]$^-$ anion are excluded for clarity. Selected bond distances (Å): Au1–C1, 2.001(6); C1–O1, 1.058(8); Au1–P1, 2.3002(11). Selected bond angles (°): P1–Au1–C1, 177.25(17).

Complex *β*-**3.2** (space group $P\bar{1}$, Figure 3.8 B) displays a structure of the cation very similar to [(**L1**)Au(CO)][SbF_6],[11] consisting of a linear geometry around the gold centre with a P1–Au1–C1 angle of 177.25(17)°. The C1–O1 bond distance of 1.058(8) Å is comparable to that of the few other gold(I) carbonyl complexes known, including [($PMes_3$)Au(CO)][SbF_6] (1.108(7) Å) and [(SIDipp)Au(CO)][SbF_6] [1.110(6) Å, SIDipp = 1,3-bis(2,6-diisopropylphenyl)imidazolin-2-ylidene].[35, 36] This distance, as well as that of other known Au–CO complexes, is shorter than free CO (1.12822 Å),[37] due to bonding being dominated by the *σ*-contribution with relatively less *π*-backdonation, as is the nature of the non-classical carbonyls (*vide infra*). The Au1–C1 bond distance of 2.001(6) Å is also similar to Au–C bond lengths for known two-coordinate gold(I)-carbonyl complexes, such as [($PMes_3$)Au(CO)][SbF_6] (2.008(6) Å) and [(SIDipp)Au(CO)][SbF_6] (1.972(5) Å).[35, 36] The solid-state packing of complex *β*-**3.2** reveals the retention of the bicapped square prismatic arrangement of [BAr$^F_4$]$^-$ anions during the transformation from complex *β*-**3.1** (Figure 3.9), as well as both 1,2-difluorobenzene and

heptane lattice solvents, with minimal change to the unit cell volume (5025.803 Å^3) compared to complex *β*-**3.1** (5040.827 Å^3).

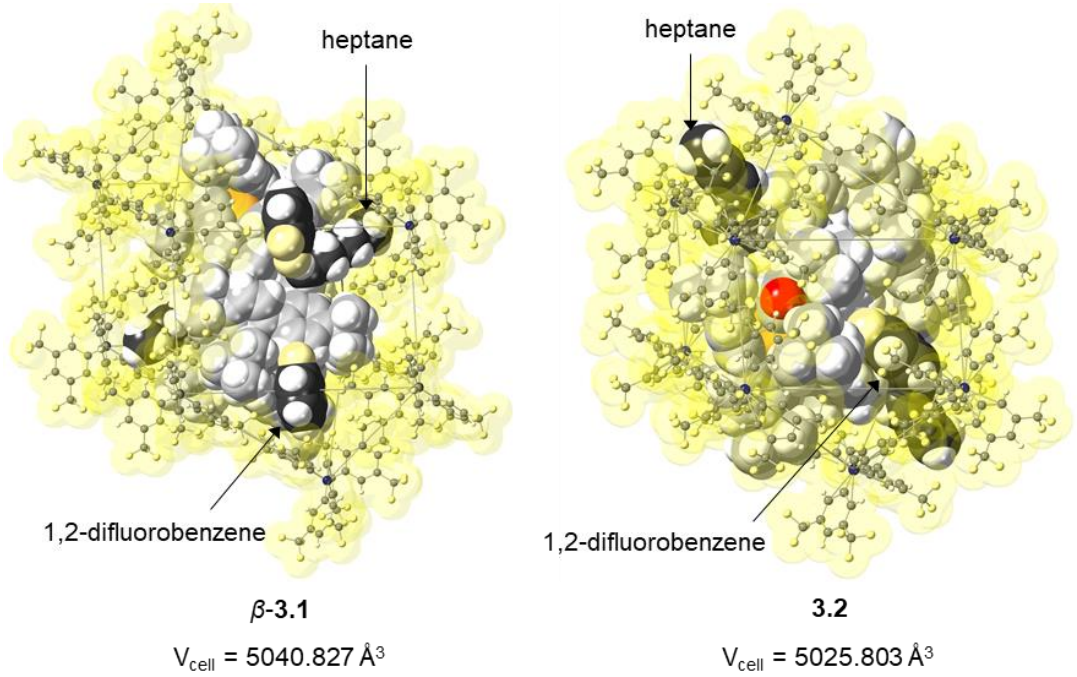

Figure 3.9 The extended solid-state structure of complexes *β*-**3.1** and **3.2**, showing that the bicapped square prismatic arrangements of [BAr$^F{}_4$]$^-$ anions and 1,2-difluorobenzene and heptane lattice solvents are retained during the SC-SC reaction from complex **3.1**, depicted as Van der Waals radii.

The ^{1}H, ^{13}C{^{1}H} and ^{31}P{^{1}H} NMR (CD_2Cl_2) spectra of the dissolved ensemble of polymorphs of complex **3.2** are analogous to the known [(**L1**)Au(CO)][SbF$_6$],[11] with the addition of peaks corresponding to the *ortho*- and *para*-BAr$^F{}_4$ protons at δ 7.72 and 7.56 respectively, as well as peaks corresponding to 1,2-difluorobenzene and heptane lattice solvent. The carbonyl peak is observed as a doublet ($^2J_{CP}$ = 110) at δ 182.3 in the solution-state, and δ 182.0 in the SSNMR spectrum. The carbonyl signal is similar to that of [(PMes$_3$)Au(CO)][SbF$_6$] (δ 182.6, $^2J_{CP}$ = 115, CD_2Cl_2) and [(SIDipp)Au(CO)][SbF$_6$] (δ 182.7, CD_2Cl_2).[35, 36] In the ^{31}P{^{1}H} NMR (CD_2Cl_2) spectrum a single peak is observed at δ 7.0.

As discussed in section 3.1, the synthesis of [(**L1**)Au(CO)][SbF$_6$] from [(**L1**)Au(η^2-C$_2$H$_4$)][SbF$_6$] is in equilibrium in the solution state.[11] This is also observed in the solid state for the [BAr$^F{}_4$]$^-$ analogue. Sampling of the crystalline ensemble of polymorphs *α*-**3.1** and *β*-**3.1** after exposure to CO (2 bar absolute) for 30 min resulted in 91% conversion to complex **3.2**, as measured by

quantitative $^{31}P\{^{1}H\}$ NMR (CD_2Cl_2) spectroscopy of dissolved crystals following the SC-SC reaction. Leaving the crystals under CO (2 bar absolute) for 1 hr and 24 hr showed no further change in the conversion of complex **3.1** to complex **3.2** (91%, Figure 3.10 A). Changing the pressure of CO (1, 2, 4 bar absolute) changes the percentage conversion to complex **3.2** (77%, 91% and 100% respectively) after 30 minutes (Figure 3.10 B). Addition of CO in the solution-state (CD_2Cl_2) results in approximately the same percentage conversion of complex **3.2** (80%, 1 bar absolute; 90%, 2 bar absolute; 100%, 4 bar absolute).

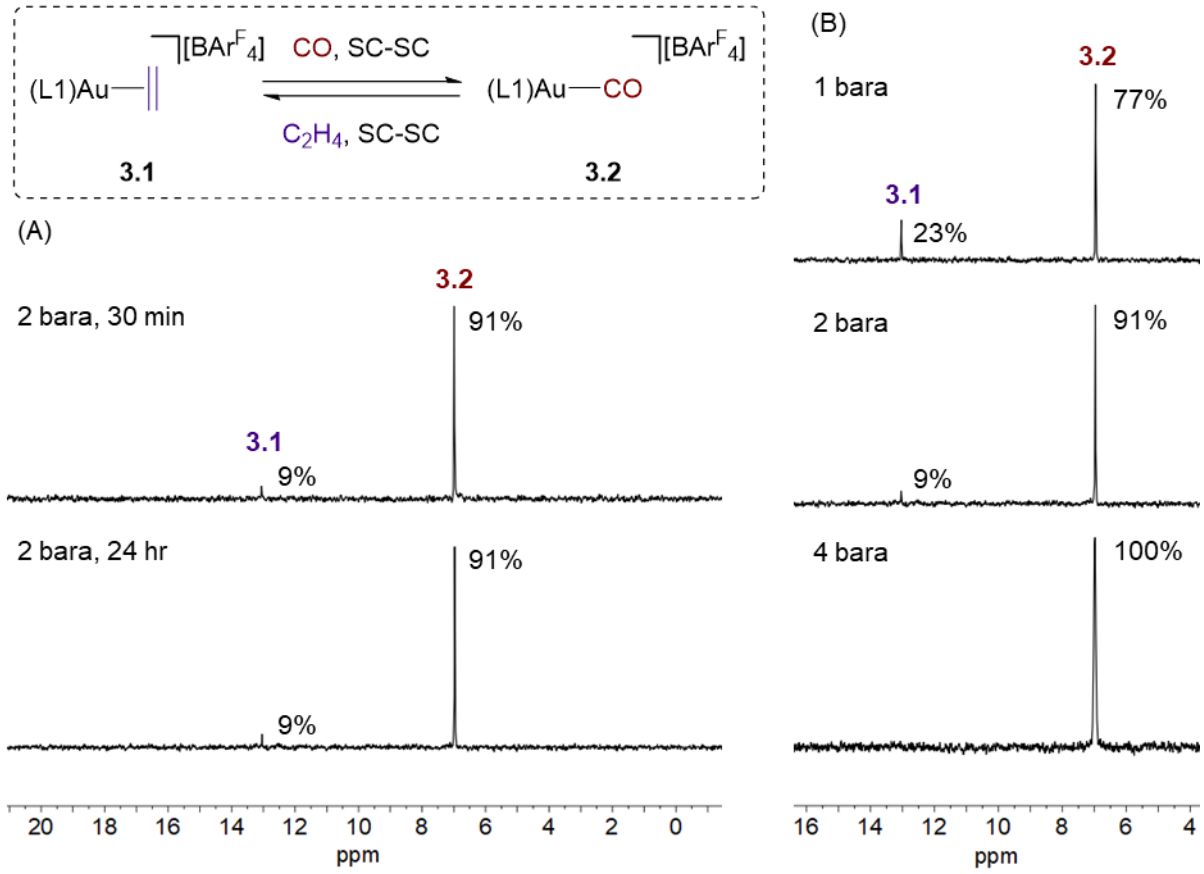

Figure 3.10 The equilibration between complexes **3.1** and **3.2** as demonstrated by the $^{31}P\{^{1}H\}$ NMR spectra of (A) 2 bar absolute CO after 30 minutes and 24 hr and (B) 1, 2 or 4 bar absolute CO after 30 minutes. (202 MHz, CD_2Cl_2, 298 K)

The solid-state IR spectrum of the ensemble of polymorphs of complex **3.2** synthesised under 4 bar absolute of CO (Figure 3.11 A) displays a sharp C–O stretch at 2170 cm^{-1}, very similar to that of [(**L1**)Au(CO)][SbF_6] (2169 cm^{-1}).[11] This is comparative to that of other gold(I) carbonyl complexes (2185 cm^{-1}, [($PMes_3$)Au(CO)][SbF_6]; 2197 cm^{-1}, [(SIDipp)Au(CO)][SbF_6]).[35, 36] The

C–O stretch is at higher wavenumber than free CO (2143 cm^{-1}),[38] which is diagnostic of coinage metal, non-classical carbonyls.[39, 40] Typically, classical metal-carbonyl bonding can be described by the Dewar-Chatt-Duncanson model where carbonyl ligands bind to metal centres *via* synergic bonding, which combines *σ*-donation from the CO to the metal and *π*-backdonation from the metal into the π^*_{CO} antibonding orbital, similar to that of alkenes and alkynes as described in section 1.2.[41, 42] Population of the π^*_{CO} orbital decreases the C–O bond strength, lengthens the C–O bond, and results in the C–O stretch moving to lower wavenumber in the IR spectrum, relative to free CO. However, as the energy of metal *d*-orbitals decreases across the transition metals, there is a weaker overlap with the CO *π** orbital. Late transition metals such as gold, which has relatively contracted *d*-orbitals as a d^{10} cation, experience negligible backbonding contribution to the metal-carbonyl bonding, favouring the $^{-}C{\equiv}O^{+}$ resonance form (Figure 3.11 B) and thus the C–O bond is weakened to a lesser extent.[37] The C–O bond is also strengthened relative to free CO due to the electrostatic effect of the metal centre inducing a change in polarisation of C–O toward the carbon atom, strengthening the ionic interactions of CO.[43] This is demonstrated in the molecular structure of complex **3.2** which has a C–O distance (1.058(8) Å) shorter than free CO (1.12822 Å),[37] as well as the IR spectrum of complex **3.2** in which the C–O stretch appears at 2170 cm^{-1}.

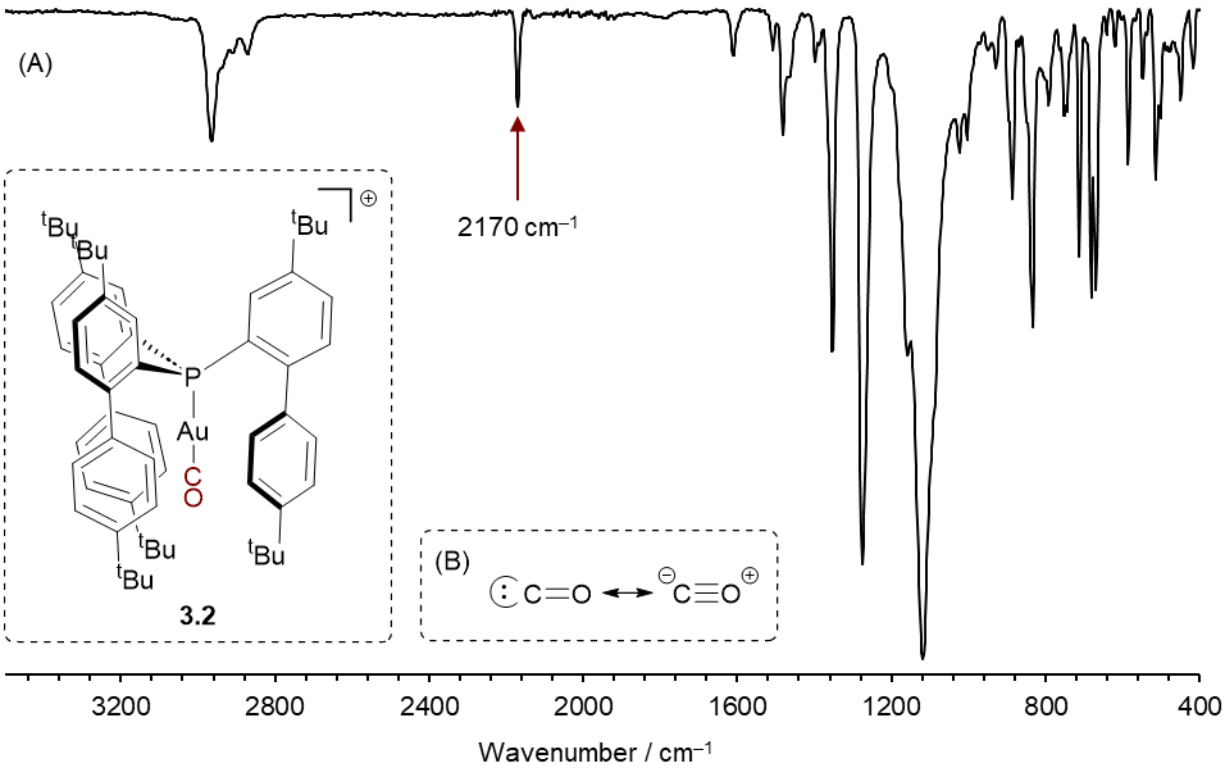

Figure 3.11 (A) The solid-state ATR-IR spectrum of the ensemble of polymorphs of complex **3.2**. (B) The different resonance forms of a carbonyl ligand.

Considering the extensive history of photochemistry with carbonyl complexes owing to their absorption of wavelengths of UV light,[44] solid-state UV experiments on complex **3.2** were attempted. However, no signs of reaction were observed (SCXRD, solution NMR) after placing crystals of complex **3.2** in an LED photoreactor (365 nm, 30 minutes) under either a static vacuum or an atmosphere of N_2 (1 bar absolute). Attempts at recording a UV-Vis absorption spectrum were hindered by the spectra being dominated by the phosphine and $[BAr^F{}_4]^-$ absorption environments, so that an absorption peak corresponding to the CO ligand could not be identified.

3.3.2 Solid/gas reactivity with amines

Having shown that the bulky phosphine system [(**L1**)Au(L)][$BAr^F{}_4$] (L = C_2H_4, CO) can support SC-SC reactivity, it was postulated that it might also undergo ligand substitution with ammonia. The SC-SC addition of NH_3 (1 bar absolute, 10 minutes) to the ensemble of polymorphs *α*-**3.1** and *β*-**3.1** resulted in 100% conversion (by NMR spectroscopy following the SC-SC reaction,

CD_2Cl_2) to [(**L1**)Au(NH_3)][BAr^F_4] (**3.3**, Figure 3.12 A) as colourless crystals. Complex **3.3** can also be accessed from complex **3.2** in a sequential SC-SC-SC reaction, as shown by solution NMR (CD_2Cl_2) spectroscopy following the reaction. No evidence of hydroamination to ethylamine was observed by ^1H gas phase NMR, as only ammonia and ethylene gas were observed. Unlike complex **3.2**, the formation of complex **3.3** is not reversible, as demonstrated by ^1H and $^{31}P\{^1H\}$ NMR (CD_2Cl_2) spectroscopy following the solid/gas addition of ethylene or CO (2 bar absolute, 10 minutes) to single-crystals of complex **3.3**, likely due to the more strongly binding nature of the ammonia ligand compared to ethylene or CO for gold(I).

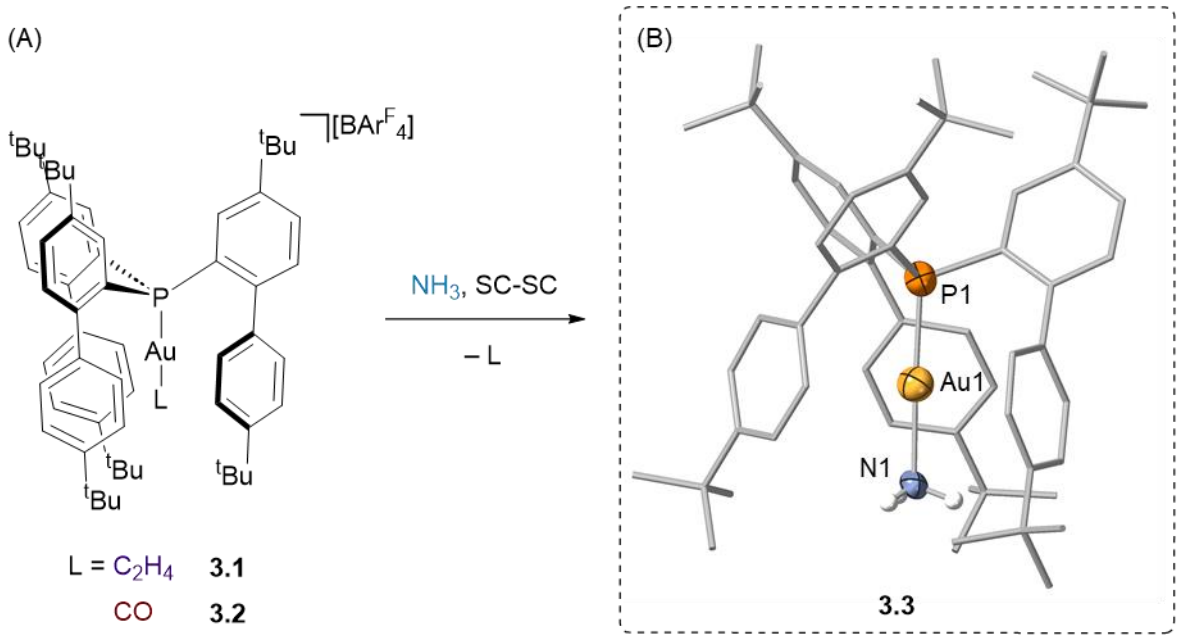

Figure 3.12 (A) The SC-SC synthesis of [(**L1**)Au(NH_3)][BAr^F_4] (**3.3**). (B) the molecular structure of the isolated cation of complex *β*-**3.3**, isolated from the SC-SC reaction from the ensemble of polymorphs of complex **3.1**. Displacement ellipsoids are set at 50% probability level. Select hydrogen atoms and $[BAr^F_4]^-$ anion are excluded for clarity. Selected bond distances (Å): Au1–N1, 2.139(7); Au1–P1, 2.234(3). Selected bond angles (°): N1–Au1–P1, 177.8(2).

The solid-state structure of complex *β*-**3.3** (space group $P\bar{1}$, Figure 3.12 B) was obtained through SC-SC methods from the ensemble of polymorphs *α*-**3.1** and *β*-**3.1**. Complex *β*-**3.3** displays a linear geometry around the gold centre with an N1–Au1–P1 angle of 177.8(2)°. The Au1–N1 bond distance of 2.139(7) Å is slightly longer than that of the only other crystallographically characterised gold(I) ammonia complex, [(CAAC)Au(NH_3)][$B(C_6F_5)_4$] (CAAC = cyclicalkylaminocarbene, 2.094(7) Å).[45] The Au1–P1 bond length (2.234(3) Å) is

shorter than complexes **3.1** (2.2861(7) Å) and **3.2** (2.3002(11) Å), likely due to the weaker *trans* influence of ammonia. The solid-state packing of complex *β*-**3.3** reveals the retention of the bicapped square prismatic arrangement of $[BAr^{F}_{4}]^{-}$ anions during the transformation from the ensemble of polymorphs *α*-**3.1** and *β*-**3.1** (Figure 3.13). However, both 1,2-difluorobenzene and heptane lattice solvents were lost in this SC-SC reaction, either induced by the movement of ammonia through the lattice or during the brief application of vacuum following the reaction to remove the ammonia and extruded ethylene from the headspace. The loss of lattice solvent results in a decrease in the unit cell volume (4515.121 $Å^3$) compared to complexes *β*-**3.1** (5040.827 $Å^3$) and **3.2** (5025.803 $Å^3$).

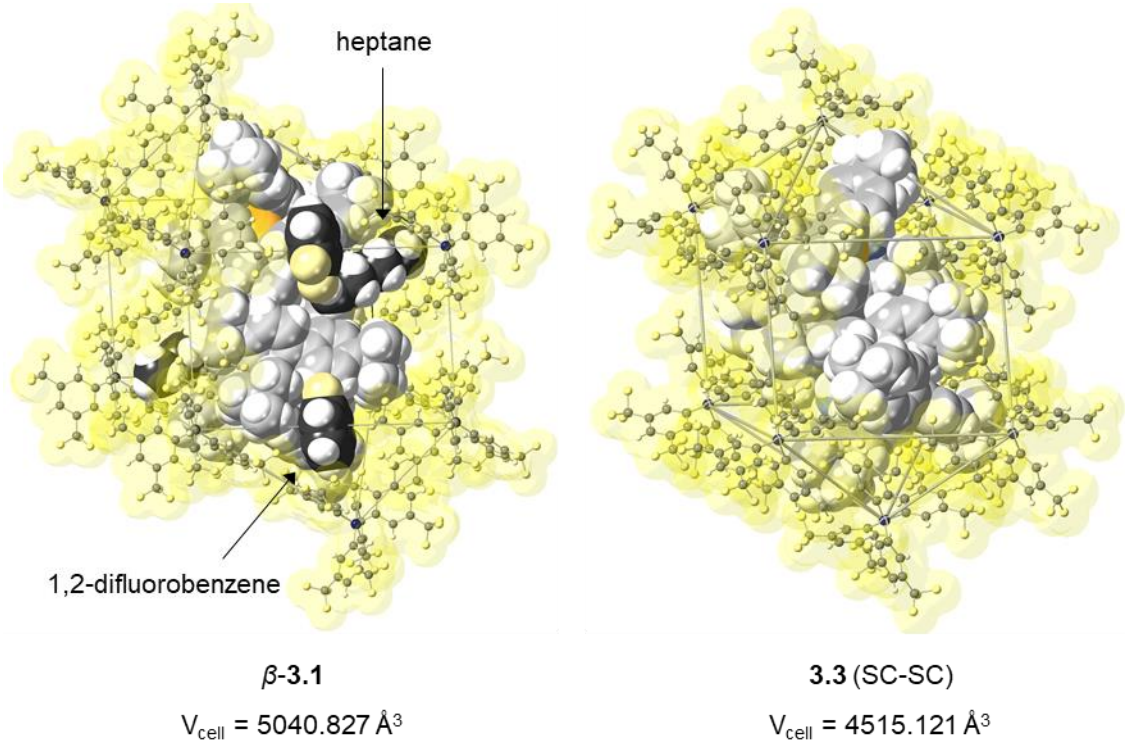

Figure 3.13 The extended solid-state structure of complexes *β*-**3.1** and **3.3** synthesised from SC-SC methods, showing that the bicapped square prismatic arrangements of $[BAr^{F}_{4}]^{-}$ anions are retained whilst the 1,2-difluorobenzene and heptane lattice solvents are lost during the SC-SC reaction from complex **3.1**, depicted as Van der Waals radii.

Whilst some degree of crystallinity is retained, unlike complex *β*-**3.1** upon loss of lattice solvent, a decrease in data quality is evident from the crystal data (R_1 = 0.1220, R_{int} = 0.1264), in comparison to complexes *β*-**3.1** (R_1 = 0.0356, R_{int} = 0.0332) and **3.2** (R_1 = 0.0601, R_{int} = 0.0569). Complex **3.3** was thus recrystallised from 1,2-difluorobenzene/heptane at –20 °C to

afford crystals of two different space groups ($P2_1/n$, *α*-**3.3**; $P\bar{1}$, *β*-**3.3**) with improved data quality (*α*-**3.3**: R_1 = 0.0336, R_{int} = 0.0337; *β*-**3.3**: R_1 = 0.0631, R_{int} = 0.0635). Crystals of polymorph *α*-**3.3** contain 1,2-difluorobenzene (0.2 occupancy) within the lattice (Figure 3.13 A) with a unit cell volume of 8917.34 Å^3, whilst polymorph *β*-**3.3** contains 1,2-difluorobenzene (0.8 occupancy) and heptane (0.7 occupancy) with a volume of 4997.376 Å^3. The unit cell volume of recrystallised polymorph *β*-**3.3** is greater than polymorph *β*-**3.3** synthesised from SC-SC methods (4515.121 Å^3), and closer to that of complexes *β*-**3.1** (5040.827 Å^3) and **3.2** (5025.803 Å^3), due to the lattice solvents being present within the lattice from recrystallisation. The bond metrics (*α*-**3.3**: Au1–N1, 2.1046(28); Au1–P1, 2.2368(9) Å; *β*-**3.3**: Au1–N1, 2.1073(67); Au1–P1, 2.2362(18) Å) are the same within error of complex **3.3** that come from SC-SC reaction (Au1–N1, 2.139(7); Au1–P1, 2.234(3) Å).

A single peak is observed in the solution-state $^{31}P\{^1H\}$ NMR (CD_2Cl_2) spectrum of the solution recrystallised ensemble of complex **3.3** at δ 3.7. The solution-state ^1H NMR (CD_2Cl_2) spectrum (Figure 3.14) of complex **3.3** shows a peak corresponding to the *ortho*-BAr^F_4 protons which overlap with one of the aryl proton environments of the biphenyl phosphine ligand at δ 7.72 (11H), whilst the *para*-BAr^F_4 protons appear as a broad singlet at δ 7.56 (4H). The remaining aryl peaks corresponding to the phosphine ligand are found at δ 7.53 (3H), 7.39 (3H), 7.14 (6H) and 6.62 (6H), whilst the *tert*-butyl protons are observed at δ 1.27 – 1.25 (59H), overlapping with heptane. There is also a triplet corresponding to 0.7 heptane at δ 0.88 (4.2H) in good agreement with the molecular structure. There is no evidence of 1,2-difluorobenzene, despite this being present within the molecular structure. This could be due to 1,2-difluorobenzene being lost under vacuum prior to vacuum transfer of the CD_2Cl_2 solvent. The NH_3 ligand is observed as a broad (fwhm = ~9 Hz) singlet at δ 0.92 (3H), which is upfield compared to the known $[(CAAC)Au(NH_3)][B(C_6F_5)_4]$ and $[(PPh_3)Au(NH_3)][ClO_4]$ at δ 2.53 and 3.85 respectively.[45, 46] The observed upfield shift is likely due to the ring current effect from the close proximity biphenyl phosphine ligand **L1** aryl groups, similar to that observed for complex **3.1**. The H–centroid (C(x)···C(y)) distances were measured similar to the C–

centroid(C(x)···C(y)) distances in complex *α*-**3.1** and found to be 3.5048(8), 3.4450(17) and 3.7706(2) Å for H1A–Cen1, H1B–Cen2 and H1C–Cen3 respectively. These close aryl centroid···ammonia contacts in the molecular structure, similar to complex *α*-**3.1**, are consistent with a ring current being observed. In CD_2Cl_2, complex **3.3** results in ~28% conversion to [(**L1**)AuCl] after 24 hrs at room temperature, as evident by the $^{31}P\{^1H\}$ NMR spectrum. This is due to activation of dichloromethane in solution, as is discussed below.

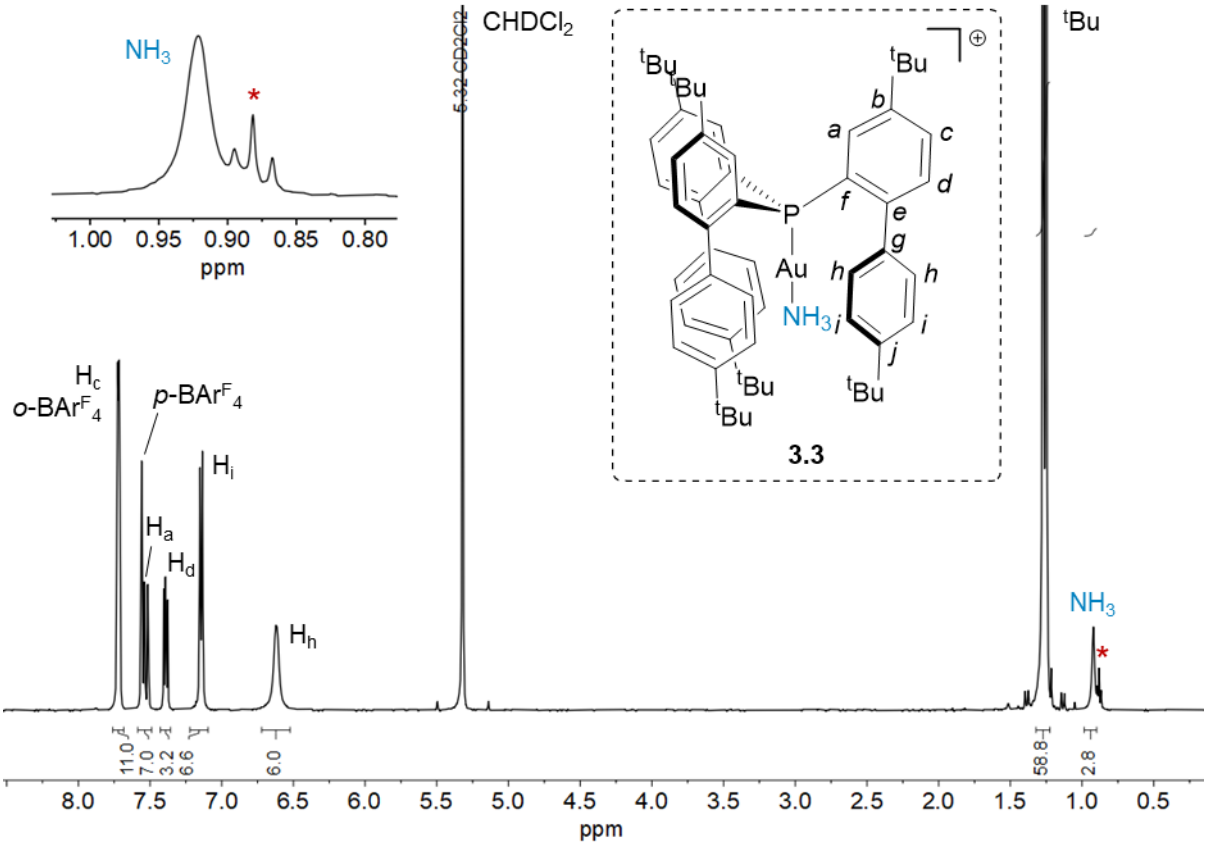

Figure 3.14 The ^1H NMR spectrum of complex **3.3** (500 MHz, CD_2Cl_2, 298 K). * Denotes lattice heptane. The inset highlights the ammonia proton environment.

As discussed previously, no sign of reaction is observed upon solid/gas addition of ethylene or CO (2 bar absolute, 10 minutes) to single-crystals of complex **3.3**. It was hypothesised that inserting a bulkier ligand within the pocket of ligand **L1** might lead to a ground-state destabilised complex that could undergo further reactivity with even weaker binding ligands. In order to probe how much steric strain could be imposed in the cavity of the phosphine ligand

L1 in the solid state, reactivity with bulkier gaseous amines (dimethylamine, trimethylamine) was therefore also explored (Scheme 3.5).

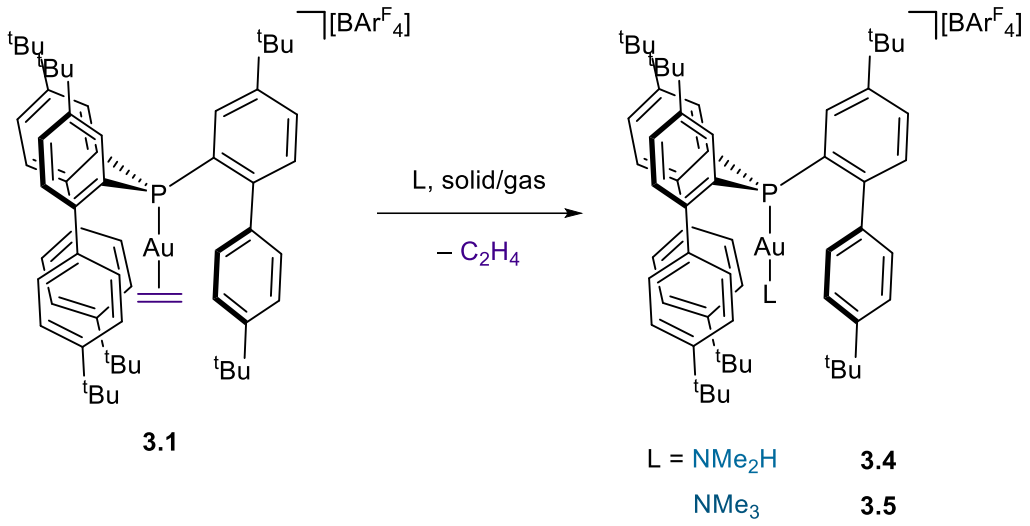

3.1 **3.4** **3.5**

Scheme 3.5 The *in crystallo* synthesis of the compounds [(**L1**)Au(L)][BAr$^F_4$] (L = NMe_2H, **3.4**; NMe_3, **3.4**).

The SC-SC addition of gaseous NMe_2H (1.5 bar absolute, 2 hr) to the ensemble of polymorphs *α*-**3.1** and *β*-**3.1** led to the formation of [(**L1**)Au(NMe_2H)][BAr$^F_4$] (**3.4**) as colourless crystals. Whilst [(**L1**)Au(N^iPr_2H)][SbF_6] is known,[13] along with other dialkylamine complexes such as diethylamine and dicylohexylamine,[47-49] this is the first example of a gold(I) dimethylamine complex. The solution-state $^{31}P\{^1H\}$ NMR (CD_2Cl_2) spectrum of complex **3.4** shows complete conversion from complex **3.1** to a complex that yields a singlet at δ 6.0. Whilst only one polymorph was measured using SCXRD (*vide infra*), it is likely that complex **3.4** exists as two polymorphs similar to complexes **3.1**–**3.3**. The solution-state ^1H NMR (CD_2Cl_2) spectrum of the dissolved ensemble of polymorphs of complex **3.4** (Figure 3.15) shows a peak corresponding to the *ortho*-BAr$^F_4$ protons which overlap with one of the aryl proton environments of the biphenyl phosphine ligand at δ 7.72 (11H), whilst the *para*-BAr$^F_4$ protons appear as a broad singlet at δ 7.56 (4H). The remaining aryl peaks corresponding to the phosphine ligand are found at δ 7.49 (3H), 7.39 (3H), 7.20 (6H) and 6.72 (6H), whilst the *tert*-butyl group protons are observed at δ 1.23 – 1.22 (55H). The methyl protons of the dimethyl amine ligand are observed as a doublet of doublets at δ 1.76 (6H, $^3J_{HH}$ = 6.1, $^4J_{HP}$ = 1.5 Hz),

which collapses into a doublet ($^3J_{HH}$ = 6.1) upon ^{31}P decoupling. No obvious peak corresponding to the amine proton is observed, due to it overlapping with the *tert*-butyl group protons within the δ 1.23 – 1.22 region, which has a relative integral of 55 protons rather than 54 as predicted for six *tert*-butyl groups. The amine proton of the similar gold(I) amine complex [(CAAC)Au(NEt$_2$H)][B(C$_6$F$_5$)$_4$] is observed at δ 2.85.[49] Complexes containing ligand **L1** experience ring current effects, as discussed for complexes **3.1**–**3.3**, which would therefore shift the amine proton upfield of reported gold(I) amines (δ 2.85) to the δ 1.23 – 1.22 region, resulting in it being obscured by the ^{t}Bu protons. This was confirmed using a ^{1}H-^{1}H COSY experiment which shows a correlation between the methyl environment at δ 1.76 and the δ 1.23 – 1.22 region. No peaks corresponding to 1,2-difluorobenzene or heptane are observed, suggesting that both lattice solvents are lost during the SC-SC reaction from complex **3.1**.

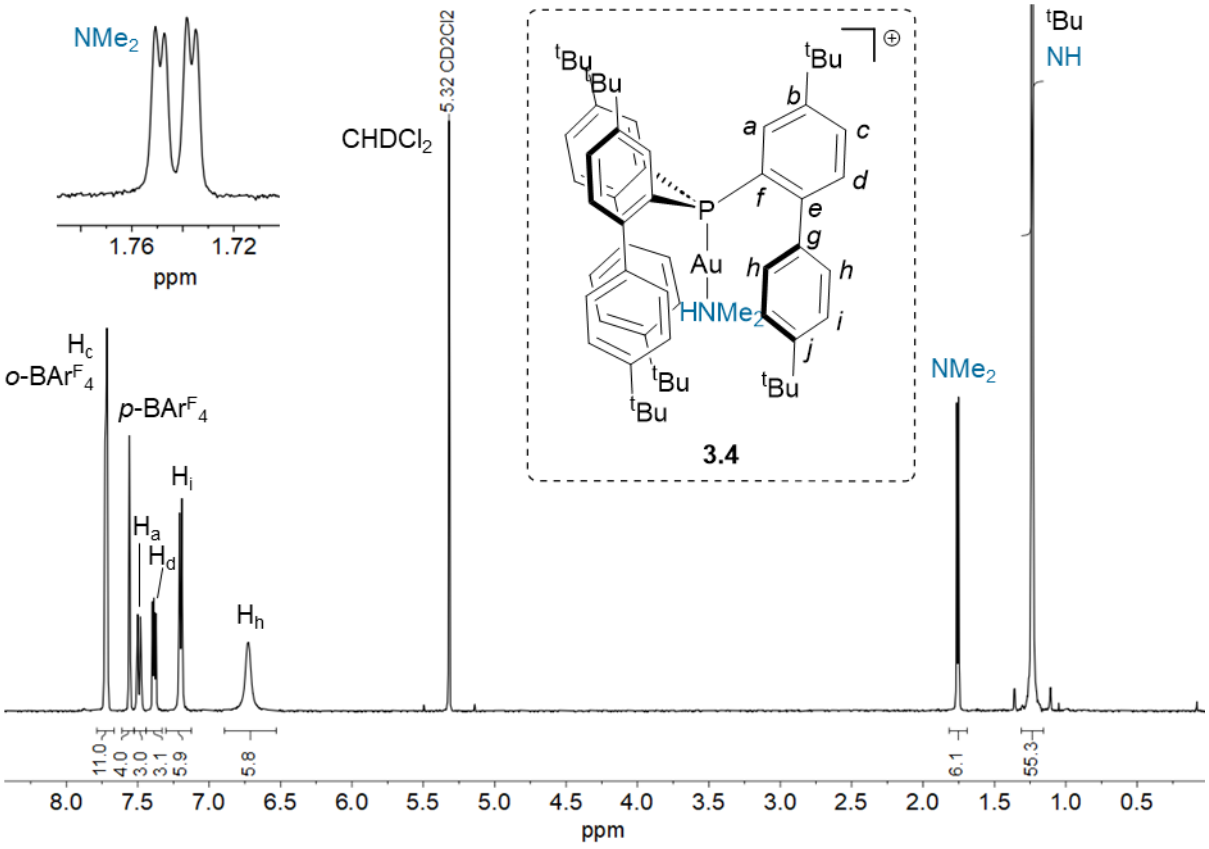

Figure 3.15 The ^{1}H NMR spectrum of the dissolved ensemble of polymorphs of complex **3.4** (500 MHz, CD_2Cl_2, 298 K). The inset highlights the methyl proton environment of the amine ligand.

The structure of complex *γ*-**3.4** accessed from SC-SC routes (space group $P\bar{1}$, Figure 3.16) contains two crystallographically distinct cations within the asymmetric unit, which both display a linear geometry around the gold centre with P–Au–N bond angles of 176.2(3) and 175.0(3)°, therefore it is not isomorphous with *β*-**3.1** and thus shall be labelled *γ*-**3.4**. The Au–N bond lengths in complex *γ*-**3.4** (2.10(1), 2.148(9) Å) are similar within error to complex *β*-**3.3** (2.139(7) Å) and [(**L1**)Au(N^{i}Pr$_2$H)][SbF$_6$] (2.120(4) Å).[13] Similar to complex *β*-**3.3**, the crystal data is of relatively poor quality (R_1 = 0.1056, R_{int} = 0.0725) in comparison to complex *β*-**3.1** (R_1 = 0.0356, R_{int} = 0.0332), likely owing to the loss of lattice solvent during the reaction, resulting in large errors for the bond metrics. The Au–P bond lengths of 2.232(2) and 2.235(2) Å are also similar to the range of that observed for complexes **3.1**–**3.3**. Similar to the ethylene, CO and ammonia ligands of complexes **3.1**–**3.3**, the dimethylamine ligand lies within close proximity of the aryl rings of the phosphine ligand, with the closest H1–centroid(C(x)···C(y)) contact of one of the cations within the unit cell being 3.0931(6) Å, resulting in a ring current effect which could result in the upfield shift of the amine proton to δ 1.23 – 1.22.

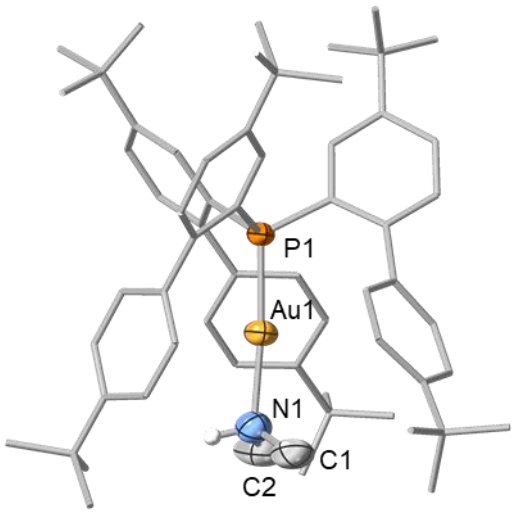

3.4

Figure 3.16 The molecular structure of one of the isolated cations of complex *γ*-**3.4**. Selected bond distances (Å): Au1–N1, 2.10(1); Au2–N2, 2.148(9); Au1–P1, 2.232(2); Au2–P2, 2.235(2). Selected bond angles (°): N1–Au1–P1, 176.2(3); N2–Au2–P2, 175.0(3). Displacement ellipsoids are set at 50% probability level. Select hydrogen atoms and [BAr$^F{}_4$]$^-$ anion are excluded for clarity.

The bulkier tertiary amine, trimethyl amine, was also explored to probe the flexibility of the pocket of ligand **L1** in the solid state. The solid/gas addition of NMe_3 (1 bar absolute, 2 hr) to crystals of the ensemble of polymorphs *α*-**3.1** and *β*-**3.1** led to a loss of crystallinity (SCXRD) and the formation of a solid which was assigned to be [(**L1**)Au(NMe_3)][BAr^F_4] (**3.5**) by $^{31}P\{^1H\}$ and ^1H NMR (CD_2Cl_2) spectroscopy. This reaction also occurs from the ensemble of polymorphs of complex **3.2** by loss of CO. Whilst only one polymorph was measured using SCXRD (*vide infra*), it is likely that complex **3.5** exists as two polymorphs similar to complexes **3.1**–**3.3**. The solution-state $^{31}P\{^1H\}$ NMR (CD_2Cl_2) spectrum of the dissolved ensemble of polymorphs of complex **3.5** shows complete conversion to a product that yields a singlet at δ 6.2. The solution-state ^1H NMR (CD_2Cl_2) spectrum of the proposed ensemble of polymorphs of complex **3.5** (Figure 3.17) shows a peak corresponding to the *ortho*-BAr^F_4 protons which overlap with one of the aryl proton environments of the biphenyl phosphine ligand at δ 7.73 (11H), whilst the *para*-BAr^F_4 protons appear as a broad singlet at δ 7.56 (4H). The remaining aryl peaks corresponding to the phosphine ligand are found at δ 7.50 (3H), 7.41 (3H), 7.22 (6H) and 6.80 (6H), whilst the *tert*-butyl group protons are observed at δ 1.23 – 1.22 (54H). The methyl protons of the trimethyl amine ligand are observed as a doublet at δ 1.63 (9H, $^4J_{HP}$ = 1.5 Hz), which collapses into a singlet upon ^{31}P decoupling. The methyl protons are shifted upfield relative to free trimethyl amine (δ 2.12)[50] and the only other known gold(I) trimethylamine complex [(Ph_3P)Au(NMe_3)][ClO_4] (δ 2.97),[51] due to the ring current effect imposed by **L1**. Consistent with this, and similar to the ligands of complexes **3.1**–**3.4**, the amine ligand lies within close proximity of the aryl rings of the phosphine ligand, with the H–centroid(C(x)···C(y)) contacts being 3.4106(10), 3.3579(7), 3.5845(19), 3.1203(14), 3.4896(14) and 3.2408(25) Å. Free NMe_3 remains within the lattice as evident by the peak at δ 2.12 (4.1H). No peaks corresponding to 1,2-difluorobenzene or heptane are observed, suggesting that the lattice solvents in both polymorphs of complex **3.1** are lost during the reaction.

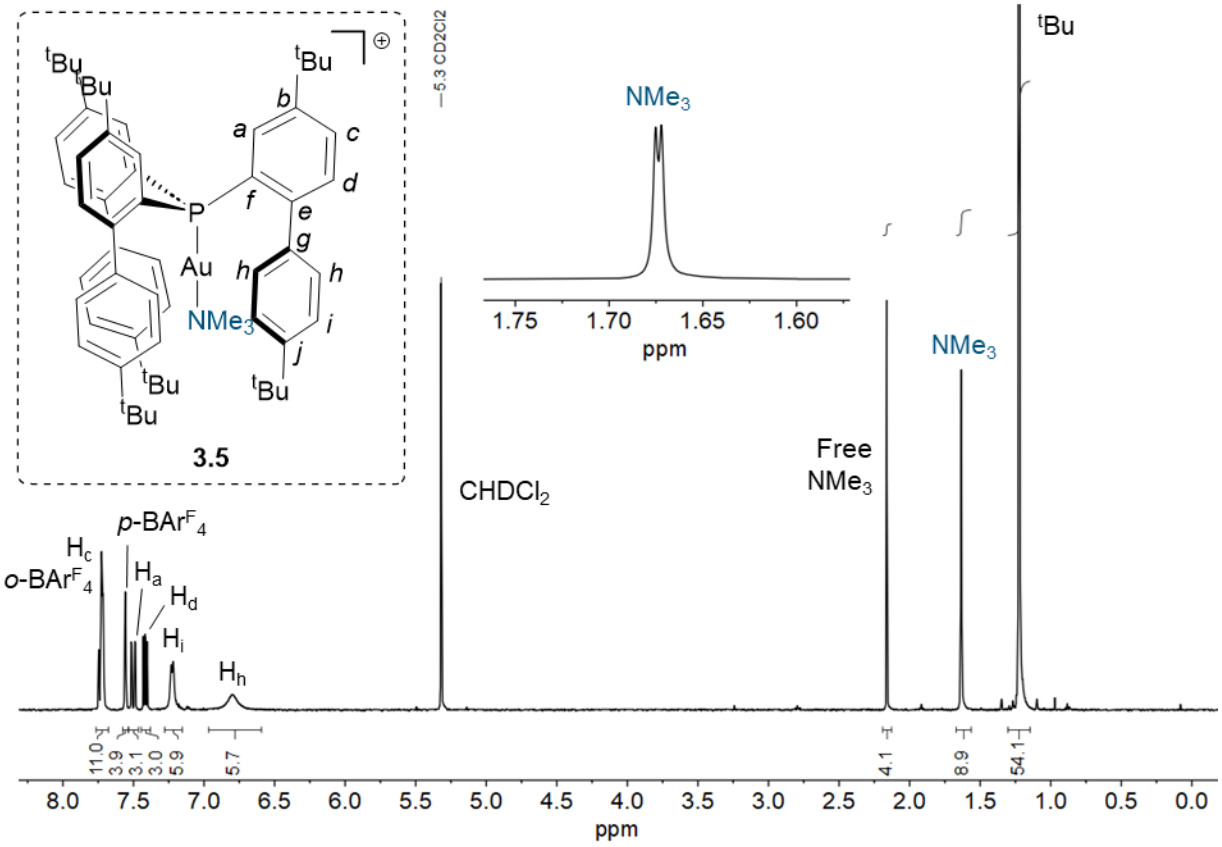

Figure 3.17 The ^{1}H NMR spectrum of the dissolved ensemble of polymorphs of complex **3.5** (500 MHz, CD_2Cl_2, 298 K). The inset highlights the methyl proton environment of the amine ligand.

Due to the relatively higher boiling point of NMe_3 (3.5 °C) compared to NH_3 (–33.3 °C), NMe_3 appeared to condense on the solid during the reaction from the ensemble of polymorphs *α*-**3.1** and *β*-**3.1**, leading to the observation of free NMe_3 in the ^{1}H NMR spectrum. The amorphous solid was recrystallised from 1,2-difluorobenzene/heptane at –20 °C, affording colourless crystals of complex *β*-**3.5** (Figure 3.18). Solution-grown crystals of complex *β*-**3.5** (space group $P\bar{1}$) display a linear geometry around the gold centre with a P1–Au1–N1 angle of 178.91(7)°. Complex *β*-**3.5** has a similar Au–N bond length (2.114(2) Å) to the known $[(Ph_3P)Au(NMe_3)][ClO_4]$ (2.108(7) Å)[51] and complex *β*-**3.3** (2.139(7) Å). The Au–P bond length of 2.2276(2) Å is also within the range observed for complexes **3.1**–**3.4** and $[(Ph_3P)Au(NMe_3)][ClO_4]$ (2.231(2) Å).[51] Complex *β*-**3.5** displays a similar bicapped square prismatic arrangement of the $[BAr^F_4]^-$ anions to complex *β*-**3.1**, with 1,2-difluorobenzene (0.5 occupancy) and heptane (0.7 occupancy) also within the lattice. The ^{1}H and ^{31}P{^{1}H} NMR

(CD_2Cl_2) spectra of the dissolved ensemble of recrystallised **3.5** are similar to that of the amorphous solid following solid/gas reaction of the ensemble of polymorphs *α*-**3.1** and *β*-**3.1** with NMe_3 gas, with the exception of the lattice solvent as no THF is observed in the recrystallised **3.5**.

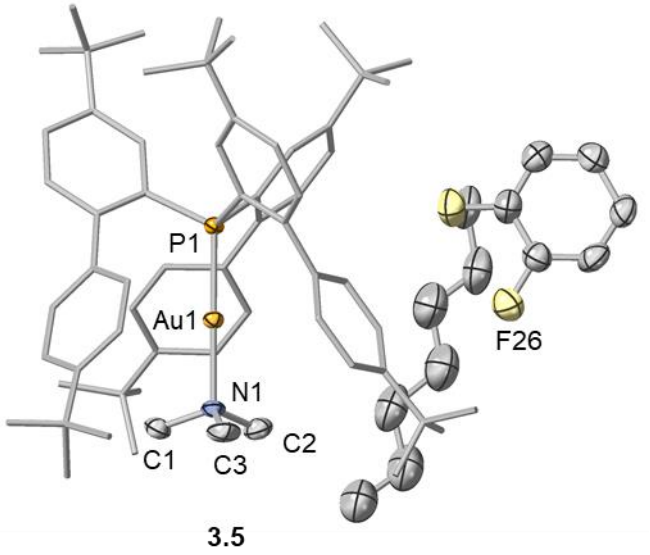

Figure 3.18 The molecular structure of the isolated cation of complex *β*-**3.5**. Selected bond distances (Å): Au1–N1, 2.114(2); Au1–P1, 2.2276(2). Selected bond angles (°): N1–Au1–P1, 178.91(7). Displacement ellipsoids are set at 50% probability level. Hydrogen atoms and $[BAr^F_4]^-$ anion are excluded for clarity.

Whilst the ensemble of complex **3.5** is stable for months in the solid state, it does not demonstrate such stability in dichloromethane solution, similar to complex **3.3**. A solution of the ensemble of complex **3.5** in CH_2Cl_2 undergoes complete conversion to [(**L1**)AuCl] and $[Me_3NCH_2Cl][BAr^F_4]$ within one week, as shown by $^{31}P\{^1H\}$ NMR spectra (CD_2Cl_2, δ 9.4). Crystallisation from dichloromethane/hexane at room temperature afforded colourless crystals of $[Me_3NCH_2Cl][BAr^F_4]$ (Figure 3.19 A). No peaks were observed in the $^{31}P\{^1H\}$ NMR spectrum (CD_2Cl_2) of the dissolved crystals, since [(**L1**)AuCl] is hexane soluble and is removed during crystallisation. The ^1H NMR spectrum (CD_2Cl_2) shows peaks at δ 7.72 (8H) and 7.56 (4H) corresponding to the *ortho*- and *para*- protons of the $[BAr^F_4]^-$ anion respectively, as well as peaks corresponding to the methylene protons of the $[Me_3NCH_2Cl]^+$ cation at δ 5.45 (2H) and the methyl protons at δ 3.30 (9H), which is consistent with the known $[Me_3NCH_2Cl][OTf]$ at δ

5.44 and 3.28 respectively (CD_3CN).[52] The formation of $[Me_3NCH_2Cl][BAr^F{}_4]$ demonstrates that the ensemble of complex **3.5** is capable of cleaving the dichloromethane C–Cl bond, forming [(**L1**)AuCl]. This process likely occurs in solution *via* dissociation of the NMe_3 ligand and binding of dichloromethane, followed by nucleophilic attack of NMe_3 at the $[(\mathbf{L1})Au(CH_2Cl_2)][BAr^F{}_4]$ intermediate (Figure 3.19 B).

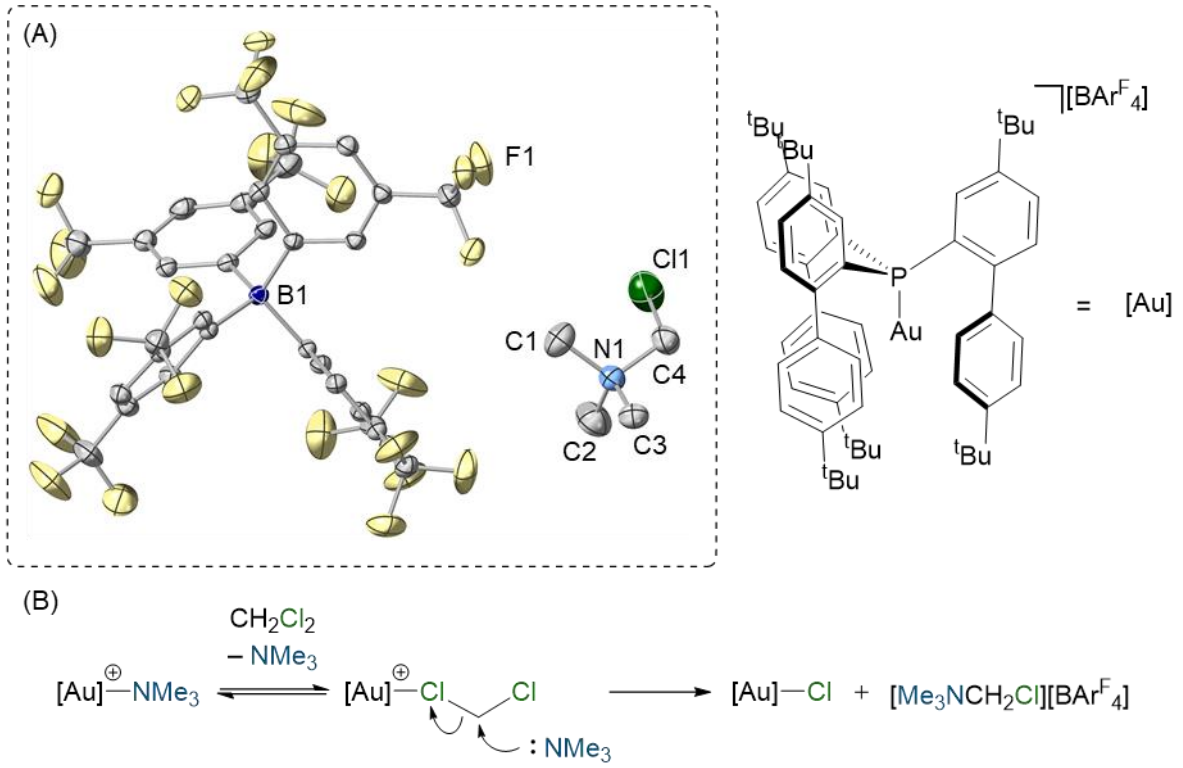

Figure 3.19 (A) The molecular structure of $[Me_3NCH_2Cl][BAr^F{}_4]$. Displacement ellipsoids are set at 50% probability level. Hydrogen atoms are excluded for clarity. Selected bond distances (Å): C1–Cl1, 1.761(4); N1–C1, 1.501(6); N1–C2, 1.491(6); N1–C3, 1.5141(51); N1–C4, 1.501(6). (B) The proposed mechanism of reactivity of complex **3.5** in dichloromethane.

Despite the additional strain within the pocket of ligand **L1**, complexes **3.3**–**3.5** do not undergo further SC-SC reactivity with CO (2 bar absolute, 20 hr) or C_2H_4 (2 bar absolute, 20 hr). In addition, no reaction was observed when crystals of complex **3.5** were heated to 60 °C under vacuum, or when placed under an atmosphere of NH_3 (1 bar absolute, 20 hr), demonstrating that despite the increased steric bulk of the trimethylamine ligand, the barrier to ligand exchange (associative) is high.

3.3.3 H/D exchange with complex 3.3

As discussed in section 1.1.1, rhodium(I) complexes have been shown to undergo H/D exchange at coordinated NH_3 ligands with D_2 in the solid state,[53] which is one of the few reported examples of solid state H/D exchange, alongside that reported for $[(Cp^*)Ir(H)_2(NH_3)]$.[54] It was hypothesised that the gold(I) ammonia complex **3.3** would also undergo rare solid state H/D exchange of ammonia.

The SC-SC addition of D_2 (2 bar absolute, 30 min) to the ensemble of polymorphs *α*-**3.3** and *β*-**3.3** resulted in the disappearance of the bound NH_3 peak at δ 0.92 in the ^{1}H NMR spectrum following the SC-SC reaction. A new peak was observed at δ 0.81 in the ^{2}H NMR spectrum (CH_2Cl_2, referenced to residual $CHDCl_2$ at δ 5.28), consistent with the formation of [(**L1**)Au(ND_3)][BAr^F_4] (**D_3-3.3**). The ND_3 resonance is observed upfield of the corresponding NH_3 (δ 0.92) signal due to isotopic perturbation of chemical shift as well as increased N–D···*π* ring current effects, as evident by the SCXRD structure of *β*-**D_3-3.3** which shows that the average D–centroid (C(x)···C(y)) distances (3.231(6), 3.455(9), 3.650(8) Å) are shorter than the average H–centroid (C(x)···C(y)) distances in complex *β*-**3.3** (3.5048(8), 3.4450(17), 3.7706(2) Å). The ND_3 signal (δ 0.81) was confirmed by independent synthesis of complex **D_3-3.3** from the solid/gas reaction of the ensemble of polymorphs *α*-**3.1** and *β*-**3.1** with ND_3 gas.

Attempts at observing the isotope exchange *via* ESI-MS (Electrospray Ionisation Mass Spectrometry, positive mode) of complex **D_3-3.3** were unsuccessful, as the molecular ion peak and isotope pattern are identical to that of complex **3.3** (1,2-difluorobenzene, obs. 1040.69 m/z, calc. 1040.55 m/z). It was postulated that this could be due to exposure to air and moisture as a consequence of the experimental conditions. The analogous solution-state experiment of the dissolved ensemble of polymorphs *α*-**3.3** and *β*-**3.3** with D_2 (2 bar absolute, 30 min) in CD_2Cl_2 also resulted in the disappearance of the NH_3 peak in the ^{1}H NMR spectrum, as well as the appearance of a peak indicative of a stoichiometric amount of H_2O (δ 1.56) in the ^{1}H NMR spectrum, which was determined to be the product of the H/D exchange. This suggests that trace water in the D_2 source undergoes the H/D exchange process rather than

D_2. Trace water in the D_2 source was confirmed by the appearance of a peak corresponding to D_2O (δ 1.55) in the ^2H NMR spectrum of the solution-state reaction.

To probe the potential of complex **3.3** to undergo H/D exchange of ammonia with D_2O in the solid state, D_2O (1 mL) was added to the bottom of a flask containing crystals of complex **3.3** on a porous glass bed, and the flask was then placed under a static vacuum for 24 hr (Figure 3.20).

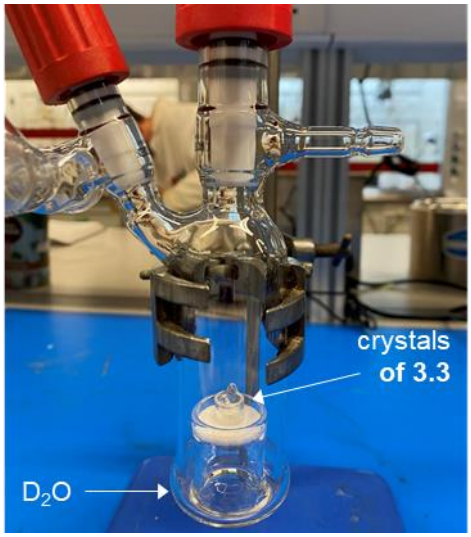

Figure 3.20 The apparatus used for the solid state reaction of complex **3.3** with D_2O vapour.

Analysis of the resulting ^1H NMR spectrum (CH_2Cl_2) of dissolved crystals of **3.3** after exposure to D_2O vapour (24 hr), resulted in the disappearance of the expected NH_3 peak at δ 0.92, and the appearance of a new ND_3 peak at δ 0.81 in the ^2H NMR spectrum (CH_2Cl_2, referenced to residual $CHDCl_2$), consistent with the formation of complex **D_3-3.3** (Figure 3.21). No change to the signals corresponding to the phosphine ligand are observed, demonstrating that H/D exchange is selective to the ammonia ligand. Crystallinity was retained during the transformation, which allowed for measurement by SCXRD. When crystals of complex **D_3-3.3** were exposed to air the resonance corresponding to the NH_3 peak of complex **3.3** (δ 0.92) reappears, suggesting that the complex reacts with trace H_2O in air and that H/D exchange is reversible, preventing the exchange being observed by ESI-MS in air.

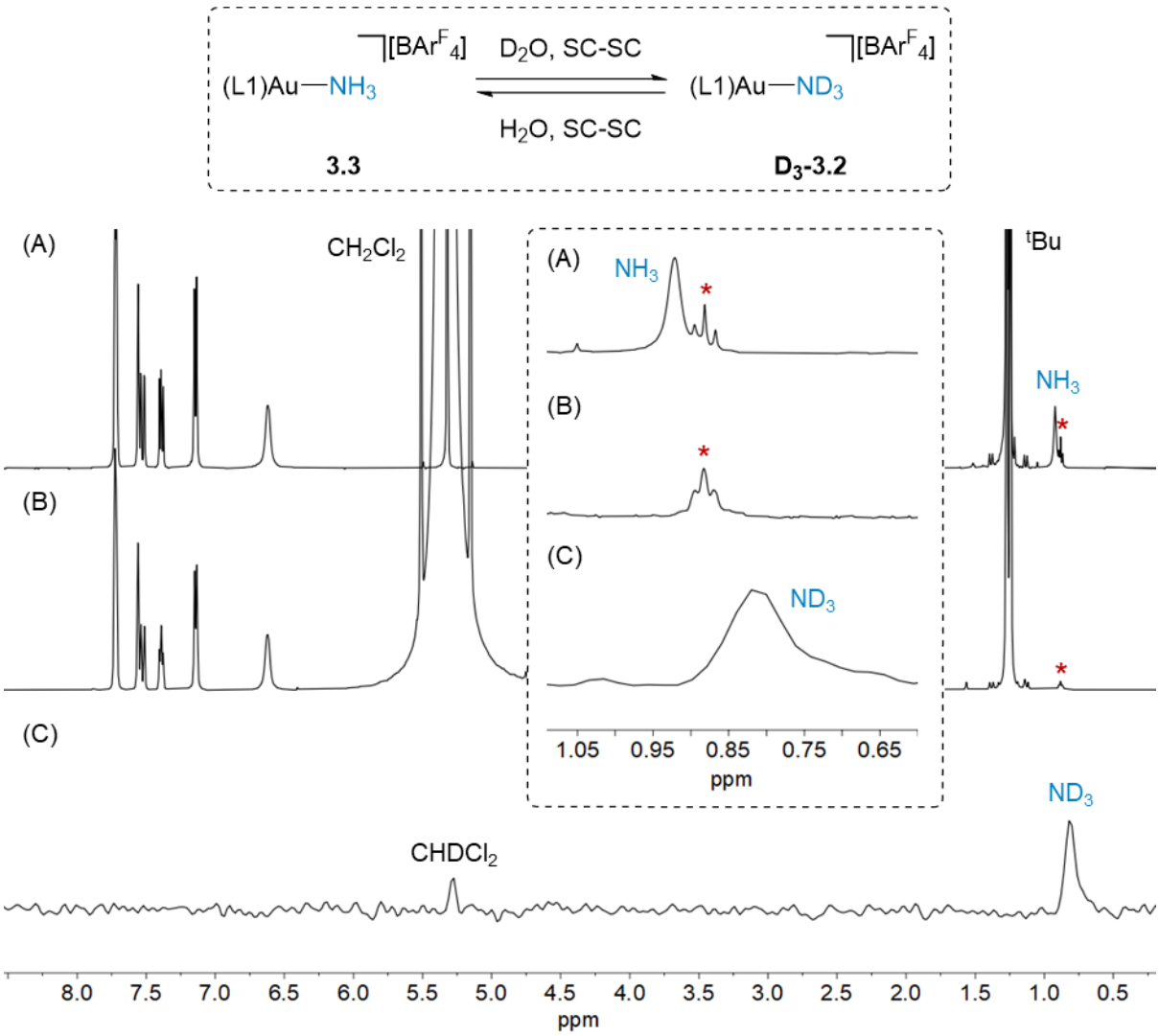

Figure 3.21 (A) The ^{1}H NMR spectrum of complex **3.3** (500 MHz, CD_2Cl_2, 298 K). (B) The ^{1}H NMR spectrum of the SC-SC reaction of complex **3.3** with D_2O (500 MHz, CH_2Cl_2, 298 K). (C) The ^{2}H NMR spectrum of the SC-SC reaction of complex **3.3** with D_2O (61 MHz, CH_2Cl_2, 298 K). * Denotes lattice heptane. The inset highlights the ammonia ligand region of the spectrum, demonstrating the disappearance of the NH_3 signal and the appearance of the corresponding ND_3 peak.

To further demonstrate the H/D exchange, the IR spectra of complexes **3.3** and **D$_3$-3.3** were compared with regard to their N–H/D stretches. The solid-state IR spectrum of complex **3.3** (Figure 3.22) displays an N–H stretch as a weak absorption band at 3359 cm^{-1}, similar to that of [(PPh$_3$)Au(NH$_3$)][ClO$_4$] at 3318 cm^{-1}.[46] This N–H stretch disappears upon exchange with deuterium, as shown by the IR spectrum of complex **D$_3$-3.3**, when measured in an argon filled glove box. Derived from the N–H stretch of 3359 cm^{-1}, the corresponding N–D absorption band should occur at approximately 2453 cm^{-1} based on the change in reduced mass

(Equation 1 and 2). Whilst no such N–D stretch is observed, the disappearance of the N–H stretch is indicative of H/D exchange.

$$\mu = \frac{m_1 m_2}{m_1 + m_2} \qquad \text{(Equation 1)}$$

$$\tilde{\nu} = \frac{1}{2\pi}\sqrt{\frac{k}{\mu}} \qquad \text{(Equation 2)}$$

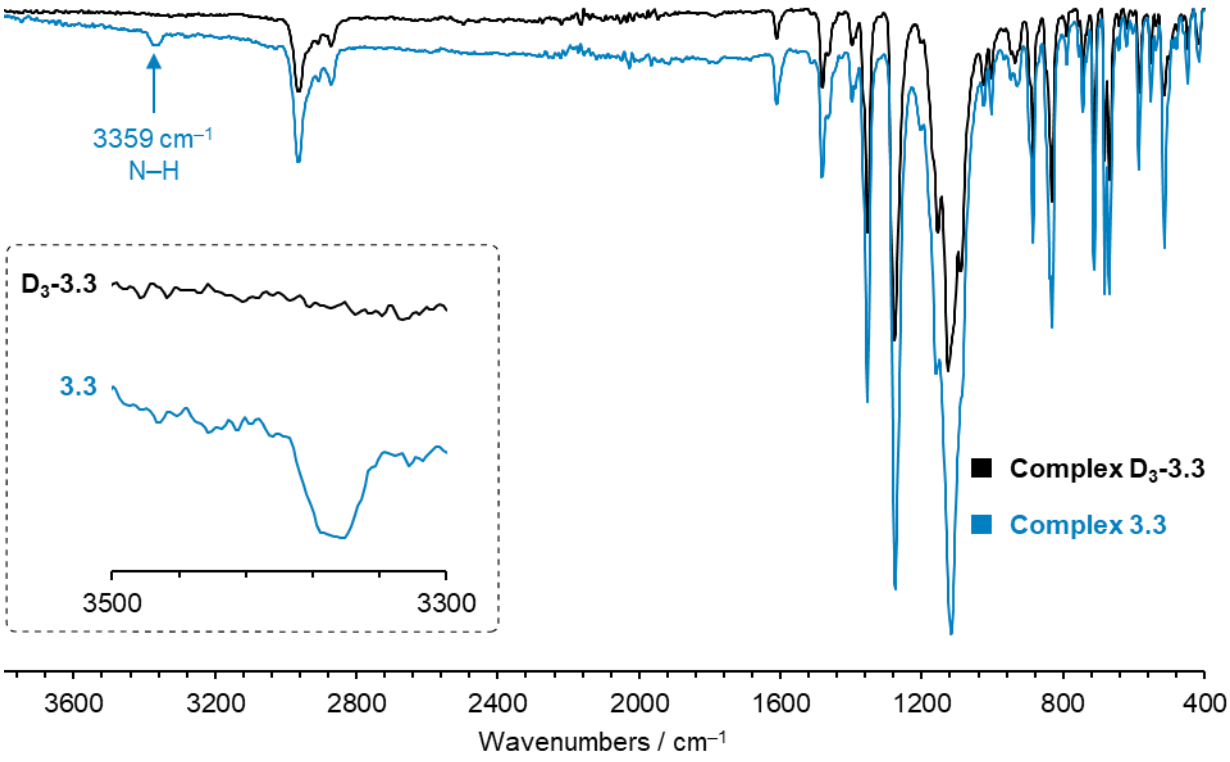

Figure 3.22 The solid-state ATR-IR spectra of complexes **3.3** and **D$_3$-3.3** measured under an argon atmosphere. The inset highlights the N–H region of the spectrum.

Another possible product of the reaction of D_2O with complex **3.3** might be a water complex, such as [(**L1**)Au(OH_2)][$BAr^F{}_4$]. A water ligand would be crystallographically indistinguishable from ammonia in the SCXRD structure, and either may correlate to the observed IR spectra. Therefore, to discount the formation of [(**L1**)Au(OH_2)][$BAr^F{}_4$], the ^{15}N labelled analogue, [(**L1**)Au($^{15}NH_3$)][$BAr^F{}_4$] (**^{15}N-3.3**), was prepared to provide an additional NMR spectroscopic handle (^{15}N, I = ½) to subsequently probe the H/D exchange. Complex **^{15}N-3.3** was synthesised using $^{15}NH_3$ (~ 0.5 bar absolute, 30 minutes) by a SC-SC reaction with complex **3.2**, then crystallised from 1,2-difluorobenzene/heptane at –20 °C. An asymmetric broad peak is observed at δ 3.9 (fwhm = ~ 353 Hz) in the $^{31}P\{^1H\}$ SSNMR spectrum of crystals of complex

^{15}N-3.3 grown from solution (Figure 3.23 B), likely due to partially collapsed coupling to the ^{15}N nuclei or quadrupolar coupling to ^{197}Au. The ^{15}N SSNMR spectrum shows a single peak at δ 6.2 (fwhm = ~ 78 Hz, Figure 3.23 C). The single peaks observed in the ^{31}P{^{1}H} and ^{15}N SSNMR spectra suggest that only one polymorph is present, however two polymorphs (*α*-**3.3** and *β*-**3.3**) are observed by SCXRD.

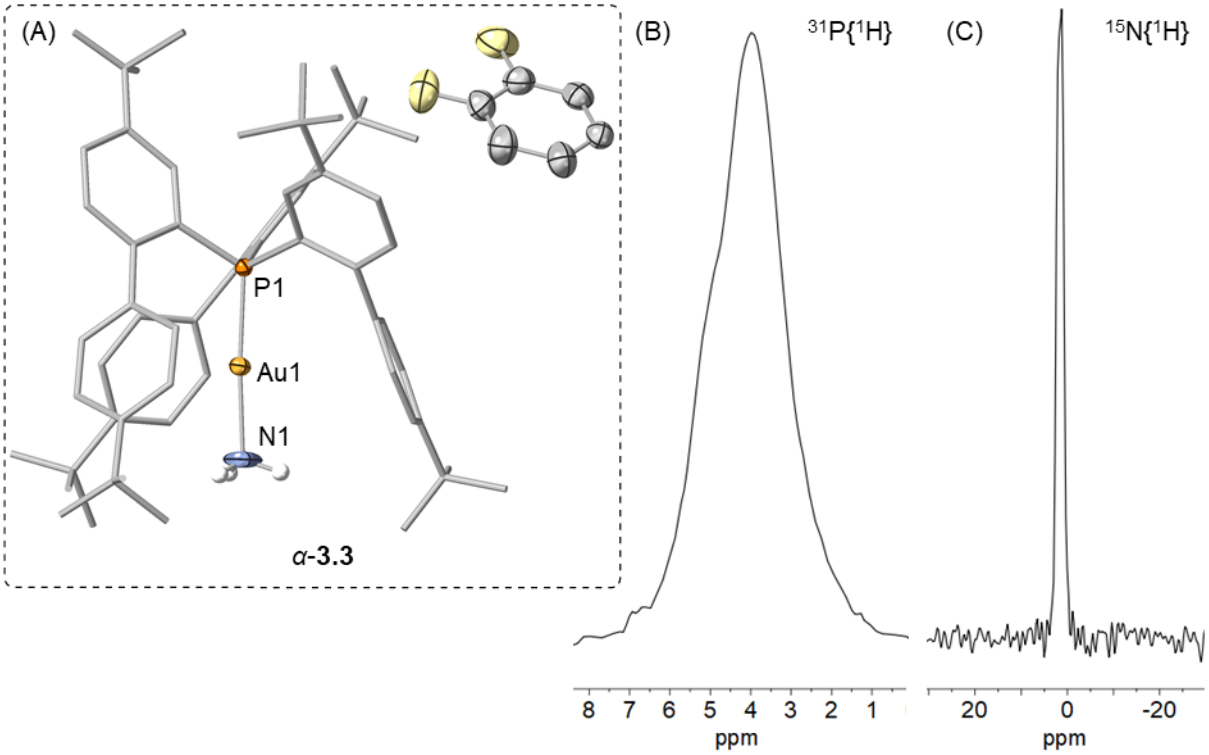

Figure 3.23 (A) The molecular structure of the isolated cation and lattice solvent of polymorph *α*-**3.3**, grown from solution. Select hydrogen atoms and $[BAr^{F}_{4}]^{-}$ anions are excluded for clarity. Displacement ellipsoids are set at 50% probability level. Selected bond distances (Å): Au1–N1, 2.1046(28); Au1–P1, 2.2368(9). Selected bond angles (°): N1–Au1–P1, 174.98(11). (B) The solid-state ^{31}P{^{1}H} CP MAS NMR spectrum of crystals of complex **3.3** grown from solution (162 MHz, 20 kHz spin rate, 298 K). (C) The solid-state ^{15}N CP MAS NMR spectrum of crystals of complex **3.3** grown from solution (40 MHz, 20 kHz spin rate, 298 K).

The ^{1}H NMR (CD_2Cl_2) spectrum of complex **^{15}N-3.3** is nearly identical to that of complex **3.3** with the exception of the ammonia signal, which is now observed as a well-defined doublet due to ^{15}N coupling (δ 0.90, 3H, $^{1}J_{HN}$ = 72 Hz, Figure 3.24 A) and shifted slightly due to isotopic perturbation of chemical shift. The $^{15}NH_3$ peak in the ^{15}N NMR (CD_2Cl_2) spectrum is observed as a quartet of doublets (δ 6.2) due to a combination of coupling to three proton nuclei ($^{1}J_{NH}$ = 72 Hz) as well as the phosphorus ($^{2}J_{NP}$ = 38 Hz), and collapses into a doublet upon proton

decoupling (Figure 3.24 B and C). The $^{31}P\{^{1}H\}$ NMR spectrum also displays coupling to ^{15}N and is now observed as a doublet (δ 3.6, $^{2}J_{PN}$ = 38 Hz, Figure 3.16 D). A small amount of unreacted complex **3.2** (7%) is also observed, likely owing to the lower pressure of $^{15}NH_3$ available (~ 0.5 bar absolute) compared to NH_3 (1 bar absolute), although this is hidden by the major peak in the $^{31}P\{^{1}H\}$ SSNMR.

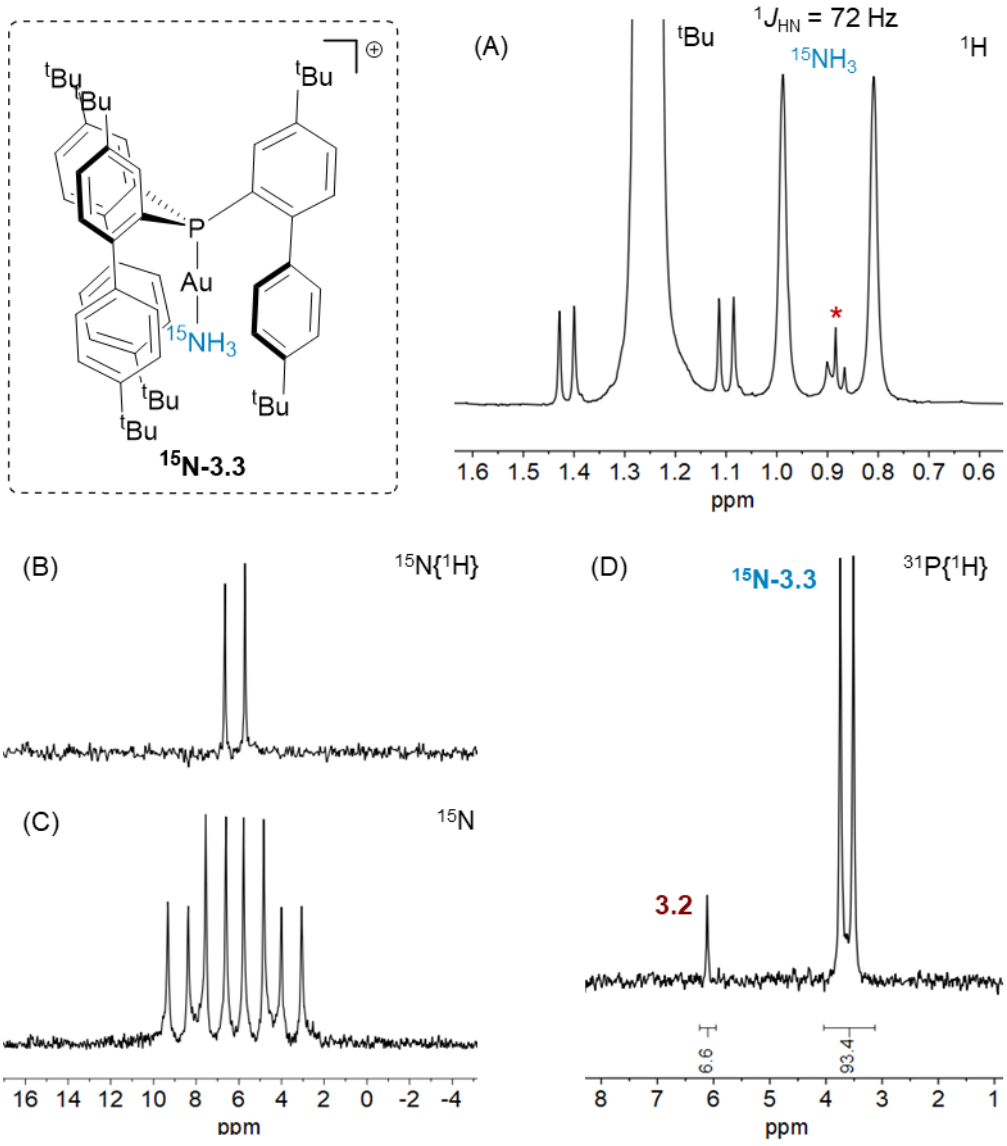

Figure 3.24 (A) The ammonia ligand region of the ^{1}H NMR spectrum (400 MHz), (B) the $^{15}N\{^{1}H\}$ NMR spectrum (40 MHz), (C) the ^{15}N NMR spectrum (40 MHz) and (D) the $^{31}P\{^{1}H\}$ NMR spectrum (161 MHz) of crystals of complex **^{15}N-3.3** grown from solution (CD_2Cl_2, 298 K).

With the ^{15}N labelled complex in hand, the reaction with D_2O with the ^{15}N labelled complex **^{15}N-3.3** was studied to validate the H/D exchange process by monitoring the ^{15}N-^{1}H and ^{15}N-

^{2}H couplings in the resulting NMR spectra. Analogous to complex **3.3**, addition of D_2O to complex **^{15}N-3.3** in CH_2Cl_2 solution results in the disappearance of the $^{15}NH_3$ peak, coupled with the appearance of H_2O (δ 1.56) as a product of the H/D exchange, in the ^{1}H NMR spectrum (Figure 3.25 A). The $^{15}ND_3$ peak in the ^{2}H NMR spectrum is now observed as a doublet due to coupling to ^{15}N (δ 0.84, $^{1}J_{DN}$ = 9 Hz, Figure 3.25 B), confirming that the deuterium nuclei is bound to the ^{15}N environment and discounting the formation of a water complex. The $^{1}J_{DN}$ coupling constant (9 Hz) of complex **^{15}N-3.3** is smaller than the $^{1}J_{HN}$ (72 Hz) of complex **3.3** due to the difference in gyromagnetic ratio of ^{1}H to ^{2}H (γ_H/γ_D = 42.58/6.54 ≈ 6). The $^{31}P\{^{1}H\}$ NMR spectrum remains unchanged from that of the starting complex **^{15}N-3.3**, showing a doublet due to coupling to ^{15}N (δ 3.6, $^{2}J_{PN}$ = 38 Hz). Upon addition of D_2O no signal is observed in the ^{15}N NMR spectrum, likely due to complex coupling to phosphorus and three deuterium nuclei (I = 1), as well as the lack of proton nuclei to provide polarisation transfer.

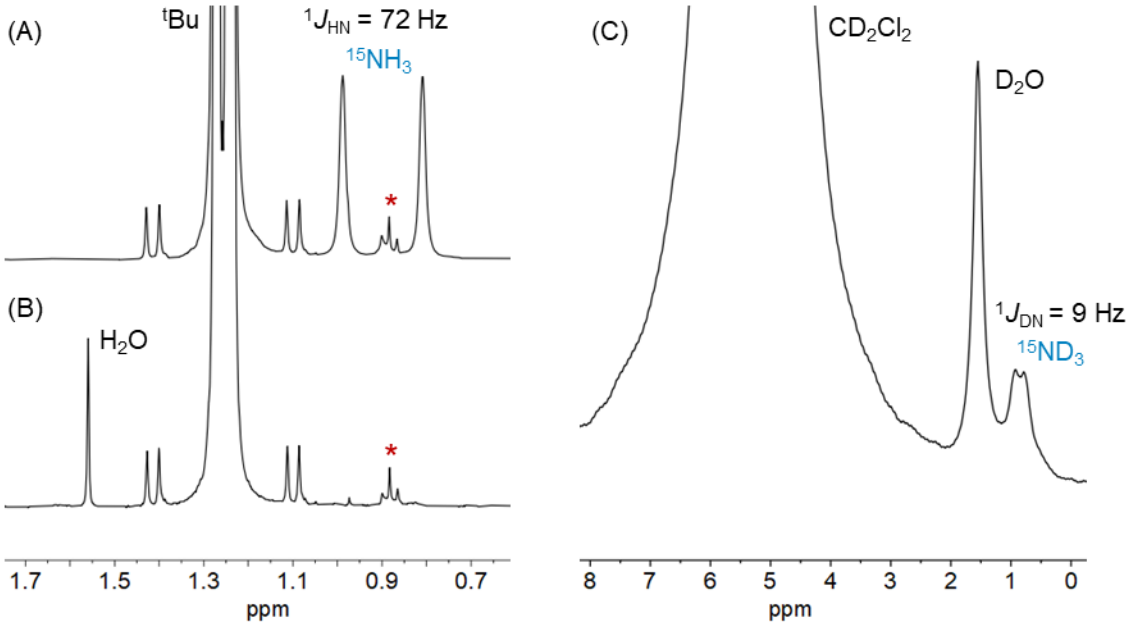

Figure 3.25 The ammonia region of the ^{1}H NMR spectrum of (A) complex **^{15}N-3.3** (400 MHz, CD_2Cl_2, 298 K) and (B) the reaction of complex **^{15}N-3.3** with D_2O in CH_2Cl_2 (400 MHz, CH_2Cl_2, 298 K). (C) The ^{2}H NMR spectrum of the reaction of complex **^{15}N-3.3** with D_2O in CH_2Cl_2 (61 MHz, CD_2Cl_2, 298 K). * Denotes lattice heptane.

Further demonstrating that the observed H/D exchange is occurring with D_2O instead of D_2, no exchange was observed between H_2 and the bound ammonia ligand of complex **3.3** in the 1D EXSY (Exchange Spectroscopy) experiment when the H_2 peak (δ 4.59) was selectively

excited. In comparison, exchange between the protons in H_2O and the bound ammonia ligand of complex **3.3** was confirmed by the 1D EXSY experiment. H_2O (0.05 mL) was added to a solution of complex **^{15}N-3.3** in CD_2Cl_2 and the H_2O peak at δ 1.56 was selectively excited. A resultant exchange peak was observed at δ 0.90 which corresponds to the $^{15}NH_3$ environment (Figure 3.26 A). No evidence of exchange with the phosphine ligand was observed. The relative integrals of the excitation and exchange peaks were measured at different mixing times (d_8) in order to calculate the rate constant at 298 K, k = 13.8347 ± 0.374 s^{-1} (Figure 3.26 B). This corresponds to a barrier of 15.9 kcal mol^{-1} at 298 K for the solution-state H/H exchange between H_2O and NH_3, which is lower than the overall computed barrier of H/H exchange of [(dibpe)Rh(NH_3)$_2$][BAr^F_4] (**1.20**) with H_2 (22.8 kcal mol^{-1}).[53] This lower barrier to exchange for **3.3** is evident experimentally as **1.20** is reported to undergo H/D exchange of the bound NH_3 ligands with H_2 in 1,2-difluorobenzene within 24 hr, whilst **3.3** undergoes H/D exchange of the bound NH_3 ligands with D_2O in CD_2Cl_2 within 10 minutes.

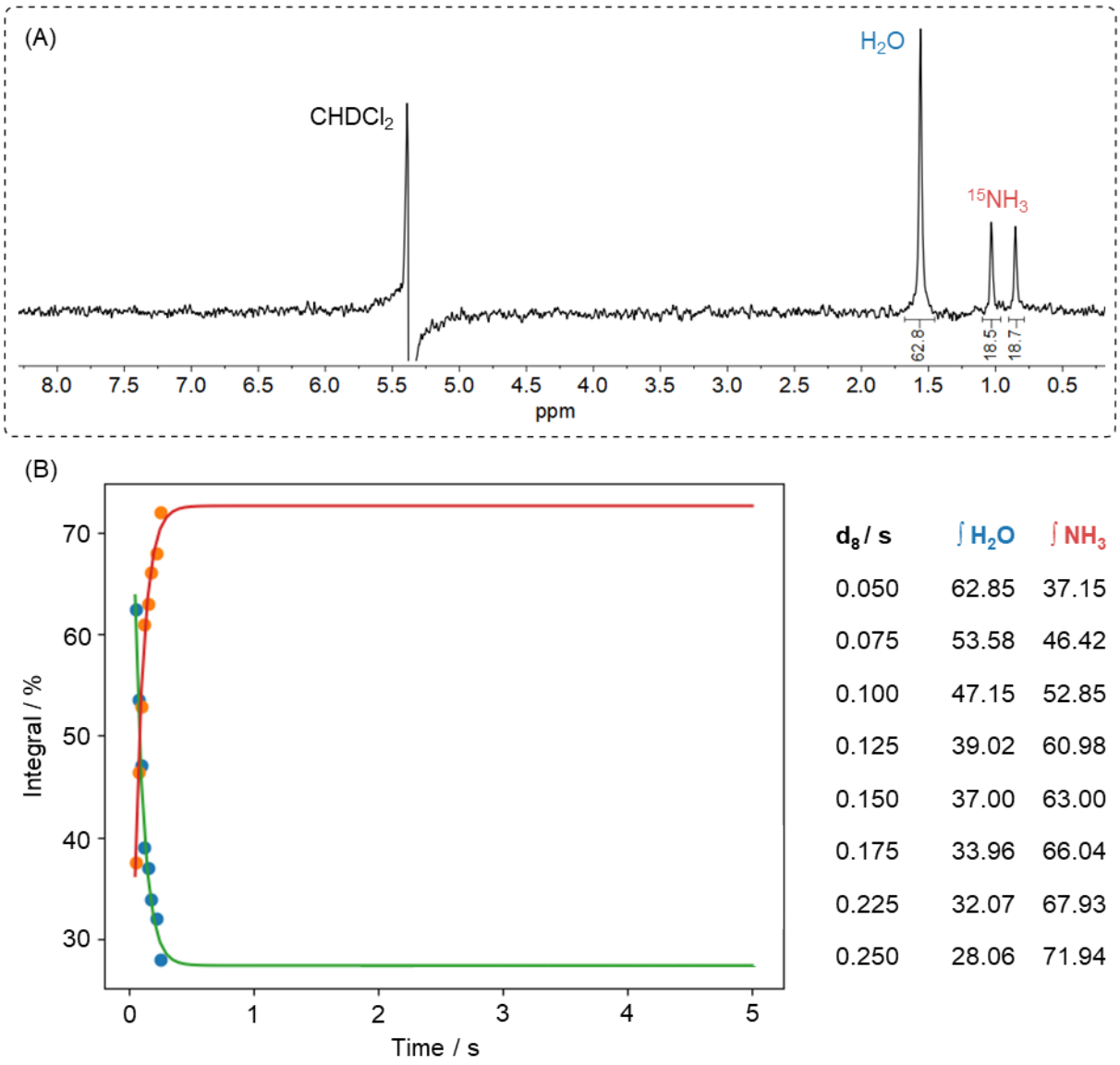

d_8 / s	∫ H_2O	∫ NH_3
0.050	62.85	37.15
0.075	53.58	46.42
0.100	47.15	52.85
0.125	39.02	60.98
0.150	37.00	63.00
0.175	33.96	66.04
0.225	32.07	67.93
0.250	28.06	71.94

Figure 3.26 (A) An example ^{1}H EXSY NMR spectrum of complex **^{15}N-3.3** (0.05 s mixing time, excitation at δ 1.56, 400 MHz, CD_2Cl_2, 298 K). (B) The plot and table of the $^{15}NH_3$ integral relative to the H_2O peak at different mixing times (d_8).

A proposed mechanism for the reversible deuteration of the ammonia ligand of complex **3.3** is *via* *σ*-bond metathesis to form an ammonium cation, $[NH_xD_{4-x}]^+$, which can re-orientate and deliver NH_xD_{3-x} back to the gold(I) centre (Scheme 3.6).

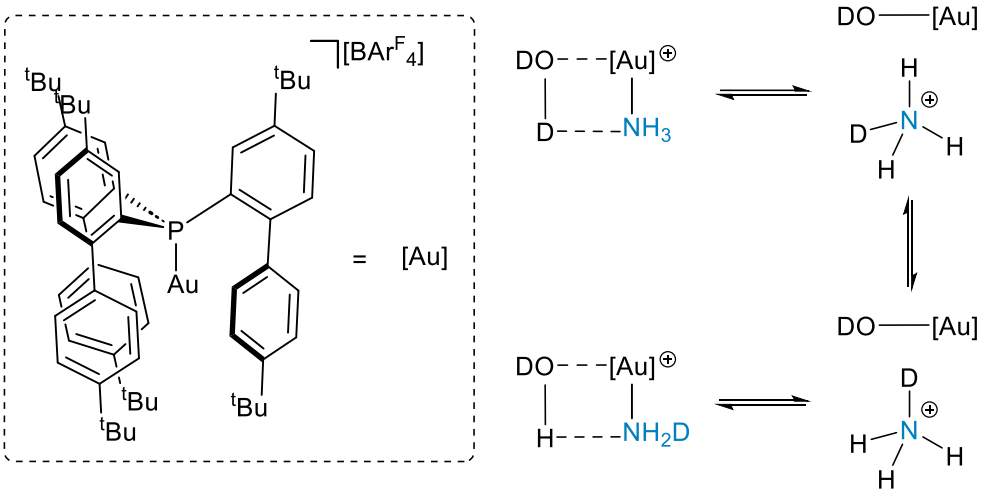

Scheme 3.6 The proposed *σ*-bond metathesis mechanism for H/D exchange of the ammonia ligand of **3.3** with D_2O.

To support the formation of an ammonium cation and thus the proposed H/D exchange mechanism, the SC-SC reaction of complex **^{15}N-3.3** with DCl (Figure 3.27 A) was investigated. It was postulated that the reaction with DCl would occur *via* a similar *σ*-bond metathesis type mechanism, forming the known [(**L1**)AuCl][11] and an ammonium cation in the solid state which may be trapped within the crystal lattice and observed by SCXRD. Addition of DCl (~0.5 bar absolute, 1 week) to crystals of complex **^{15}N-3.3** results in ~27% conversion to [(**L1**)AuCl] as shown by the resulting solid and solution-state $^{31}P\{^1H\}$ NMR spectra (Figure 3.27 C and D). The $[NH_3D]^+$ cation is not observed in the ^1H solution NMR and ^{15}N SSNMR spectra, likely due to its low relative occupancy (27%) and coupling to ^{15}N and ^2H. Full conversion was achieved when left for 1 month under DCl, as evident by the SCXRD structure following SC-SC reaction (Figure 3.27 B). The crystal structure of the SC-SC reaction of complex **^{15}N-3.3** with DCl has a P1–Au1–Cl1 angle of 176.57(4)° and an Au1–Cl1 bond distance of 2.3236(30) Å, slightly longer than the corresponding value for the known [(**L1**)AuCl] which has a Au–Cl distance of 2.3029(10) and a P–Au–Cl angle of 178.87(3)°.[11]

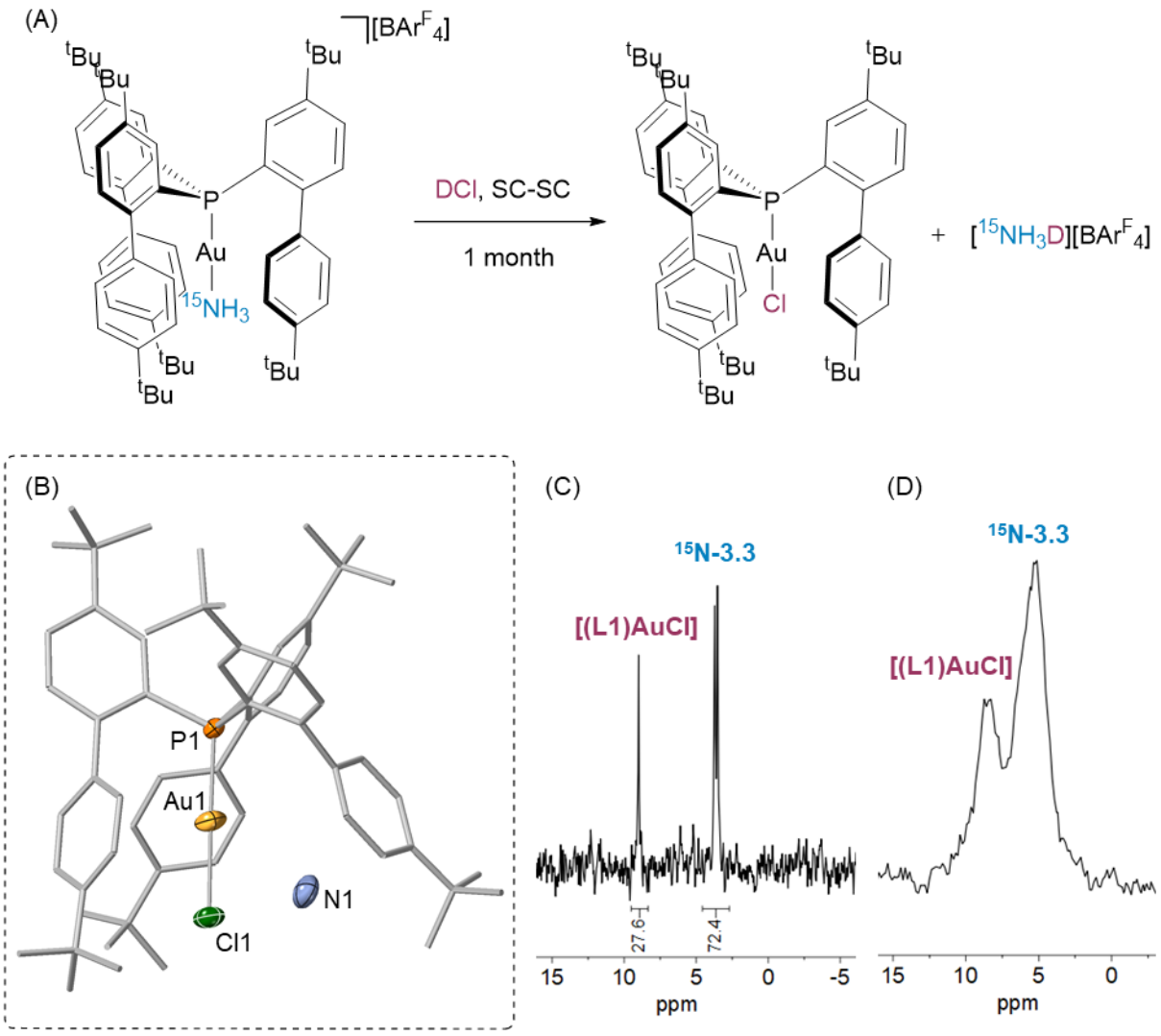

Figure 3.27 (A) The SC-SC reaction of **^{15}N-3.3** with gaseous DCl. (B) The molecular structure of the isolated cation of the reaction of **^{15}N-3.3** with gaseous DCl after 1 month. Select hydrogen atoms and $[BAr^F_4]^-$ anions are excluded for clarity. Displacement ellipsoids are set at 50% probability level. (C) The $^{31}P\{^1H\}$ NMR (202 MHz, CD_2Cl_2, 298 K) and (D) solid-state $^{31}P\{^1H\}$ CP MAS NMR (162 MHz, 20 kHz spin rate, 298 K) spectra of the reaction of **^{15}N-3.3** with gaseous DCl after 1 week.

3.3.4 SC-SC reactivity with isobutylene

Considering the weakly binding nature of alkene ligands to gold(I), it was hypothesised that a substituted gaseous alkene might provide a weakly binding, sterically imposing, environment which could undergo subsequent SC-SC reactivity. Therefore, reactivity with isobutylene was explored. The SC-SC addition of isobutylene (2 bar absolute, 10 minutes) to the ensemble of polymorphs *α*-**3.1** and *β*-**3.1** resulted in 100% conversion (by ^{31}P NMR spectroscopy) to [(**L1**)Au(H_2CCMe_2)][BAr$^F_4$] (**3.6**, Scheme 3.7, Figure 3.28) as colourless crystals. This reaction

is reversible, similar to the synthesis of complex **3.2**, reforming complex **3.1** upon addition of ethylene (2 bar absolute, 10 minutes).

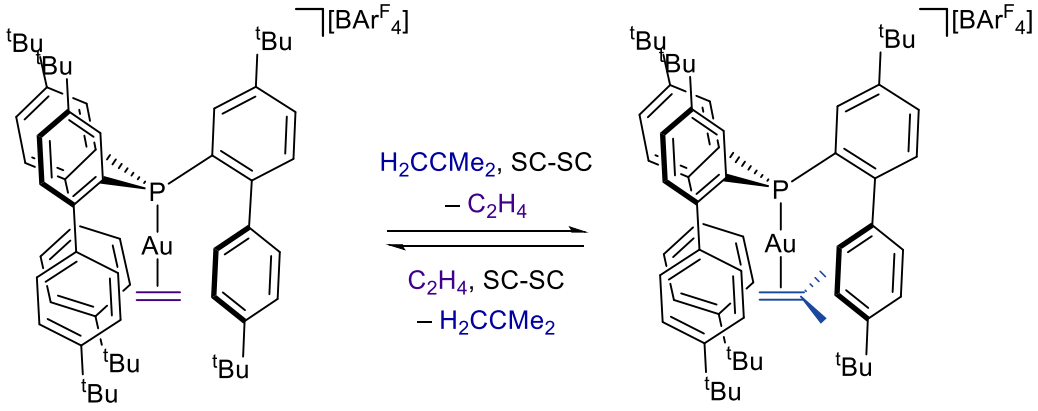

Scheme 3.7 The SC-SC synthesis of complex **3.6**.

Complex *β*-**3.6** (space group $P\bar{1}$) displays a linear geometry around the gold centre with a P1–Au1–centroid(C1···C2) angle of 177.612(12)°. The C1–C2 alkene distance of 1.339(8) Å (110 K) is longer than complex *α*-**3.1** (1.302(5) Å, 100 K) due to the rigidity imposed upon the alkene bond by the methyl substituents hindering a similar torsional libration to that observed in the molecular structure of complex *α*-**3.1**. The C1–C2 distance is similar to that of [(P^{t}Bu$_3$)Au(H_2CCMe_2)][SbF_6] (1.349(14) Å) and [(IPr)Au(H_2CCMe_2)][SbF_6] (IPr = 1,3-bis(2,6-diisopropylphenyl)imidazol-2-ylidine; 1.331(7) Å).[55, 56] The ligand is slightly slipped with a shorter Au1–C1 distance to the CH_2 carbon (2.214(5) Å) than the Au1–C2 to the CMe_2 carbon (2.341(4) Å), with the Au1–C1 distance being similar to complex *α*-**3.1** (2.219(3) Å). This slippage is similar to [(P^{t}Bu$_3$)Au(H_2CCMe_2)][SbF_6] as evidenced by the Au–C distances (2.224(9) and 2.350(8) Å), as well as [(IPr)Au(H_2CCMe_2)][SbF_6] (2.199(5) and 2.285(5) Å). The Au1–P1 distance of 2.271(1) is within range of that of complexes **3.1**–**3.5**. The lattice contains 1,2-difluorobenzene (0.7 occupancy) and heptane (0.6 occupancy), showing that the lattice solvents are retained during the reaction from complex *β*-**3.1** (0.90 1,2-difluorobenzene, 0.75 heptane) but decrease slightly in relative occupancy, likely due to the brief application of

vacuum in order to remove the argon headspace before addition of isobutylene and after the reaction.

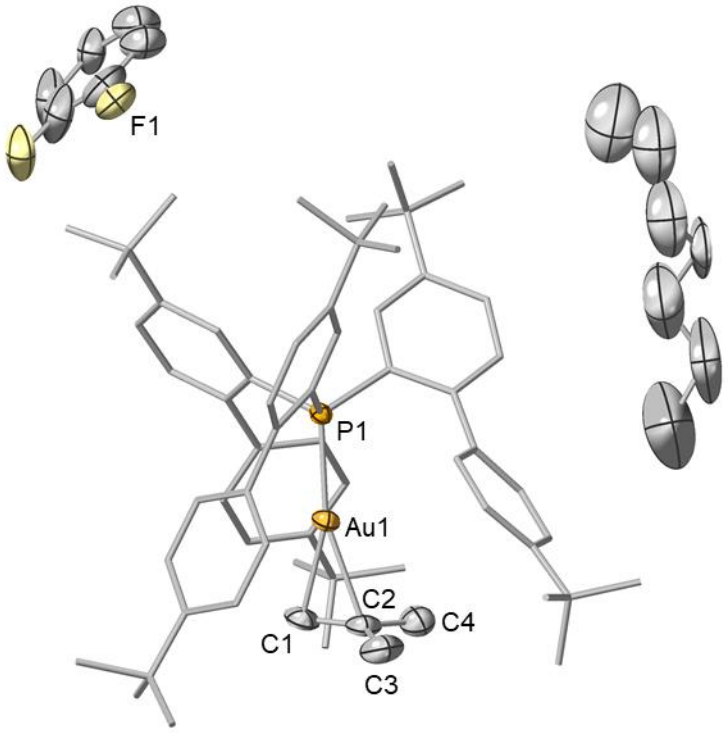

Figure 3.28 The molecular structure of the isolated cation of complex **3.6**. Selected bond distances (Å): C1–C2, 1.339(8); Au1–C1, 2.214(5); Au1–C2, 2.3418(4); Au1–P1, 2.2715(1). Select bond angles (°): P1–Au1–centroid(C1···C2), 177.612(12). Displacement ellipsoids are set at 50% probability level. Select hydrogen atoms and $[BAr^F_4]^-$ anion are excluded for clarity.

The ^{1}H NMR (CD_2Cl_2) spectrum of complex **3.6** (Figure 3.29) shows multiplet peaks corresponding to the *ortho*- and *para*-BAr^F_4 protons at δ 7.72 and 7.56 respectively. The diastereotopic alkene protons are observed as multiplets at δ 3.10 (1H, $^3J_{HP}$ = 2.6, $^2J_{HH}$ = 2.2 Hz) and 2.99 (1H, $^3J_{HP}$ = 2.6, $^2J_{HH}$ = 2.2 Hz) due to coupling to one another, as well as the ^{31}P nuclei as evident by comparison to the ^{1}H{^{31}P} NMR spectrum for which two doublets are observed ($^2J_{HH}$ = 2.2 Hz). The alkene protons are shifted upfield compared to the known $[(P^tBu_3)Au(H_2CCMe_2)][SbF_6]$ (δ 5.19) and $[(IPr)Au(H_2CCMe_2)][SbF_6]$ (δ 4.40),[55, 56] due to ring current effects (closest H1–centroid(C(x)···C(y)) distances of 3.8392(62) and 4.0409(61) Å). The inequivalent proton environment is likely due to the phosphine pocket of **L1**, as evident by comparison to the broad singlet of $[(P^tBu_3)Au(H_2CCMe_2)][SbF_6]$ at δ 5.19 which does not encapsulate the gold(I) centre. Broad multiplets corresponding to the 1,2-difluorobenzene

lattice solvent are observed at δ 7.18–7.22 (0.6H), overlapping with the phosphine aryl environments, which corresponds to 0.15 1,2-difluorobenzene. This is lower than that observed within the crystal structure of complex **3.6** likely due to the application of vacuum prior to vacuum transfer of the CD_2Cl_2 solvent. A triplet peak at δ 0.88 (1.2H) corresponding to the terminal CH_3 of 0.2 heptane is also observed. The peak corresponding to the CH_2 of heptane is overlapping with the *tert*-butyl protons of the phosphine ligand at δ 1.27–1.25 (59H), which is also overlapping with one of the inequivalent methyl proton environments of the isobutylene ligand. The other methyl environment is observed as a broad singlet at δ 1.29 (3H) which sharpens upon ^{31}P decoupling. Both signals were confirmed using a ^{31}P-^{1}H HMBC experiment which showed a correlation between the singlet at δ 14.1 in the $^{31}P\{^{1}H\}$ NMR (CD_2Cl_2) spectrum and both the peaks at δ 1.29 and δ 1.27–1.25 in the ^{1}H spectrum. Similar to the alkene protons, the isobutylene methyl protons are also observed upfield of $[(P^tBu_3)Au(H_2CCMe_2)][SbF_6]$ (δ 2.38) and $[(IPr)Au(H_2CCMe_2)][SbF_6]$ (δ 1.80) due to ring current effects of **L1**. A SSNMR spectrum was not obtained due to time constraints and the small scale of the reaction (< 10 mg).

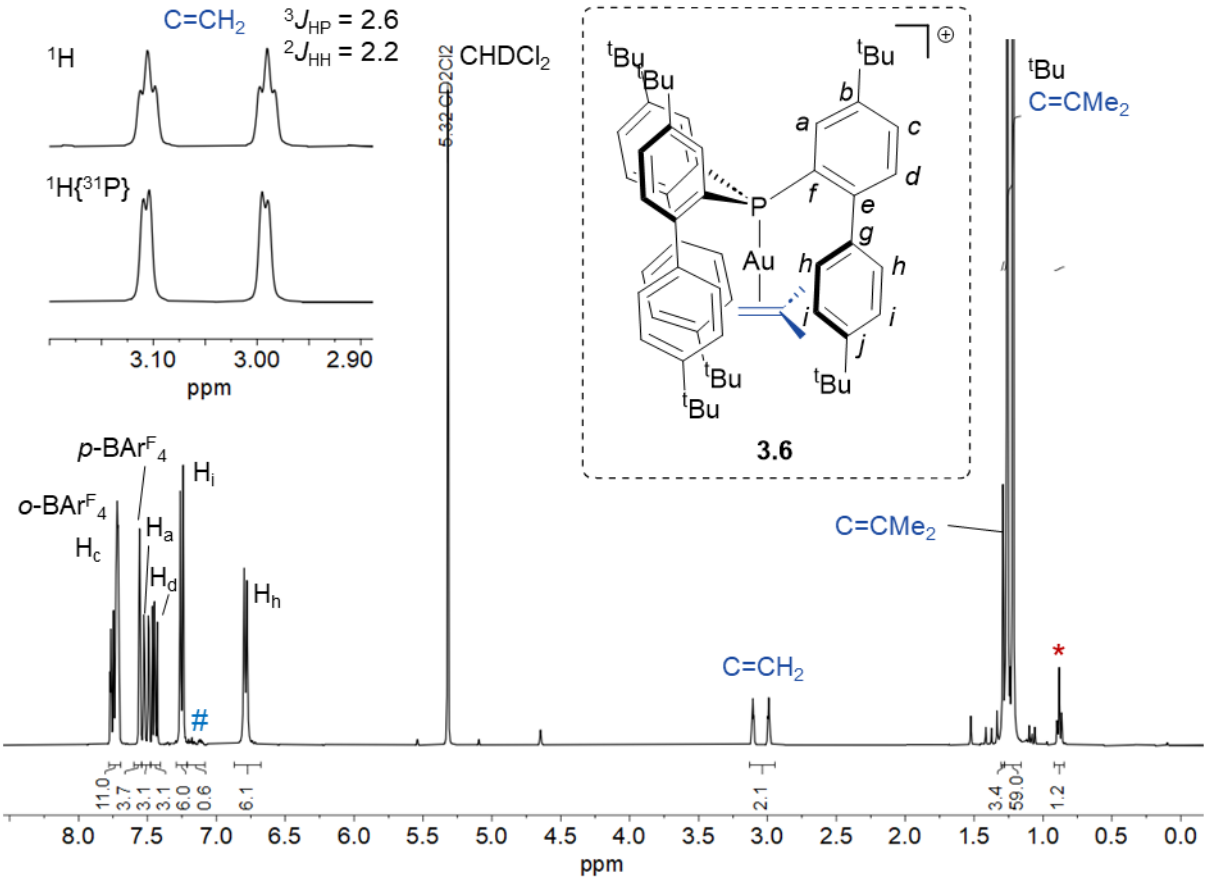

Figure 3.29 The ^{1}H NMR spectrum of complex **3.6** (500 MHz, CD_2Cl_2, 298 K). # Denotes lattice 1,2-difluorobenzene, * denotes lattice heptane. The inset highlights the alkene proton environment.

The flexibility of the pocket of ligand **L1** is exemplified by the distances between the calculated centroid(C(x)···C(y)) of the aryl groups (Figure 3.30), which range from 5.7006(54)–5.9688(92) Å for the smallest ligands, CO and ammonia, and expand to 6.2371(14)–6.6572(2) Å for bigger ligands such as dimethylamine. This flexibility allows for the solid/gas formation of complexes **3.1**–**3.6** even within the constraints of the solid state.

(A)

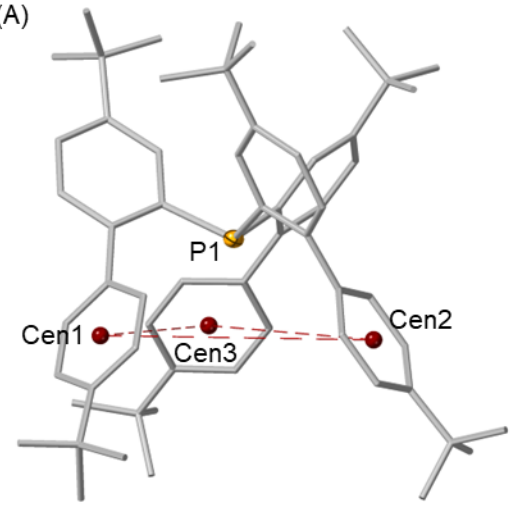

(B)

Complex	Ligand	Centroid···Centroid distances / Å		V_{cell} / Z' Å
β*-3.1	C_2H_4	Cen1···Cen2	6.1896(48)	2520
		Cen2···Cen3	6.0920(46)	
		Cen1···Cen3	5.8737(26)	
***β*-3.2** (SC-SC)	CO	Cen1···Cen2	5.7212(93)	2513
		Cen2···Cen3	5.7006(54)	
		Cen1···Cen3	5.9688(92)	
***β*-3.3** (SC-SC)	NH_3	Cen1···Cen2	5.7565(104)	2258
		Cen2···Cen3	5.8776(251)	
		Cen1···Cen3	5.7605(110)	
***γ*-3.4** (SC-SC)	NMe_2H	Cen1···Cen2	5.7317(24)	4687
		Cen2···Cen3	6.7186(36)	
		Cen1···Cen3	6.4502(27)	
β*-3.5	NMe_3	Cen1···Cen2	6.2371(14)	2730
		Cen2···Cen3	6.6572(2)	
		Cen1···Cen3	6.2563(30)	
***β*-3.6** (SC-SC)	H_2CCMe_2	Cen1···Cen2	6.3860(15)	2694
		Cen2···Cen3	6.6641(3)	
		Cen1···Cen3	6.1933(40)	

Figure 3.30 (A) The **L1** fragment of the molecular structure of complex **3.5**, as an example showing the calculated aryl centroids. (B) A table of the centroid–centroid distances (Å) of complexes **3.1**–**3.6**, demonstrating the flexibility of the pocket of the phosphine ligand. * Denotes structures collected following recrystallisation in solution.

3.4 Isolation of a gold(I) acetylene complex (3.7) *via in crystallo* techniques

As discussed in section 1.2, gold(I) *π*-acetylene complexes are prone to decomposition in the solution-state.[14] This solution-state instability is evident by the attempted reaction of [(**L1**)AuCl] with $Ag[SbF_6]$ under acetylene (1.5 bar absolute) in dichloromethane which led to the

formation of Au(0) as a black precipitate and a mixture of unidentified products in the $^{31}P\{^{1}H\}$ and ^{1}H NMR (CD_2Cl_2) spectra within 5 minutes. In contrast, the solution-state (CD_2Cl_2) addition of acetylene (1.5 bar absolute) to [(**L1**)Au(η^2-C_2H_4)][SbF_6] resulted in partial conversion (55%) after 30 minutes to a new product which was assigned as [(**L1**)Au(C_2H_2)][SbF_6], which yields a peak at δ 8.9 in the $^{31}P\{^{1}H\}$ NMR spectrum. No further conversion was observed when left for an additional 18 hr. Minor impurities were observed in the ^{1}H NMR spectrum of the reaction, including 0.13 acetone (δ 2.12,[29] 0.8H) likely from the acetone carrier solvent of the acetylene gas, and a peak at δ 9.79 (0.05H) which corresponds to 0.05 acetaldehyde, likely produced from the reaction of [(**L1**)Au(C_2H_2)][SbF_6] with trace water in the acetylene gas.[57] Other impurities could be due to acetone decomposition or dimerization, showing peaks of similar chemical shifts (δ 3.48, 2.32, 1.67, 1.13 in CD_2Cl_2) to 4-hydroxy-4-methyl-2-pentanone (δ 3.81, 2.64, 2.18, 1.26 in $CDCl_3$), which is the product of acetone aldol condensation.[58] Recharging the reaction with additional acetylene (freeze-pump-thaw, 1.5 bar absolute) resulted in a slight increase in [(**L1**)Au(C_2H_2)][SbF_6] to 58% (^{31}P NMR spectroscopy), however this also led to an increase in the impurities observed in the ^{1}H NMR spectrum (acetaldehyde, 0.3H) as well as an unidentified peak at δ 16.4 (7%) in the $^{31}P\{^{1}H\}$ NMR spectrum (Figure 3.31).

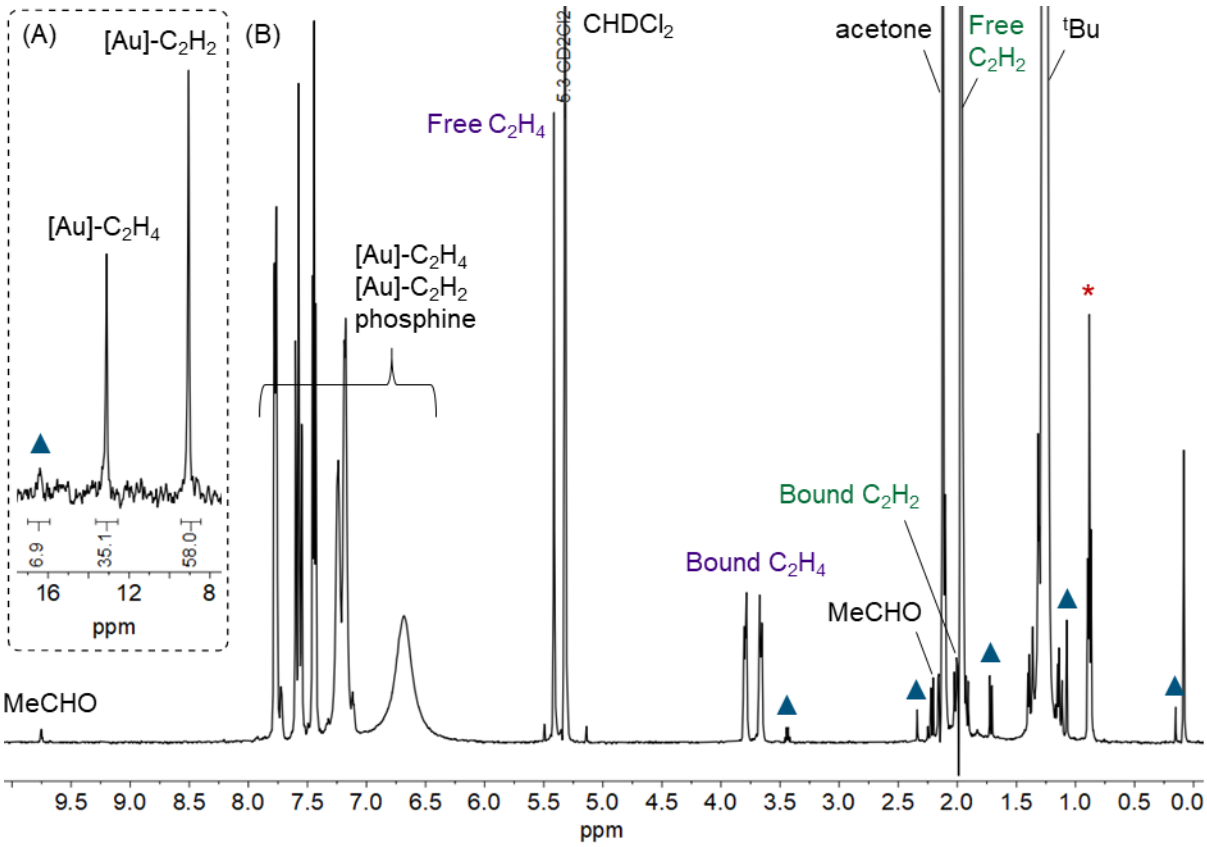

Figure 3.31 (A) The $^{31}P\{^{1}H\}$ NMR spectrum of the reaction of [(**L1**)Au(η^2-C_2H_4)][SbF_6] with acetylene after recharge. (202 MHz, CD_2Cl_2, 298 K). (B) The ^{1}H NMR spectrum of the reaction of [(**L1**)Au(η^2-C_2H_4)][SbF_6] with acetylene after recharge. (500 MHz, CD_2Cl_2, 298 K). [Au]-C_2H_4 denotes [(**L1**)Au(η^2-C_2H_4)][SbF_6], [Au]-C_2H_2 denotes [(**L1**)Au(η^2-C_2H_2)][SbF_6], * denotes lattice heptane, ▲ denotes unidentified impurity.

The incomplete formation of [(**L1**)Au(η^2-C_2H_2)][SbF_6], as well as the formation of impurities and decomposition products, led to investigation of the more stabilising weakly coordinating anion [BAr^F_4]$^-$. Anion effects on reactivity and deactivation in gold(I) catalysis has been explored previously, and often more coordinating anions lead to more rapid deactivation.[59] However, switching to the [BAr^F_4]$^-$ anion still led to only partial conversion of complex **3.1** to the new product (δ 8.9, 60%, 1 hr) upon addition of acetylene (1.5 bar absolute) in CD_2Cl_2. Recharging with additional acetylene (freeze-pump-thaw, 1.5 bar absolute, 10 minutes) led to greater, though still partial, conversion (86%). In contrast, addition of acetylene (1.5 bar absolute) to complex **3.2** resulted in full conversion in 10 minutes. However, removal of the acetylene atmosphere and CD_2Cl_2 solvent under vacuum resulted in the formation of Au(0) as a black precipitate and ligand **L1** at δ 25.3 (~20%) in the $^{31}P\{^{1}H\}$ NMR spectrum. This is likely due to dissociation of the acetylene ligand and reactivity with the CD_2Cl_2 solvent.

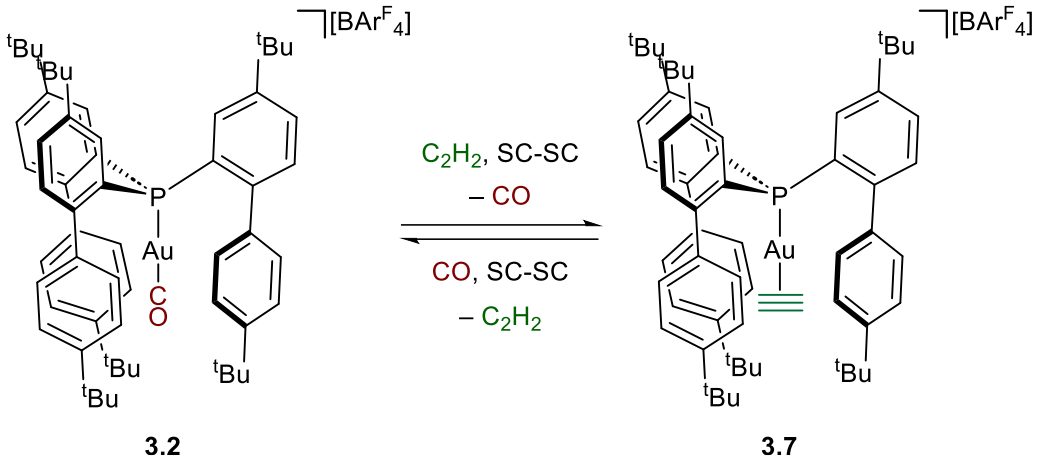

Scheme 3.8 The SC-SC synthesis of the first reported gold(I) acetylene complex, [(**L1**)Au(η^2-C_2H_2)][BAr$^F_4$] (**3.7**).

Considering the decomposition observed in solution upon removal of the acetylene atmosphere under vacuum, which is likely caused by deleterious reactivity with solvent, it was hypothesised that the gold(I) *π*-acetylene complex might instead by accessed in the solid state through the application of SMOM techniques. Addition of acetylene (1.5 bar absolute, 30 minutes) to crystals of the ensemble of polymorphs *α*-**3.1** and *β*-**3.1** led to the formation of free ethylene (gas phase ^{1}H NMR) and [(**L1**)Au(η^2-C_2H_2)][BAr$^F_4$] (**3.7**) as colourless crystals in 85% conversion (15% unreacted complex **3.1**), as shown by ^{31}P{^{1}H} and ^{1}H NMR (CD_2Cl_2) spectroscopy of the crystals following the reaction. The 85% conversion observed is likely due to the finely balanced equilibrium between the complexes **3.1** and **3.7**. In contrast, the analogous reaction with of the ensemble of polymorphs *α*-**3.2** and *β*-**3.2** led to full conversion to the ensemble of polymorphs *α*-**3.7** and *β*-**3.7** (Scheme 3.8). These reactions are reversible, and addition of ethylene or CO gas to crystals of the ensemble of polymorphs *α*-**3.7** and *β*-**3.7** results in full conversion to complexes **3.1** or **3.2** respectively.

Application of vacuum to crystals of the ensemble of polymorphs *α*-**3.7** and *β*-**3.7** accessed from the SC-SC reaction resulted in a loss of lattice heptane and a significant decrease in crystal quality (R_1 = 0.1137, R_{int} = 0.1720) for which the acetylene ligand could not be resolved. However, NMR spectroscopy showed that the acetylene ligand was retained even after 72 hr under vacuum (10^{-2} mbar).

3.4.1 Solid-state characterisation of complex 3.7

Recrystallisation of complex **3.7** from 1,2-difluorobenzene/heptane at –20 °C allowed for the measurement of two crystalline polymorphs, $P2_1/n$ (*α*-**3.7**) and $P\bar{1}$ (*β*-**3.7**), similar to **3.1**. The $[BAr^F{}_4]^-$ anions of both polymorphs *α*-**3.7** and *β*-**3.7** are arranged in a bicapped square prismatic motif, which differ only in lattice solvent. Polymorph *α*-**3.7** contains just 1,2-difluorobenzene (0.35 occupancy), whilst polymorph *β*-**3.7** contains both 1,2-difluorobenzene (0.9 occupancy) and heptane (0.75 occupancy).

Two peaks are observed in the $^{31}P\{^1H\}$ SSNMR spectrum of the ensemble of polymorphs *α*-**3.7** and *β*-**3.7** directly after the SC-SC reaction at δ 10.2 and 8.0 due to the two distinct crystal morphologies (Figure 3.34 A). Small unidentified peaks at δ 26.9 and 2.3 are also observed, potentially due to exposure of the ensemble of polymorphs *α*-**3.7** and *β*-**3.7** to air in the SSNMR rotor, as these peaks are not observed in the solution $^{31}P\{^1H\}$ NMR (CD_2Cl_2) spectrum of the same batch of crystals and dissolution instead results in the formation of a single peak at δ 8.9. When placed under dynamic vacuum (20 hr, 10^{-3} mbar), the peak at δ 8.0 appears to broaden compared to the peak at δ 10.2 (Figure 3.34 B), potentially due to the peak at δ 8.0 corresponding to polymorph *β*-**3.7** which turns amorphous upon loss of lattice heptane under vacuum, as shown by SCXRD similar to *β*-**3.1**. The loss of lattice heptane is evident from the disappearance of the corresponding peaks in the $^{13}C\{^1H\}$ SSNMR spectrum. The acetylene environment is observed as two peaks at δ 76.3 and 75.2 in the $^{13}C\{^1H\}$ SSNMR spectrum due to the two distinct crystalline polymorphs, with the peak at δ 75.2 also experiencing a broadening similar to the $^{31}P\{^1H\}$ environment and shifting slightly to δ 75.6 (Figure 3.34 C and D), therefore likely corresponding to *β*-**3.7**. The $^{13}C\{^1H\}$ SSNMR spectrum from the SC-SC reaction is otherwise similar to that prior to vacuum. Similar to complex **3.1**, no quadrupolar coupling to ^{197}Au is observed.

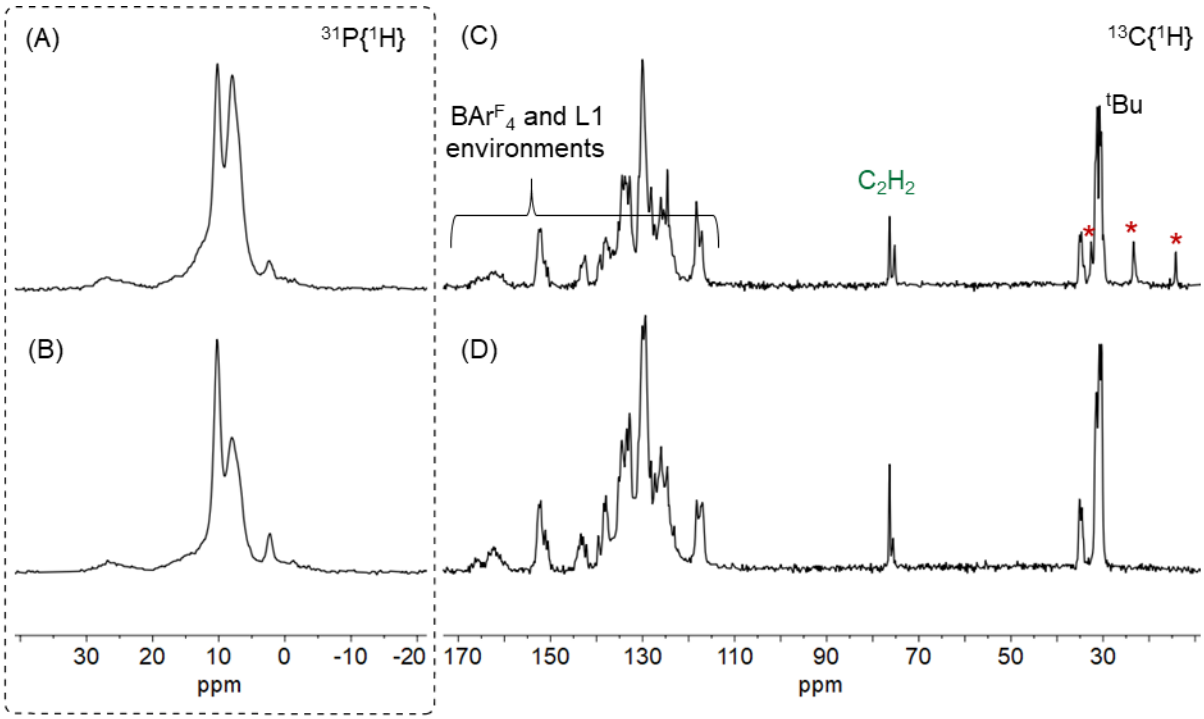

Figure 3.34 The solid-state $^{31}P\{^{1}H\}$ CP MAS NMR spectra of the ensemble of polymorphs *α*-**3.7** and *β*-**3.7** (162 MHz, 20 kHz spin rate, 298 K) (A) after 30 minutes argon purge and (B) after 20 hr under dynamic vacuum. The solid-state $^{13}C\{^{1}H\}$ CPTOSS MAS NMR spectra of the ensemble of polymorphs *α*-**3.7** and *β*-**3.7** (100 MHz, 10 kHz spin rate, 298 K). * Denotes lattice heptane. (C) after 30 minutes argon purge and (D) after 20 hr under dynamic vacuum.

The cationic structures of polymorphs *α*-**3.7** and *β*-**3.7** are the same within error (*α*-**3.7**, 110 K: C1–C2, 1.023(11) Å; *β*-**3.7**, 110 K: C1–C2, 1.034(10) Å), and therefore discussion of the cation structure shall be limited to that of polymorph *α*-**3.7**. The molecular structure of polymorph *α*-**3.7** displays a linear structure with the acetylene ligand coordinated in an η^2 fashion with a P1–Au1–centroid(C1···C2) angle of 179.038(10)° (Figure 3.32 A). The C1–C2 distance (1.023(11) Å) is shorter than free acetylene (1.2033(2) Å),[25] likely due to torsional libration of the acetylene bond, similar to complex *α*-**3.1**, which results in the acetylene bond appearing artificially short. The C1–C2 distance decreases at higher collection temperatures [110 K, 1.023(11); 150 K, 0.980(9); 200 K, 0.923(11) Å] (Figure 3.32 B), albeit these distances are within error. The Au–C bond lengths in polymorph *α*-**3.7** also shorten at higher temperature, with a more significant shortening of the Au1–C1 distance [Au1–C1: 110 K, 2.197(7); 150 K, 2.184(5); 200 K, 2.157(9). Au1–C2: 110 K, 2.179(6); 150 K, 2.188(6); 200 K, 2.186(6) Å]. The Au–C distances suggest that there is a torsional pivot around the Au1–C2 bond when

compared to the Au–C distances of [(P^{t}Bu$_3$)Au(^{t}BuC≡CMe)][SbF$_6$] (2.238(12), 2.239(10) Å)[60] which do not experience such torsional libration. The Au1–P1 distance changes minimally from 110 K (2.2747(7) Å) to 200 K (2.2732(7) Å), showing that only the C1–C2 bond experiences the significant torsional libration.

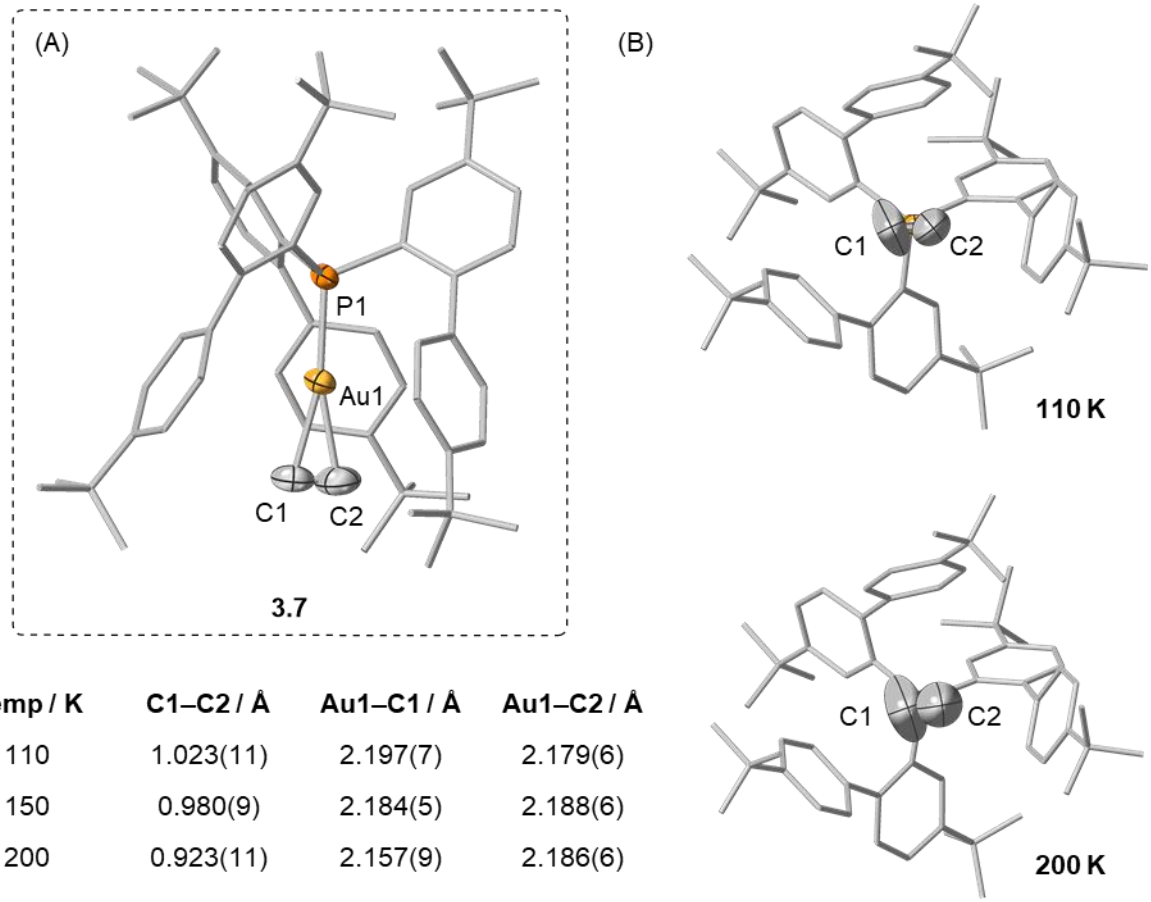

Temp / K	C1–C2 / Å	Au1–C1 / Å	Au1–C2 / Å
110	1.023(11)	2.197(7)	2.179(6)
150	0.980(9)	2.184(5)	2.188(6)
200	0.923(11)	2.157(9)	2.186(6)
Calc	1.24	2.27	2.24

Figure 3.32 (A) The molecular structure of the isolated cation of complex *α*-**3.7** collected at 110 K. Displacement ellipsoids are set at 50% probability level. Hydrogen atoms, lattice solvent and [BAr$^F{}_4$]$^-$ anion are excluded for clarity. (B) Alternative representation of complex *α*-**3.7** showing the torsional disorder at 110 K and 200 K data, highlighting the ethylene atomic displacement parameters, with a table noting selected bond distances of complex *α*-**3.7** at different data collection temperatures, and the calculated values. Au1–P1 bond distances (Å): 2.2747(7), 110 K; 2.2744(7), 150 K; 2.2732(7), 200 K. Select bond angles (°): P1–Au1–centroid(C1···C2), 179.038(10).

3.4.2 Solution-state characterisation of complex 3.7

The ^{1}H NMR (CD_2Cl_2) spectrum of the dissolved ensemble of polymorphs *α*-**3.7** and *β*-**3.7** from the SC-SC reaction (Figure 3.33) reveals the *ortho*-BAr$^F{}_4$ protons are observed at δ 7.72

(8H), whilst the *para*-BAr^F_4 protons are observed as a broad singlet at δ 7.56 (4H). The remaining aryl peaks corresponding to the phosphine ligand are observed at δ 7.77 (3H), 7.59 (3H), 7.44 (3H), and 6.68 (6H), as well as overlapping with lattice 1,2-difluorobenzene at δ 7.19 – 7.16 (7H). The *tert*-butyl protons are observed at δ 1.27 – 1.23 (62H), overlapping with heptane. The triplet of the terminal protons of heptane are observed at δ 0.88 (4H). The acetylene environment is observed as a doublet at δ 2.02 (4H, $^3J_{HP}$ = 2.8), which collapses to a singlet upon phosphorus decoupling. One peak is observed for the acetylene protons due to fast rotation of the acetylene ligand making them equivalent on the NMR timescale, which is consistent with the torsional libration in the variable temperature SCXRD experiment. The acetylene peak is downfield relative to free acetylene (δ 1.80), which is in contrast to complexes **3.1**–**3.6** which experience upfield shifts relative to the corresponding free ligand due to ring current effects. The acetylene peak of complex **3.7** is however significantly upfield compared to related d^{10} metal acetylene complexes such as [(L)Pd(η^2-C_2H_2)] (L = dtbpe, δ 6.91; 1,2-bis(di-*iso*-propylphosphino)ethane, δ 6.78).[61] The acetylene peak is also observed as a doublet in the $^{13}C\{^1H\}$ NMR (CD_2Cl_2) spectrum at δ 76.0 ($^2J_{CP}$ = 9), downfield of free acetylene (δ 71.9).

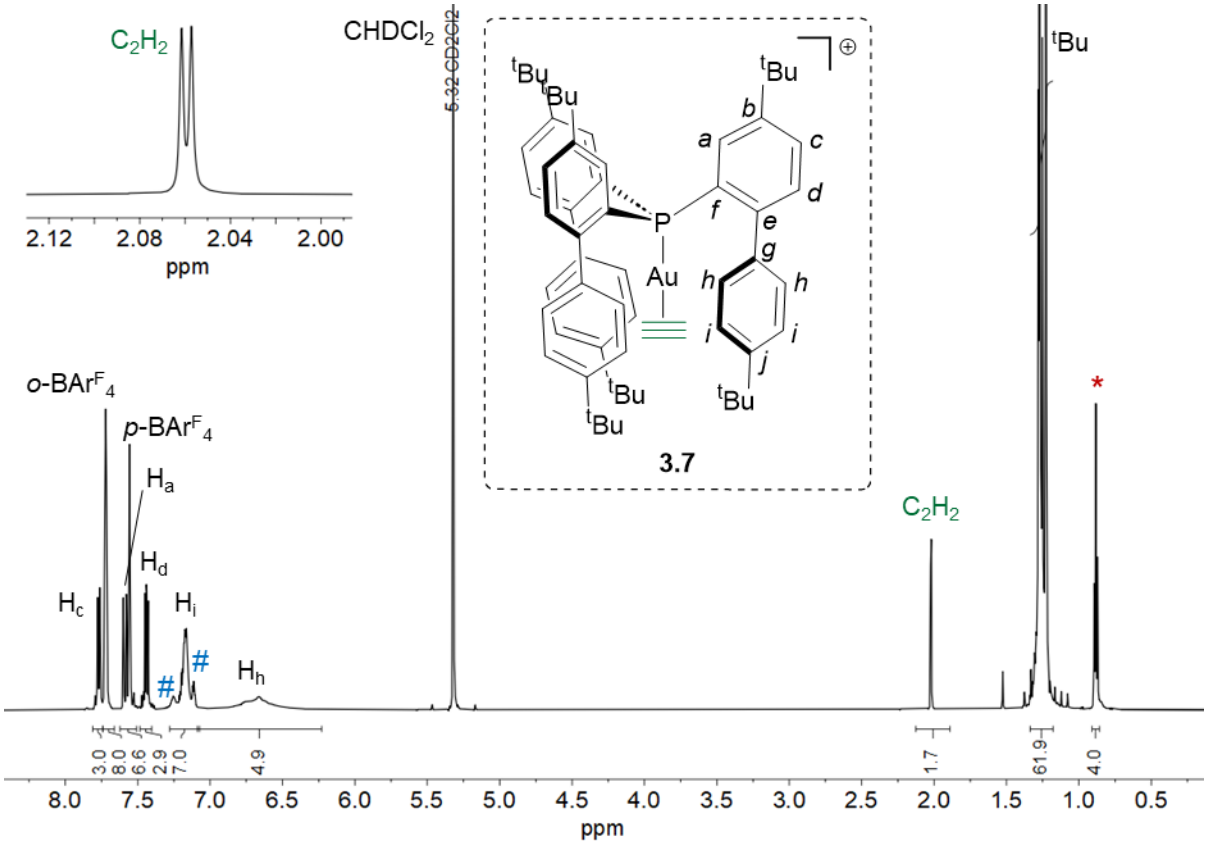

Figure 3.33 The ^{1}H NMR spectrum of the dissolved ensemble of polymorphs *α*-**3.7** and *β*-**3.7** (500 MHz, CD_2Cl_2, 298 K). # Denotes lattice 1,2-difluorobenzene, * denotes lattice heptane. The inset highlights the acetylene proton environment.

Crystals of the isotopologue, [(**L1**)Au(η^{2}-$^{13}C_2H_2$)][BAr$^{F}_4$] (**^{13}C-3.7**) can be accessed from the solid/gas addition of doubly ^{13}C labelled acetylene gas, $^{13}C_2H_2$ to complex **3.2**. The ethylene complex [(**L1**)Au(η^{2}-$^{13}C_2H_4$)][BAr$^{F}_4$] (**^{13}C-3.1**, ~10%) is also observed in the ^{31}P{^{1}H} and ^{1}H NMR (CD_2Cl_2) spectra due to the presence of $^{13}C_2H_4$ in the $^{13}C_2H_2$ source, as confirmed by gas phase ^{1}H NMR spectroscopy of the $^{13}C_2H_2$. In the ^{13}C{^{1}H} NMR (CD_2Cl_2) spectrum of the dissolved ensemble of polymorphs *α*-**3.7** and *β*-**3.7**, the acetylene peak is observed as a doublet at δ 76.0 ($^{2}J_{CP}$ = 9). In the ^{13}C NMR spectrum of the dissolved ensemble of polymorphs *α*-**^{13}C-3.7** and *β*-**^{13}C-3.7** the environment is observed as an AA'MM'X spin system (Figure 3.35 A and B). The ^{1}H NMR spectra for complexes **^{13}C-3.7** and **3.7** are analogous apart from the acetylene resonances which are also observed as a AA'MM'X spin system. The ^{13}C NMR spectrum of complex **^{13}C-3.7** was simulated using the gNMR modelling software to provide estimated coupling constants (Figure 3.35 C), including the $^{1}J_{CH}$ coupling constant which was

estimated to be 261 Hz, which is larger than free acetylene (248 Hz).[62] Coupling is dictated by the *s*-character of a bond, as described by the Fermi contact mechanism, therefore a smaller $^{1}J_{CH}$ coupling constant would be expected upon complexation to metals due to the C–H bond being weakened. This is seen in [(dtbpe)Pd(η^2-C_2H_2)] which has a $^{1}J_{CH}$ (211 Hz) smaller than free acetylene (248 Hz).[61] It is interesting to note that the $^{1}J_{CH}$ of complex **^{13}C-3.7** (261 Hz) is larger than free acetylene, however larger $^{1}J_{CH}$ coupling constants compared to free ligand is not unusual for d^{10} coinage metal complexes. Related coinage metal ethylene complexes such as [(^{t}Bu$_2$P(NSiMe$_3$)$_2$)Cu(η^2-C_2H_4)], [(Me$_2$B(6-(CF$_3$)Py)$_3$)Cu(η^2-C_2H_4)] and [(Me$_2$B(6-(CF$_3$)Py)$_3$)Au(η^2-C_2H_4)] also report larger $^{1}J_{CH}$ coupling constants (158, 160 and 162 Hz respectively) than free ethylene (156 Hz).[63, 64] The $^{2}J_{CH}$ coupling constants of 47 Hz is smaller than free acetylene (49 Hz)[65] as would be expected. The $^{1}J_{CC}$ coupling constant (134 Hz) is also smaller than free acetylene (172 Hz),[64] due to the C≡C bond being weakened as described by the Dewar-Chatt-Duncanson model of metal-alkyne bonding (section 1.2).[41, 42] The acetylene protons also couple to one another, with a $^{3}J_{HH}$ coupling constant of 8 Hz, and couple to phosphorus with a $^{4}J_{HP}$ coupling constant of 3 Hz.

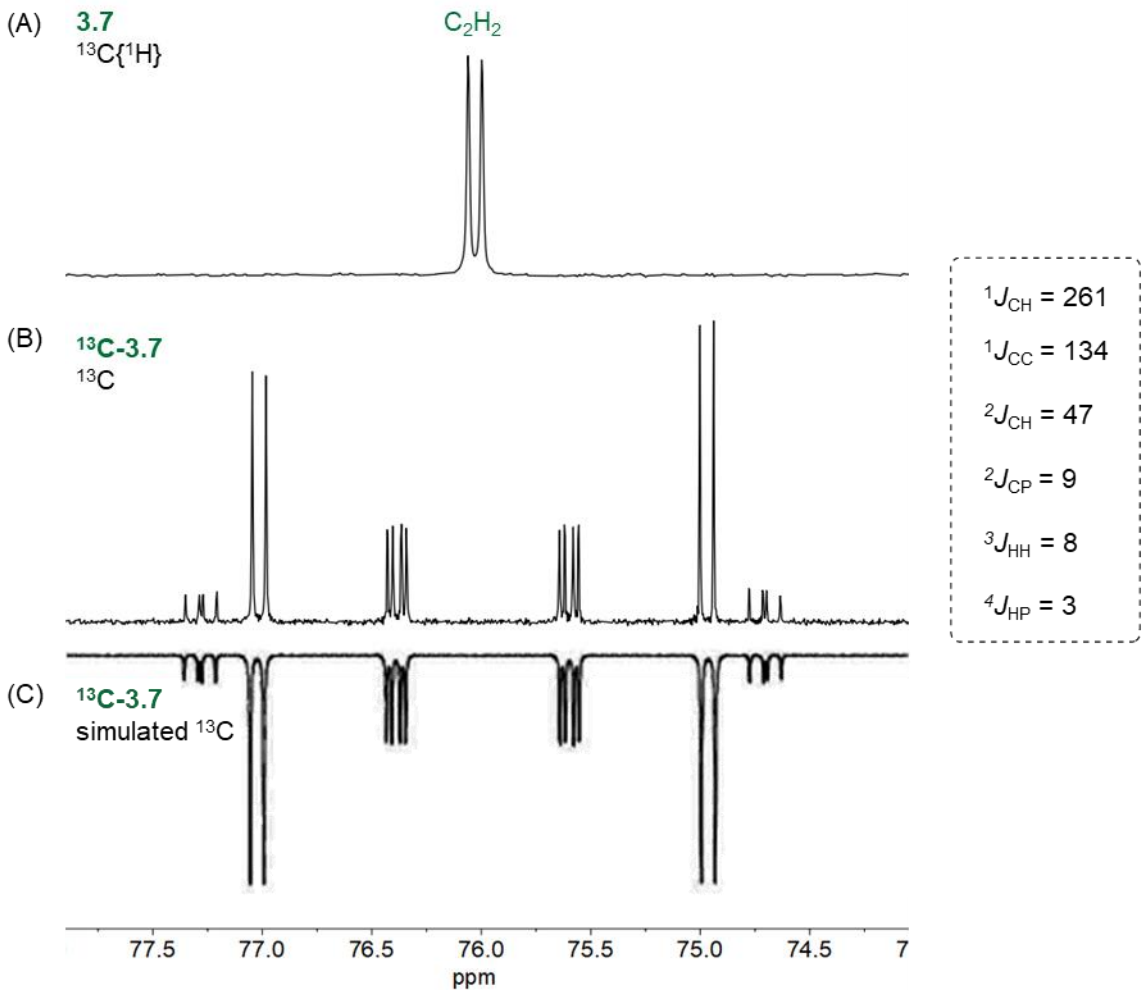

Figure 3.35 The acetylene region of the (A) $^{13}C\{^1H\}$ NMR spectrum of the dissolved ensemble of polymorphs *α*-**3.7** and *β*-**3.7**, (B) ^{13}C NMR spectrum of the dissolved ensemble of polymorphs *α*-**^{13}C-3.7** and *β*-**^{13}C-3.7** (150 MHz, CD_2Cl_2, 298 K) and (C) the simulated (gNMR) ^{13}C NMR spectrum of complex **^{13}C-3.7**. Quoted coupling constants are in Hz.

In the IR spectrum of the ensemble of polymorphs *α*-**3.7** and *β*-**3.7**, the C≡C stretch is observed at 1656 cm^{-1} (Figure 3.36), at lower wavenumber than free acetylene (1974 cm^{-1}), but similar to the d^{10} *π*-acetylene complexes [(L)Pd(η^2-C_2H_2)] (L = dtbpe, 1626 cm^{-1}; 1,2-bis(di-*iso*-propylphosphino)ethane, 1619 cm^{-1})[61] although significantly shifted in comparison to tricoordinate coinage metal *π*-acetylene complexes such as [(1,10-phenanthroline)Cu(η^2-C_2H_2)] (1800 cm^{-1})[66] and [(dipyridylamine)Cu(η^2-C_2H_2)][BF_4] (1795 cm^{-1}).[67] This observed red shift to lower wavenumber than free acetylene is in contrast to the blue shift to higher wavenumber than free CO observed for complex **3.2**. This is due to the vibrational Stark effect, which describes the impact the electric field has on vibrational transition energies and

demonstrates that electrostatic contributions to bonding are significant.[68] The acetylene C–H band of complex **3.7** is observed at 3185 cm^{-1}. The IR bands were identified by comparison to the IR spectrum of complex **^{13}C-3.7**, for which the C–H stretch is shifted to 3175 cm^{-1} (calculated 3176 cm^{-1}) due to the difference in the reduced mass (Equations 1 and 2). The C≡C stretch (calculated 1592 cm^{-1}) is no longer observed due to it being masked by a broad C–H band corresponding to **L1** at 1611 cm^{-1}.

$$\mu = \frac{m_1 m_2}{m_1 + m_2} \qquad \text{(Equation 1)}$$

$$\tilde{\nu} = \frac{1}{2\pi}\sqrt{\frac{k}{\mu}} \qquad \text{(Equation 2)}$$

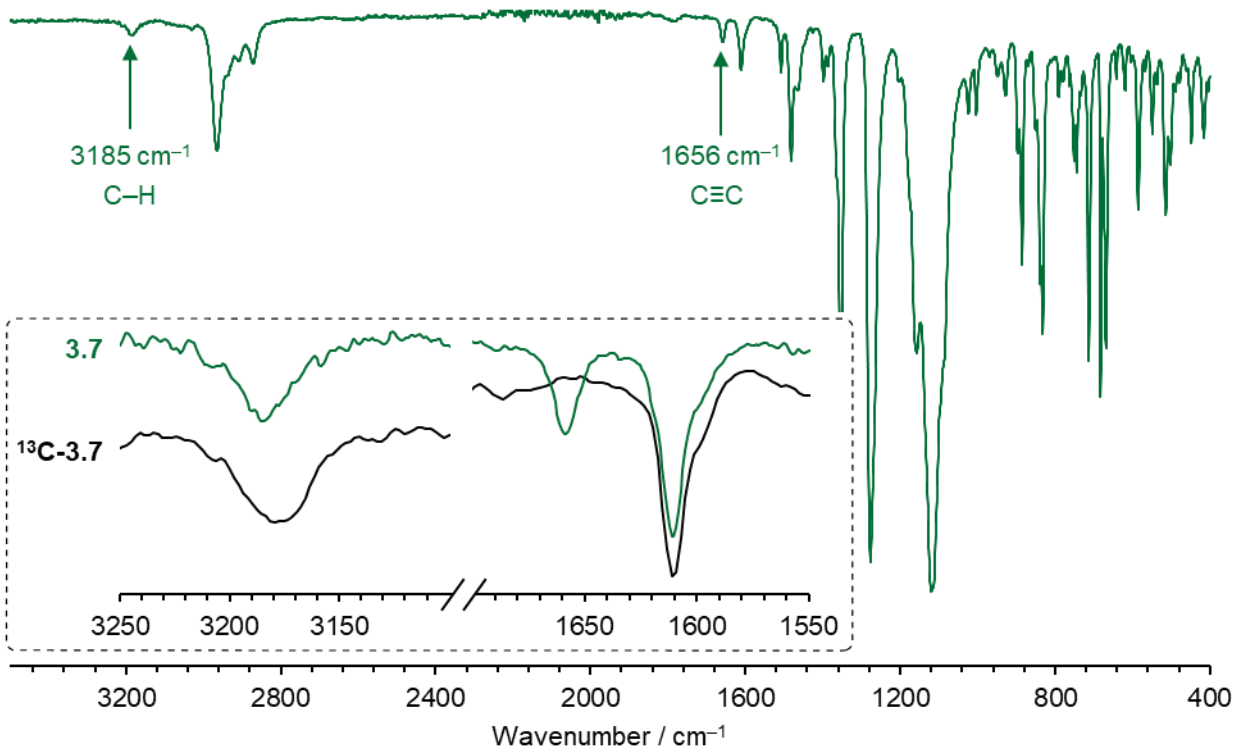

Figure 3.36 The solid-state IR spectrum of the ensemble of polymorphs *α*-**3.7** and *β*-**3.7**. The inset highlights the C≡C and C–H regions of the spectrum of complexes **3.7** and **^{13}C-3.7**.

3.4.3 Computational analysis of complex 3.7

Considering that the torsional libration observed in the SCXRD structure of complex *β*-**3.7** results in an artificial shortening of the C1–C2 bond to 1.023(11) Å, the C1–C2 distance of the structure was fully optimised in the solid state using periodic DFT. The calculated C1–C2 distance is 1.24 Å, the same within error of [(P^{t}Bu$_3$)Au(^{t}BuC≡CMe)][SbF$_6$] (1.220(18) Å), which does not experience such torsional libration.[60] The Au–C distances of 2.24 and 2.27 Å are

asymmetric, similar to that observed in the experimental structure at 200 K (2.157(9) and 2.186(6) Å). This is seen in calculations of both the solid state and the isolated cation, due to the acetylene ligand being orientated so that one C–H bond points at the centroid of one aryl phosphine **L1** aryl ring whilst the other C–H bond is directed between the other two rings.

To further understand the acetylene binding, the natural bond orbital (NBO) analysis of the cation **3.7**$^{+}$ was also explored (Figure 3.37). The most prominent contribution to bonding is *σ*-donation from the acetylene ligand to an Au–P *σ** orbital, which has a perturbation theory energy of 58.24 kcal mol^{-1}, approximately three times that of the relative contribution of *π*-backdonation (19.70 kcal mol^{-1}). The *π*-backdonation denotes the Au(5d) to the $\pi^*_{C\equiv C}$ antibonding orbital of the acetylene ligand, and previous reports describe *π*-backdonation from gold(I) to be significant in *π*-ethylene and *π*-acetylene complexes,[69, 70] despite the relatively poor overlap of contracted *d*-orbitals and high energy antibonding orbitals seen in d^{10} coinage metal cationic complexes as described in section 1.2.

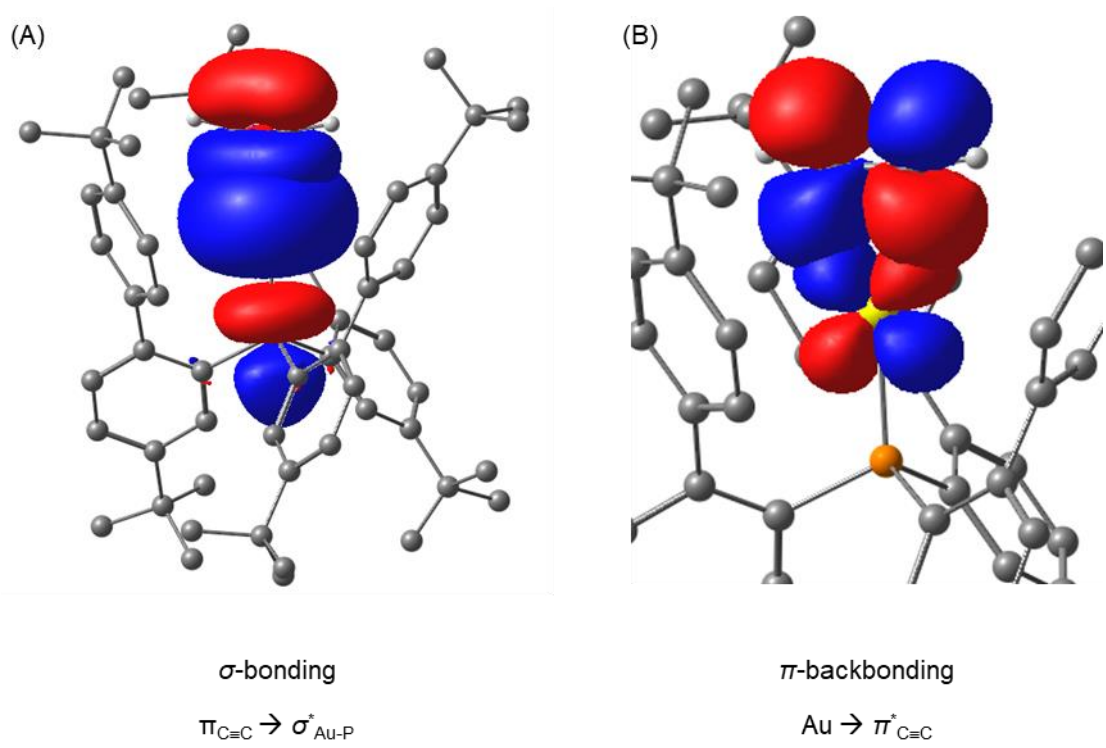

Figure 3.37 The most prominent NBO donor-acceptor orbital pairs in the cation **3.7**$^{+}$.

Quantum Theory of Atoms in Molecules (QTAIM)[71] is a method which analyses the electron density of a complex in order to calculate bond paths within the structure. The QTAIM plot of the cation **3.7**$^{+}$ confirms that the acetylene ligand is bound to the gold(I) centre as Au···C bond paths were located. The QTAIM plot also confirms that there are weak interactions between the acetylene and the phosphine aryl groups (Figure 3.38 A). Weak interactions between the acetylene and the phosphine pocket are further highlighted by the DFT calculated non-covalent interaction (NCI) plot of the cation **3.7**$^{+}$, which displays interactions between the acetylene ligand and the surrounding **L1** pocket, as denoted by the green isosurfaces (Figure 3.38 B). The overall interaction energy of the cation **3.7**$^{+}$ was calculated to be –41.3 kcal mol^{-1}, which is comprised of stabilising orbital interactions, dispersion, and destabilising steric interactions of –57.6, –6.6 and 22.9 kcal mol^{-1} respectively. When the structure is calculated with protons in place of the ^{t}Bu substituents, the interaction energy is lowered to –35.8 kcal mol^{-1} due to the decrease in dispersion interactions (–1.2 kcal mol^{-1}). The calculated interaction energies, and QTAIM and NCI plots, further demonstrate the added stability that the complete phosphine ligand **L1** provides to [(**L1**)Au(L)][BAr$^{F}_{4}$] complexes, not only in the steric profile of **L1** but also through the weak stabilising interactions with the acetylene ligand.

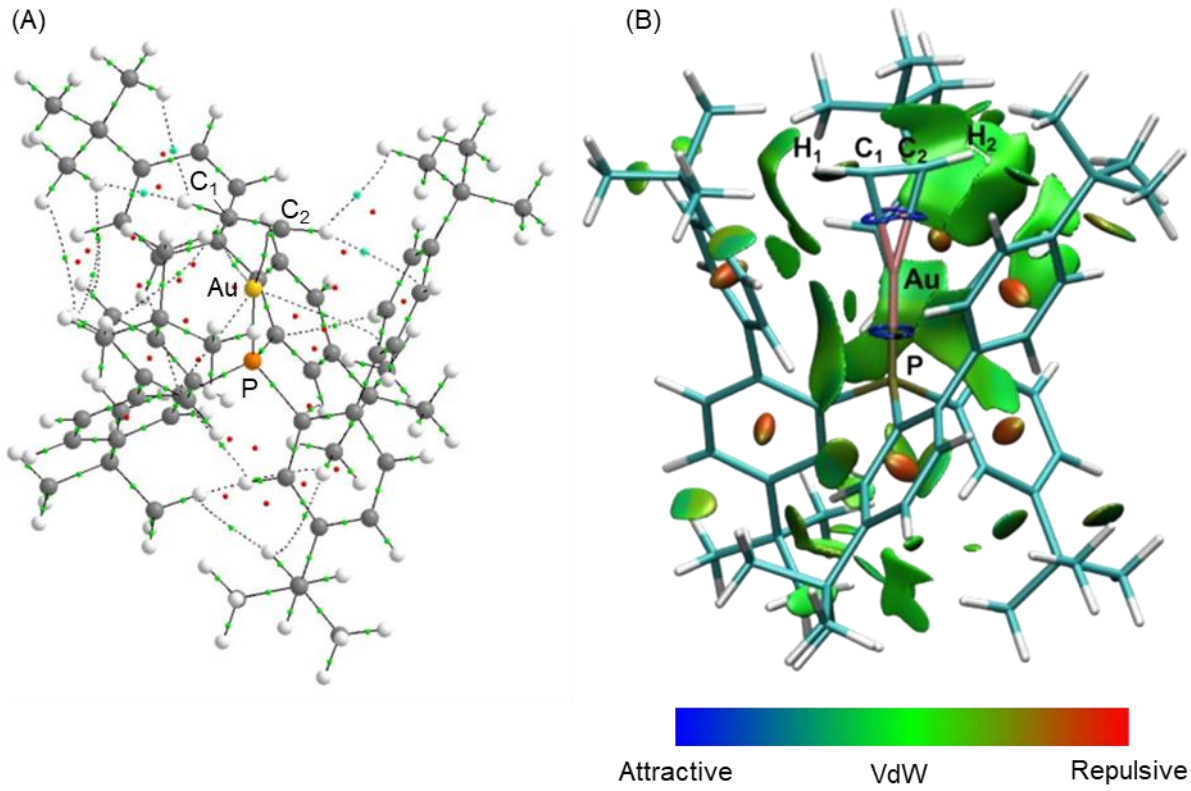

Figure 3.38 (A) Full QTAIM molecular graph of the cation **3.7**$^{+}$, highlighting bond paths between H1 and H2 and the surrounding **L1** ligand. Bond critical points (BCPs) are shown in green and ring critical points (RCPs) in red. BCP $\rho(r)$ values for the C−H···**L1** bond paths lie in the range 0.003 – 0.007 a.u. (B) The NCI plot of the cation **3.7**$^{+}$. Isosurfaces generated for $\sigma = 0.3$ a.u. and $-0.07 < \rho < 0.07$ a.u.. VdW = Van der Waals interactions.

3.5 Summary and Conclusions

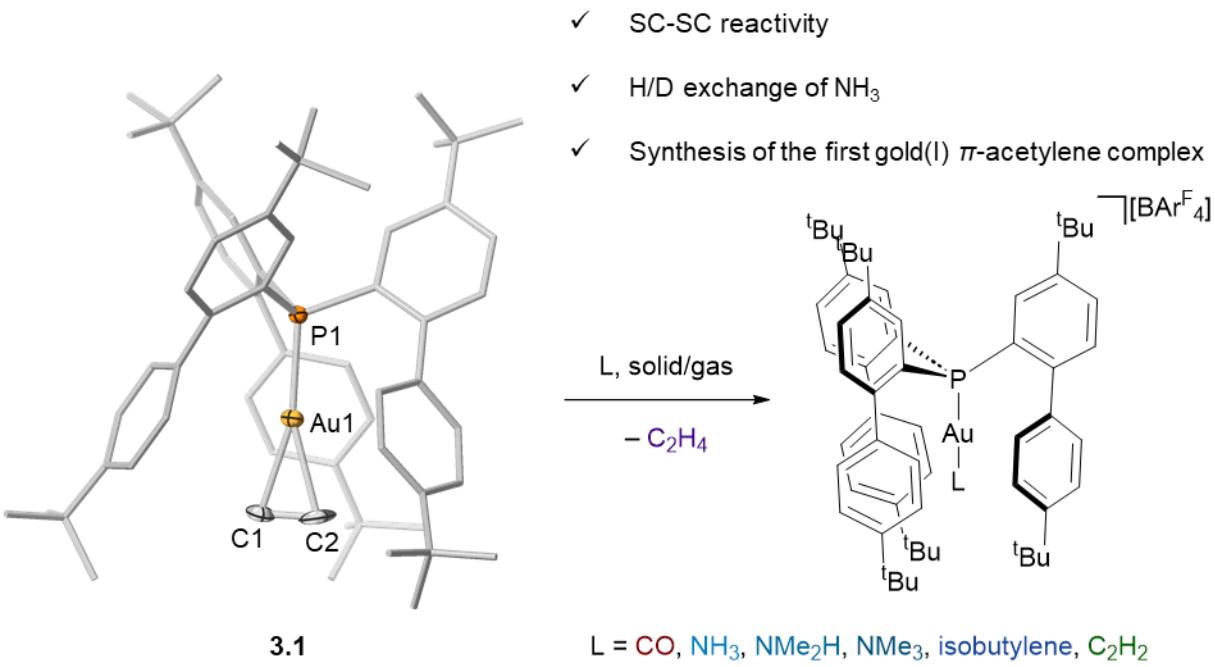

Figure 3.39 A summary of the work presented in chapter 3 of this thesis.

This chapter has presented the characterisation and *in crystallo* reactivity of the gold(I) *π*-ethylene complex [(**L1**)Au(η^2-C_2H_4)][BAr^F_4] (**3.1**) to form [(**L1**)Au(L)][BAr^F_4] (L = CO, NH_3, $NHMe_2$, NMe_3, isobutylene, C_2H_2, $^{13}C_2H_2$; Figure 3.39). SC-SC reactivity with CO has revealed a pressure dependant equilibrium in the solid state, whilst the formation of amine complexes (NH_3, NMe_2H, NMe_3) is irreversible. The bound ammonia ligand of [(**L1**)Au(NH_3)][BAr^F_4] (**3.3**) undergoes H/D exchange with D_2O in both solution and the solid state, which is proposed to occur *via* the formation of an ammonium cation. The SC-SC reactivity of complex **3.1** also includes the isolation of the first gold(I) *π*-acetylene complex, [(**L1**)Au(η^2-C_2H_2)][BAr^F_4], **3.7**. Whilst complex **3.7** can also be accessed in the solution state, it is susceptible to acetylene loss under vacuum meaning that it is difficult to prepare free of an acetylene atmosphere. The application of SMOM techniques allows for the simple isolation of pure (solution and solid-state NMR, XRD, IR) complex **3.7** which is stable under vacuum. It has been demonstrated that the bulky phosphine ligand, **L1**, is pivotal to the isolation of complex **3.7** due to its steric profile and weakly stabilising interactions to the acetylene ligand. Complex **3.7** has been characterised by solution and solid-state NMR spectroscopy, SCXRD, ^{13}C isotope labelling,

IR, and DFT calculations, and it has been demonstrated that *σ*-donation is the dominant contribution to acetylene binding, approximately three times that of the relative contribution of *π*-backdonation.

Whilst there are several examples of topotactic chemistry with gold complexes, including polymorphism and X-ray induced reduction transformations,[72-75] as described in section 1.2, these are the first examples of solid/gas ligand substitution chemistry of gold(I) in the solid state, as well as the first example of a gold(I) *π*-acetylene complex.

3.6 Experimental

For general procedures see appendix section 7.1 of this thesis. Ligand **L1** was synthesised by Dr Miquel Navarro at the Instituto de Investigaciones Químicas and University of Sevilla and used as received. Na[BAr^F_4],[76] [(**L1**)AuCl] and [(**L1**)Au(η^2-C_2H_4)][SbF_6][11] were prepared according to literature methods. All chemical shifts (δ) are quoted in ppm and coupling constants (*J*) in Hz.

3.6.1 [(L1)Au(η^2-C_2H_4)][BAr^F_4] (3.1)

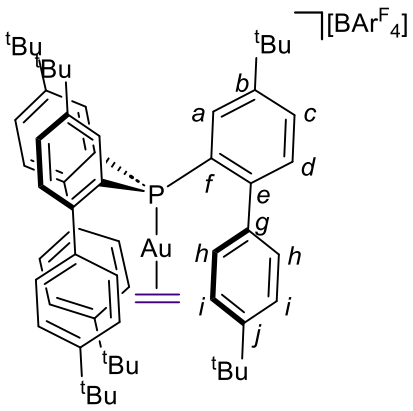

A suspension of Na[BAr^F_4] (70 mg, 79 μmol) in dichloromethane (5 mL) was added dropwise to a solution of [(**L1**)Au(η^2-C_2H_4)][SbF_6] (101 mg, 78 μmol) in dichloromethane (2 mL) at 0 °C. The reaction mixture was allowed to warm to room temperature then filtered via cannula. Crystallisation from 1,2-difluorobenzene/heptane at –20 °C afforded colourless crystals of polymorphs *α*-**3.1** and *β*-**3.1**. (Yield: 119 mg, 62 μmol, 79%)

^{1}H NMR (500 MHz, CD_2Cl_2, 298 K): δ 7.77 (dt, 3H, $^{3}J_{HH}$ = 8.1, $^{4}J_{HH}$ = 1.8, H_c), 7.72 (m, 8H, *ortho*-$BAr^F{}_4$), 7.56 (s and dd, 7H, $^{3}J_{HP}$ = 12.4, $^{4}J_{HH}$ = 1.9, overlapping *para*-$BAr^F{}_4$ and H_a), 7.44 (dd, 3H, $^{3}J_{HH}$ = 7.9, $^{4}J_{HP}$ = 6.0, H_d), 7.22 (br s and m, fwhm = 18 Hz, 7H, overlapping 1,2-$C_2H_4F_2$ and H_i), 7.18 (m, 1,2-$F_2C_6H_4$), 7.11 (m, 1,2-$F_2C_6H_4$), 6.69 (br s, fwhm = 90 Hz, 6H, H_h), 3.77 (m, 2H, C_2H_4), 3.64 (m, 2H, C_2H_4), 1.27–1.25 (m, s and s, 61H, overlapping ^{t}Bu and heptane), 0.88 (t, $^{3}J_{HH}$ = 7.2, 4.2 H, heptane).

^{31}P{^{1}H} NMR (202 MHz, CD_2Cl_2, 298 K): δ 13.0.

^{13}C{^{1}H} NMR (125 MHz, CD_2Cl_2, 298 K): δ 162.2 (q, $^{1}J_{CB}$ = 50, $BAr^F{}_4$), 152.2 (d, $^{3}J_{CP}$ = 8, C_b), 152.2 (s, C_j), 143.0 (d, $^{2}J_{CP}$ = 16, C_e), 138.5 (d, $^{3}J_{CP}$ = 8, C_g), 135.2 (s, *ortho*-$BAr^F{}_4$), 133.5 (d, $^{2}J_{CP}$ = 4, C_a), 133.4 (s, C_d), 129.9 (d, $^{3}J_{CP}$ = 2, C_c), 129.7 (s, C_h), 129.3 (qq, $^{2}J_{CF}$ = 32, $^{4}J_{CF}$ = 3, *meta*-$BAr^F{}_4$), 127.6 (d, $^{1}J_{CP}$ = 63, C_f), 125.8 (s, C_i), 125.1 (t, $^{3}J_{CF}$ = 5, 1,2-$C_6H_4F_2$), 125.0 (q, $^{1}J_{CF}$ = 270, CF_3), 117.9 (septet, $^{3}J_{CF}$ = 3, *para*-$BAr^F{}_4$), 117.7 (m, $^{3}J_{CF}$ = 5, 1,2-$C_6H_4F_2$), 109.4 (d, $^{2}J_{CP}$ = 9, C_2H_4), 35.3 (s, $\underline{C}(CH_3)_3$), 35.0 (s, $\underline{C}(CH_3)_3$), 32.3 (heptane), 31.4 (s, $C(\underline{C}H_3)_3$), 31.2 (s, $C(\underline{C}H_3)_3$), 29.4 (heptane), 23.1 (heptane), 14.3 (heptane).

^{31}P{^{1}H} SSNMR (162 MHz, 10 kHz spin rate, 298 K): δ 16.6, 11.7.

^{13}C{^{1}H} SSNMR (100 MHz, 10 kHz spin rate, 298 K): δ 162.0, 152.5, 151.6, 142.9, 142.1, 138.5, 134.4, 133.1, 129.6, 126.2, 124.6, 117.9 ($BAr^F{}_4$ and phosphine aryl environments), 109.4 (C_2H_4), 34.7 ($\underline{C}(CH_3)_3$), 31.8, 30.3 ($C(\underline{C}H_3)_3$), 23.3 and 14.3 (heptane).

ESI-MS m/z (CH_2Cl_2) found (calculated) for $Au_1C_{62}H_{79}P_1$ $[M]^+$: 1051.5592 (1051.5585)

Elemental analysis calc for $C_{94}H_{91}Au_1B_1F_{24}P_1$: C 58.94; H 4.79; N 0; found: C 58.51; H 4.79; N 0.

3.6.2 [(L1)Au(CO)][BAr$^{F}_{4}$] (3.2)

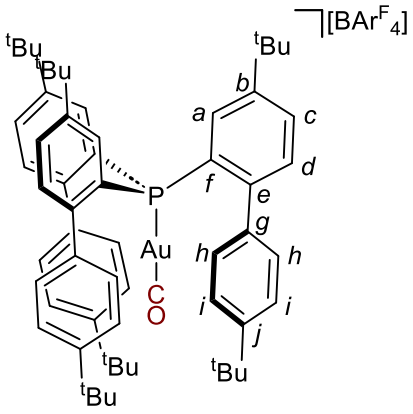

Single-crystals of the ensemble of polymorphs *α*-**3.1** and *β*-**3.1** (35 mg, 18 μmol) were placed under CO (4 bar absolute, ca. 323 μmol) in a J-Young NMR tube for 10 minutes. The volatiles were removed under reduced pressure to afford colourless single-crystals of complex **3.2**. (isolated yield: 33 mg, 17 μmol, 94%)

^{1}H NMR (500 MHz, CD_2Cl_2, 298 K): δ 7.78 (dt, 3H, $^{3}J_{HH}$ = 8.1, $^{4}J_{HH}$ = 1.6, H_c), 7.72 (m, 8H, *ortho*-BAr$^{F}_{4}$), 7.56 and 7.55 (s and dd, 7H, $^{3}J_{HP}$ = 12.4, $^{4}J_{HH}$ = 2.0, overlapping *para*-BAr$^{F}_{4}$ and H_a), 7.46 (dd, 3H, $^{3}J_{HH}$ = 8.2, $^{4}J_{HP}$ = 5.9, H_d), 7.25 (br s, fwhm = 18 Hz, 6H, H_i), 7.19 (m, 1,2-$F_2C_6H_4$), 7.12 (m, 1,2-$F_2C_6H_4$), 6.67 (br s, fwhm = 87 Hz, 3H, H_h), 1.28–1.25 (m, s and s, 56H, overlapping ^{t}Bu and heptane), 0.88 (t, $^{3}J_{HH}$ = 7.2, 1.5 H, heptane).

^{31}P{^{1}H} NMR (202 MHz, CD_2Cl_2, 298 K): δ 7.0.

^{13}C{^{1}H} NMR (125 MHz, CD_2Cl_2, 298 K): δ 182.3 (d, $^{2}J_{CP}$ = 110, CO), 162.1 (q, $^{1}J_{CB}$ = 50, BAr$^{F}_{4}$), 152.6 (s, C_j), 152.5 (d, $^{3}J_{CP}$ = 8, C_b), 143.4 (d, $^{2}J_{CP}$ = 16, C_e), 138.1 (d, $^{3}J_{CP}$ = 8, C_g), 135.2 (s, *ortho*-BAr$^{F}_{4}$), 133.0 (d, $^{4}J_{CP}$ = 6, C_d), 132.7 (d, $^{2}J_{CP}$ = 9, C_a), 130.3 (d, $^{3}J_{CP}$ = 2, C_c), 130.1 (s, C_h), 129.4 (qq, $^{2}J_{CF}$ = 32, $^{4}J_{CF}$ = 3, *meta*-BAr$^{F}_{4}$), 126.2 (s, C_i), 125.9 (d, $^{1}J_{CP}$ = 66, C_f), 125.1 (q, $^{1}J_{CF}$ = 270, CF_3), 117.9 (septet, $^{3}J_{CF}$ = 3, *para*-BAr$^{F}_{4}$), 35.3 (s, $\underline{C}(CH_3)_3$), 35.0 (s, $\underline{C}(CH_3)_3$), 32.3 (heptane), 31.3 (s, C($\underline{C}H_3)_3$), 31.2 (s, C($\underline{C}H_3)_3$), 29.4 (heptane), 23.1 (heptane), 14.3 (heptane).

^{31}P{^{1}H} SSNMR (162 MHz, 10 kHz spin rate, 298 K): δ 8.6, 5.7.

$^{13}C\{^1H\}$ SSNMR (100 MHz, 10 kHz spin rate, 298 K): δ 182.0 (d, $^2J_{CP}$ = 110, CO), 165.8, 163.8, 153.2, 152.0, 150.8 144.5, 143.4, 139.0, 138.3, 134.5, 133.0, 131.5, 130.7, 129.7, 127.5, 126.8, 125.7, 125.2, 123.6, 117.4 (BAr^F_4 and phosphine aryl environments), 35.1, 34.6 ($\underline{C}(CH_3)_3$), 31.1, 30.1 ($C(\underline{C}H_3)_3$).

IR (ATR) ν_{CO} 2170 (w, s) cm^{-1}.

ESI-MS m/z (CH_2Cl_2) found (calculated) for $Au_1C_{61}H_{75}O_1P_1$ $[M]^+$: 1051.5226 (1051.5221)

Elemental analysis calc for $C_{93}H_{87}Au_1B_1F_{24}O_1P_1$: C 58.32; H 4.58; N 0; found: C 58.03; H 4.50; N 0.

3.6.3 [(L1)Au(NH$_3$)][BAr$^F_4$] (3.3)

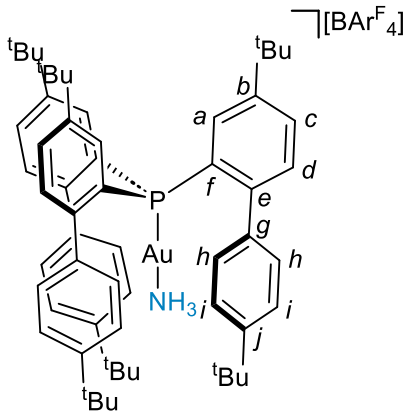

Single-crystals of the ensemble of polymorphs *α*-**3.1** and *β*-**3.1** (30 mg, 16 μmol) were placed under NH_3 (1 bar absolute) in a J-Young NMR tube for 10 minutes. The volatiles were removed under reduced pressure to afford colourless single-crystals of complex **3.3**. (isolated yield: 23 mg, 12 μmol, 75%)

^1H NMR (500 MHz, CD_2Cl_2, 298 K): 7.72 (m, 11H, overlapping H_c and *ortho*-BAr^F_4), 7.56 (s, 4H, *para*-BAr^F_4), 7.53 (dd, 3H, $^3J_{HP}$ = 12.3, $^4J_{HH}$ = 1.7, H_a), 7.39 (dd, 3H, $^3J_{HH}$ = 8.0, $^4J_{HP}$ = 5.6, H_d), 7.14 (br d, 6H, $^3J_{HH}$ = 8.5, H_i), 6.62 (br s, 6H, H_h), 1.27 – 1.25 (m, s and s, 61H, overlapping ^{t}Bu and heptane), 0.92 (br s, 3H, NH_3), 0.88 (t, $^3J_{HH}$ = 7.2, 4.2 H, heptane).

$^{31}P\{^1H\}$ NMR (202 MHz, CD_2Cl_2, 298 K): δ 3.7.

$^{13}C\{^1H\}$ NMR (125 MHz, CD_2Cl_2, 298 K): δ 161.7 (q, $^1J_{CB}$ = 50, *ipso*-BAr^F_4), 151.4 (d, $^3J_{CP}$ = 7.9, C_b), 151.2 (s, C_j), 143.4 (d, $^2J_{CP}$ = 15.9, C_e), 138.9 (d, $^3J_{CP}$ = 7.7, C_g), 134.8 (*ortho*-BAr^F_4), 132.4 (d, $^4J_{CP}$ = 5.4, C_d), 132.2 (d, $^2J_{CP}$ = 8.9, C_a), 129.9 (s, C_h), 128.9 (d, $^3J_{CP}$ = 2.4, C_c), 128.9 (q, $^2J_{FC}$ = 32, *meta*-BAr^F_4), 127.7 (d, $^1J_{CP}$ = 65.7, C_f), 124.6 (q, $^1J_{FC}$ = 270, CF_3), 124.4 (s, C_i), 117.4 (*para*-BAr^F_4), 34.8 (s, $\underline{C}(CH_3)_3$), 34.5 (s, $\underline{C}(CH_3)_3$), 31.9 (heptane), 31.3 (s, $C(\underline{C}H_3)_3$), 30.8 (s, $C(\underline{C}H_3)_3$), 29.0 (heptane), 22.7 (heptane), 13.9 (heptane).

IR (ATR) ν_{NH} 3359 (w, br) cm^{-1}.

Elemental analysis calc for $C_{92}H_{90}Au_1B_1F_{24}N_1P_1$: C 58.02; H 4.75; N 0.74; found: C 57.67; H 4.48; N 0.76.

3.6.4 Independent synthesis of [(L1)Au(ND_3)][BAr^F_4] (D_3-3.3)

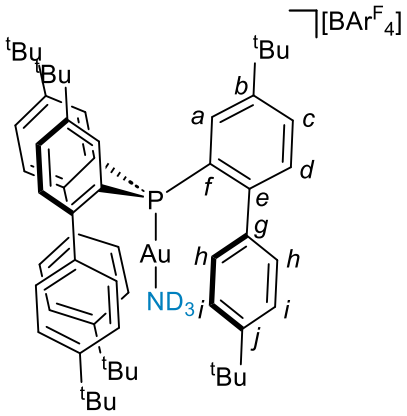

Tetraglyme (5 mL) was added to a flask containing ND_4Cl (278.4 mg, 4.8 mmol) and NaH (200.8 mg, 8.4 mmol) at –40 °C, freezing immediately upon addition. The headspace was removed under vacuum and the solution thawed and stirred at 0 °C. ND_3 was condensed into a receiving flask under a static vacuum, and freeze-pump-thawed to remove the H_2 side product.

Single-crystals of the ensemble of polymorphs *α*-**3.1** and *β*-**3.1** (29 mg, 15 μmol) were exposed to the ND_3 flask (~1 bar absolute) in a J-Young NMR tube for 30 minutes. The volatiles were removed under reduced pressure to afford colourless single-crystals of complex **D_3-3.3**. (isolated yield: 21 mg, 11 μmol, 73%)

^{1}H NMR (500 MHz, CD_2Cl_2, 298 K): 7.72 (m, 11H, overlapping H_c and *ortho*-$BAr^F{}_4$), 7.56 (s, 4H, *para*-$BAr^F{}_4$), 7.53 (dd, 3H, $^{3}J_{HP}$ = 12.3, $^{4}J_{HH}$ = 1.7, H_a), 7.39 (dd, 3H, $^{3}J_{HH}$ = 8.0, $^{4}J_{HP}$ = 5.6, H_d), 7.14 (br d, 6H, $^{3}J_{HH}$ = 8.5, H_i), 6.62 (br s, 6H, H_h), 1.27 – 1.25 (m, s and s, 57H, overlapping ^{t}Bu and heptane), 0.88 (t, $^{3}J_{HH}$ = 7.2, 2.6 H, heptane).

^{2}H NMR (61 MHz, CD_2Cl_2, 298 K): δ 0.81 (s, ND_3).

^{31}P{^{1}H} NMR (202 MHz, CD_2Cl_2, 298 K): δ 3.6.

3.6.5 [(L1)Au($^{15}NH_3$)][$BAr^F{}_4$] (^{15}N-3.3)

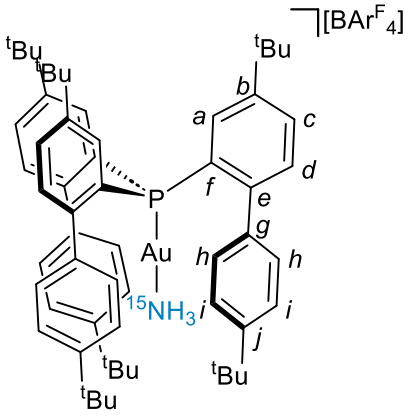

Single-crystals of the ensemble of polymorphs of complex **3.2** (34 mg, 18 μmol) were placed under $^{15}NH_3$ (~0.5 bar absolute) in a J-Young NMR tube for 30 minutes. The volatiles were removed under reduced pressure to afford colourless single-crystals of complex **^{15}N-3.3**. (isolated yield: 27 mg, 14 μmol, 79%)

^{1}H NMR (400 MHz, CD_2Cl_2, 298 K): 7.72 (m, 11H, overlapping H_c and *ortho*-$BAr^F{}_4$), 7.56 (s, 4H, *para*-$BAr^F{}_4$), 7.53 (dd, 3H, $^{3}J_{HP}$ = 12.3, $^{4}J_{HH}$ = 1.7, H_a), 7.39 (dd, 3H, $^{3}J_{HH}$ = 8.0, $^{4}J_{HP}$ = 5.6, H_d), 7.14 (br d, 6H, $^{3}J_{HH}$ = 8.5, H_i), 6.62 (br s, 6H, H_h), 1.27 – 1.25 (m, s and s, 61H, overlapping ^{t}Bu and heptane), 0.90 (d, 3H, $^{1}J_{HN}$ = 72, NH_3), 0.88 (t, $^{3}J_{HH}$ = 7.2, 4.2 H, heptane).

^{31}P{^{1}H} NMR (161 MHz, CD_2Cl_2, 298 K): δ 7.0 (s, **3.2**), 3.6 (d, $^{2}J_{NP}$ = 38, **^{15}N-3.3**).

^{15}N NMR (40 MHz, CD_2Cl_2, 298 K): δ 6.2 (qd, $^{1}J_{NH}$ = 72, $^{2}J_{NP}$ = 38).

^{15}N{^{1}H} NMR (40 MHz, CD_2Cl_2, 298 K): δ 6.2 (d, $^{2}J_{NP}$ = 38).

^{31}P{^{1}H} SSNMR (162 MHz, 20 kHz spin rate, 298 K): δ 3.9 (s).

^{15}N SSNMR (40 MHz, 20 kHz spin rate, 298 K): δ 6.2 (s).

3.6.6 [(L1)Au(NMe$_2$H)][BAr$^F_4$] (3.4)

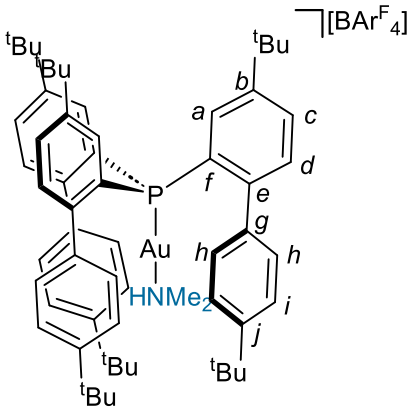

Single-crystals of the ensemble of polymorphs *α*-**3.1** and *β*-**3.1** (42 mg, 22 μmol) were placed under $NHMe_2$ (1.5 bar absolute) in a J-Young NMR tube for 2 hr. The volatiles were removed under reduced pressure to afford colourless single-crystals of complex **3.4**. (isolated yield: 33 mg, 17 μmol, 77%)

^{1}H NMR (500 MHz, CD_2Cl_2, 298 K): 7.72 (m, 11H, overlapping H_c and *ortho*-BAr$^F_4$), 7.56 (s, 4H, *para*-BAr$^F_4$), 7.49 (dd, 3H, $^3J_{HP}$ = 12.5, $^4J_{HH}$ = 2.0, H_a), 7.39 (dd, 3H, $^3J_{HH}$ = 7.8, $^4J_{HP}$ = 5.9, H_d), 7.20 (br d, 6H, $^3J_{HH}$ = 8.4, H_i), 6.72 (br s, 6H, H_h), 1.76 (dd, 6H, $^3J_{HH}$ = 6.1, $^4J_{HP}$ = 1.5, $N(CH_3)_2$), 1.23 – 1.22 (s and s, 55 H, overlapping ^{t}Bu and NH).

^{31}P{^{1}H} NMR (202 MHz, CD_2Cl_2, 298 K): δ 6.0.

^{13}C{^{1}H} NMR (125 MHz, CD_2Cl_2, 298 K): δ 162.2 (q, $^1J_{CB}$ = 50, *ipso*-BAr$^F_4$), 151.7 (d, $^3J_{CP}$ = 7.9, C_b), 151.3 (s, C_j), 143.7 (d, $^2J_{CP}$ = 15.0, C_e), 139.0 (d, $^3J_{CP}$ = 6.9, C_g), 135.2 (*ortho*-BAr$^F_4$), 133.6 (d, $^2J_{CP}$ = 9.7, C_a), 133.2 (d, $^4J_{CP}$ = 6.1, C_d), 129.9 (s, C_h), 129.4 (d, $^3J_{CP}$ = 2.0, C_c), 129.3 (q, $^2J_{FC}$ = 31.5, *meta*-BAr$^F_4$), 127.5 (d, $^1J_{CP}$ = 64.5, C_f), 125.0 (q, $^1J_{FC}$ = 270, CF_3), 125.3 (s, C_i), 117.9 (*para*-BAr$^F_4$), 42.8 (d, $^3J_{CP}$ = 2.5, NMe_2), 42.6 (d, $^3J_{CP}$ = 2.5, NMe_2), 35.2 (s, $\underline{C}(CH_3)_3$), 34.9 (s, $\underline{C}(CH_3)_3$), 31.4 (s, $C(\underline{C}H_3)_3$), 31.2 (s, $C(\underline{C}H_3)_3$).

Elemental analysis calc for $C_{94}H_{94}Au_1B_1F_{24}N_1P_1$: C 58.42; H 4.90; N 0.72; found: C 58.02; H 4.54; N 0.74.

3.6.7 [(L1)Au(NMe$_3$)][BAr$^F_4$] (3.5)

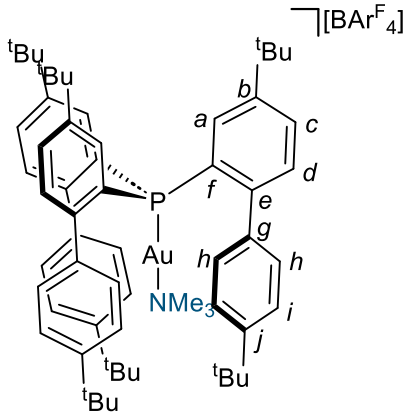

Single-crystals of the ensemble of polymorphs *α*-**3.1** and *β*-**3.1** (20 mg, 11 μmol) were placed under an atmosphere of NMe_3 (1 bar absolute) for 2 hr, resulting in an amorphous solid which was recrystallised from 1,2-difluorobenzene/heptane to afford colourless crystals of **3.5**. (isolated yield: 14 mg, 7 μmol, 64%)

^{1}H NMR (500 MHz, CD_2Cl_2, 298 K): 7.73 (m, 11H, overlapping H_c and *ortho*-BAr$^F_4$), 7.56 (s, 4H, *para*-BAr$^F_4$), 7.50 (dd, 3H, $^3J_{HP}$ = 13.1, $^4J_{HH}$ = 2.0, H_a), 7.41 (dd, 3H, $^3J_{HH}$ = 8.1, $^4J_{HP}$ = 5.9, H_d), 7.22 (br d, 6H, $^3J_{HH}$ = 6.7, H_i), 6.80 (br s, 6H, H_h), 1.63 (d, 9H, $^4J_{HP}$ = 1.40, $N(CH_3)_3$), 1.23 – 1.22 (s and s, 54 H, overlapping ^{t}Bu).

^{31}P{^{1}H} NMR (202 MHz, CD_2Cl_2, 298 K): δ 6.2.

^{13}C{^{1}H} NMR (125 MHz, CD_2Cl_2, 298 K): δ 161.7 (q, $^1J_{CB}$ = 50, *ipso*-BAr$^F_4$), 151.9 (d, $^3J_{CP}$ = 7.9, C_b), 150.7 (s, C_j), 143.4 (d, $^2J_{CP}$ = 16.0, C_e), 137.9 (d, $^3J_{CP}$ = 7.7, C_g), 134.8 (*ortho*-BAr$^F_4$), 132.9 (d, $^4J_{CP}$ = 5.5, C_d), 132.5 (d, $^2J_{CP}$ = 8.8, C_a), 129.9 (s, C_h), 128.9 (d, $^3J_{CP}$ = 2.4, C_c), 128.9 (q, $^2J_{FC}$ = 32, *meta*-BAr$^F_4$), 127.5 (d, $^1J_{CP}$ = 65.7, C_f), 124.6 (q, $^1J_{FC}$ = 270, CF_3), 124.6 (s, C_i), 117.4 (*para*-BAr$^F_4$), 53.0 (t, $^3J_{CP}$ = 3.0, NMe_3), 35.0 (s, $\underline{C}(CH_3)_3$), 34.7 (s, $\underline{C}(CH_3)_3$), 31.5 (s, $C(\underline{C}H_3)_3$), 31.3 (s, $C(\underline{C}H_3)_3$).

Elemental analysis calc for $C_{95}H_{96}Au_1B_1F_{24}N_1P_1$: C 58.62; H 4.97; N 0.72; found: C 58.70; H 4.92; N 0.31.

3.6.8 [(L1)Au(H$_2$CCMe$_2$][BAr$^F{}_4$] (3.6)

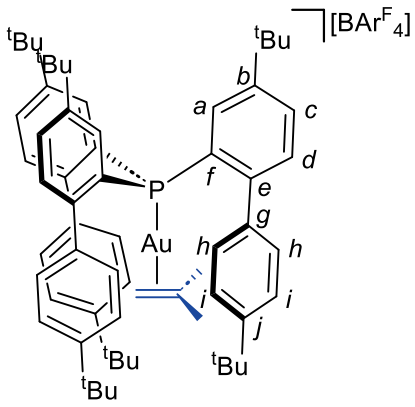

Single-crystals of the ensemble of polymorphs *α*-**3.1** and *β*-**3.1** (20 mg, 11 μmol) were placed under an atmosphere of isobutylene (2 bar absolute) for 1 hr, resulting in colourless crystals of **3.6**. (isolated yield: 16 mg, 8 μmol, 73%)

^{1}H NMR (500 MHz, CD$_2$Cl$_2$, 298 K): δ 7.75 (dt, 3H, $^3J_{HH}$ = 8.0, $^4J_{HH}$ = 2.1, H$_c$), 7.72 (m, 8H, *ortho*-BAr$^F{}_4$), 7.56 (s, *para*-BAr$^F{}_4$), 7.50 (dd, 7H, $^3J_{HP}$ = 12.4, $^4J_{HH}$ = 2.0z, H$_a$), 7.44 (dd, 3H, $^3J_{HH}$ = 8.1, $^4J_{HP}$ = 5.8, H$_d$), 7.25 (d, $^3J_{HH}$ = 8.5, 6H, H$_i$), 7.18-7.11 (m, 1,2-F$_2$C$_6$H$_4$, 0.6H), 6.79 (d, $^3J_{HH}$ = 7.9, 6H, H$_h$), 3.10 (m, 1H, $^3J_{HP}$ = 2.6, $^2J_{HH}$ = 2.2, C=CH$_2$), 2.99 (m, 1H, $^3J_{HP}$ = 2.6, $^2J_{HH}$ = 2.2, C=CH$_2$), 1.29 (s, 3H, C=CMe$_2$), 1.26–1.22 (m, s and s, 59H, overlapping ^{t}Bu, C=CMe$_2$ and heptane), 0.88 (t, $^3J_{HH}$ = 7.2, 1.2H, heptane).

^{1}H{^{31}P} NMR (500 MHz, CD$_2$Cl$_2$, 298 K): δ 7.75 (dt, 3H, $^3J_{HH}$ = 8.0, $^4J_{HH}$ = 2.1, H$_c$), 7.72 (m, 8H, *ortho*-BAr$^F{}_4$), 7.56 (s, *para*-BAr$^F{}_4$), 7.50 (dd, 7H, $^3J_{HP}$ = 12.4, $^4J_{HH}$ = 2.0z, H$_a$), 7.44 (dd, 3H, $^3J_{HH}$ = 8.1, $^4J_{HP}$ = 5.8, H$_d$), 7.25 (d, $^3J_{HH}$ = 8.5, 6H, H$_i$), 7.18-7.11 (m, 1,2-F$_2$C$_6$H$_4$, 0.6H), 6.79 (d, $^3J_{HH}$ = 7.9, 6H, H$_h$), 3.10 (d, 1H, $^2J_{HH}$ = 2.2, C=CH$_2$), 2.99 (d, 1H, $^2J_{HH}$ = 2.2, C=CH$_2$), 1.29 (s, 3H, C=CMe$_2$), 1.26–1.22 (m, s and s, 59H, overlapping ^{t}Bu, C=CMe$_2$ and heptane), 0.88 (t, $^3J_{HH}$ = 7.2, 1.2H, heptane).

^{31}P{^{1}H} NMR (202 MHz, CD$_2$Cl$_2$, 298 K): δ 14.1.

^{13}C{^{1}H} NMR (125 MHz, CD$_2$Cl$_2$, 298 K): δ 162.2 (q, $^1J_{CB}$ = 50, BAr$^F{}_4$), 152.2 (s, C$_b$), 152.2 (s, C$_j$), 143.4 (d, $^2J_{CP}$ = 16, C$_e$), 138.7 (d, $^3J_{CP}$ = 7, C$_g$), 135.4 (s, *ortho*-BAr$^F{}_4$), 134.5 (d, $^2J_{CP}$ = 10,

C_a), 134.0 (s, C_d), 130.1 (s, C_h), 130.0 (d, $^3J_{CP}$ = 2, C_c), 129.3 (qq, $^2J_{CF}$ = 32, $^4J_{CF}$ = 3, *meta*-$BAr^F{}_4$), 127.6 (d, $^1J_{CP}$ = 61, C_f), 126.2 (s, C_i), 125.0 (q, $^1J_{CF}$ = 270, CF_3), 117.9 (septet, $^3J_{CF}$ = 3, *para*-$BAr^F{}_4$), 109.2 (s, $^2J_{CP}$ = 9, C=$\underline{C}H_2$), 104.5 (s, $^2J_{CP}$ = 8, C=$\underline{C}Me_2$), 35.4 (s, $\underline{C}(CH_3)_3$), 35.2 (s, $\underline{C}(CH_3)_3$), 32.5 (heptane), 31.6 (s, $C(\underline{C}H_3)_3$), 31.3 (s, $C(\underline{C}H_3)_3$), 30.3 (heptane), 23.1 (heptane), 14.5 (heptane).

Elemental analysis calc for $C_{96}H_{95}Au_1B_1F_{24}P_1$: C 59.33; H 4.93; N 0; found: C 58.98; H 4.79; N 0.

3.6.9 [(L1)Au(η²-C_2H_2)][$BAr^F{}_4$] (3.7)

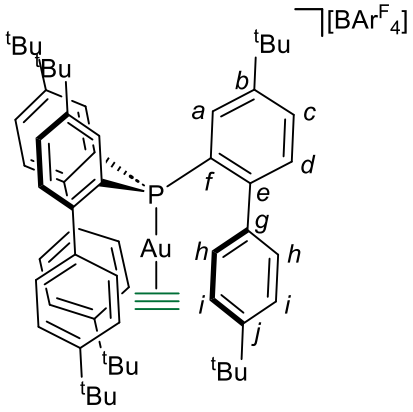

Single-crystals of complex **3.2** (25 mg, 13 μmol) were placed under an atmosphere of acetylene C_2H_2 (1.5 bar absolute, ca. 121 μmol) in a J-Young NMR tube for 5 minutes. The volatiles were removed under reduced pressure to afford complex **3.7**, which was recrystallised from 1,2-difluorobenzene/heptane at –20 °C to yield colourless single-crystals of **3.7**. (isolated yield: 21 mg, 11 μmol, 85%)

^{1}H NMR (500 MHz, CD_2Cl_2, 298 K): 7.77 (dt, 3H, $^3J_{HH}$ = 8.1, $^4J_{HH}$ = 1.8, H_c), 7.72 (m, 8H, *ortho*-$BAr^F{}_4$), 7.59 (dd, 3H, $^3J_{HP}$ = 12.4, $^4J_{HH}$ = 2.0, H_a), 7.56 (s, 4H, *para*-$BAr^F{}_4$), 7.44 (dd, 3H, $^3J_{HH}$ = 8.1, $^4J_{HP}$ = 6.0, H_d), 7.19 – 7.16 (m, 7H, $^4J_{HP}$ = 6.5, overlapping H_i and 1,2-$F_2C_6H_4$), 7.12 (m, 1,2-$F_2C_6H_4$), 6.68 (br s, 6H, fwhm = 110 Hz, H_h), 2.02 (d, 2H, $^3J_{HP}$ = 2.8, C_2H_2), 1.27–1.23 (m, s and s, 53H, overlapping ^{t}Bu and heptane), 0.88 (t, $^3J_{HH}$ = 7.2, 0.7 H, heptane).

^{31}P{^{1}H} NMR (202 MHz, CD_2Cl_2, 298 K): δ 8.9.

$^{13}C\{^1H\}$ NMR (125 MHz, CD_2Cl_2, 298 K): δ 162.2 (q, $^1J_{CB}$ = 50, $BAr^F{}_4$), 152.3 (s and d, $^3J_{CP}$ = 8, overlapping C_b and C_j), 143.4 (d, $^2J_{CP}$ = 16, C_e), 138.6 (d, $^3J_{CP}$ = 8, C_g), 135.2 (s, *ortho*-$BAr^F{}_4$), 133.3 (d and s, $^2J_{CP}$ = 5, overlapping C_a and C_d), 129.9 (m, overlapping C_h and C_c), 129.3 (qq, $^2J_{CF}$ = 32, $^4J_{CF}$ = 3, *meta*-$BAr^F{}_4$), 127.3 (d, $^1J_{CP}$ = 64, C_f), 125.7 (s, C_i), 125.1 (q, $^1J_{CF}$ = 270, CF_3), 117.9 (septet, $^3J_{CF}$ = 4, *para*-$BAr^F{}_4$), 76.0 (d, $^2J_{CP}$ = 10, C_2H_2), 35.3 (s, $\underline{C}(CH_3)_3$), 34.9 (s, $\underline{C}(CH_3)_3$), 31.5 (s, $C(\underline{C}H_3)_3$), 31.2 (s, $C(\underline{C}H_3)_3$).

$^{31}P\{^1H\}$ SSNMR (162 MHz, 10 kHz spin rate, 298 K): δ 27.0, 10.2, 8.0, 2.4.

$^{13}C\{^1H\}$ SSNMR (100 MHz, 10 kHz spin rate, 298 K): δ 162.0, 152.0, 142.5, 139.2, 138.3, 135.2, 133.6, 132.8, 130.0, 128.2, 126.1, 124.6, 118.4, 117.1 ($BAr^F{}_4$ and phosphine aryl environments), 76.3, 75.2 (C_2H_2), 34.7 ($\underline{C}(CH_3)_3$), 32.6, 31.4, 30.6 ($C(\underline{C}H_3)_3$), 29.8, 23.4, 14.2 (heptane).

IR (ATR) ν_{CH} 3185 cm^{-1}, ν_{CC} 1656 (w, s) cm^{-1}.

3.6.10 [(L1)Au(η^2-$^{13}C_2H_2$)][$BAr^F{}_4$] (^{13}C-3.7)

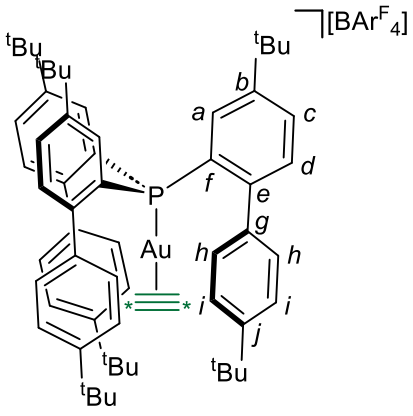

Single-crystals of complex **3.2** (30 mg, 16 μmol) were placed under an atmosphere of ^{13}C-acetylene $^{13}C_2H_2$ (1.3 bar absolute, ca. 105 μmol) in a J-Young NMR tube for 5 minutes. The volatiles were removed under reduced pressure to afford complex **^{13}C-3.7**, with ~10% **^{13}C-3.1** present due to the presence of ^{13}C-ethylene in the ^{13}C-acetylene gas. (isolated yield: 23 mg, 12 μmol, 75%)

^{1}H NMR (500 MHz, CD_2Cl_2, 298 K): 7.77 (dt, 3H, $^{3}J_{HH}$ = 8.1, $^{4}J_{HH}$ = 1.8, H_c), 7.72 (m, 8H, *ortho*-$BAr^F{}_4$), 7.60 (dd, 3H, $^{3}J_{HP}$ = 12.4, $^{4}J_{HH}$ = 2.0, H_a), 7.56 (s, 4H, *para*-$BAr^F{}_4$), 7.44 (dd, 3H, $^{3}J_{HH}$ = 8.1, $^{4}J_{HP}$ = 6.0, H_d), 7.19 – 7.16 (m, 6H, $^{4}J_{HP}$ = 6.5, overlapping H_i and 1,2-$F_2C_6H_4$), 6.68 (br s, 6H, fwhm = 110 Hz, H_h), 2.02 (m, 2H, $^{1}J_{HC}$ = 261, $^{2}J_{HC}$ = 47, $^{3}J_{HH}$ = 8, $^{3}J_{HP}$ = 3, $^{13}C_2H_2$), 1.27–1.23 (m, s and s, 61H, overlapping ^{t}Bu and heptane), 0.88 (t, $^{3}J_{HH}$ = 7.2, 1.1 H, heptane).

^{31}P{^{1}H} NMR (202 MHz, CD_2Cl_2, 298 K): δ 13.1 (**^{13}C-3.1**), 8.9 (**^{13}C-3.7**).

^{13}C{^{1}H} NMR (125 MHz, CD_2Cl_2, 298 K): δ 152.2 (m, C_b and C_j), 138.6 (m, C_g), 135.2 (s, *ortho*-$BAr^F{}_4$), 133.3 (m, overlapping C_a and C_d), 130.0 (m, overlapping C_h and C_c), 125.7 (s, C_i), 125.1 (q, $^{1}J_{CF}$ = 270, CF_3), 117.9 (m, *para*-$BAr^F{}_4$), 109.5 (d, $^{2}J_{CP}$ = 9, $^{13}C_2H_4$), 76.0 (d, $^{2}J_{CP}$ = 10, $^{13}C_2H_2$), 35.3 (s, $\underline{C}(CH_3)_3$), 34.9 (s, $\underline{C}(CH_3)_3$), 31.5 (s, $C(\underline{C}H_3)_3$), 31.2 (s, $C(\underline{C}H_3)_3$).

^{31}P{^{1}H} SSNMR (162 MHz, 10 kHz spin rate, 298 K): δ 14.8 (**^{13}C-3.1**), 10.8 (**^{13}C-3.7**), 2.4.

^{13}C{^{1}H} SSNMR (100 MHz, 10 kHz spin rate, 298 K): δ 166.3, 162.5, 152.2, 151.2, 142.8, 139.7, 138.1, 137.5, 135.3, 133.6, 132.8, 130.2, 129.5, 127.3, 126.1, 124.6, 118.4, 117.1 ($BAr^F{}_4$ and phosphine aryl environments), 109.6 ($^{13}C_2H_4$), 76.3 ($^{13}C_2H_2$), 35.2, 34.3 ($\underline{C}(CH_3)_3$), 31.9, 31.4, 30.5 ($C(\underline{C}H_3)_3$).

IR (ATR) ν_{CH} 3175 cm^{-1}.

3.7 References

1. M. Fianchini, C. F. Campana, B. Chilukuri, T. R. Cundari, V. Petricek and H. V. R. Dias, *Organometallics*, **2013**, *32*, 3034-3041.
2. G. Santiso-Quiñones, A. Reisinger, J. Slattery and I. Krossing, *Chem. Comm.*, **2007**, 5046-5048.
3. H. V. R. Dias, M. Fianchini, T. R. Cundari and C. F. Campana, *Angew. Chem. Int. Ed.*, **2008**, *47*, 556-559.
4. I. Krossing and A. Reisinger, *Angew. Chem. Int. Ed.*, **2003**, *42*, 5725-5728.
5. J. Schaefer, D. Himmel and I. Krossing, *Eur. J. Inorg. Chem.*, **2013**, *2013*.
6. J. A. Flores and H. V. R. Dias, *Inorg. Chem.*, **2008**, *47*, 4448-4450.
7. H. V. R. Dias and J. Wu, *Angew. Chem. Int. Ed.*, **2007**, *46*, 7814-7816.
8. M. Navarro, A. Toledo, S. Mallet-Ladeira, E. D. S. Carrizo, K. Miqueu and D. Bourissou, *Chem. Sci.*, **2020**, *11*, 2750-2758.
9. M. J. Harper, C. J. Arthur, J. Crosby, E. J. Emmett, R. L. Falconer, A. J. Fensham-Smith, P. J. Gates, T. Leman, J. E. McGrady, J. F. Bower and C. A. Russell, *J. Am. Chem. Soc.*, **2018**, *140*, 4440-4445.
10. Y. Yang, P. Antoni, M. Zimmer, K. Sekine, F. F. Mulks, L. Hu, L. Zhang, M. Rudolph, F. Rominger and A. S. K. Hashmi, *Angew. Chem. Int. Ed.*, **2019**, *58*, 5129-5133.

11. M. Navarro, J. Miranda-Pizarro, J. J. Moreno, C. Navarro-Gilabert, I. Fernández and J. Campos, *Chem. Comm.*, **2021**, *57*, 9280-9283.
12. J. Keller, C. Schlierf, C. Nolte, P. Mayer and B. F. Straub, *Synthesis*, **2006**, *2*, 354-365.
13. M. Navarro, M. G. Alférez, M. d. Sousa, J. Miranda-Pizarro and J. Campos, *ACS Catal.*, **2022**, *12*, 4227-4241.
14. A. Noonikara-Poyil, S. G. Ridlen, I. Fernández and H. V. R. Dias, *Chem. Sci.*, **2022**, *13*, 7190-7203.
15. S. D. Pike, A. L. Thompson, A. G. Algarra, D. C. Apperley, S. A. Macgregor and A. S. Weller, *Science*, **2012**, *337*, 1648-1651.
16. E. N. de Silva, G. A. Bowmaker and P. C. Healy, *J. Mol. Struct.*, **2000**, *516*, 263-272.
17. S. K. Mallissery and D. Gudat, *Dalton Trans.*, **2010**, *39*, 4280-4284.
18. K. Angermair, G. A. Bowmaker, E. N. d. Silva, P. C. Healy, B. E. Jones and H. Schmidbaur, *J. Chem. Soc., Dalton Trans.*, **1996**, 3121-3129.
19. F. Mark Chadwick, A. I. McKay, A. J. Martinez-Martinez, N. H. Rees, Tobias Krämer, S. A. Macgregor and A. S. Weller, *Chem. Sci.*, **2017**, *8*, 6014-6029.
20. I. J. Vitórica-Yrezábal, S. Libri, J. R. Loader, G. M. Espallargas, M. Hippler, A. J. Fletcher, S. P. Thompson, J. E. Warren, D. Musumeci, M. D. Ward and L. Brammer, *Chem. Eur. J.*, **2015**, *21*, 8799-8811.
21. I. Halasz, *Cryst. Growth Des.*, **2010**, *10*, 2817-2823.
22. M. R. Gyton, M. A. Sajjad, D. J. Storm, K. M. Altus, J. C. Goodall, C. L. Johnson, S. J. Page, A. J. Edwards, R. Piltz, S. B. Duckett, S. A. Macgregor and A. S. Weller, *J. Am. Chem. Soc.*, Submitted, ja-2024-18122t.
23. G. J. H. Nes and A. Vos, *Acta Crystallogr., Sect. B.*, **1979**, *35*, 2593-2601.
24. A. Reisinger, N. Trapp, I. Krossing, S. Altmannshofer, V. Herz, M. Presnitz and W. Scherer, *Angew. Chem. Int. Ed.*, **2007**, *46*, 8295-8298.
25. H. Fast and H. L. Welsh, *J. Mol. Spectrosc.*, **1972**, *41*, 203-221.
26. J. Harada, K. Ogawa and S. Tomoda, *J. Am. Chem. Soc.*, **1995**, *117*, 4476-4478.
27. P. Pyykkö, *Chem. Rev.*, **1997**, *97*, 597-636.
28. H. Schmidbaur and A. Schier, *Chemical Society Reviews*, **2011**, *41*, 370-412.
29. G. R. Fulmer, A. J. M. Miller, N. H. Sherden, H. E. Gottlieb, A. Nudelman, B. M. Stoltz, J. E. Bercaw and K. I. Goldberg, *Organometallics*, **2010**, *29*, 2176-2179.
30. S. P. Brown, T. Schaller, U. P. Seelbach, F. Koziol, C. Ochsenfeld, F.-G. Klärner and H. W. Spiess, *Angew. Chem. Int. Ed.*, **2001**, *40*, 717-720.
31. G. Huang, Y. Ide, Y. Hashikawa, T. Hirose and Y. Murata, *Chem. Eur. J.*, **2023**, *29*, e202301161.
32. A. J. Bukvic, A. L. Burnage, G. J. Tizzard, A. J. Martínez-Martínez, A. I. McKay, N. H. Rees, B. E. Tegner, T. Krämer, H. Fish, M. R. Warren, S. J. Coles, S. A. Macgregor and A. S. Weller, *J. Am. Chem. Soc.*, **2021**, *143*, 5106-5120.
33. F. M. Chadwick, N. H. Rees, A. S. Weller, T. Krämer, M. Iannuzzi and S. A. Macgregor, *Angew. Chem. Int. Ed.*, **2016**, *55*, 3677-3681.
34. J. C. Goodall, M. Arif Sajjad, E. A. Thompson, S. J. Page, A. M. Kerrigan, H. T. Jenkins, J. M. Lynam, S. A. Macgregor and A. S. Weller, *Chem. Comm.*, **2023**, *59*, 10749-10752.
35. C. Dash, P. Kroll, M. Yousufuddin and H. V. R. Dias, *Chem. Comm.*, **2011**, *47*, 4478-4480.
36. H. V. R. Dias, C. Dash, M. Yousufuddin, M. A. Celik and G. Frenking, *Inorg. Chem.*, **2011**, *50*, 4253-4255.
37. G. Bistoni, S. Rampino, N. Scafuri, G. Ciancaleoni, D. Zuccaccia, L. Belpassi and F. Tarantelli, *Chem. Sci.*, **2016**, *7*, 1174-1184.
38. G. H. K. P. Huber, *Molecular Spectra and Molecular Structure IV: Constants of Diatomic Molecules*, Van Nostrand Reinhold Co, New York, 1979.
39. P. K. Hurlburt, J. J. Rack, J. S. Luck, S. F. Dec, J. D. Webb, O. P. Anderson and S. H. Strauss, *J. Am. Chem. Soc.*, **1994**, *116*, 10003-10014.
40. J. Schaefer, A. Kraft, S. Reininger, G. Santiso-Quinones, D. Himmel, N. Trapp, U. Gellrich, B. Breit and I. Krossing, *Chem. Eur. J.*, **2013**, *19*, 12468-12485.

41. M. J. S. Dewar, *Bull. Soc. Chim Fr.*, **1951**, *18*, C71-79.
42. J. Chatt and L. A. Duncanson, *J. Chem. Soc.*, **1953**, 2939-2947.
43. A. S. Goldman, K. Krogh-Jespersen, *J. Am. Chem. Soc.*, **1996**, *118*, 48, 12159-12166.
44. B. Dinda, in *Essentials of Pericyclic and Photochemical Reactions*, Springer, Cham, 2017, vol. 93, pp. 241-275.
45. V. Lavallo, G. D. Frey, B. Donnadieu, M. Soleilhavoup and G. Bertrand, *Angew. Chem. Int. Ed.*, **2008**, *47*, 5224-5228.
46. José Vicente, María-Teresa Chicote, R. Guerrero, P. G. Jones and M. C. R. d. Arellano, *Inorg. Chem.*, **1997**, *36*, 4438-4443.
47. P. G. Jones and B. Ahrens, *New J. Chem.*, **1998**, *22*, 1041-1042.
48. C. Döring and P. G. Jones, *Z. Naturforsch. B*, **2013**, *68*, 474-492.
49. X. Zeng, M. Soleilhavoup and G. Bertrand, *Org. Lett.*, **2009**, *11*, 3166-3169.
50. M. Lacey, C. Macdonald, A. Pross, J. Shannon and S. Sternhell, *Aust. J. Chem.*, **1970**, *23*, 1421-1429.
51. J. Vicente, M.-T. Chicote, R. Guerrero and P. G. Jones, *Dalton Trans.*, **1995**, *0*, 1251-1254.
52. C. S. Chin, D. Chong, B. Lee, H. Jeong, G. Won, Y. Do and Y. J. Park, *Organometallics*, **2000**, *19*, 638-648.
53. S. D. Pike, T. Krämer, N. H. Rees, S. A. Macgregor and A. S. Weller, *Organometallics*, **2015**, *34*, 1487-1497.
54. A.-K. Jungton, C. Herwig, T. Braun and C. Limberg, *Chem. Eur. J.*, **2012**, *18*, 10009-10013.
55. T. J. Brown, M. G. Dickens and R. A. Widenhoefer, *J. Am. Chem. Soc.*, **2009**, *131*, 6350-6351.
56. T. N. Hooper, M. Green, J. E. McGrady, J. R. Patel and C. A. Russell, *Chem. Comm.*, **2009**, 3877-3879.
57. L. Hintermann and A. Labonne, *Synthesis*, **2007**, *8*, 1121-1150.
58. H. Maxell, I. Masahiro, M. Ichiji, Japanese Pat., Patent no. JP05208936 A, **1993**.
59. Z. Lu, T. Li, S. R. Mudshinge, B. Xu and G. B. Hammond, *Chem. Rev.*, **2021**, *121*, 8452-8477.
60. T. N. Hooper, Michael Green and C. A. Russell, *Chem. Comm.*, **2010**, *46*, 2313-2315.
61. J. Krause, W. Bonrath and K. R. Poerschke, *Organometallics*, **1992**, *11*, 1158-1167.
62. Y. N. Luzikov and N. M. Sergeyev, *J. Magn. Reson.,*, **1984**, *60*, 177-183.
63. B. F. Straub, F. Eisenträger and P. Hofmann, *Chem. Comm.*, **1999**, 24, 2507-2508.
64. B. T. Watson, M. Vanga, A. Noonikara-Poyil, A. Muñoz-Castro and H. V. R. Dias, *Inorg. Chem.*, **2023**, *62*, 1636-1648.
65. R. M. Lynden-Bell and N. Sheppard, *Proc. Roy. Soc. London Ser. A.*, **1962**, *269*, 385.
66. M. Munakata, S. Kitagawa, I. Kawada, M. Maekawa and H. Shimono, *J. Chem. Soc., Dalton Trans.*, **1992**, 2225-2230.
67. J. S. Thompson and J. F. Whitney, *Inorg. Chem.*, **1984**, *23*, 2813-2819.
68. G. L. Parker, R. V. Lommel, N. Roig, M. Alonso and A. B. Chaplin, *Chem. Eur. J.*, **2022**, *28*, 69, e202202283.
69. M. S. Nechaev, Víctor M. Rayón and G. Frenking, *J. Phys. Chem. A*, **2004**, *108*, 3134-3142.
70. A. Muñoz-Castro and H. V. R. Dias, *J. Comput. Chem.*, **2022**, *43*, 1848-1855.
71. R. F. W. Bader, *Atoms in Molecules: A Quantum Theory*, 1994.
72. N. K. Sethi, A. C. Whitwood and D. W. Bruce, *Inorg. Chem.*, **2018**, *57*, 13524-13532.
73. S. H. Lim, M. M. Olmstead and A. L. Balch, *J. Am. Chem. Soc.*, **2011**, *133*, 10229-10238.
74. S. H. Lim, M. M. Olmstead and A. L. Balch, *Chem. Sci.*, **2013**, *4*, 311-318.
75. H. Ito, M. Muromoto, S. Kurenuma, S. Ishizaka, N. Kitamura, H. Sato and T. Seki, *Nat. Commun.*, **2013**, *4*.
76. A. J. Martínez-Martínez and A. S. Weller, *Dalton Trans.*, **2019**, *48*, 3551-3554.

Chapter 4: A new Ir(I)/Ir(III) adamantyl pincer system

The experimental work presented in this chapter was carried out by this thesis author at the University of York. The synthesis and kinetic data for [(^{tBu}PONOP)Ir(N_2)][BAr^F_4] (**1.54**), obtained from [(^{tBu}PONOP)Ir(Me)(H)][BAr^F_4] (**1.50**), were carried out in collaboration with Dr Matthew Gyton at the University of York. Solid-State NMR (SSNMR) data were collected by Dr Kristof Altus at the University of York or Dr Samuel Page at the University of Durham.

4.1 Introduction

As discussed in section 1.4, the iridium(III) pincer system [(^{tBu}PONOP)Ir(Me)(H)][BAr^F_4] (**1.50**) is in rapid endergonic equilibrium with the iridium(I) σ-methane complex [(^{tBu}PONOP)Ir(CH_4)][BAr^F_4] in solution at –105 °C, and rapidly liberates methane at room temperature.[1] Despite this solution-state instability, complex **1.50** is remarkably stable in the solid state, although it is capable of undergoing SC-SC reactivity to form an iridium(III) cyclometalated product (**1.53**) by the elimination of methane under high vacuum (5×10^{-5} mbar) at 80 °C (Figure 4.1 A and B).[2] The mechanism for the solid state formation of complex **1.53** was probed by DFT and predicted to occur *via* reductive coupling to initially form the σ-methane complex, [(^{tBu}PONOP)Ir(CH_4)][BAr^F_4], followed by dissociation of methane to form the highly reactive transient 14 electron intermediate, [(^{tBu}PONOP)Ir][BAr^F_4], which undergoes cyclometalation to form complex **1.53** (Figure 4.1 A).

Remarkably, the cyclometalated complex **1.53** can then undergo further SC-SC reactivity (Figure 4.1 C). For example, the SC-SC reaction with N_2 at 80 °C forms [(^{tBu}PONOP)Ir(N_2)][BAr^F_4] (**1.54**). Complex **1.53** also C–H activates methane in the solid state *via* the 14 electron [(^{tBu}PONOP)Ir][BAr^F_4], resulting in a pressure-dependent equilibrium between complex **1.53** and regenerated complex **1.50**. In contrast, activation of ethane by complex **1.53** results in the formation of a 1:1 mixture of the corresponding ethylene and dihydride[3] complexes *via* a dehydrogenation reaction.

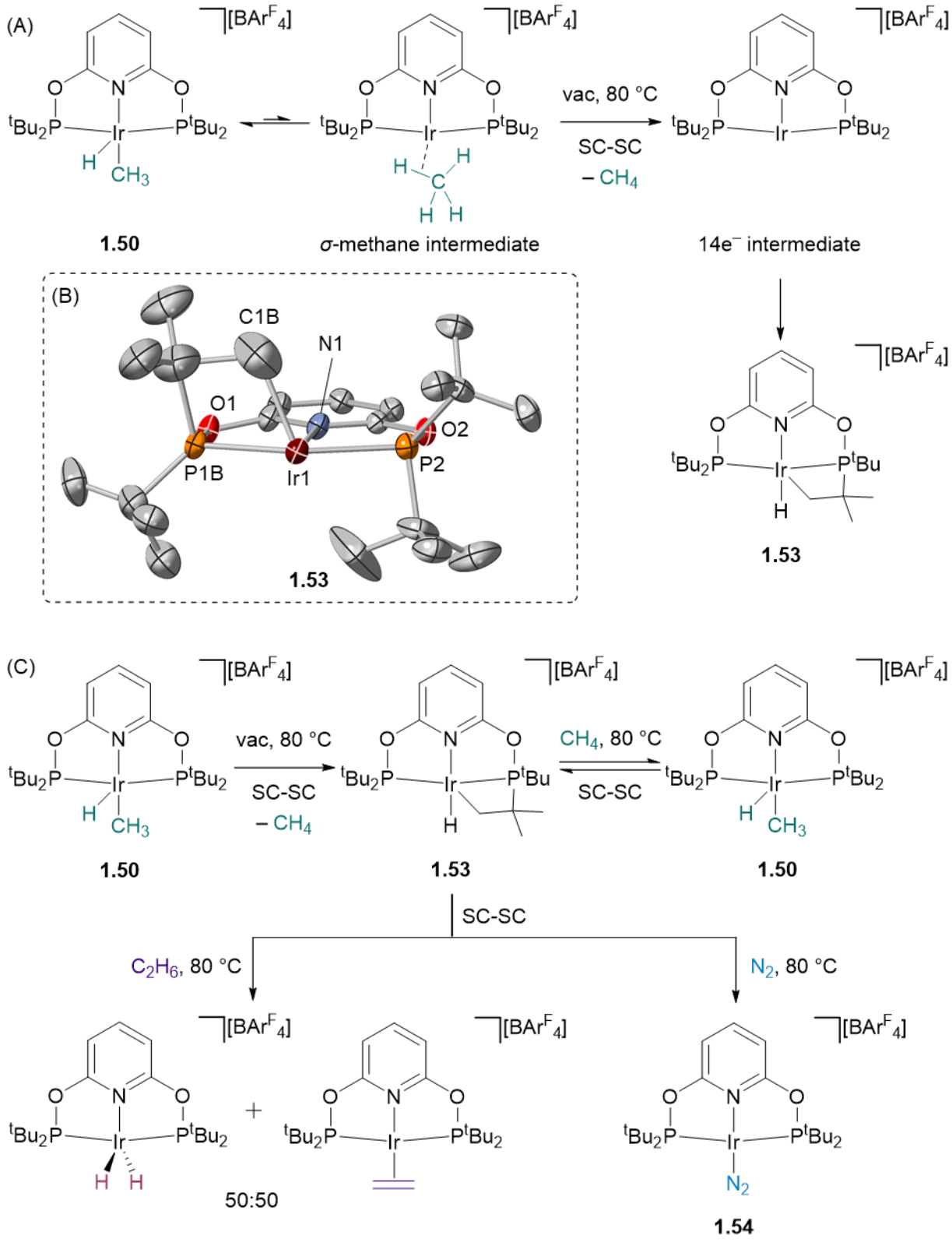

Figure 4.1 (A) The SC-SC formation of the cyclometalated complex **1.53** which proceeds *via* a 14 electron iridium(I) intermediate. (B) The molecular structure of the isolated cation of complex **1.53**. Hydrogen atoms and $[BAr^F_4]^-$ anion are excluded for clarity. Displacement ellipsoids are set at 30% probability level. (C) The *in crystallo* reactivity of complex **1.53** with methane, ethane and N_2.

Highly reactive 14 electron Ir(I) pincer complexes such as [(^{tBu}PONOP)Ir][BAr$^{F}_{4}$] ([Ir]) are often postulated as key intermediates in alkane dehydrogenation catalysis (Scheme 4.1), which occurs *via* C–H bond activation and subsequent *β*-H elimination. However, such 14 electron Ir(I) pincer complexes have yet to be observed experimentally,[4, 5] although similar Rh(I) 14 electron complexes stabilised by strong *σ*-donating ligands which cannot cyclometalate, such as the bioxazoline-derived NHC used in [(IBioxMe$_4$)$_3$Rh]Cl, have been reported.[6]

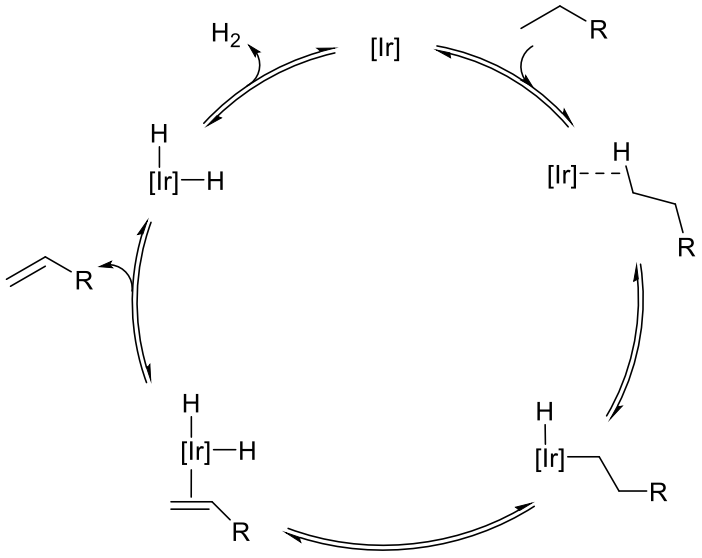

Scheme 4.1 A simplified alkane dehydrogenation cycle *via* a 14 electron Ir(I) intermediate, [Ir].

Considering that the isolation of the highly reactive 14 electron intermediate [(^{tBu}PONOP)Ir][BAr$^{F}_{4}$] is prevented by onward cyclometalation to form complex **1.53**, it was hypothesised that using a ligand set which does not cyclometalate may allow for the isolation of the corresponding 14 electron intermediate. It was hypothesised that such a 14 electron iridium(I) intermediate, [(^{Ad}PONOP)Ir][BAr$^{F}_{4}$], might be accessed by preventing the cyclometalation pathway using Ad substituents, which are often resistant to cyclometalation, through the reductive elimination of methane from a methyl hydride complex equivalent to complex **1.50**. During the writing of this thesis, Gade and coworkers reported the isolation of a latent rhodium(I) 14 electron species in the solution-state by using a bicyclic PNP-type pincer ligand (Scheme 4.2).[7] Whilst the ^{t}Bu analogue forms the corresponding cyclometalated rhodium(III) complex, cyclometalation is suppressed when using more constrained, cage-like

adamantyl (Ad) groups, instead forming a 14 electron rhodium(I) complex with a Rh···H–C agostic interaction (Rh···H, 1.99(4) Å). Both complexes react with N_2 to form the corresponding rhodium(I) dinitrogen complex.

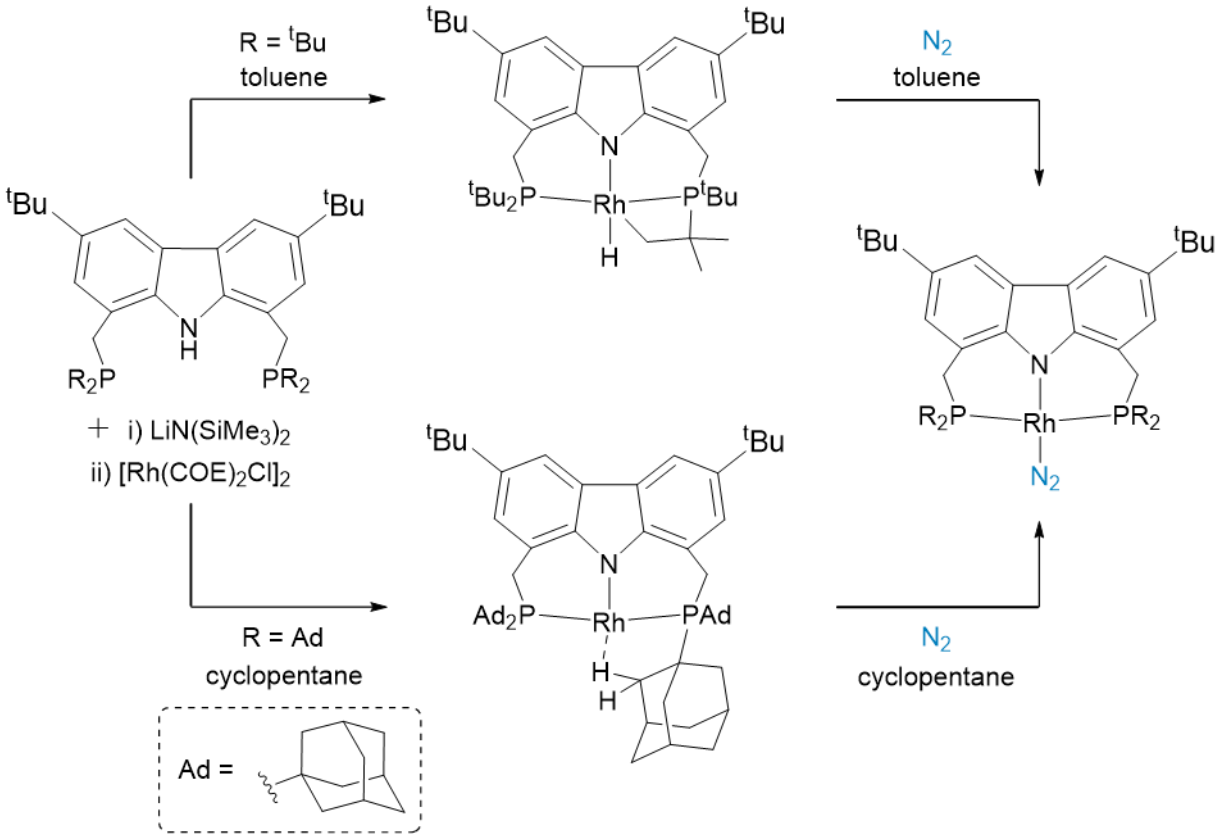

Scheme 4.2 The synthesis of rhodium(I) or rhodium(III) species, as dictated by the substituent of the pincer ligand, and their ongoing reactivity with N_2.

The simple monodentate phosphine, PAd_3, is also known to be resistant to cyclometalation in $[(PAd_3)Pd(Ph)(OAc)]$ even at 90 °C. This is attributed to the significant torsional strain required to form the corresponding cyclometalated complex, in comparison to the more flexible ^{t}Bu analogue $[(P^tBu_3)Pd(3\text{-}(CH_2F)C_6H_4)(OAc)]$ which cyclometalates at 60 °C (Scheme 4.3).[8, 9]

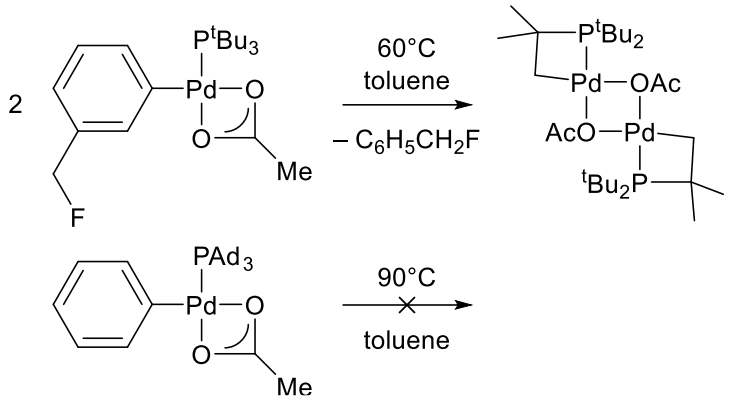

Scheme 4.3 Comparison of the reactivity of two Pd(II) phosphine complexes.

Despite the rigid structure of Ad groups, their apparent resistance to cyclometalation is not always the case. Examples of cyclometalation of ligands bearing Ad substituents are known for NHC ligands, likely due to the more acute M–X–C angle (X = N) that places the Ad group close to the metal. Methylation of [(IAdMes)Co(PPh$_3$)Cl] (IAdMes = 1-mesityl-3-adamantyl-4,5-dimethylimidazol-2-ylidene) with MeLi results in the formation of a cyclometalated cobalt(I) complex *via* the elimination of methane (Scheme 4.4 A).[10] Alternatively, halide abstraction from [(SIAdMes)RuCl$_2$(=CH-*o*-(O^{i}Pr)C$_6$H$_4$)] forms a cyclometalated ruthenium catalyst (Scheme 4.4 B) which is active in the ring-closing metathesis of diethyldiallyl malonate and the ring-opening metathesis polymerisation of norbornene.[11]

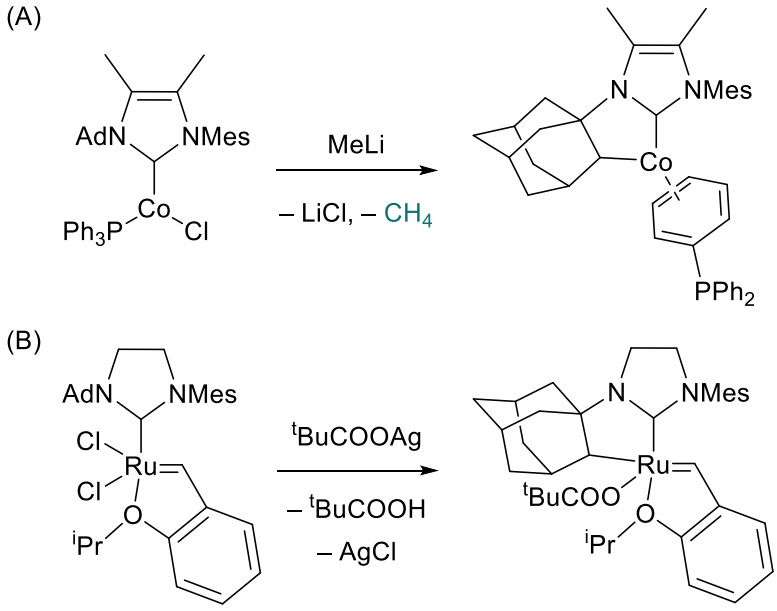

Scheme 4.4 Examples of complexes that exhibit C–H bond activated adamantyl ligand substituents.

There are only a few adamantyl pincer complexes known (Scheme 4.5 A). This includes the ligand ^{Ad}PCP (^{Ad}PCP = 2,6-(Ad$_2$PCH$_2$)$_2$C$_6$H$_3$), which forms the iridium(I) carbonyl and the iridium(III) dihydride complexes, [(^{Ad}PCP)Ir(CO)] and [(^{Ad}PCP)Ir(H)$_2$] respectively.[12] The latter complex, [(^{Ad}PCP)Ir(H)$_2$], demonstrates slightly higher levels of activity in the acceptorless dehydrogenation of cyclodecane (TON = turnover number = 543, 96 hours) compared to the ^{t}Bu analogue, [(^{tBu}PCP)Ir(H)$_2$] (TON = 314, 96 hours). As evident by monitoring by ^{31}P NMR spectroscopy at 250 °C, [(^{Ad}PCP)Ir(H)$_2$] is also more thermally robust than the ^{t}Bu and ^{i}Pr analogues, and thus more resistant to catalyst decomposition at the high temperatures required for alkane dehydrogenation catalysis (250 °C).

The bis[2-(diadamantylphosphino)ethyl]amine ligand is also known, and was shown to be poorly reactive in the isomerisation of allyl alcohols to ketones when complexed with cobalt (no reaction), carbonylation of formaldehyde with rhodium (2%), or in the upgrading of ethanol to butanol with manganese (10%), though this poor catalytic activity was not discussed further.[13-15] The adamantyl analogue of ^{tBu}PONOP, bis(di-adamantylphosphino)-2,6-dioxypyridine (**L2**), has yet to be reported despite the ^{t}Bu and ^{i}Pr analogues being well known.[1, 16]

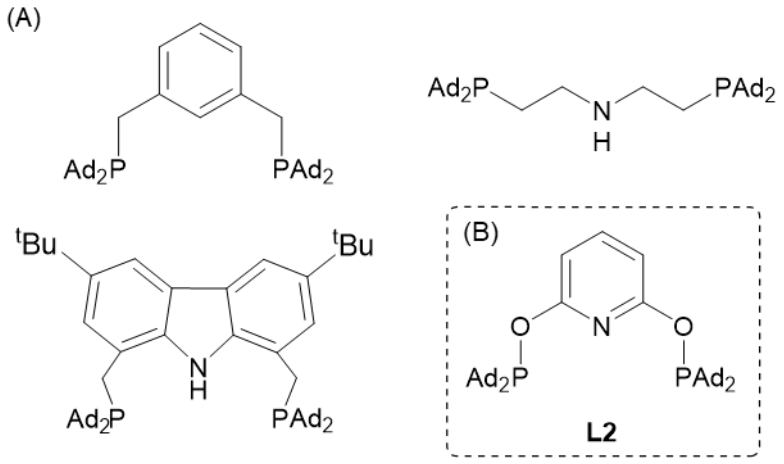

Scheme 4.5 (A) Known adamantyl substituted pincer ligands. (B) The target of this work, ligand **L2**.

This chapter describes the synthesis and characterisation of ligand **L2**, and the formation of the target iridium(III) methyl hydride complex [(**L2**)Ir(Me)(H)][BAr^F_4] (**4.5**). Methane loss from complex **4.5** in both the solution (CD_2Cl_2, 1,2-difluorobenzene) and solid state (vacuum, N_2, H_2) is explored, in an attempt to access the 14 electron complex [(**L2**)Ir][BAr^F_4]. The solution- and solid state behaviour of complex **4.5** is compared to that of [(^{tBu}PONOP)Ir(Me)(H)][BAr^F_4] (**1.50**) to probe the importance of a cyclometalated intermediate, such as complex **1.53**, in its reactivity.

4.2 Synthesis of the adamantyl pincer ligand, L2

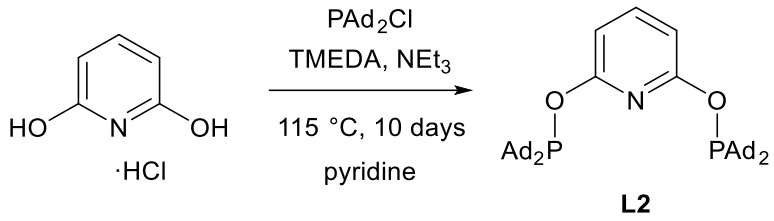

Scheme 4.6 The synthesis of the new pincer ligand, (di-adamantylphosphino)- 2,6-dioxypyridine (**L2**).

After repeat synthesis attempts using different conditions (base = triethylamine, TMEDA (tetramethylethylenediamine); temp = 65 °C, 80 °C, 115 °C; solvent = THF, pyridine; time = 7 days, 10 days), the pincer ligand **L2** was cleanly synthesised from the reaction of 2,6-dihydroxypyridine hydrochloride with diadamantylchloride in pyridine, TMEDA and triethylamine at 115 °C for 10 days (Scheme 4.6). Extraction into toluene, followed by washing with pentane at 0 °C yielded ligand **L2** as an off-white solid powder (4.4 g, 87%). Exposure of ligand **L2** to air for 24 hours led to ~30% formation of a new peak at δ 56.6 which likely corresponds to the phosphine oxide, therefore ligand **L2** was treated as air sensitive. Crystallisation from a pentane solution at –80 °C afforded colourless crystals of ligand **L2** (Figure 4.2). Ligand **L2** crystallises in the space group $P\bar{1}$. In the solid-state structure, the phosphorus atoms point slightly above and below the plane of the pyridine backbone in a twisted arrangement. The P–O bond distances (1.694(2), 1.693(2) Å) are longer than

^{tBu}POCOP (1.674(1), 1.678(1) Å).[17] The P–C distances of ligand **L2** (1.871(2), 1.864(3), 1.868(2), 1.870(2) Å) are similar to ^{tBu}POCOP (1.873(2), 1.873(2), 1.864(2), 1.875(2) Å).

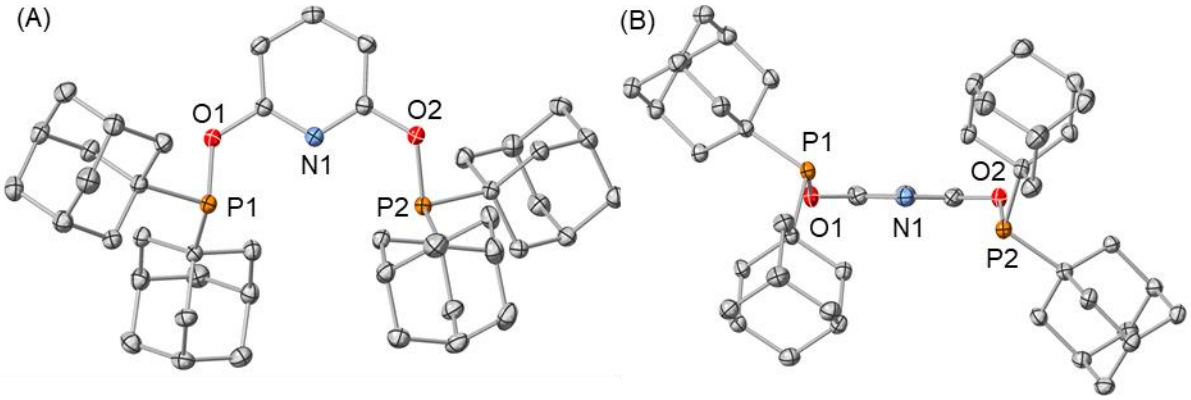

Figure 4.2 A view of the molecular structure of **L2** (A) from above and (B) looking down the plane of the pyridine ring. Displacement ellipsoids are set at 50% probability. Hydrogen atoms are excluded for clarity. Select bond distances (Å): P1–O1, 1.694(2); P2–O2, 1.693(2); P1–C6, 1.871(2); P1–C16, 1.864(3); P2–C26, 1.868(2); P2–C36, 1.870(2).

The ^{1}H NMR (C_6D_6) spectrum of crystalline ligand **L2** (Figure 4.3) shows a triplet and doublet ($^{3}J_{HH}$ = 7.3 Hz) at δ 7.19 (1H) and 6.65 (2H) respectively corresponding to the *para*- and *meta*-protons of the pyridine ring. Peaks corresponding to 0.13 equivalents of toluene are also observed at δ 7.02 (0.4H) and at 7.13, the latter overlapping with the residual C_6D_5H solvent peak at δ 7.16, although this is too low occupancy to be observed in the crystal structure. In solution, the Ad groups are equivalent, showing one set of NMR signals due to time-averaged C_{2v} symmetry in the solution-state. The pair of H_b adamantyl protons are observed as overlapping tightly coupled AB doublets at δ 2.14 and 2.11 (24H) due to the two protons being diastereotopic. The H_c proton signal is observed as a singlet at δ 1.91 (12H), whilst the diastereotopic proton pair for H_d are observed as overlapping AB doublets centred at δ 1.71 and 1.67 (24H). The adamantyl environment assignments H_b and H_d were confirmed by the ^{1}H-^{13}C HSQC (Heteronuclear Single Quantum Coherence) spectrum, which revealed cross peaks to the adamantyl carbons C_b and C_d. The adamantyl carbons C_a, C_b and C_c are observed as doublets at δ 40.3, 39.2 and 28.9 with decreasing J_{CP} coupling constants ($^{1}J_{CP}$ = 29, $^{2}J_{CP}$ = 14 and $^{3}J_{CP}$ = 8 Hz respectively) due to the longer bond path to the ^{31}P nucleus. In contrast, remote C_d is observed as a singlet at δ 37.5. Diastereotopic proton environments

have been noted before for pincer ligands featuring adamantyl substituents, for example with a similar peak pattern being reported for the adamantyl group resonances of [(^{Ad}PCP)Ir(H)$_2$] as AB doublets at δ 2.14 ($^2J_{HH}$ = 12.0 Hz, 12H) and 2.08 ($^2J_{HH}$ = 11.0 Hz, 12H), a singlet at δ 1.83 (12H), and AB doublets at δ 1.63 ($^2J_{HH'}$ = 12.0 Hz, 12H) and 1.57 ($^2J_{HH}$ = 10.5 Hz, 12H).[12] A singlet peak is observed at δ 151.3 in the ^{31}P{^{1}H} NMR spectrum of ligand **L2**, due to the equivalent phosphorus environments.

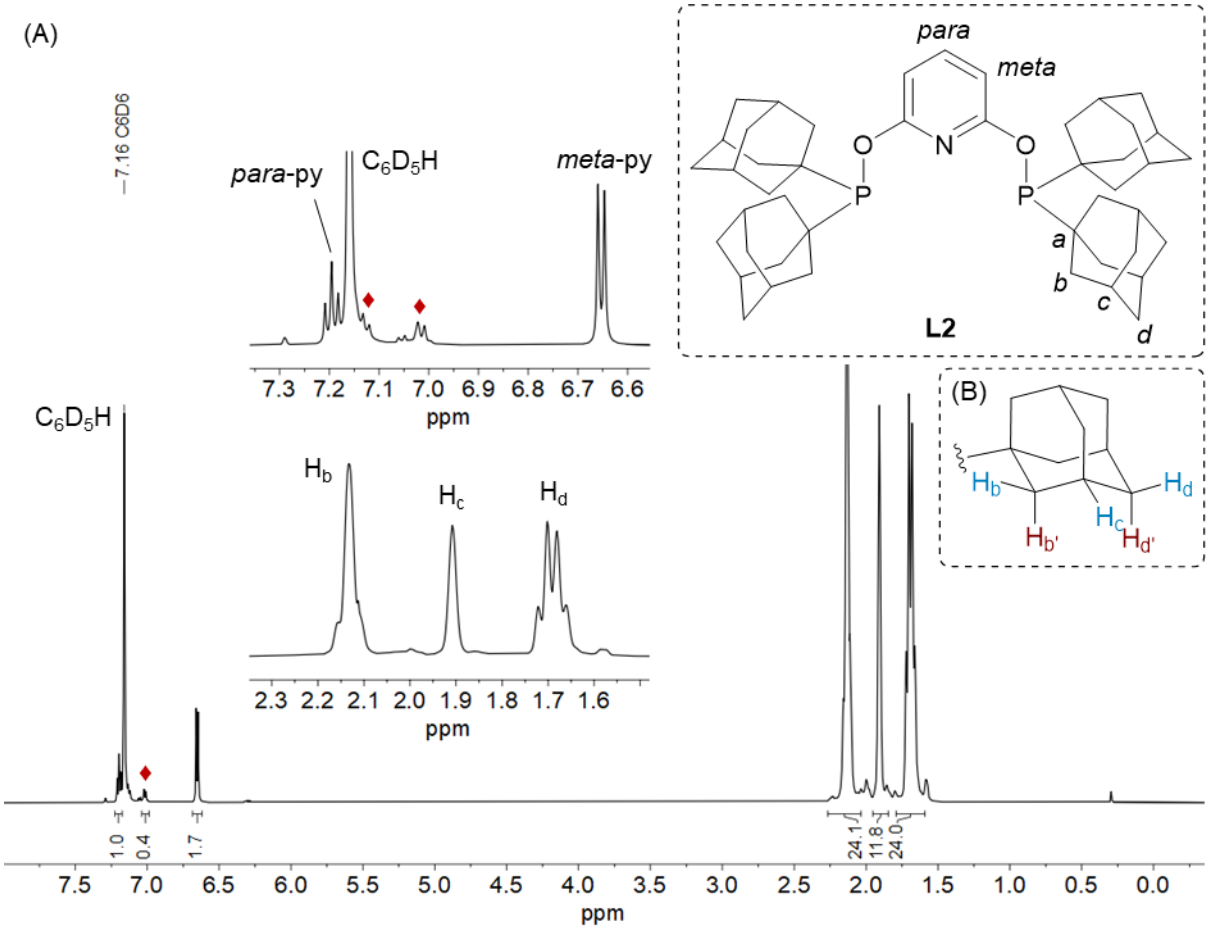

Figure 4.3 (A) The ^{1}H NMR spectrum of ligand **L2** (500 MHz, C_6D_6, 298 K). ♦ Denotes toluene. The inset NMR expansions highlight the pyridine and Ad regions. (B) The fused chair confirmation of the Ad substituent which results in diastereotopic proton pairs for H_b and H_d.

4.3 Synthesis of an iridium(III) methyl hydride complex, 4.5

Brookhart's complex, [(^{tBu}PONOP)Ir(Me)(H)][BAr$^F_4$] (**1.50**), is synthesised by a multistep synthesis, beginning with the preparation of [(^{tBu}PONOP)IrCl] obtained from the reaction of [Ir(COE)$_2$Cl]$_2$ and ^{tBu}PONOP under ethylene.[1] An analogous synthesis with ligand **L2** was attempted to access the target [(**L2**)IrCl] compound (**4.3**). However, the reaction of ligand **L2**

with $[Ir(COE)_2Cl]_2$ in C_6D_6 led to an intractable mixture of products, including unreacted ligand **L2**, as evident from the ^1H and $^{31}P\{^1H\}$ NMR spectra (Figure 4.4). Multiple hydride signals are observed in the ^1H NMR spectrum, showing the numerous C–H activation products present.

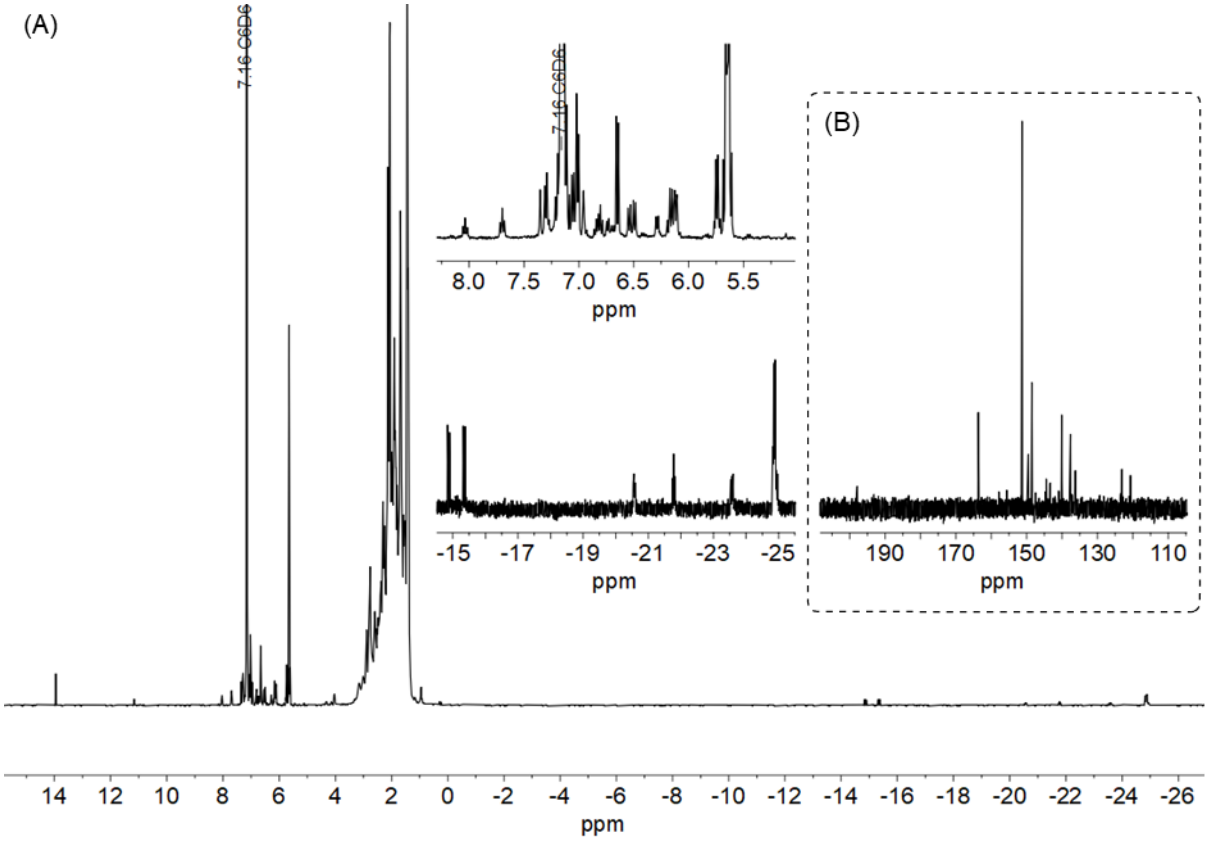

Figure 4.4 The (A) ^1H (400 MHz) and (B) $^{31}P\{^1H\}$ NMR spectra of the reaction of ligand **L2** with $[Ir(C_2H_4)_2Cl]_2$ (161 MHz, C_6D_6, 298 K). Insets highlight the PONOP and hydride regions of the ^1H NMR spectrum.

Considering the mixture of C–H activation products observed from the reaction of ligand **L2** with $[Ir(COE)_2Cl]_2$ under C_2H_4, a different route using an $[Ir(CO)_2Cl]_2$ dimer was instead investigated. The $[Ir(CO)_2Cl]_2$ used was synthesised according to literature procedure[18] by the reaction of $[Ir(COE)_2Cl]_2$ with CO in toluene at room temperature. Reaction of $[Ir(CO)_2Cl]_2$ with ligand **L2** in acetonitrile was subsequently carried out at room temperature for 20 hours, followed by extraction into toluene, to afford the iridium(I) carbonyl complex, [(**L2**)Ir(CO)]Cl (**4.1**), as a yellow solid (0.3 g, 78%, Scheme 4.7).

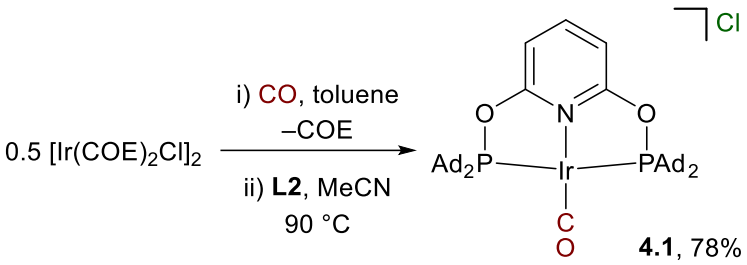

Scheme 4.7 The synthesis of complex **4.1**.

In the ^{1}H NMR (CD_2Cl_2) spectrum of complex **4.1** (Figure 4.5) a triplet and doublet ($^{3}J_{HH}$ = 8.2 Hz) are observed at δ 8.14 (1H) and 7.09 (2H) corresponding to the *para*- and *meta*- positions of the pyridine ring respectively. Two AB doublets ($^{2}J_{HH}$ = 11.0 Hz) appear at δ 2.29 (12H) and 2.07 and connect *via* one-bond couplings to the same carbon environment at δ 29.4 (^{1}H-^{13}C HSQC, Figure 4.6) and are assigned to the diastereotopic adamantyl H_b protons. These peaks are now better separated than the corresponding signals for ligand **L2** due to coordination to the iridium(I) centre. The latter peak for H_b (δ 2.07) is overlapping with a singlet at δ 2.09 (24H total) which corresponds to H_c. In contrast, the peak corresponding to H_d again appears as two tightly coupled AB doublets at δ 1.82 and 1.77 (24H).

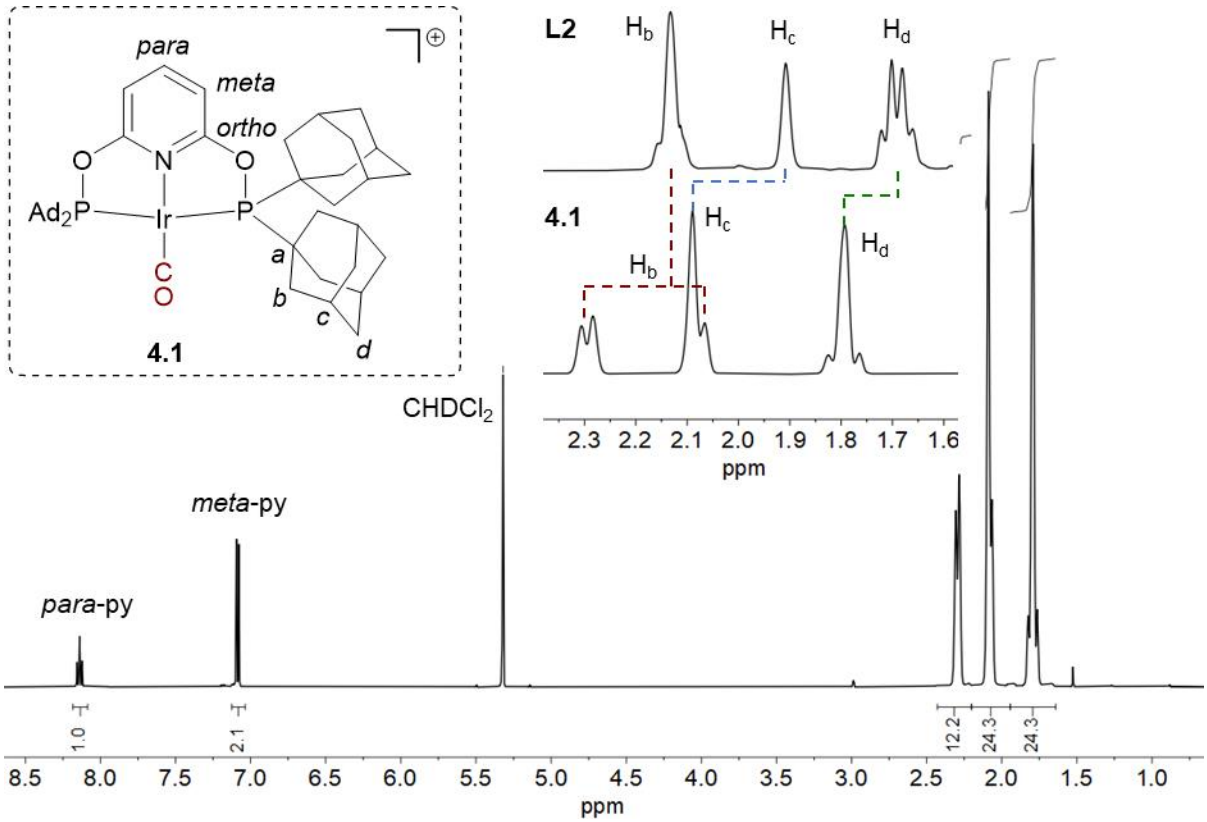

Figure 4.5 The ^{1}H NMR spectrum of complex **4.1** (500 MHz, CD_2Cl_2, 298 K). Inset NMR expansions highlight the adamantyl proton region of the spectra for **L2** and complex **4.1**.

Complex **4.1** is observed to yield a singlet at δ 196.5 in the $^{31}P\{^{1}H\}$ NMR spectrum. Its carbonyl carbon is observed as a triplet ($^{2}J_{CP}$ = 7 Hz) at δ 183.9 due to coupling to two ^{31}P nuclei. This reflects a similar shift to that found in [(^{Ad}PCP)Ir(CO)] ($^{2}J_{CP}$ = 4 Hz, δ 182.2)[12] and [(^{tBu}PONOP)Ir(CO)][BAr$^{F}_{4}$] ($^{2}J_{CP}$ = 7 Hz, δ 182.2).[19]

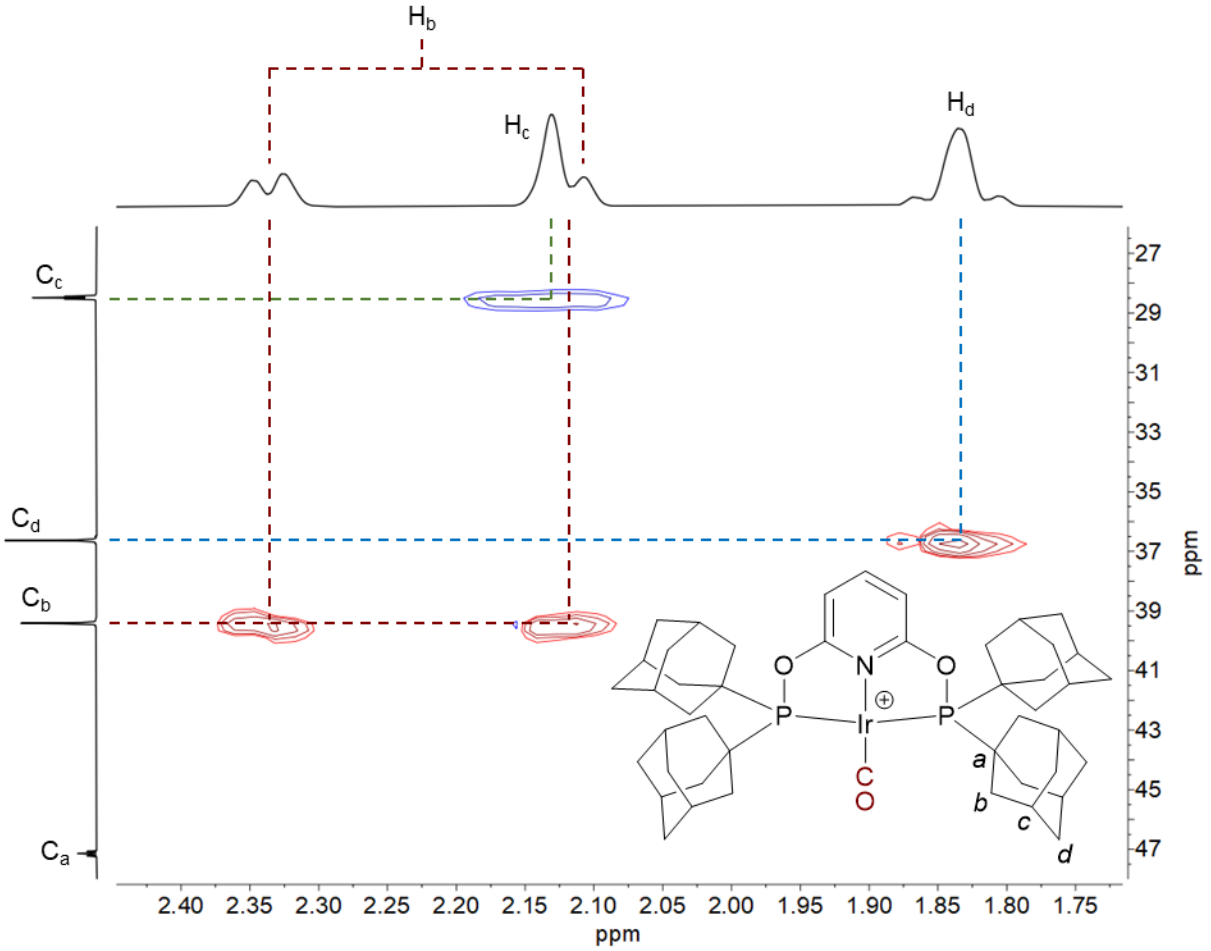

Figure 4.6 The adamantyl region of the ^{1}H-^{13}C HSQC NMR spectrum of complex **4.1** (500 MHz, CD_2Cl_2, 298 K).

All crystallisation attempts (solvents = dichloromethane/hexane, dichloromethane/pentane, 1,2-difluorobenzene/hexane; temp = –20 °C, 0 °C, room temp) for complex **4.1** were unsuccessful. As compounds of $[BAr^F_4]^-$ are often easier to crystallise, owing to their insolubility in alkane solvents such as hexane, salt metathesis with $Na[BAr^F_4]$ in dichloromethane was carried out on small scale (3 mg) to access the crystal structure of [(**L2**)Ir(CO)][BAr^F_4] (**4.2**). The ^{1}H NMR (CD_2Cl_2) spectrum of complex **4.2** is the same as that of complex **4.1** with the addition of peaks at δ 7.72 (multiplet, 8H) and 7.56 (singlet, 4H) corresponding to the *ortho*- and *meta*-BAr^F_4 protons respectively. Crystallisation from dichloromethane/hexane at room temperature resulted in yellow crystals of complex **4.2**.

Complex **4.2** crystallises in the space group $P\bar{1}$ and displays a pseudo square planar geometry around the iridium(III) centre with an P1–Ir1–P2 angle of 160.57(4)° (Figure 4.7). The CO

ligand is located *trans* to the nitrogen of the **L2** ligand, with an Ir1–C1 bond distance of 1.838(6) Å and a C1–O1 distance of 1.147(7) Å, which are the same within error as those reported for [(^{tBu}PONOP)Ir(CO)][BAr$^{F}_{4}$] (1.841(3) and 1.158(4) Å respectively)[20] and [(^{R1}PONOP)Ir(CO)][BAr$^{F}_{4}$] (R1 = 2-(CF$_3$)C$_6$H$_4$; Ir–C, 1.858(3); C–O 1.137(4) Å).[21] The Ir–C distance of complex **4.2** is shorter than that of other iridium(I) carbonyls bearing macrocyclic POCOP ligands, for example [(^{R2}POCOP)Ir(CO)] (R2 = tetradecamethylene; Ir–C, 1.879(4) Å).[22] The phosphorus atoms are crystallographically inequivalent, with Ir–P distances of 2.289(3) and 2.282(2) Å, similar to [(^{tBu}PONOP)Ir(CO)][BAr$^{F}_{4}$] (2.2846(8) and 2.2892(8) Å).[20] The Ir1–N1 distance of 2.068(4) Å is also within error of [(^{tBu}PONOP)Ir(CO)][BAr$^{F}_{4}$] (2.054(3) Å), demonstrating that there is no significant impact on the bond metrics upon switching from ^{t}Bu to Ad substituents.

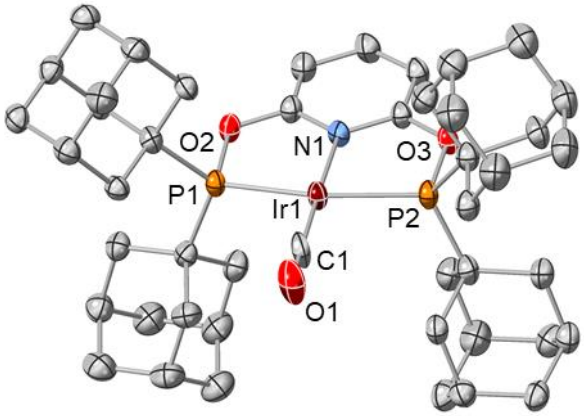

Figure 4.7 The molecular structure of the isolated cation of complex **4.2**. Displacement ellipsoids are set at 50% probability. Hydrogen atoms and [BAr$^{F}_{4}$]$^{-}$ anion are excluded for clarity. Select bond distances (Å): Ir1–C1, 1.838(6); Ir1–P1, 2.289(3); Ir1–P2, 2.282(2); Ir1–N1, 2.068(4); C1–O1, 1.147(7). Select bond angles (°): P1–Ir1–P2, 160.57(4).

Despite the large size of the adamantyl substituents, the space-filling structure of the cation in complex **4.2** shows the adamantyl groups to be pushed back away from the iridium centre, so that the iridium(I) centre is similarly exposed as that in [(^{tBu}PONOP)Ir(CO)][BAr$^{F}_{4}$] (Figure 4.8 A).[20] This effect can also be demonstrated by the percent buried volume of the ligand (%V$_{Bur}$). %V$_{Bur}$ is the percent volume of a sphere which is occupied by a ligand, wherein the metal centre is the centre of the sphere, and is often used to compare steric profiles of phosphine or

NHC ligands.[23] The $\%V_{Bur}$ of ligand **L2** was calculated by removing the CO ligand in complex **4.2** in the programme Sambvca 2.1.[24, 25] Ligand **L2** has a similar buried volume (83.0%) to that of the analogous [(^{tBu}PONOP)Ir(CO)][PF_6] (83.5%),[20] showing that despite the bulkier adamantyl substituents, the steric profile around the iridium(I) is similar (Figure 4.8 B).

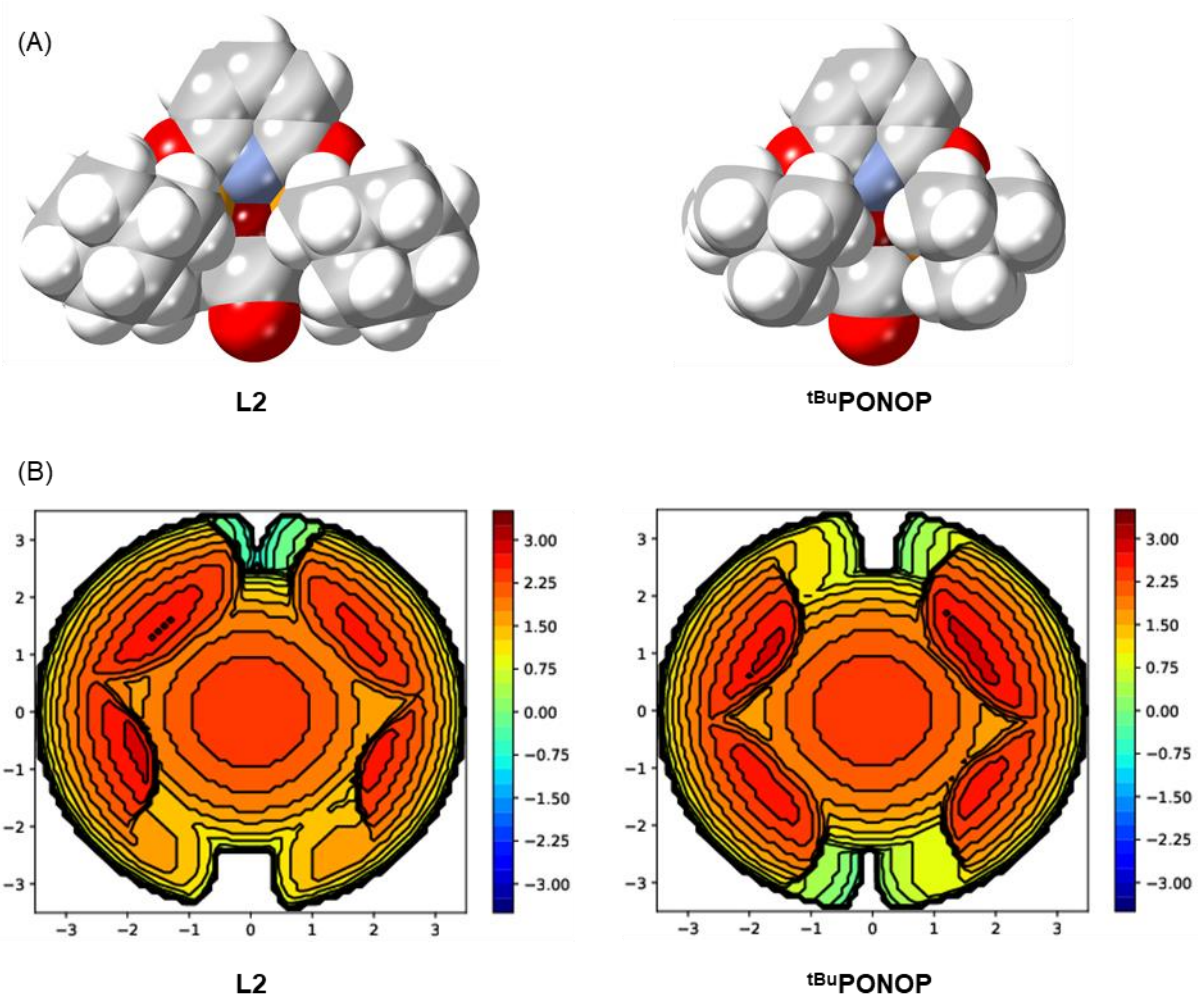

Figure 4.8 (A) The space-filling structures of the cations of complex **4.2** and [(^{tBu}PONOP)Ir(CO)][PF_6]. (B) The percent buried volume maps of ligand **L2** and ^{tBu}PONOP from the corresponding iridium(I) carbonyl complexes, looking down the Ir–CO bond.

The solid-state IR spectrum of complex **4.2** (Figure 4.9) displays a sharp C–O stretch at 1988 cm^{-1}. This is at a lower wavenumber than free CO (2143 cm^{-1})[26] due to the iridium(I) centre behaving as a classical carbonyl complex, wherein the π-backdonation into the π^*_{CO} orbital has a significant contribution to bonding, resulting in a decrease in the C–O bond strength and lengthening of the C–O bond, moving the C–O stretch to a lower wavenumber. The IR stretch

of carbonyl ligands has been utilised previously to compare the donor properties of pincer ligands,[22, 27] by reporting the change in *π*-backdonation upon switching the ligand substituents from acyclic to macrocyclic pincer ligands. The C–O stretch of complex **4.2** is observed at lower wavenumber than [(^{tBu}PONOP)Ir(CO)][BAr$^F_4$] (2003 cm^{-1}),[28] demonstrating that changing the ^{t}Bu substituents to Ad results in increased electron donation to the metal by the pincer ligand, so that the CO reporter ligand experiences more *π*-backdonation.

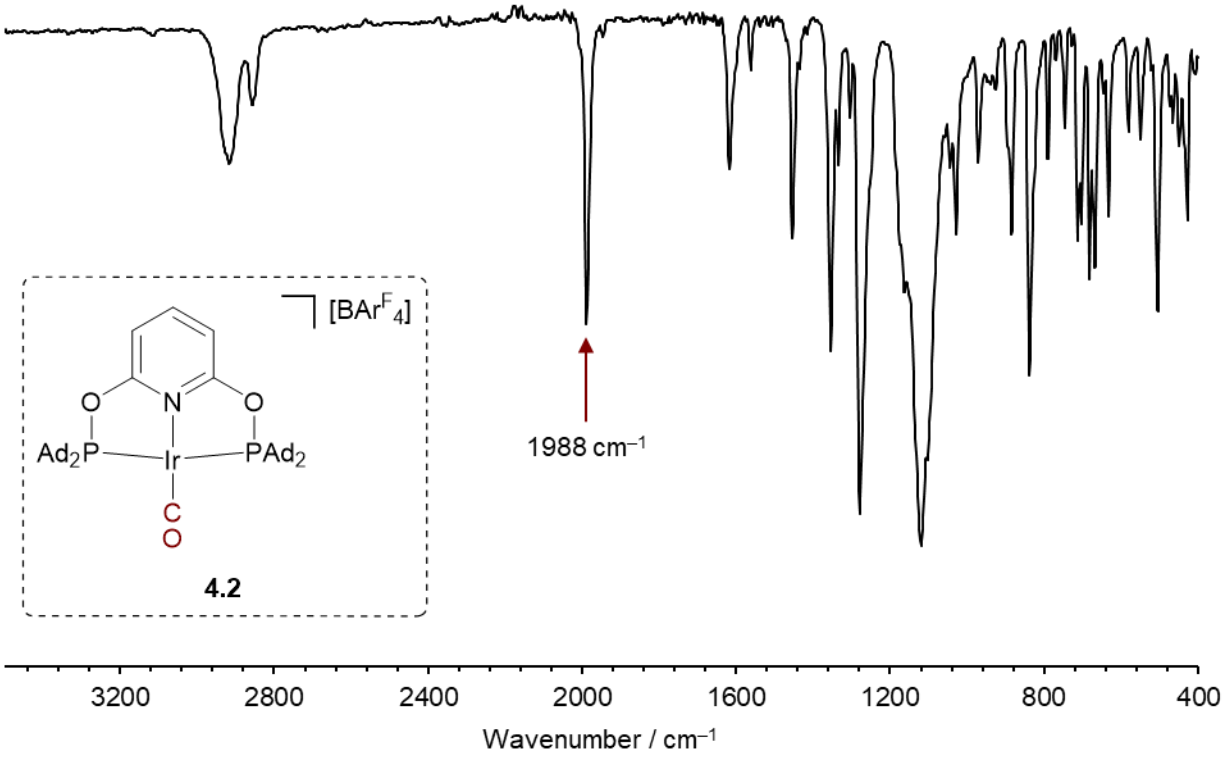

Figure 4.9 The solid-state ATR-IR spectrum of complex **4.2**.

With complex **4.1** in hand, methylation was attempted to access [(**L2**)Ir(Me)] (**4.4**). However, repeat attempts at methylation by the addition of methyl lithium, dimethyl magnesium or tetramethyl tin to complex **4.1** under different reaction conditions led to an unidentified mixture of products as inferred from the ^{31}P{^{1}H} NMR spectra. It was hypothesised that trimethylamine *N*-oxide (TMNO) might abstract the carbonyl ligand from complex **4.1** to form the target chloride complex, [(**L2**)IrCl] (**4.3**, Scheme 4.8), which could then be cleanly methylated. The reaction of complex **4.1** with TMNO in THF at room temperature for 24 hours, followed by

extraction in toluene, afforded the iridium(I) chloride complex **4.3** as an air sensitive orange solid (547.2 mg, 67%).

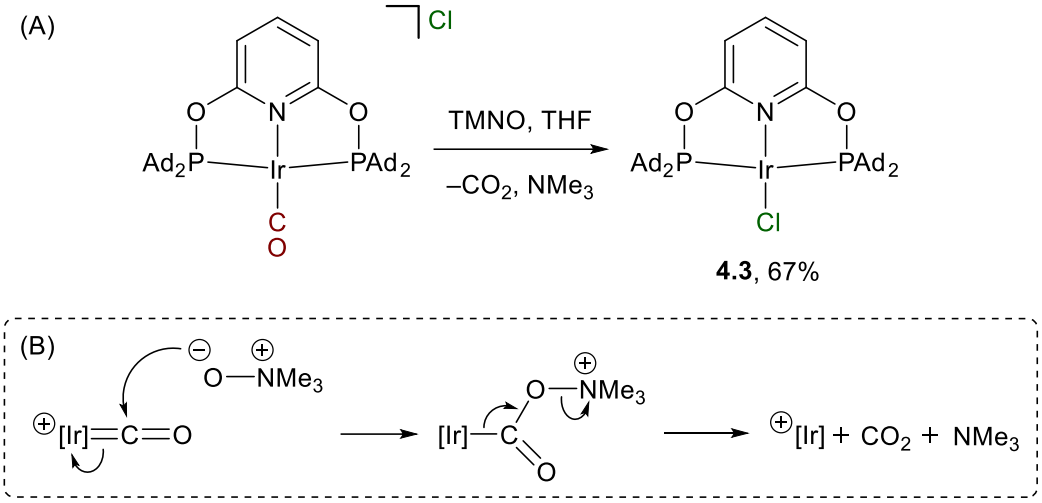

Scheme 4.8 (A) The synthetic route to complex **4.3**. (B) The mechanism by which CO is abstracted from a metal carbonyl by TMNO. [Ir] = [(**L2**)Ir].

The ^{1}H NMR (C_6D_6) spectrum of complex **4.3** (Figure 4.10) shows a triplet and doublet ($^{3}J_{HH}$ = 8.0 Hz) at δ 7.25 (1H) and 6.13 (2H) corresponding to the *para*- and *meta*- positions of the pyridine ring respectively. One set of signals are observed for the Ad protons, with similar appearance to those of complex **4.1**, at δ 2.67 (12H) and 2.54 (12H) for H_b, at δ 1.91 (12H) for H_c, and at δ 1.75 (12H) and 1.61 (12H) corresponding to H_d. The broad peak at δ 3.26 corresponds to unreacted TMNO.[29] There are several other broad peaks observed at the base of the adamantyl peaks which correspond to a small amount of unidentified side product, however only one peak is observed in the ^{31}P{^{1}H} NMR spectrum at δ 172.7. There is no peak observed in the carbonyl region (δ ~180) of the ^{13}C{^{1}H} spectrum, verifying that the carbonyl ligand has been removed. Although a crystal structure could not be obtained for this product despite repeat attempts at crystallisation, a peak corresponding to 9H for NMe_3 was also not observed, suggesting that the complex is not the NMe_3 adduct. Free NMe_3 is reported at δ 2.12, and although there is a peak present at δ 2.11, its integral is too low (5.1H rather than the expected 9H) and instead corresponds to 1.9 equivalents of recalcitrant toluene, for which the corresponding aryl toluene peaks are also observed at δ 7.02 (4.9 H) and at 7.13 (2.9H).

Although the purity was not otherwise established, complex **4.3** proceeds to cleanly form the corresponding methyl complex [(**L2**)IrMe] (**4.4**, *vide infra*), in an analogous way to how Brookhart's [(^{tBu}PONOP)IrCl] complex reacts to form [(^{tBu}PONOP)IrMe], using methyl lithium.[1] This indirectly supports both the identity of complex **4.3** and its purity.

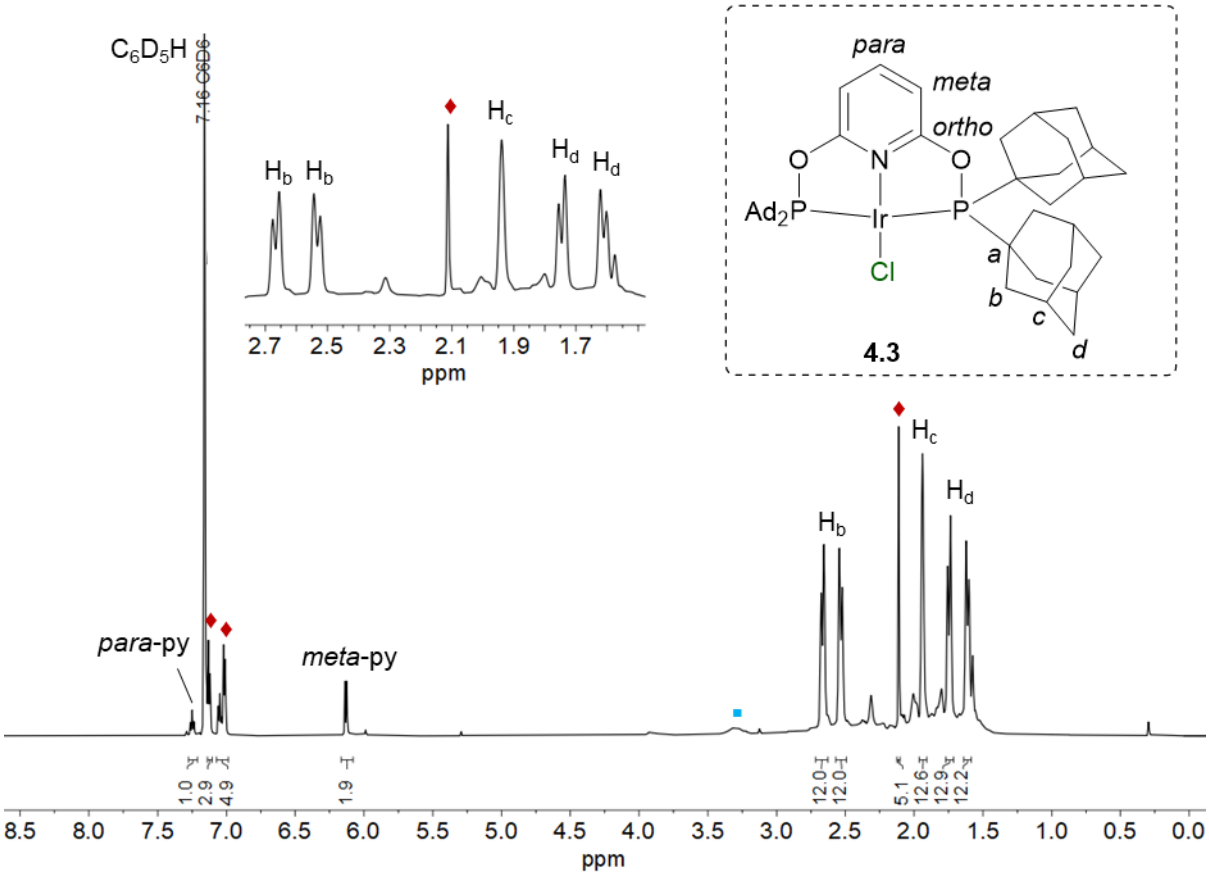

Figure 4.10 The ^{1}H NMR spectrum of complex **4.3** (500 MHz, C_6D_6, 298 K). ♦ Denotes recalcitrant toluene, ■ denotes unreacted TMNO. Inset highlights the adamantyl proton region.

The reaction of complex **4.3** with methyl lithium in THF and 1,4-dioxane at 90 °C for 3 hours, followed by extraction in toluene, afforded the iridium(I) complex, [(**L2**)IrMe] (**4.3**) as an air sensitive dark red solid (168.7 mg, 58%, Scheme 4.9). Crystallisation from toluene at –20 °C led to dark red crystals of complex **4.3**.

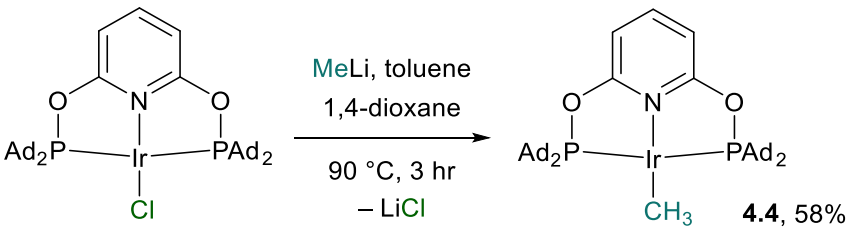

Scheme 4.9 The synthetic route to complex **4.4**.

The ^{1}H NMR (C_6D_6) spectrum of the crystals of complex **4.4** (Figure 4.11) shows a triplet and doublet ($^{3}J_{HH}$ = 7.9 Hz) at δ 7.49 (1H) and 6.27 (2H) corresponding to the *para*- and *meta*-positions of the pyridine ring respectively. One set of signals are observed for the Ad protons, that are similar to those of complexes **4.1**–**4.3**, at δ 2.63 (12H) and 2.40 (12H) for H_b, δ 1.93 (12H) for H_c, and at δ 1.74 (12H) and 1.63 (12H) corresponding to H_d. The methyl protons are observed as a triplet ($^{3}J_{HP}$ = 4 Hz) at δ 2.29 (3H) which collapses into a singlet upon ^{31}P decoupling (Figure 4.11 B and C). The methyl protons of complex **4.5** are slightly downfield compared to complex **1.50** (δ 2.11) but have a similar coupling constant ($^{3}J_{HP}$ = 5 Hz).[1] A singlet is observed at δ 179.7 in the solution ^{31}P{^{1}H} NMR spectrum of complex **4.5**, which shows a cross peak with the methyl and H_b adamantyl protons in the ^{1}H-^{31}P HMBC spectrum (Figure 4.12).

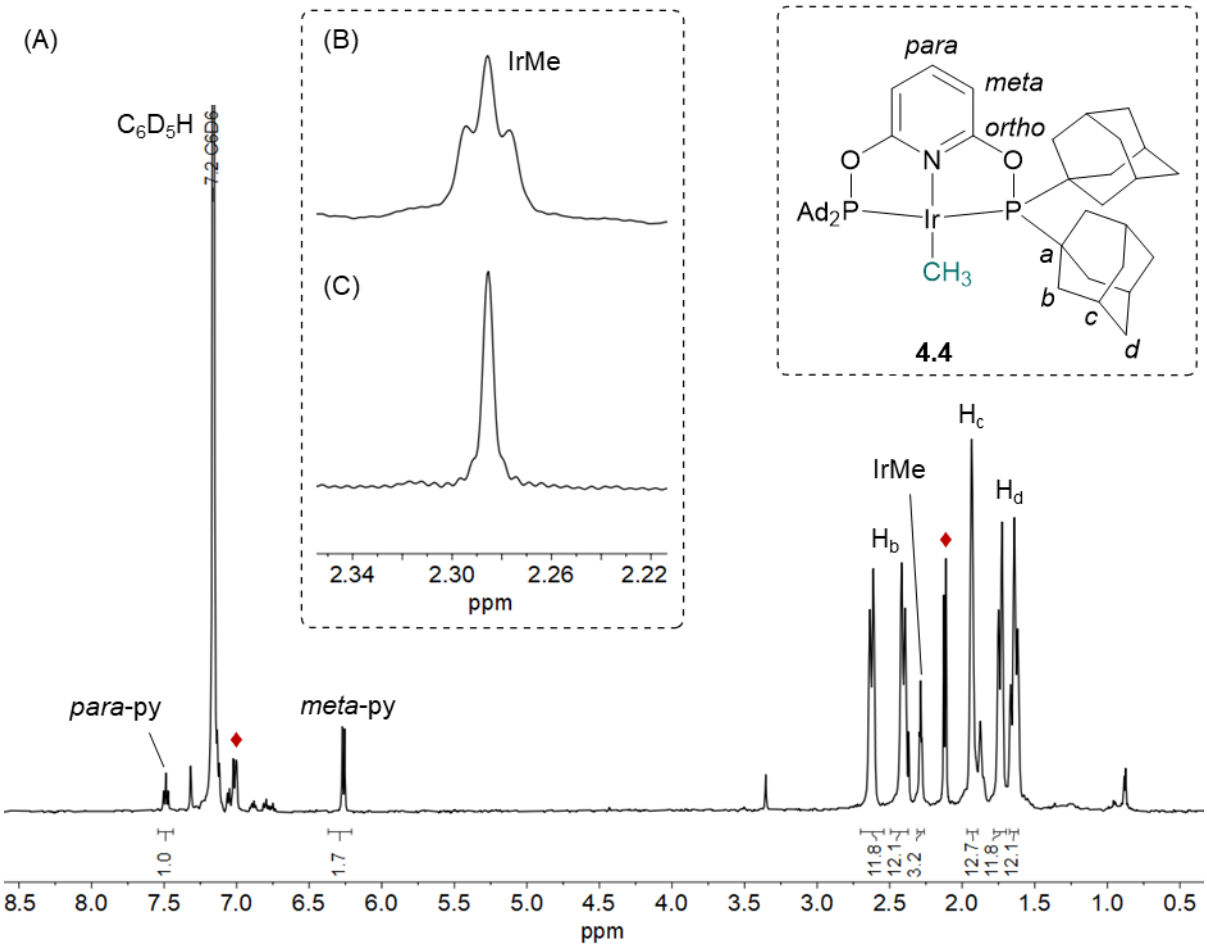

Figure 4.11 (A) The ^{1}H NMR spectrum of complex **4.4** (500 MHz, C_6D_6, 298 K). ♦ Denotes lattice toluene. Inset highlights the methyl environment in the (B) ^{1}H and (C) ^{1}H{^{31}P} NMR spectrum.

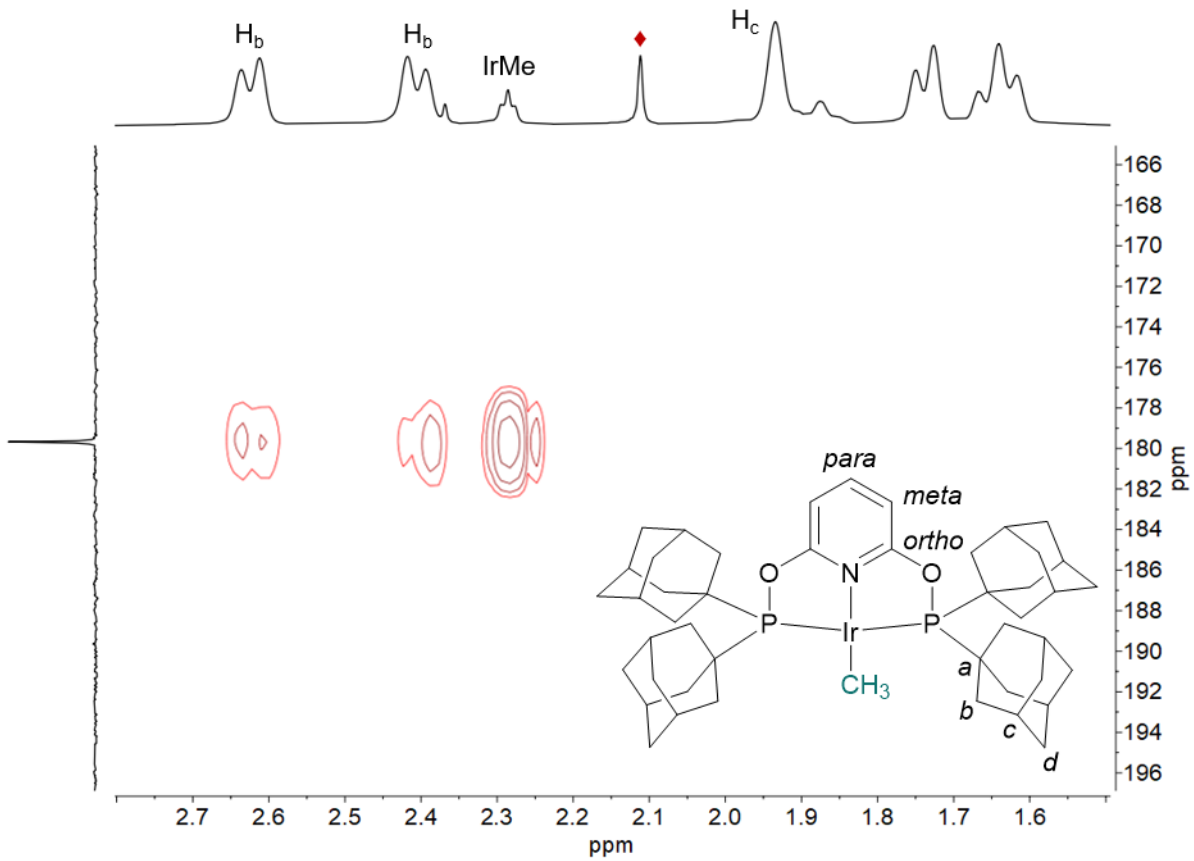

Figure 4.12 The adamantyl region of the ^{1}H-^{31}P HMBC NMR spectrum of complex **4.4** (500 MHz, C_6D_6, 298 K). ♦ Denotes recalcitrant toluene.

In the ^{31}P{^{1}H} SSNMR spectrum, a single peak is observed at δ 178.0 (Figure 4.13 A). The methyl carbon is observed at δ –25.8 in the solution ^{13}C{^{1}H} NMR spectrum of complex **4.4**, similar to complex **1.50** (δ –24.8), and shows a ^{1}H-^{13}C HSQC correlation to the methyl proton peak at δ 2.29 in the ^{1}H NMR spectrum. The ^{13}C{^{1}H} SSNMR spectrum of complex **4.4** is similar to the solution-state spectrum, aside from the methyl carbon which is shifted upfield slightly to δ –27.9 (Figure 4.13 B).

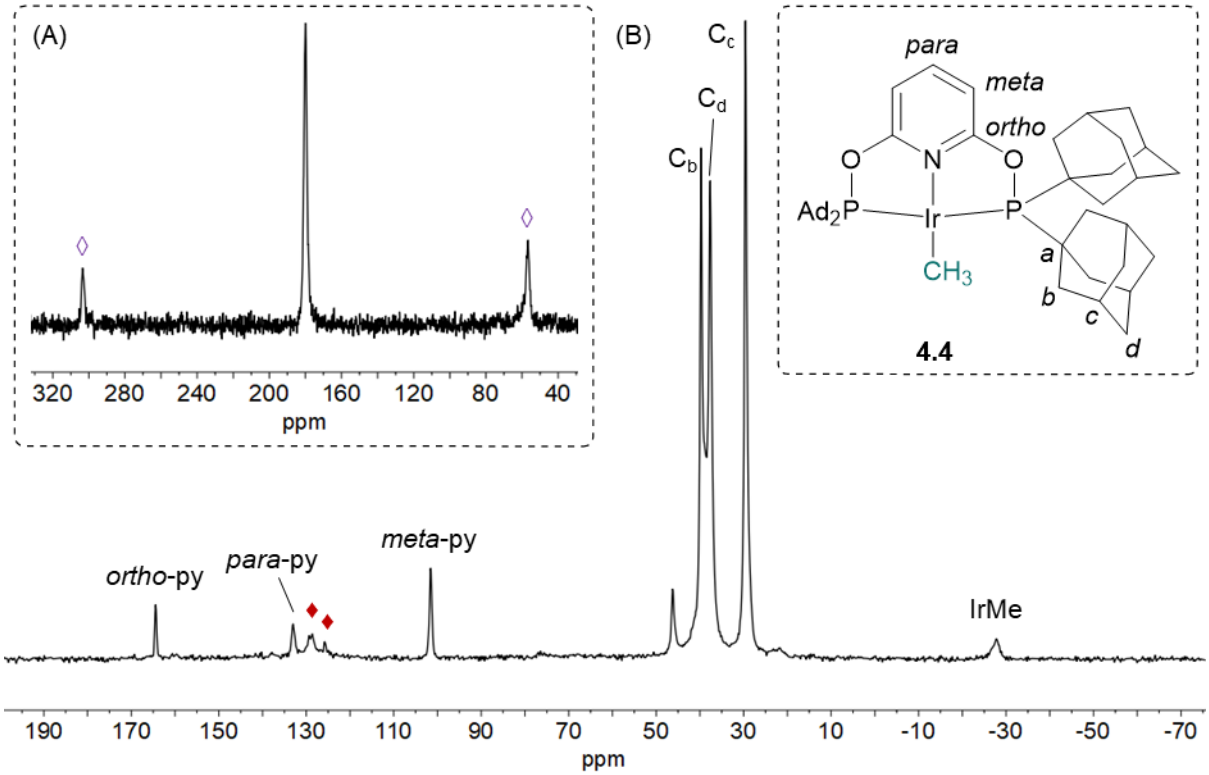

Figure 4.13 (A) The solid-state $^{31}P\{^{1}H\}$ CP MAS NMR spectrum of complex **4.4** (162 MHz, 20 kHz spin rate, 298 K). ◊ Denotes spinning side bands. (B) The solid-state $^{13}C\{^{1}H\}$ CPTOSS MAS NMR spectrum of complex **4.4** (100 MHz, 20 kHz spin rate, 298 K). ♦ Denotes recalcitrant toluene.

Complex **4.4** crystallises in the space group *C*2/*c* and displays a pseudo square planar geometry around the iridium(III) centre with an P1–Ir1–P2 angle of 161.134(9)° (Figure 4.14). The complex lies on a crystallographic two-fold position with the iridium(I) centre at a special position, resulting in crystallographically equivalent phosphorus and oxygen atoms, and adamantyl substituents. The Ir–C1 distance is 2.115(4) Å, the Ir1–P1 distance is 2.229(1) Å and the Ir1–N1 distance is 2.058(3) Å.

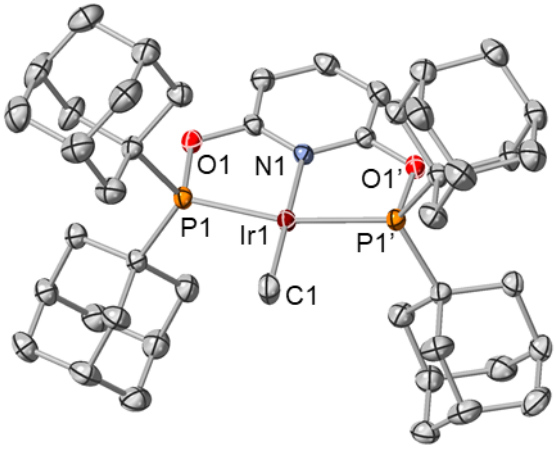

Figure 4.14 The molecular structure of complex **4.4**. Displacement ellipsoids are set at 50% probability. Hydrogen atoms are excluded for clarity. Select bond distances (Å): Ir1–C1, 2.115(4); Ir1–P1, 2.229(1); Ir1–N1, 2.058(3). Select bond angles (°): P1–Ir1–P2, 161.134(9).

4.4 Characterisation of complex 4.5

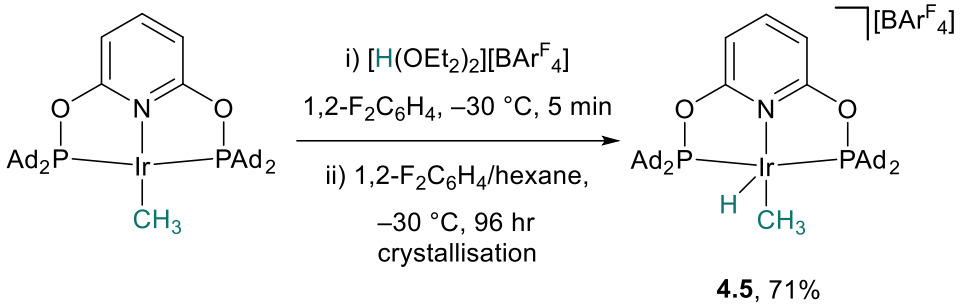

Scheme 4.10 The synthetic route to complex **4.5**.

The reaction of complex **4.4** with $[H(OEt_2)_2][BAr^F{}_4]$ in 1,2-difluorobenzene at –30 °C, followed by crystallisation from 1,2-difluorobenzene/hexane at –30 °C afforded the target complex **4.5** (Scheme 4.10). Complex **4.5** begins to lose methane above 273 K in solution (*vide infra*) and therefore synthesis and crystallisation was carried out at –30 °C. Complex **4.5** crystallises as two different polymorphs in space groups *C*2/*c* (*α*-**4.5**) and $P\bar{1}$ (*β*-**4.5**).

Consideration of the extended lattice structures of polymorphs *α*-**4.5** and *β*-**4.5** show that the polymorphs form different packing arrangements of $[BAr^F{}_4]^-$ anions (Figure 4.15). Polymorph *α*-**4.5** forms an ortho gyrobifastigium with two capping $[BAr^F{}_4]^-$ anions above and below the central plane of six $[BAr^F{}_4]^-$ anions, with ten total $[BAr^F{}_4]^-$ anions. This encapsulates two crystallographically equivalent cations and lattice hexane (0.5 occupancy), with a V_{cell}/Z' of

1936 Å^3. Polymorph *β*-**4.5** forms a hexagonal prismatic packing arrangement of twelve $[BAr^F{}_4]^-$ anions also encapsulating two crystallographically identical cations, as well as two molecules of lattice hexane (0.9 and 0.6 occupancy) with a V_{cell}/Z' of 2310 Å^3. Residual electron density peaks in the structure of polymorph *β*-**4.5** suggests that more solvent may also be present in the lattice which could not be modelled, therefore the SQUEEZE tool was applied to the structure. This is likely 1,2-difluorobenzene from the crystallisation solvents, as evident in the ^{1}H NMR (CD_2Cl_2, 193 K) spectrum (*vide infra*) which contains 0.1 equivalents of 1,2-difluorobenzene at δ 7.18–7.22 (0.4H), which is too low occupancy to be modelled in the crystal structure.

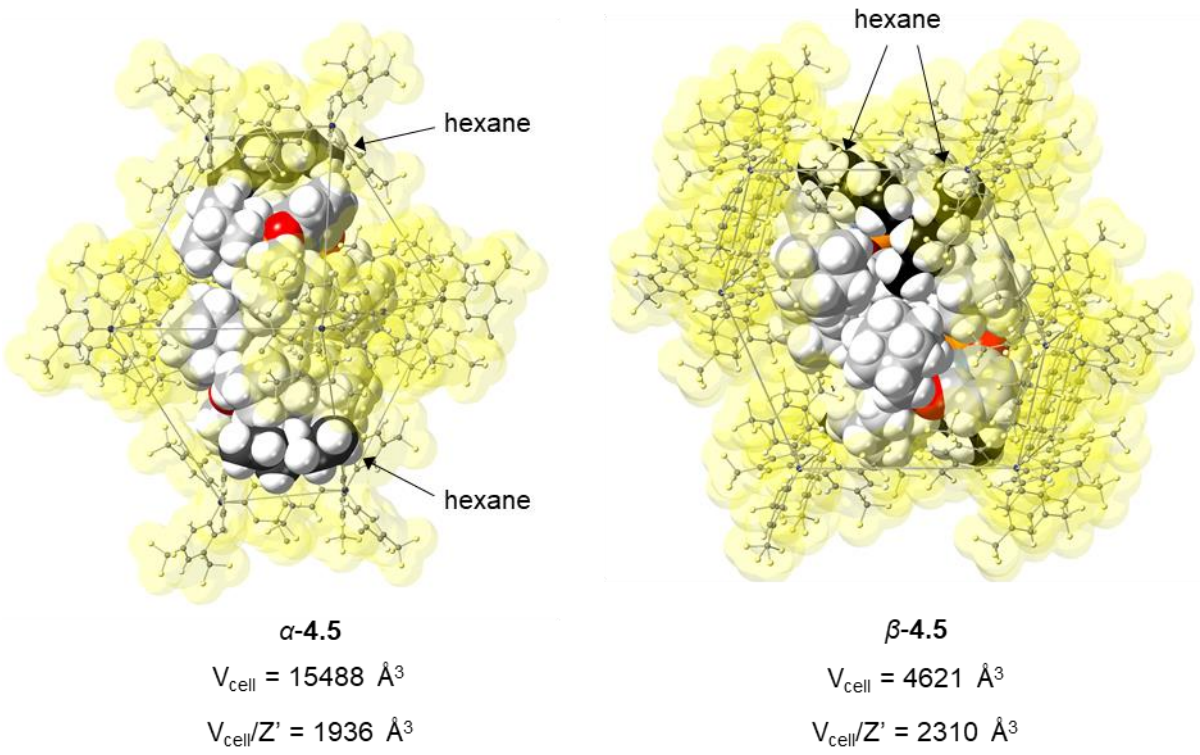

Figure 4.15 The extended solid-state structure of the two polymorphs of **4.5**, showing the ortho gyrobifastigium or hexagonal prismatic arrangements of $[BAr^F{}_4]^-$ anions, and hexane lattice solvents, depicted as Van der Waals radii.

As discussed in section 3.2, it is important to isolate a single polymorph as different morphologies may have differing reactivity and stabilities.[30-32] The ^{t}Bu analogue, complex **1.50**, also crystallises as two distinct polymorphs which can be separated by graded sieving, due to the difference in their crystal sizes. However, due to the similar size of the crystals of

polymorphs *α*-**4.5** and *β*-**4.5**, repeated attempts at separating them by graded sieving or different crystallisation conditions (temperature, solvents) were unsuccessful, as evident from the resulting SCXRD and $^{31}P\{^{1}H\}$ SSNMR data (*vide infra*).

Polymorphs *α*-**4.5** and *β*-**4.5** display the same cation structure within error (*α*-**4.5**, Ir1–C1, 2.085(4) Å; *β*-**3.1**, Ir1–C1, 2.111(5) Å) therefore discussion of the cation structure shall be limited to that of polymorph *α*-**4.5**. Polymorph *α*-**4.5** displays a pseudo square planar geometry around the iridium(III) centre with an P1–Ir1–P2 angle of 160.914(7)° (Figure 4.16 A). The methyl ligand is *trans* to the nitrogen of the **L2** ligand, with an Ir1–C1 bond distance of 2.085(4) Å, similar to complex **1.50** (2.091(4) Å).[1] The Ir1–C1 bond length (2.085(4) Å) is shorter than complex **4.4** (2.115(4) Å). The phosphorus atoms are crystallographically inequivalent, with Ir–P distances of 2.280(1) and 2.281(1) Å, similar to complex **1.50** (2.2875(9) and 2.2840(9) Å). The Ir1–N1 distance (2.094(3) Å) is also similar to complex **1.50** (2.091(4) Å). The similar bond metrics between complexes **1.50** and *α*-**4.5** show that switching substituents has little effect on the structure around the iridium(III) centre. Although the hydride ligand could not be located in the electron density map of complex *α*-**4.5**, a hydride is observed in the solution ^{1}H NMR spectrum (CD_2Cl_2, 193 K, *vide infra*) of the dissolved ensemble of polymorphs of complex **4.5** as a triplet at δ –40.91. The relatively upfield hydride signal position is consistent with a hydride ligand *trans* to a vacant site, which tend to be observed in this region.[33, 34] In both polymorphs *α*-**4.5** and *β*-**4.5** the Ir–C bond of the overlapping cations point toward one another, revealing one face of the cation is more open than the other, indicating the likely position of the hydride ligand (Figure 4.16 B). This is supported by the fact that the distance between the two Ad groups on this face (C20···C30, 5.5897(4) Å) is significantly longer than that between the two adamantyl groups on the opposite face (C8···C40, 3.6766(6) Å), in order to accommodate the hydride ligand. This is further demonstrated by the C20–P2–Ir1 and C30–P1–Ir1 angles (103.742(3) and 100.019(4)° respectively) which are significantly wider than that of C8–P2–Ir1 and C40–P1–Ir1 (85.579(4) and 77.151(6)° respectively). These data combined place the hydride ligand on the ‘open face’ between the C20 and C30 Ad groups.

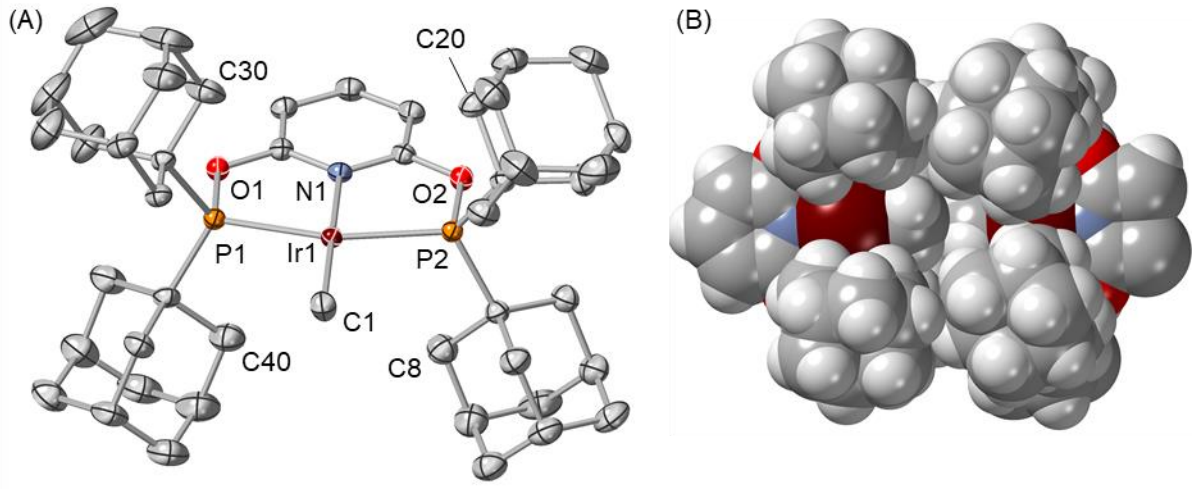

Figure 4.16 (A) The molecular structure of the isolated cation of complex *α*-**4.5**. Displacement ellipsoids are set at 50% probability. Hydrogen atoms, lattice solvent and $[BAr^{F}_{4}]^{-}$ anion are excluded for clarity. Select bond distances (Å): Ir1–C1, 2.085(4); Ir1–P1, 2.280(1); Ir1–P2, 2.281(1); Ir1–N1, 2.094(3); C20···C30, 5.5897(4); C8···C40, 3.6766(6). Select bond angles (°): P1–Ir1–P2, 160.915(7). (B) A space filling view of the cations of complex *α*-**4.5**.

The solution $^{31}P\{^{1}H\}$ NMR (CD_2Cl_2, 193 K) spectrum of the dissolved ensemble of polymorphs *α*-**4.5** and *β*-**4.5** shows a singlet peak at δ 172.6, consistent with the polymorphs being the same in the solution-state once solid state packing effects are removed. At 193 K the ^{1}H NMR spectrum of the dissolved ensemble of polymorphs *α*-**4.5** and *β*-**4.5** (Figure 4.17) shows a mutually coupled triplet and doublet ($^{3}J_{HH}$ = 8.2 Hz) at δ 7.81 (1H) and 6.98 (2H) corresponding to the *para*- and *meta*- positions of the pyridine ring respectively. The *ortho*- and *meta*-BAr^{F}_{4} protons are observed as singlets at δ 7.72 (8H) and 7.53 (4H) respectively. The methyl environment is observed as a broad multiplet at δ 1.81 (3H), at a similar shift to [(^{tBu}PONOP)Ir(Me)(H)][BAr^{F}_{4}] (**1.50**, δ 1.83),[1] which collapses into a singlet upon ^{31}P decoupling. The methyl peak assignment at δ 1.81 was confirmed by correlation to the phosphorus peak at δ 172.6 in the ^{1}H-^{31}P HMBC spectrum (Figure 4.18 A). The methyl carbon is observed at δ –26.0 in the solution $^{13}C\{^{1}H\}$ NMR spectrum (CD_2Cl_2, 193 K), significantly upfield of complex **1.50** (δ –20.6).[1] This chemical shift could be due to a solution-state equilibrium between complex **4.5** and a *σ*-methane intermediate (*vide infra*), residing closer to the higher energy *σ*-methane tautomer than in the corresponding equilibrium of complex **1.50**, as *σ*-methane complexes are observed at relatively upfield shifts, such as

[(^{tBu}PONOP)Rh(CH_4)][BAr^F_4] (**1.51**) at δ –41.7 and [(Cp)Os(CO)$_2$(CH_4)][Al(OC(CF_3)$_3$)$_4$] at δ –56.3.[35, 36] The hydride of complex **4.5** is observed as a triplet ($^2J_{HP}$ = 12.0 Hz) at δ –40.91 (1H) which collapses into a singlet upon ^{31}P decoupling, slightly downfield of the hydride peak of complex **1.50** which is observed at δ –41.79 ($^2J_{HP}$ = 13 Hz). The hydride signal of complex **4.5** is also slightly closer to that of the *σ*-methane complexes [(^{tBu}PONOP)Rh(CH_4)][BAr^F_4] (**1.51**) and [(Cp)Os(CO)$_2$(CH_4)][Al(OC(CF_3)$_3$)$_4$] at δ –0.86 and –2.16 respectively.[35, 36] As discussed previously, the relatively upfield hydride signal of complex **4.5** is consistent with a hydride ligand *trans* to a vacant site. Peaks corresponding to ~0.15 lattice hexane are observed at δ 0.88 (0.9H) and 1.27 (1.3H), and 0.1 1,2-difluorobenzene (0.4H) at δ 7.18–7.22. At 193 K, the adamantyl protons are observed as broad overlapping signals at δ 2.02–1.96 (30H) 1.76 (6H) and 1.66–1.61 (24H) in the ^{1}H NMR spectrum as the time-averaged C_{2v} symmetry has been lost. Although the ^{1}H NMR spectrum does not provide clear information, the ^{13}C{^{1}H} NMR spectrum demonstrates that the complex has effective C_s symmetry as six signals at δ 47.1, 43.1, 36.9, 36.6, 35.2 and 26.9 are observed (Figure 4.18 A). Although eight carbon signals might be expected rather than the observed six for the adamantyl groups, the peak height of the C_d signal is approximately double the size as that of each C_b signal, suggesting that the C_d signals are coincident. The carbon peaks at δ 47.1 and 43.1 correlate to C_a, as they are observed as triplets due to coupling to the ^{31}P nuclei in close proximity ($^1J_{CP}$ = 10 Hz), and they have no proton correlation in the ^{1}H-^{13}C HSQC spectrum of the dissolved ensemble of polymorphs *α*-**4.5** and *β*-**4.5**. The carbon peak at δ 26.9 was assigned to C_c as its HSQC correlation peak (Figure 4.18 C) is in opposite phase to the other adamantyl peaks due to it being a CH environment rather than CH_2. This in turn identified one of the overlapping peaks at δ 2.02–1.96 as correlating to the 12 protons of H_c. H_b was identified by the ^{1}H-^{31}P HMBC spectrum (Figure 4.18 B), which shows a correlation between the overlapping signal at δ 2.02–1.96 and the phosphorus peak at δ 172.6, suggesting that it is in close proximity with the ^{31}P nuclei and one of the overlapping environments, which have a total integral of 30 H, can be assigned to 18 of the H_b protons. One of the overlapping peaks at δ 2.02–1.96 have a HSQC correlation to the overlapping carbon signals at δ 36.9–36.6, which in turn correlate to the

proton peak at δ 1.76 with an integral of 6H, therefore the proton peak at δ 1.76 likely corresponds to 6 of the inequivalent H_b protons. The H_d protons are observed at δ 1.66–1.61 and have a HSQC correlation to the carbon peak at δ 35.2. The inequivalent nature of the adamantyl H_c protons is likely due to the the hydride ligand perpendicular to the plane of the pyridine backbone making the adamantyl groups inequivalent, leading to C_s symmetry.

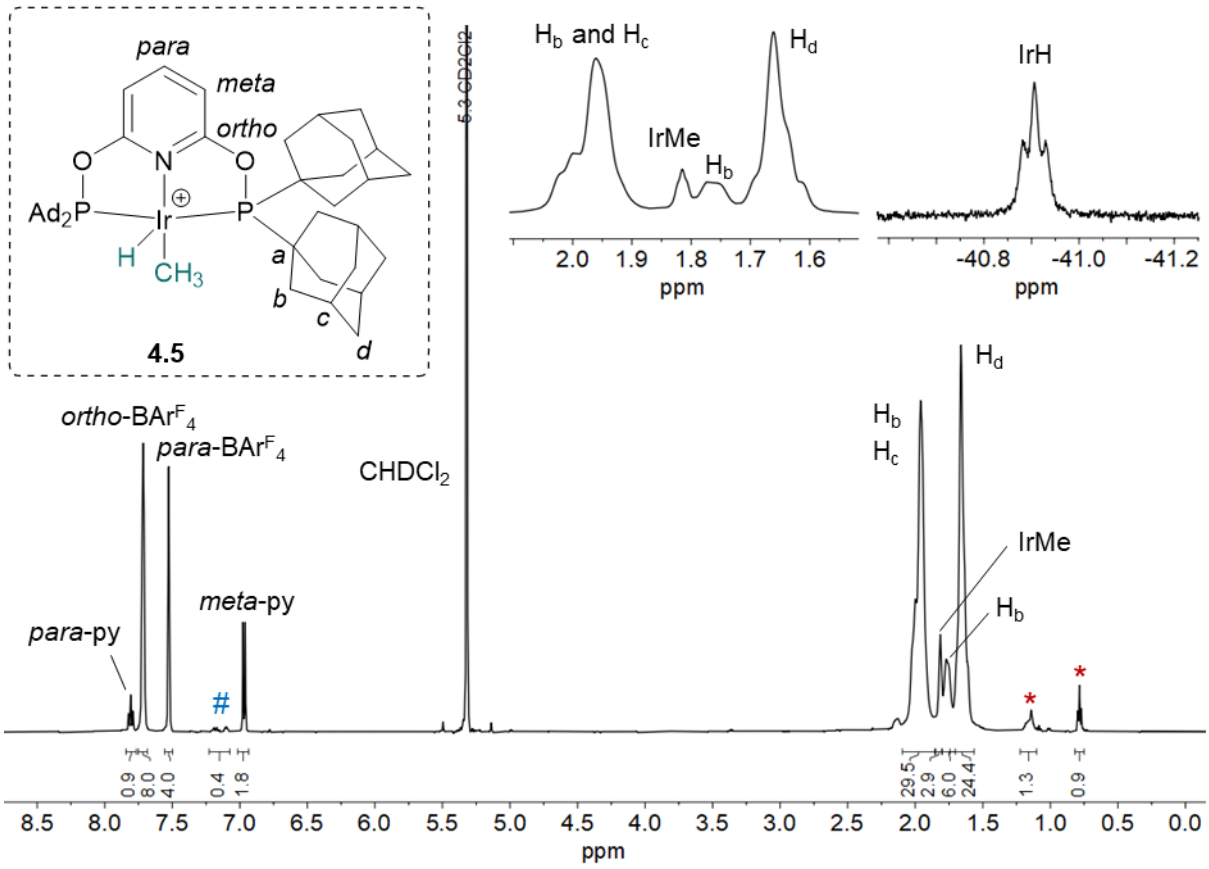

Figure 4.17 The ^{1}H NMR spectrum of the dissolved ensemble of polymorphs *α*-**4.5** and *β*-**4.5** (500 MHz, CD_2Cl_2, 193 K). # Denotes lattice 1,2-difluorobenzene, * denotes lattice hexane. Insets highlight the adamantyl proton region and the hydride peak.

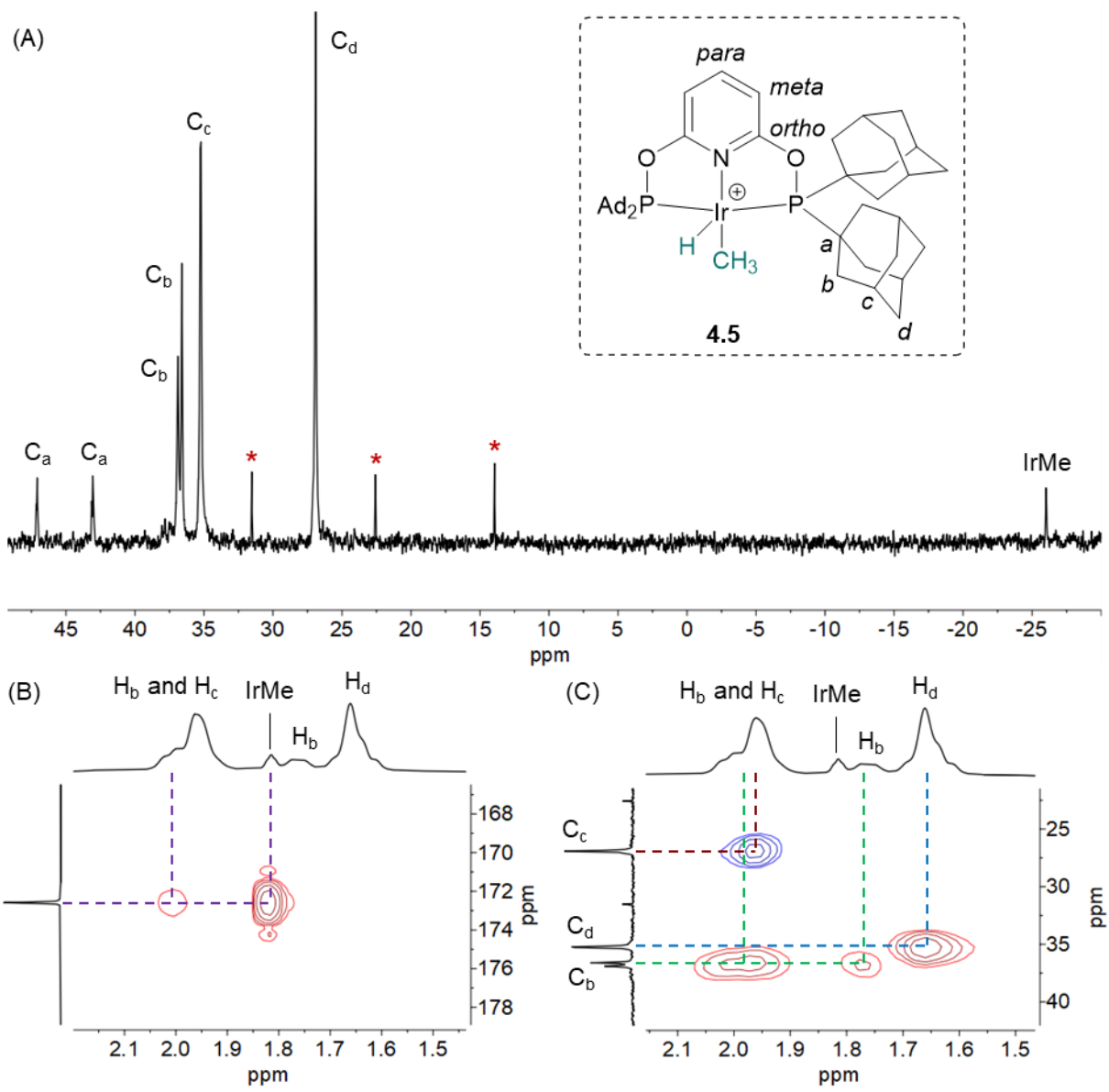

Figure 4.18 (A) The adamantyl and methyl region of the $^{13}C\{^1H\}$ NMR spectrum of the dissolved ensemble of polymorphs *α*-**4.5** and *β*-**4.5**. (125 MHz, CD_2Cl_2, 193 K). (B) The adamantyl region of the ^1H-^{31}P HMBC spectrum of the dissolved ensemble of polymorphs *α*-**4.5** and *β*-**4.5**. (C) The adamantyl region of the ^1H-^{13}C HSQC-edited spectrum of the dissolved ensemble of polymorphs *α*-**4.5** and *β*-**4.5** (500 MHz, CD_2Cl_2, 193 K).

As the temperature is increased from 193 K, the hydride peak (δ –40.91) of complex **4.5** begins to broaden and disappears completely at 223 K (Figure 4.19 B). The methyl peak (δ 1.81) also disappears, although this is less clear due to the adamantyl signals being in close proximity. The hydride and methyl signals reappear upon cooling back to 193 K as the ^1H spectrum is re-established, demonstrating that the complex has not changed through cycling the temperature. The disappearance of the methyl and hydride peaks is consistent with an

exchange process which is faster at higher temperatures so that the signals become one signal at the weighted frequency averaged position (Figure 4.19 A). However, no new signal was detected as the temperature was increased to 273 K, as the rate of exchange is not fast enough to see coalescence of the peaks at δ 1.81 and δ –40.91. At 298 K the time-averaged C_{2v} symmetry is regained, demonstrated by the adamantyl groups becoming equivalent in the ^{1}H NMR spectrum taken immediately after warming to 298 K, and a similar peak pattern to that seen for a complex with time averaged C_{2v} symmetry, such as of complex 4.1, is observed. This is consistent with a rapid and reversible formation of a *σ*-methane intermediate in solution (Figure 4.19 A) which can rotate and deliver the hydride to both possible positions perpendicular to the plane of the pyridine ring. However, methane loss occurs above 273 K leading to decomposition within 24 hours (*vide infra*) and therefore the NMR experiments were conducted at 193 K. Above 273 K in CD_2Cl_2, complex **4.5** begins to lose methane, as evident by the appearance of free methane (δ 0.21).[37] This results in the formation of a mixture of products in the ^{1}H and $^{31}P\{^{1}H\}$ NMR spectra within 20 hours at 298 K (Figure 4.20).

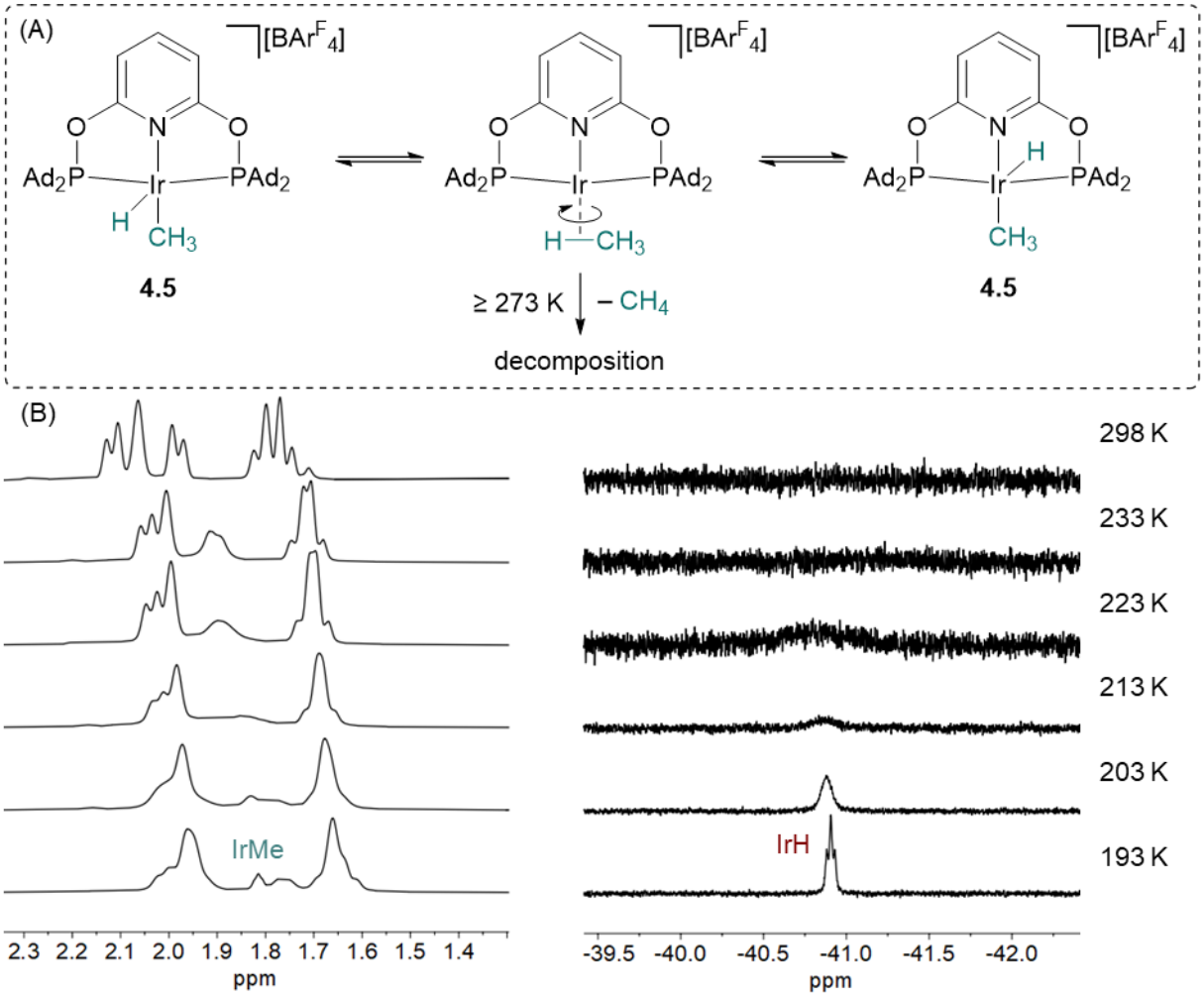

Figure 4.19 (A) The proposed mechanism for exchange between the methyl and proton environments in complex **4.5**. (B) The methyl and hydride regions of the variable temperature ^{1}H NMR spectra of the dissolved ensemble of polymorphs *α*-**4.5** and *β*-**4.5** as a function of temperature. (500 MHz, CD_2Cl_2).

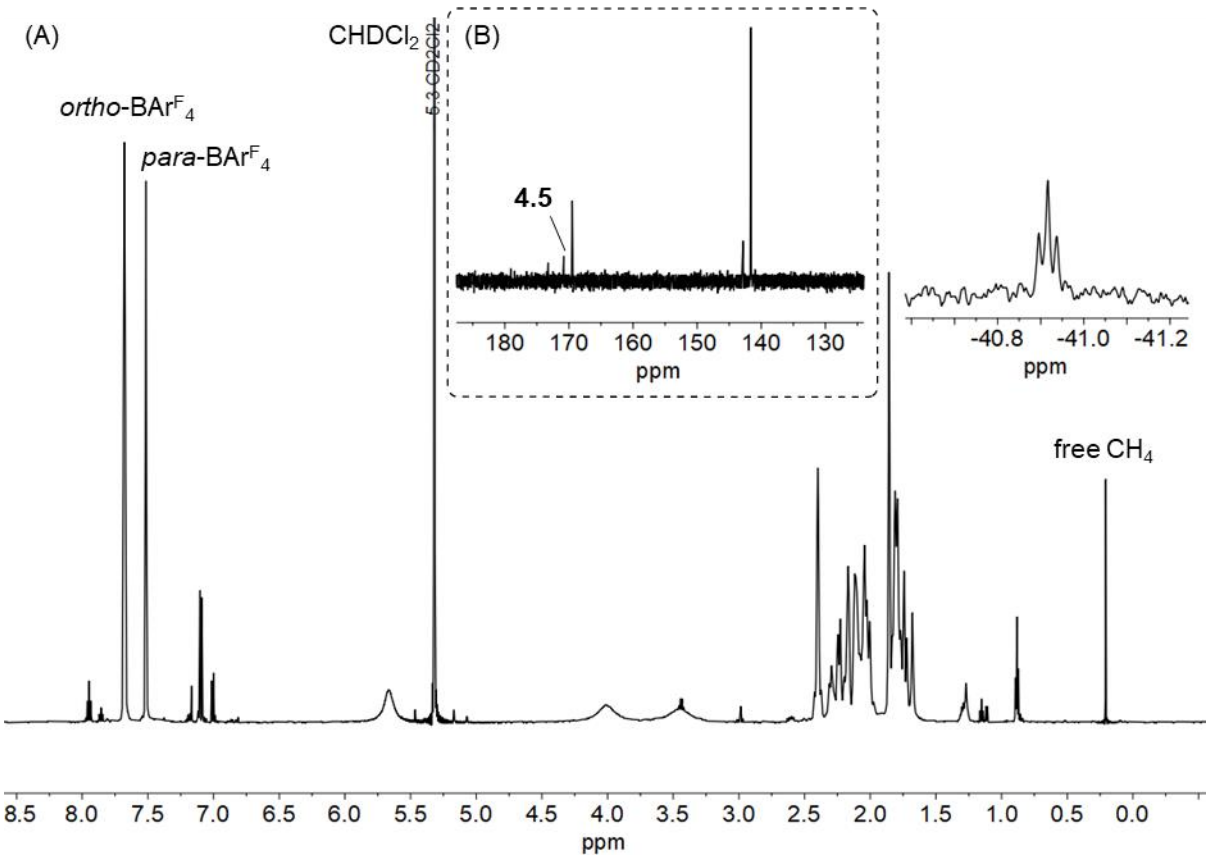

Figure 4.20 (A) The ^{1}H (500 MHz) and (B) ^{31}P{^{1}H} (202 MHz) NMR spectra illustrating the partial decomposition of the dissolved ensemble of polymorphs *α*-**4.5** and *β*-**4.5** after 20 hours at room temperature (CD_2Cl_2, 298 K). Inset highlights the hydride region of the ^{1}H spectrum.

The mixture of decomposition products formed from the dissolved ensemble of polymorphs *α*-**4.5** and *β*-**4.5** at 298 K includes [(**L2**)Ir(H)(Cl)][BAr^F_4]. This is evident by the observation of a new hydride peak at δ –40.92 and by picking out a crystal of [(**L2**)Ir(H)(Cl)][BAr^F_4] from a solid mixture formed from the layering of the CD_2Cl_2 solution with hexane. The chloride ligand has an occupancy of 0.9, suggesting that it has positional disorder between the position *trans* to the nitrogen of ligand **L2** and *trans* to the vacant site, the latter of which can also be modelled with an occupancy of 0.1 (Figure 4.21). Only one hydride signal is observed in the solution ^{1}H NMR (CD_2Cl_2) spectrum, at a shift (δ –40.92) typical of a hydride ligand *trans* to a vacant site and similar to [(^{Ad}PCP)Ir(H)(Cl)] (δ –43.94),[12], suggesting that the minor complex (Cl') is either in too low occupancy to be observed by NMR spectroscopy or the crystal measured is not representative of the bulk.

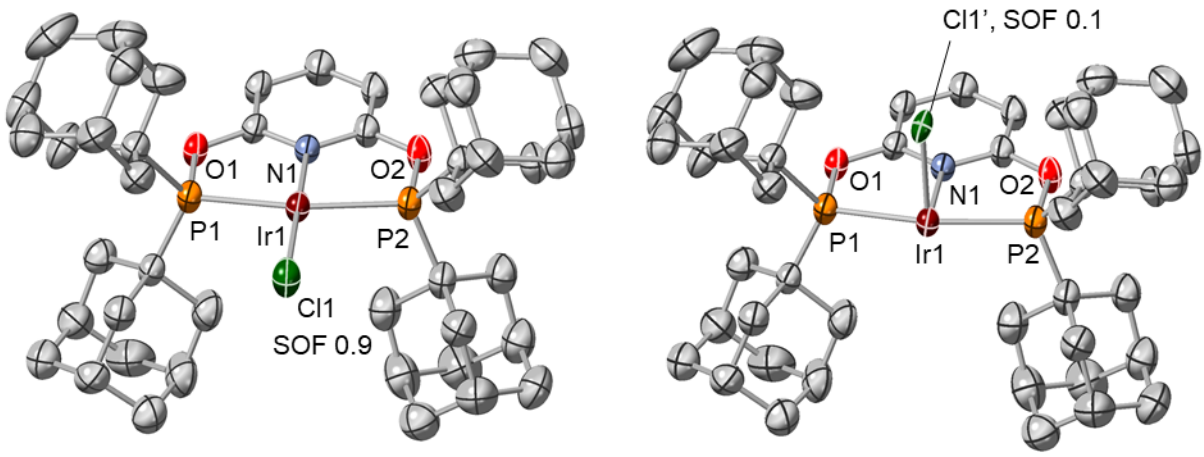

Figure 4.21 The molecular structure of the isolated cation of [(**L2**)Ir(H)(Cl)][BAr^F_4], showing the two different positional isomers of the chloride ligand. Displacement ellipsoids are set at 50% probability. Hydrogen atoms and [BAr^F_4]$^-$ anion are excluded for clarity. Select bond distances (Å): Ir1–Cl1, 2.323(4); Ir1–Cl1', 2.400(1), Ir1–P1, 2.302(3); Ir1–P2, 2.293(3); Ir1–N1, 2.039(5). Select bond angles (°): P1–Ir1–P2, 162.109(2). SOF = Site Occupancy Factor.

To explore the site exchange between the hydride and methyl protons of complex **4.5**, a series of low temperature quantitative 1D EXSY NMR experiments (CD_2Cl_2, T = 178, 183, 193, 198, 203, 208, 213 K) with different mixing times (d_8) and temperatures were conducted (experimental section 4.8.9, Table 4.1). The hydride ligand (δ –40.91) was selectively excited, resulting in an exchange peak observed at δ 1.81 which corresponds to the methyl protons (Figure 4.22 A). No evidence of exchange with the adamantyl ligands or phosphine backbone was observed. The relative integrals of the excitation and exchange peaks were measured at different mixing times, and the resulting rate constants were calculated for each temperature. The rate constants were plotted using the Eyring equation to give an enthalpy ($\Delta H^‡$) of 42.6 ± 0.9 kJ mol^{-1} and entropy ($\Delta S^‡$) of 0.3 ± 0.9 J K^{-1} mol^{-1} (Figure 4.22 B). The $\Delta S^‡ \approx 0$ term indicates that the reductive coupling of methane is likely intramolecular, rather than a dissociative process for which a positive entropy value would be expected. The transition state energy barrier ($\Delta G^‡_{168\,K}$) of site exchange was calculated using the $\Delta H^‡$ and $\Delta S^‡$ values to be $\Delta G^‡_{168\,K}$ = 42.6 ± 0.9 kJ mol^{-1}, slightly higher than that of complex **1.50** which is $\Delta G^‡_{168\,K}$ = 38.9 ± 1.2 kJ mol^{-1} at 168 K.[1] The site exchange, combined with the variable temperature NMR spectra of complex **4.5**, suggests that a *σ*-methane intermediate is being rapidly and reversibly

formed in solution as described *vide supra* (Figure 4.19), similar to that outlined for complex **1.50**.

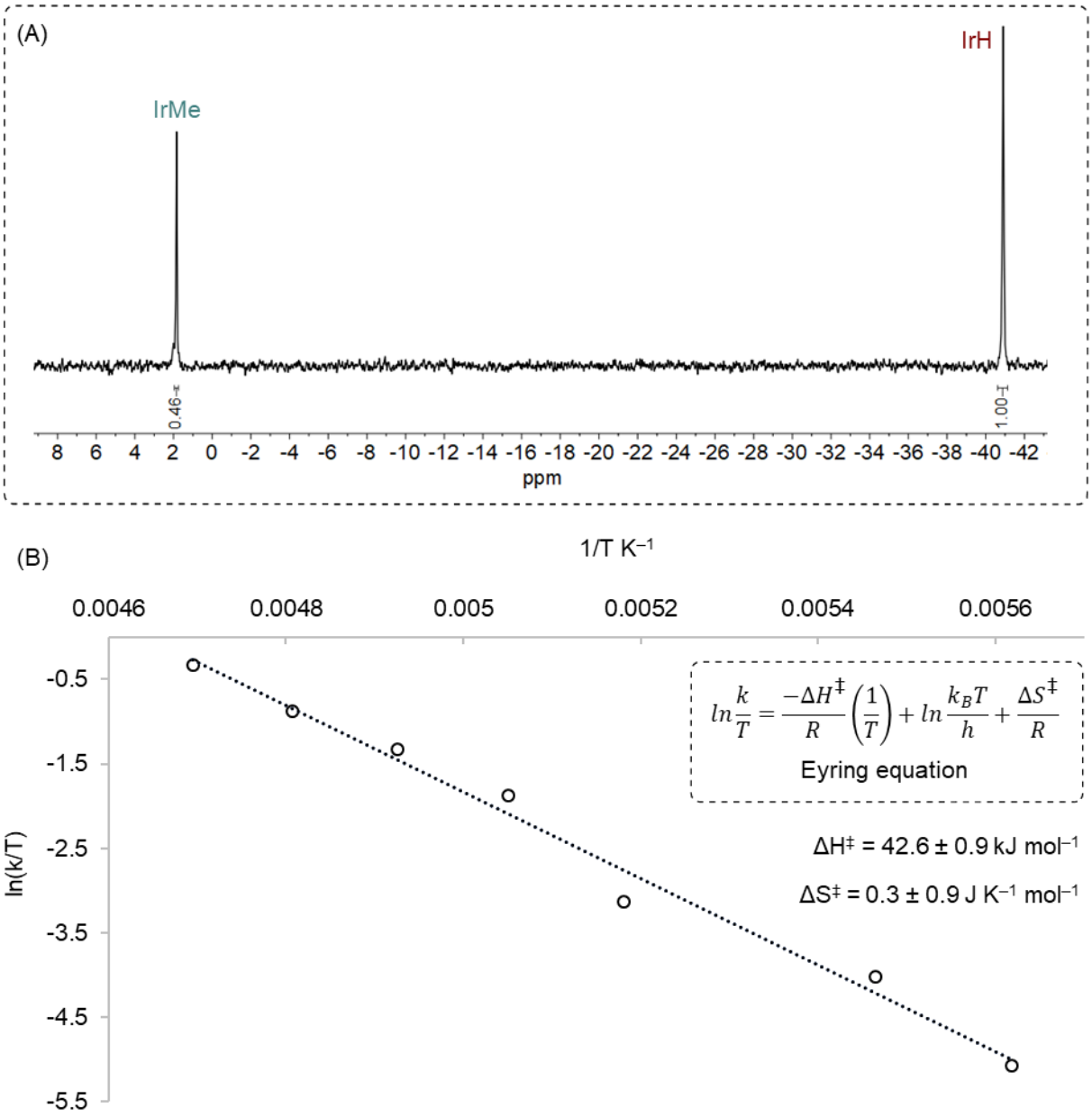

Figure 4.22 (A) Example ^{1}H EXSY NMR spectrum of the dissolved ensemble of polymorphs *α*-**4.5** and *β*-**4.5** (0.05 s mixing time, excitation at δ –40.91, 400 MHz, CD_2Cl_2, 193 K). (B) The Eyring plot of the ^{1}H EXSY NMR data of complex **4.5** (T = 178, 183, 193, 198, 203, 208, 213 K).

At 193 K, two sets of peaks are observed in the ^{31}P{^{1}H} SSNMR spectrum of the ensemble of polymorphs *α*-**4.5** and *β*-**4.5**, centred at δ 175.3 and 170.0 (Figure 4.23), which likely manifest as broad tightly coupled AB doublets due to *trans* ^{31}P coupling of the inequivalent phosphorus

groups. Two sets of peaks are observed due to the crystallographically inequivalent phosphorus environments of the two distinct crystal morphologies of complex **4.5**, *α*-**4.5** and *β*-**4.5**. Consistent with this interpretation, in solution only one peak is observed at δ 172.6 at 193 K. Upon warming in the solid state, the peaks appear to converge at δ 173.5 at 298 K, similar to the shift observed in solution at 298 K (δ 173.2), and continue to shift to δ 174.1 at 353 K. The two peaks reappear upon cooling back to 193 K. These changes are likely due to the temperature affecting the chemical shift which causes the peaks corresponding to the two polymorphs to be observed at coincident chemical shifts at higher temperatures.

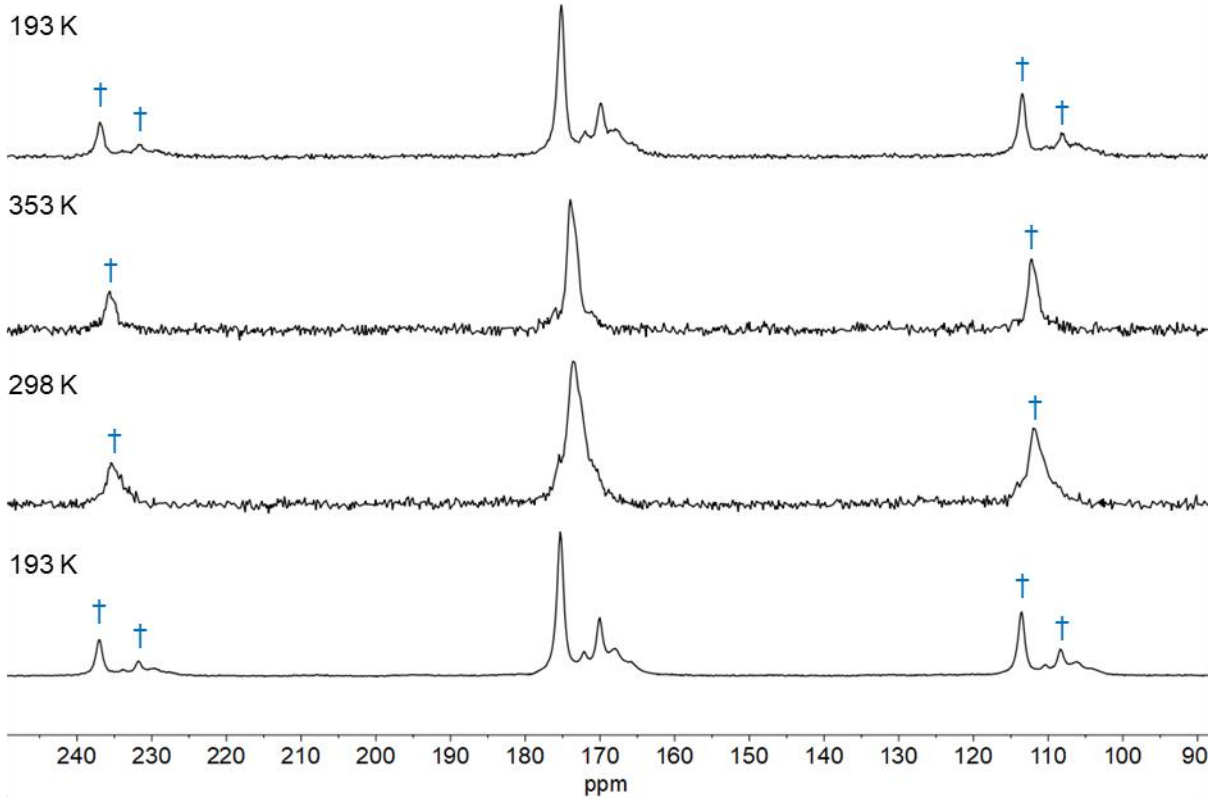

Figure 4.23 The variable temperature solid-state $^{31}P\{^{1}H\}$ CP MAS NMR spectrum of complex **4.5** (162 MHz, 10 kHz spin rate). † Denotes spinning sidebands.

In the $^{13}C\{^{1}H\}$ SSNMR spectrum of the ensemble of polymorphs *α*-**4.5** and *β*-**4.5**, two broad signals at δ –19.4 and –31.1 (Figure 4.24) are assigned to the methyl carbon due to the two distinct crystal morphologies. Only one peak is observed at the frequency averaged position of δ –26.0 in the corresponding solution (CD_2Cl_2, 193 K) NMR spectrum. No peaks were observed in the negative region above 273 K, similar to the solution-state disappearance of

the hydride and methyl environments in the ^{1}H NMR (CD_2Cl_2) spectrum, suggesting that the transient *σ*-methane complex is reversibly formed in the solid state, although no new peak is observed even at 353 K in the ^{13}C SSNMR spectrum (Figure 4.24 B). The peaks at δ –19.4 and –31.1 reappear upon cooling back to 193 K, giving validity to their existence and linking with the ^{31}P{^{1}H} SSNMR behaviour. An unknown peak at δ 65.8 is also observed in the ^{13}C{^{1}H} SSNMR spectrum at all temperatures, although this is not observed in the solution ^{13}C{^{1}H} NMR (CD_2Cl_2) spectrum of the same material at 193 K. Future work includes repeating the ^{13}C{^{1}H} SSNMR experiment to see if the peak at δ 65.8 remains.

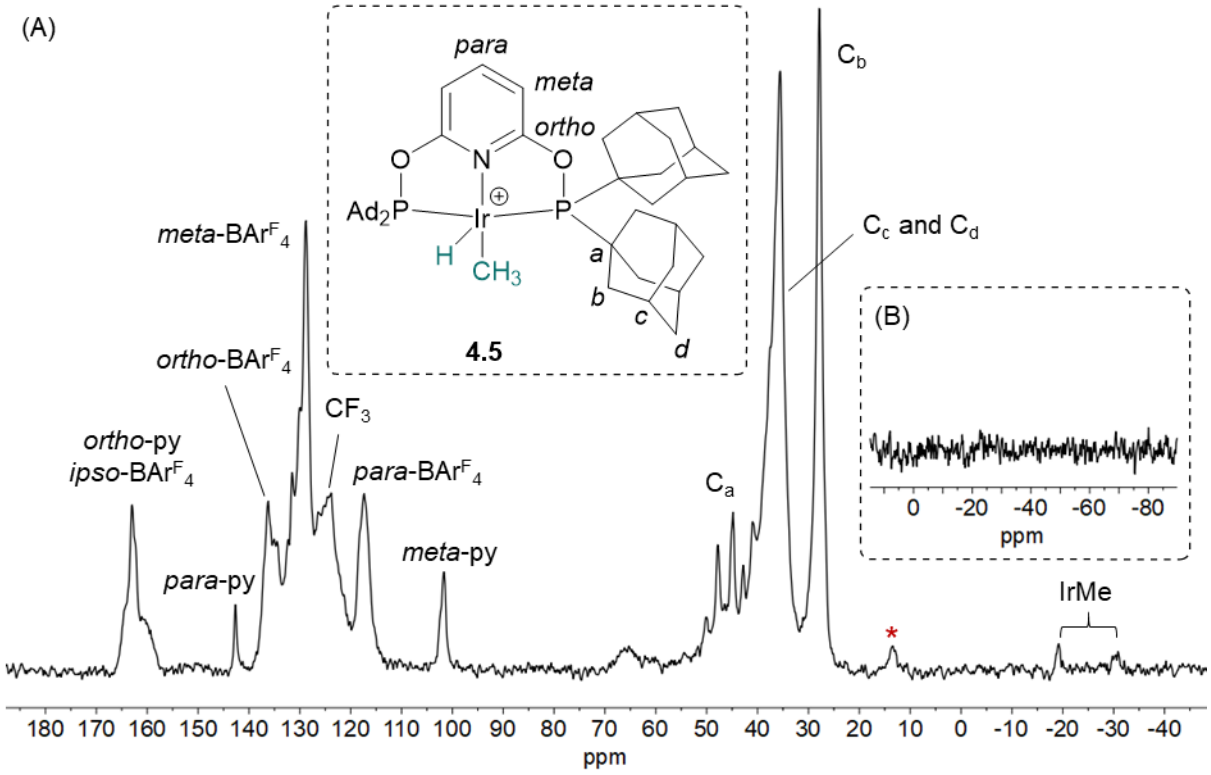

Figure 4.24 (A) The solid-state ^{13}C{^{1}H} CP MAS NMR spectrum of the ensemble of polymorphs *α*-**4.5** and *β*-**4.5** (100 MHz, 10 kHz spin rate, 193 K). * Denotes lattice hexane. (B) The negative region of the ^{13}C{^{1}H} CP MAS NMR spectrum at 353 K.

The presence of two polymorphs, with analogous solid-state bond metrics, and similar solution-state behaviour, demonstrates that complex **4.5** thus far acts similarly to the [(^{tBu}PONOP)Ir(Me)(H)][BAr$^{F}_4$] (**1.50**) analogue. Both complexes undergo rapid and reversible formation of a *σ*-methane intermediate and lose methane in solution. Therefore, further

reactivity of complex **4.5** was subsequently explored (*vide infra*) to probe the formation of the proposed 14 electron intermediate.

4.5 C–H activation of 1,2-difluorobenzene with complex 4.5

The activation of fluoroarenes using iridium pincer complexes has previously been investigated, and is proposed to occur *via* transient 14 electron iridium(I) intermediates similar to that targeted in this chapter.[38-40] For example, exposure of [(^{tBu}PCP)Ir(CO)] (^{tBu}PCP = 2,6-(P^{t}Bu$_2$CH$_2$)$_2$C$_6$H$_3$) to UV light in a closed system forms [(^{tBu}PCP)Ir(Ar)(H)(CO)] (Ar = $C_6H_3F_2$) in 1,2-difluorobenzene solution. This does not occur in the absence of UV light, due to photolysis being required to generate the highly reactive 14 electron iridium(I) intermediate [(^{tBu}PCP)Ir] *via* loss of CO. [(^{tBu}PCP)Ir] then undergoes C–H activation of 1,2-difluorobenzene and re-coordinates the CO.[41]

It was hypothesised that the C–H bond activation of 1,2-difluorobenzene with complex **4.5** to form [(**L2**)Ir(Ar)(H)][BAr$^F_4$] (**4.6**, Ar = $C_6H_3F_2$), might provide insight into the feasibility of forming the proposed 14 electron intermediate, [Ir], following methane loss in solution (Scheme 4.11).

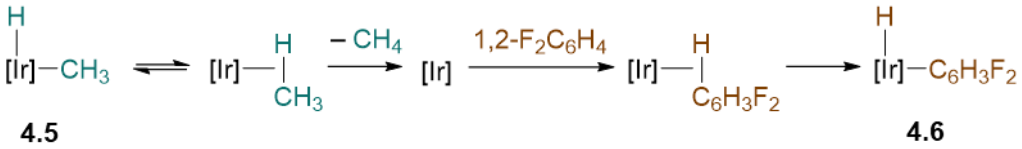

Scheme 4.11 Proposed activation of 1,2-difluorobenzene by complex **4.5**. [Ir] = [(**L2**)Ir][BAr$^F_4$].

Complex **4.6** is easily accessed from the dissolution of the ensemble of polymorphs *α*-**4.5** and *β*-**4.5** in 1,2-difluorobenzene within 24 hours at 298 K (Scheme 4.12). The layering with 1,2-difluorobenzene/hexane at room temperature afforded orange crystals of complex **4.6** upon diffusion.

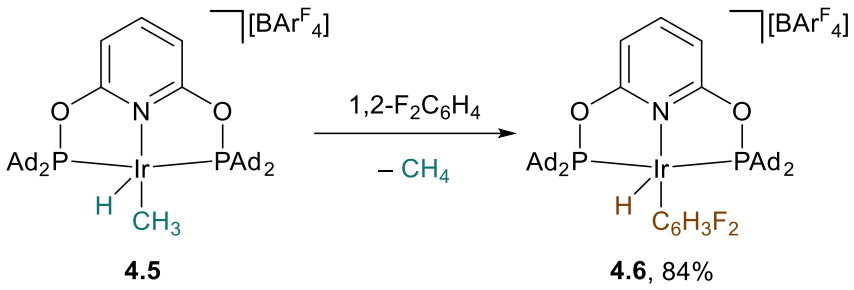

4.5 **4.6**, 84%

Scheme 4.12 The synthetic route to complex **4.6**.

Complex **4.6** crystallises in the space group $P\bar{1}$. The structure displays a pseudo square planar geometry around the iridium(III) centre with an P1–Ir1–P2 angle of 160.120(8) ° and the aryl ring of the 1,2-difluoroarene orthogonal to the pyridine backbone (Figure 4.25 A). The Ir1–C1 bond distance of 2.059(3) Å is similar to [(^{tBu}PONOP)Ir(Ph)(H)][BAr$^F_4$] (2.05(1) Å).[1] The only other crystallographically characterised complex of an activated 1,2-difluorobenzene iridium(III) complex is [(^{tBu}PCP)Ir(Ar)(H)(CO)] which has an Ir1–C1 bond distance of 2.150(2) Å,[41] longer than complex **4.6**. The Ir–P bond lengths of 2.302(1) and 2.296(1) Å are slightly longer than complex *α*-**4.5** (2.280(1) and 2.281(1) Å, whilst the Ir–N distance of complex **4.6** (2.085(2) Å) is the same within error of complex *α*-**4.5** (2.094(3) Å). The aryl ring lies within the cleft of two of the [BAr$^F_4$]$^-$ anion aromatic rings, with distances between the proton in the *para* position to the iridium centre and the centroids of the [BAr$^F_4$]$^-$ aromatic rings (H4–Centroid(C52···C57) and H4–Centroid(C60···C65)) of 2.711(1) and 2.817(2) Å respectively (Figure 4.25 B). The hydride ligand could not be located in the electron density map of complex **4.6**. Two fractional 1,2-difluorobenzene molecules (0.7 and 0.9 occupancy) are also present within the lattice.

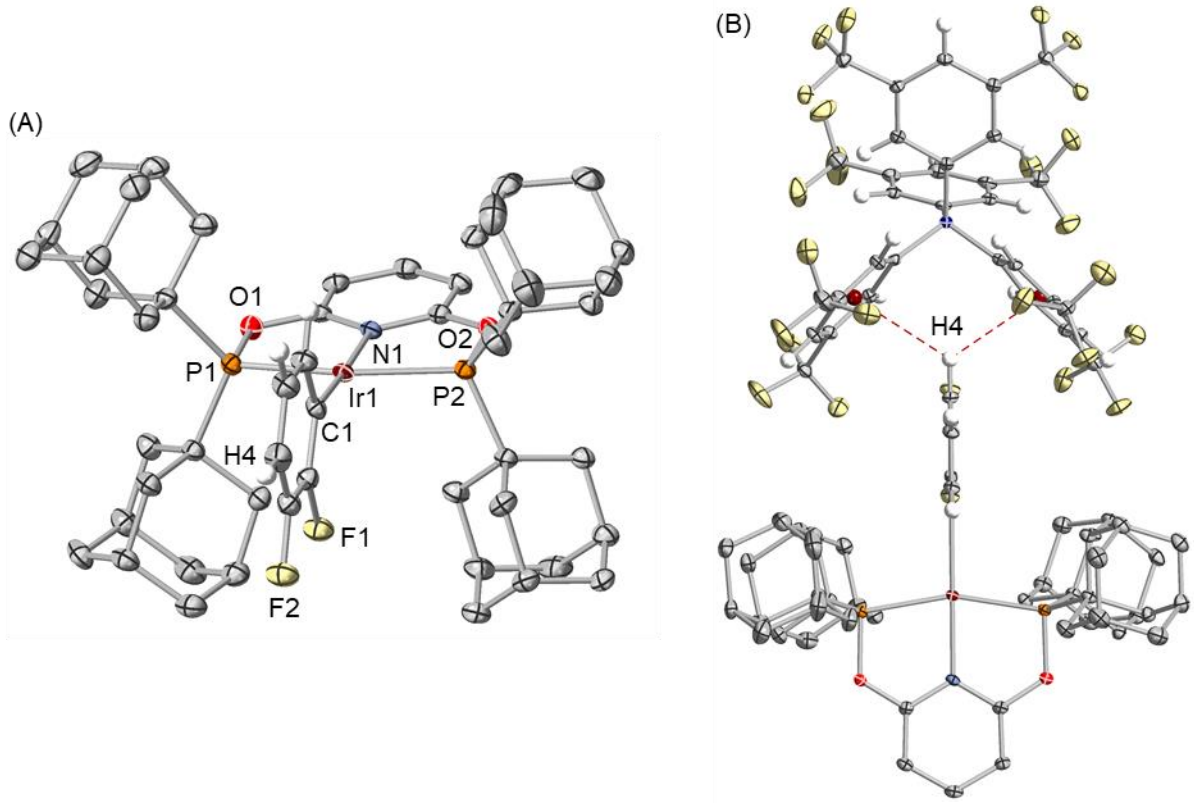

Figure 4.25 (A) The molecular structure of the isolated cation of complex **4.6**. Displacement ellipsoids are set at 50% probability. Hydrogen atoms, lattice solvent and $[BAr^{F}_{4}]^{-}$ anion are excluded for clarity. Select bond distances (Å): Ir1–C1, 2.059(3); Ir1–P1, 2.302(1); Ir1–P2, 2.296(1); Ir1–N1, 2.085(2); (H4–Centroid(C52···C57), 2.711(1); H4–Centroid(C60···C65)), 2.817(2). Select bond angles (°): P1–Ir1–P2, 160.120(8). (B) An alternative view of complex **4.6**, showing the aryl ligand situated within the cleft of the $[BAr^{F}_{4}]^{-}$ aromatic rings.

The ^{1}H NMR (CD_2Cl_2, 298 K) spectrum of the crystals of complex **4.6** (Figure 4.26) shows a triplet ($^{3}J_{HH}$ = 8.1 Hz) at δ 7.98 (1H) corresponding to the *para*- position of the pyridine ring. Multiple peaks are observed at δ 7.19–6.85 (8H) for the overlapping signals of the *meta*-py proton, the protons of the 1,2-$F_2C_6H_3$ ligand and the two lattice 1,2-difluorobenzene molecules (0.7 and 0.9 occupancy). The *ortho*- and *meta*-BAr^{F}_{4} protons are observed as singlets at δ 7.72 (8H) and 7.55 (4H) respectively. The adamantyl protons are observed as overlapping signals at δ 2.04–1.75 (60H), similar to that of complex **4.5** at 193 K. Two hydride signals are observed as broad singlets at δ –38.28 (0.7H) and –41.54 (0.3H) at 298 K, rather than a single environment which would be expected. These two signals lie within the region typically associated with hydrides *trans* to a vacant site,[33, 34] and reflect the different non-equilibrating orientations of the 1,2-difluoroarene ring. This is not unusual for iridium(III) difluoroarene

complexes, as the similar complex [(^{tBu}PCP)Ir(H)($C_6H_3F_2$)(CO)] also displays two hydride signals in the ^{1}H NMR spectrum at δ –8.88 and –9.66 and two signals in the ^{31}P{^{1}H} NMR spectrum at δ 54.7 and 52.2 due to the restricted rotation between rotamers.[41] Although only one signal is observed in the solution ^{31}P{^{1}H} NMR (CD_2Cl_2) spectrum of complex **4.6** at δ 170.7, it is broad (fwhm = 147 Hz) likely due to the two different ^{31}P environments. Only one orientation is observed for the well-ordered 1,2-difluorobenzene ring in the SCXRD structure of complex **4.6**, similar to [(^{tBu}PCP)Ir(H)($C_6H_3F_2$)(CO)], suggesting that one orientation is preferred when slowly crystallised on the laboratory timescale (~72 hours), as redissolution of this crystalline material gives the same two rotamers in the resulting NMR spectrum. At 193 K, the hydride ligand signals sharpen into two triplets at δ –38.39 (0.7H) and –41.48 (0.3H) with $^2J_{HP}$ coupling constants of 11.3 and 10.9 Hz respectively, similar to the hydride observed at δ –40.91 ($^2J_{HP}$ = 12 Hz) in the ^{1}H NMR spectrum of complex **4.5** at 193 K. These triplet signals collapse into singlets upon ^{31}P decoupling.

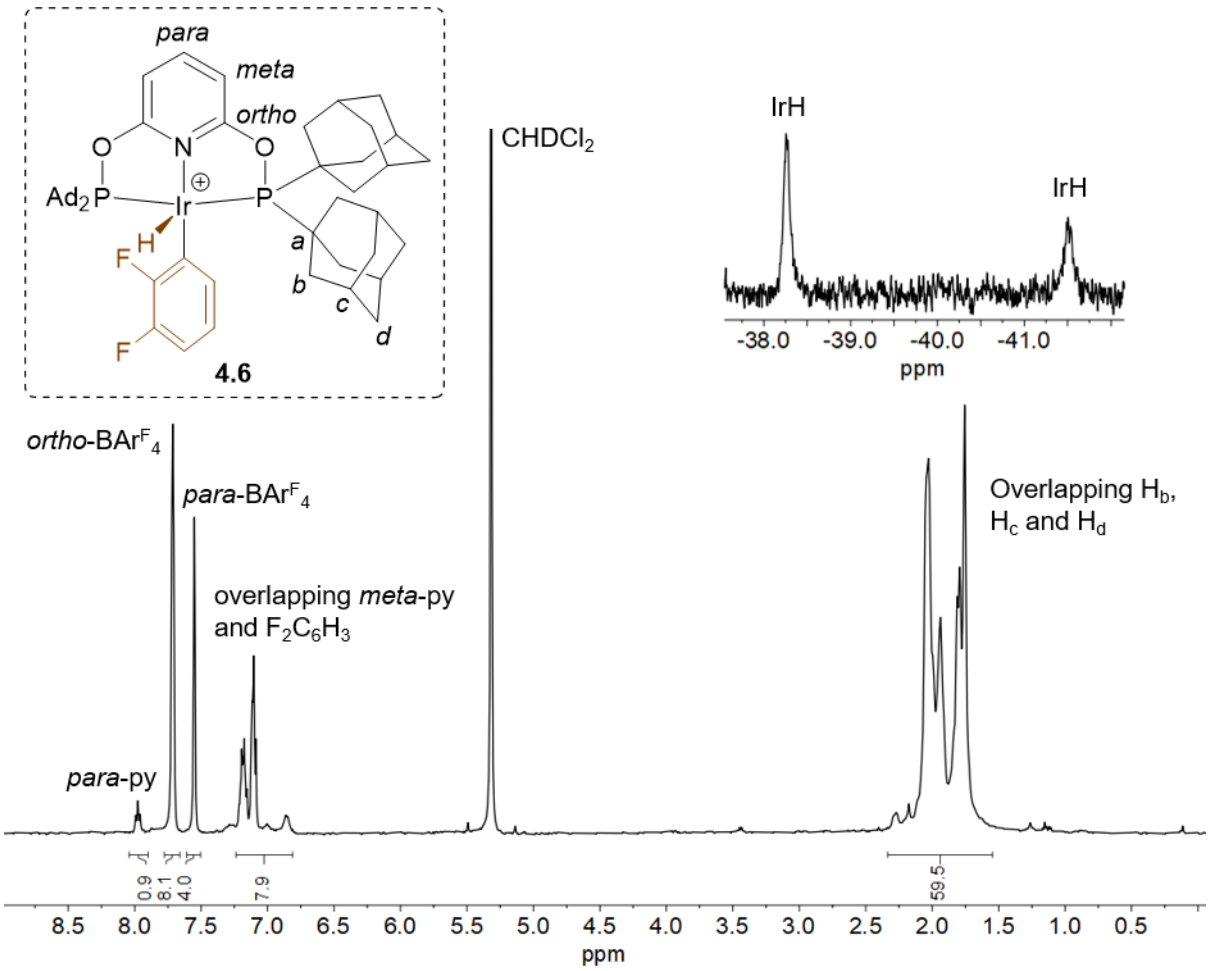

Figure 4.26 The ^{1}H NMR spectrum of complex **4.6** (500 MHz, CD_2Cl_2, 298 K). Inset highlights the hydride environments.

To further explore the observation of two hydride signals, a variable temperature ^{1}H NMR experiment on complex **4.6** was conducted. 1,1,2,2-tetrachloroethane-d_2 was used as the solvent due to its higher boiling point (147 °C)[42] than CD_2Cl_2 (40 °C)[42] thereby enabling measurement at higher temperatures. This revealed that the two hydride signals observed at 193 K broaden as the temperature is increased and disappear at 343 K (Figure 4.27). The peaks are re-established upon cooling back to 193 K, demonstrating that the complex has not changed upon heating. The disappearance of the two signals is consistent with the orientations of the 1,2-difluoroarene aryl ring becoming equivalent at high temperatures so that the peaks become one signal at the frequency averaged position. However, a new signal did not appear within the temperature upper stabilisation limit of the NMR spectrometer (368 K), demonstrating that the exchange is slow even at 368 K. Whilst the equilibration of the

hydride signals could be due to rotation of the aryl ring, the hydride peak pattern and its behaviour at different temperatures is similar to that observed for complex **4.5.** Therefore this could also indicate the formation of a transient *σ*-fluoroarene intermediate, similar to the *σ*-methane intermediate described *vide supra* for complex **4.5**. Future work includes investigating this further by using DFT to calculate the barrier to rotation, as well as deuteration experiments to monitor any possible isotopic perturbation of equilibrium.

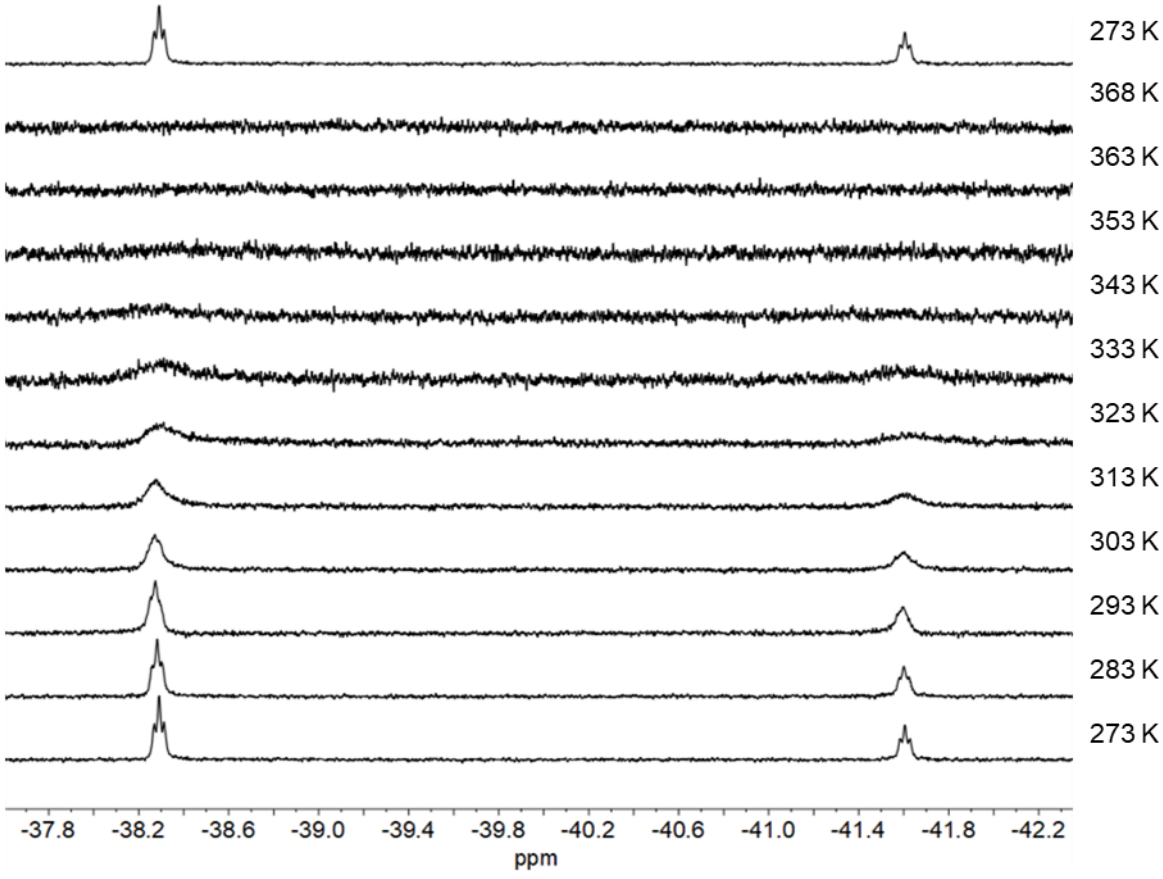

Figure 4.27 The hydride region of the stacked variable temperature ^{1}H NMR spectra of complex **4.6**. (500 MHz, 1,1,2,2-$Cl_4C_2D_2$). The top spectrum shows the sample cooled back down to 273 K from 368 K, showing that the sample remains unchanged from heating.

With the synthesis and characterisation of complex **4.6** established, the conversion of complex **4.5** to complex **4.6** was monitored using quantitative $^{31}P\{^{1}H\}$ NMR spectroscopy in 1,2-difluorobenzene at different temperatures (T = 298, 303, 308, 313 K). The resulting time course data were modelled using first order reaction kinetics in the kinetic modelling software COPASI[43] to provide the reaction rate constants (Figure 4.28; experimental section 4.8.10,

Table 4.2). An Eyring plot was generated which gave an activation enthalpy of 114.6 ± 1.2 kJ mol^{-1} and an activation entropy of 34.9 ± 0.3 J K^{-1} mol^{-1} (Figure 4.29 A). The transition state energy barrier ($\Delta G^{\ddagger}_{298\ K}$) was calculated to be $\Delta G^{\ddagger}_{298\ K}$ = 104.2 ± 1.2 kJ mol^{-1} at 298 K. The analogous experiment of the conversion of complex **1.50** to [(^{tBu}PONOP)Ir(Ar)(H)][BAr$^{F}_{4}$] was also carried out (see experimental section 4.8.10, Table 4.3), and the Eyring plot (Figure 4.29 B) provided an activation enthalpy of 113.4 ± 0.6 kJ mol^{-1} and an activation entropy of 34.7 ± 0.6 J K^{-1} mol^{-1}, which gives a transition state energy barrier of $\Delta G^{\ddagger}_{298\ K}$ = 103.0 ± 0.6 kJ mol^{-1}, similar to that of complex **4.5**. These data demonstrate that the rates of C–H bond activation of 1,2-difluorobenzene are similar for complexes **4.5** and **1.50**. Therefore, thus far the complexes react in the same way in solution, showing that changing the phosphine substituent (Ad, ^{t}Bu) does not have a great effect on solution-state reactivity.

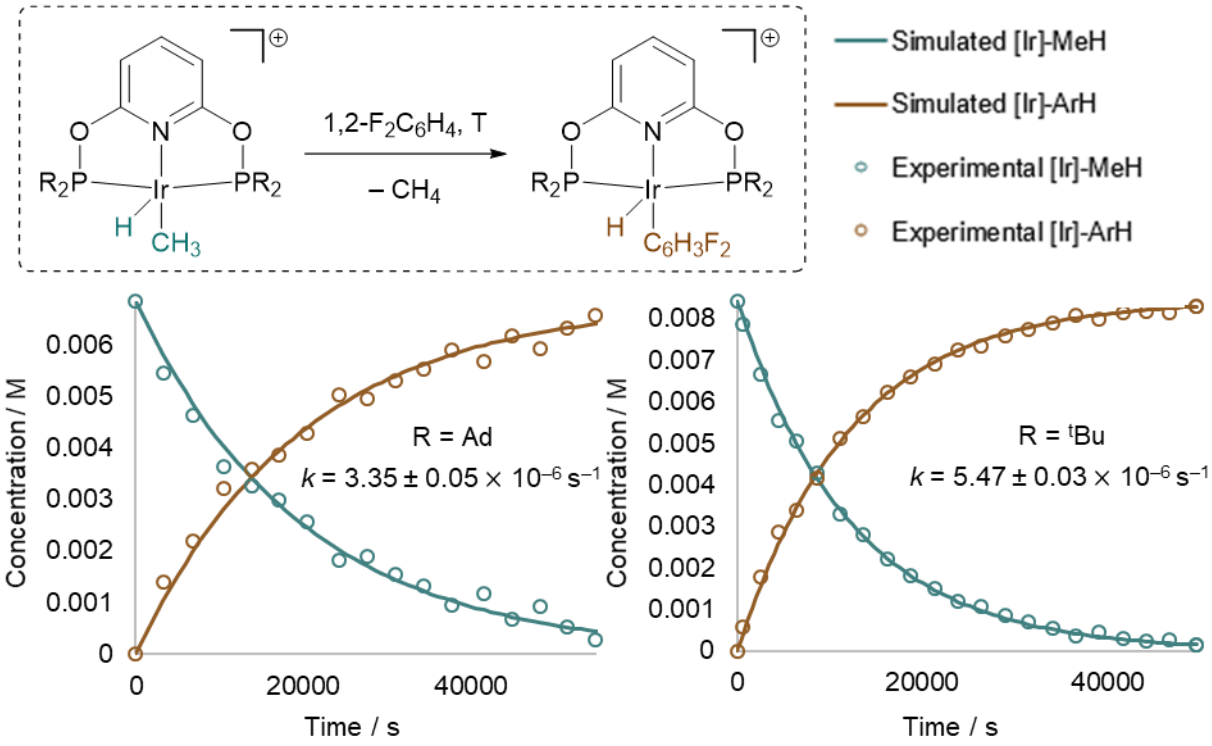

Figure 4.28 Example time-course plots of experimental and simulated data for the conversion of the complex **4.5** to complex **4.6** at 298 K and complex **1.50** to [(^{tBu}PONOP)Ir(Ar)(H)][BAr$^{F}_{4}$] at 298 K by quantitative ^{31}P{^{1}H} NMR spectroscopy. Open circles denote experimental data, solid lines denote simulated data derived from a simple first order process in COPASI. Blue denotes [(R)Ir(Me)(H)][BAr$^{F}_{4}$], brown denotes [(R)Ir(Ar)(H)][BAr$^{F}_{4}$].

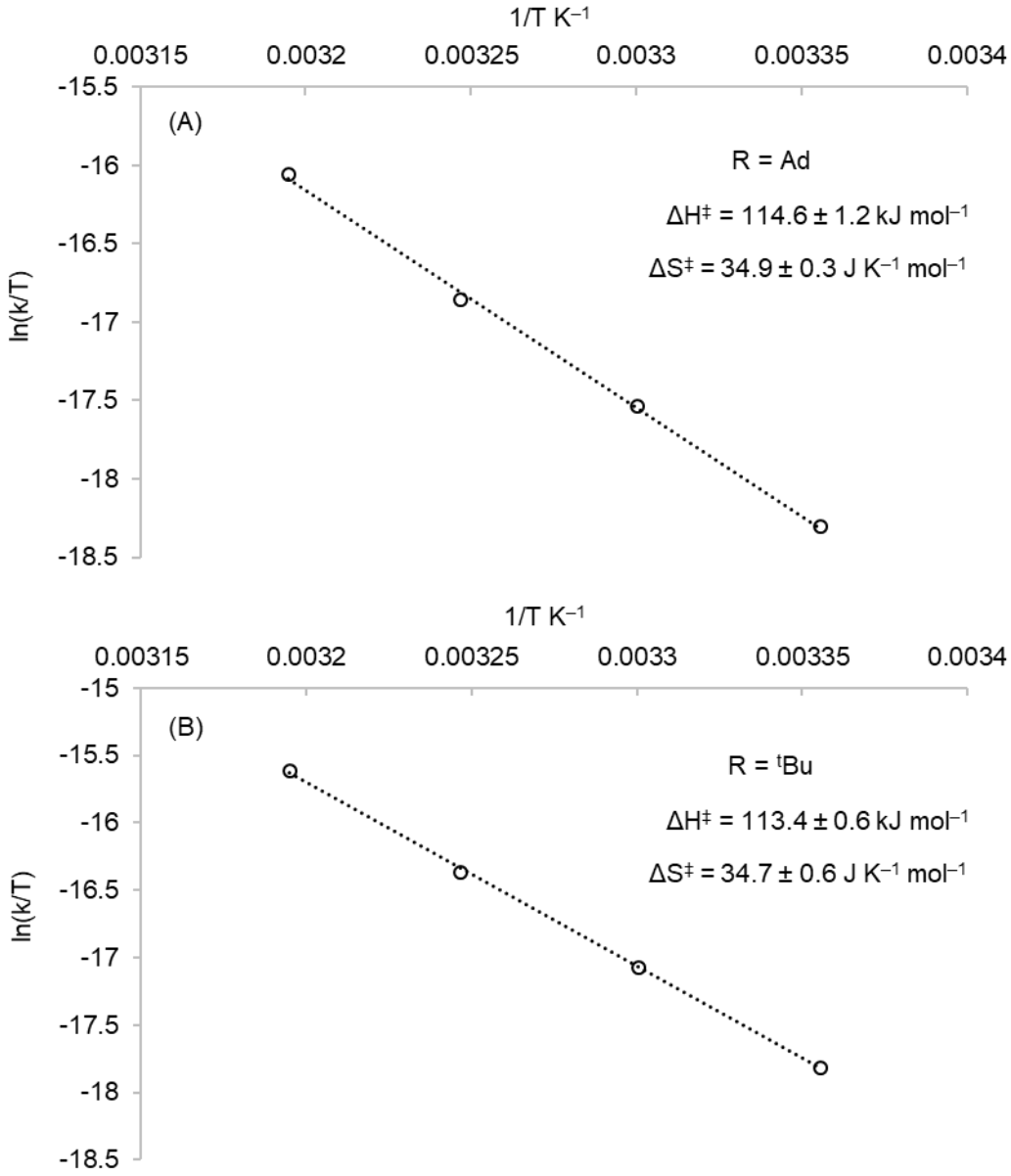

Figure 4.29 The Eyring plot of the conversion of (A) complex **4.5** to complex **4.6** and (B) complex **1.50** to [(^{tBu}PONOP)Ir(Ar)(H)][BAr$^{F}_{4}$] (T = 298, 303, 308, 313 K).

4.6 *In crystallo* chemistry of complex 4.5

As previously discussed, it was hypothesised that ligand **L2** would not cyclometalate to form the complex analogous to the cyclometalated complex **1.53**, which can be accessed from the SC-SC loss of methane from complex **1.50** under high vacuum (5×10^{-5} mbar) at 80 °C for 1-3 days (Scheme 4.13). To investigate the cyclometalation of ligand **L2**, a similar reaction with complex **4.5** was attempted. Crystals of the ensemble of polymorphs *α*-**4.5** and *β*-**4.5** were placed under high vacuum (5×10^{-5} mbar) for 2 days at 80 °C, then CD_2Cl_2 was added for

analysis by NMR spectroscopy at 193 K. The resulting ^{1}H and $^{31}P\{^{1}H\}$ NMR (CD_2Cl_2, 193 K) spectra are identical to those of the dissolved ensemble of polymorphs *α*-**4.5** and *β*-**4.5**, indicating that no reaction has occurred (Scheme 4.13).

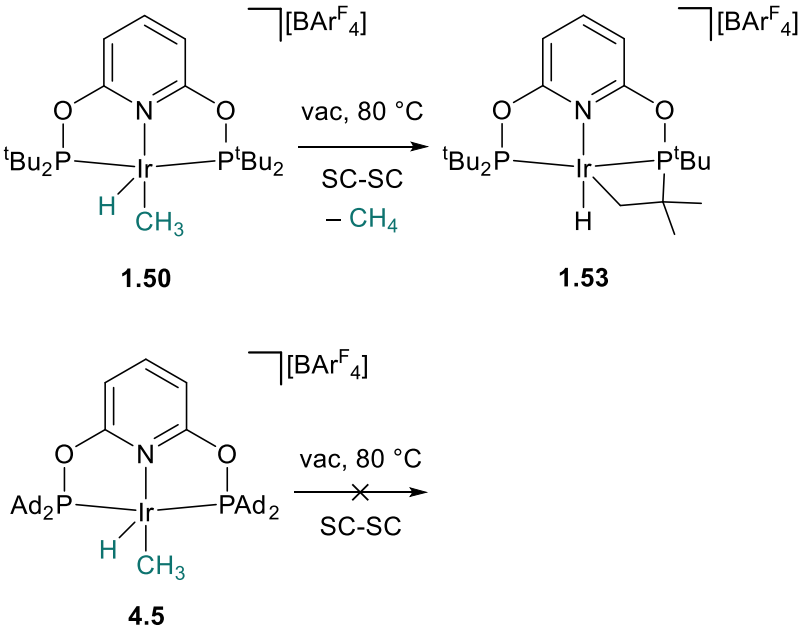

Scheme 4.13 The cyclometalation of complex **1.50** under vacuum at 80 °C, and the attempted cyclometalation of complex **4.5** under the same conditions.

In an attempt to encourage the loss of methane, the reaction was repeated at 120 °C for three days, leading to the formation of several unidentified peaks in the $^{31}P\{^{1}H\}$ NMR (CD_2Cl_2, 193 K) spectrum (Figure 4.30 B), including a peak at δ 193.3 which corresponds to the iridium(III) dihydride complex [(**L2**)Ir(H)$_2$][BAr$^F_4$] (**4.7**, *vide infra*), alongside a major peak (53%) corresponding to unreacted complex **4.5**. In the ^{1}H NMR spectrum (Figure 4.30 A), two new hydride peaks are observed at δ –10.31 (m), –25.51 (t, $^{2}J_{HP}$ = 10.1 Hz), as well as the dominant hydride at δ –40.91 which corresponds to complex **4.5**. The peak at δ –25.51 corresponds to complex **4.7**. The peak at δ –10.31 is at a similar chemical shift to the hydride ligand of the cyclometalated complex **1.53** (δ –9.24),[2] yet only has an integral of 0.06H.

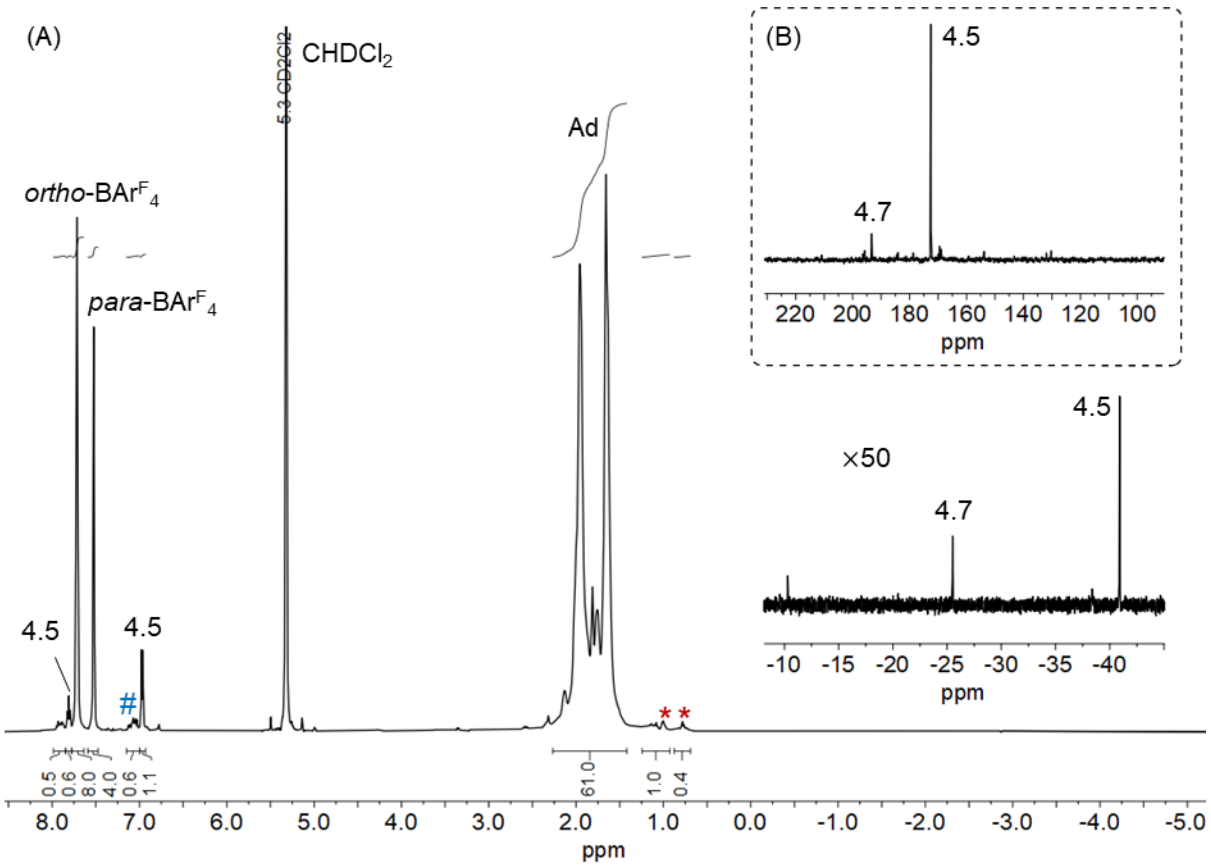

Figure 4.30 (A) The ^{1}H (500 MHz) and (B) ^{31}P{^{1}H} (202 MHz) NMR spectra of the attempted SC-SC reaction of the ensemble of polymorphs *α*-**4.5** and *β*-**4.5** under high vacuum for 3 days at 80 °C (CD_2Cl_2, 193 K). Inset highlights the hydride region of the ^{1}H spectrum, for which the y-gain has been increased ×50.

Although the reaction of complex **4.5** under vacuum at 80 °C for 2 days was carried out using the ensemble of polymorphs *α*-**4.5** and *β*-**4.5**, the structure of polymorph *α*-**4.5** could not be obtained due to a loss of long-range order following exposure to vacuum at 80 °C, likely due to loss of hexane. However, the structure of complex *β*-**4.5** after vacuum at 80 °C (*β*-**4.5b**) could be measured with a slight decrease in crystal quality reflected by larger ADPs, and shows the same cationic structure as complex *β*-**4.5** before exposure to vacuum. The closest Ir···C distance to a C_b adamantyl carbon is 3.3069(307) Å, much larger than that of the cyclometalated Ir–C bond of complex **1.53** (2.04(1) Å),[2] demonstrating that no cyclometalation has occurred. Whilst there is no reaction at the iridium cation, the two molecules of lattice hexane in complex *β*-**4.5** (0.9 and 0.6 occupancy) are no longer present, having been removed under vacuum in a SC-SC manner. Loss of lattice solvent results in a movement of the $[BAr^F_4]^-$

anions and decrease in unit cell volume from 4621 Å^3 to 3720 Å^3. The $[BAr^F{}_4]^-$ anions now form a bicapped square prism with ten $[BAr^F{}_4]^-$ anions encapsulating two crystallographically equivalent cations (Figure 4.31). This is in contrast to the hexagonal prismatic packing arrangement of twelve $[BAr^F{}_4]^-$ anions observed for complex ***β*-4.5** and demonstrates the flexibility of the SMOM anionic framework, as crystallinity is retained during this reordering of $[BAr^F{}_4]^-$ anions. As described in section 1.1.2, lateral movement of $[BAr^F{}_4]^-$ anions have been reported during the reaction of $[(^{iPr}PONOP)Mn(CO)_2(THF)][BAr^F{}_4]$ (**1.32**) with CO to yield $[(^{iPr}PONOP)Mn(CO)_3][BAr^F{}_4]$ (**1.33**),[44] yet this results in fracturing of the crystals so that MicroED techniques were required to obtain the crystal structure, whilst that of complex ***β*-4.5b** could still be measured by SCXRD. No crystals of ***α*-4.5** after vacuum were found during crystal screening, potentially due to the more significant decrease in crystal quality upon loss of lattice solvent.

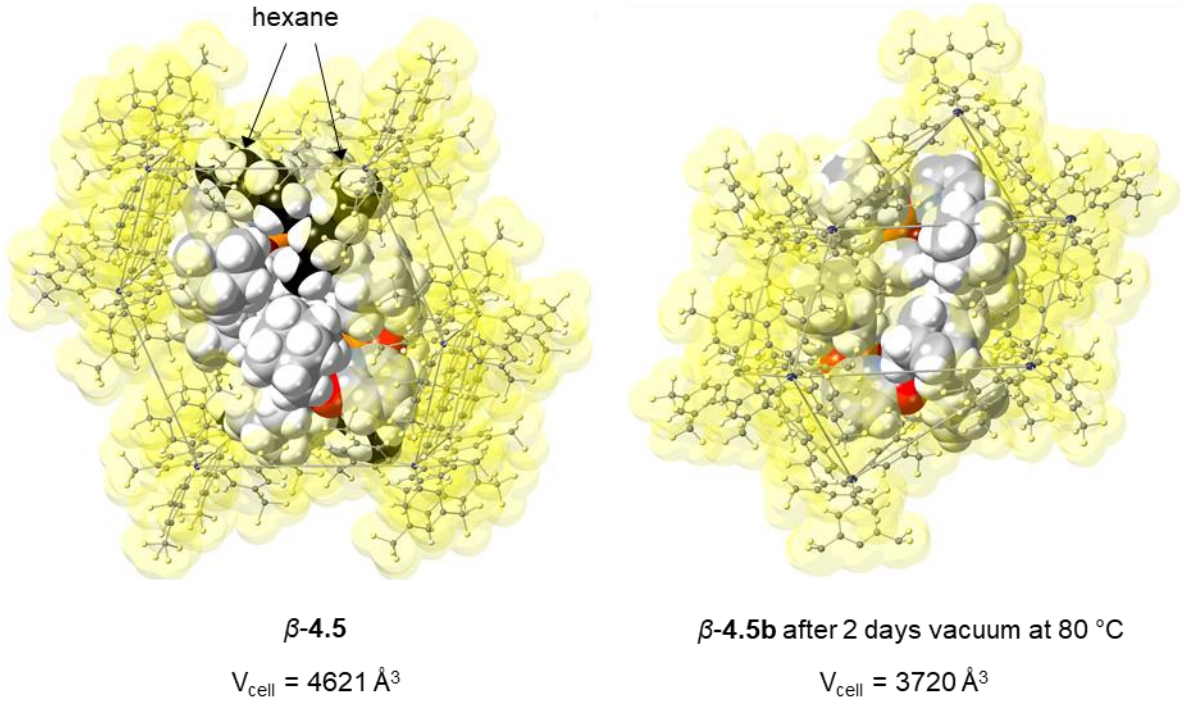

Figure 4.31 The change in the extended solid-state structure of ***β*-4.5** before and after 2 days under vacuum at 80 °C (***β*-4.5b**), showing the change from hexagonal prismatic to bicapped square prismatic arrangements of $[BAr^F{}_4]^-$ anions, and loss of hexane lattice solvent, depicted as Van der Waals radii.

The attempted reactions of the ensemble of polymorphs *α*-**4.5** and *β*-**4.5** under vacuum demonstrate that complex **4.5** does not cleanly cyclometalate even at 120 °C, revealing a stark difference upon switching ^{t}Bu groups for Ad groups. The mechanism of cyclometalation of [(^{tBu}PONOP)Ir(Me)(H)][BAr$^{F}_{4}$] (**1.50**) occurs *via* reductive coupling of methane followed by methane loss as the rate determining step to form the 14 electron [(^{tBu}PONOP)Ir][BAr$^{F}_{4}$], which subsequently cyclometalates to form complex **1.53**.[2] For complex **4.5**, methane loss is likely prevented in the solid state due to the 14 electron [(^{Ad}PONOP)Ir][BAr$^{F}_{4}$], which would be formed following methane loss, being thermodynamically inaccessible owing to the lack of onward reactivity *via* cyclometallation of the adamantyl groups. This is in contrast to the solution-state behaviour of complex **4.5** due to the presence of solvent for onward reactivity (dichloromethane, 1,2-difluorobenzene). Solid-state methane loss might also be hindered by packing effects of the cation, as in both polymorphs *α*-**4.5** and *β*-**4.5** the Ir–C bond of the cations face one another (Figure 4.32), potentially blocking the loss of methane. In contrast, the Ir–C bond of the cations of both polymorphs of the ^{t}Bu analogue complex **1.50** point toward the [BAr$^{F}_{4}$]$^{-}$ anions of the surrounding lattice, leaving space around the methyl ligand to undergo reductive coupling and providing an open route for the methane through the channels provided by the [BAr$^{F}_{4}$]$^{-}$ lattice.

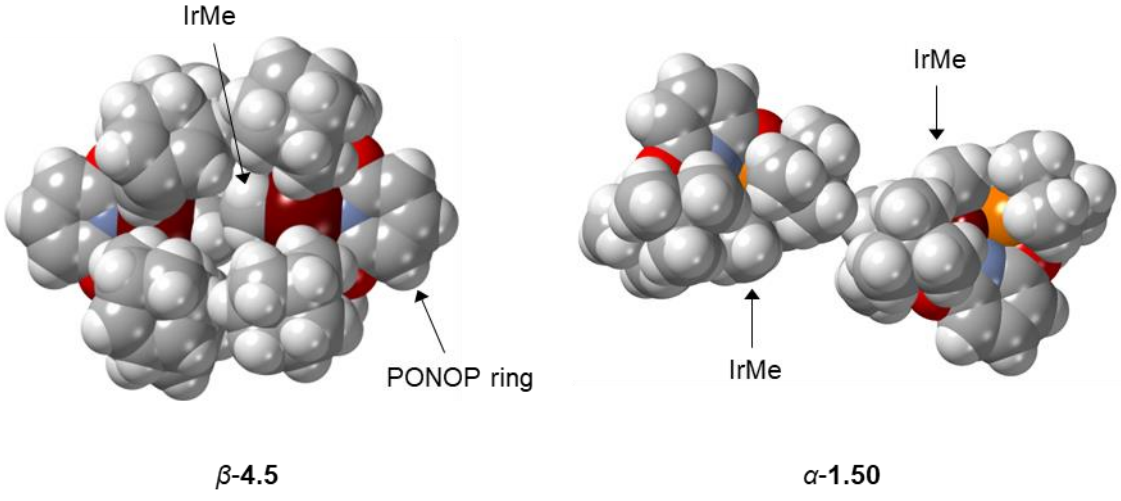

Figure 4.32 A space filling view of the cations of complexes *β*-**4.5** and *β*-**1.50** within the corresponding [BAr$^{F}_{4}$]$^{-}$ lattice. [BAr$^{F}_{4}$]$^{-}$ anions are omitted for clarity.

To probe the importance of methane loss and subsequent cyclometalation on SC-SC reactivity, the reaction of the ^{t}Bu and Ad analogues of [(^{R}PONOP)Ir(Me)(H)][BAr$^{F}_{4}$] with N_2 were compared, beginning with ^{t}Bu. As discussed in section 4.1, it is possible to access [(^{tBu}PONOP)Ir(N_2)][BAr$^{F}_{4}$] (**1.54**) from the cyclometalated complex, **1.53**.[2] Here the synthesis of complex **1.54** from the SC-SC complex **1.50** with N_2 is also presented (N_2 filled glovebox, 80 °C, 10 days). The reaction was carried out in an open flask to prevent back reactivity with methane, and monitored by removing an aliquot of crystals at different timepoints and analysis by quantitative $^{31}P\{^{1}H\}$ NMR (CD_2Cl_2, 193 K) spectroscopy, in a similar manner to how solid-state reaction kinetics have been monitored previously.[45] The reaction was shown to occur *via* the cyclometalated complex **1.50** as an intermediate species, as evident by the distinct signals in the $^{31}P\{^{1}H\}$ NMR spectrum (Figure 4.33) and its temporal profile in the time course plot (Figure 4.34).

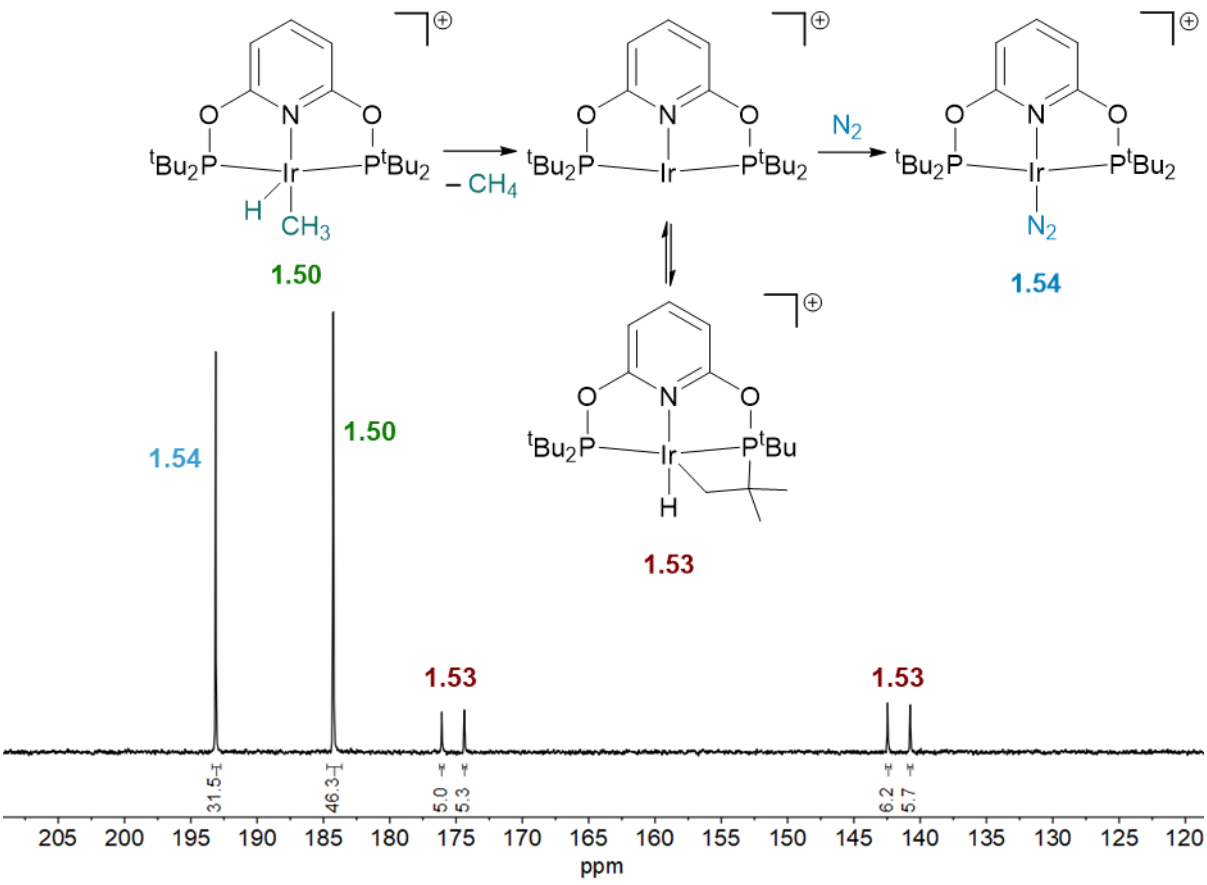

Figure 4.33 An example $^{31}P\{^{1}H\}$ NMR spectrum of the SC-SC reaction of complex **1.50** with N_2 after 48 hours at 80 °C (202 MHz, CD_2Cl_2, 193 K).

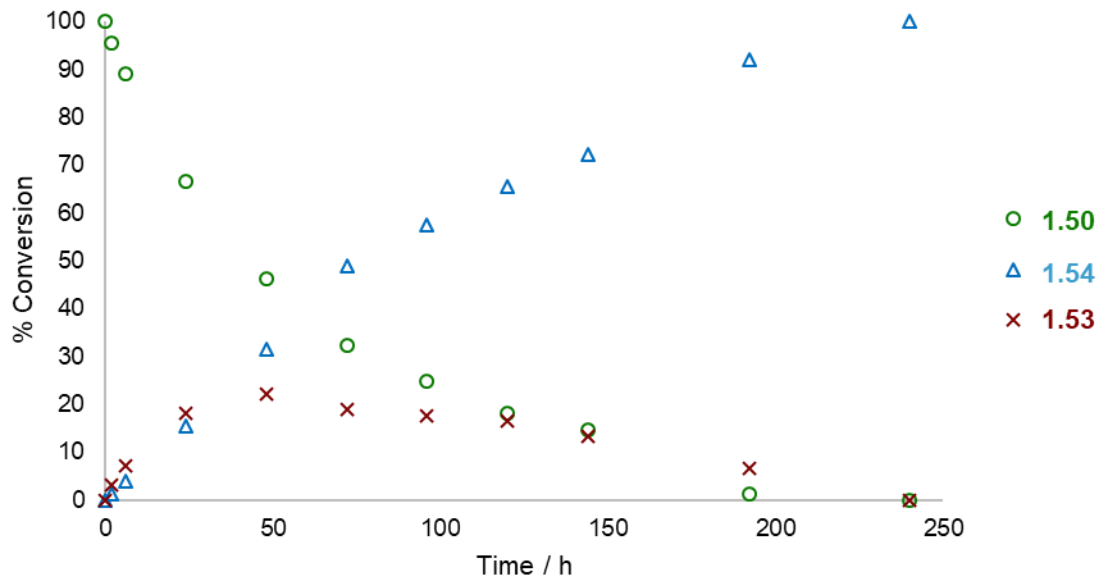

Figure 4.34 The time course profile for the SC-SC reaction of complex **1.50** with N_2 at 80 °C, as measured by quantitative $^{31}P\{^1H\}$ NMR spectroscopy. Green denotes complex **1.50**, red denotes complex **1.53**, blue denotes complex **1.54**.

To compare this reactivity with that of complex **4.5**, the SC-SC reaction of the ensemble of polymorphs *α*-**4.5** and *β*-**4.5** with N_2 (80 °C, 10 days) was carried out. A new peak is observed in the $^{31}P\{^1H\}$ NMR (CD_2Cl_2, 193 K) spectrum at δ 184.4, shifted downfield from complex **4.5** at δ 172.6 (Figure 4.34 A). This was tenuously assigned to the target [(**L2**)Ir(N_2)][BAr^F_4] complex as no other ligand peaks are observed in the ^1H NMR spectrum and the chemical shift change (Δδ = 11.8) is similar to that exhibited between complexes **1.50** and **1.54** (Δδ = 8.8). However, only 30% conversion to the product giving the peak at δ 184.4 was observed even after 10 days at 80 °C, in contrast to the full conversion observed for complex **1.50**. The identity of the peak at δ 184.4 could not be confirmed by SCXRD due to its low occupancy, as the structure was consistent with complex *β*-**4.5**, albeit disordered. Leaving the reaction for one month at 80 °C in a sealed system of N_2 in an attempt to drive the reaction to completion resulted in the formation of several unidentified products observed in the resulting ^1H and $^{31}P\{^1H\}$ NMR spectra (CD_2Cl_2, 193 K, Figure 4.35 B), including only 24% of the product giving the peak at δ 184.4, suggesting that the system is not stable at 80 °C for one month. Considering that complexes **1.50** and **4.5** lose methane at similar rates in the solution-state,

the significantly slower reactivity of complex **4.5** with N_2 compared to complex **1.50** is likely due to complex **4.5** being resistant to cyclometalation.

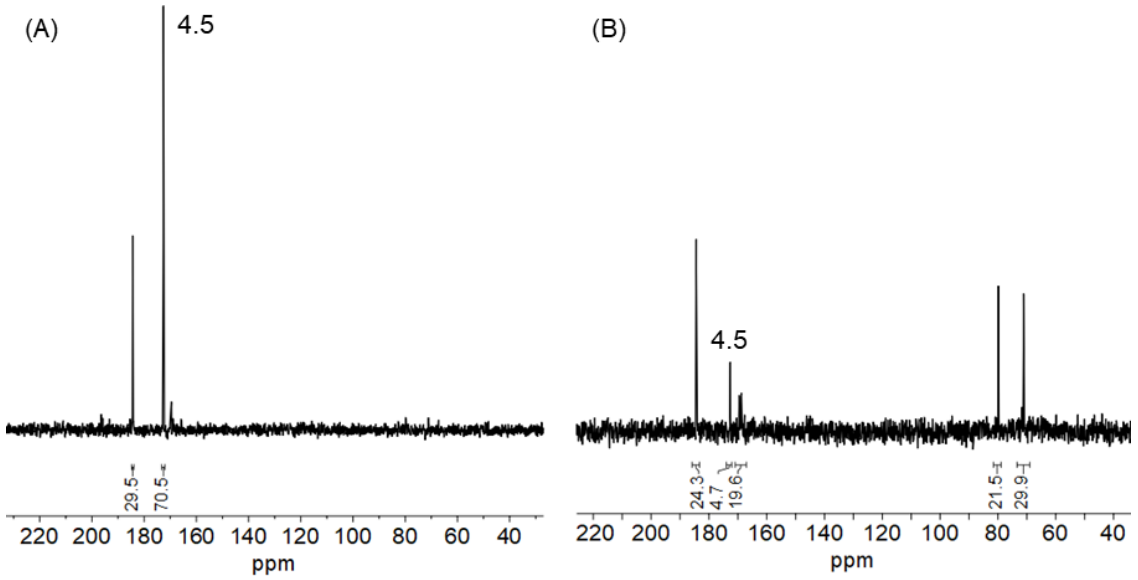

Figure 4.35 The $^{31}P\{^1H\}$ NMR spectrum of the SC-SC reaction of the dissolved ensemble of polymorphs *α*-**4.5** and *β*-**4.5** with N_2 after (A) 7 days and (B) one month at 80 °C (202 MHz, CD_2Cl_2, 193 K).

Given that the ensemble of polymorphs *α*-**4.5** and *β*-**4.5** does not lose methane in the solid state due to steric interactions of the neighbouring cations, it was hypothesised that methane might instead be liberated in a SC-SC manner by the addition of a ligand which would bind *trans* to the hydride ligand and undergo different reactivity, such as H_2 (Scheme 4.14 A). The SC-SC addition of H_2 (4 bar absolute, 10 minutes) to the ensemble of polymorphs *α*-**4.5** and *β*-**4.5** resulted in the successful isolation of [(**L2**)Ir$(H)_2$][$BAr^F{}_4$] (**4.7**, Scheme 4.15 B, Figure 4.36) as orange crystals, in 100% conversion as shown by ^1H and $^{31}P\{^1H\}$ NMR (CD_2Cl_2) spectroscopy following the SC-SC reaction, with an isolated yield of 88%. The full conversion of the ensemble of polymorphs *α*-**4.5** and *β*-**4.5** to complex **4.7** suggest that both polymorphs react, however only one polymorph (*β*-**4.7**) was measured by SCXRD due to time constraints.

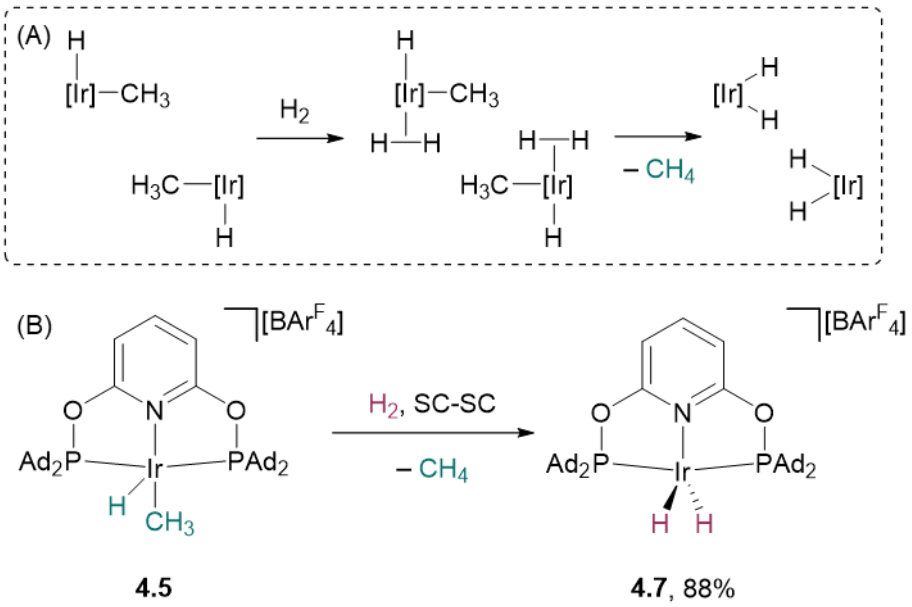

Scheme 4.15 (A) A proposed σ-H_2 intermediate and the dihydride product, postulated to negate steric interactions upon methane loss. [Ir] = [(**L2**)Ir][BAr^F_4]. (B) The SC-SC synthesis of [(**L2**)Ir$(H)_2$][BAr^F_4] (**4.7**).

The hydride ligands of complex *β*-**4.7** (space group $P\bar{1}$) could not be located in the electron density map due to the limitations of the experiment, however the presence of hydride ligands was confirmed by ^{1}H NMR (CD_2Cl_2) spectroscopy following the reaction (*vide infra*). The Ir–P distances (2.289(2), 2.263(3) Å) are within the range of complex *α*-**4.5** (2.2801(10), 2.2811(10) Å), and the P1–Ir1–P2 angle is 161.525(6)°. The Ir1–N1 distance (2.094(5) Å) is also similar to complex *α*-**4.5** (2.0938(26) Å), demonstrating that there is no structural impact on the binding of ligand **L2** upon the formation of the dihydride *via* methane loss. The closest Ir–C contacts with the adamantyl substituents (Ir1···C27, 3.030(6); Ir1···C19, 3.689(7); Ir1···C9, 3.698(8); Ir1···C37, 3.954(7) Å), show that one of the adamantyl groups (C27) resides closer to the iridium centre, likely to minimise steric interactions between the bulky adamantyl groups. Although ~0.1 hexane is observed in the ^{1}H NMR (CD_2Cl_2) spectrum (*vide infra*), no lattice solvent is located in the crystal structure due to the low occupancy of hexane, which has likely been removed from the crystal under vacuum before and after addition of H_2.

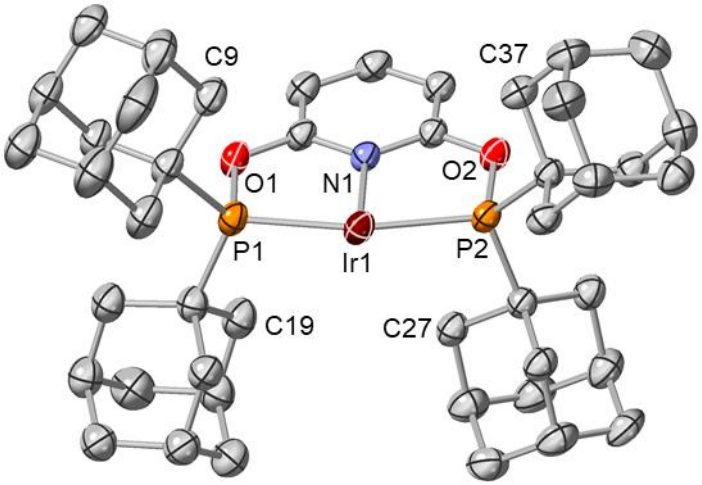

Figure 4.36 The molecular structure of the isolated cation of complex *β*-**4.7**. Displacement ellipsoids are set at 50% probability. Hydrogen atoms and $[BAr^{F}_{4}]^{-}$ anion are excluded for clarity. Select bond distances (Å): Ir1–P1, 2.289(2); Ir1–P2, 2.263(3); Ir1–N1, 2.094(5); Ir1···C27, 3.030(6); Ir1···C19, 3.689(7); Ir1···C9, 3.698(8); Ir1···C37, 3.954(7). Select bond angles (°): P1–Ir1–P2, 161.525(6).

The $[BAr^{F}_{4}]^{-}$ anions in complex *β*-**4.7** form an ortho gyrobifastigium with two capping $[BAr^{F}_{4}]^{-}$ anions above and below the two crystallographically equivalent cations, with eight total $[BAr^{F}_{4}]^{-}$ anions (Figure 4.37). This is in contrast to the hexagonal prismatic packing arrangement of twelve $[BAr^{F}_{4}]^{-}$ anions observed for complex *β*-**4.5** and the bicapped square prism of ten $[BAr^{F}_{4}]^{-}$ anions observed for complex *β*-**4.5** after 2 days under vacuum at 80 °C, and instead similar to the ortho gyrobifastigium observed for complex *α*-**4.5** despite the difference in space group for complex *α*-**4.5** ($P2_1/n$). The two molecules of lattice hexane observed in complex *β*-**4.5** (0.9 and 0.6 occupancy) have also been lost during the SC-SC reaction. The movement of $[BAr^{F}_{4}]^{-}$ anions, coupled with the loss of lattice hexane, results in a decrease in unit cell volume from 4621 Å^3 for complex *β*-**4.5** to 3680 Å^3 for complex *β*-**4.7**, similar to the volume change observed when complex *β*-**4.5** is exposed to vacuum for 2 days at 80 °C (3720 Å^3).

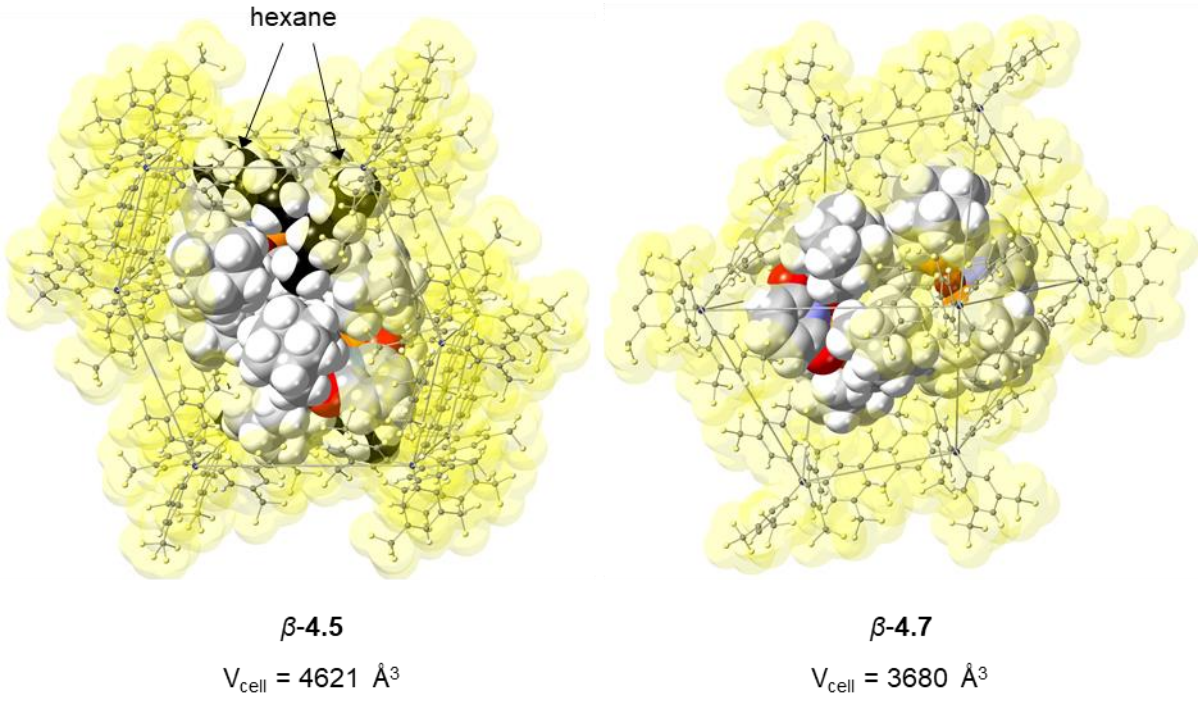

Figure 4.37 The extended solid-state structure of complexes *β*-**4.7** and *β*-**4.5**, showing the change in arrangements of $[BAr^F_4]^-$ anions and loss of hexane lattice solvent during the SC-SC reaction from complex *β*-**4.5**, depicted as Van der Waals radii.

The ^{1}H NMR (CD_2Cl_2) spectrum of the dissolved ensemble of polymorphs of complex **4.7** (Figure 4.38) following the SC-SC reaction from the ensemble of polymorphs *α*-**4.5** and *β*-**4.5** shows a triplet and doublet ($^3J_{HH}$ = 8.3 Hz) at δ 7.87 (1H) and 7.03 (2H) corresponding to the *para*- and *meta*- positions of the pyridine ring respectively. Peaks at δ 7.72 (multiplet, 8H) and 7.56 (singlet, 4H) correspond to the *ortho*- and *meta*-BAr^F_4 protons respectively. The adamantyl protons are observed as a broad multiplet at δ 1.91 (24H) for H_b, a singlet at δ1.74 (12H) for H_c and a broad singlet at δ 1.63 (24H) for H_d. The hydride environment is observed as a triplet ($^2J_{HP}$ = 10.1 Hz) at δ –25.51 (2H) which collapses into a singlet upon ^{31}P decoupling. The hydride shift is observed further downfield than that of complex **4.5** (δ –40.91) and complex **4.6** (δ –38.28, –41.54) due to the hydride ligands being *cis* to one another, rather than *trans* to a vacant site. This also contrasts with [(^{Ar}POCOP)Ir$(H)_2(H_2)$], formed from the SC-SC addition of H_2 to [(^{Ar}POCOP)Ir(N_2)] as described in section 1.1, which shows a hydride peak at δ –9.21 with an integral of 4H, due to the ligands of the tetrahydride being in rapid exchange, causing the peak to be observed relatively downfield, as is typical of iridium

tetrahydride complexes.[37, 46] The hydride ligand shift in complex **4.7** (δ –25.51, $^{2}J_{HP}$ = 10.1 Hz) is observed closer to that of the dihydride complexes [(^{Ad}PCP)Ir(H)$_2$] (δ –19.15, $^{2}J_{HP}$ = 9.3 Hz)[12] and [(^{tBu}PONOP)Ir(H)$_2$][BAr$^{F}_4$] (δ –25.07, $^{2}J_{HP}$ = 12 Hz).[3] Lattice hexane (0.1) is observed at δ 0.88 (0.6H) and 1.27 (1.5H), showing that some hexane is retained during the SC-SC transformation. The dissolved ensemble of polymorphs of complex **4.7** is observed as a singlet peak at δ 193.3 in the ^{31}P{^{1}H} NMR spectrum. Due to time constraints, the ^{31}P{^{1}H} and ^{13}C{^{1}H} SSNMR spectra could not be obtained.

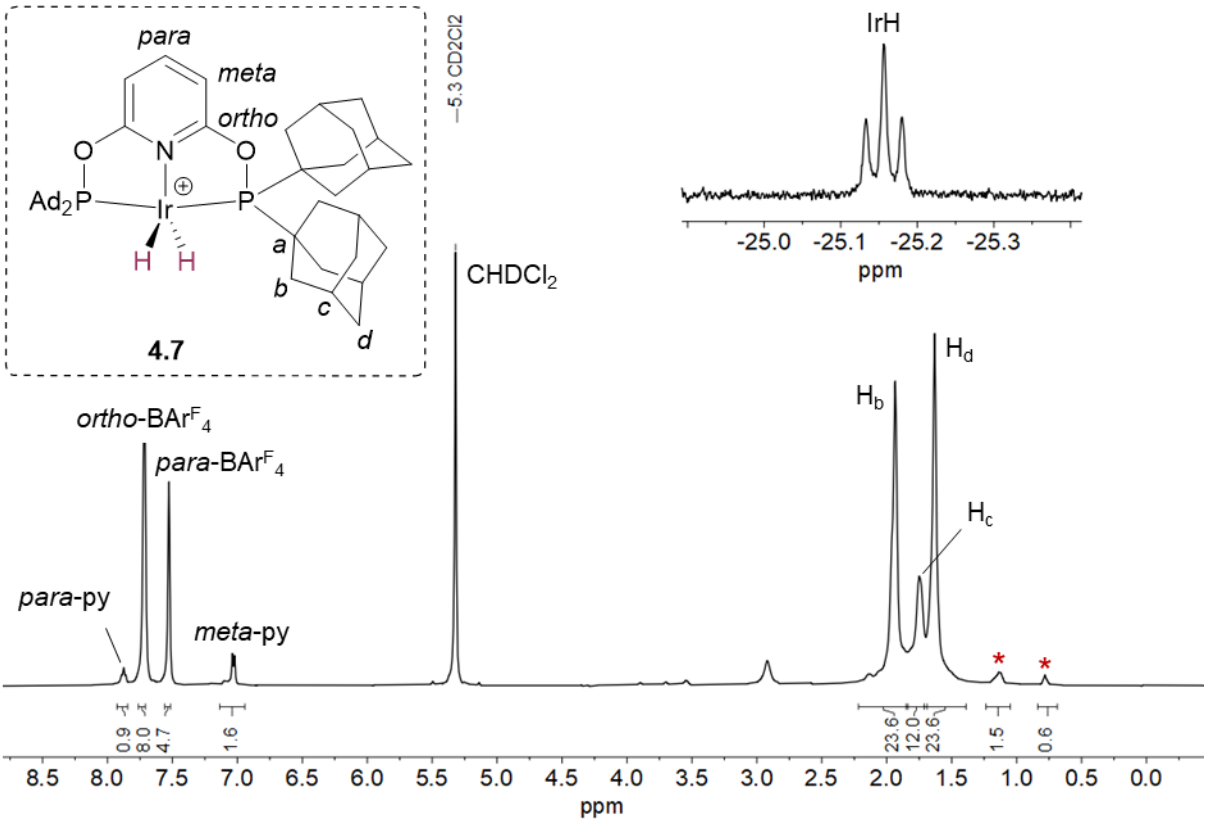

Figure 4.38 The ^{1}H NMR spectrum of the dissolved ensemble of polymorphs of complex **4.7** (500 MHz, CD_2Cl_2, 298 K). Inset highlights the hydride environment. * Denotes lattice hexane.

The SC-SC formation of complex **4.7** demonstrates that whilst the ensemble of polymorphs *α*-**4.5** and *β*-**4.5** is not capable of methane loss in the solid state under vacuum, the system is capable of SC-SC methane loss upon addition of hydrogen, due to a different mechanism operating.

4.7 Summary and Conclusions

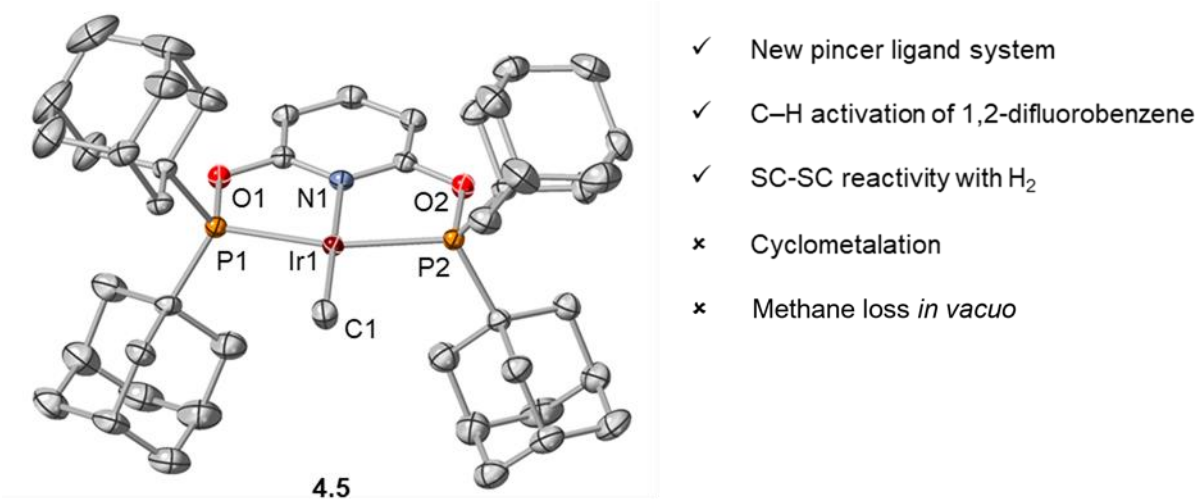

Figure 4.39 A summary of the work presented in chapter 4 of this thesis.

This chapter has presented the synthesis, characterisation and reactivity of an iridium(III) methyl hydride system, [(**L2**)Ir(Me)(H)][BAr^F_4] (**4.5**), featuring a new pincer ligand system, ^{Ad}PONOP (**L2**), which features rigid, cage-like adamantyl substituents (Figure 4.39). A different synthetic route to that reported for the known complex [(^{tBu}PONOP)Ir(Me)(H)][BAr^F_4] (**1.50**)[1] has been presented, which occurs *via* an iridium(I) carbonyl complex, [(**L2**)Ir(CO)]Cl (**4.1**). By comparison of their carbonyl stretching frequencies, **L2** was shown to be a slightly stronger donor than ^{tBu}PONOP. Complexes **4.5** and **1.50** have similar behaviour in the solution-state, showing site exchange between the hydride and methyl protons, losing methane at room temperature, and C–H bond activating 1,2-difluorobenzene to form the corresponding iridium(III) aryl hydride complexes, [(L)Ir(Ar)(H)][BAr^F_4] (L = ^{tBu}PONOP, **L2**), at similar rates. The similarities between the reactivity of complexes **4.5** and **1.50** end in the solid state, as complex **4.5** does not lose methane under the same conditions as complex **1.50**, or at harsher temperatures (120 °C), likely due to the 14-electron iridium(I) complex being thermodynamically inaccessible, owing to its inability to onward cyclometalate. The corresponding dinitrogen complex, [(**L2**)Ir(N_2)][BAr^F_4], could not be isolated from complex **4.5**, demonstrating the importance of the cyclometalated intermediate seen for complex **1.50**.

Despite this, complex **4.5** rapidly undergoes SC-SC reactivity with H_2 to form the iridium(III) dihydride, [(**L2**)Ir(H_2)][BAr^F_4] (**4.7**), demonstrating the SC-SC capabilities of complex **4.5**.

4.8 Experimental

For general procedures see appendix section 7.1 of this thesis. Na[BAr^F_4],[47] [$H(OEt_2)_2$][BAr^F_4][48] and [$Ir(CO)_2Cl]_2$[18] were prepared according to literature methods. All chemical shifts (δ) are quoted in ppm and coupling constants (*J*) in Hz.

4.8.1 (di-adamantylphosphino)-2,6-dioxypyridine (L2)

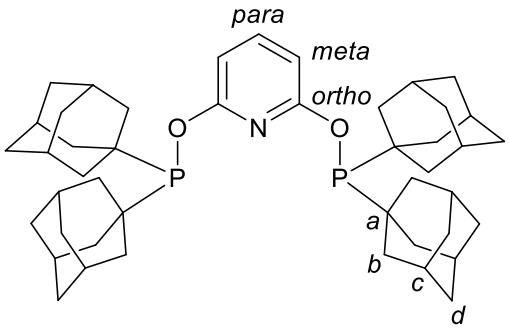

Pyridine (100 mL) was added to an ampoule charged with PAd_2Cl (5.0 g, 14.8 mmol) and 2,6-dihydroxypyridine hydrochloride (1.0 g, 7.1 mmol). NEt_3 (2 mL) and TMEDA (6 mL) were added. The solution was stirred for 10 days at 115 °C. The volatiles were removed *in vacuo* then the light blue solid was washed with pentane at 0 °C and extracted into toluene to afford an off-white solid of **L2** (Yield: 4.4 g, 6.2 mmol, 87%)

^{1}H NMR (500 MHz, C_6D_6, 298 K): δ 7.19 (t, 1H, $^3J_{HH}$ = 7.3, *para*-py), 6.65 (d, 2H, $^3J_{HH}$ = 7.3, *meta*-py), 2.13 (m, 24H, H_b), 1.91 (s, 12H, H_c), 1.71–1.67 (d, 24H, $^2J_{HH}$ = 12.1, H_d).

^{31}P{^{1}H} NMR (202 MHz, C_6D_6, 298 K): δ 151.3.

^{13}C{^{1}H} NMR (125 MHz, C_6D_6, 298 K): δ 165.0 (d, $^2J_{CP}$ = 10, *ortho*-py), 141.3 (s, *para*-py), 137.9 (s, toluene), 129.3 (s, toluene), 128.6 (s, toluene), 125.7 (s, toluene), 105.0 (d, 2H, $^3J_{CP}$ = 6, *meta*-py), 40.3 (d, $^1J_{CP}$ = 29, C_a), 39.2 (d, $^2J_{CP}$ = 14, C_b), 37.5 (s, C_d), 28.9 (d, $^3J_{CP}$ = 8, C_c), 21.4 (s, toluene).

Elemental analysis calc for $C_{45}H_{63}O_2P_2N_1$: C 75.92; H 8.92; N 1.97; found: C 75.56; H 8.54; N 1.63.

4.8.2 [(L2)Ir(CO)]Cl (4.1)

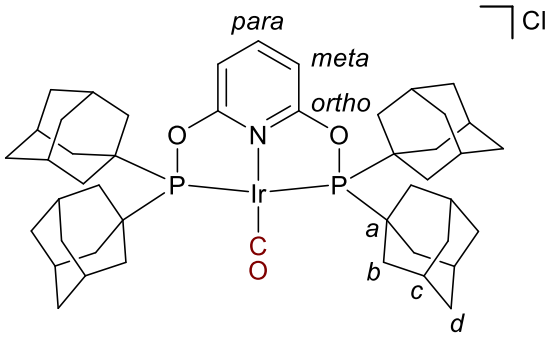

An orange solution of $[Ir(COE)_2Cl]_2$ (0.5 g, 0.6 mmol) in toluene (20 mL) was charged with CO (2 bar absolute) at room temperature, immediately forming a black precipitate. The volatiles were removed *in vacuo* and the resulting solid was washed with hexane to afford $[Ir(CO)_2Cl]_2$ as a black precipitate. (Yield: 0.3 g, 0.5 mmol, 95%)

Acetonitrile (20 mL) was added to an ampoule containing ligand **L2** (0.5 g, 0.7 mmol) and $[Ir(CO)_2Cl]_2$ (0.2 g, 0.4 mmol), and stirred at room temperature for 6 hours to give a dark yellow solution. The volatiles were removed *in vacuo* and toluene added. The reaction mixture was stirred at 90 °C for 18 hours then dried *in vacuo* and washed with hexane to afford complex **4.1** as a yellow solid. (Yield: 0.3 g, 0.3 mmol, 78%)

^{1}H NMR (500 MHz, CD_2Cl_2, 298 K): δ 8.14 (t, 1H, $^3J_{HH}$ = 8.2, *para*-py), 7.09 (d, 2H, $^3J_{HH}$ = 8.2, *meta*-py), 2.29 (d, 12H, $^2J_{HH}$ = 11.0, H_b), 2.09–2.06 (s and d, 24H, overlapping H_c and H_b), 1.82–1.77 (m, 24H, H_d).

^{31}P{^{1}H} NMR (161 MHz, CD_2Cl_2, 298 K): δ 196.5.

^{13}C{^{1}H} NMR (125 MHz, CD_2Cl_2, 298 K): δ 183.9 (t, $^2J_{CP}$ = 7, IrCO), 165.1 (t, $^3J_{CP}$ = 3), 147.9 (s, *para*-py), 104.1 (t, $^3J_{CP}$ = 2, *meta*-py), 47.1 (t, $^1J_{CP}$ = 10, C_a), 39.4 (s, C_b), 36.6 (s, C_d), 28.5 (t, $^3J_{CP}$ = 5, C_c).

ESI-MS m/z (CH_2Cl_2) found (calculated) for $Ir_1C_{46}H_{63}O_3P_2N_1$ $[M]^+$: 932.3934 (932.3913)

Elemental analysis calc for $C_{46}H_{63}Ir_1O_3P_2N_1Cl_1$: C 57.10; H 6.56; N 1.45 ; found: C 56.81; H 6.94; N 1.47.

4.8.3 [(L2)Ir(CO)][BAr$^F_4$] (4.2)

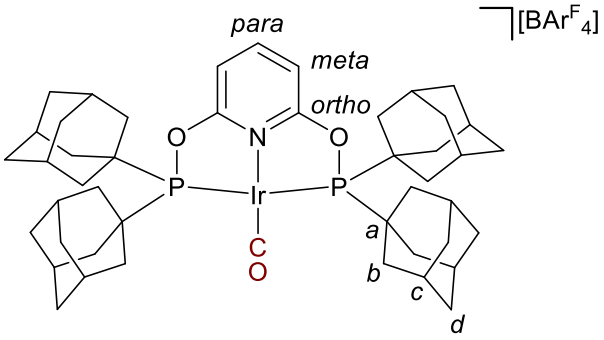

CD_2Cl_2 (0.4 mL) was added to a J-Youngs NMR tube containing complex **4.1** (3.1 mg, 3.1 µmol) and Na[BAr$^F_4$] (3.5 mg, 4.0 µmol). The solution was filtered, and the layering of CD_2Cl_2/hexane at room temperature afforded yellow crystals of complex **4.2**. (Yield: 3.4 mg, 1.9 µmol, 61%)

^{1}H NMR (500 MHz, CD_2Cl_2, 298 K): δ 8.14 (t, 1H, $^3J_{HH}$ = 8.2, *para*-py), 7.72 (s, 8H, *ortho*-BAr$^F_4$), 7.56 (s, 4H, *meta*-BAr$^F_4$),7.09 (d, 2H, $^3J_{HH}$ = 8.2, *meta*-py), 2.29 (d, 12H, $^3J_{HH}$ = 11.0, H_b), 2.09–2.06 (s and d, 24H, overlapping H_c and H_b), 1.82–1.77 (m, 24H, H_d).

^{31}P{^{1}H} NMR (161 MHz, CD_2Cl_2, 298 K): δ 196.8.

^{13}C{^{1}H} NMR (125 MHz, CD_2Cl_2, 298 K): δ 183.9 (t, $^2J_{CP}$ = 7, IrCO), 165.1 (t, $^2J_{CP}$ = 3, *ortho*-py), 162.1 (q, $^1J_{CB}$ = 50 Hz, *ipso*-BAr$^F_4$), 147.9 (s, *para*-py), 135.0 (s, *ortho*-BAr$^F_4$), 130.2 (s, *meta*-BAr$^F_4$), 124.4 (q, $^1J_{CF}$ = 272 Hz, CF_3), 118.0 (s, *para*-BAr$^F_4$), 104.1 (t, $^3J_{CP}$ = 2, *meta*-py), 47.1 (t, $^1J_{CP}$ = 10, C_a), 39.4 (s, C_b), 36.6 (s, C_d), 28.5 (t, $^3J_{CP}$ = 5, C_c).

IR (ATR) ν_{CO} (w, s) 1988 cm^{-1}.

4.8.4 [(L2)IrCl] (4.3)

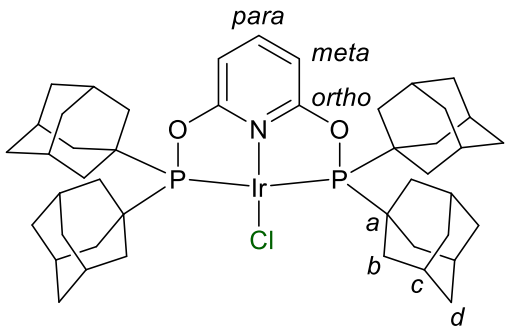

THF (30 mL) was added to an ampoule containing complex **4.1** (850.2 mg, 0.9 mmol) and TMNO (150.4 mg, 2.0 mmol). The ampoule was then placed in a sonicator for 15 minutes before stirring the solution for 24 hours. The volatiles were removed *in vacuo* and the resulting solid extracted into toluene, dried *in vacuo* and washed with hexane to afford complex **4.3** as an orange solid. (Yield: 547.2 mg, 0.6 mmol, 67%)

^{1}H NMR (500 MHz, C_6D_6, 298 K): δ 7.25 (t, 1H, $^{3}J_{HH}$ = 7.7, *para*-py), 7.13 (m, 2.9H, toluene), 7.02 (m, 4.9H, toluene), 6.13 (d, 2H, $^{2}J_{HH}$ = 8.0, *meta*-py), 2.67 (d, 12H, $^{2}J_{HH}$ = 11.2, H_b), 2.54 (d, 12H, $^{2}J_{HH}$ = 11.2, H_b), 2.11 (s, 5.1H, toluene) 1.94 (s, 12H, H_c), 1.75 (d, 12H, $^{2}J_{HH}$ = 10.8, H_d), 1.61 (d, 12H, $^{2}J_{HH}$ = 10.8, H_d).

^{31}P{^{1}H} NMR (202 MHz, C_6D_6, 298 K): δ 172.7.

^{13}C{^{1}H} NMR (125 MHz, C_6D_6, 298 K): δ 164.5 (*ortho*-py), 137.9 (s, toluene), 129.6 (*para*-py), 128.6 (s, toluene), 125.7 (s, toluene), 101.7 (*meta*-py), 38.1 (Ad_b), 36.7 (Ad_d), 32.2 (Ad_c), 21.4 (s, toluene).

4.8.5 [(L2)Ir(Me)] (4.4)

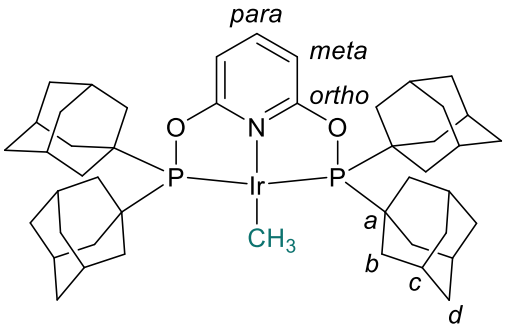

Methyl lithium in Et_2O (0.5 mL, 0.6 mmol) was added to a solution of complex **4.3** (300.2 mg, 318.6 µmol) in toluene (30 mL) and 1,4-dioxane (5 mL). The reaction mixture was stirred for three hours at 90 °C. The volatiles were removed *in vacuo* and the solid crystallised from toluene at –90 °C to afford dark red crystals of complex **4.4**. (Yield: 168.7 mg, 183.2 µmol, 58%)

^{1}H NMR (500 MHz, C_6D_6, 298 K): δ 7.49 (t, 1H, $^{3}J_{HH}$ = 7.9, *para*-py), 6.27 (d, 2H, $^{3}J_{HH}$ = 8, *meta*-py), 2.63 (d, 12H, $^{2}J_{HH}$ = 12, Ad_b), 2.40 (d, 12H, $^{2}J_{HH}$ = 12, Ad_b), 2.29 (t, 3H, $^{3}J_{HP}$ = 4, IrMe), 1.93 (br s, 12H, Ad_c), 1.74 (d, 12H, $^{2}J_{HH}$ = 12, Ad_d), 1.63 (d, 12H, $^{2}J_{HH}$ = 12, Ad_d).

^{1}H{^{31}P} NMR (500 MHz, C_6D_6, 298 K): δ 7.49 (t, 1H, $^{3}J_{HH}$ = 7.9, *para*-py), 6.27 (d, 2H, $^{3}J_{HH}$ = 8, *meta*-py), 2.63 (d, 12H, $^{2}J_{HH}$ = 12, Ad_b), 2.40 (d, 12H, $^{2}J_{HH}$ = 12, Ad_b), 2.29 (s, 3H, IrMe), 1.93 (br s, 12H, Ad_c), 1.74 (d, 12H, $^{2}J_{HH}$ = 12, Ad_d), 1.63 (d, 12H, $^{2}J_{HH}$ = 12, Ad_d).

^{31}P{^{1}H} NMR (202 MHz, C_6D_6, 298 K): δ 179.7.

^{13}C{^{1}H} NMR (125 MHz, C_6D_6, 298 K): δ 164.1 (*ortho*-py), 137.9 (s, toluene), 129.3 (*para*-py), 101.5 (*meta*-py), 38.9 (Ad_b), 37.1 (Ad_d), 29.2 (Ad_c), 21.4 (s, toluene), –25.8 (IrMe).

^{31}P{^{1}H} SSNMR (162 MHz, 20 kHz spin rate, 298 K): δ 180.0.

^{13}C{^{1}H} SSNMR (100 MHz, 20 kHz spin rate, 298 K): δ 164.4 (*ortho*-py), 133.0 (*para*-py), 129.4 (toluene), 128.6 (toluene), 125.8 (toluene), 101.5 (*meta*-py), 46.2, 39.8 (Ad_b), 37.6 (Ad_d), 29.6 (Ad_c), –27.9 (IrMe).

Elemental analysis calc for $C_{46}H_{66}Ir_1O_2P_2N_1$: C 60.11; H 7.24; N 1.52; found: C 60.43; H 7.39; N 1.82.

4.8.6 [(L2)Ir(Me)(H)][BAr$^F_4$] (4.5)

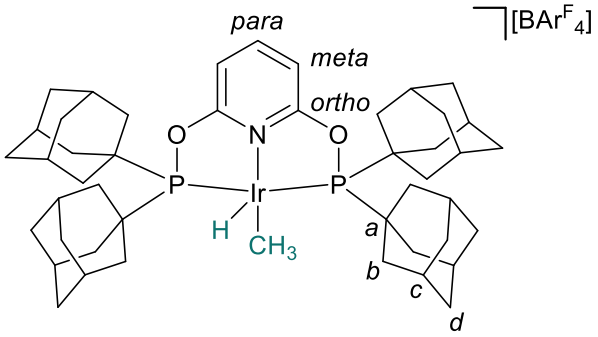

1,2-difluorobenzene (5 mL) was added to an ampoule containing [H(OEt$_2$)$_2$][BAr$^F_4$] (70.3 mg, 73.3 μmol) and complex **4.4** (53.4 mg, 58.0 μmol) at –30 °C. The resultant orange solution was dried *in vacuo*. Crystallisation by 1,2-difluorobenzene/hexane at –30 °C afforded a mixture of orange crystals of polymorphs *α*-**4.5** and *β*-**4.5**, and a dark orange oil. The oil was separated and recrystallised by 1,2-difluorobenzene/hexane at –30 °C to yield more orange crystals of polymorphs *α*-**4.5** and *β*-**4.5**. (Total crystallised yield: 60.7 mg, 41.3 μmol, 71%)

^{1}H NMR (500 MHz, CD_2Cl_2, 193 K): δ 7.81 (t, $^3J_{HH}$ = 8.2, 1H, *para*-py), 7.72 (s, 8H, *ortho*-BAr$^F_4$), 7.53 (s, 4H, *meta*-BAr$^F_4$), 7.18 (m, 0.2H, 1,2-$F_2C_6H_4$), 7.10 (m, 0.2H, 1,2-$F_2C_6H_4$), 6.98 (d $^3J_{HH}$ = 8.2, 2H, *meta*-py), 2.02–1.96 (m, 30H, overlapping H_b and H_c), 1.81 (m, 3H, IrMe), 1.76 (br s, 6H, H_b), 1.66–1.61 (m, 24H, H_d), 1.14 (m, 1.3H, hexane), 0.78 (0.9H, $^3J_{HH}$ = 7, hexane), –40.91 (t, $^2J_{HP}$ = 12.0, 1H, IrH).

^{1}H{^{31}P} NMR (500 MHz, CD_2Cl_2, 193 K): δ 7.81 (t, $^3J_{HH}$ = 8.2, 1H, *para*-py), 7.72 (s, 8H, *ortho*-BAr$^F_4$), 7.53 (s, 4H, *meta*-BAr$^F_4$), 7.18 (m, 0.2H, 1,2-$F_2C_6H_4$), 7.10 (m, 0.2H, 1,2-$F_2C_6H_4$), 6.98 (d $^3J_{HH}$ = 8.2, 2H, *meta*-py), 2.02–1.96 (m, 30H, overlapping H_b and H_c), 1.81 (s, 3H, IrMe), 1.76 (br s, 6H, H_b), 1.66–1.61 (m, 24H, H_d), 1.14 (m, 1.2H, hexane), 0.78 (0.9H, $^3J_{HH}$ = 7, hexane), –40.91 (s, 1H, IrH).

^{31}P{^{1}H} NMR (202 MHz, CD_2Cl_2, 193 K): δ 172.6.

$^{13}C\{^1H\}$ NMR (125 MHz, CD_2Cl_2, 193 K): δ 162.0 (s, *ortho*-py), 161.3 (q, $^1J_{CB}$ = 50 Hz, *ipso*-BAr^F_4), 142.8 (s, *para*-py), 134.0 (s, *ortho*-BAr^F_4), 128.0 (q, $^2J_{CF}$ = 32, *meta*-BAr^F_4), 123.4 (q, $^1J_{CF}$ = 272 Hz, CF_3), 117.0 (s, *para*-BAr^F_4), 103.0 (*meta*-py), 47.1 (t, $^1J_{CP}$ = 10, C_a), 43.1 (t, $^1J_{CP}$ = 10, C_a), 36.9 (s, C_b), 36.6 (s, C_b), 35.2 (s, C_d), 31.5 (hexane), 26.9 (s, C_c), 22.6 (hexane), 13.9 (hexane), –26.0 (s, IrMe).

$^{31}P\{^1H\}$ SSNMR (162 MHz, 10 kHz spin rate, 193 K): δ 175.3, 170.0.

$^{13}C\{^1H\}$ SSNMR (100 MHz, 10 kHz spin rate, 193 K): δ 163.0 (overlapping *ortho*-py and *ipso*-BAr^F_4), 142.7 (*para*-py), 136.3 (*ortho*-BAr^F_4), 129.0 (*meta*-BAr^F_4), 123.9 (CF_3), 117.4 (*para*-BAr^F_4), 101.7 (*meta*-py), 47.8 (C_a), 44.7 (C_a), 37.5 (overlapping s, C_b), 35.4 (C_d), 31.5 (hexane), 27.7 (C_c), 13.4 (hexane), –19.4 (IrMe), –31.1 (IrMe).

$^{31}P\{^1H\}$ SSNMR (162 MHz, 10 kHz spin rate, 298 K): δ 173.5.

$^{13}C\{^1H\}$ SSNMR (100 MHz, 10 kHz spin rate, 298 K): δ 162.7 (overlapping *ortho*-py and *ipso*-BAr^F_4), 142.9 (*para*-py), 135.9 (*ortho*-BAr^F_4), 129.1 (*meta*-BAr^F_4), 124.6 (CF_3), 117.9z (*para*-BAr^F_4), 101.9 (*meta*-py), 48.2 (C_a), 44.7 (C_a), 39.1 (overlapping s, C_b), 36.2 (C_d), 28.4 (C_c).

ESI-MS m/z (CH_2Cl_2) found (calculated) for $C_{46}H_{67}Ir_1O_2P_2N_1$ $[M]^+$: 920.4288 (920.4276)

Elemental analysis calc for $C_{78}H_{79}Ir_1O_2P_2N_1B_1F_{24}$: C 52.53; H 4.56; N 0.89; found: C 50.03; H 3.22; N 0.68. Repeat attempts also led to discrepancies between the found and calculated values both before and after accounting for lattice solvent, the reason for which could not be identified. Despite this, the complex was pure by NMR, SCXRD, and ESI-MS, and so was used for subsequent reactivity.

4.8.7 [(L2)Ir(Ar)(H)][BAr$^{F}_{4}$] (4.6)

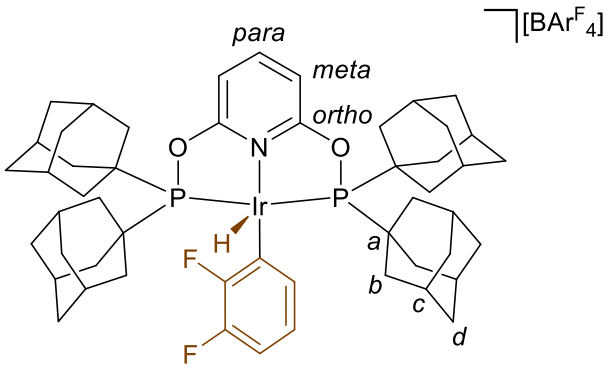

The ensemble of polymorphs *α*-**4.5** and *β*-**4.5** (20.8 mg, 14.1 μmol) was stirred in 1,2-difluorobenzene (5 mL) for 24 hours at room temperature, then the reaction product crystallised from the layering of 1,2-difluorobenzene/hexane to afford orange crystals of complex **4.6**. (Yield: 18.6 mg, 11.9 μmol, 84%)

^{1}H NMR (500 MHz, CD_2Cl_2, 298 K): δ 7.98 (t, $^{3}J_{HH}$ = 8.1, 1H, *para*-py), 7.72 (s, 8H, *ortho*-BAr$^{F}_{4}$), 7.55 (s, 4H, *meta*-BAr$^{F}_{4}$), 7.19–6.85 (m, 9H, overlapping 1,2-$F_2C_6H_4$, *meta*-py), 2.04 (m, 24H, Ad), 1.94 (s, 12H, Ad), 1.81–1.75 (m, 24H, Ad), –38.3 (s, 0.7H, IrH), –41.5 (s, 0.3H, IrH).

^{1}H{^{31}P} NMR (500 MHz, CD_2Cl_2, 298 K): δ 7.98 (t, $^{3}J_{HH}$ = 8.1, 1H, *para*-py), 7.72 (s, 8H, *ortho*-BAr$^{F}_{4}$), 7.55 (s, 4H, *meta*-BAr$^{F}_{4}$), 7.19–6.85 (m, 9H, overlapping 1,2-$F_2C_6H_4$, *meta*-py), 2.04 (m, 24H, Ad), 1.94 (s, 12H, Ad), 1.81–1.75 (m, 24H, Ad), –38.3 (s, 0.7H, IrH), –41.5 (s, 0.3H, IrH).

^{1}H NMR (500 MHz, CD_2Cl_2, 193 K): δ 7.93 (t, $^{3}J_{HH}$ = 8.1, 1H, *para*-py), 7.72 (s, 8H, *ortho*-BAr$^{F}_{4}$), 7.55 (s, 4H, *meta*-BAr$^{F}_{4}$), 7.40–6.77 (m, 9H, overlapping 1,2-$F_2C_6H_4$, *meta*-py), 1.93–0.98 (overlapping m, 60H, Ad), –38.3 (t, $^{2}J_{HP}$ = 11.3, 0.7H, IrH), –41.5 (t, $^{2}J_{HP}$ = 10.9, 0.3H, IrH).

^{31}P{^{1}H} NMR (202 MHz, CD_2Cl_2, 298 K): δ 170.7.

^{19}F NMR (470 MHz, CD_2Cl_2, 298 K): δ –62.9 (s, BAr^F_4), –110.1 (br s, 1,2-$F_2C_6H_3$), –113.9 (br s, 1,2-$F_2C_6H_3$), –138.4 (br s, 1,2-$F_2C_6H_3$), –139.4 (t, $^3J_{FH}$ = 9.8, 1,2-$F_2C_6H_4$), –140.0 (br s, 1,2-$F_2C_6H_3$).

^{13}C{^{1}H} NMR (125 MHz, CD_2Cl_2, 298 K): δ 163.8 (s, *ortho*-py), 161.3 (q, $^1J_{CB}$ = 50 Hz, *ipso*-BAr^F_4), 150.0 (s, 1,2-$F_2C_6H_3$), 145.6 (s, *para*-py), 135.1 (s, *ortho*-BAr^F_4), 129.3 (q, $^2J_{CF}$ = 32, *meta*-BAr^F_4), 124.9 (q, $^1J_{CF}$ = 272 Hz, CF_3), 117.9 (s, *para*-BAr^F_4), 104.1 (*meta*-py), 101.7 (s, 1,2-$F_2C_6H_3$), 50.1 (s, C_a), 38.8–37.5 (overlapping s, C_c), 36.4 (s, C_d), 28.3 (d, $^2J_{CP}$ = 20, C_b).

ESI-MS m/z (CH_2Cl_2) found (calculated) for $C_{51}H_{67}Ir_1O_2P_2N_1$ $[M]^+$: 980.4289 (980.4277).

Elemental analysis calc for $C_{83}H_{79}Ir_1O_2P_2N_1B_1F_{24}$: C 54.08; H 4.32; N 0.76; found: C 54.32; H 4.03; N 0.79.

4.8.8 [(L2)Ir(H)$_2$][BAr$^F_4$] (4.7)

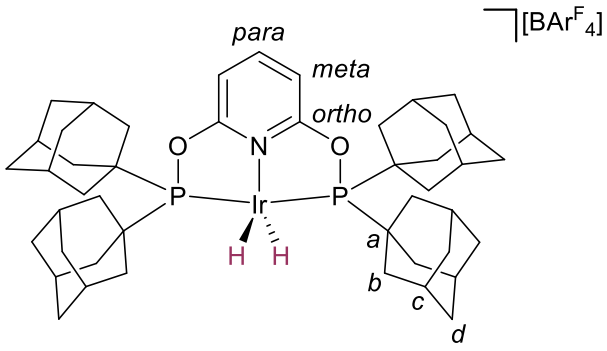

Single-crystals of the ensemble of polymorphs *α*-**4.5** and *β*-**4.5** (22.3 mg, 15.7 μmol) were placed under H_2 (4 bar absolute) in a J-Young NMR tube for 10 minutes. The volatiles were removed under reduced pressure to afford orange single-crystals of complex **4.7**. (Yield: 20.1 mg, 13.8 μmol, 88%)

^{1}H NMR (500 MHz, CD_2Cl_2, 298 K): δ 7.87 (t, $^3J_{HH}$ = 8.3, 1H, *para*-py), 7.72 (s, 8H, *ortho*-BAr^F_4), 7.53 (s, 4H, *meta*-BAr^F_4), 7.03 (d $^3J_{HH}$ = 8.3, 2H, *meta*-py), 1.91 (m, 24H, H_b), 1.74 (s, 12H, H_c), 1.63 (s, 24H, H_d), 1.14 (m, 1.5H, hexane), 0.78 (0.6H, $^3J_{HH}$ = 7, hexane), –25.51 (t, $^2J_{HP}$ = 10.1, 2H, IrH).

$^{1}H\{^{31}P\}$ NMR (500 MHz, CD_2Cl_2, 298 K): δ 7.87 (t, $^{3}J_{HH}$ = 8.3, 1H, *para*-py), 7.72 (s, 8H, *ortho*-BAr^{F}_{4}), 7.53 (s, 4H, *meta*-BAr^{F}_{4}), 7.03 (d $^{3}J_{HH}$ = 8.3, 2H, *meta*-py), 1.91 (m, 24H, H_b), 1.74 (s, 12H, H_c), 1.63 (s, 24H, H_d), 1.14 (m, 1.5H, hexane), 0.78 (0.6H, $^{3}J_{HH}$ = 7, hexane), –25.51 (s, 2H, IrH).

$^{31}P\{^{1}H\}$ NMR (202 MHz, CD_2Cl_2, 298 K): δ 193.3.

$^{13}C\{^{1}H\}$ NMR (125 MHz, CD_2Cl_2, 298 K): δ 163.7 (s, *ortho*-py), 162.1 (q, $^{1}J_{CB}$ = 50 Hz, *ipso*-BAr^{F}_{4}), 145.3 (s, *para*-py), 135.2 (s, *ortho*-BAr^{F}_{4}), 129.2 (q, $^{2}J_{CF}$ = 32, *meta*-BAr^{F}_{4}), 125.0 (q, $^{1}J_{CF}$ = 272 Hz, CF_3), 117.9 (s, *para*-BAr^{F}_{4}), 103.8 (*meta*-py), 46.5 (s, C_a), 39.0 (s, C_c), 36.5 (s, C_d), 28.3 (s, C_b).

IR (ATR) ν_{IrH} (br) 2109 cm^{-1}.

ESI-MS m/z (CH_2Cl_2) found (calculated) for $C_{45}H_{65}Ir_1O_2P_2N_1$ $[M]^+$: 906.4110 (906.4120)

Elemental analysis calc for $C_{77}H_{77}Ir_1O_2P_2N_1B_1F_{24}$: C 52.27; H 4.39; N 0.79; found: C 52.64; H 4.01; N 0.83.

4.8.9 EXSY Data for complex 4.5

Table 4.1 The integral and rate constant data for the exchange between the hydride and methyl ligand of complex **4.5** at different mixing times and temperatures.

Temperature / K	Mixing time / d_8	∫IrH	∫IrMe
178	0.0750	1	0.0793
	0.1000	1	0.1144
	0.1250	1	0.1339
183	0.0250	1	0.0492
	0.1000	1	0.2131
	0.1250	1	0.3083
	0.1500	1	0.3225
193	0.0250	1	0.2329
	0.0500	1	0.4787
	0.0750	1	0.7644
	0.1000	1	1.0347

	0.1250	1	1.4363
198	0.0050	1	0.1493
	0.0075	1	0.2321
	0.0100	1	0.3420
	0.0150	1	0.5314
	0.0250	1	0.8932
203	0.0025	1	0.1365
	0.0050	1	0.3087
	0.0100	1	0.6219
	0.0150	1	0.9821
	0.0250	1	1.7088
208	0.0025	1	0.2427
	0.0050	1	0.5605
	0.0075	1	1.0225
	0.0100	1	1.2352
	0.0150	1	2.8436
213	0.0070	1	1.3111
	0.0080	1	1.4415
	0.0090	1	1.6610
	0.0100	1	1.7428

4.8.10 Kinetic data for the C–H activation of 1,2-difluorobenzene by complexes 4.5 and 1.50

Table 4.2 The rate constants of the conversion of complex **4.5** to complex **4.6** at different temperatures.

Temperature / K	k / s^{-1}
298	$3.35 \pm 0.05 \times 10^{-6}$
303	$7.78 \pm 0.12 \times 10^{-6}$
308	$1.50 \pm 0.15 \times 10^{-5}$
313	$3.34 \pm 0.12 \times 10^{-5}$

Table 4.3 The rate constants of the conversion of complex **1.50** to [(^{tBu}PONOP)Ir(Ar)(H)][BAr^F_4] at different temperatures.

Temperature / K	k / s^{-1}
298	$5.47 \pm 0.03 \times 10^{-6}$
303	$1.18 \pm 0.01 \times 10^{-5}$
308	$2.45 \pm 0.02 \times 10^{-5}$
313	$5.18 \pm 0.07 \times 10^{-5}$

4.9 References

1. W. H. Bernskoetter, S. K. Hanson, S. K. Buzak, Z. Davis, P. S. White, R. Swartz, K. I. Goldberg and M. Brookhart, *J. Am. Chem. Soc.*, **2009**, *131*, 8603-8613.
2. M. R. Gyton, M. A. Sajjad, D. J. Storm, K. M. Altus, J. C. Goodall, C. L. Johnson, S. J. Page, A. J. Edwards, R. Piltz, S. B. Duckett, S. A. Macgregor and A. S. Weller, *J. Am. Chem. Soc.*, Submitted, ja-2024-18122t.
3. M. Findlater, K. M. Schultz, W. H. Bernskoetter, A. Cartwright-Sykes, D. M. Heinekey and M. Brookhart, *Inorg. Chem.*, **2012**, *51*, 4672-4678.
4. Kenton B. Renkema, Yury V. Kissin and A. S. Goldman, *J. Am. Chem. Soc.*, **2003**, *125*, 7770-7771.
5. S. Biswas, M. J. Blessent, B. M. Gordon, T. Zhou, S. Malakar, D. Y. Wang, K. Krogh-Jespersen and A. S. Goldman, *ACS Catal.*, **2021**, *11*, 12038-12051.
6. A. B. Chaplin, *Organometallics*, **2014**, *33*, 3069-3077.
7. L. K. P. Darian, J. Ballmann and L. H. Gade, *Angew. Chem. Int. Ed.*, **2024**, e202416814.
8. B. P. Carrow and L. Chen, *Synlett*, **2017**, *28*, 280-288.
9. Y. Tan, F. Barrios-Landeros and J. F. Hartwig, *J. Am. Chem. Soc.*, **2012**, *134*, 3683-3686.
10. Y. Gao, Q. Chen, X. Leng and L. Deng, *Dalton Trans.*, **2019**, *48*, 9676-9683.
11. K. Endo and R. H. Grubbs, *J. Am. Chem. Soc.*, **2011**, *133*, 8525-8527.
12. B. Punji, T. J. Emge and A. S. Goldman, *Organometallics*, **2010**, *29*, 2702-2709.
13. B. Spiegelberg, A. Dell'Acqua, T. Xia, A. Spannenberg, S. Tin, S. Hinze and J. G. d. Vries, *Chem. Eur. J.*, **2019**, *25*, 7820-7825.
14. T. Meyer, R. Konrath, P. C. J. Kamer and X.-F. Wu, *Asian J. Org. Chem.*, **2021**, *10*, 245-250.
15. N. V. Kulkarni, W. W. Brennessel and W. D. Jones, *ACS Catal.*, **2018**, *8*, 997-1002.
16. H. Salem, L. J. W. Shimon, Y. Diskin-Posner, G. Leitus, Y. Ben-David and D. Milstein, *Organometallics*, **2009**, *28*, 4791-4806.
17. B. Vabre, D. M. Spasyuk and D. Zargarian, *Organometallics*, **2012**, *31*, 8561-8570.
18. D. Roberto, E. Cariati, R. Psaro and R. Ugo, *Organometallics*, **2002**, *13*, 4227-4231.
19. J. Campos, S. Kundu, D. R. Pahls, M. Brookhart, E. Carmona and T. R. Cundari, *J. Am. Chem. Soc.*, **2013**, *135*, 1217-1220.
20. G. Hu, J. J. Jiang, H. R. Kelly, A. J. Matula, Y. Wu, N. Romano, B. Q. Mercado, H. Wang, V. S. Batista, R. H. Crabtree and G. W. Brudvig, *Chem. Comm.*, **2020**, *56*, 9126-9129.
21. E. W. Poole, I. Bustos, T. M. Hood, J. E. Smart and A. B. Chaplin, *Dalton Trans.*, **2023**, *52*, 1096-1104.
22. B. Leforestier, M. R. Gyton and A. B. Chaplin, *Dalton Trans.*, **2020**, *49*, 2087-2101.
23. H. Clavier and S. P. Nolan, *Chem. Comm.*, **2010**, *46*, 841-861.
24. L. Falivene, Z. Cao, A. Petta, L. Serra, A. Poater, R. Oliva, V. Scarano and L. Cavallo, *Nat. Chem.*, **2019**, *11*, 872-879.
25. A. Poater, B. Cosenza, A. Correa, S. Giudice, F. Ragone, V. Scarano and L. Cavallo, *Eur. J. Inorg. Chem.*, **2009**, *2009*, 1759-1766.

26. G. H. K. P. Huber, *Molecular Spectra and Molecular Structure IV: Constants of Diatomic Molecules*, Van Nostrand Reinhold Co, New York, 1979.
27. T. M. Hood, M. R. Gyton and A. B. Chaplin, *Dalton Trans.*, **2020**, *49*, 2077-2086.
28. T. M. Hood, B. Leforestier, M. R. Gyton and A. B. Chaplin, *Inorg. Chem.*, **2019**, *58*, 7593-7601.
29. R. Pohl, M. Dračínský, L. Slavětínská and M. Buděšínský, *Magn. Reson. Chem.*, **2011**, *49*, 320-327.
30. F. Mark Chadwick, A. I. McKay, A. J. Martinez-Martinez, N. H. Rees, Tobias Krämer, S. A. Macgregor and A. S. Weller, *Chem. Sci.*, **2017**, *8*, 6014-6029.
31. I. J. Vitórica-Yrezábal, S. Libri, J. R. Loader, G. M. Espallargas, M. Hippler, A. J. Fletcher, S. P. Thompson, J. E. Warren, D. Musumeci, M. D. Ward and L. Brammer, *Chem. Eur. J.*, **2015**, *21*, 8799-8811.
32. I. Halasz, *Cryst. Growth Des.*, **2010**, *10*, 2817-2823.
33. P. Hrobárik, V. Hrobáriková, F. Meier, M. Repiský, S. Komorovský and M. Kaupp, *J. Phys. Chem. A*, **2011**, *115*, 5654-5659.
34. L. J. L. Häller, E. Mas-Marzá, A. Moreno, J. P. Lowe, S. A. Macgregor, M. F. Mahon, P. S. Pregosin and M. K. Whittlesey, *J. Am. Chem. Soc.*, **2009**, *131*, 9618-9619.
35. W. H. Bernskoetter, C. K. Schauer, K. I. Goldberg and M. Brookhart, *Science*, **2009**, *326*, 553-556.
36. J. D. Watson, L. D. Field and G. E. Ball, *Nat. Chem.*, **2022**, *14*, 801-804.
37. G. R. Fulmer, A. J. M. Miller, N. H. Sherden, H. E. Gottlieb, A. Nudelman, B. M. Stoltz, J. E. Bercaw and K. I. Goldberg, *Organometallics*, **2010**, *29*, 2176-2179.
38. S. A. Hauser, I. Prokes and A. B. Chaplin, *Chem. Comm.*, **2015**, *51*, 4425-4428.
39. Lei Fan, Sean Parkin and O. V. Ozerov, *J. Am. Chem. Soc.*, **2005**, *127*, 16772-16773.
40. Eyal Ben-Ari, Mark Gandelman, Haim Rozenberg, Linda J. W. Shimon and D. Milstein, *J. Am. Chem. Soc.*, **2003**, *125*, 4714-4715.
41. S. A. Hauser, J. Emerson-King, S. Habershon and A. B. Chaplin, *Chem. Comm.*, **2017**, *53*, 3634-3636.
42. S. Budavari, M. J. O'Neil, A. Smith and P. E. Heckelman, *The Merck index: An encyclopedia of chemicals, drugs, and biologicals: - Eleventh Edition*, Merck Co., Inc, Rahway, NJ, 1989.
43. S. Hoops, S. Sahle, R. Gauges, C. Lee, J. Pahle, N. Simus, M. Singhal, L. Xu, P. Mendes and U. Kummer, *Bioinform.*, **2006**, *22*, 3067-3074.
44. J. C. Goodall, M. Arif Sajjad, E. A. Thompson, S. J. Page, A. M. Kerrigan, H. T. Jenkins, J. M. Lynam, S. A. Macgregor and A. S. Weller, *Chem. Comm.*, **2023**, *59*, 10749-10752.
45. L. R. Doyle, M. R. Galpin, S. K. Furfari, B. E. Tegner, A. J. Martínez-Martínez, A. C. Whitwood, S. A. Hicks, G. C. Lloyd-Jones, S. A. Macgregor and A. S. Weller, *Organometallics*, **2022**, *41*, 284-292.
46. Z. Huang, P. S. White and M. Brookhart, *Nature*, **2010**, *465*, 598-601.
47. A. J. Martínez-Martínez and A. S. Weller, *Dalton Trans.*, **2019**, *48*, 3551-3554.
48. M. Brookhart, B. Grant and A. F. V. Jr., *Organometallics*, **1992**, *11*, 3920-3922.

Chapter 5: Overview

This thesis presents the solution and solid-state reactivity and characterisation of target group IX and XI organometallic systems, focusing on a silver(I) [Ag(NBE)(η^2:η^2-$BAr^F{}_4$)] zwitterion (*Chapter 2*), a gold(I) [(**L1**)Au(L)][$BAr^F{}_4$] system (*Chapter 3*) and an iridium(III) methyl hydride complex [(**L2**)Ir(Me)(H)][$BAr^F{}_4$] (*Chapter 4*).

This work highlights some of the key advantages of SMOM chemistry, primarily the isolation of catalytically relevant, highly reactive intermediates which cannot be accessed in the solution state, as shown by the isolation of the first reported gold(I) π-acetylene complex (*Chapter 3*). *Chapter 3* also describes the H/D exchange of the gold(I) ammonia complex [(**L1**)Au(NH_3)][$BAr^F{}_4$], which reacts with dichloromethane solvent to form the corresponding [(**L1**)AuCl] in the solution state yet is stable for months in the solid state, demonstrating how another advantage to SMOM chemistry is in the prevention of deleterious reactivity induced by solvent. Solid state chemistry also allows for different chemistry to be accessed, as evident by the solid state characterisation of a silver(I) [Ag(NBE)(η^2:η^2-$BAr^F{}_4$)] zwitterion and its contrasting solution state behaviour, which points toward a proposed, rare Ag···H–C agostic complex in the solution state (*Chapter 2*).

However, this work has also presented some limitations of the SMOM approach. For example, the confinements imposed by the solid-state may also prevent reactivity, as demonstrated by the lack of methane loss from the iridium(III) methyl hydride complex, [(**L2**)Ir(Me)(H)][$BAr^F{}_4$], *in vacuo* (*Chapter 4*).

This work has demonstrated the versatility of SMOM chemistry in that it can be applied to the chemical space beyond that of rhodium σ-alkane complexes featuring bidentate phosphine ligands, to that of group IX and XI complexes featuring monodentate and pincer phosphine ligands.

Chapter 6: Future Work

Chapter 2 proposed a silver(I) complex featuring a rare Ag···H–C agostic interaction, however this could not be further explored due to time constraints. Therefore, future work might include attempts at the structural characterisation of this complex.

The solid/gas chemistry described in *Chapter 3* reports sequential SC-SC transformations with a gold(I) system to access a variety of alkene, carbonyl, amine and acetylene complexes. Such systems are often proposed intermediates in gold(I) catalysis. This presents an opportunity to investigate new areas of solid-state catalysis such as the catalytic hydroamination of alkenes or the hydration of alkynes, which could be explored as future work.

Considering the similar solution-state behaviour between complexes **4.5** and **1.50**, as highlighted in *Chapter 4*, it would also be interesting to explore the formation of the rhodium analogue, [(^{Ad}PONOP)Rh(CH_4)][BAr^F_4]. Future investigations might include the detection of this complex by low temperature NMR spectroscopy and attempts at its solid-state characterisation.

Chapter 7: Appendix

7.1 General Considerations

All manipulations, unless otherwise stated, were performed using standard Schlenk line and glovebox techniques under an argon (BOC, N4.8 purity) atmosphere. Glassware was dried overnight at 140 °C and flame dried under vacuum before use. Pentane, hexane and dichloromethane were dried using a Grubbs-type solvent purification system (Innovative Technologies)[1] under nitrogen and degassed with three freeze-pump-thaw cycles. Pentane and hexane were stored under argon. Dichloromethane was stored over 3 Å molecular sieves under argon. Heptane was purchased anhydrous from Sigma-Aldrich, decanted by cannula into resealable glass ampoules and stored over 3 Å molecular sieves under nitrogen. 1,2-difluorobenzene (pre-dried over alumina) was distilled from CaH_2, degassed with three freeze-pump-thaw cycles and stored over 3 Å molecular sieves under argon. d_2-dichloromethane, TMEDA, NEt_3 and pyridine was dried over CaH_2, vacuum distilled, degassed with three freeze-pump-thaw cycles and stored over 3 Å molecular sieves under argon. Key starting materials were prepared according to literature methods as denoted in the relevant chapters. All other chemicals were from commercial sources and used without further purification.

Solution-state NMR data were collected on a Bruker AVIIIHD 400 MHz, 500 MHz or 600 MHz or Bruker AVANCE NEO-300, AVANCE NEO-400 or AVANCE NEO-500 spectrometers at the temperatures specified. The ^{1}H and $^{13}C\{^{1}H\}$ solution spectra were referenced to the residual solvent peaks. $^{31}P\{^{1}H\}$ spectra were referenced externally to 85% H_3PO_4 in D_2O. Solid-state NMR samples were prepared in an argon filled glovebox by pre-loading 60–100 mg or 10–20 mg of crushed material into a 4.0 mm or 2.5 mm zirconia solid-state NMR rotor and sealed with Kel-F or Vespel caps. Spectra were recorded on a Bruker Avance III HD spectrometer, operating at 100 MHz ($^{13}C\{^{1}H\}$) and 162 MHz ($^{31}P\{^{1}H\}$) at the MAS rates and temperatures specified. All $^{13}C\{^{1}H\}$ CP MAS spectra were referenced to adamantane where the upfield methane resonance was taken to be δ_C = 29.5 ppm, secondarily referenced to $\delta_C(SiMe_4)$ =

0.0 ppm.[4] $^{31}P\{^{1}H\}$ CP MAS spectra were referenced to triphenylphosphine (δ_P = -9.3 ppm relative to H_3PO_4) or calcium hydrogen phosphate (δ_P = 1.4 ppm relative to H_3PO_4).[2]

IR spectra were collected in an argon filled glovebox on a Bruker ALPHA FT-IR spectrometer. Electrospray Ionisation Mass Spectrometry (ESI-MS) was carried out using a Bruker compact® Time of Flight mass spectrometer by Mr Karl Heaton at the University of York. Elemental microanalyses were performed by Ms Orfhlaith McCullough at London Metropolitan University.

Powder X-ray crystallography was performed by Dr Adrian Whitwood at the University of York on a Panalytical Aeris X-ray diffractometer equipped with a 600 W copper source and a PIXcel1D-Medipix3 detector. The instrument was operated in reflectance mode, with a scan range of 2θ = 5−70° and a scan rate of 0.026° s^{-1}.

7.2 Single-Crystal X-ray Diffraction

Single-crystal X-Ray diffraction data for all complexes were collected Rigaku SuperNova diffractometer with Cu-Kα (λ = 1.54184 Å) radiation equipped with nitrogen gas Oxford Cryosystems Cryostream unit.[3] Diffraction images from raw frame data were reduced using the CrysAlisPro suite of programmes. The structures were solved using SHELXT[4] and refined to convergence on F^2 against all independent reflections by full-matrix least-squares using SHELXL[5, 6] (version 2018/3) through the Olex2 GUI.[7] All non-hydrogen atoms were refined anisotropically and hydrogen atoms were geometrically placed and allowed to ride on their parent atoms. Disorder of the -CF_3 groups on the $[BAr^F{}_4]^-$ anions was treated by introducing a S28 split-site model and restraining geometries and displacement parameters. Distances and angles were calculated using the full covariance matrix. Published crystallographic data for complexes **3.1**, **3.2** and **3.7** are available free of charge via the Cambridge Crystallographic Data Centre, under deposition numbers 2336525-2336535.

7.2.1 Crystallographic Data Tables

Table S1. Selected crystallographic data for compounds **2.1·DFB**, **2.2** and **2.3**

Chapter 2	**2.1·DFB**	**2.2**	**2.3**
Formula	$C_{53}H_{42}AgBF_{24}$ ·0.9($F_2C_6H_4$)	$C_{39}H_{22}AgBF_{24}$	$C_{44}H_{42}AgBF_{24}O_6$
Formula weight	1379.04	1065.39	1241.45
Temperature/K	110.15	110.15	110.05(10)
Crystal system	Monoclinic	Monoclinic	Orthorhombic
Space group	$P2_1/n$	$P2_1/c$	Pnna
a/Å	14.5043(3)	13.17010(10)	22.3313(2)
b/Å	16.6750(4)	18.31760(10)	18.32137(17)
c/Å	25.0876(4)	16.43240(10)	12.51340(11)
α/°	90	90	90
β/°	101.935(2)	103.4400(10)	90
γ/°	90	90	90
Volume/Å^3	5936.5(2)	3855.66(5)	5119.74(8)
Z	4	4	4
ρ_{calc}g/cm^3	1.543	1.835	1.611
μ/mm^{-1}	3.819	5.573	4.375
F(000)	2767	2096	2488
Radiation	CuKα (λ = 1.54184)	CuKα (λ = 1.54184)	CuKα (λ = 1.54184)
2Θ range/°	7.202 to 153.69	6.9 to 153.91	7.918 to 154.766
Reflections collected	42020	48135	61315
R_{int}	0.0691	0.0286	0.0363
Data/restraints/param	12037/537/924	8022/176/653	5406/135/403
Goodness-of-fit	1.052	1.039	1.090
R_1 [I>=2σ (I)]	0.0926	0.0363	0.0642
wR_2 [all data]	0.2664	0.0917	0.2020
Largest peak/hole/eÅ^{-3}	2.27/-0.95	1.44 /-1.12	1.81/-1.58

Table S2. Selected crystallographic data for compounds **2.4** and **2.5**

Chapter 2	**2.4**	**2.5**
Formula	$C_{53}H_{51}BClF_{24}IrNO_2P_2$	$C_{61}H_{62}BClF_{25}P_2Pt$
Formula weight	1489.35	1573.39
Temperature/K	110.15	110.15
Crystal system	Monoclinic	Triclinic
Space group	$P2_1/n$	P-1
a/Å	16.52290(10)	14.0516(2)
b/Å	18.23040(10)	14.9380(2)
c/Å	21.26850(10)	16.9051(2)
α/°	90	89.8200(10)
β/°	109.7880(10)	65.5790(10)
γ/°	90	88.0440(10)
Volume/$Å^3$	6028.19(7)	3228.84(8)
Z	4	2
$\rho_{calc}g/cm^3$	1.641	1.618
μ/mm^{-1}	6.234	5.910
F(000)	2946	1566
Radiation	CuKα (λ = 1.54184)	CuKα (λ = 1.54184)
2Θ range/°	7.474 to 154.054	6.914 to 153.724
Reflections collected	76418	40537
R_{int}	0.0331	0.0255
Data/restraints/param	12524/444/891	13093 /236/940
Goodness-of-fit	1.064	1.019
R_1 [I>=2σ (I)]	0.0378	0.0225
wR_2 [all data]	0.0684	0.0554
Largest peak/hole/$eÅ^{-3}$	0.82/-0.94	1.22/-0.76

Table S3. Selected crystallographic data for compound *α*-**3.1** at 100, 150 and 200 K.

Chapter 3	*α*-**3.1** (100 K)	*α*-**3.1** (150 K)	*α*-**3.1** (200 K)
CCDC Number	2336526	2336527	2336528
Formula	$C_{94}H_{91}AuBF_{24}P \cdot 0.35(F_2C_6H_4)$	$C_{94}H_{91}AuBF_{24}P \cdot 0.35(F_2C_6H_4)$	$C_{94}H_{91}AuBF_{24}P \cdot 0.35(F_2C_6H_4)$
Formula weight	1955.34	1956.05	1956.31
Temperature/K	102.2(6)	151(2)	200.2(2)
Crystal system	monoclinic	monoclinic	monoclinic
Space group	$P2_1/n$	$P2_1/n$	$P2_1/n$
a/Å	14.85350(10)	14.91475(8)	14.98980(10)
b/Å	33.45610(10)	33.61425(14)	33.7897(2)
c/Å	18.95250(10)	18.99658(10)	19.05230(10)
α/°	90	90	90
β/°	107.5560(10)	107.4225(5)	107.3090(10)
γ/°	90	90	90
Volume/Å^3	8979.58(9)	9086.97(8)	9212.99(11)
Z	4	4	4
ρ_{calc}g/cm^3	1.446	1.430	1.410
μ/mm^{-1}	4.090	4.041	3.987
F(000)	3961	3963	3963
Radiation	Cu Kα (λ = 1.54184)	Cu Kα (λ = 1.54184)	Cu Kα (λ = 1.54184)
2Θ range/°	6.778 to 153.962	7.152 to 154.078	7.124 to 154.144
Reflections collected	109045	113258	61354
R_{int}	0.0321	0.0348	0.0317
Data/restraints/param	18683/150/1275	18940/552/1362	18678/804/1394
Goodness-of-fit	1.052	1.050	1.052
R_1 [I>=2σ (I)]	0.0290	0.0304	0.0343
wR_2 [all data]	0.0748	0.0796	0.0942
Largest peak/hole/eÅ^{-3}	1.06/-0.81	0.96/-0.79	0.76/-0.56

Table S4. Selected crystallographic data for compound *α*-**3.1** at 250 and 298 K, and *β*-**3.1**.

Chapter 3	*α*-**3.1** (250 K)	*α*-**3.1** (298 K)	*β*-**3.1**
CCDC Number	2336529	2336530	2336525
Formula	$C_{94}H_{91}AuBF_{24}P \cdot 0.35(F_2C_6H_4)$	$C_{94}H_{91}AuBF_{24}P \cdot 0.4(F_2C_6H_4)$	$C_{94}H_{91}AuBF_{24}P \cdot 0.75(C_7H_{16})0.9(F_2C_6H_4)$
Formula weight	1954.33	1959.63	2093.24
Temperature/K	250.2(3)	291(7)	110.15(10)
Crystal system	monoclinic	monoclinic	triclinic
Space group	$P2_1/n$	$P2_1/n$	P-1
a/Å	15.07100(10)	15.1759(2)	15.69430(13)
b/Å	33.9351(3)	34.0854(4)	18.7599(2)
c/Å	19.1239(2)	19.1920(2)	19.84623(19)
α/°	90	90	114.3315(10)
β/°	107.1640(10)	106.9280(10)	101.6610(7)
γ/°	90	90	98.3366(8)
Volume/Å^3	9345.06(15)	9497.4(2)	5040.83(9)
Z	4	4	2
ρ_{calc}g/cm^3	1.389	1.370	1.379
μ/mm^{-1}	3.930	3.870	3.696
F(000)	3957	3967	2131
Radiation	Cu Kα (λ = 1.54184)	Cu Kα (λ = 1.54184)	CuKα (λ = 1.54184)
2Θ range/°	7.096 to 154.026	7.064 to 155.18	6.908 to 154.116
Reflections collected	62944	112663	68229
R_{int}	0.0355	0.0386	0.0332
Data/restraints/param	19006/713/1386	19822/1203/1459	20573/153/1312
Goodness-of-fit	1.029	1.037	1.063
R_1 [I>=2σ (I)]	0.0356	0.0414	0.0356
wR_2 [all data]	0.0995	0.1208	0.0993
Largest peak/hole/eÅ^{-3}	0.54/-0.49	0.48/-0.43	2.21/-0.71

Table S5. Selected crystallographic data for compound **3.2**, and **3.3** from either SC-SC methods or solution recrystallisation**.**

Chapter 3	**3.2**	*β*-**3.3** (SC-SC)	*α*-**3.3** (solution)
CCDC Number	2336531		
Formula	$C_{93}H_{87}AuBF_{24}OP \cdot 0.75(C_7H_{16})0.9(F_2C_6H_4)$	$C_{92}H_{90}AuBF_{24}NP$	$C_{94}H_{94}AuBF_{24}NP \cdot 0.2(F_2C_6H_4)$
Formula weight	2093.20	1899.60	1934.20
Temperature/K	109.95(10)	110.15	110.15
Crystal system	triclinic	triclinic	Monoclinic
Space group	P-1	P-1	$P2_1/n$
a/Å	15.7067(3)	15.6853(10)	14.80710(10)
b/Å	18.9173(4)	16.4299(10)	33.32830(10)
c/Å	20.0078(5)	19.4505(12)	18.94520(10)
α/°	116.551(2)	75.532(5)	90
β/°	102.402(2)	68.977(6)	107.4860(10)
γ/°	97.137(2)	89.130(5)	90
Volume/$Å^3$	5026.1(2)	4515.1(5)	8917.34(9)
Z	2	2	4
$\rho_{calc}g/cm^3$	1.383	1.397	1.441
μ/mm^{-1}	3.715	4.042	4.110
F(000)	2127	1922	3919
Radiation	Cu Kα (λ = 1.54184)	Cu Kα (λ = 1.54184)	Cu Kα (λ = 1.54184)
2Θ range/°	7.844 to 153.78	7.854 to 154.342	6.798 to 154.156
Reflections collected	56297	50070	110401
R_{int}	0.0569	0.1264	0.0337
Data/restraints/param	20300/816/1524	18248/372/1254	18532/321/1244
Goodness-of-fit	1.035	1.062	1.046
R_1 [I>=2σ (I)]	0.0602	0.1220	0.0336
wR_2 [all data]	0.1611	0.3354	0.0858
Largest peak/hole/$eÅ^{-3}$	2.67/-2.66	3.91/-1.73	1.49/-1.15

Table S6. Selected crystallographic data for compounds *β*-**3.3**, *γ*-**3.4** and **3.5**

Chapter 3	***β*-3.3**	***γ*-3.4**	**3.5**
CCDC Number			
Formula	$C_{94}H_{94}AuBF_{24}NP \cdot 0.7(C_7H_{16})0.8(F_2C_6H_4)$	$C_{188}H_{185}Au_2B_2F_{48}N_2P_2$	$C_{95}H_{96}AuBF_{24}NP \cdot 0.7(C_7H_{16})0.5(F_2C_6H_4)$
Formula weight	2020.50	3861.86	2066.28
Temperature/K	111.15	110.15	110.15
Crystal system	Triclinic	Triclinic	Triclinic
Space group	P-1	P-1	P-1
a/Å	15.77460(10)	17.0470(3)	14.77177(15)
b/Å	18.65070(10)	17.3229(3)	19.46539(14)
c/Å	19.98960(10)	33.5564(8)	21.41331(14)
α/°	116.8900(10)	97.8418(16)	111.2570(7)
β/°	100.2080(10)	93.9465(15)	94.5726(7)
γ/°	98.0400(10)	106.0287(14)	104.3377(8)
Volume/$Å^3$	4997.37(7)	9375.8(3)	5460.66(8)
Z	2	2	2
$\rho_{calc}g/cm^3$	1.343	1.368	1.257
μ/mm^{-1}	3.715	3.902	3.394
F(000)	2048	3914	2112
Radiation	Cu Kα (λ = 1.54184)	Cu Kα (λ = 1.54184)	Cu Kα (λ = 1.54184)
2Θ range/°	6.68 to 154.044	8.03 to 154.108	8.04 to 153.856
Reflections collected	66800	107300	64949
R_{int}	0.0362	0.0725	0.0265
Data/restraints/param	20402/48/1194	37787/24/2236	22229/578/1431
Goodness-of-fit	1.069	1.133	1.060
R_1 [I>=2σ (I)]	0.0631	0.1054	0.0403
wR_2 [all data]	0.1891	0.2632	0.1196
Largest peak/hole/$eÅ^{-3}$	3.53/-1.48	3.44/-2.78	2.15/-1.02

Table S7. Selected crystallographic data for compounds **3.6**, and *α*-**3.7** at 110 K.

Chapter 3	**3.6**	*α*-**3.7** (110 K)
CCDC Number		2336532
Formula	$C_{96}H_{95}AuBF_{24}P$ $\cdot 0.6(C_7H_{16})0.7(F_2C_6H_4)$	$C_{94}H_{89}AuBF_{24}P$ $\cdot 0.4(F_2C_6H_4)$
Formula weight	2016.33	1959.03
Temperature/K	110.15	109.7(6)
Crystal system	Triclinic	monoclinic
Space group	P-1	$P2_1/n$
a/Å	15.1179(2)	14.87570(10)
b/Å	19.3533(3)	33.5769(2)
c/Å	20.9001(3)	18.90000(10)
α/°	109.9300(10)	90
β/°	97.4790(10)	107.5460(10)
γ/°	105.0510(10)	90
Volume/$Å^3$	5388.08(14)	9000.97(11)
Z	2	4
$\rho_{calc}g/cm^3$	1.243	1.446
μ/mm^{-1}	3.429	4.084
F(000)	2045	3965
Radiation	Cu Kα (λ = 1.54184)	Cu Kα (λ = 1.54184)
2Θ range/°	5.138 to 160.378	7.17 to 153.962
Reflections collected	68903	62786
R_{int}	0.0356	0.0352
Data/restraints/param	21693/105/1279	18350/450/1303
Goodness-of-fit	1.076	1.055
R_1 [I>=2σ (I)]	0.0501	0.0425
wR_2 [all data]	0.1523	0.1187
Largest peak/hole/$eÅ^{-3}$	1.88/-1.45	4.40/-1.70

Table S8. Selected crystallographic data for compound *α*-**3.7** at 150 and 200 K, and *β*-**3.7**.

Chapter 3	*α*-**3.7** (150 K)	*α*-**3.7** (200 K)	*β*-**3.7**
CCDC Number	2336533	2336534	2336535
Formula	$C_{94}H_{89}AuBF_{24}P \cdot 0.4(F_2C_6H_4)$	$C_{94}H_{89}AuBF_{24}P \cdot 0.4(F_2C_6H_4)$	$C_{94}H_{89}AuBF_{24}P \cdot 0.75(C_7H_{14})0.9(F_2C_6H_4)$
Formula weight	1959.03	1954.67	2087.08
Temperature/K	149.90(14)	200.00(10)	110.00(10)
Crystal system	monoclinic	monoclinic	triclinic
Space group	$P2_1/n$	$P2_1/n$	P-1
a/Å	14.92330(10)	14.99450(10)	15.69063(18)
b/Å	33.7104(2)	33.8964(2)	18.8505(3)
c/Å	18.94640(10)	19.01810(10)	19.9062(2)
α/°	90	90	114.7143(13)
β/°	107.4800(10)	107.3690(10)	101.9107(11)
γ/°	90	90	98.0673(10)
Volume/$Å^3$	9091.23(11)	9225.37(11)	5060.35(12)
Z	4	4	2
$\rho_{calc}g/cm^3$	1.431	1.407	1.370
μ/mm^{-1}	4.043	3.979	3.678
F(000)	3965	3955	2122
Radiation	Cu Kα (λ = 1.54184)	Cu Kα (λ = 1.54184)	CuKα (λ = 1.54184)
2Θ range/°	7.15 to 153.946	7.122 to 153.862	7.95 to 155.056
Reflections collected	62668	61137	64522
R_{int}	0.0359	0.0375	0.0448
Data/restraints/param	18499/811/1421	18745/1338/1556	20534/644/1418
Goodness-of-fit	1.037	1.049	1.043
R_1 [I>=2σ (I)]	0.0395	0.0421	0.0520
wR_2 [all data]	0.1102	0.1195	0.1468
Largest peak/hole/$eÅ^{-3}$	3.26/-1.16	2.83/-0.89	1.68/-1.65

Table S9. Selected crystallographic data for compounds **L2**, **4.2** and **4.4**.

Chapter 4	**L2**	**4.2**	**4.4**
Formula	$C_{45}H_{63}NO_2P_2$	$C_{78}H_{75}BF_{24}IrNO_3P_2$	$C_{23}H_{33}Ir_{0.5}N_{0.5}OP$
Formula weight	52.73	1795.34	459.57
Temperature/K	110.15	110.05(10)	110.15
Crystal system	triclinic	triclinic	Monoclinic
Space group	P-1	P-1	C2/c
a/Å	11.2218(2)	14.5127(3)	17.0062(2)
b/Å	11.3807(2)	15.8814(3)	10.69030(10)
c/Å	15.3793(3)	16.4329(4)	21.8212(2)
α/°	79.918(2)	94.846(2)	90
β/°	80.813(2)	99.946(2)	90.3320(10)
γ/°	78.763(2)	92.036(2)	90
Volume/$Å^3$	1880.61(6)	3712.38(14)	3967.06(7)
Z	2	2	8
$\rho_{calc}g/cm^3$	1.257	1.606	1.539
μ/mm^{-1}	1.343	4.865	7.574
F(000)	772	1804	1888
Radiation	Cu Kα (λ = 1.54184)	Cu Kα (λ = 1.54184)	Cu Kα (λ = 1.54184)
2Θ range/°	8.01 to 154.008	7.466 to 154.814	8.104 to 159.866
Reflections collected	20787	42757	21148
R_{int}	0.0411	0.0635	0.0290
Data/restraints/param	7625/0/451	15135/311/1085	4122/0/238
Goodness-of-fit	1.065	1.069	1097
R_1 [I>=2σ (I)]	0.0467	0.0505	0.0211
wR_2 [all data]	0.1307	0.1275	0.0526
Largest peak/hole/$eÅ^{-3}$	0.79/-0.45	1.73/-3.13	0.54/-0.60

Table S10. Selected crystallographic data for compounds *α*-**4.5**, *β*-**4.5** and **4.6**.

Chapter 4	***α*-4.5**	***β*-4.5**	**4.6**
Formula	$C_{78}H_{79}IrO_2P_2NBF_{24}\cdot 0.5(C_7H_{14})$	$C_{78}H_{79}IrO_2P_2NBF_{24}\cdot 1.5(C_7H_{14})$	$C_{83}H_{79}IrO_2P_2NBF_{24}\cdot 1.8(F_2C_6H_4)$
Formula weight	1823.96	1945.37	1937.46
Temperature/K	110.15	110.15	110.15
Crystal system	Monoclinic	Triclinic	Triclinic
Space group	C2/c	P-1	P-1
a/Å	29.61410(10)	14.0252(2)	14.4442(3)
b/Å	21.61910(10)	18.3289(3)	16.3542(2)
c/Å	24.21800(10)	20.5051(5)	18.1811(3)
α/°	90	66.704(2)	86.0690(10)
β/°	92.6320(10)	72.918(2)	73.787(2)
γ/°	90	80.574(2)	81.4330(10)
Volume/$Å^3$	15488.74(11)	4621.05(17)	4076.34(13)
Z	8	2	2
$\rho_{calc}g/cm^3$	1.564	1.398	1.578
μ/mm^{-1}	4.662	3.940	4.524
F(000)	7366	1983	1948
Radiation	Cu Kα (λ = 1.54184)	Cu Kα (λ = 1.54184)	Cu Kα (λ = 1.54184)
2Θ range/°	5.062 to 160.262	5.258 to 160.014	5.064 to 160.774
Reflections collected	57319	60284	50873
R_{int}	0.0290	0.0273	0.0374
Data/restraints/param	15663/388/1126	18651/731/1242	16428/168/1101
Goodness-of-fit	1.053	1.054	1.081
R_1 [I>=2σ (I)]	0.0326	0.0329	0.0284
wR_2 [all data]	0.0835	0.0891	0.0745
Largest peak/hole/$eÅ^{-3}$	1.00/-0.72	1.15/-0.87	1.17/-0.72

Table S11. Selected crystallographic data for complex **4.7**.

Chapter 4	**4.7**
Formula	$C_{77}H_{77}IrO_2P_2NBF_{24}$
Formula weight	1767.33
Temperature/K	110.15
Crystal system	Triclinic
Space group	P-1
a/Å	14.9375(3)
b/Å	15.0792(3)
c/Å	16.7653(3)
α/°	92.016(2)
β/°	101.982(2)
γ/°	94.017(2)
Volume/$Å^3$	3680.17(13)
Z	2
$\rho_{calc}g/cm^3$	1.595
μ/mm^{-1}	4.886
F(000)	1776.0
Radiation	Cu Kα (λ = 1.54184)
2Θ range/°	5.396 to 160.752
Reflections collected	40281
R_{int}	0.0548
Data/restraints/param	0.1489
Goodness-of-fit	1.047
R_1 [I>=2σ (I)]	0.0548
wR_2 [all data]	0.1489
Largest peak/hole/$eÅ^{-3}$	5.05/-1.93

7.3 Computational Methods

Molecular calculations employed the Gaussian 16 (Revision A.03) program package[8] and employed the PBE GGA functional was used in combination with Grimme's D3 correction for dispersion interactions. Stuttgart-Dresden (SDD)[9] relativistic effective core potentials (ECP) in combination with the associated basis sets were utilized to describe Au and P, with S41 polarization functions added for P (ζ = 0.387).[10] 6-31G(d,p) basis sets[11, 12] were used on the remaining atoms. All electronic structure analyses were performed on the geometry of the 3.7+ cation extracted from the fully optimised structures calculated with periodic DFT with CP2K. The topology of the electron density was analysed by means of Quantum Theory of Atoms in Molecules (QTAIM),[13] as implemented in the AIMALL package.[14] Inner-shell electrons on Au and P modelled by ECPs were represented by core density functions (extended wavefunction format). The QTAIM molecular graphs and the associated BCP metrics were used to assess different model geometries of the 3.7+ cation derived from (a) the fully optimised 3.7 geometry from periodic DFT (b) the partially optimised 3.7 geometry from periodic DFT and (c) the fully optimised geometry of the isolated cation in the gas-phase. The data show the choice of model geometry does not significantly affect the outcome and so the geometry of the 3.7+ cation from model (a) was used for all other analyses. Natural Bond Orbital (NBO) calculations were performed using the NBO 6.0 program[15] implemented with Gaussian 09 (Revision D.01).[16] Non-Covalent Interaction (NCI) plots were produced using the NCIPLOT program,[17, 18] and used the promolecular electron density with isosurfaces generated for s = 0.3 au and $-0.07 \leq \rho \leq 0.07$ au.

7.4 References

1. Amy B. Pangborn, Michael A. Giardello, Robert H. Grubbs, Robert K. Rosen and F. J. Timmers, *Organometallics*, **1996**, *15*, 1518-1520.
2. B. Hu and I. D. Gay, *Langmuir*, **1998**, *15*, 477-481.
3. J. Cosier, Glazer, A M, *J. Appl. Cryst*, **1986**, *19*, 105-107.
4. G. M. Sheldrick, *Acta Crystallogr., Sect. A.*, **2008**, *64*, 112-122.
5. G. M. Sheldrick, *Acta Crystallogr., Sect. A.*, **2015**, *71*, 3-8.
6. D. Kratzert, J. J. Holstein and I. Krossing, *J. Appl. Crystallogr.*, **2015**, *48*, 933-938.
7. O. V. Dolomanov, L. J. Bourhis, R. J. Gildea, J. A. K. Howard and H. Puschmann, *J. Appl. Cryst*, **2009**, *42*, 339-341.

8. G. W. T. M. J. Frisch, H. B. Schlegel, G. E. Scuseria, M. A. Robb, J. R. , G. S. Cheeseman, V. Barone, G. A. Petersson, H. Nakatsuji, X. Li, M. , A. V. M. Caricato, J. Bloino, B. G. Janesko, R. Gomperts, B. Mennucci, H. P. , J. V. O. Hratchian, A. F. Izmaylov, J. L. Sonnenberg, D. Williams-Young, F. Ding, F. , F. E. Lipparini, J. Goings, B. Peng, A. Petrone, T. Henderson, D. Ranasinghe, V. , J. G. G. Zakrzewski, N. Rega, G. Zheng, W. Liang, M. Hada, M. Ehara, K. Toyota, , J. H. R. Fukuda, M. Ishida, T. Nakajima, Y. Honda, O. Kitao, H. Nakai, T. , K. T. Vreven, J. J. A. Montgomery, J. E. Peralta, F. Ogliaro, M. J. Bearpark, J. , E. N. B. J. Heyd, K. N. Kudin, V. N. Staroverov, T. A. Keith, R. Kobayashi, J. , K. R. Normand, A. P. Rendell, J. C. Burant, S. S. Iyengar, J. Tomasi, M. , J. M. M. Cossi, M. Klene, C. Adamo, R. Cammi, J. W. Ochterski, R. L. Martin, K. and O. F. Morokuma, J. B. Foresman, D. J. Fox, *Gaussian, Inc, Wallingford CT*, **2016**.
9. D. Andrae, U. Häußermann, M. Dolg, H. Stoll, H. Preuß, D. Andrae, U. Häußermann, M. Dolg, H. Stoll and H. Preuß, *Theor. Chim. Acta*, **1990**, *77*, 123-141.
10. A. Höllwarth, M. Böhme, S. Dapprich, A. W. Ehlers, A. Gobbi, V. Jonas, K. F. Köhler, R. Stegmann, A. Veldkamp and G. Frenking, *Chem. Phys. Lett.*, **1993**, *208*, 237-240.
11. W. J. Hehre, R. Ditchfield, J. A. Pople, W. J. Hehre, R. Ditchfield and J. A. Pople, *J. Chem. Phys.*, **1972**, *56*, 2257-2261.
12. P. C. Hariharan, J. A. Pople, P. C. Hariharan and J. A. Pople, *Theor. Chim. Acta*, **1973**, *28*, 213-222.
13. R. F. W. Bader, *Atoms in Molecules: A Quantum Theory*, Clarendon Press, **1994**.
14. AIMAll (Version 17.11.14), T. A. Keith, TK Gristmill Software, Overland Park KS, USA, **2017** (aim.tkgristmill.com)
15. NBO 6.0. E. D. Glendening, J. K. Badenhoop, A. E. Reed, J. E. Carpenter, J. A. Bohmann, C. M. Morales, C. R. Landis, and F. Weinhold (Theoretical Chemistry Institute, University of Wisconsin, Madison, WI, **2013**); http://nbo6.chem.wisc.edu/
16. G. W. T. M. J. Frisch, H. B. Schlegel, G. E. Scuseria, M. A. Robb, J. R. , G. S. Cheeseman, V. Barone, B. Mennucci, G. A. Petersson, H. Nakatsuji, M. , X. L. Caricato, H. P. Hratchian, A. F. Izmaylov, J. Bloino, G. Zheng, J. L. Sonnenberg, , M. E. M. Hada, K. Toyota, R. Fukuda, J. Hasegawa, M. Ishida, T. Nakajima, Y. , O. K. Honda, H. Nakai, T. Vreven, J. A. Montgomery, J. E. Peralta, F. Ogliaro, M. , J. J. H. Bearpark, E. Brothers, K. N. Kudin, V. N. Staroverov, T. Keith, R. , J. N. Kobayashi, K. Raghavachari, A. Rendell, J. C. Burant, S. S. Iyengar, J. , M. C. Tomasi, N. Rega, J. M. Millam, M. Klene, J. E. Knox, J. B. Cross, V. Bakken, , J. J. C. Adamo, R. Gomperts, R. E. Stratmann, O. Yazyev, A. J. Austin, R. , C. P. Cammi, J. W. Ochterski, R. L. Martin, K. Morokuma, V. G. Zakrzewski, G. , P. S. A. Voth, J. J. Dannenberg, S. Dapprich, A. D. Daniels, O. Farkas, J. B. and J. V. O. Foresman, J. Cioslowski, D. J. Fox,, *Gaussian, Inc, Wallingford CT,*, **2013**.
17. E. R. Johnson, S. Keinan, P. Mori-Sánchez, J. Contreras-García, A. J. Cohen and W. Yang, *J. Am. Chem. Soc.*, **2010**, *132*, 6498-6506.
18. J. Contreras-García, E. R. Johnson, S. Keinan, R. Chaudret, J.-P. Piquemal, D. N. Beratan and W. Yang, *J. Chem. Theory Comput.*, **2011**, *7*, 625-632.